Binary star population synthesis

Progenitors of gravitational wave driven mergers

Dissertation

zur

Erlangung des Doktorgrades (Dr. rer. nat.)

der

Mathematisch-Naturwissenschaftlichen Fakultät

der

Rheinischen Friedrich-Wilhelms-Universität Bonn

in Astrophysik

vorgelegt von

Matthias U. Kruckow

aus

Sömmerda

Bonn, March 2018

1. Gutachter

Prof. Dr. Thomas M. Tauris

Argelander-Institut für Astronomie, Universität Bonn
Auf dem Hügel 71, 53121 Bonn

2. Gutachter

Prof. Dr. Norbert Langer

Argelander-Institut für Astronomie, Universität Bonn
Auf dem Hügel 71, 53121 Bonn

Angefertigt mit Genehmigung der Mathematisch-Naturwissenschaftlichen Fakultät der Rheinischen Friedrich-Wilhelms-Universität Bonn

Tag der Promotion: 11. Juni 2018

Erscheinungsjahr: 2018

Abstract

The binarity of a star may influence its life drastically. Evolution in a binary system enables a large variety of additional interactions between stars. Some events, like the recently detected gravitational wave mergers, happen mainly in binaries. The new stellar grid based populations synthesis code ComBinE was developed in order to investigate the possible paths of binary evolution. The results of its first application to double compact object binaries, containing black holes, neutron stars and white dwarfs, and final mergers driven by gravitational wave radiation are presented in this thesis.

During binary evolution, uncertain phases, including one or more mass-transfer phases, a common-envelope phase or possible kicks during a supernova explosion, have to be investigated. The least understood among them is the common-envelope phase. A detailed analysis of the consequences of the conversion of the energy of available reservoirs into the ejection of the gas of the common envelope is performed at two metallicities, that of the Milky Way ($Z = Z_{\rm MW} \equiv 0.0088$) and that of the dwarf galaxy IZwicky18 ($Z = Z_{\rm IZw18} \equiv 0.0002$). This analysis allows the derivation of the minimum masses of an in-spiralling object needed for a successful common-envelope ejection. The most crucial aspect is the bifurcation point which separates the remaining core from the lost material.

The influence of the different phases are further studied statistically. A variety of parameters of the phases during the binary evolution are used to investigate their effect on observable stages during the evolution and the final gravitational wave driven merger. The simulations performed with ComBinE are able to reproduce the observed double neutron star population with respect to orbital parameters and, to some extend, measured mass distributions. Simultaneously, all published merger events of double black hole binaries and the double neutron star merger, GW170817, are reflected at appropriate metallicities.

With population synthesis methods, the nature of an unseen companion star, here in the case of PSR J1755−2550, is probed, to narrow the search window for the companion.

Investigations of the different parameters of binary evolution yield predictions on them. The valid ranges of each parameter will refine by further observations. ComBinE also allows the incorporation of new developments in stellar evolution in an easy and self-consistent way.

Contents

0 Preface **v**
- 0.1 Definitions . . . v
- 0.2 Acronyms . . . vi
- 0.3 Constants and variables . . . viii

1 Introduction and theoretical background **1**
- 1.1 Astronomical observations . . . 1
  - 1.1.1 Optical observations . . . 1
  - 1.1.2 Radio observations . . . 3
  - 1.1.3 High frequency observations . . . 3
  - 1.1.4 Laser interferometers . . . 3
- 1.2 Single star evolution . . . 4
  - 1.2.1 Young stars . . . 4
  - 1.2.2 Main sequence evolution . . . 7
  - 1.2.3 Giant phases . . . 11
  - 1.2.4 Helium stars . . . 13
  - 1.2.5 Remnants . . . 13
- 1.3 Binary star evolution . . . 15
  - 1.3.1 Orbital evolution . . . 16
  - 1.3.2 Mass transfer . . . 18
- 1.4 Stars in galaxies . . . 22
- 1.5 Population synthesis . . . 23

2 Common-envelope ejection in massive binary stars **25**
- 2.1 Introduction . . . 26
- 2.2 Criterion for common-envelope ejection . . . 27
- 2.3 Results . . . 28
  - 2.3.1 CE ejectability and companion star masses . . . 29
  - 2.3.2 CE ejection: NS-NS and WD-WD binaries . . . 30
  - 2.3.3 Bifurcation point of envelope ejection . . . 30
  - 2.3.4 Response of donor star to mass loss . . . 31
- 2.4 Discussions . . . 32
  - 2.4.1 Bifurcation point revisited . . . 32
  - 2.4.2 Other energy sources . . . 32
  - 2.4.3 Ejection efficiency parameter . . . 34

2.4.4 Post-CE orbital separations in population synthesis 34
2.4.5 Post-CE merger before core collapse? 35
2.4.6 Extended envelopes of helium stars 36
2.4.7 Luminous blue variables 36
2.4.8 Convective core overshooting 36
2.5 Implications for LIGO detected BH-BH binaries 36
2.5.1 GW150914 36
2.5.2 GW151226 36
2.5.3 Comparison to other work 36
2.5.4 BH-BH formation: stability of the first RLO 36
2.6 Conclusions 37
2.7 Acknowledgements 38
2.8 References 38
2.9 Supplementary material 39

3 Progenitors of gravitational wave mergers 41
3.1 Introduction 42
3.1.1 Double compact object merger rates 43
3.1.2 Résumé of double compact object formation 43
3.1.3 Population synthesis studies 44
3.2 The ComBinE code 44
3.2.1 Initial conditions 44
3.2.2 Evolutionary phases 45
3.2.3 Galactic motion 50
3.2.4 Computed quantities 50
3.3 Stellar grids 50
3.3.1 Hydrogen-rich stars 50
3.3.2 Helium stars 51
3.3.3 Core-envelope boundary 52
3.4 Results 52
3.4.1 Progenitor zero-age main-sequence masses 52
3.4.2 Compact object masses 53
3.4.3 Orbital parameters 56
3.4.4 Gravitational wave-driven merger rates 58
3.5 Discussion 61
3.5.1 Parameter studies 61
3.5.2 Comparison to other studies and observations 65
3.5.3 Recycled pulsars orbiting black holes 70
3.5.4 Alternative formation channels 70
3.6 Summary and conclusions 71
3.7 Acknowledgements 72
3.8 References 72
3.9 Appendix A: Interpolation of stellar grids 75
3.9.1 Grid structure and interpolation 75
3.9.2 Placing a star on the stellar grid 75

3.10 Appendix B: Efficient mass transfer . . . 76
3.10.1 Progenitor zero-age main-sequence masses . . . 76
3.10.2 Compact object masses . . . 76
3.10.3 Orbital parameters . . . 77
3.10.4 Gravitational wave-driven merger rates . . . 78
3.10.5 Merger rate density . . . 78
3.11 Appendix C: Formation channels . . . 79
3.12 Appendix D: Further parameter variations . . . 82
3.12.1 Iron-core collapse supernovae . . . 82
3.12.2 Mass-transfer efficiency . . . 82
3.12.3 Internal energy parameter ($\alpha_{\rm th}$) . . . 83
3.13 Supplementary material . . . 84
3.13.1 Stellar models . . . 84
3.13.2 How binaries evolve in ComBinE . . . 89
3.13.3 Physical parameter variations . . . 92
3.13.4 Intermediate efficient mass transfer . . . 94

4 A young radio pulsar with a massive, compact companion 97
4.1 Introduction . . . 98
4.2 Radio timing observations . . . 99
4.2.1 Observational set-up . . . 99
4.2.2 Derivation of times-of-arrival and the timing solution . . . 99
4.2.3 Pulse profile and polarization study . . . 101
4.3 Formation scenario . . . 101
4.3.1 Formation of binary pulsars . . . 101
4.3.2 PSR J1755−2550 – the case of a young pulsar . . . 102
4.3.3 A MS star companion? . . . 102
4.3.4 Mass function of PSR J1755−2550 . . . 102
4.4 Population synthesis . . . 103
4.4.1 Orbital period and eccentricity . . . 104
4.4.2 Relative formation rate of WDNS versus DNS systems . . . 104
4.4.3 On the possibility of a MS companion star . . . 105
4.4.4 Merging WDNS systems and Ca-rich SNe . . . 105
4.5 Observable clues . . . 106
4.5.1 Optical search of a first-formed WD . . . 106
4.5.2 Search for radio pulsation from the potential first-formed NS 107
4.6 Conclusion . . . 109
4.7 Acknowledgements . . . 109
4.8 References . . . 109
4.9 Supplementary material . . . 111

5 Conclusions and outlook 113

A ComBinE Manual **117**
A.1 Introduction . . . 118
A.2 Run the code . . . 118
A.2.1 Set parameters . . . 118
A.2.2 Input parameter description . . . 120
A.2.3 Single run . . . 125
A.2.4 Population synthesis . . . 125
A.2.5 Output files . . . 126
A.2.6 Stellar tables . . . 128
A.3 Code structure . . . 128
A.3.1 Main structure . . . 128
A.3.2 Constants . . . 129
A.3.3 Structure definitions . . . 130
A.3.4 Read stellar tables . . . 133
A.3.5 Initial conditions . . . 133
A.3.6 Evolutionary phases . . . 134
A.3.7 Analysing the binary . . . 136
A.3.8 Histograms . . . 136
A.3.9 User interface . . . 137
A.4 Warnings and errors . . . 140
A.4.1 Warning messages . . . 141
A.4.2 Error messages . . . 143
A.5 References . . . 150

B Additional figures **153**
B.1 Figures of Section 3.13.1.2 . . . 153
B.1.1 At maximum radius . . . 153
B.1.2 At maximum core mass . . . 157
B.1.3 At the end of the stellar calculation . . . 162
B.1.4 He-stars at He-ZAMS . . . 166
B.1.5 He-stars at their end of the stellar calculation . . . 170
B.2 Figures of Section 3.13.2 . . . 175
B.3 Figures of Section 3.13.3 . . . 182
B.4 Figures of Section 3.13.4 . . . 188

Acknowledgements **193**

List of figures **I**

List of tables **VI**

Bibliography **VII**

Curriculum Vitae **XXIII**

List of publications **XXIV**

Chapter 0

Preface

This thesis deals with many different topics, therefore the following sections provide a simple overview.

0.1 Definitions

The following list of definitions is meant to be easily understandable and provide a quick look-up table. The more precise explanations are incorporated in Chapter 1.

binary
: A binary consists of two stars or stellar remnants that are gravitationally bound to each other.

black hole
: A black hole is an object which is to dense that light or information can escape from it.

core
: The core of a star is the region which is enriched with some nuclear burning products.

envelope
: The envelope of a star contains all the material of the star which is not part of the core.

giant
: A giant is an extended star during its shell burning.

hydrostatic equilibrium
: Hydrostatic equilibrium is reached when the net forces are balanced which leads to a static, nearly time independent, structure of an object.

merger
: A merger is the coalescence of two stars or stellar remnants.

neutron star
: A neutron star is a stellar remnant balanced by the degeneracy of neutrons.

primary (star)
The primary star is the more massive star in a binary directly after its formation.

secondary (star)
The secondary star is the less massive star in a binary directly after its formation.

star
A star is an object which is self gravitating and produces its energy by nuclear fusion.

stellar remnant
A stellar remnant is the compact object, e.g. a black hole, a neutron star or a white dwarf, which remains when a all fusion processes in a star stopped.

thermal equilibrium
Thermal equilibrium is reached when the energy determining the structure of an object remains constant, i.e. the produced and lost energy have the same amount.

white dwarf
A white dwarf is a stellar remnant balanced by the degeneracy of electrons.

0.2 Acronyms

IZw18 (dwarf galaxy) IZwicky18 23
BEC binary evolution code (hydrodynamic code) 10
BH black hole 13
C carbon 9
CC SN core-collapse supernova 14
CE common envelope 20
CHE chemically homogeneous evolution 18
ComBinE computing binary evolution (population synthesis code) 23
DCO double compact object 15
DNS double neutron star system 22
EC SN electron-capture supernova 14
EoS equation-of-state 10
Fe iron 12
GR general relativity 4
GRB gamma-ray burst 3
GW gravitational wave 3

GWR gravitational-wave radiation 18
H hydrogen 6
He helium 6
HMXB high-mass X-ray binary 22
HRD Hertzsprung-Russell diagram 2
IMF (stellar) initial-mass function 7
JWST James Webb Space Telescope 3
LBV luminous blue variable 13
LIGO laser interferometer gravitational-wave observatory 4
LMC Large Magellanic Cloud 23
LMXB low-mass X-ray binary 22
Mg magnesium 12
MOB massive overcontact binary 21
MS main sequence 2
MSP millisecond radio pulsar 3
MW Milky Way 23
N nitrogen 9
Ne neon 12
NS neutron star 13
O oxygen 9
PISN pair-instability supernova 15
PSF point spread function 2
PSR (radio) pulsar 3
RLO (stable) Roche-lobe overflow 19
SKA Square-Kilometre Array 3
SMC Small Magellanic Cloud 23
SN supernova 14
SSB solar system barycentre 3
TOA time-of-arrival 3
WD white dwarf 13
ZAMS zero-age main sequence 6

0.3 Constants and variables

Table 1: Units (Olive & Particle Data Group, 2014).

symbol (value in SI units)	name
$\mathrm{au} = 1.495978707 \cdot 10^{11}$ m	astronomical unit (mean distance between Earth and Sun)
$\mathrm{days} = 86\,164.09053$ s	(mean sidereal) day (some times only d)
$\mathrm{eV} = 1.602176565 \cdot 10^{-19}$ kg m^2 s^{-2}	electronvolt
$\mathrm{L}_\odot = 3.828 \cdot 10^{26}$ kg m^2 s^{-3}	solar luminosity
$\mathrm{m_u} = 1.660538921 \cdot 10^{-27}$ kg	atomic mass unit
$\mathrm{M}_\odot = 1.9885 \cdot 10^{30}$ kg	solar mass
$\mathrm{pc} = 3.08567758149 \cdot 10^{16}$ m	parsec (distance in which a 1 au object is one arc second)
$\mathrm{R}_\odot = 6.9551 \cdot 10^{8}$ m	solar radii
$\mathrm{yr} = 31\,558\,149.8$ s	(sidereal) year

Table 2: Constants (Olive & Particle Data Group, 2014).

symbol (value)	name	page
$a = 7.5657 \cdot 10^{-26}$ kg m^{-1} s^{-2} K^{-4}	radiation constant	6
$c = 299\,792\,458$ m s^{-2}	speed of light	4
$G = 6.67384 \cdot 10^{-11}$ m^3 kg^{-1} s^{-2}	gravitational constant	5
$k = 1.3806488 \cdot 10^{-23}$ kg m^2 s^{-2} K^{-1}	Boltzmann constant	10
$K_{\mathrm{non-rel}} = 1.00 \cdot 10^{7}$ kg$^{-\frac{2}{3}}$ m^4 s^{-2}	pressure constant for non-relativistic degenerate electrons	10
$K_{\mathrm{rel}} = 1.24350 \cdot 10^{10}$ kg$^{-\frac{1}{3}}$ m^3 s^{-2}	pressure constant for relativistic degenerate electrons	10
$\sigma = 5.670373 \cdot 10^{-8}$ kg s^{-3} K^{-4}	Stefan-Boltzmann constant	6
$\sigma_{\mathrm{T}} = 0.6652458734 \cdot 10^{-28}$ m^2	Thomson cross section of electrons	46
$t_{\mathrm{hubble}} = 1.381 \cdot 10^{10}$ yr	Hubble time (age of the Universe)	23

Table 3: Variables.

symbol	name	page
a	semi-major axis	16
$\hat{a}$ & $\tilde{a}$	amplitudes of GW polarisations	4
$\alpha_{\rm CE}$	CE efficiency (some times shortened as α)	21
$\alpha_{\rm IMF}$	IMF slope	7
$\alpha_{\rm ov}$	overshooting parameter	8
$\alpha_{\rm RLO}$	fraction of material lost in a direct wind mass during stable RLO	20
$\alpha_{\rm th}$	internal energy parameter	21
$\beta_{\rm min}$	minimum value of $\beta_{\rm RLO}$	20
$\beta_{\rm RLO}$	fraction of material re-emitted from the accretor during stable RLO	20
$c_{\#}$	core mass (# specifies the material or He-core at a track point)	85
γ	size parameter of a circumbinary torus (also parameter of angular momentum loss during CE in Section 1.3.2.3)	21
$\delta_{\rm RLO}$	fraction of material transferred to a circumbinary torus during stable RLO	21
e	eccentricity	16
$E_{\rm nuc}$	available total nuclear energy	9
$E_{\rm orb}$	orbital energy	16
ϵ	mass-transfer efficiency	20
$\epsilon_{\rm gr}$	energy by gravity	7
ϵ_{ν}	energy change by neutrinos	7
$\epsilon_{\rm nuc}$	energy change by nuclear fusion	7
$\eta_{\mu\nu}$	Minkowski metric with indices μ and ν indicating the four space-time dimensions $\in \{0, 1, 2, 3\}$	4
$f_{\mu\nu}$	perturbation from Minkowski metric with indices μ and ν indicating the four space-time dimensions $\in \{0, 1, 2, 3\}$	4
g	local gravitational acceleration	8
$g_{\mu\nu}$	space-time metric with indices μ and ν indicating the four space-time dimensions $\in \{0, 1, 2, 3\}$	4
$H_{\rm p}$	pressure scale height	8
$J_{\rm orb}$	orbital angular momentum	17
κ	opacity	6
L	total luminosity	5
l	local luminosity	6
$L_{\#}$	luminosity (# specifies the track point)	86

Table 3 continued.

symbol	name	page
$L_{\rm acc}$	accretion luminosity	5
λ	structure parameter of the envelope (measure for the strength of binding to the core of the star)	21
$\lambda_{\rm B}^{\#}$	structure parameter of the envelope including the internal binding energy (# specifies the track point)	88
$\lambda_{\rm G}^{\#}$	gravitational structure parameter of the envelope (# specifies the track point)	87
M	total mass of the system (cloud, singe star or binary system)	5
m	mass coordinate	6
$\mathcal{M}$	chirp mass	18
m_1 & m_2	the two masses of a binary	16
$m_{\#}$	mass (# specifies the track point)	85
$M_{\rm J}$	Jeans mass	5
$\dot{M}$	mass accretion rate	5
μ	mean-molecular weight	6
$\mu_{\rm e}$	mean molecular weight per free electron	10
n	number density	5
$\nabla_{\rm ad}$	adiabatic temperature gradient	6
$\nabla_{\rm rad}$	radiative temperature gradient	6
∇_{μ}	mean molecular weight gradient	8
ω	frequency of a wave	4
Ω	orbital angular velocity	17
p	pressure (in textbooks usually P, to avoid confusions with the period, p is used instead)	6
$P_{\rm orb}$	orbital period (some times only P)	17
q	mass ratio	19
$q_{\rm limit}$	mass-ratio limit for stable mass transfer	20
R	radius of an object (cloud or singe star)	5
r	radius coordinate	7
$\mathcal{R}$	curvature scalar	4
$R_{\rm L}$	radius of Roche lobe	19
$R_{\#}$	radius (# specifies the track point)	86
r_j	reaction rates	10

Table 3 continued.

symbol	name	page
$\mathcal{R}_{\mu\nu}$	Ricci tensor with indices μ and ν indicating the four space-time dimensions $\in \{0, 1, 2, 3\}$	4
ρ	(local) density	7
s	specific entropy	7
T	temperature	5
t	time	7
$t_{\#}$	age or time since ZAMS (# specifies the track point)	85
T_{eff}	effective temperature	6
$T_{\mathrm{eff}}^{\#}$	effective temperature (# specifies the track point)	87
τ_{dyn}	dynamical timescale or free fall timescale	5
τ_{nuc}	nuclear timescale	9
τ_{th}	thermal timescale or Kelvin-Helmholz timescale	5
X	H abundance	6
Y	He abundance	6
Z	metal abundance or metallicity	6
z	redshift	23

Chapter 1

Introduction and theoretical background

This chapter presents the physical concepts which are used in this thesis.

1.1 Astronomical observations

Half of all day only a single star is visible with human eyes. It is the closest star to Earth. It is the Sun. As all other stars are much farther away, many people consider the stars and the Sun to be different kinds of objects. When the Sun disappears and the night begins the other stars seem to arise. Since antiquity the stars are observed by humans. The brightest stars are combined to constellations. Those constellations are related with old mythology and help to orientate at night. The first maps of the positions of stars at the sky are created in order to enable stars to become a reliable tool for navigation.

1.1.1 Optical observations

Further, more detailed, observations of stars with the first telescopes bring up new questions. Those telescopes operate in the optical regime, which is the part of the electromagnetic spectrum accessible to the human eye. The operating principle of these telescopes is to focus the light coming from a particular direction in the eye of the observer. The telescope should additionally block stray light which does not originate from the object of interest. Light coming from different directions is simply blocked by some non-transparent material. Apparently close objects can be differentiated by colour. This is done by putting a filter on the telescope which absorbs light in most of the optical regime and only allows a given frequency range to pass through. As a result one gets a way of differentiating between astronomical objects.

The human eye already differentiates between objects of different brightness. The usage of more than one filter allows to observe the brightness of astronomical objects in different colours. Measurements by human eyes are given in magnitudes, which is a logarithmic scale of the flux in units of a reference flux. Hence, the stars

can be put into a colour-magnitude diagram. There the magnitude in one chosen filter is displayed against the difference of the magnitudes relative to a second filter.

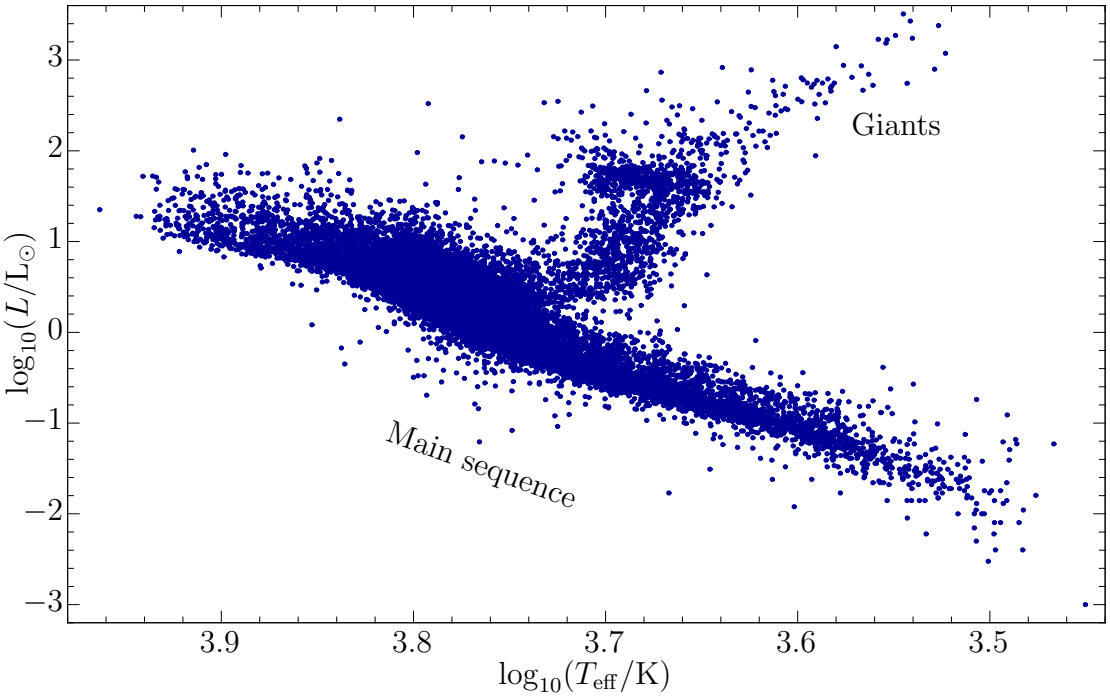

Figure 1.1: A theoretical Hertzsprung-Russell diagram of stars in the solar neighbourhood. The shown data, being part of the star catalogue by McDonald et al. (2017), is limited to stars which are within 100 pc around the solar system and are measured with fractional errors below 0.1 in effective temperature, T_{eff}, and luminosity, L. Most of the stars are on the main sequence (MS, Section 1.2.2) while the more luminous ones are evolved to their giant phases (Section 1.2.3). The most massive stars ended their lives already and are not visible in this plot.

Ejnar Hertzsprung and Henry Norris Russell classified stars in a diagram (e.g. Russell, 1914), the Hertzsprung-Russell diagram (HRD), showing the absolute magnitude (or luminosity) and the spectral type (or effective temperature) of a star (Fig. 1.1). This is similar to the colour-magnitude diagram but avoids apparent observables which depend on the distance to the star.

Modern telescopes are much more precise than their antecessors, therefore it becomes necessary to correct for artifacts originating in the telesecopes own optics. Each telescope has its characteristic point spread function (PSF) which decribes how light from a point source is spread while penetrating through the telescopes' optics. Very distant sources, like stars, behave similarly when passing through the optics. The signal is also modified by other material on the line of sight, e.g. the Earth's atmosphere. In order to isolate information of the unperturbed light of a star all this need to be taken into account. One of the simple correction techniques is a calibration of the telescope by observing a well known object. Since the atmosphere is a major source of background noise, new telescopes are build

at high altitude and places where the air is clean. Alternatively, the telescope is spaceborn and placed outside the atmosphere like the Hubble Space Telescope (STScI, 2017), operating from ultraviolet to near-infrared, or the James Webb Space Telescope (JWST, NASA, 2017a), mainly operating in the infrared.

1.1.2 Radio observations

The Earth's atmosphere blocks several parts of the electromagnetic spectrum. Besides the optical, the radio regime is the most prominent one which is observable by ground based telescopes. The largest telescopes, build so far, detect radio signals. In the radio regime even larger virtual telescopes are operating by combing several individual telescopes. The Square-Kilometre Array (SKA, SKA Organisation, 2017), under construction, is an example of such a virtual telescope. The sky looks different in radio frequencies compared to the usual known optical regime, e.g. there is an overall microwave background.

There are variable objects observable, e.g. radio pulsars (PSRs). These PSRs show a remarkable constant period in the detected pulses and are believed to be rotating[1] neutron stars (Section 1.2.5.2). These neutron stars emit radio signals in a collimated beam pointing regularly in the direction of the Earth. The majority of PSRs show pulse periods of about 1 s. The fastest rotating PSRs are the millisecond radio pulsars (MSPs), while slow rotating ones showing the strongest magnetic fields are called magnetars. To make use of the stable periods very precise measurements of the time-of-arrival (TOA) of each pulse are required. As stable, long term observations are of spezial interest, the measurements are often transferred into solar system barycentre (SSB), a system where the solar system is stationary and the origin is its center of mass, to be independent from the movement of the Earth around the Sun.

1.1.3 High frequency observations

Other electromagnetic regimes include the X-ray regime and the even more energetic gamma-ray regime. However, these parts of the electromagnetic spectrum are efficiently blocked by Earth's atmosphere, which protects life from the destructive impact of this highly energetic radiation. Hence, observations of X-rays or gamma-rays require space-based observatories, e.g. Fermi (NASA, 2017b). Large amounts of high energy photons, like X-rays or gamma-rays, are mainly emitted by extreme, astrophysical events and therefore appear as a single gamma-ray bursts (GRBs).

1.1.4 Laser interferometers

In order to observe the Universe outside the electromagnetic spectrum, the gravitational wave (GW) spectrum is investigated by building large observatories in recent years. The main instrument in each of these observatories is a laser operating in the near-infrared. This light is sent through a long-arm interferometer. At

[1] The rotation of PSRs is also called the spin of the PSRs.

the end of each arm are freely moveable mirrors connected to a test mass. If this test mass is moved, the interference pattern changes, allowing precise measurements of the displacement. The idea is that the test masses are displaced when a GW passes the interferometer.

GWs (Einstein, 1918) are a consequence of general relativity (GR) which was introduced by Einstein (1916). GWs are a solution of the Einstein equation in vacuum

$$\mathcal{R}_{\mu\nu} - \frac{1}{2} g_{\mu\nu} \mathcal{R} = 0. \tag{1.1}$$

$\mathcal{R}_{\mu\nu}$ is the Ricci tensor, $\mathcal{R}$ is the curvature scalar, and $g_{\mu\nu}$, the space-time metric. To solve Eq. (1.1) for a given application $g_{\mu\nu}$ is often linearised by the assumtion $g_{\mu\nu} = \eta_{\mu\nu} + f_{\mu\nu}$ where the Minkowski metric is

$$\eta_{\mu\nu} = \begin{pmatrix} \text{-1} & 0 & 0 & 0 \\ 0 & 1 & 0 & 0 \\ 0 & 0 & 1 & 0 \\ 0 & 0 & 0 & 1 \end{pmatrix}, \tag{1.2}$$

and $f_{\mu\nu}$ is a small perturbation depending on the application. In the case of a GW propagating in x_3-direction $f_{\mu\nu}$ could read

$$f_{\mu\nu} = \begin{pmatrix} 0 & 0 & 0 & 0 \\ 0 & \hat{a} \cdot \cos(\frac{\omega}{c} \cdot x_3 - \omega \cdot t) & \tilde{a} \cdot \cos(\frac{\omega}{c} \cdot x_3 - \omega \cdot t) & 0 \\ 0 & \tilde{a} \cdot \cos(\frac{\omega}{c} \cdot x_3 - \omega \cdot t) & -\hat{a} \cdot \cos(\frac{\omega}{c} \cdot x_3 - \omega \cdot t) & 0 \\ 0 & 0 & 0 & 0 \end{pmatrix} \tag{1.3}$$

where ω is the frequency, and $\hat{a}$ and $\tilde{a}$ are the amplitudes of the two polarisations of the wave, respectively (e.g. Hobson et al., 2006). Most GWs have so small amplitudes that Einstein expected them to be not measureable. The advanced techniques, decsribed above, allowed for the first detection of a strong GW passing the Earth in 2015 (Abbott et al., 2016b). The so far measured events are detected by the laser interferometer gravitational-wave observatory (LIGO, LIGO Scientific Collaboration, 2017) and the Virgo experiment (The Virgo Collaboration, 2017). The signal of the first observed GWs must have originated in some extreme event as an energy of about 3.0 $M_\odot \cdot c^2$ is emitted in GWs (Abbott et al., 2016b), where c is the speed of light. This event was likely a merger of two BHs (see Section 1.2.5.3).

1.2 Single star evolution

This section deals with single and isolated stars with the assumption of spherical symmetry, see e.g. Kippenhahn & Weigert (1990).

1.2.1 Young stars

Stars are born from a cloud of gas. These clouds are usually in a state of pressure equilibrium. From time to time, this equilibrium is perturbed by, e.g. random

fluctuations happening on small scales or a shock wave propagating through them on large scales. If the cloud becomes too massive or too dense, it collapses under its own gravity. Due to gravity, overdensities can grow by accumulating more and more material from the gas cloud. The critical mass leading to collapse is called the Jeans mass,

$$M_{\mathrm{J}} \approx 10^5\ \mathrm{M}_\odot \cdot \left(\frac{T}{100\ \mathrm{K}}\right)^{\frac{3}{2}} \cdot (n \cdot\ \mathrm{cm}^3)^{-\frac{1}{2}}, \tag{1.4}$$

where T is the temperature of the gas and n is its number density.

1.2.1.1 Dynamical timescale

The collapse of a gas cloud happens on the dynamical, or free fall, timescale of the cloud,

$$\tau_{\mathrm{dyn}} \approx \sqrt{\frac{R^3}{G \cdot M}}, \tag{1.5}$$

where G is the gravitational constant, R and M are the radius and mass of the cloud, respectively. As the density grows, the critical mass limit for collapse decreases and the collapse accelerates. During this continuing collapse the cloud fragments due to inhomogeneities. Each individual fragment collapses further.

As the fragments grow and get denser, they become opaque for photons. Therefore, the central part of the fragments get heated and increase accordingly the gas pressure. A new pressure, or hydrostatic, equilibrium is established and the collapse slows down. The individual fragments become protostellar cores. These cores continue to accrete material from the surrounding gas. The accretion releases gravitational energy with the luminosity

$$L_{\mathrm{acc}} = \frac{G \cdot M \cdot \dot{M}}{2 \cdot R}, \tag{1.6}$$

where M and R are the mass and radius of the protostellar core, and $\dot{M}$ is the mass accretion rate. In spherical symmetry, this rate is limited by the fact that the accretion itself generates luminosity. The luminosity puts a restraining photon pressure on the in-coming material. The in-falling gas probably forms an accretion disk, caused by conservation of angular momentum. Therefore, the factor 0.5 arises in Eq. (1.6).

1.2.1.2 Thermal timescale

The accretion process continues on the dynamical timescale, defined in Eq. (1.5). τ_{dyn} is shorter than the thermal, or Kelvin-Helmholtz, timescale,

$$\tau_{\mathrm{th}} \approx \frac{G \cdot M^2}{2 \cdot R \cdot L}, \tag{1.7}$$

where L is the luminosity. Therefore, the protostar is not able to reach a stable thermal structure and heats up adiabatically. As the temperature increases further,

hydrogen molecules begin to dissociate. Consequently, the protostellar core enters a new phase of rapid, dynamical collapse until nearly all hydrogen molecules are dissociated into atomic hydrogen. A similar effect occures when the ionisation temperatures of hydrogen (H) and helium (He) are reached. These are the two most abundant elements with mass fractions of $X \approx 0.7$ and $Y \lesssim 0.3$, respectively. The existence of heavier elements, which are called metals $Z \gtrsim 0$, can absorb energy caused by their dissociation and ionisation as well.

When the accretion rate becomes very low, or zero, the protostar develops a stable thermal structure on the corresponding timescale, defined in Eq. (1.7). The central part of the protostar generates energy by contracting further and the surface cools by radiation.

As long as temperatures are low ($\lesssim 10^5$ K), the radiative temperature gradient in hydrostatic equilibrium,

$$\nabla_{\mathrm{rad}} = \left(\frac{\mathrm{d}\log(T)}{\mathrm{d}\log(p)}\right)_{\mathrm{rad}} = \frac{3 \cdot \kappa \cdot l \cdot p}{16 \cdot \pi \cdot a \cdot c \cdot G \cdot m \cdot T^4}, \tag{1.8}$$

is larger than the adiabatic one, ∇_{ad}, and the energy transport is dominated by convection (Section 1.2.2.2). κ is the opacity, l and m are the local luminosity and mass coordinate, respectively, a is the radiation constant, and p and T are the pressure and temperature, respectively. When the temperature becomes even larger, the convection in the center of the protostar stops and the core becomes radiative. This continues until the star starts nuclear fusion and reaches its zero-age main sequence (ZAMS).

1.2.1.3 Zero-age main sequence

When computing stellar evolution the ZAMS is usually used as the initial configuration for the simulation of a star. At this point of the evolution, with the assumption of an ideal gas in hydrostatic and thermal equilibrium, a relation between the mass and luminosity can be obtained as

$$L \propto \frac{\mu^4 \cdot M^3}{\kappa}, \tag{1.9}$$

where μ is the mean-molecular weight. In the same way, depending on the energy production a mass-radius relation can be received as

$$R \propto \mu^{\frac{\nu-4}{\nu+3}} \cdot M^{\frac{\nu-1}{\nu+3}}, \tag{1.10}$$

where the parameter ν depends on the dominating burning reaction during the MS evolution, e.g. $\nu \approx 4$ for p-p chain or $\nu \approx 18$ for CNO cycle (Section 1.2.2.3). The effective temperature, T_{eff}, can be obtained from the luminosity and radius as

$$L = 4 \cdot \pi \cdot R^2 \cdot \sigma \cdot T_{\mathrm{eff}}^4, \tag{1.11}$$

where σ is the Stefan-Boltzmann constant. The combination of Eqs (1.9) to (1.11) gives a relation in the HRD only depending on the mass of the star and its composition on the ZAMS, cf. Figs 1.1 (lower left boundary of the MS), 3.3 (left beginning of the curves) and 3.5.

1.2.1.4 Stellar initial-mass function

As the position at the ZAMS and the further evolution of the star depends on its mass, a distribution of stellar masses at the ZAMS is needed. There are different types of stellar initial-mass functions (IMFs) which are used, e.g. a simple power-law with exponent $-\alpha_{\mathrm{IMF}}$ (Salpeter, 1955; Scalo, 1986; Kroupa, 2001) or a log-normal (Miller & Scalo, 1979; Chabrier, 2003). Some more details are given in Section 3.2.1.1.

1.2.2 Main sequence evolution

The stars spend most of their lives on the MS.

1.2.2.1 Stellar structure equations

To consider the evolution of a star, the stellar structure equations (1.12) to (1.15) need to be solved.

$$\frac{\mathrm{d}r}{\mathrm{d}m} = \frac{1}{4 \cdot \pi \cdot r^2 \cdot \rho}, \tag{1.12}$$

$$\frac{\mathrm{d}p}{\mathrm{d}m} = -\frac{G \cdot m}{4 \cdot \pi \cdot r^4} - \frac{1}{4 \cdot \pi \cdot r^2} \cdot \frac{\partial^2 r}{\partial t^2} \approx -\frac{G \cdot m}{4 \cdot \pi \cdot r^4}, \tag{1.13}$$

$$\frac{\mathrm{d}l}{\mathrm{d}m} = \epsilon_{\mathrm{nuc}} - \epsilon_{\nu} + \epsilon_{\mathrm{gr}} \approx \epsilon_{\mathrm{nuc}}, \tag{1.14}$$

$$\frac{\mathrm{d}T}{\mathrm{d}m} = -\frac{G \cdot m \cdot T \cdot \nabla}{4 \cdot \pi \cdot r^4 \cdot p}. \tag{1.15}$$

The first stellar structure equation (1.12) follows from the principle of mass conservation. It connects the local density ρ with the radius, r and mass coordinate, m. Here, a static situation without a time, t, dependent mass flow is assumed.

From conservation of momentum, the second stellar structure equation (1.13) arises. It simplifies under the assumption of hydrostatic equilibrium, where the acceleration, $\frac{\partial^2 r}{\partial t^2}$, vanishes.

The third stellar structure equation (1.14) represents conservation of energy. The local luminosity changes accordingly to the energy generated by nuclear fusion, ϵ_{nuc}, and energy loss into weakly interacting particles, the neutrinos, ϵ_{ν}. Furthermore, it can vary due to gravitational contraction or expansion, $\epsilon_{\mathrm{gr}} = -T \cdot \frac{\partial s}{\partial t}$, where s is the specific entropy of the gas. When the star is in thermal equilibrium, $\epsilon_{\mathrm{gr}} = 0$, the equation simplifies. If neutrino losses are low, $\epsilon_{\nu} \approx 0$, a further simplification can be made.

While the main energy generation is taking place in the center of the star, most of the energy is lost at the surface, the energy transport is considered in the fourth stellar structure equation (1.15). Depending on the temperature gradients, there are mainly two regimes. If $\nabla_{\mathrm{rad}} \leq \nabla_{\mathrm{ad}}$ (Schwarzschild criterion) the energy transport is radiative and therefore $\nabla = \nabla_{\mathrm{rad}}$, see Eq. (1.8), otherwise it is convective and the gradient consists of an adiabatic and a super adiabatic term.

If there are chemically inhomogeneous layers, the mean molecular weight gradient, $\nabla_\mu = \frac{\mathrm{d}\log(\mu)}{\mathrm{d}\log(p)}$, has to be taken into account, leading to the Ledoux criterion, $\nabla_{\mathrm{rad}} \leq \nabla_{\mathrm{ad}} + \nabla_\mu$ for an ideal gas.

1.2.2.2 Convection

During stellar evolution, there are three main reasons for convection to occur. In cool regions, the low temperature causes the opacity to increase, which results in an increase of ∇_{rad}, cf. Eq. (1.8). This mostly happens in very low mass stars ($M \lesssim 0.35\ \mathrm{M}_\odot$) and only in the outer envelopes of Sun-like stars ($M \lesssim 1.5\ \mathrm{M}_\odot$) during their MS evolution. Especially extended regions, e.g. during the giant phases (Section 1.2.3), show convection for this reason and a second effect occurs similarly. In cases where the low temperature and density leads to only partially ionized regions, the adiabatic temperature gradient can decrease and therefore enable convection in thin layers.

There is a third reason for convection, which is caused by very high energy production $\epsilon_{\mathrm{nuc}} \approx \frac{l}{m}$. This happens during core-burning phases of massive stars ($M \gtrsim 1.2\ \mathrm{M}_\odot$). In burning regions a chemical gradient usually arises between the unburned fuel and the already burned ashes. If this region becomes convective, the material mixes efficiently.

For simplicity convection is treated within the mixing length theory in most cases. This theory assumes that a convectively moving cell of gas mixes into its surrounding after traveling a given mixing length. Usually this length is set to be similar to the pressure scale height,

$$H_{\mathrm{p}} = \frac{p}{\rho \cdot g}, \tag{1.16}$$

where g is the local gravitational acceleration.

As the moving cells usually have a non-zero velocity, it is not possible to have a sharp boundary between convective and non-convective regions. At the boundary of a convective region, the movement of material penetrates into non-convective layers. This mechanism is called overshooting. This is especially important where a chemical gradient limits convection. Overshooting will lead to some mixing and therefore weaken the chemical boundary. This can extend burning processes when the mixing provides more fuel. The overshooting parameter, α_{ov}, which is the fraction of a pressure scale height where additional mixing happens, therefore needs to be calibrated by observations (Section 3.13.1.1).

1.2.2.3 Hydrogen core burning

The first, nuclear reactions take place in the center of a star. There the required temperature and density is reached first to produce energy by fusion. The temperature dependence, in particular, is very strong. The reason for this is the repulsive electric force between two similar charged particles. Here, mainly ionized hydrogen needs to overcome a Coulomb barrier. Only at high temperatures the most energetic particles have a sufficient probability to penetrate through this barrier via the quantum-tunnelling effect.

The p-p chains

On the MS, hydrogen (H) burns into helium (He). Each stable ^{4}He-particle needs four ^{1}H-particles to be produced. Reactions where only two particles interact are much more likely than multiple particle reactions, so in intermediate steps other isotopes like ^{2}H and ^{3}He are generated and reprocessed. The net reaction can be represented as

$$4\,{}^1\mathrm{H} \rightarrow {}^4\mathrm{He} + 2\,\mathrm{e}^+ + 2\,\nu_\mathrm{e} + 2\,\gamma.$$

Side products are positrons (e^+), electron neutrinos (ν_e) and photons (γ). The released energy, which is carried by reaction products, is about 26.73 MeV. The energy imparted on the neutrinos can leave the star efficiently. Therefore, this energy does not contribute to the photon luminosity and pressure which balances the gravity to prevent a further collapse.

Further reactions involve beryllium, lithium and boron isotopes. In those reactions, the energy lost by neutrinos is larger per resulting He nucleus. The reactions converting these intermediate isotopes into He via proton capture work already at lower temperatures, which efficiently depletes these isotopes, e.g. lithium, in stars.

The CNO cycle

Heavier elements like carbon (C), nitrogen (N), oxygen (O) and some others with the different isotopes can help to convert H into He. The overall amount of these heavier elements remain constant during this process and build up a characteristic relative abundance. Usually the heavier elements have a larger Coulomb barrier, therefore require higher burning temperatures. On the other hand, reactions involving these elements are favoured at lower densities. At lower densities the intermediate products of the p-p chains may decay before they react further. Those conditions of low density are fulfilled in more massive stars ($M \gtrsim 2\ \mathrm{M}_\odot$).

While the total amount of the catalysing elements remains constant, individual nuclei react to become different isotopes, but after a loop is completed they become the same isotopes again and H is converted into He. These cycles involving heavier elements can only take place in stars with $Z > 0$. Such stars need to form from a gas cloud containing the heavier elements before the star formation begins, as those elements will only be produced in later stages of stellar evolution (Section 1.2.3.1). Enrichment of these elements originates in previous generations of stars, e.g. ejected during supernovae (Section 1.2.5.2).

Nuclear timescale

The fusion of light elements into heavier ones takes a long time and operates on the nuclear timescale

$$\tau_\mathrm{nuc} = \frac{E_\mathrm{nuc}}{L}, \tag{1.17}$$

where E_nuc is the available total nuclear energy. When taking only the energy released by the fusion of H to He, and assuming a constant luminosity, this timescale corresponds to the lifetime of the star on its MS.

The energy deposition, $\epsilon_\mathrm{nuc} - \epsilon_\nu$, needed in the third stellar structure equation (1.14), is calculated from the burning reactions. Therefore, the abundances

of the different elements and their isotopes have to be determined. The number density of each considered isotope, n_i, changes accordingly to all rates, r_j, of reactions where the isotope is involved. The isotope's number density increases where it is produced and decreases where consumed. This adds another set of differential equations

$$\frac{\mathrm{d}n_i}{\mathrm{d}t} = \sum_{\text{reactions producing } i} r_j - \sum_{\text{reactions consuming } i} r_j, \tag{1.18}$$

where the reaction rates depend on the number densities of the reacting particles and the average of the product of their relative velocity and their velocity dependent reaction cross section.

1.2.2.4 Equation-of-state

As there are to many unknowns in the stellar structure equations, another equation is required. This is the equation-of-state (EoS). It connects the pressure with the density, temperature and the composition of the material. A few examples for different regimes are listed here:

- For an ideal gas, the EoS is

$$p_{\mathrm{gas}} = \frac{k \cdot \rho \cdot T}{\mu \cdot \mathrm{m_u}}, \tag{1.19}$$

  where k is the Boltzmann constant and $\mathrm{m_u}$ the atomic mass unit.

- For non-relativistic degenerate electrons, the EoS is

$$p_{\mathrm{e}} = K_{\mathrm{non-rel}} \cdot \left(\frac{\rho}{\mu_{\mathrm{e}}}\right)^{\frac{5}{3}}, \tag{1.20}$$

  where $K_{\mathrm{non-rel}}$ is constant and μ_{e} is the mean molecular weight per free electron.

- For highly relativistic degenerate electrons, the EoS is

$$p_{\mathrm{e}} = K_{\mathrm{rel}} \cdot \left(\frac{\rho}{\mu_{\mathrm{e}}}\right)^{\frac{4}{3}}, \tag{1.21}$$

  where K_{rel} is constant and different from $K_{\mathrm{non-rel}}$.

- For pure radiation, the EoS is

$$p_{\mathrm{rad}} = \frac{1}{3} \cdot a \cdot T^4. \tag{1.22}$$

The overall EoS is a combination of the individual ones, however in most cases one of the regimes dominates. During the MS, ideal gas dominates. In massive stars ($M \gtrsim 50\ \mathrm{M_\odot}$), radiation also needs to be considered.

All of the differential Eqs (1.12) to (1.15) and (1.18) are solved numerically in hydrodynacmic stellar evolution codes. The stellar evolution code used in this work is the one-dimensional binary evolution code (BEC).

1.2.3 Giant phases

When the fuel in the center of the star is exhausted, core burning terminates. As a consequence of the missing energy source, powering the stabilizing pressure, the central region begins to contract further. This increases the temperature until the layers above the He-core become hot enough to ignite the remaining hydrogen there. This burning takes place in a shell around the core[2], while the core itself contracts further. Now there are two energy sources the contracting core and the burning shell. This leads to an expansion of the envelope. To keep the conditions, i.e. decreasing density and pressure in the core, on one side of the burning shell in equilibrium with the other, the envelope expands further to get back to an equilibrium state. This reverse behaviour of the core and the envelope is called mirror principle of a stable burning shell.

As some of the energy is consumed by the expansion, the luminosity of the star decreases a bit. This restructuring of the star happens on its thermal timescale (Section 1.2.1.2). The star enters the red giant branch when the expansion of the envelope decreases the surface temperature and effective temperature. Hence, the outer-most layers become unstable against convection. Once large parts of the envelope are convective, the luminosity increases while the star continues to expand. In less massive stars ($M \lesssim 2\ \mathrm{M}_\odot$) the convection of the envelope can reach down to the shells where partial H burning took place and lead to a, so called, dredge-up. During dredge-up burning products are transported to the surface where they can be observed directly.

1.2.3.1 Helium burning

Meanwhile, the core temperature increases and at some point the He may ignite[3], otherwise the core becomes degenerate (Section 1.2.5.1). He burning happens in a two-step process, called the triple-α process. As the beryllium produced is not stable, a second reaction is required where it has to capture another He particle to produce C. When the C reacts with further He nuclei, part of the C is converted into O. Thus, C and O production dominates and therefore, a CO-core is built up. The nuclear timescale (Section 1.2.2.3) of He burning is about $\frac{1}{10}$ of the nuclear timescale of H burning, as the released energy per He particle is only $\frac{1}{10}$ compared to H burning. As soon as the core contraction is stopped[4], the envelope do not expand any further. When the H burning shell moves outwards, the envelope has to contract a bit to ensure stable nuclear burning conditions. Any decrease of the released burning energy would reduce the pressure and therefore lead to a contraction of the envelope. This results to a self-regulating system.

[2] In stars where the H-burning core is not convective, the burning region continuously moves away from the center into a burning shell.

[3] In low mass stars ($M \lesssim 2\ \mathrm{M}_\odot$), He burning may lead to flashes.

[4] The energy production may lead to a small expansion of the core.

1.2.3.2 Late burning

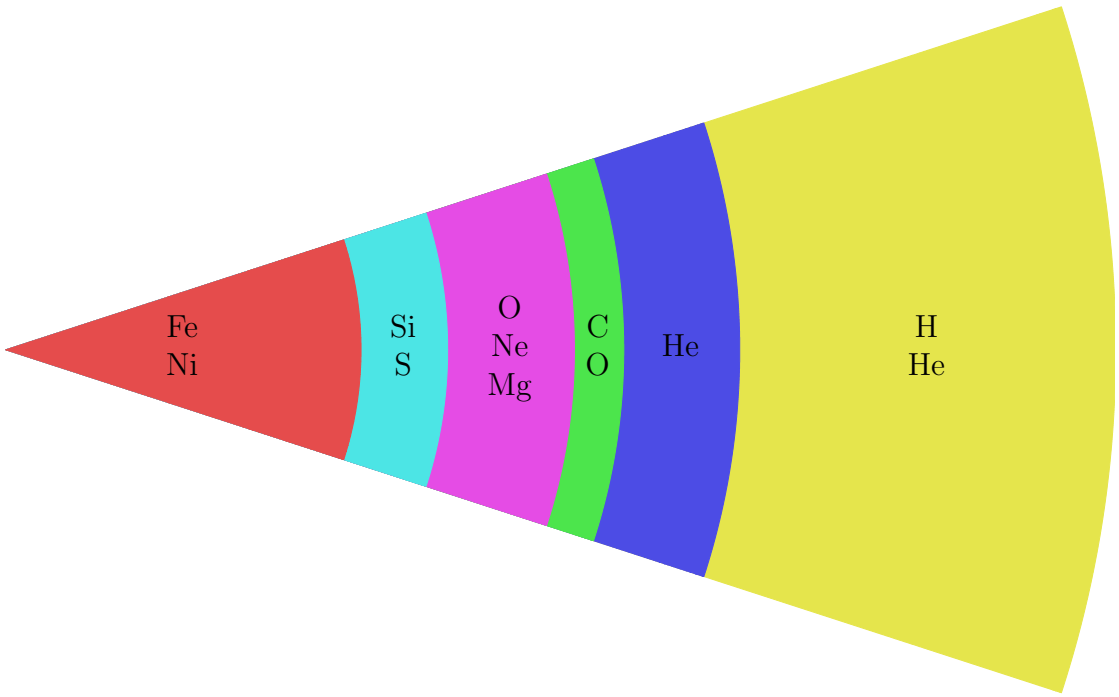

Figure 1.2: Example of the onion-like structure of the burning products in a star with an initial mass of 15 $M_\odot$ (Woosley et al., 2002). The layers are labelled with the most abundant elements representing more than 90 per cent of the mass of each shell.
Acronyms used in the figure are H: hydrogen; He: helium; C: carbon; O: oxygen; Ne: neon; Mg: magnesium; Si: silicon; S: sulphur; Fe: iron; Ni: nickel.

At even higher core temperatures, created when the core contracts further, heavier elements can burn. First, C is converted into unstable magnesium (Mg), which decays into neon (Ne) or sodium, which reacts to Ne. Ne subsequently reacts with He particles into stable Mg. Before O burns, Ne is converted into stable Mg by providing He nuclei from its own decay into O. Once mostly O and Mg remains in the core, O burning may produce silicon and sulphur. Most of these subsequently burns until iron (Fe) and nickel, which decays into iron. The later reactions in the burning sequence provide less specific energy. This consequently leads to shorter nuclear timescales in which those burning processes are active. Finally, the fusion processes stop completely as no more energy can be gained by building up heavier elements than Fe. Ultimately, a massive star develops a structure like illustrated in Fig. 1.2.

1.2.3.3 Luminous blue variables

Very massive stars ($M \gtrsim 50\ M_\odot$) are quite large on the MS. As the luminosity of those stars is very large, they develop strong stellar winds. When those winds

occur in an unstable way, one observes repeating phases of outbursts with mass losses above 10^{-3} $M_\odot$/yr. Such a star is called a luminous blue variable (LBV, e.g. Humphreys & Davidson, 1994). During core H burning these outbursts may eject the entire envelope of the star.

1.2.4 Helium stars

If a star loses its H envelope, it becomes a naked He star or a type of Wolf-Rayet star, which have optically think winds. The He stars have also a MS, the HeMS (Fig. 3.5), where they burn He in their cores. The subsequent burning processes are the same as for the giants (Section 1.2.3.2). Less massive naked He stars ($M_{\rm He} \lesssim 5$ $M_\odot$) also expand like giants (Section 1.2.3) after their MS evolutions, but having no H in their envelopes. More massive naked He stars may develop inflated envelopes early on, see Section 2.4.6.

1.2.5 Remnants

After the last nuclear fusion stopped, stars end their lives and leave behind different remnants depending on their final core masses. The least massive stars with a ZAMS mass $\lesssim$ 8 $M_\odot$ are believed to become a white dwarf (WD). The more massive ones probably end as a neutron star (NS) or a stellar mass black hole (BH). Further details can be found in Section 3.2.2.5 and Shapiro & Teukolsky (1983).

1.2.5.1 White dwarfs

During the contraction, before a burning process can start in the core, the material could become so dense that the electrons become degenerate. According to the Pauli exclusion principle, the electron gas can only occupy each quantum state with a single electron. In cases of a degenerate electron gas, the pressure becomes dominated by the terms in Eqs (1.20) or (1.21). This stops further contraction and prevents the core from reaching the ignition temperature required for the next burning process. The envelope still expands and cools. Consequently, the envelope becomes more and more convective. At some point, the convection may extend into layers containing the ashes of earlier shell burning. This leads to a dredge-up.

Later in the evolution, when the burning shell becomes very thin, the burning becomes thermally unstable. This leads to burning flashes and pulsations. Depending on the depth of the pulsations they may induce further dredge-up. This is called third dredge-up. By this process, the core grows in every pulse until there is nearly no fuel left in the envelope. Material ejected may form a planetary nebulae around the old star. When the thin burning shell approaches the surface of the star, its effective temperature increases. Hence, molecules may dissociate and parts of the surrounding gas in the nebula ionize.

At some time, the cooling decreases the temperature in the last burning shell below the required temperature for nuclear fusion. After the last burning stopped, the remaining core, lacking of nuclear energy generation, cools and decreases its

luminosity. The degenerate core becomes the WD. Depending on the mass of the initial star the resulting WDs have different compositions. This is a consequence of the maximum temperature reached during the evolution of the star and the required temperatures to ignite the different burning processes. The most massive WDs contain mainly O, Ne and Mg. Their maximum mass, where the electron degeneracy can stabilize the WD, is given by the Chandrasekhar mass (Chandrasekhar, 1931). Less massive WDs never started C burning and therefore end as a CO WD, as long as they went through He burning. If they also failed to ignite He, they become a He WD[5]. Due to the low luminosity, it is difficult to observe WDs, see Section 4.5.1.

1.2.5.2 Neutron stars

Massive stars which are able to burn until Fe in their core does not become fully stabilized by electron degeneracy. The burning shells usually do not reach the surface, therefore the stars develop an onion like structure (Fig. 1.2) with layers of the burning ashes of all the burning processes (Sections 1.2.3.1 and 1.2.3.2) which took place during the evolution. Some of them may get partially mixed by convection. Further nuclear reactions would not generate energy (Section 1.2.3.2). The energy production by fusion prevented the collapse of the central core. Hence, the central Fe core collapses. The electron degeneracy drops when the central temperature becomes large enough so that the electrons can overcome the binding energy of the Fe nuclei[6]. This leads to electron capture making the material more neutron rich. Alternatively, the photodisintegration of Fe can produce neutrons at extremely high temperatures. In this case, the photon pressure drops which leads to the final core collapse.

When the particles becomes neutral in electric charge, the density can increase further. The free falling collapse of the core frees a large amount of energy in a short time. When the density of nuclear matter is exceeded the collapse is suddenly stopped in the center of the star. As the material further out is still falling freely onto the material whose density exeeds that of nuclear matter, it rebounces back outwards. Parts of the rebounced material becomes unbound to the core and is ejected in a supernova (SN). During this process, a lot of neutrinos, photons and some high energetic neutrons are produced. Thus, neutron rich and ionized material is ejected and recombines when it cools. This material dominates the late observations of a SN, showing some prominent features of the nuclear decays of nickel or cobalt in the SN light curve.

Depending on the main mechanism responsible for the free collapse, SNe are classified into electron-capture supernovae (EC SNe), where the electron capture dominates, and Fe core-collapse supernovae (CC SNe), where the photodisintegration of Fe dominates. As SN explosions are very rapid, small deviations from spherical symmetry can lead to asymmetric ejection of the material. Hence, the

[5]Observable He WDs need to form in binaries as their progenitor's lifetime is longer than the age of the Universe.

[6]This may also partially happen to massive cores consisting of ONeMg or heavier elements.

remaining core gets a net momentum kick. A prescription of these kicks imparted onto the SN remnant is shown in Table 3.1 and described in Section 3.2.2.6. In cases where the remnant is stabilized by the degeneracy of neutrons it is called a NS. The overall EoS of NSs is still not finally understood and part of current research (e.g. Steiner et al., 2013; Özel & Freire, 2016).

NSs are even smaller than WDs. This makes optical observations of them very difficult. They can be observed, when they are active (radio) PSRs (e.g. Manchester & Taylor, 1977) and their pulse beam points in our direction some of the time. Whether they are active in the radio regime depends on the magnetic field and the spin of the NS. In most models, it is assumed that the beam of the radio emission aligns with the dipole magnetic field giving rise to two beams, one at each of the two magnetic poles of the NS. Only if the spin and magnetic field axis of the NS are not aligned the direction of the radio beam changes rapidly and therefore it can be observed as a PSR. In a binary (Section 1.3), any misalignment of the magnetic field axis and the orbit of the PSR causes additional long time periods on the observable pulses.

1.2.5.3 Black holes

When the remnant of a SN cannot be stabilized by the degeneracy of neutrons, it collapses further until the density is so high that no light can escape from the remnant, which is then called a BH. As no information can escape the event horizon of a BH, its interior cannot be constrained by direct observations. A BH is only indirectly observable, when there is some material being accreted by it. Therefore, the number of such objects in the Universe is quite unknown.

One can predict the number of BHs based on the numbers of massive stars which potentially end their lives as a BH. As the transition between NS and BH progenitors is not fully constrained, the unseen BH population remains uncertain. Additionally, there is a possibility that not all stars too massive to become a NS become a BH instead. If during the late phase of massive star evolution the core gets too hot, while its internal pressure is dominated by radiation, the star may die in a pair-instability supernova (PISN, Heger & Woosley, 2002). In this case, there will be no compact remnant left.

1.3 Binary star evolution

Many stars, especially massive ones, seem to have a companion star (e.g. Sana et al., 2012). For the initial conditions of a binary, see Section 3.2.1.

This section deals with the influence of binarity on a star and its evolution. If the two stars of a binary are separated far enough, they practically evolve as two single stars. In this case, the fact that they are in a binary does not change the evolution of the stars. If the binaries with massive stars remain bound after their SNe, they may form a double compact object (DCO) binary.

1.3.1 Orbital evolution

The gravitational force accelerates each of the two binary components in the direction of the other one. If the stars have an initially zero relative velocity, they would fall towards each other, but this relative velocity is in general not zero. The reason for this goes back to the formation of a binary. The two stars form at the same time from the same gas cloud. They are simply two different fragments which become protostars (see Section 1.2.1). Conservation of angular momentum in the whole of the cloud causes an initial relative velocity of the two components of a binary.

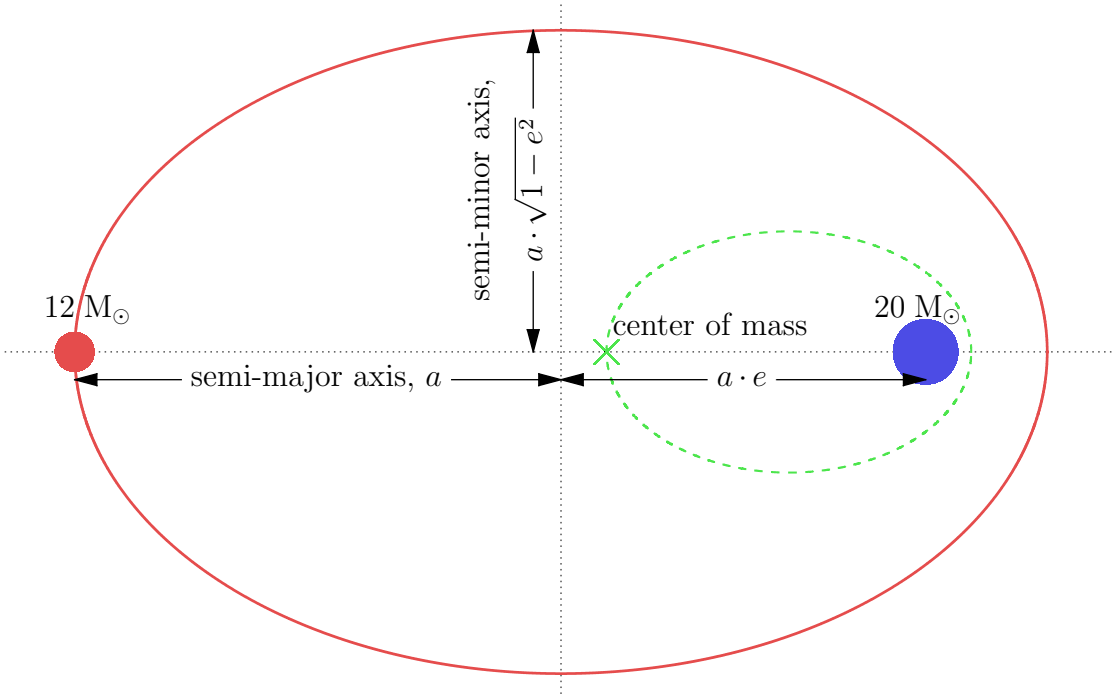

Figure 1.3: Top view of an orbit of the secondary (red, solid) with an eccentricity $e = 0.75$ in the rest frame of the primary star (20 $M_\odot$, blue). The barycentre, or center of mass, is indicated with the green cross and has also an orbit (dashed) in the primary stars' rest frame.

As the stars are attracted by gravity, they move around each other. For a system with two masses the solutions of the equation of motion are Keplerian orbits. If the binary is bound, the orbit is closed. Keplerian orbits, like the one shown in Fig. 1.3, are characterised by the two masses, m_1 and m_2, of the stars and two further parameters, the semi-major axis, a, and the eccentricity, e. The semi-major axis is related to the energy stored in the orbit

$$E_{\mathrm{orb}} = -\frac{G \cdot m_1 \cdot m_2}{2 \cdot a}. \tag{1.23}$$

This, together with the eccentricity also determines the angular momentum of the

orbit

$$J_{\rm orb} = \sqrt{\frac{G}{M}} \cdot m_1 \cdot m_2 \cdot \sqrt{a \cdot (1 - e^2)}, \tag{1.24}$$

where $M = m_1 + m_2$ is the total mass of the binary. Kepler's third law connects the semi-major axis with the period of the orbit

$$\Omega \equiv \frac{2 \cdot \pi}{P_{\rm orb}} = \sqrt{\frac{G \cdot M}{a^3}}, \tag{1.25}$$

where Ω is the angular velocity of the orbit.

As long as the orbital energy and angular momentum are conserved, the two stars remain on the Keplerian orbit determined by the semi-major axis and the eccentricity. There are several physical condition that may cause changes in the orbital parameters, which are discussed in the following subsections and Section 1.3.2.

1.3.1.1 Wind mass loss

The simplest reason for a change in energy and angular momentum of the orbit is the loss of material from the binary system. During its evolution, any star loses mass on its surface through a stellar wind. The material ejected in the wind escapes from the star's surface if its kinetic energy is large enough to overcome the gravitational potential. The mean kinetic energy of the material in the outermost layers depends on its temperature and therefore also determines the strength and the density of the wind. The gravitational force at the surface limits the wind. This results in very different winds depending on the mass and the evolutionary phase of the star (see Sections 1.2.2 to 1.2.4). As a result, the semi-major axis changes depending on the total amount of material lost (Section 3.2.2.1).

1.3.1.2 Tides

As stars are extended objects, the gravitational force caused by the companion varies in different parts of the star. This causes tides (e.g. Hut, 1981). As a consequence of the tides, orbits tend to circularise, decreasing the eccentricity. While tides exchange energy between the orbit and the stars, the angular momentum is conserved. This results in a change of the semi-major axis and accordingly the eccentricity changes. The full circularisation acts on a timescale which strongly depends on the extension of the stars and the semi-major axis (e.g. Claret & Cunha, 1997; Zahn, 1975, 1984). A prescription of full circularisation is shown in Section 3.2.2.2.

An other effect of tides is the synchronisation of angular velocity of the stellar surface and the orbit[7]. Especially in close orbits, the correspondingly short synchronisation timescale causes the rotation of the star to be locked to the orbit. Otherwise, the overall rotation of a star changes according to angular momentum conservation during the episodes of contraction or expansion (Section 1.2). In the most extreme case of rotation, this can lead to chemically homogeneous evolution

[7]In other words, the spin period of the star becomes equal to the orbital period.

(CHE), as rotation induces additional mixing. Thus, expansion during the giant phase would be suppressed and appear to be less prominent.

1.3.1.3 Magnetic breaking

Most stellar material is at least partially ionized and therefore the individual particles are charged. Hence, they are effected by electromagnetic fields. Especially in low mass stars, the magnetic field of the stars influences the outflowing charged material. Hence, the angular momentum loss is changed when the charged particles carry away a different amount of angular momentum compared to a situation without magnetic field. The angular momentum change also acts on the spin of the stars, which may couple back to the orbit through tides.

1.3.1.4 Gravitational-wave radiation

Orbiting massive objects emit GWs. This emission depends on the masses and the orbital separation, or period. The more massive and closer the massive objects, i.e. stars, the stronger is the gravitational-wave radiation (GWR, e.g. Peters & Mathews, 1963). Thus, the strongest GW signals are emitted by very compact, massive objects in tight orbits, e.g. immediately before the two objects touch each other. An example for these kinds of objects are stellar remnants in binaries. During their merging event, GWs are produced, which have an amplitude which is detectable with the modern GW detectors (Section 1.1.4).

In order to get a binary to this final merger stage, it has to survive the evolution of its components and end up in a tight orbit. This evolution involves several uncertainties studied in this thesis. The emission of GWs prior to the merger leads to a shrinkage of the orbit. Nevertheless, the orbit of the DCO binary needs to be close and/or eccentric after the formation of the second compact object. As GW emission depends on the separation, the time it takes for the GWR to shrink the orbit until a merger happens can be calculated, see Section 3.2.2.7 and Peters (1964). Most of the time during GWR is spent in a wide orbit. The final orbits with the largest shrinking only last a few seconds. The very last orbit before the merger results in a typical chirp-like signal. This signal is related to a combination of the masses of the merging objects, the so called chirp mass

$$\mathcal{M} = \frac{(m_1 \cdot m_2)^{\frac{3}{5}}}{M^{\frac{1}{5}}}. \tag{1.26}$$

1.3.2 Mass transfer

Tight DCO binaries show orbits which are smaller than the maximum extent of the components' progenitors during their giant phases. Therefore there must have been some interaction between the stars during their evolution. Each star in the binary sits in its own gravitational potential. When a star expands (Section 1.2) or the orbit shrinks (Section 1.3.1), material can be transferred from one star to its companion.

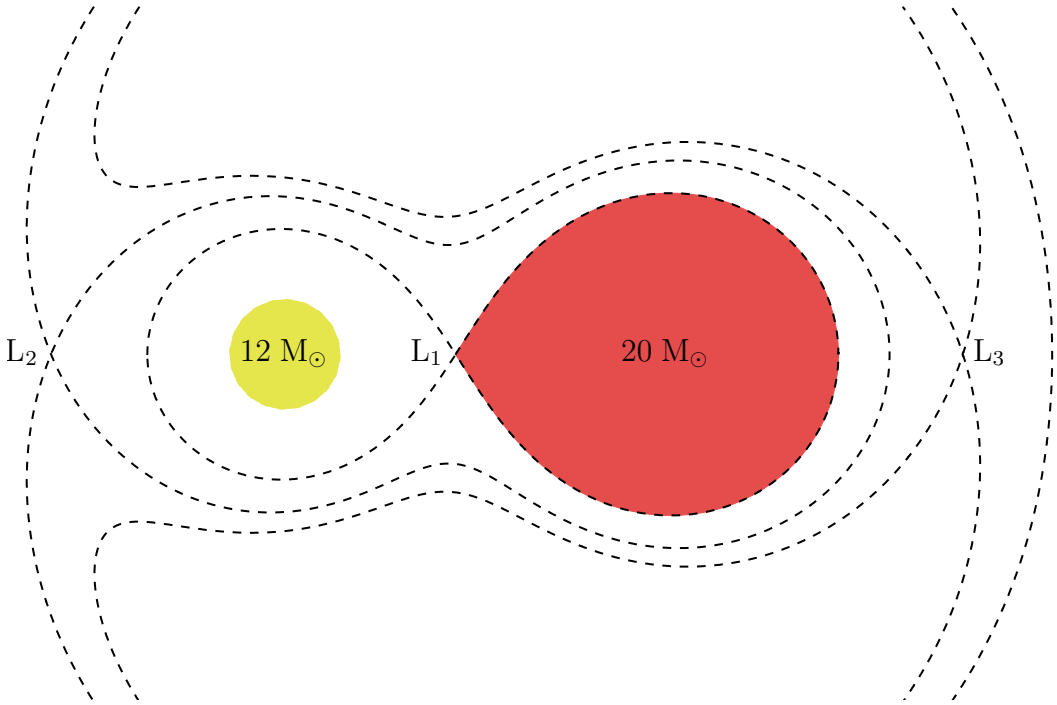

Figure 1.4: Top view of a mass-transferring binary where the Roche-lobe filling star (20 $M_\odot$) begins to transfer mass through the first Lagrangian point (L_1) to its companion (12 $M_\odot$). The three dashed lines show the equipotential lines (projections of the equipotential[8] surfaces) of the first three Lagrangian points.

The equipotential[8] surface which defines where the material is mainly bound to one star is called its Roche lobe. Consequently, the loss of material is called Roche-lobe overflow (RLO). Usually, lost material falls into the nearest available gravitational potential. In a binary, the material is attracted by the companion star. Hence, the gas moves usually through the first Lagrangian point, as illustrated in Fig. 1.4. The Lagrangian points are saddle points in the potential. Therefore, material will be able to escape through Lagrangian points first.

The Roche-lobe radius, R_L, which is the radius of a spherical symmetric star with the same volume as the non-symmetric Roche lobe filling star, can be approximated (Eggleton, 1983) as

$$R_\mathrm{L} = \frac{a \cdot 0.49 \cdot q^{\frac{2}{3}}}{0.6 \cdot q^{\frac{2}{3}} + \ln\left(1 + q^{\frac{1}{3}}\right)}, \tag{1.27}$$

where q is the mass ratio. In Eq. (1.27) the ratio is taken to be the mass of the considered star divided by its companion's mass.

[8]The effective potential is caused by the gravitational and centrifugal force.

1.3.2.1 Stability of Roche-lobe overflow

Depending on the conditions, the mass transfer can proceed in a stable or unstable way. The first case is called just RLO while the second case usually results in a situation where the material lost from the donor engulfs both stars and forms a so called common envelope (CE). There are three main changes which need to be considered when differentiating between stable RLO and the formation of a CE.

Firstly, the reaction of the mass-losing star, the donor, can be different depending on the conditions of the mass loss. Usually, removal of radiation dominated material leads to a contraction of the donor. But the donor expands further when convective material is removed (Hjellming & Webbink, 1987). In this case, the mass transfer enhances. Thus, a criterion based on the radial extent of the donor, and therefore how convective its surface layers are, is shown in Section 2.9.

Secondly, the reaction of the mass-gaining star, the accretor, could also be contraction, e.g. material accreted onto a degenerate object, or expansion. Depending on the strength of the expansion, such a star may fill its own Roche lobe with the new material, leading to a CE. This is usually the case if the potential of the accretor is not very deep, i.e. if it is much less massive than the donor, the accretion happens close to the Eddington limit of the accretor[9], or the new material initiates a structure change similar to the situation when the stars become giants to ensure stable nuclear burning conditions.

Thirdly, the change of the orbit according to the mass transfer can enhance the mass loss further. As a consequence of conservation of angular momentum, the orbit shrinks as long as mass is transferred from the more massive star to the less massive one. Hence, the two last considerations are often considered by a comparison to a threshold in the mass ratio of the donor to accretor mass, $q_{\rm limit}$ (Section 3.2.2.3). The influence of the mass-ratio limit on binary evolution is investigated in Sections 3.5.1.5 and 3.13.3.

1.3.2.2 Stable Roche-lobe overflow

The outcome of stable mass transfer depends on several parameters which describe where material is lost and where it ends up. The overall mass-transfer efficiency, giving the relative amount of material transferred from the donor to the accretor, is $\epsilon = 1 - \alpha_{\rm RLO} - \beta_{\rm RLO} - \delta_{\rm RLO}$, which includes the three main processes happening to the lost material.

First, material is partially lost directly from the vicinity of the donor, $\alpha_{\rm RLO}$. This material escapes the binary in a direct fast wind instead of moving to the companion.

Second, some material is ejected as the accretors luminosity pushes it out of the system, $\beta_{\rm RLO}$. Usually all material which exceeds the amount the accretor can assimilate is lost as re-emission from the accretor. Therefore, a minimum value for this fraction of re-emitted material is set, $\beta_{\rm min}$, while the full re-emission depends on the exact conditions of accretion.

[9]The Eddington limit is reached when the radiation pressure would stop a further increase of the accretion rate of in-falling material.

Third, some of the material lost from the donor may remain close to the binary in a circumbinary torus, $\delta_{\rm RLO}$, with a radius of $\gamma^2 \cdot a$. This amount is usually the smallest of the three and therefore neglected, $\delta_{\rm RLO} \approx 0$.

Depending where the material is finally lost and where it ends up, a different amount is lost from the orbital angular momentum of the binary. With the assumption of effective tides the binary keeps circularised (Section 1.3.1.2). Thus, the final separation after mass transfer results from the change in orbital angular momentum. More details are given in Section 3.2.2.3. To get a better understanding of the mass-transfer efficiency, the effect of the main parameters is investigated in Sections 3.5.1.4 and 3.13.3.

1.3.2.3 Common envelope evolution

When the mass transfer becomes unstable, more and more material will flow to the accretor which will be unable to accumulate all of it. Hence, the material surrounds both stars and forms a CE. The ejection of the CE is believed to proceed in different phases.

Before the onset of the CE, tides will have synchronised the rotational period of the stars with the orbital period. As there is now some additional friction on the accreting companion by the CE, this corotation is lost in the first phase. In the second phase, the plunge-in, the orbital separation drastically shrinks while the envelope becomes sparse due to the enhanced heating. When the density drops low enough, the in-spiral enters a phase of self-regulation, the third phase, on the thermal timescale. Instabilities may push a system back and forth between the second and third phase (e.g. Taam & Ricker, 2010; Ivanova et al., 2013).

The final phase can either be a successful ejection of the CE or a merger of the two stars. This bifurcation has a strong influence on the subsequent evolution of the binary or the merger product. A merger prevents the binary from becoming a DCO. Therefore, such a merger will be called an "early merger", as it happens during the evolution prior to the formation of a DCO.

To eject the CE successfully, the binary needs to get rid of the gas in the CE. There are two broadly used ways of how to determine the situation after the ejection of the CE. First, the energy required to eject the envelope is balanced with the available energy. Here, the main source of energy is the energy stored in the orbit of the two stars. This leads to the (α-λ)-formalism, see Sections 2.2 and 3.2.2.4. The two parameters of this formalism are the efficiency of converting the available energy into kinetic energy of the CE, $\alpha_{\rm CE}$, and the structure parameter of the envelope, λ. Other energy reservoirs which may help to eject the CE are discussed in Section 2.4.2. The amount of thermal energy which could be provided by the envelope itself is given by the parameter $\alpha_{\rm th}$. A second way of determining the outcome of common envelope evolution is to consider the angular momentum lost from the orbit. This leads to the γ prescription (e.g. Nelemans & Tout, 2004).

Recently it is suggested by Marchant et al. (2016) that very massive stars undergoing CHE may keep evolving in a stable way even with both stars filling their Roche lobes. In these so-called massive overcontact binaries (MOBs), mass

is transferred back and forth until they reach similar masses. Such MOBs, which could end in a tight double BH system, are only possible to form at high stellar masses and at low metallicity to enable CHE.

1.3.2.4 Accretion

Material which is transferred to a star or a stellar remnant has to overcome the counter pressure from the accretor. In the first place, there is the photon pressure resulting from the luminosity of the accretor. This pressure is enhanced by the photons emitted from the in-falling material as the accretion produces its own, additional luminosity, see Eq. (1.6). In the case of a star or a stellar remnant with a magnetic field, especially NSs, the magnetic pressure limits accretion and redirects charged particles.

In an isotropic situation mostly a spherical accretion is first established. But the conservation of angular momentum often leads to the build up of an accretion disk and the ejection of some material in two jets perpendicular to the disk. As the luminosity is radiated in all directions, the accretion of material through a disk is more efficient than spherical accretion, as only a fraction of the overall luminosity puts photon pressure on the material in the accretion disk.

Systems with ongoing accretion are observable in several parts of the electromagnetic spectrum, e.g. in X-rays. There are two main classes of X-ray binaries, high-mass X-ray binaries (HMXBs) and low-mass X-ray binaries (LMXBs). HMXBs usually contain a high-mass star and a compact object which accretes material from the wind of the companion star. On the other hand, there are the LMXBs which have a less massive donor which fills its Roche lobe and transfers material via stable RLO. As single BHs are usually not detectable in the eletromagnetic spectrum, they can only be detected as long as they are accreting material. Similarly, NSs are seen when they are actively accreting material.

It is more likely to observe systems containing NSs which are active as radio sources. In a double neutron star system (DNS) the chances are highest to observe at least one of them as a PSR. As PSRs are precise clocks they allow to infer several parameters of the binary. This works best when both NSs are observable as PSRs or when the system is tight enough and allows for the measurement of post-Newtonian parameters which describe effects appearing only in full GR.

1.4 Stars in galaxies

Independent, if stars are part of a binary or not, they are usually not completely isolated. They appear in star clusters or galaxies (e.g. Binney & Tremaine, 1987). In star clusters the stars are born from the same primordial gas cloud therefore the initial composition of these stars is very similar. In a galaxy the stars and the star clusters are associated in a larger ensemble. Also in a galaxy several episodes of star formation enrich the primordial gas cloud of later generations of stars with metals. The metal-rich ejecta from SNe may trigger new star formation.

Therefore, most galaxies cover a range of metallicities over different populations. There is usually a single most common metallicity in a galaxy as most galaxies experienced an enhanced star formation episode.

The closest galaxy is the spiral galaxy which contains the solar system, the Milky Way (MW). Stellar models which should resemble stellar evolution in the MW are calculated with a metallicity of $Z = 0.0088$ following Brott et al. (2011).

The two most prominent satellite galaxies of the MW are the Small Magellanic Cloud (SMC) and the Large Magellanic Cloud (LMC), which have, on average, lower metallicities than the MW. To investigate a very low metallicity, the stellar evolution in the dwarf galaxy IZwicky18 (IZw18) is studied by Szécsi et al. (2015). There, the matallicity is as low as about $Z = 0.0002$. Stellar models of these four metallicity environments are used to investigate GW driven mergers with ComBinE (Appendix A) in Chapter 3.

The distance between galaxies is much larger than the distance between individual stars or star clusters. Hence, observations of a distant galaxies are unable to resolve the individual stars. All information coming from a distant galaxy is therefore a superposition of its individual stars. Only the most extreme events, e.g. SNe, GRBs or GW driven mergers, are distinguishable from the overall galaxy to infer the nature of its origin. Observation of a distant galaxy always means looking back in time by at least millions of years. One needs to consider that stellar evolution and propagation of light take time and have to fit within the age of the Universe, to be observable nowadays. The time since the beginning of the Universe is known as the Hubble time, $t_{\rm hubble}$. When looking at distant astrophysical events, cosmological implications influence the coherent probabilities of the observation, see e.g. Section 3.5.2.3. One example is the expansion of the Universe which causes a characteristic redshift, z, to all observations. This is used as a distance or age measure of the most distant galaxies.

1.5 Population synthesis

The aim of population synthesis is to simulate a large and representative sample of stellar systems to understand global properties and underlying physics (see Sections 3.5.1 and 3.13.3) by comparison to observations of selected kinds of systems and events. In Chapter 2, this thesis deals with the investigation of binary systems in order to make predictions of the most uncertain phase of binary interaction, CE evolution. In Chapter 3, the current NS population and GW merger events are compared to the outcome of population synthesis simulations with the here newly developed code ComBinE (Appendix A). The statistics of a large population can also help to constrain the origin of a single, observed system. In Chapter 4, this is demonstrated with the young radio pulsar PSR J1755−2550 by simulating its possible formation to make predictions about the nature of its unseen companion star.

Chapter 2

Common-envelope ejection in massive binary stars: Implications for the progenitors of GW150914 and GW151226

In this chapter, a detailed discussion about the CE evolution is presented (published in Kruckow et al., 2016, Astronomy & Astrophysics, 596, A58).

Astronomy & Astrophysics manuscript no. 29420
October 20, 2016

Common-envelope ejection in massive binary stars

Implications for the progenitors of GW150914 and GW151226

M. U. Kruckow[1,⋆], T. M. Tauris[2,1], N. Langer[1], D. Szécsi[1,3], P. Marchant[1] and Ph. Podsiadlowski[4,1]

[1] Argelander-Institut für Astronomie, Universität Bonn, Auf dem Hügel 71, 53121 Bonn, Germany
[2] Max-Planck-Institut für Radioastronomie, Auf dem Hügel 69, 53121 Bonn, Germany
[3] Astronomical Institute of the Czech Academy of Sciences, Ondřejov, Czech Republic
[4] Department of Astronomy, Oxford University, Oxford OX1 3RH, UK

Received July 28, 2016; accepted October 14, 2016

ABSTRACT

Context. The recently detected gravitational wave signals (GW150914 and GW151226) of the merger event of a pair of relatively massive stellar-mass black holes (BHs) calls for an investigation of the formation of such progenitor systems in general.
Aims. We analyse the common-envelope (CE) stage of the traditional formation channel in binaries where the first-formed compact object undergoes an in-spiral inside the envelope of its evolved companion star and ejects the envelope in this process.
Methods. We calculated envelope binding energies of donor stars with initial masses between 4 and 115 $M_\odot$ for metallicities of $Z = Z_{\rm Milky\,Way} \simeq Z_\odot/2$ and $Z = Z_\odot/50$, and derived minimum masses of in-spiralling objects needed to eject these envelopes.
Results. In addition to producing double white dwarf and double neutron star binaries, CE evolution may also produce massive BH-BH systems with individual BH component masses of up to $\sim 50 - 60\ M_\odot$, in particular for donor stars evolved to giants beyond the Hertzsprung gap. However, the physics of envelope ejection of massive stars remains uncertain. We discuss the applicability of the energy-budget formalism, the location of the bifurcation point, the recombination energy, and the accretion energy during in-spiral as possible energy sources, and also comment on the effect of inflated helium cores.
Conclusions. Massive stars in a wide range of metallicities and with initial masses of up to at least 115 $M_\odot$ may shed their envelopes and survive CE evolution, depending on their initial orbital parameters, similarly to the situation for intermediate- and low-mass stars with degenerate cores. In addition to being dependent on stellar radius, the envelope binding energies and λ-values also depend on the applied convective core-overshooting parameter, whereas these structure parameters are basically independent of metallicity for stars with initial masses below 60 $M_\odot$. Metal-rich stars $\gtrsim 60\ M_\odot$ become luminous blue variables and do not evolve to reach the red giant stage. We conclude that based on stellar structure calculations, and in the view of the usual simple energy budget analysis, events like GW150914 and GW151226 might be produced by the CE channel. Calculations of post-CE orbital separations, however, and thus the estimated LIGO detection rates, remain highly uncertain.

Key words. stars: evolution – binaries: close – X-rays: binaries – stars: black holes – gravitational waves

1. Introduction

The majority of all massive stars are found in close binaries that will eventually interact through mass transfer during their stellar lifetimes (Sana et al. 2012). This sometimes leads to the formation of compact stellar X-ray sources (e.g. Tauris & van den Heuvel 2006) and, in some cases, to the eventual production of a pair of compact objects merging within a Hubble time. The evolution of massive single stars (e.g. Heger et al. 2003) has been investigated for many years and is still far from being well understood. The evolution of massive (interacting) binary stars is even more complex and can be significantly different (Podsiadlowski et al. 1992; Langer 2012).

Common-envelope (CE) evolution is thought to play a key role in the formation of many close-orbit binaries containing two compact objects, that is, white dwarfs (WDs), neutron stars (NSs), or black holes (BHs). Given their current small orbital separation (often much smaller that the radii of their progenitor stars), a binary interaction process must have been at work to reduce the orbital energy and angular momentum significantly. CE evolution is a good candidate for such a process since it is accompanied by a drag-force, arising from the motion of the in-spiralling object through the envelope of its companion star, which leads to dissipation of orbital angular momentum and deposition of orbital energy in the envelope. Hence, the global outcome of a CE phase is a reduced binary separation and ejected envelope, unless the system coalesces. The final post-CE separation, however, is difficult to predict as a result of our poor understanding of the complex physical processes involved in envelope ejection. The huge ranges in both length scales and timescales make hydrodynamical simulations troublesome. For general reviews on CE evolution, see for instance Iben & Livio (1993); Taam & Sandquist (2000); Podsiadlowski (2001); Ivanova et al. (2013).

There is strong evidence of past orbital shrinkage (i.e. similar to the expected outcome of a CE phase) in a number of observed close binary pulsars and WD pairs with orbital periods of a few hours or less. Examples include PSR 1913+16 (Hulse & Taylor 1975), PSR J0737−3039 (Burgay et al. 2003), CSS 41177 (Bours et al. 2014), and J0651+2844 (Brown et al. 2011). These systems are tight enough that gravitational-wave radiation will bring the two compact objects (e.g. NS-NS or WD-WD binary) into contact within a Gyr, which in some cases leads to a merger event.

⋆ e-mail: mkruckow@astro.uni-bonn.de

Similarly, the recent, and first, gravitational wave detection GW150914 (Abbott et al. 2016b) of the merger event of two relatively massive stellar-mass BHs ($36 + 29\ M_\odot$) raises interesting questions about its origin. This system has also been suggested to form through CE evolution (Belczynski et al. 2016). However, for massive stars there are other formations channels in which a binary system may evolve to become a tight pair of BHs. Three main formation channels to produce such a BH-BH pair are

i) the CE formation channel (i.e. traditional channel),
ii) the chemically homogeneous evolution (CHE) channel with or without a massive overcontact binary (MOB), and
iii) the dynamical channel in dense stellar environments.

i) The CE formation channel for BHs is similar to that which is believed to produce tight double NS systems (e.g. Tauris & van den Heuvel 2006, and references therein). In this scenario, the systems always enter a CE phase following the high-mass X-ray binary (HMXB) stage, during which the O-type star becomes a red supergiant and captures its BH companion. There are many uncertainties, however, involved in calculations of the in-spiral and the subsequent CE ejection. The evolution is often tidally unstable, and the angular momentum transfer, dissipation of orbital energy, and structural changes of the donor star take place on very short timescales ($< 10^3$ yr, Podsiadlowski 2001). A complete study of the problem requires detailed multi-dimensional hydrodynamical calculations, although early studies in this direction have difficulties ejecting the envelope and securing deep in-spiral (Taam & Sandquist 2000; Passy et al. 2012; Ricker & Taam 2012; Nandez et al. 2014; Ohlmann et al. 2016). The calculations along this route are therefore highly uncertain owing to our current poor knowledge of CE physics (Ivanova et al. 2013). As a consequence, the predicted detection rate of BH-BH mergers from the CE channel is uncertain by several orders of magnitude (Abadie et al. 2010), also partly as a result of the unknown amount of (asymmetric) mass loss that is associated with a possible supernova explosion (i.e. imparted momentum kick) when a BH is formed. Examples of population syntheses investigations of BH-BH binaries following the traditional channel with a CE scenario include Belczynski et al. (2002); Voss & Tauris (2003); Belczynski et al. (2008); Dominik et al. (2012); Mennekens & Vanbeveren (2014); Belczynski et al. (2016); Eldridge & Stanway (2016).

ii) The two other formation channels of BH-BH binaries avoid the CE phase altogether. In the CHE scenario for binaries (de Mink et al. 2009; Mandel & de Mink 2016; de Mink & Mandel 2016), the stars avoid the usual strong post-main sequence expansion as a result of effective mixing enforced through the rapidly rotating stars through tidal interactions. Hence, this works only for massive stars at low metallicity where strong angular-momentum loss due to stellar winds can be avoided. Marchant et al. (2016) presented the first detailed CHE models leading to the formation of BH-BH systems and demonstrated that MOB systems are particularly suited for this channel, enabling formation of very massive stellar-mass BH-BH mergers, that is in agreement with the detection of GW150914. Lower-mass BH-BH mergers like GW151226 ($14 + 8\ M_\odot$), however, cannot be formed from this scenario.

iii) Finally, the dynamical formation channel (e.g. Sigurdsson & Hernquist 1993; Portegies Zwart & McMillan 2000; Banerjee et al. 2010; Rodriguez et al. 2016) produces BH-BH mergers through encounter interactions in dense stellar clusters and thereby circumvents the need for mass transfer and CE evolution. In analogy to the other production channels mentioned above, the rate of BH-BH mergers from the dynamical formation channel is also difficult to constrain. Recent studies predict that this channel probably accounts for less than about 10% of all BH-BH mergers (e.g. Rodriguez et al. 2016).

In this paper, we investigate the prospects of envelope ejection from massive stars during the CE stage with an in-spiralling compact object, following the CE formation channel. In Sect. 2 we introduce the CE ejection criterion based on energy budget considerations. In Sect. 3 we present our calculated envelope binding energies and so-called λ-values of donor stars with initial zero-age main-sequence (ZAMS) masses between 4 and 115 $M_\odot$ for different metallicities (Milky Way-like: $Z_{\rm MW} \approx Z_\odot/2$, and IZw18-like: $Z = Z_\odot/50$), and derive minimum masses of in-spiralling compact objects (or non-degenerate stars) needed to eject these envelopes based on simple energy considerations. In addition, we analyse the stellar structure of pre-CE donor stars, with the aim of better understanding the location of the core boundary. A general discussion of our results is given in Sect. 4, where we also revisit the question of locating the bifurcation point of envelope ejection, debate the possibility of additional energy input from liberated recombination energy or accretion during in-spiral, and comment on the effect of inflated helium cores. Finally, we briefly discuss our results in relation to the LIGO merger events GW150914 and GW151226 in Sect. 5, before summarising our conclusions in Sect. 6.

2. Criterion for common-envelope ejection

The central problem in question is whether a massive binary will survive a CE evolution or result in an early merger event without ever forming a BH-BH system. Whether the donor star envelope is ejected successfully depends on the binding energy of the envelope, the available energy resources to expel it, and the ejection mechanism.

Following the (α, λ)-formalism introduced by Webbink (1984) and de Kool (1990), we can write the criterion for successful envelope ejection as $E_{\rm bind} \leq \alpha\,\Delta E_{\rm orb}$, where α is the efficiency of converting released orbital energy into kinetic energy that provides the outward ejection of the envelope. The total binding energy (gravitational plus internal thermodynamic contributions) of the donor star envelope at onset of the CE is given by

$$E_{\rm bind} = \int_{M_{\rm core}}^{M_{\rm donor}} \left(-\frac{GM(r)}{r} + U\right) dm \equiv -\frac{GM_{\rm donor}M_{\rm env}}{\lambda\, R_{\rm donor}}\,, \quad (1)$$

where G is the gravitational constant, $M(r)$ is the mass within the radius coordinate r of the donor star with total radius, $R_{\rm donor}$, total mass, $M_{\rm donor}$, core mass, $M_{\rm core}$, envelope mass, $M_{\rm env} \equiv M_{\rm donor} - M_{\rm core}$, and U is the specific internal energy (Han et al. 1994). Given that $E_{\rm bind}$ is evaluated at the moment the evolved donor star fills its Roche-lobe and initiates dynamically unstable mass transfer, leading to formation of the CE, we do not include the gravitational potential from the in-spiralling companion when calculating $E_{\rm bind}$ (see e.g. Podsiadlowski et al. 1992; Iben & Livio 1993, for alternative descriptions).

¿From integrations of detailed stellar models, the values of λ in Eq. (1) can be calculated (Dewi & Tauris 2000, 2001; Podsiadlowski et al. 2003) and tabulated (e.g. for use in population synthesis codes). Differences in λ-values may arise, for example, from the use of different stellar models, the degree of available recombination energy (Ivanova et al. 2015), enthalpy considerations (Ivanova & Chaichenets 2011; Wang et al. 2016),

and, in particular, from using different definitions of the core-envelope boundary (Tauris & Dewi 2001). The last problem is discussed in Sect. 4.1.

Since the in-spiral of the companion star often decreases the orbital separation by a factor of ~ 100 or more, we can approximate the change in orbital energy as

$$\Delta E_{\rm orb} = -\frac{GM_{\rm core}M_{\rm X}}{2\,a_{\rm f}} + \frac{GM_{\rm donor}M_{\rm X}}{2\,a_{\rm i}} \simeq -\frac{GM_{\rm core}M_{\rm X}}{2\,a_{\rm f}}\,, \qquad (2)$$

where $a_{\rm i}$ and $a_{\rm f}$ denote the initial (pre-CE) and final (post-CE) orbital separation, respectively, and $M_{\rm X}$ is the mass of the in-spiralling object (e.g. $M_{\rm BH}$ for a BH).

It is crucial for our purposes to investigate whether the ability of CE ejection depends on the masses of the two stars; that is to say, whether it is possible that the CE ejection will work for producing [8+8 $M_\odot$] BH-BH systems, for instance, but not [30+30 $M_\odot$] BH-BH systems. Hydrodynamical simulations and some observational evidence (see Sect. 3.2) indicate that the envelope ejection efficiency α does depend on the mass of the in-spiralling object, at least in the formation of WD-WD binaries. Furthermore, massive stars producing BHs have more tightly bound envelopes, and therefore higher values of $E_{\rm bind}$, than somewhat less massive stars with the same radius. The reason for this are the combined effects of a more shallow decline in mass density with radial coordinate and more envelope mass located outside the core boundary compared to less massive stars. On the other hand, the more massive stars are also able to release more orbital energy from in-spiral to a given final orbital separation. Therefore, we can consider the ratio $E_{\rm bind}/\Delta E_{\rm orb}$, which can be rewritten as

$$\frac{E_{\rm bind}}{\Delta E_{\rm orb}} = \frac{M_{\rm donor}}{M_{\rm X}}\,\frac{2(1-x)}{r_{\rm L}(q')\,x}\,\frac{R_{\rm core}}{\lambda\,R_{\rm donor}}, \qquad (3)$$

where $x \equiv M_{\rm core}/M_{\rm donor}$, $q' \equiv M_{\rm core}/M_{\rm X}$ and $r_{\rm L}(q') \equiv R_{\rm core}/a_{\rm f}$ is the dimensionless Roche-lobe radius (Eggleton 1983) of the stripped core with mass $M_{\rm core}$ and radius $R_{\rm core}$ (see Sect. 4.6 for discussions). For the values of $\Delta E_{\rm orb}$, it is assumed that the in-spiral stops just when the remaining core would fill its Roche lobe.

As a boundary of the remaining core, we take in this study the mass coordinate where the hydrogen abundance $X_H = 0.1$ (see Sects. 3.3 and 4.1 for extensive discussions).

In the above energy formalism, we have assumed a minimum energy requirement, that is, we have neglected any kinetic energy of the ejected matter and simply assumed that the velocity of the gas is zero at infinity. In reality, the material may be ejected from the binary with a higher velocity. For example, it has been argued (Nandez et al. 2014) that the kinetic energy of the ejecta material at infinity might be comparable to the initial binding energy of the envelope of the donor star. In addition, orbital energy transferred to the ejected material might not have been thermalised (Ivanova et al. 2013). The applied energy formalism used to predict the post-CE separation does not take these effects into account, unless a value of α lower than unity is chosen (see also Sect. 4.3).

As mentioned above, for successful envelope ejection, it is required that $(E_{\rm bind}/\Delta E_{\rm orb}) \leq \alpha$ (Livio & Soker 1988). We now investigate $E_{\rm bind}$ and λ for various stellar models and calculate for which values of $M_{\rm X}$ envelope ejection is possible if the sole energy source to eject the envelope is released orbital energy from the in-spiralling object (which can be a compact object, a star, or a planet).

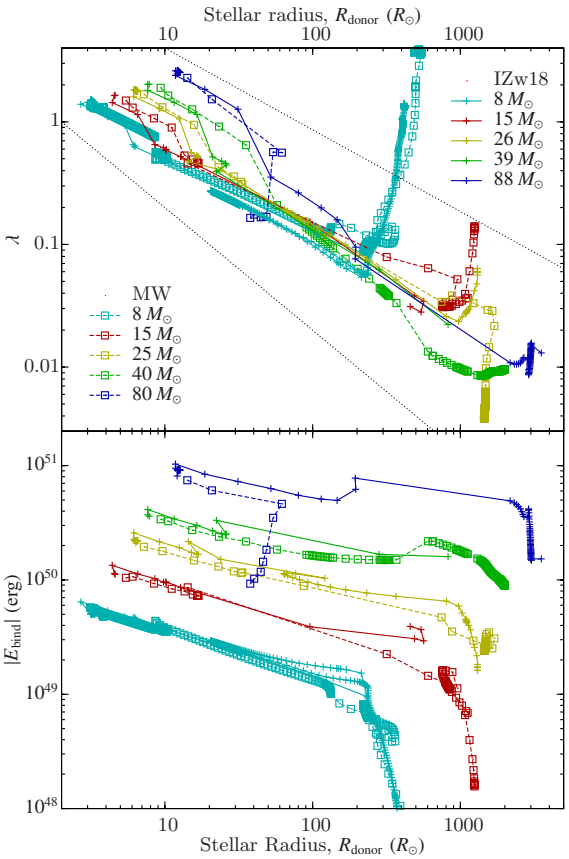

Fig. 1. Binding energy of the envelope, $|E_{\rm bind}|$ (lower panel), and its associated λ-value (upper panel), as a function of total stellar radius for two sets of models with $Z = Z_\odot/50$ (full lines, crosses) and $Z = Z_{\rm MW}$ (dashed lines, squares). Independent of mass and metallicity, and before reaching the giant stages ($R \lesssim 1000\ R_\odot$), the λ-values almost follow a power law with an exponent between $-2/3$ and -1 (upper and lower grey lines, respectively). The exceptions are stars with initial masses $\gtrsim 60\ M_\odot$ at $Z = Z_{\rm MW}$ (dashed blue line), which either become LBV stars, see Sect. 4.7, or have their envelopes stripped by enhanced wind-mass loss. The absolute binding energies of the 8 $M_\odot$ stars drop below the plotted range, down to approximately 2.7×10^{47} erg and 7.3×10^{46} erg for $Z = Z_\odot/50$ and $Z = Z_{\rm MW}$, respectively.

3. Results

In Fig. 1 we have plotted our calculated values of λ and $|E_{\rm bind}|$ according to Eq. (1) as a function of stellar radii, $R_{\rm donor}$, using the stellar models of Szécsi et al. (2015) for a metallicity of $Z = Z_\odot/50$ (resembling the metallicity of the irregular dwarf galaxy: IZwicky 18) and Brott et al. (2011) for $Z = 0.00876 \approx Z_\odot/2$ (which we assume to represent the average metallicity of the Milky Way, $Z_{\rm MW}$). The 8 $M_\odot$ models are calculated using the same code and input physics as the models of Szécsi et al. (2015) and Brott et al. (2011), respectively.

It is seen that, in general, the envelope becomes less bound with increasing values of $R_{\rm donor}$. Until the giant stages, the val-

ues of $|E_{\rm bind}|$ are moderately declining due to a combination of structural changes (i.e. growing core mass) and wind-mass loss, which affects the mass-density profile and decreases the mass of the envelope. The evolution at these early stages is more or less independent of metallicity, except for stars with ZAMS masses $\gtrsim 60\ M_\odot$, which become luminous blue variable (LBV) stars at high metallicities, cf. Sect. 4.7, or have their envelopes stripped by enhanced wind mass loss (Vink et al. 2001), and therefore do not evolve to become red supergiants (cf. the dashed blue track of the 80 $M_\odot$ star with $Z = Z_{\rm MW}$, which does not expand above 60 $R_\odot$).

The resulting change of λ with stellar radius (upper panel) is seen to be significantly stronger than changes caused by different stellar masses or metallicities. During the early stages of the expansion phase (up to $R \simeq 1000\ R_\odot$), the dependence on radius almost follows a power law with an exponent between $-2/3$ and -1.

The stellar tracks in Fig. 1 terminate at different evolutionary stages. Depending on stellar mass, the stars will reach the Eddington limit (Sect. 4.7) at different epochs of evolution. When a star reaches the Eddington limit, it initiates cycles of large-amplitude radial pulsations. This explains the horizontal clustering of points at the end of the stellar tracks in the $(R, |E_{\rm bind}|)$–diagram. This also explains why some tracks have increasing λ–values near the end (e.g. 15 $M_\odot$ stars at $Z = Z_{\rm MW}$, evolved beyond core carbon burning), whereas others have decreasing values of λ (e.g. 25 $M_\odot$ stars at $Z = Z_{\rm MW}$, only evolved to the end of core helium burning), or more or less constant values of λ (e.g. 40 $M_\odot$ stars at $Z = Z_{\rm MW}$, even less evolved to hydrogen shell burning). A careful inspection of the 15 $M_\odot$ track at $Z = Z_{\rm MW}$ shows decreasing and increasing λ-values before reaching the pulsating stage as a giant. This star experiences a final giant stage with significant radial expansion (up to $R = 1585\ R_\odot$), which results in the strong decline in $|E_{\rm bind}|$, causing the increase in λ.

Our calculated λ-values for massive stars (with initial masses of up to 115 $M_\odot$) are in broad agreement with those of Dewi & Tauris (2001) and Loveridge et al. (2011). The latter authors demonstrated that the calculated λ-values are largely independent of metallicity and applied wind mass-loss prescription. Our calculations more or less confirm this result, except for massive metal-rich stars (LBVs) or in case models are calculated with a very low mass-loss rate (much lower than for $Z = Z_\odot/50$), in which case the λ-values become higher for evolved stars (Podsiadlowski et al. 2003).

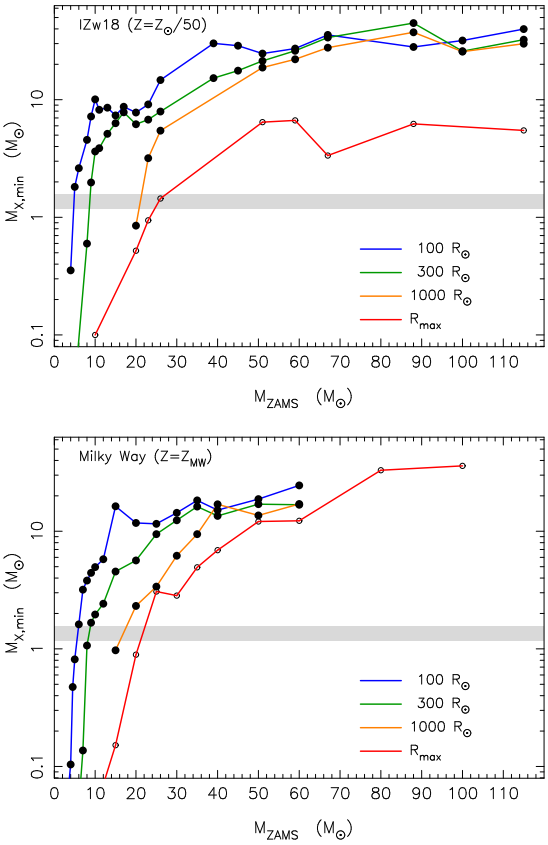

Fig. 2. Minimum mass of the in-spiralling object, $M_{\rm X,min}$ which is needed to expel the envelope during a CE evolution with $\alpha = 1$, for a given donor star radius as indicated by the coloured lines, as a function of ZAMS mass of the donor star, $M_{\rm ZAMS}$ for $Z = Z_\odot/50$ (upper panel) and $Z = Z_{\rm MW}$ (lower panel). $R_{\rm max}$ is the maximum radial extent during the stellar evolution. The grey band between 1.17 and 1.56 $M_\odot$ indicates masses of NSs observed in double NS systems (Martinez et al. 2015).

3.1. CE ejectability and companion star masses

To investigate the ejectability of the CE, we plot in Fig. 2 the minimum mass of the in-spiralling object, $M_{\rm X,min}$ which is needed to successfully expel the envelope during a CE evolution of stars with a given mass and metallicity at different evolutionary stages. The core radii of the stripped donor stars were calculated for naked helium star models (Sect. 4.6) using the stellar evolution code BEC (Yoon et al. 2010), which was also used to calculate our applied models of Szécsi et al. (2015) and Brott et al. (2011).

As expected from the decreasing values of $|E_{\rm bind}|$ with increasing stellar radius (Fig. 1), it is seen in Fig. 2 that evolved (expanded) donor stars more easily have their envelopes ejected by a relatively less massive in-spiralling companion than less evolved donor stars. In particular for the low-metallicity models ($Z = Z_\odot/50$, upper panel), we note the significant difference in envelope ejectability between massive stars evolved to radii $R \lesssim 1000\ R_\odot$ (blue, green, and orange lines) and giants ($R > 1000\ R_\odot$; red line). For example, for the 88 $M_\odot$ model with $Z = Z_\odot/50$ we find that it requires an in-spiralling object with a mass of at least $30 - 50\ M_\odot$ to eject the envelope in the former case, but only an object of $\sim 6\ M_\odot$ in case the envelope is ejected when the donor star is an evolved giant near its maximum radius of $\sim 3500\ R_\odot$.

The scatter of points along the coloured lines in Fig. 2 can be understood from the non-monotonic behaviour of $|E_{\rm bind}|$ as a function of stellar radius. For a given stellar mass, we see from Fig. 1 that $|E_{\rm bind}|$ is not monotonically decreasing as a function of increasing value of R. The reason for this are changes in the core structure during the stellar evolution.

We conclude that envelope ejection is facilitated for giant stars compared to less evolved stars, and as long as the in-spiralling BH masses are high enough (above the coloured lines in Fig. 2), they probably succeed in ejecting the envelopes of their host stars. Hence, for a given donor star mass and mass

of in-spiralling object, we can define a certain interval of stellar radii of each pre-CE donor star where CE ejection is possible (see Sect. 4.4), which translates into a range of pre-CE orbital periods combining Kepler's third law with an expression for the dimensionless Roche-lobe radius of the donor star (e.g. Eggleton 1983). For example, our 115 $M_\odot$ model star ($Z = Z_\odot/50$) might have its envelope ejected successfully when the mass of the in-spiralling BH is above $30 - 40$ $M_\odot$ and the star has evolved to $R \gtrsim 100$ $R_\odot$ (cf. Fig. 2, upper panel). The maximum radius reached by this star as a giant is 3922 $R_\odot$, at which point $M \simeq 93$ $M_\odot$. Hence, the orbital period interval for successful ejection of the envelope in this particular binary is between 875 and 7750 days for a 30 $M_\odot$ BH.

We stress the important caveat that the above calculations in Fig. 2 all assume a certain core boundary criterion ($X_H = 0.10$). We investigate in Sect. 3.3 more carefully at which bifurcation point we might expect CE ejection. Furthermore, we assume formation of a CE for all binary systems in Fig. 2. It is quite likely that several of these systems, especially with less evolved donor stars or mass ratios close to unity, may undergo stable Roche-lobe overflow (RLO, Pavlovskii et al. 2016). We also recall that in Fig. 2 we solely investigate the possibility of CE ejection regardless of the formation of any given binary. Some of the implied binary configurations in Fig. 2 are unlikely to be produced in nature in an isolated binary system. For example, it would be unexpected to have a 6 $M_\odot$ BH orbiting an 88 $M_\odot$ star (and, in particular, a 100 or a 115 $M_\odot$ star). The reason is that in order for the primary star (the initially most massive of the two ZAMS stars) to evolve first and eventually produce a BH, it must have had a ZAMS mass of more than ~ 60 $M_\odot$ (otherwise the initially least massive of the two stars, the secondary, would not be able to accrete sufficient material to reach 88 $M_\odot$). However, the core mass of a 60 $M_\odot$ star is ~ 30 $M_\odot$ and thus most likely too massive to leave a BH with a mass of only 6 $M_\odot$.

Finally, we note that the cores of the most massive (≥ 100 $M_\odot$) low-metallicity stars exceed 60 $M_\odot$ and probably terminate their lives in pair-instability SNe, which lead to the total disruption of the star without leaving behind any BH (Heger & Woosley 2002; Chatzopoulos & Wheeler 2012).

All calculations in Fig. 2 were performed assuming an envelope ejection efficiency parameter of $\alpha = 1$. The plotted curves therefore represent the most optimistic case for ejectability. Applying more realistic efficiencies of $\alpha < 1$ would require higher values of $M_{\mathrm{X,min}}$ and shift all plotted curves upward. On the other hand, we assumed that the release of orbital binding energy is the sole energy source available to eject the envelope. It is possible that other energy sources are at work as well (see Sect. 4.2), in which case the curves in Fig. 2 would be shifted downward to lower values of $M_{\mathrm{X,min}}$, reflecting that envelope ejection would be facilitated.

3.2. CE ejection: NS-NS and WD-WD binaries

Another interesting result seen in Fig. 2 is that HMXB systems with in-spiralling NSs are also able to eject the envelopes of donor stars with initial masses of up to about $22 - 25$ $M_\odot$ (depending on metallicity). These systems eventually evolve to become double NS systems following a post-CE episode of so-called Case BB Roche-lobe overflow (Dewi et al. 2002; Ivanova et al. 2003; Tauris et al. 2015). The grey band between 1.17 and 1.56 $M_\odot$ in Fig. 2 indicates the interval of measured NS masses in double NS systems (Martinez et al. 2015). Similarly, we note that evolved donors with masses lower than $8 - 10$ $M_\odot$ can have their envelopes ejected by even sub-solar mass objects, thereby allowing formation of tight double WD systems through CE evolution, as confirmed by observations (e.g. Zorotovic et al. 2010).

Interestingly enough, Ivanova et al. (2015) found that less massive in-spiralling stars plunge in faster than more massive in-spiralling stars, which results in a relatively higher heating rate, and low-mass intruders are therefore more effective in ejecting the envelopes since a smaller fraction of the released orbital energy is dissipated in the outer parts of the envelope. This suggests that low-mass stars are more efficient in removing the envelope (i.e. these binaries should have higher α-values than binaries with more massive companion stars, see also Podsiadlowski 2001). This hypothesis is supported by observations that indicate that the ejection efficiency increases for less massive companion stars (de Marco et al. 2011; Davis et al. 2012).

3.3. Bifurcation point of envelope ejection

One of the main problems in our understanding of CE ejection is the difficulty of localising the physical point of envelope ejection, that is, the bifurcation point, which separates the ejected envelope from the remaining core (Tauris & Dewi 2001). The three main categories proposed for determining the bifurcation point are nuclear energy generation, chemical composition, and thermodynamic quantities. A first-order constraint on the location of the core boundary (i.e. bifurcation point) can be taken as follows: it has to be somewhere between the hydrogen-depleted core ($X_H = 0$) and the mass coordinate of the bottom of the convection zone in the pre-CE star. From studies of direct collisions between a NS and a red giant, it was found (Lombardi et al. 2006) that some amount of hydrogen remains bound to the stellar core, following envelope ejection. This result therefore indicates $X_H > 0$. The problem with the upper limit is that the bottom of the outer convection zone often moves in mass coordinate during the CE ejection.

Our chosen core boundary criterion ($X_H = 0.10$) is easy to apply in practice to stars at most evolutionary stages. Changing the mass coordinate of the core-mass boundary by 1% results in only minor different values of E_{bind} and λ (of the order 10%) for stars in the Hertzsprung gap, whereas the effect of changing M_{core} by 1% is much larger (up to a factor 2) for stars on the giant branch that possess a steep density gradient near the core boundary.

In Fig. 3 we plot the integrated binding energy (solid lines) and the released orbital energy (dashed lines, calculated as the difference between E_{orb} at the starting point and the end point of the in-spiral) as a function of mass coordinate of our 88 $M_\odot$ stellar model ($Z = Z_\odot/50$) at two different evolutionary epochs of the star. The in-spiralling object corresponds here to either a NS (with a mass of 1.3 $M_\odot$) or a BH with a mass between 5 and 80 $M_\odot$. The upper panel is based on the structure of the star for $R = 194.5$ $R_\odot$ ($M = 86.94$ $M_\odot$, $M_{\mathrm{core}} = 51.82$ $M_\odot$) during hydrogen shell burning (Hertzsprung gap star), while the lower panel is for $R = 3530$ $R_\odot$ ($M = 76.65$ $M_\odot$, $M_{\mathrm{core}} = 52.35$ $M_\odot$) at its maximum expansion point as a giant.

In each panel in Fig. 3, the black points indicate when (during in-spiral) the released orbital energy will become lower than the binding energy of the layers outside the location of these points. Hence, if the in-spiralling object moves further inward than these crossing points, there is no possibility of ejecting the envelope, and the system merges. The location of these black crossing points should be compared to our defined location of

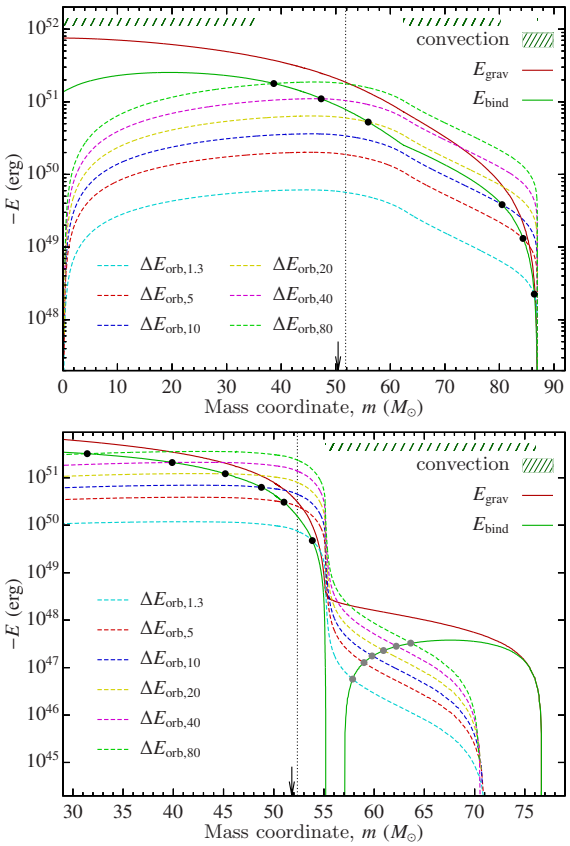

Fig. 3. Energy budget of the in-spiral process for the 88 $M_\odot$ donor star model with $Z = Z_\odot/50$ at two different evolutionary epochs: at the beginning of the Hertzsprung gap, $R = 194\ R_\odot$ (upper panel), and when the star reaches its maximum extent as a giant star, $R = 3530\ R_\odot$ (lower panel). The two solid lines mark the integrated binding energy of the material between the given mass coordinate and the surface. The green line (E_{bind}) includes the total energy (internal and gravitational binding energy, cf. Eq. (1)), while the red line (E_{grav}) only considers the gravitational binding energy. The six dashed curves represent the released orbital energy, ΔE_{orb} of an in-spiralling object with a given mass between 1.3 and 80 $M_\odot$ (cf. mass values in the legend). For the values of ΔE_{orb}, it is assumed that the in-spiral stops just when the remaining star would fill its Roche lobe. The vertical dotted line indicates the core boundary according to the $X_H = 0.10$ criterion (cf. Sect. 2), and the arrow marks the location of the maximum-compression point (cf. Sect. 4.1). The hatched regions shown at the top indicate convective layers. The black and grey dots mark the crossings when $E_{bind} = \Delta E_{orb}$, see Sect. 3.3 for details.

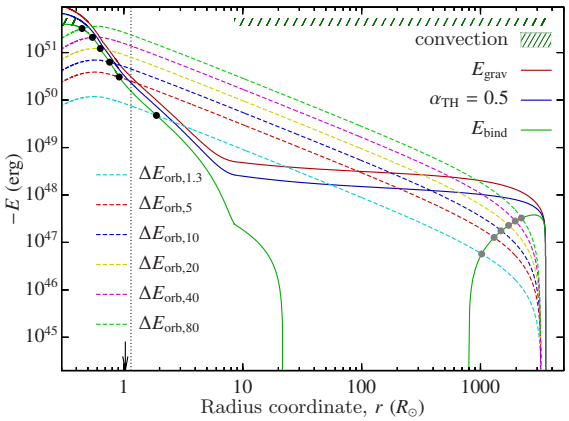

Fig. 4. Lower panel of Fig. 3 in radius coordinates. The additional blue solid line indicates where 50% of the internal energy is included in the calculated binding energy of the envelope.

the core boundary, shown as a vertical dotted line ($X_H = 0.10$). If the black crossing points are located outside (to the right of) our assumed core boundary, the system is expected to merge. In the upper panel (Hertzsprung gap star), this is the case for $M_X = 1.3-20\ M_\odot$, whereas $M_X = 40\ M_\odot$ and $80\ M_\odot$ succeed in envelope ejection. In the lower panel (star at the tip of the giant branch), all in-spiralling objects with masses $M_X \gtrsim 5\ M_\odot$ are in principle able to eject the envelope of the star[1].

In the lower panel of Fig. 3, the additional grey points mark the crossing where the released orbital energy exceeds the binding energy for the first time. Hence, an in-spiralling object has to spiral in at least to this depth to eject the material farther out. As long as there are no other energy sources, the in-spiral leading to successful envelope ejection is expected to stop somewhere between the grey and the black points. Depending on the amount of the internal energy that can actually be used to eject the envelope (see e.g. Han et al. 1994; Ivanova et al. 2015, for discussions), the crossing points should be be located somewhere between the solid green and red lines. The less the available internal energy, the deeper the in-spiral, and the more difficult it is for the binary system to eject the envelope (and survive instead of merging).

It should be noted that the region between the two crossings of ΔE_{orb} and E_{bind} shown in Fig. 3 has previously been discussed in terms of 'the energy expense' (Ivanova 2011), that is, the normalised excess energy available to the envelope after removal of all matter above a given mass coordinate.

3.4. Response of donor star to mass loss

The immediate adiabatic response of the remaining envelope layers depends on whether they are convective or radiative (Hjellming & Webbink 1987). On a longer timescale, the reaction of stripped cores to loss of their envelope depends on the amount of residual material remaining in the envelope. The expansion or contraction of the remaining shell occurs on the thermal timescale of the remaining layer. The resid-

[1] In Fig. 2 the limiting mass for the same model is slightly higher (about 6 $M_\odot$) because of differences in estimating the core radius. In Fig. 2 we applied naked (post-CE) helium star models (i.e. with zero pressure at their surfaces), whereas Fig. 3 probes the interior structure before envelope removal (i.e. with a non-zero surface pressure at a given point from the surrounding outer layers). Hence, in the latter case the in-spiralling object can penetrate deeper for a given core mass coordinate, thereby releasing more orbital energy and thus slightly facilitating envelope ejection. See also Sect. 4.6 on extended envelopes of helium stars.

ual hydrogen content following envelope ejection has been studied in the formation of WDs (Deinzer & von Sengbusch 1970), and in particular in LMXB systems (Tauris & Savonije 1999; Podsiadlowski et al. 2002; Istrate et al. 2016). However, for more massive stars the situation is less well explored.

In Fig. 4 we plot the lower panel of Fig. 3 in radius coordinates. The convective envelope of this massive giant star spans a wide range in radius, although its mass is lower than the core mass. The core boundary is located near a radius coordinate of $r \simeq 1\ R_\odot$. At first sight, the in-spiral might be expected to stop at the grey point, considering that at this location enough energy is released to unbind to material of the envelope farther out. However, when this point is well within hydrogen-rich material (which is clearly the case here), the system will not undergo final detachment at this location. As discussed above, the hydrogen-rich layers of the star will re-expand (and during this thermal adjustment the star may develop strong thermal pulses, cf. Ivanova et al. 2013). Hence, the mass transfer will continue and rebuild the CE. At this point, however, the drag force might be too weak to cause significant further in-spiral before the core of the donor star collapses (see e.g. Appendix A in Tauris et al. 2015, for an estimate of the timescale of the in-spiral). It is also possible that a self-regulated in-spiral is followed by additional RLO from either the core of the donor star (depending on the amount of residual hydrogen) or the in-spiralling companion star, and this leads to further plunge-in. This plunge could in turn be followed by an additional self-regulated phase, and so on, such that a repetitive pattern may occur (Ivanova et al. 2013). This pattern may repeat until the in-spiralling object reaches non-convective layers, at which point re-expansion of radiative material will process on a longer timescale. In the case of our giant star model in Fig. 4, the pre-CE convective boundary is located at a radius coordinate of about 8 $R_\odot$.

The removal of the innermost hydrogen-rich layers may possibly proceed through dynamical stable mass transfer (this still has to be confirmed by numerical calculations), until the mass of the diluted giant envelope reaches below a critical threshold value and the remaining envelope collapses and the binary finally becomes detached. If mass is removed to below the bifurcation point, then the remaining core contracts on its thermal timescale.

To summarise the above, we conclude that the termination point of the in-spiral is difficult to estimate accurately. We expect that at first, the plunge-in of the in-spiral will stop somewhere in the interval where the green curves bent vertically downward (i.e. where $E_{\rm bind} \gtrsim 0$) in Fig. 3 (lower panel) and Fig. 4. The further evolution and the final post-CE orbital separation is not trivial to calculate and depends on the details of the physics of the CE ejection process, the response of the remaining core to mass loss, and the amount of liberated accretion energy.

We also conclude that the in-spiral will only come to an end and lead to successful CE ejection when both of the following conditions are fulfilled:

- The remaining amount of hydrogen is below the threshold for re-expansion of an envelope (i.e. the bifurcation point is located in a radiative layer with $X_H > 0$).
- The released orbital energy is sufficient to remove the envelope (i.e. the final location where in-spiral ends is between the black and grey points in Figs. 3 and 4).

The last point illustrates once again the difficulty in population synthesis modelling of final post-CE orbital separations and thus explains the huge uncertainty in the LIGO merger rates determined from this method (Abadie et al. 2010). Whereas the separation between the black and grey points for the massive giant star plotted in Figs. 3 (lower panel) and 4 may cover a spread in mass coordinates of about 4 $M_\odot$ (less than 8% of the remaining core mass), the corresponding spread in radius coordinates (and thus the spread in final post-CE orbital separation) is an astonishing factor 500!

It is therefore evident from our analysis that LIGO merger rates estimated from population synthesis of the CE formation channel (e.g. Belczynski et al. 2002; Voss & Tauris 2003; Belczynski et al. 2008; Dominik et al. 2012; Mennekens & Vanbeveren 2014; Belczynski et al. 2016; Eldridge & Stanway 2016) must be highly uncertain and all quoted rates should be taken with a huge grain of salt (let alone other uncertain effects in addition to CE evolution).

4. Discussions

4.1. Bifurcation point revisited

A method suggested by Ivanova (2011) is to locate the core boundary, after thermal readjustment, at the (pre-CE) mass coordinate in the hydrogen shell corresponding to the local maximum of the sonic velocity (i.e. at the maximum-compression point, $M_{\rm cp}$ where P/ρ has a local maximum). It was argued that if a post-CE star has a final mass smaller than $M_{\rm cp}$, then the star will shrink. However, if it has any mass beyond this location, the star will continue to expand on the local thermal timescale. This may give rise to a new episode of mass transfer, or possibly a pulse.

For our calculations of the core boundary in this study, we chose to use the $X_H = 0.10$ criterion (Dewi & Tauris 2000), which is often used in the literature. Interestingly enough, we find that this point coincides closely to the maximum-compression point in the hydrogen shell burning layer in most of our models. For all stellar models we investigated that are evolved beyond core hydrogen burning (independent of mass and metallicity), the locations of the core boundary using the $X_H = 0.10$ criterion and the maximum-compression point $M_{\rm cp}$ are often consistent to within 1%, and always within 4% (except for our few high-metallicity models with masses $< 10\ M_\odot$, where the discrepancy can be up to 8% in mass coordinate).

This general agreement is evident from comparing our λ-values, calculated with the $X_H = 0.10$ criterion, with those recently calculated by Wang et al. (2016) for population I stars of up to 60 $M_\odot$, using the $M_{\rm cp}$ criterion.

4.2. Other energy sources

According to Ivanova et al. (2013), the question of additional energy sources, other than the release of orbital energy, depends partly on the extent to which the envelope is ejected directly by spiral shocks, developing from the orbital motion and tidal arms trailing the two stars (Ricker & Taam 2012), or indirectly by heating and a pressure gradient. If the donor star core expands as a consequence of mass loss, it could do mechanical work on the envelope and change the boundary conditions for the integral in Eq. (1). Enforcing corotation of the envelope through tidal heating may produce an energy sink.

Ivanova et al. (2015) demonstrated that heat input leading to kinetic energy deposition within the envelope is not just a simple function of radius and mass. It depends on the structure of the pre-CE donor star (e.g. mass density profile and the degree of corotation), the initial mass ratio between the two stars, and on how angular momentum is transported through the CE. In other

words, the authors concluded that the envelope ejection process depends on i) the amount, ii) the location, and iii) how rapidly the released energy is transferred to the envelope, and they predict two types of outcomes: 'runaway' and 'self-regulated' envelope ejection.

4.2.1. Recombination energy

The inclusion of recombination energy of hydrogen and helium (e.g. Han et al. 1994) has been argued to be a promising candidate for producing successful envelope ejection (e.g. Ivanova et al. 2015, and references therein). Recent 3D hydrodynamical modelling (Nandez et al. 2015) taking the released recombination energy reservoir into account, let to the first successful CE ejection and production of a post-CE double WD system.

Figure 5 shows the significance of recombination energy in units of the total internal energy U in the envelopes of our stellar models. Within the core of the star, the internal energy is fully dominated by radiation and gas pressure. The recombination energy contributes strongest to the total internal energy in the outer regions of the envelope with a mass density inversion.

Whereas the recombination energy can be an important contribution (up to $\sim 55\%$ of U) for low- and intermediate-mass stars, it does not play a role for massive stars when we apply the $X_{\rm H} = 0.10$ criterion for the core boundary (red and blue arrows). For BH progenitors, the contribution is typically lower than 1%, which may potentially lead to problems using current hydrodynamical simulation codes because they apparently only succeed to eject the envelope of low-mass stars when taking the released recombination energy into account (Nandez et al. 2015). As Fig. 5 points out, the metallicity content has no significant effect on this general behaviour.

Changing the bifurcation point criterion, however, such that the remaining core is assumed to include 1 $M_\odot$ of hydrogen, causes the relative contribution of recombination energy to be more important (green arrows) and thus play a role in facilitating CE ejection. An additional effect that favours successful ejection of CEs in wide systems is that the released recombination energy is highest for the most extended (coldest) stars.

4.2.2. Enthalpy

Ivanova & Chaichenets (2011) argued that including the enthalpy in the energy budget typically results in λ-values that are higher by a factor of 2 to 3 (see also Wang et al. 2016). Whether enthalpy should be included in the CE energy budget at all is controversial and may depend on the timescale of the CE ejection. Rather than being a new energy source, the main contribution of the P/ρ term is that it redistributes energy: it adds more kinetic energy to the gas ejected from the outer envelope regions at the expense of the energy of the inner regions of the envelope (Ivanova et al. 2013). This may cause the formation of a circumbinary disk if the inner envelope material is barely ejected at the escape velocity. Such a circumbinary disk can act as an additional sink of orbital angular momentum losses (e.g. Soberman et al. 1997; Spruit & Taam 2001). As a result of the dispute and uncertainty of potentially including the P/ρ term in Eq. (1), we disregard this term in our modelling.

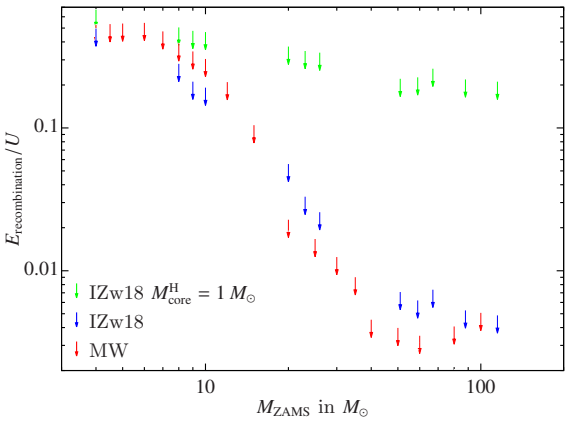

Fig. 5. Recombination energy in the envelope as a function of ZAMS mass. The plot shows the maximum contribution of recombination energy (from H, He and H_2) to the total internal energy (U) obtained during the evolution of the stars. These maximum values are always reached when the stars are near their largest radial expansion as giants. The red arrows are for $Z = Z_{\rm MW}$ and the blue ones for $Z = Z_\odot/50$. The green arrows are also calculated for our $Z = Z_\odot/50$ models, but assume a larger remaining core that includes 1 $M_\odot$ of hydrogen.

4.2.3. Liberated accretion energy

Release of accretion energy is an additional energy source. This contribution may even dominate that of orbital energy release in the beginning of the in-spiral, for the reason that in the outer envelope layers the in-spiral timescale is relatively long and the binding energy per unit mass is low. In recent studies of hydrodynamical simulations, MacLeod & Ramirez-Ruiz (2015a,b) found that a compact object such as a NS embedded in a CE only accretes a very modest amount of material during its in-spiral as a result of a density gradient across its accretion radius, which strongly limits accretion by imposing a net angular momentum to the flow around the NS. This conclusion supports earlier work by Ricker & Taam (2012), who also found that the true accretion rate of the accreting star is much lower than predicted by the Bondi-Hoyle prescription. Nevertheless, even modest accretion rates constrained by the Eddington limit can contribute significant heat to the CE energy budget.

Voss & Tauris (2003) introduced in their simulations the inclusion of released accretion energy from the in-spiralling compact object (thus facilitating envelope ejection), and hence demonstrated that the expected aLIGO detection rate of BH-BH mergers should strongly dominate that of NS-NS systems. The energy input from accretion onto a BH during a CE phase is given by $\Delta E_{\rm acc} = \eta\,\dot{M}_{\rm Edd} c^2\,\tau_{\rm CE}$, where the Eddington accretion limit (van den Heuvel 1994) can be estimated as

$$\dot{M}_{\rm Edd} = 4.4 \times 10^{-9}\ M_\odot\,{\rm yr}^{-1} \left(\frac{M_{\rm BH}}{M_\odot}\right) \frac{r_*}{(1+X_H)}\,, \qquad (4)$$

yielding

$$\Delta E_{\rm acc} = 1.6 \times 10^{48}\ {\rm erg} \left(\frac{M_{\rm BH}}{M_\odot}\right) \left(\frac{\tau_{\rm CE}}{1000\ {\rm yr}}\right) \left(\frac{\eta}{0.20}\right) \frac{r_*}{(1+X_H)}\,. \qquad (5)$$

Here, $\tau_{\rm CE} < 10^3$ yr is the duration of the CE phase (dictated by the thermal timescale of the envelope, Ivanova et al. 2013), X_H is the mass fraction of hydrogen in the donor-star envelope, η is the accretion radiation efficiency, and $r_* = R_{\rm ISCO}/(GM_{\rm BH}/c^2)$ is the location of the innermost stable circular orbit (ISCO). Both $\eta = 0.06 - 0.42$ and $r_* = 1 - 6$ depend on the (here assumed to be prograde) spin of the accreting BH.

As an example, a 35 $M_\odot$ BH with an Eddington-limited accretion rate ($\sim 10^{-7}$ $M_\odot$ yr^{-1}) would therefore be able to accrete about 10^{-4} $M_\odot$ while embedded in a CE and release a total energy output of $\sim 5 \times 10^{49}$ erg, which can potentially be used to eject the envelope. As can be seen from Fig. 4, a heat input of this amount could significantly facilitate envelope ejection even in massive stars. However, as we discuss in Sect. 4.2.4 below, this possibility depends on the physics of energy transport in the envelope to be ejected.

In addition to heating, we note that accretion can also help in envelope ejection by the possible formation of a jet by the inspiralling object (Soker 2004, 2016). Especially BHs and NSs are expected to potentially launch very energetic jets. In a scenario recently suggested by Soker (2015), so-called grazing envelope evolution might be made possible if a compact companion star manages to accrete matter at a high rate and launch a jet that removes the outskirts of the giant envelope, hence preventing the formation of a CE. However, further investigation of this model is needed.

4.2.4. Convective energy transport

In order to eject a CE, the liberated energy, either from the inspiral of the compact companion, from accretion onto this compact companion, or from the recombination of ionised envelope material needs to be converted into mechanical energy. If all these processes take place inside a fully convective envelope, the question arises whether a part of the liberated energy, which is at first present in the form of heat, would be quickly transported to the top of the envelope, where it would be radiated away.

The efficiency of this energy loss will depend on the ratio of the timescale of energy liberation to the convective timescale. If it is small, then convective energy loss will be negligible. If the ratio is near one or higher, convective energy loss may be important. As the convective timescale is of the order of the dynamical timescale of the star, it appears possible that convective energy loss is relevant for all three forms of energy liberation mentioned above. It will require models of time-dependent convection to quantify this effect.

4.3. Ejection efficiency parameter

So far, we have not addressed the value of the ejection efficiency parameter, which we have simply assumed to be $\alpha = 1$. There are several reasons, however, why a realistic value of the ejection efficiency parameter would be $\alpha < 1$. An example is radiative losses from the CE (e.g. as discussed above in Sect. 4.2.4) or internal and kinetic energy of the ejecta material.

Energy loss from the envelope photosphere is relevant for relatively slow, thermal timescale CE events (in which case there might also be significant energy input from the naked, hot stellar core). Moreover, recent work by Nandez et al. (2015) demonstrated a case where between 25% to 50% of the released orbital energy is taken away as kinetic energy of the ejected material, implying $\alpha < 0.75$ from this effect alone.

Assuming lower and more realistic values of α (e.g. 0.3 – 0.7) would cause all the solid lines in Fig. 2 to move up, and all dashed lines in Figs. 3 and 4 to move down. For example, in Figs. 3 and 4, the line of the 5 $M_\odot$ in-spiralling object for $\alpha = 1$ is comparable to that of a 10 $M_\odot$ in-spiralling object with $\alpha \approx 0.5$.

4.4. Post-CE orbital separations in population synthesis

For a discussion of predicted LIGO detection rates of merging BH-BH, NS-NS, or BH-NS binaries, it is of interest to evaluate the amount of fine-tuning needed for a given binary system to survive CE evolution, and to probe how the mapping of pre-CE orbital separations to post-CE orbital separations are performed in a typical population synthesis code. In such codes, it is usually assumed that all material is removed above a core boundary at $X_H = 0.10$. In the discussion below we therefore apply this bifurcation point criterion.

In Fig. 6 we plot post-CE orbital separations, $a_{\rm f}$ as a function of pre-CE orbital separations, $a_{\rm i}$ for the 88 $M_\odot$ ($Z = Z_\odot/50$) donor star investigated in this paper. In the upper panel, we show the results for in-spiralling companions (BHs) of masses: 5, 10, 35 and 80 $M_\odot$, in all cases assuming an envelope ejection efficiency parameter of $\alpha = 1$. In the lower panel, we assume $M_{\rm X} = 35$ $M_\odot$ (i.e. resembling the progenitor system of GW150914) for different values of α (0.25, 0.50, 0.75 and 1), and including one additional case (for $\alpha = 1$) where we assumed injection of released accretion energy of $\Delta E_{\rm acc} = 5 \times 10^{49}$ erg.

In each panel we show GW and CE lines, corresponding to post-CE orbital separations below which the system will merge within a Hubble time (13.8 Gyr) and thus become detectable as a gravitational wave source, or coalesce during the CE in-spiral and thus not survive as a binary system, respectively. For each system, the intervals of $a_{\rm i}$, for which the binary successfully survives and eventually produces a LIGO merger event within a Hubble time, are marked with a hatched pattern. For example, the upper panel shows that only the two in-spiralling objects with masses $M_{\rm X} = 80$ $M_\odot$ and $M_{\rm X} = 35$ $M_\odot$ can successfully eject the CE of our donor star (which has an initial mass of 88 $M_\odot$ and $Z = Z_\odot/50$) before it reaches its giant stage. The in-spiralling object with $M_{\rm X} = 10$ $M_\odot$ is only able to eject the envelope of the donor star when the latter has evolved to its very last expansion phase as a giant. The in-spiralling 5 $M_\odot$ cannot eject the envelope at all (see also Fig. 2). For $M_{\rm X} > 27$ $M_\odot$, there are two windows of $a_{\rm i}$ intervals that allow CE ejection.

Whereas for a massive in-spiralling object of 80 $M_\odot$ we find solutions for the entire interval $60 \leq a_{\rm i} < 10\,000$ $R_\odot$, an in-spiralling object with $M_{\rm X} = 35$ $M_\odot$ only has solutions for $130 < a_{\rm i} < 400$ $R_\odot$ and $1300 < a_{\rm i} < 8000$ $R_\odot$. Given their lower values of $a_{\rm f}$, the $M_{\rm X} = 35$ $M_\odot$ systems produce shorter delay-time binaries (i.e. they merge on a shorter timescale following the CE ejection than the $M_{\rm X} = 80$ $M_\odot$ systems).

In the lower panel of Fig. 6, an envelope ejection efficiency close to 100% ($\alpha = 1$) is needed for the system with $M_{\rm X} = 35$ $M_\odot$ to survive. An injection of $\Delta E_{\rm acc} = 5 \times 10^{49}$ erg will result in somewhat less in-spiral and therefore wider post-CE binaries with longer delay-times.

The points on each curve in Fig. 6 were calculated using a specific subroutine of the binary population synthesis code of Kruckow et al. (in prep.), which estimates the post-CE orbital separations. This code makes use of interpolations of stellar tracks using a finite grid resolution of stellar radii that is combined with the dimensionless Roche-lobe radius (Eggleton 1983) to determine $a_{\rm i}$ for each value of $M_{\rm X}$. The values of $a_{\rm f}$

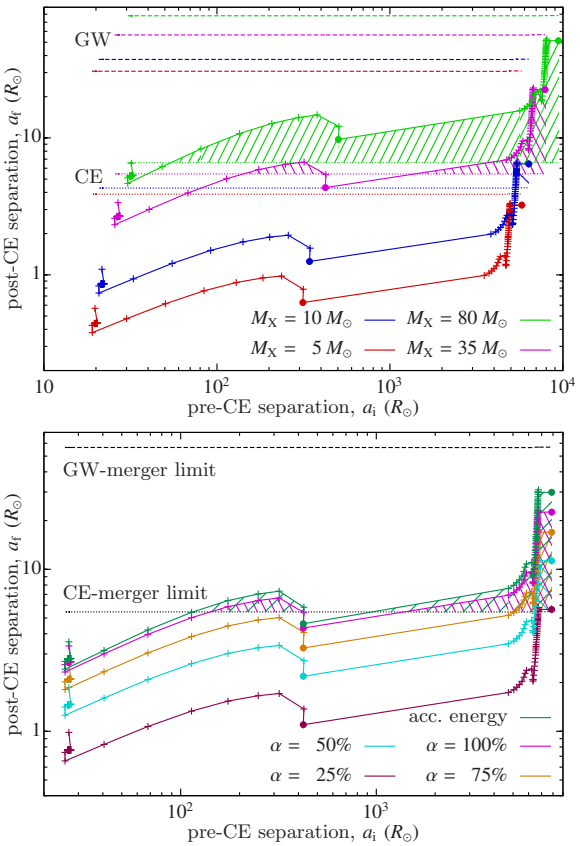

Fig. 6. Mapping of pre-CE to post-CE orbital separations as done in population synthesis (see Sect. 4.4) when applying the (α, λ)-formalism. The donor is assumed to be our 88 $M_\odot$ ($Z = Z_\odot/50$) star. The in-spiralling objects (BHs) have masses of between 5 and 80 $M_\odot$. Below the dashed GW lines, the post-CE systems will merge within a Hubble time. Below the dotted CE lines, the in-spiral continues to the core of the donor star and leads to coalescence (i.e. the relaxed He-core fills its Roche-lobe, cf. Sect. 4.6, and the binary will not survive). In the upper panel, the different colours mark the mass of the in-spiralling object (using $\alpha = 1$); in the lower panel, they represent different values of α (for a fixed value of $M_X = 35\ M_\odot$). The dark green (upper) line in the lower panel was calculated for $\alpha = 1$ and an additional accretion energy of 5×10^{49} erg, see Sect. 4.2.3. The hatched regions indicate systems that are expected to successfully produce LIGO sources. The solid dots mark the models shown in Figs. 3 and 4.

are then determined from tabulated values of λ associated with the stellar grids, following Eq.(1) and combined with $|E_{\rm bind}| = \alpha \cdot |\Delta E_{\rm orb}| + \Delta E_{\rm acc}$.

4.5. Post-CE merger before core collapse?

For massive binaries undergoing CE evolution with deep in-spiral of the BH, we investigated if it is possible that the timescale of gravitational-wave radiation (GWR) of the post-CE binary is shorter than the remaining lifetime of the exposed core. The result is illustrated in Fig. 7. We studied the fate of our 88 $M_\odot$ star ($Z = Z_\odot/50$) under the assumption of onset of a CE when this star is near its maximum extent as a giant ($R = 3530\ R_\odot$ at an age of 2.83 Myr, cf. Fig. 3 (lower panel) and Fig. 4). Furthermore, we assumed a mass of the in-spiralling BH of 30 $M_\odot$.

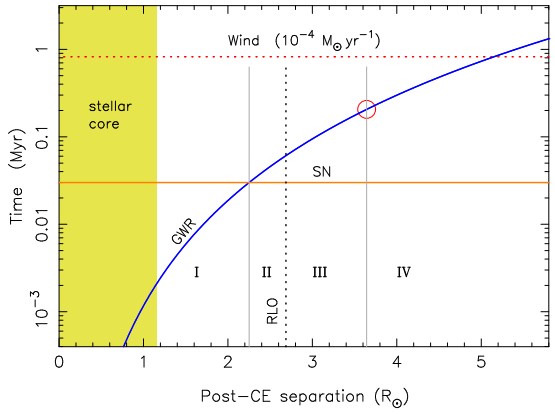

Fig. 7. Final fate of a post-CE binary system composed of a naked helium core and a BH as a function of orbital separation after envelope ejection. The chosen donor star model is that of the 88 $M_\odot$ star ($Z = Z_\odot/50$) at its maximum extent as a giant, cf. Figs. 3 (lower panel) and 4. The mass of the exposed helium core is $M = 52.35\ M_\odot$ and the BH is assumed to have a mass of 30 $M_\odot$. The blue line (GWR) represents the merger time due to gravitational-wave radiation, the orange line (SN) represents the remaining lifetime of the core until it collapses, and the red dotted line (Wind) represents the timescale $(a/\dot{a}_{\rm wind})$ of orbital widening due to stellar wind mass loss. The yellow shaded region marks the core region ($X_H < 0.10$). See Sect. 4.5.

In Fig. 7 region I marks the extreme case where GWR would be strong enough to merge the binary before a BH-BH binary is produced, that is, before the collapse of the exposed core. However, the vertical dotted line marks the orbital separation of the BH where the core would fill its Roche lobe and continue mass transfer. Hence, regions I and II would most likely lead to an early merger in any case. In region III, the orbit will decrease in size before core collapse as a result of GWR, while in region IV the orbit widens before core collapse as a result of the stellar wind.

For this system, we estimate the remaining lifetime of the post-CE exposed core ($M = 52.35\ M_\odot$) to be about 30 kyr (given that the progenitor star was evolved close to the onset of carbon burning). For the merger time of the binary we find from integration (assuming time-independent point masses M_1 and M_2 in a circular orbit with separation, a, following Peters 1964)

$$\tau_{\rm GRW} = \frac{1}{4}\frac{a}{|\dot{a}_{\rm GWR}|} = \frac{5}{256}\frac{c^5}{G^3}\frac{a^4}{M_1 M_2 (M_1 + M_2)}\,, \qquad (6)$$

where c is the speed of light. The steep dependence on a means that systems will spend most of their in-spiral time at a large separation. They only evolve to half their initial separation in about 94% of the full merger time calculated from Eq. (6).

Therefore, taking into account the finite size of the exposed core only changes the true merger time slightly.

It is seen in Fig. 7 that if a post-CE survival criterion is that the exposed core is not allowed to fill its Roche lobe (i.e. ruling out all post-CE orbital separations to the left of the vertical dotted line), then at least for this particular system, it is not possible for the post-CE system to merge as a result of GWR before the naked core terminates its life and undergoes core collapse to form a BH. Hence, all systems to the right of the dotted line would produce BH-BH binaries and eventually become LIGO sources.

We can determine the critical separation at which the orbital decay due to GWR ($\dot{a}_{\rm GWR}$) is exactly opposed by the orbital widening due to (fast, Jeans mode) stellar wind mass loss ($\dot{a}_{\rm wind}$) with a rate of $\dot{M}_{\rm wind}$ as

$$a_{\rm crit} = \left(\frac{64}{5} \frac{G^3}{c^5} \frac{M_1 M_2 (M_1 + M_2)^2}{\dot{M}_{\rm wind}} \right)^{1/4} . \quad (7)$$

For the system in Fig. 7, we find $a_{\rm crit} = 3.65\ R_\odot$ (cf. red circle) for $\dot{M}_{\rm wind} = 10^{-4}\ M_\odot\,{\rm yr}^{-1}$.

4.6. Extended envelopes of helium stars

Massive, luminous stars, both hydrogen-rich and helium (Wolf-Rayet) stars, reach the Eddington limit in their interiors and develop inflated and extremely diluted envelopes (Ishii et al. 1999; Petrovic et al. 2006; Sanyal et al. 2015). Applying these extended radii for naked helium star models would prevent inspiral to small separations if a criterion for survival of the CE ejection would be that the exposed helium core is not allowed to fill its Roche lobe. Hence, our estimated values of $R_{\rm core}$ (and thus $M_{\rm X,min}$) would be much higher if such a conservative criterion was at work, which would make CE ejection even more difficult.

In our estimates of $R_{\rm core}$ for naked helium stars, we followed Sanyal et al. (2015) and defined the core radius as the distance from the centre of the star to where the ratio β of gas pressure to total pressure drops below 0.15 for the first time. This definition agrees fairly well with the location of the point where the density gradient is steepest ($\partial^2 \log\rho / \partial m^2 = 0$).

To check the validity of this relaxed criterion for $R_{\rm core}$, we performed calculations of Roche-lobe overflow for a BH placed inside the extended envelope of a helium star, using the stellar evolution code BEC (Yoon et al. 2010, and references therein). As expected, the BH simply peels off the outer envelope of the star, which might have been lost in a strong wind in any case.

To summarise, applying the relaxed criterion on $R_{\rm core}$ does not result in yet another episode of dynamically unstable mass transfer, and by applying these smaller core radii, we therefore probe the conditions under which the CE is most easily ejected.

4.7. Luminous blue variables

In our galaxy as well as in the Large Magellanic Cloud, stars more massive than $\sim 60\ M_\odot$ are not found to be cooler than about 20 000 K (Humphreys & Davidson 1994; Castro et al. 2014). That single stars in the considered luminosity range are thought to develop into hydrogen-poor Wolf-Rayet stars (Langer et al. 1994; Meynet & Maeder 2005) implies that they do loose their envelope even without the help from a binary companion. The so-called luminous blue variables (LBVs) are located close the this observational border (Smith et al. 2004), and the LBV variability and outbursts are thought to be connected to the stellar Eddington limit (Ulmer & Fitzpatrick 1998; Sanyal et al. 2015).

The envelopes of stellar models near the Eddington limit may have very low binding energies (Gräfener et al. 2012; Sanyal et al. 2015). In the limit of near zero binding energies, a companion star could indeed kick off these envelopes without the requirement of a significant in-spiral. A similar situation is reached in the final phases of the AGB evolution of low- and intermediate mass stars. For stars in this mass range, there is observational evidence that in some cases, the common envelope ejection occurs with an insignificant orbital decay (Nelemans et al. 2000).

Consequently, stars near their Eddington limit, when they capture a companion into their envelope, may be prone to loose their envelope easily, but they will not produce sufficiently tight binaries to serve as progenitors for double compact mergers. The mapping of the Eddington limit throughout the parameter space of mass and metallicity is far from complete. Ulmer & Fitzpatrick (1998) pointed out that the Eddington limit is reached at higher masses for lower metallicity. This is confirmed by Sanyal et al. (2016, in prep.), who find a limiting mass of $\sim 100\ M_\odot$ at the metallicity of the Small Magellanic Cloud.

4.8. Convective core overshooting

The models presented in this work apply a convective core-overshooting parameter of $\delta_{\rm OV} = 0.335$ pressure scale heights ($H_{\rm p}$), meaning that the radius of the convective core is equal to the radius given by the Ledoux criterion at the formal core boundary plus an extension equal to $0.335\,H_{\rm p}$. Neglecting, or strongly reducing, the amount of convective core overshooting leads to a significantly different interior structure, not only because of its reduced core mass, but also owing to the star burning the main part of its helium core already in the Hertzsprung gap, before ascending the giant branch. For example, for our 20 $M_\odot$ model with $Z = Z_{\rm MW}$ at the base of the giant branch, the central helium mass abundance, $Y_c = 0.24$ for $\delta_{\rm OV} = 0.0$ compared to the case of $Y_c = 0.99$ for $\delta_{\rm OV} = 0.335$. The calculated envelope binding energies and λ-values are therefore also affected by the choice of $\delta_{\rm OV}$. For example, for the 20 $M_\odot$ star mentioned above, we find that when it is evolved to a radius of $R = 1200\ R_\odot$, then $|E_{\rm bind}|$ can be almost a factor 10 smaller (and λ a factor of 10 larger) using $\delta_{\rm OV} = 0.0$ compared to $\delta_{\rm OV} = 0.335$. The corresponding core masses are about 5.9 $M_\odot$ and 7.2 $M_\odot$, respectively. However, for the former case ($\delta_{\rm OV} = 0.0$) the central mass density is significant higher, leading to less tightly bound envelopes. For a 40 $M_\odot$ star we find that the impact of changing $\delta_{\rm OV}$ is smaller.

5. Implications for LIGO detected BH-BH binaries

5.1. GW150914

The two merging BHs in GW150914 were located at a redshift of about $z \simeq 0.09$ (~ 400 Mpc) and reported to have masses of $36^{+5}_{-4}\ M_\odot$ and $29^{+4}_{-4}\ M_\odot$ (Abbott et al. 2016b). These masses, as well as preliminary aLIGO detection rate estimates, agree well with the predictions of Marchant et al. (2016) and de Mink & Mandel (2016). Unfortunately, the spins of the individual BHs were not well constrained from this event. The question is whether the CE formation channel can also reproduce an event like GW150914.

Based on the analysis presented in this paper, we conclude that the CE formation channel might work (in a low-metallicity

environment) to produce relatively massive BH-BH systems like GW150914 (which require $M_{\rm ZAMS} \gtrsim 50\ M_\odot$). A caveat is that there are still many uncertain aspects of CE ejection and that 3D hydrodynamical modelling in this direction is only at its infant stage, so far with no simulations of envelope ejections from a compact object embedded in the envelope of a massive star.

5.2. GW151226

GW151226 was reported to consist of a pair of BHs of masses $14^{+8}_{-4}\ M_\odot$ and $7.5^{+2.3}_{-2.3}\ M_\odot$ and is also located at a redshift of $z \simeq 0.09$ (Abbott et al. 2016a). It is notable that its total mass is about three times lower than the spectacular first event GW150914. Thus the formation of GW151226 cannot be explained by the CHE/MOB scenario (which in addition to BH masses $\gtrsim 25\ M_\odot$ also predicts a mass ratio very close to unity). From the simple energy budget analysis presented here, the CE formation channel could work for GW151226 in both a low- and high-metallicity environment (see Fig. 2), assuming that the 14 $M_\odot$ BH formed first. In the (somewhat unlikely) case that the 7.5 $M_\odot$ BH formed first, however, an origin in a high-metallicity environment seems difficult. According to Fig. 2, we can see that such a BH can only remove the CE of a $Z = Z_{\rm MW}$ star when the star has an initial mass lower than about 40 $M_\odot$ (and only when it is evolved to near its very maximum radial extent on the giant branch), which means that the mass of the collapsing core would be lower than about 18 $M_\odot$, according to our models. Hence, even modest mass loss of $\gtrsim 4\ M_\odot$ in the BH formation process would rule out this possibility, depending on the exact masses of the two BHs.

5.3. Comparison to other work

In a recent paper by Belczynski et al. (2016), a CE formation channel was put forward for GW150914. While the various aspects of CE evolution discussed here in this paper are generic, comparing our results directly with those of Belczynski et al. (2016) is difficult since few details of their applied stellar models are given. From their model (see their Fig. 1), we can deduce that the suggested 82.2 $M_\odot$ donor star ($Z \simeq Z_\odot/30$) has a radius of about 1700 $R_\odot$ at the onset of the CE phase with a 35.1 $M_\odot$ BH accretor. From our computed stellar structure models of an 80.0 $M_\odot$ star, we find $\lambda \sim 0.01$ (in agreement with Dewi & Tauris 2001), which yields $|E_{\rm env}| \simeq 5 \times 10^{50}$ erg. However, after the in-spiral of the BH, the orbital separation in the Belczynski et al. model is quoted to be $a_{\rm f} = 43.8\ R_\odot$, which corresponds to a released orbital energy of $|E_{\rm orb}| \simeq 5.4 \times 10^{49}$ erg, that is, about 10 times too small to eject the envelope. However, such an apparent discrepancy could be an artefact of simply applying different convective core-overshooting parameters, and given the relatively low stellar core masses in their illustrated scenario, we suspect that Belczynski et al. (2016) applied stellar models with small convective core overshooting. Alternatively, it is possible that they included released accretion energy as a main energy source in their budget, although this aspect is not discussed in their paper.

5.4. BH-BH formation: stability of the first RLO

Following the CE scenario for producing BH-BH binaries, we can also make predictions for the dynamical stability of the first mass-transfer phase (RLO). To lower the binding energy of the envelope during the CE phase and thus enhance the chance for surviving the in-spiral of the BH, the pre-CE binary system must be wide to secure an evolved donor star (Figs. 1 and 2). To fulfil the requirement of a wide pre-CE system, this means that the first mass-transfer phase from the primary star (the progenitor of the first-formed BH) to the (less evolved) secondary star must be dynamically stable or, in case of unstable RLO (see also Sect. 4.7), the orbital separation is only slightly reduced. Otherwise, if this first mass-transfer phase would form an effective CE, it would either reduce the orbital size drastically or result in an early coalescence, thus preventing the subsequent formation of a BH-BH system. However, the stability of mass transfer in massive binaries with non-degenerate stars is largely unexplored in the literature. In particular, we question to which extent binary systems would be dynamically stable at this stage since the timescale of the mass transfer is often much shorter than the thermal timescale of the accreting star. As a possible result, the accreting star may expand, initiate mass loss through the second Lagrangian point and result in a CE. It cannot be ruled out therefore that a significant fraction of the systems would merge already in this early phase. However, further investigations are needed in this direction before any conclusion can be drawn.

6. Conclusions

We have analysed the CE ejection process in post-HMXB systems. From our investigation of stellar structures and energy budget considerations, we find that CE evolution, in addition to producing double WD and double NS binaries, may in principle also produce massive BH-BH systems with individual BH component masses of up to 60 $M_\odot$ (beyond which point a pair-instability SN is expected to lead to complete disruption of the progenitor star and not leaving behind any compact remnant, cf. Heger & Woosley 2002; Chatzopoulos & Wheeler 2012). The potential for successful CE ejection is particularly good for donor stars evolved to giants beyond the Hertzsprung gap.

We find that the change in the λ-parameter with stellar radius is significantly more important than changes caused by different stellar masses or metallicities (although some mass dependence is noted on the giant branch). The associated binding energies of the stellar envelopes increase with stellar mass (independent of evolutionary status), but are generally independent of metallicity (except for massive high-metallicity stars that evolve to become LBV stars). The convective core-overshooting parameter applied in stellar models, $\delta_{\rm OV}$, however, can strongly affect the calculated values of λ and $E_{\rm bind}$ (up to a factor of 10).

Based on our detailed analysis of the evolution of the interior structure of massive stars, it is evident that the difficulty in determining the precise bifurcation point (core boundary) remains the key uncertain aspect of the outcome of CE evolution (Tauris & Dewi 2001). Whereas the hydrogen abundance ($X_{\rm H} = 0.10$, Dewi & Tauris 2000) and the maximum-compression point criteria (Ivanova 2011) roughly yield similar locations for the core boundary, it remains uncertain if the in-spiral continues significantly below the bottom of the convection zone in the envelope. Until future 3D hydrodynamical simulations will succeed in ejecting the CE of massive stars, the estimated LIGO detection rates from population synthesis of merging BH-BH and NS-NS binaries (Abadie et al. 2010) will remain highly uncertain, not to mention all other aspects of binary evolution and interactions not investigated in this work.

We explored the importance of additional energy sources to help ejecting the CE. We confirm that recombination energy makes an important contribution to the total internal energy in low- and intermediate-mass stars. However, for massive

($> 30\ M_\odot$) stars the contribution may be less than 1%, depending on the core boundary. Hence, liberated recombination energy may not play any significant role in forming BH-BH binaries through CE evolution.

The release of accretion energy, on the other hand, from an in-spiralling compact object (BH or NS), can be significant for the energy budget and may help to facilitate the CE ejection process. However, models of time-dependent energy transport in the convective envelope are needed to quantify this effect.

Although a deep in-spiral of a BH is possible in massive binaries that may eject their envelope, the exposed core will most likely terminate its evolution, and collapse before GWR would cause such post-CE binaries to coalesce. Hence, once a post-CE system is formed composed of a helium (Wolf-Rayet) star and a BH, the outcome is expected to be a BH-BH binary.

While it is difficult to estimate the outcome of CE evolution with high confidence, the arguments presented in this paper taken together suggest that it seems realistic to expect that production of BH-BH binaries are possible through the CE formation channel, leading to events such as GW150914 and GW151226.

Acknowledgements. MUK acknowledges financial support by the DFG Grant: TA 964/1-1 awarded to TMT. D.Sz. was supported by GAČR grant 14-02385S.

References

Abadie, J., Abbott, B. P., Abbott, R., et al. 2010, Classical and Quantum Gravity, 27, 173001
Abbott, B. P., Abbott, R., Abbott, T. D., et al. 2016a, Physical Review Letters, 116, 241103
Abbott, B. P., Abbott, R., Abbott, T. D., et al. 2016b, Physical Review Letters, 116, 061102
Banerjee, S., Baumgardt, H., & Kroupa, P. 2010, MNRAS, 402, 371
Belczynski, K., Holz, D. E., Bulik, T., & O'Shaughnessy, R. 2016, ArXiv e-prints
Belczynski, K., Kalogera, V., & Bulik, T. 2002, ApJ, 572, 407
Belczynski, K., Kalogera, V., Rasio, F. A., et al. 2008, ApJS, 174, 223
Bours, M. C. P., Marsh, T. R., Parsons, S. G., et al. 2014, MNRAS, 438, 3399
Brott, I., de Mink, S. E., Cantiello, M., et al. 2011, A&A, 530, A115
Brown, W. R., Kilic, M., Hermes, J. J., et al. 2011, ApJ, 737, L23
Burgay, M., D'Amico, N., Possenti, A., et al. 2003, Nature, 426, 531
Castro, N., Fossati, L., Langer, N., et al. 2014, A&A, 570, L13
Chatzopoulos, E. & Wheeler, J. C. 2012, ApJ, 748, 42
Davis, P. J., Kolb, U., & Knigge, C. 2012, MNRAS, 419, 287
de Kool, M. 1990, ApJ, 358, 189
de Marco, O., Passy, J., Moe, M., et al. 2011, MNRAS, 28
de Mink, S. E., Cantiello, M., Langer, N., et al. 2009, A&A, 497, 243
de Mink, S. E. & Mandel, I. 2016, ArXiv e-prints
Deinzer, W. & von Sengbusch, K. 1970, ApJ, 160, 671
Dewi, J. D. M., Pols, O. R., Savonije, G. J., & van den Heuvel, E. P. J. 2002, MNRAS, 331, 1027
Dewi, J. D. M. & Tauris, T. M. 2000, A&A, 360, 1043
Dewi, J. D. M. & Tauris, T. M. 2001, in Astronomical Society of the Pacific Conference Series, Vol. 229, Evolution of Binary and Multiple Star Systems, ed. P. Podsiadlowski, S. Rappaport, A. R. King, F. D'Antona, & L. Burderi , 255
Dominik, M., Belczynski, K., Fryer, C., et al. 2012, ApJ, 759, 52
Eggleton, P. P. 1983, ApJ, 268, 368
Eldridge, J. J. & Stanway, E. R. 2016, ArXiv e-prints
Gräfener, G., Owocki, S. P., & Vink, J. S. 2012, A&A, 538, A40
Han, Z., Podsiadlowski, P., & Eggleton, P. P. 1994, MNRAS, 270, 121
Heger, A., Fryer, C. L., Woosley, S. E., Langer, N., & Hartmann, D. H. 2003, ApJ, 591, 288
Heger, A. & Woosley, S. E. 2002, ApJ, 567, 532
Hjellming, M. S. & Webbink, R. F. 1987, ApJ, 318, 794
Hulse, R. A. & Taylor, J. H. 1975, ApJ, 195, L51
Humphreys, R. M. & Davidson, K. 1994, PASP, 106, 1025
Iben, Jr., I. & Livio, M. 1993, PASP, 105, 1373
Ishii, M., Ueno, M., & Kato, M. 1999, PASJ, 51, 417
Istrate, A., Marchant, P., Tauris, T. M., et al. 2016, ArXiv 1606.04947
Ivanova, N. 2011, ApJ, 730, 76
Ivanova, N., Belczynski, K., Kalogera, V., Rasio, F. A., & Taam, R. E. 2003, ApJ, 592, 475
Ivanova, N. & Chaichenets, S. 2011, ApJ, 731, L36
Ivanova, N., Justham, S., Chen, X., et al. 2013, A&A Rev., 21, 59
Ivanova, N., Justham, S., & Podsiadlowski, P. 2015, MNRAS, 447, 2181
Langer, N. 2012, ARA&A, 50, 107
Langer, N., Hamann, W.-R., Lennon, M., et al. 1994, A&A, 290
Livio, M. & Soker, N. 1988, ApJ, 329, 764
Lombardi, Jr., J. C., Proulx, Z. F., Dooley, K. L., et al. 2006, ApJ, 640, 441
Loveridge, A. J., van der Sluys, M. V., & Kalogera, V. 2011, ApJ, 743, 49
MacLeod, M. & Ramirez-Ruiz, E. 2015a, ApJ, 803, 41
MacLeod, M. & Ramirez-Ruiz, E. 2015b, ApJ, 798, L19
Mandel, I. & de Mink, S. E. 2016, ArXiv e-prints
Marchant, P., Langer, N., Podsiadlowski, P., Tauris, T., & Moriya, T. 2016, ArXiv e-prints
Martinez, J. G., Stovall, K., Freire, P. C. C., et al. 2015, ApJ, 812, 143
Mennekens, N. & Vanbeveren, D. 2014, A&A, 564, A134
Meynet, G. & Maeder, A. 2005, A&A, 429, 581
Nandez, J. L. A., Ivanova, N., & Lombardi, J. C. 2015, MNRAS, 450, L39
Nandez, J. L. A., Ivanova, N., & Lombardi, Jr., J. C. 2014, ApJ, 786, 39
Nelemans, G., Verbunt, F., Yungelson, L. R., & Portegies Zwart, S. F. 2000, A&A, 360, 1011
Ohlmann, S. T., Röpke, F. K., Pakmor, R., & Springel, V. 2016, ApJ, 816, L9
Passy, J.-C., De Marco, O., Fryer, C. L., et al. 2012, ApJ, 744, 52
Pavlovskii, K., Ivanova, N., Belczynski, K., & Van, K. X. 2016, ArXiv e-prints
Peters, P. C. 1964, Physical Review, 136, 1224
Petrovic, J., Pols, O., & Langer, N. 2006, A&A, 450, 219
Podsiadlowski, P. 2001, in Astronomical Society of the Pacific Conference Series, Vol. 229, Evolution of Binary and Multiple Star Systems, ed. P. Podsiadlowski, S. Rappaport, A. R. King, F. D'Antona, & L. Burderi , 239–+
Podsiadlowski, P., Joss, P. C., & Hsu, J. J. L. 1992, ApJ, 391, 246
Podsiadlowski, P., Rappaport, S., & Han, Z. 2003, MNRAS, 341, 385
Podsiadlowski, P., Rappaport, S., & Pfahl, E. D. 2002, ApJ, 565, 1107
Portegies Zwart, S. F. & McMillan, S. L. W. 2000, ApJ, 528, L17
Ricker, P. M. & Taam, R. E. 2012, ApJ, 746, 74
Rodriguez, C. L., Chatterjee, S., & Rasio, F. A. 2016, Phys. Rev. D, 93, 084029
Sana, H., de Mink, S. E., de Koter, A., et al. 2012, Science, 337, 444
Sanyal, D., Grassitelli, L., Langer, N., & Bestenlehner, J. M. 2015, A&A, 580, A20
Sigurdsson, S. & Hernquist, L. 1993, Nature, 364, 423
Smith, N., Vink, J. S., & de Koter, A. 2004, ApJ, 615, 475
Soberman, G. E., Phinney, E. S., & van den Heuvel, E. P. J. 1997, A&A, 327, 620
Soker, N. 2004, New A, 9, 399
Soker, N. 2015, ApJ, 800, 114
Soker, N. 2016, ArXiv:1605.02672
Spruit, H. C. & Taam, R. E. 2001, ApJ, 548, 900
Szécsi, D., Langer, N., Yoon, S.-C., et al. 2015, A&A, 581, A15
Taam, R. E. & Sandquist, E. L. 2000, ARA&A, 38, 113
Tauris, T. M. & Dewi, J. D. M. 2001, A&A, 369, 170
Tauris, T. M., Langer, N., & Podsiadlowski, P. 2015, MNRAS, 451, 2123
Tauris, T. M. & Savonije, G. J. 1999, A&A, 350, 928
Tauris, T. M. & van den Heuvel, E. P. J. 2006, Formation and evolution of compact stellar X-ray sources (Cambridge University Press), 623–665
Ulmer, A. & Fitzpatrick, E. L. 1998, ApJ, 504, 200
van den Heuvel, E. P. J. 1994, in Saas-Fee Advanced Course 22: Interacting Binaries, ed. S. N. Shore, M. Livio, E. P. J. van den Heuvel, H. Nussbaumer, & A. Orr, 263–474
Vink, J. S., de Koter, A., & Lamers, H. J. G. L. M. 2001, A&A, 369, 574
Voss, R. & Tauris, T. M. 2003, MNRAS, 342, 1169
Wang, C., Jia, K., & Li, X.-D. 2016, ArXiv:1605.03668
Webbink, R. F. 1984, ApJ, 277, 355
Yoon, S., Woosley, S. E., & Langer, N. 2010, ApJ, 725, 940
Zorotovic, M., Schreiber, M. R., Gänsicke, B. T., & Nebot Gómez-Morán, A. 2010, A&A, 520, A86

2.9 Supplementary material

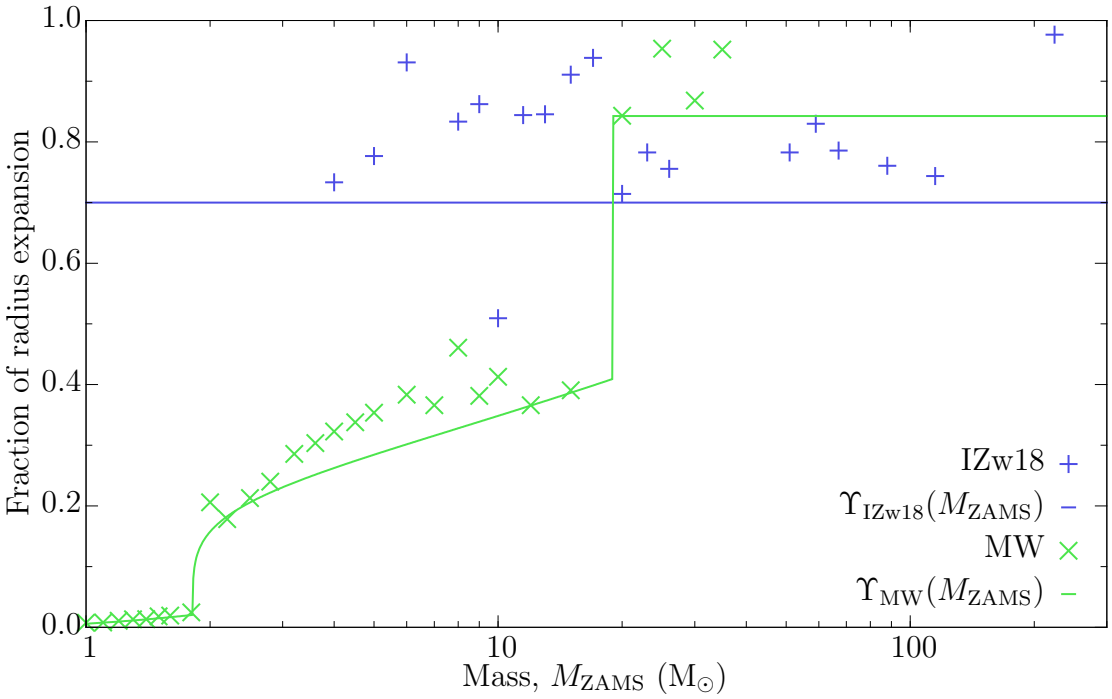

Figure 2.8: The fractional expansion (in units of the maximum radius) of stars at the point when at least 10% of the envelope mass is convective, plotted as a function of the ZAMS mass.

To parametrise when a stellar envelope is convective, an inspection of the stellar models at MW and IZw18 metallicity leads to Fig. 2.8. A minimum value for the fractional expansion when the envelope becomes too convective for a potentially stable mass transfer is set by

$$r_{\rm conv} = \Upsilon(m_{\rm ZAMS}) \cdot r_{\rm max}, \tag{2.1}$$

where $r_{\rm max}$ is the maximum radius reached during the expansion phase as a giant star. For the two metallicities the mass dependency is estimated by

$$\Upsilon_{\rm MW}(m) = \begin{cases} -0.01208 + 0.01796 \cdot \frac{m}{\rm M_\odot} & m < 1.816\ \rm M_\odot \\ 0.02054 + 0.2022 \cdot \left(\frac{m}{\rm M_\odot} - 1.816\right)^{0.23} & \text{for } m < 19\ \rm M_\odot \\ 0.8426 & m \geq 19\ \rm M_\odot \end{cases} \tag{2.2}$$

and

$$\Upsilon_{\rm IZw18}(m) = 0.7. \tag{2.3}$$

Chapter 3

Progenitors of gravitational wave mergers: Binary evolution with the stellar grid based code ComBinE

In this chapter, the code ComBinE is presented and applied to simulate the origin of the recently detected GW mergers. Furthermore, simulations with ComBinE are performed to understand the influence of several physical parameters to constrain the physics of the progenitors of GW mergers (Kruckow et al., 2018, submitted to MNRAS, arXiv: 1801.05433).

MNRAS **000**, 1–42 (2018) Preprint 18 January 2018 Compiled using MNRAS LATEX style file v3.0

Progenitors of gravitational wave mergers: Binary evolution with the stellar grid based code ComBinE

Matthias U. Kruckow,[1]★ Thomas M. Tauris,[2,1] Norbert Langer,[1,2] Michael Kramer,[2] Robert G. Izzard[3]

[1] *Argelander-Institut für Astronomie, Universität Bonn, Auf dem Hügel 71, 53121 Bonn, Germany*
[2] *Max-Planck-Institut für Radioastronomie, Auf dem Hügel 69, 53121 Bonn, Germany*
[3] *Astrophysics Research Group, Faculty of Engineering and Physical Sciences, University of Surrey, Guildford, Surrey, GU2 7XH, United Kingdom*

Submitted December 19, 2017

ABSTRACT

The first gravitational wave detections of mergers between black holes and neutron stars represent a remarkable new regime of high-energy transient astrophysics. The signals observed with LIGO-Virgo detectors come from mergers of extreme physical objects which are the end products of stellar evolution within close binary systems. To better understand their origin and merger rates, we have performed binary population syntheses at different metallicities using the new stellar grid based populations synthesis code ComBinE. Starting from newborn pairs of stars, we follow their evolution including mass loss, mass transfer and accretion, common envelopes and supernova explosions. We apply the binding energies of common envelopes based on dense grids of detailed stellar structure models, make use of improved investigations of the subsequent Case BB Roche-lobe overflow and scale supernova kicks according to the stripping of the exploding stars. We demonstrate that all the double black hole mergers, GW150914, LVT151012, GW151226, GW170104, GW170608 and GW170814, as well as the recently reported double neutron star merger GW170817, are accounted for in our models in the appropriate metallicity regime. Our binary interaction parameters are calibrated in particular to match the accurately determined properties of Galactic double neutron star systems, and we discuss their masses and types of supernova origin. Using our default values for the input physics parameters, we find a double neutron star merger rate of about 3.0 Myr^{-1} for Milky-Way equivalent galaxies. Our absolute upper limit to the merger-rate density of double neutron star systems is $\mathcal{R} \simeq 400\ \mathrm{yr}^{-1}\ \mathrm{Gpc}^{-3}$ in the local Universe ($z = 0$).

Key words: gravitational waves – stars: evolution – binaries: close – stars: neutron – stars: black holes – gamma-ray burst: general

1 INTRODUCTION

The evolution of massive binary stars and subsequent production of pairs of compact objects in tight orbits plays a central role in many areas of modern astrophysics, including: the origin of different types of supernova (SN) explosions (Yoon et al. 2010), accretion processes in X-ray binaries (Lewin & van der Klis 2006) and the formation of millisecond radio pulsars (MSPs, Bhattacharya & van den Heuvel 1991). Furthermore, the final outcome of massive binary evolution may in some cases be fatal collisions between neutron stars (NSs) and/or black holes (BHs). These events give rise to powerful emission of gravitational waves (GWs), as recently detected by advanced LIGO and Virgo (Abbott et al. 2016b,c, 2017a,b,c). They also lead to short gamma-ray bursts (GRBs, Eichler et al. 1989; Berger 2014; Abbott et al. 2017c) as well as chemical enrichment of the interstellar medium by heavy *r*-process elements (e.g. Lattimer & Schramm 1974; Rosswog 2015; Just et al. 2015; Abbott et al. 2017c).

Double compact objects (DCOs) – in the following defined as binary systems with a pair of NSs, BHs or one of each type – represent the end point of massive binary stellar evolution. According to their various formation channels, the progenitor systems have survived two SN explosions and multiple stages of mass transfer, often with one or more

★ E-mail: mkruckow@astro.uni-bonn.de

common-envelope (CE) episodes (e.g. Voss & Tauris 2003; Tauris & van den Heuvel 2006; Belczynski et al. 2008; Dominik et al. 2012; Marchant et al. 2016; Mandel & de Mink 2016; Belczynski et al. 2016; Tauris et al. 2017). Their observed properties are fossil records of their past evolutionary history and DCOs can therefore be used as key probes of binary stellar astrophysics. For a recent review of the formation of double NS systems, see Tauris et al. (2017). For general investigations and reviews of massive star evolution in pre-SN binaries, see e.g. Podsiadlowski et al. (1992); Wellstein & Langer (1999); Langer (2012); De Marco & Izzard (2017).

DCOs hosting a radio pulsar are also of special interest since their ultra-stable spin-down nature allows for precise timing of their motion in relativistic orbits and thereby tests of gravitational theories in the strong-field regime (Damour & Taylor 1992; Kramer et al. 2006; Wex 2014). Finally, observations of NS binaries help to constrain the long-sought-after equation-of-state (EoS) of nuclear matter at high densities (Antoniadis et al. 2013; Özel & Freire 2016).

1.1 Double compact object merger rates

The Galactic formation and merger rate of DCO systems has been estimated for almost four decades (e.g. Clark et al. 1979). As will be described below, the standard formation scenario of DCO binaries involves a number of highly uncertain aspects of binary interactions. The main uncertainties include, in particular, the treatment of CE evolution (Ivanova et al. 2013; Kruckow et al. 2016) and SN kicks (Janka 2012, 2017). Together, these processes lead to an uncertainty in the expected merger rates of several orders of magnitude. As an example, the simulated values of the double NS merger rate based on population synthesis covers a broad range of about $1 - 100\,\mathrm{Myr}^{-1}$ per Milky Way equivalent galaxy (Abadie et al. 2010). After the recent success in also detecting GW signals from merging NSs (Abbott et al. 2017c), it is expected that GWs from a large number of colliding systems will soon determine the double NS merger-rate density in the local Universe. It is also anticipated that collisions of mixed BH/NS systems will be detected in the near future. Thus, it will soon be possible to obtain broad DCO merger rate constraints from GW detectors like advanced LIGO, Virgo, KAGRA and LIGO India, and finally determine which species of DCO binaries dominate the detection rate. A (perhaps slightly naïve) hope, but a difficult task due to the degeneracy involved, is that the empirical detection rate from advanced LIGO and sister observatories can be inverted to infer constraints on CE physics and SN momentum kicks (e.g. Dominik et al. 2012; Dvorkin et al. 2017; Barrett et al. 2017b).

1.2 Résumé of double compact object formation

Previous theoretical work on the physics of DCO formation includes: Bisnovatyi-Kogan & Komberg (1974); Wheeler et al. (1974); Flannery & van den Heuvel (1975); Srinivasan & van den Heuvel (1982); van den Heuvel (1994); Ivanova et al. (2003); Dewi & Pols (2003); Podsiadlowski et al. (2004); van den Heuvel (2004); Dewi et al. (2005); Tauris et al. (2015, 2017). From these papers, a *standard scenario*[1] has emerged (e.g. Bhattacharya & van den Heuvel 1991; Tauris & van den Heuvel 2006; Belczynski et al. 2008) which we now summarize in more detail.

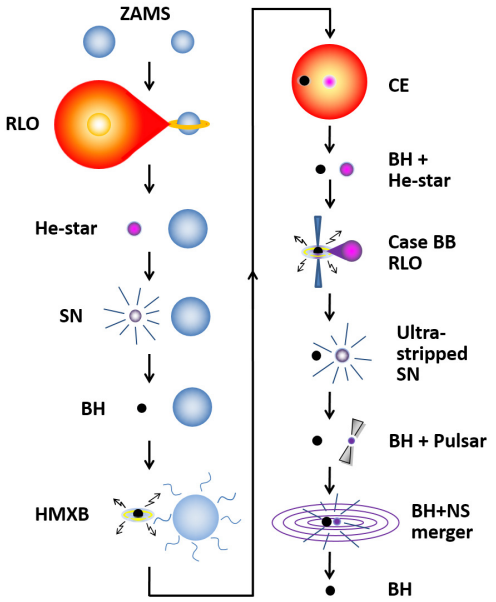

Figure 1. Illustration of the formation of a BH-NS system which merges within a Hubble time and produces a single BH, following a powerful burst of GWs and a short GRB. Acronyms used in this figure: ZAMS: zero-age main sequence; RLO: Roche-lobe overflow (mass transfer); He-star: helium star; SN: supernova; BH: black hole; HMXB: high-mass X-ray binary; CE: common envelope; NS: neutron star.

In Fig. 1, we illustrate the formation of a DCO system. The initial system contains a pair of OB-stars which are massive enough to terminate their lives in a core-collapse SN. The secondary (initially least massive) star may, in principle, be a $5 - 7\,\mathrm{M}_\odot$ star which accretes mass from the primary (initially most massive) star to reach the threshold limit for core collapse at $\sim 8 - 12\,\mathrm{M}_\odot$ (Jones et al. 2013; Woosley & Heger 2015). The donor (primary) star loses its hydrogen-rich envelope, via Roche-lobe overflow (RLO) to the secondary star, and becomes a helium star. If such a star is more massive than about $8\,\mathrm{M}_\odot$ it is often observable as a Wolf-Rayet star (Crowther 2007). Whether or not the system survives the following SN explosion depends on the orbital separation and the kick imparted onto the newborn NS or BH (Flannery & van den Heuvel 1975; Hills 1983; Tauris & Takens 1998). If the binary system remains bound after the first SN explosion (which is of type Ib/c, Yoon et al. 2010), the system eventually becomes observable as a HMXB. Before this stage, and if the first-born compact object is a NS, the system may also be detectable as a radio

[1] See Section 5.4 for discussions on alternative formation scenarios and Table C1 for several further sub-channels.

pulsar orbiting an OB-star, e.g. as in PSRs B1259−63 and J0045−7319 (Johnston et al. 1992; Kaspi et al. 1994).

When the secondary star expands and initiates RLO during the HMXB stage, the system may eventually become dynamically unstable on a timescale that could be as short as a few 100 yr (Savonije 1978). This leads to the formation of a CE (Paczynski 1976; Ivanova et al. 2013) where dynamical friction of the motion of the compact object (NS or BH) inside the giant star's envelope often causes extreme loss of orbital angular momentum and energy. In case the hydrogen-rich envelope is successfully ejected and the binary system survives the CE phase, it consists of a NS or BH orbiting a helium star (the naked core of the former giant star). Depending on the orbital separation and the mass of the helium star, an additional phase of mass transfer which mostly leads to further shrinkage of the orbit (Case BB RLO, Habets 1986; Tauris et al. 2015) may be initiated. This stage of mass transfer is important since it enables a relatively long phase of accretion onto the compact object, whereby the first-formed compact object is recycled to a high spin rate. In addition, it allows for extreme stripping of the helium star prior to its explosion (in a so-called *ultra-stripped* SN, Tauris et al. 2013, 2015; Suwa et al. 2015; Moriya et al. 2017).

If the post-SN orbital period after the second explosion is short enough (and especially if the eccentricity is large) the DCO system will eventually merge due to GW radiation. The final remnant is in most cases a BH, although for double NS mergers a massive NS (or, at least, a meta-stable NS) may be left behind instead depending on the EoS (Vietri & Stella 1998; Falcke & Rezzolla 2014).

1.3 Population synthesis studies

To estimate the formation and merger rates of DCO binaries, the nature of the merging compact objects and their delay timescales, and thus the offset of the associated short GRBs and kilonovae from their birth places, it is necessary to evolve a larger number of binary systems. Many binary star interactions, however, are uncertain and various input distributions are often used to quantify key physical parameters by the use of e.g. Monte Carlo techniques. This is the essence of population synthesis.

Based on observational evidence and theoretical development of the necessary input physics from stellar evolution and binary interactions, a large number of population synthesis studies have emerged over the last two decades to investigate the formation and evolution of DCO binaries. Examples include Bloom et al. (1999); Belczynski et al. (2002); Voss & Tauris (2003); Belczynski et al. (2008); Dominik et al. (2012); Mennekens & Vanbeveren (2014); Belczynski et al. (2016); Eldridge & Stanway (2016); Stevenson et al. (2017a); Chruslinska et al. (2017).

Here, we present new results based on a significantly improved version of the population synthesis code applied by Voss & Tauris (2003). The innovative aspect comes in when applying updated stellar evolution models (at different metallicities) with high resolution of the stellar structure, and a proper treatment of Case BB RLO. For example, in the last couple of years the calculations of the final stage of close binary evolution with an accreting NS has been advanced to a new stage, towards the end of oxygen burning, providing evidence for the existence of ultra-stripped SNe (Tauris et al. 2013, 2015). It was demonstrated that for such SNe the total envelope mass surrounding the metal core can even be $< 0.1\ M_\odot$, which results in very little mass ejection during the SN. This is important for the subsequent calculations of the resulting NS kicks (Tauris et al. 2017) which strongly affect the estimated number of mergers that GW observatories will detect and the offsets from their host galaxies (relevant for short GRBs and electromagnetic follow-up observations).

The applied population synthesis code ComBinE and our newly developed upgrades to this code will be described in Section 2. In Section 3, our default grid of stellar models extracted from detailed stellar evolution calculations is presented. The results and first comparisons to observations are given in Section 4. This is followed in Section 5 with further discussions with respect to observations, the influence of the different population synthesis input parameters and a comparison to other publications. We conclude our findings in Section 6. Additional material can be found in Appendix A–D.

2 THE ComBinE CODE

ComBinE is a rapid binary population synthesis code. It is a significantly upgraded version of the code developed by Voss & Tauris (2003), which again is based on the original code of Tauris & Bailes (1996). Another version of this code has been applied in e.g. Tauris & Takens (1998); Tauris et al. (1999); Tauris & Sennels (2000). Compared to the older versions, the new one is faster and allows for e.g. simultaneous evolution of the two stars as well as RLO from the secondary star to the primary star before the primary star has terminated its nuclear evolution (i.e. mass-transfer reversals). Several updates on the input physics are included as well. It is faster than other binary population synthesis codes like *StarTrack* (Belczynski et al. 2008) or *binary_c* (Izzard et al. 2004, 2006, 2009, 2017). ComBinE does not rely on fitting formulae for the stellar evolution (e.g. Hurley et al. 2002) which often leads to usage outside their range of validity when studying formation of massive DCO binaries. Our code interpolates in tabulated data from a dense grid of detailed stellar models (for more details see Section 3). This allows for a more accurate treatment of, for example, the CE evolution which is still the most uncertain part in binary star population synthesis. Additionally, we have implemented the latest results of detailed numerical Case BB RLO calculations (Tauris et al. 2015).

2.1 Initial conditions

Usually stellar or binary population synthesis start with stars on their zero-age main sequence (ZAMS). There are several distribution functions in the literature to describe the statistical distribution of the most important parameters of a binary system. We now discuss the most important ones applied in ComBinE.

2.1.1 Stellar masses

The first fundamental parameters of a binary system are the two masses of the stars which build the binary.

The primary mass, $m_{\rm p}$, is defined to be the mass of the initially more massive star. It is selected from an initial-mass function (IMF) for single stars. By default the Salpeter-IMF (Salpeter 1955; Scalo 1986) is used,

$$\xi(m_{\rm p}) \propto m_{\rm p}^{-\alpha_{\rm IMF}} \quad \text{with} \quad \alpha_{\rm IMF} = 2.7. \tag{1}$$

Different IMF slopes are considered in Section 5.1.6. Other IMFs, (e.g. Kroupa 2008, where $\alpha_{\rm IMF}$ depends on the mass range) are implemented as well for comparison. According to the chosen IMF, the primary mass is selected randomly.

The minimum and maximum masses of the primary and secondary stars can be varied to fix the desired mass ranges for the ZAMS stars. When considering NS and BH progenitors at solar metallicity, our primary star mass range starts at 8 and 22 $M_\odot$, respectively. As a result of mass transfer, however, the initial ZAMS mass of the secondary star can be smaller (see below).

The secondary mass, $m_{\rm s}$, is chosen based on the primary mass and a distribution function for the mass ratio, $q \equiv m_{\rm s}\, m_{\rm p}^{-1}$. Our default distribution is

$$f(q) = \frac{2}{(1+q)^2} \tag{2}$$

form Kuiper (1935). Alternatively, we can apply e.g. a flat distribution for q or investigate other distributions based on recent empirical data, such as Sana et al. (2012) and Moe & Di Stefano (2017). It is also possible to set a range for the secondary mass and ComBinE will automatically calculate the relevant range for the mass ratio. However, de Mink & Belczynski (2015) demonstrated that their DCO merger rates are almost independent of the initial distributions of mass ratios and orbital periods, compared to the strong dependence on input physics parameters governing binary interactions and SNe. Our test simulations yield a similar conclusion. We compared our DCO merger-rate results using Equation (2) for the mass ratios and a flat distribution of initial orbital periods (see below) to the results obtained using the input distributions of Sana et al. (2012), and we find that our merger rates only change by a factor of $2-3$.

If the secondary star gains mass as a result of mass-transfer processes in a binary, even lower ZAMS masses than needed in an isolated evolution must be considered for the secondary star when producing selected compact objects. As an example, it has been demonstrated that secondary stars with ZAMS masses of e.g. $6-7\,M_\odot$ may accrete sufficient material to end up producing a NS (Tauris & Sennels 2000; Zapartas et al. 2017).

2.1.2 Orbital parameters

Given the two stellar masses, the orbital energy of the binary system is determined by the semi-major axis, a. The value of a is calculated from Kepler's third law once the orbital period has been chosen. Orbital period distributions often used in the literature are flat in $\log(P)$ (Abt 1983). Alternative distributions have been proposed (e.g. Kroupa 2008; Sana et al. 2012) and are also included in the ComBinE code. Again, we emphasize that the properties of the final DCO binaries and their merger rates are only weak functions of the initial input distributions (de Mink & Belczynski 2015, and Section 2.1.1). The minimum and maximum orbital separations can be specified, although the former is limited by the condition that none of the stars must fill their Roche lobe (see Section 2.2.3) on the ZAMS. The latter can only be specified as a fixed value (Table 2 in Section 4).

Another orbital parameter is the eccentricity, e. Close systems circularise with time due to tidal effects (Zahn 1977). Therefore, our default simulations are always initiated with circular orbits, $e = 0$ (Hurley et al. 2002). Other possibilities included in ComBinE are a thermal (Heggie 1975) or a flat distribution in eccentricity, as well as a flat distribution in the orbital angular momentum.

2.1.3 Further parameters

In addition to the above, there are further parameters which can influence the evolution of a binary system. Stars usually possess rotation. In a close binary tidal forces tend to synchronise the stellar spin with the orbit (Zahn 1977). The influence of the rotation on the evolution of a star is very limited as long as the star spins much more slowly than its break-up velocity (e.g. Brott et al. 2011), where the centrifugal force fully compensates the gravity. Hence, for most purposes a differentiation between slow and very fast rotating stars is sufficient. Here we focus on non-rotating stars.

The metallicity may also have an important effect on the evolution of a star (Langer 2012). It varies between galaxies and for different generations of star formation within each galaxy. Finally, depending on the stellar density, there could be dynamical interactions with other stars or binary systems (Portegies Zwart & McMillan 2000; Rodriguez et al. 2016a; Banerjee 2017; Park et al. 2017) which can change the orbital and stellar evolution compared to that of an isolated binary. Such dynamical interactions are not considered in this investigation.

2.2 Evolutionary phases

In the following, we highlight our treatment of various evolutionary phases in ComBinE, including: stellar winds, tides, mass transfer/loss (RLO, CE), SNe and GWs. Further details on the orbital evolution can be found in van den Heuvel (1994); Soberman et al. (1997). For a general review, see e.g. Tauris & van den Heuvel (2006).

If a binary system is initially very wide (and remains wide throughout its evolution), the two stars evolve as if they where isolated. They just follow their evolutionary tracks of single stars taken from the stellar girds (see Section 2.4, and also Appendix A1 for a list of all stellar quantities calculated). These tracks are assumed to be extended by a short-lasting phase of burning elements heavier than helium prior to the core collapse. In this case of isolated star evolution, the only changes to the orbital separation are caused by stellar winds and SN explosions.

For a close binary system, or a system initially in a wide orbit that later becomes tight after the first SN (Kalogera 1998), however, we consider in each individual case whether some or all of the phases described below apply.

2.2.1 Stellar winds

Following the stellar wind models prescribed for our applied stellar grids (Section 3), we calculate the orbital widening by assuming that the average angular momentum (per unit mass) carried away by a spherically symmetric wind at high velocity is the same as the average orbital angular momentum of the mass-losing star. This leads to a simple expression for the orbital widening given by

$$\frac{a}{a_0} = \frac{M_0}{M}, \tag{3}$$

where M is the total mass of the binary, a is the semi-major axis, and indices "0" refer to the values prior to wind mass loss. The above expression also holds in the case of simultaneous wind mass loss from both stars.

2.2.2 Circularisation

In close systems, the tides on the stars will circularise the orbit and synchronise their spins with the orbital phase (Sutantyo 1974). Prior to mass transfer, when the donor star is close to filling its Roche lobe, the tidal effects are particularly strong and the orbit is likely to circularise on a short timescale. For this process, angular momentum conservation yields the orbital changes for a given eccentricity, e_0,

$$\frac{a}{a_0} = 1 - e_0^2. \tag{4}$$

The orbit is assumed to be fully circularised at the onset of mass transfer.

2.2.3 Roche-lobe overflow

The change in orbital separation upon non-conservative[2] mass transfer depends crucially on the specific angular momentum of the matter lost – which is rather poorly known.

When the donor star expands and fills its Roche lobe (Eggleton 1983), large scale mass transfer to its companion star initiates. This transfer of matter will continue in a stable or unstable way depending on the reaction of the two stars upon the mass transfer. We refer to stable mass transfer as RLO, while dynamically unstable mass transfer is assumed to result in a CE (Section 2.2.4).

For stellar components on the main sequence (i.e. during core hydrogen burning) the stability of mass transfer is evaluated in ComBinE by comparing their mass ratio, q at the onset of the mass transfer to a threshold value, $q_{\rm limit}$ (e.g. Nelson & Eggleton 2001; de Mink et al. 2008, and see discussion in Section 5.1.5). Additionally, to avoid a Darwin instability and ensure dynamically stable mass transfer with a hydrogen-rich donor star, we require that the system has a minimum orbital period $\gtrsim 3$ d (Pablo Marchant, priv. comm.). Giant donor stars have a deep convective envelope which often leads to unstable mass transfer (Hjellming & Webbink 1987; Tauris & Savonije 1999; Tauris et al. 2000; Podsiadlowski et al. 2002; Pavlovskii et al. 2017), in many cases resulting in a CE. In ComBinE, we check for the depth of the convective envelope and assume a CE forms if RLO is initiated for donor stars which have convective envelops exceeding 10 per cent in mass coordinate.

For helium star donors (Case BB RLO) and non-degenerate accretors we apply the same stability criterion as for hydrogen-rich donors mentioned above. If a helium star transfers mass onto a compact object, however, the applied default stability of the mass transfer is given by the orbital period and we apply the numerical results from Tauris et al. (2015).

In order to calculate the orbital period changes due to RLO, we adopt the isotropic re-emission model (Tauris & van den Heuvel 2006, and references therein). Here, the change in orbital angular momentum caused by mass loss, $\dot{J}_{\rm ml}$, in terms of the orbital angular momentum, $J_{\rm orb}$, from the binary system (usually the dominant term in the orbital angular momentum balance equation) is given by

$$\frac{\dot{J}_{\rm ml}}{J_{\rm orb}} = \frac{\alpha_{\rm RLO} + \beta_{\rm RLO}\, q^2 + \delta_{\rm RLO}\, \gamma\, (1+q)^2}{1+q}\, \frac{\dot{m}_2}{m_2}, \tag{5}$$

where $\alpha_{\rm RLO}$, $\beta_{\rm RLO}$ and $\delta_{\rm RLO}$ are the fractions of mass lost from the donor in the form of a direct fast wind, the mass ejected from the vicinity of the accretor and from a circumbinary coplanar toroid (with radius, $a_{\rm r} = \gamma^2\, a$), respectively (van den Heuvel 1994; Soberman et al. 1997). The accretion efficiency of the accreting star (here index 1) is thus given by: $\epsilon = 1 - \alpha_{\rm RLO} - \beta_{\rm RLO} - \delta_{\rm RLO}$, or equivalently

$$\partial m_1 = -\epsilon\, \partial m_2, \tag{6}$$

where m_2 refers to the donor star mass and $\partial m_2 < 0$ is its mass loss. These factors are functions of time as the binary system evolves during the mass-transfer phase. In ComBinE, we assume $\alpha_{\rm RLO}$, $\beta_{\rm RLO}$ and $\delta_{\rm RLO}$ to be constant during the entire RLO. In our default model $\delta_{\rm RLO} = 0$. In this case, we obtain for the change in the orbital separation,

$$\frac{a}{a_0} = \left(\frac{q}{q_0}\right)^{2\,\alpha_{\rm RLO}-2} \left(\frac{1+q}{1+q_0}\right)^{-1} \left(\frac{1+\epsilon\, q}{1+\epsilon\, q_0}\right)^{2\,\frac{\alpha_{\rm RLO}\,\epsilon^2+\beta_{\rm RLO}}{\epsilon\,(1-\epsilon)}+3}. \tag{7}$$

The parameter $\alpha_{\rm RLO}$ is discussed further in Section 5.1.4.

The response of the accreting star is taken into account in ComBinE by checking its Eddington limit[3],

$$\dot{m}_{\rm Edd} = 4\,\pi\, c\, G\, m_1\, \frac{m_{\rm H}\, \mu_{\rm e}}{\varepsilon\, \sigma_{\rm T}}, \tag{8}$$

where c is the speed of light, G is the gravitational constant, m_1 is the accretor mass, $m_{\rm H}$ is the proton mass, $\mu_{\rm e}$ is the mean molecular weight per electron of the accreted hydrogen- or helium-rich material, $\sigma_{\rm T}$ is the Thomson cross section and ε is the sum of released energy per unit mass from released gravitational binding energy and nuclear burning of accreted material. If $\dot{m}_1 > \dot{m}_{\rm Edd}$, we either reduce the mass-accretion efficiency, ϵ, by automatically increasing the re-emission fraction of the accretor, $\beta_{\rm RLO}$, to ensure $\dot{m}_1 = \dot{m}_{\rm Edd}$ (the default in case the accretor is a compact object), or otherwise assume the onset of a CE (Section 2.2.4).

[2] Meaning that total mass and orbital angular momentum are not conserved within the binary system.

[3] In addition, for low-mass stars, the thermal timescale of the accretor should be compared to the timescale of the RLO as well. This is not included here, because for relatively massive stars the thermal timescale of the accretor is always smaller than, or comparable to, that of the RLO – thus avoiding a contact phase.

Therefore, as the value of $\beta_{\rm RLO}$ is potentially readjusted we refer to this input parameter as $\beta_{\rm min}$ (Section 5.1.4). It is simply assumed that $\beta_{\rm min}$ takes the same value for all accreting stars (non-degenerate stars and compact objects).

The accreting star is assumed to be fully rejuvenated and we attach it to a new evolutionary track depending on its core mass and total mass (Section 3 and Appendix A2). If the rejuvenated accretor, or the relaxed core of the donor, fills its Roche lobe, then the system remains attached and we assume that it coalesces.

The donor star is always assumed to lose its mass down to its core-envelope boundary, see Section 3.3. Therefore, every hydrogen-rich donor becomes a helium star (Section 3.2) and a helium rich donor leaves behind a naked metal core which is composed of carbon and heavier elements. In the latter case, we assume it terminates its life and becomes a compact object, see Section 2.2.5, before any other binary interaction is dealt with in ComBinE. We assume that any RLO typically proceeds on the thermal timescale of the donor star, which depends on its internal structure at the onset of RLO. In addition, the duration of the mass transfer is adjusted by rescaling with a factor of 1 or 3, for helium- and hydrogen-rich donor stars, respectively.

2.2.4 *Common-envelope evolution*

If the mass transfer in a binary is unstable, we assume a CE will be formed, engulfing the two stars. In the standard formation channel for DCO binaries which become GW mergers (Fig. 1), the systems often enter a CE phase during RLO in the HMXB stage as a result of enhanced orbital shrinking due to a large mass ratio between the donor star and the accretor. Here, at the latest when it becomes a red supergiant, the massive donor star captures its NS/BH companion and causes it to spiral in. For a successful CE ejection, it is believed that the envelope will be lost from the system on a short timescale of $\lesssim 1000$ yr (Podsiadlowski 2001).

There are many uncertainties in calculations of the in-spiral process and the subsequent ejection of the CE. This causes large uncertainties in the predicted rates for GW merger events obtained from population synthesis (Abadie et al. 2010). A full understanding of the CE phase requires detailed multi-dimensional hydrodynamical calculations. Early studies in this direction have difficulties ejecting the envelope and securing deep in-spiral (Taam & Sandquist 2000; Passy et al. 2012; Ricker & Taam 2012; Nandez et al. 2014; Ohlmann et al. 2016).

As a result of the current limited knowledge of CE physics (Ivanova et al. 2013) a simple but robust prescription is implemented in ComBinE. The outcome of the CE ejection is calculated according to the (α, λ)-formalism (Webbink 1984; de Kool 1990). In this framework, it is assumed that a certain fraction, $\alpha_{\rm CE}$, of the released orbital energy, caused by frictional torques acting on the in-spiralling star, is converted into kinetic energy in the envelope. We assume $\alpha_{\rm CE}$ to be a fixed parameter for all stars and our default value is $\alpha_{\rm CE} = 0.5$. The influence of this parameter is further discussed in Section 5.1.3.

The released orbital energy from in-spiral, $|\Delta E_{\rm orb}|$, is given by

$$\Delta E_{\rm orb} = -\frac{G\, m_{2,\rm core}\, m_1}{2\, a} + \frac{G\, m_2\, m_1}{2\, a_0}, \tag{9}$$

where m_1 and m_2 denote the pre-CE companion star mass and donor star mass, respectively, while $m_{2,\rm core}$ is the core mass of the donor star (Section 3.3). The pre- and post-CE orbital separations are denoted by a_0 and a.

A successful CE ejection can only occur in systems where $|E_{\rm bind}| \leq \alpha_{\rm CE}\, |\Delta E_{\rm orb}|$. Here, the binding energy of the envelope of the donor star is given by

$$E_{\rm bind} \equiv -\frac{G\, m_2\, m_{2,\rm env}}{\lambda\, R}, \tag{10}$$

where R denote the pre-CE donor star radius and $m_{2,\rm env} = m_2 - m_{2,\rm core}$ is its envelope mass. The value of λ is not a constant but depends strongly on the mass and the evolutionary status of the donor star (Dewi & Tauris 2000, 2001; Kruckow et al. 2016). From our detailed stellar structure models (Section 3) we calculate the relevant λ values and determine the outcome of the CE event from the energy budget.

The total binding energy of the envelope is the sum of the gravitational binding energy and the internal thermodynamic energy,

$$E_{\rm bind} = -\int_{m_{2,\rm core}}^{m_2} \frac{G\, m(r)}{r}\, {\rm d}m + \alpha_{\rm th} \int_{m_{2,\rm core}}^{m_2} U\, {\rm d}m, \tag{11}$$

where $m(r)$ is the mass within the radius coordinate r and U is calculated following Han et al. (1995). The latter involves the basic thermal energy for a simple perfect gas, the energy of radiation, as well as terms due to ionization of atoms and dissociation of molecules. The value of $\alpha_{\rm th}$ depends on the details of the ejection process. In our default model we assume $\alpha_{\rm th} = 0.5$; other values are discussed in Appendix D3.

If the binary system is not able to eject the CE, we assume that its stellar components merge and we disregard further evolution of the product (Glebbeek et al. 2013). If the system survives and ejects the CE, the change in orbital separation according to the in-spiral is calculated from

$$\frac{a}{a_0} = \frac{m_{2,\rm core}}{m_2} \left(1 + \frac{2}{\alpha_{\rm CE}\, \lambda}\, \frac{m_{2,\rm env}}{m_1}\, \frac{a_0}{R}\right)^{-1}. \tag{12}$$

ComBinE also takes the released energy of accretion onto a compact object, $E_{\rm acc}$, and the associated additional nuclear-burning energy, $E_{\rm nuc}$, into account. This rescales (increases) the final semi-major axis by a factor $1 + (E_{\rm acc} + E_{\rm nuc})\, |E_{\rm bind}|^{-1}$. For detailed discussions on CE ejection from massive stars (NS and BH progenitors), we refer to Kruckow et al. (2016).

If the binary system survives the CE phase, the donor star becomes a naked core similar to the case of stable RLO. If the pre-CE donor star is a hydrogen-rich star, ComBinE places the exposed stellar core on the ZAMS helium-star track. If the pre-CE donor star is a helium-rich donor, then the exposed metal core is assumed to end its life in a SN or becomes a white dwarf (WD) before any further binary interactions will occur.

2.2.5 *Formation of compact objects*

When a star finishes nuclear burning its core contracts and it either forms a WD remnant or it produces a NS or a

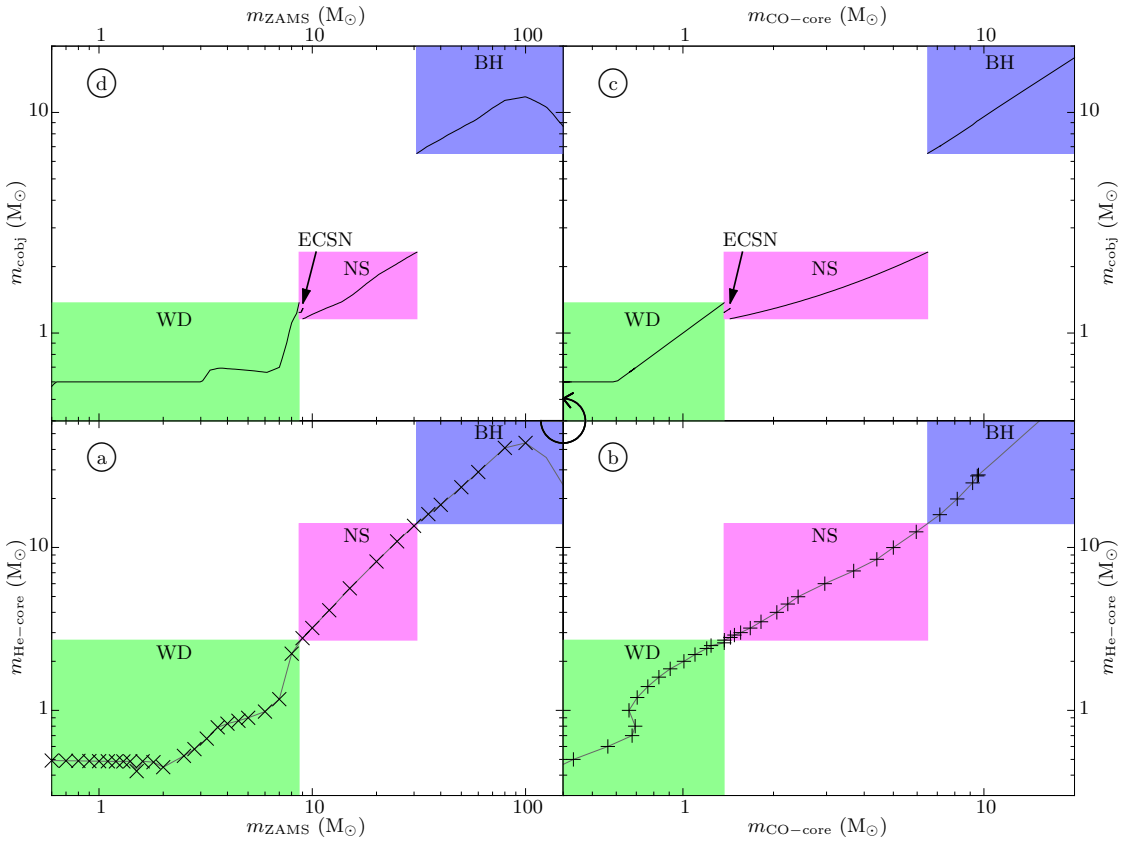

Figure 2. Mapping of single star ZAMS mass, $m_{\rm ZAMS} \in [0.6 : 150]\ M_\odot$, to final stellar remnant mass, $m_{\rm cobj}$, for stellar tracks (data points of Figs 3 and 5 are marked by × and +, respectively) at Milky Way metallicity (panel d, inferred from panels a to c for single stars). As intermediate steps, the He-core mass, $m_{\rm He-core}$, (panel a) and CO-core mass, $m_{\rm CO-core}$, (panel b) are calculated to obtain the compact object masses (panel c). In binary stars, the remnant masses differ because of additional mass loss or mass gain from the companion star. Acronyms: ZAMS: zero-age main sequence; WD: white dwarf; NS: neutron star; BH: black hole; ECSN: electron capture supernova.

BH. The nature and mass of the stellar remnant depends on the mass of its progenitor star. Fig. 2 shows the relations between ZAMS mass, He-core mass, CO-core mass – based on the stellar grids applied in ComBinE – and estimated compact object mass.

The compact remnants resulting from our single star evolution grids (Section 3) are assumed to be WDs with masses $m_{\rm WD} < 1.37\ M_\odot$, NSs with masses $1.16\ M_\odot < m_{\rm NS} < 2.33\ M_\odot$ and BHs with masses $m_{\rm BH} > 6.52\ M_\odot$, depending on the collapsing core mass. In binary star systems, however, ComBinE can produce BHs with masses down to $5.2\ M_\odot$ if their helium envelope is stripped off prior to core collapse.

WDs produced in our binaries can be either He WDs, CO WDs or ONeMg WDs, depending on the mass of their progenitor cores, $m_{\rm CO-core} < 1.37\ M_\odot$. Our NSs result from either an electron capture SN if $1.37\ M_\odot \leq m_{\rm CO-core} < 1.435\ M_\odot$ or an iron-core collapse SN if $1.435\ M_\odot \leq m_{\rm CO-core} < 6.5\ M_\odot$, following binary star calculations in Tauris et al. (2015). In the first case, a reduction of 10 per cent in gravitational mass is assumed during formation (Hüdepohl et al. 2010), leading to NS masses in the range 1.24 to $1.29\ M_\odot$. In the second case, we follow Lattimer & Yahil (1989). We note that the NSs produced with the very smallest masses (see Fig. 2) come from iron-core collapse SNe (Timmes et al. 1996).

Our BHs are assumed to be formed from the collapsing CO-cores with $m_{\rm CO-core} > 6.5\ M_\odot$ and receive in addition a partial fallback of 80 per cent of the mass of their surrounding helium envelopes. Studies of BH formation via hydrodynamical calculations (e.g. Fryer et al. 1999; Fryer 2006) show that the fallback fraction ranges from 0 (no fallback) to 1 (complete fallback) and may depend on the mass of the collapsing star in a complex manner. Here, for simplicity, we assume a constant partial fallback for the formation of all BHs. We account for the release of gravitational binding energy during BH formation and calculate the resulting

Table 1. Projected 1-dimensional root-mean-square kick velocities $\left(w_{\rm rms}^{\rm 1D}\right)$, or 3-dimensional kick velocity ranges*, applied to various exploding stars in the first and second SN in a binary.

SN type	first SN	second SN
Electron capture SN*	0 – 50 km s^{-1}	0 – 50 km s^{-1}
Iron-core collapse SN depending on the NS progenitor:		
– Isolated star or wide binary	265 km s^{-1}	265 km s^{-1}
– Close binary, no H env.**	120 km s^{-1}	120 km s^{-1}
– Close binary, no He env.**	60 km s^{-1}	30 km s^{-1}
Formation of BH*	0 – 200 km s^{-1}	0 – 200 km s^{-1}

* The stated velocity interval corresponds to 3-dimensional velocities and we applied a flat probability distribution rather than applying a Maxwellian distribution.
** For iron-core collapse SNe in close systems, we applied a bimodal kick distribution such that the above $w_{\rm rms}^{\rm 1D}$ values for a Maxwellian distribution account for 80 per cent of the cases and in the remaining 20 per cent of the cases we applied a larger kick using $w_{\rm rms}^{\rm 1D} = 200$ km s^{-1} (see Section 2.2.6).

gravitational mass by lowering the total (baryonic) mass by 20 per cent.

In the regime of pair-instability SNe (PISNe), no remnant will be left behind (Heger & Woosley 2002). While this effect is included in ComBinE the occurrence of pulsational PISNe (Woosley 2017) is not considered in the current version. Pulsational PISNe may eject the outer layers and thus reduce the mass of the star prior to its final core collapse. This reduces the mass of the BH remnant, because the amount of potential fallback material is decreased.

2.2.6 *Supernova kicks in* ComBinE

Massive stars usually end their life in a SN. A core-collapse SN (CC SN) ejects the envelope while the core collapses to become a NS or a BH. As the SN is not spherically symmetric, the explosion usually leads to a kick imparted on the newborn compact remnant (Janka 2012). In the following, we discuss the treatment of SN kicks in ComBinE. A summary is given in Table 1.

For an electron capture SN (EC SN, Nomoto 1987) we apply a flat 3-dimensional kick distribution up to 50 km s^{-1}. This choice of a small kick is motivated by arguments based on the pre-SN stellar structure as well as SN simulations showing that such SNe usually result in small kicks (Podsiadlowski et al. 2004; Kitaura et al. 2006; Dessart et al. 2006). EC SNe account for the small population of NSs shown in Fig. 2 which are produced from the lowest mass ZAMS stars.

For an iron-core collapse SN (FeCC SN) a Maxwell-Boltzmann distribution

$$f(w) = \sqrt{\frac{54}{\pi}}\,\frac{w^2}{w_{\rm rms}^3}\,\exp\left(-\frac{3}{2}\,\frac{w^2}{w_{\rm rms}^2}\right) \tag{13}$$

is used for the kick velocity, w. The default value for the projected 1-dimensional root-mean-square velocity is $w_{\rm rms}^{\rm 1D} = 265$ km s^{-1}, taken from (Hobbs et al. 2005). The 3-dimensional $w_{\rm rms}$ of the Maxwell-Boltzmann distribution is then found by $w_{\rm rms} = \sqrt{3}\,w_{\rm rms}^{\rm 1D}$. We select the kick magnitude and orientation for each SN event using Monte Carlo techniques. The kick orientation is assumed to be isotropic.

If the progenitor of the exploding star loses its hydrogen envelope as a consequence of mass loss to its companion star, $w_{\rm rms}^{\rm 1D}$ is reduced to 120 km s^{-1}. An even more stripped progenitor star, which also loses its helium envelope prior to the core collapse (via Case BB RLO, Habets 1986), is treated with $w_{\rm rms}^{\rm 1D} = 60$ km s^{-1}, unless this star has a compact object companion. If the exploding star forms the second-born compact star of the binary, it undergoes an ultra-stripped SN (Tauris et al. 2013, 2015; Suwa et al. 2015; Moriya et al. 2017) because of severe mass stripping by the nearby compact object, leaving an almost naked metal core at the time of the explosion. For such ultra-stripped SNe we apply $w_{\rm rms}^{\rm 1D} = 30$ km s^{-1}.

Although the kick magnitudes are generally believed to be smaller for the core collapse of stripped stars, there is evidence from observations that a minor fraction of the FeCC SNe still produce rather large kicks. For ultra-stripped SNe this is motived by the kinematics of known double NS systems; see detailed discussions in Tauris et al. (2017). According to this work, such a difference in kick magnitudes is possibly related to the mass of the final iron core and thus to the mass of the resulting NS. As a result, for these stripped and ultra-stripped stars we apply in ComBinE a bimodal kick distribution with 80 per cent of the explosions receiving reduced kick magnitudes as stated above, and the remaining 20 per cent receiving a large kick of $w_{\rm rms}^{\rm 1D} = 200$ km s^{-1}. We remind the reader that in a Maxwellian distribution the average 3-dimensional kick magnitude is $\sqrt{8/\pi}\,w_{\rm rms}^{\rm 1D} \simeq 1.60\,w_{\rm rms}^{\rm 1D}$.

Regarding kicks on newly formed BHs less is known (Nelemans et al. 1999; Janka 2013; Repetto & Nelemans 2015; Mandel 2016). Therefore, a simple flat 3-dimensional distribution up to 200 km s^{-1} is used as our default distribution.

To solve for the post-SN orbital dynamics (also including the SN shell impact on the companion star) we apply the formulae of Tauris & Takens (1998), where a circular pre-SN orbit is assumed. To deal with eccentric orbits, the pre-SN separation and orbital velocity are taken at a random orbital phase from a flat distribution of the eccentric anomaly of the orbit. Any resulting changes of the mass of the companion star from the SN shell impact leads to a new stellar track following the prescription in Appendix A2. Depending on the SN mass loss and the kick velocity (magnitude and direction) the system may survive, disrupt or coalesce. A post-SN binary is assumed to coalesce in case the companion star fills its Roche lobe directly after the explosion.

2.2.7 *Gravitational wave radiation*

GW radiation leads to a shrinking of the binary orbit. Thus for a tight DCO binary, this may eventually lead to a merger event. ComBinE uses the prescription by Peters (1964) to calculate the delay time of a merger after the formation of the two compact objects:

$$t_{\rm merge} = \frac{15}{304}\,\frac{a_0^4\,c^5}{G^3\,m_1\,m_2\,M}\,\Xi(e_0), \tag{14}$$

where a_0 is the semi-major axis after the formation of the DCO binary, m_1 and m_2 are the two component masses,

$M = m_1 + m_2$ is the total mass and

$$\Xi(e_0) \equiv \left[\left(1 - e_0^2\right) e_0^{-\frac{12}{19}} \left(1 + \frac{121}{304} e_0^2\right)^{-\frac{870}{2299}}\right]^4 \cdot \int_0^{e_0} \frac{e^{\frac{29}{19}} \left(1 + \frac{121}{304} e^2\right)^{\frac{1181}{2299}}}{\left(1 - e^2\right)^{\frac{3}{2}}} \mathrm{d}e. \quad (15)$$

This time delay strongly depends on the separation of the two compact objects and the orbital eccentricity, e_0.

2.3 Galactic motion

Because a DCO binary often needs a long time to merge it can move a significant distance from its birth site within its host galaxy before the merger event. To follow the motion of a binary within a galaxy, a simple Runge-Kutta 4 integrator is used. As a default gravitational potential we apply a Milky Way-like potential (Allen & Santillan 1991) where the initial distribution of our binaries follow the mass density distribution of the disk component.

2.4 Computed quantities

To keep track of the evolution, ComBinE calculates the age, mass, core mass, radius, luminosity, effective temperature and the envelope structure parameter, λ, for both stars in the binary. The semi-major axis (orbital period), eccentricity, galactic position and velocity of each binary system is also tracked. Finally, after the DCO is formed, the time until the merger of the two compact objects is determined.

3 STELLAR GRIDS

ComBinE interpolates in dense girds of detailed stellar models. The underlying stellar models are calculated with the stellar evolution code BEC (e.g. Yoon et al. 2010, and references therein). In the following, we describe how we calculate the stellar grids from hydrogen-rich stars and helium stars, and how we determine the core-envelope boundary.

3.1 Hydrogen-rich stars

On the ZAMS, stars consists mainly of hydrogen. Brott et al. (2011) calculated grids of massive stars at various metallicities. Our computed grid takes its basis in similar calculations, performed with the same stellar code (BEC) but having more frequent full structure output to calculate the structure parameter of the envelope, λ.

3.1.1 Milky Way metallicity

For a Milky Way (MW)-like metallicity ($Z = Z_{MW} \equiv 0.0088$), the grid calculated by (Brott et al. 2011) contains evolved models starting from ZAMS stars with masses from 3 $M_\odot$ to 100 $M_\odot$. To make use of this grid for the ComBinE code, we extended it to lower ZAMS masses (down to 0.5 $M_\odot$) and added some more intermediate-mass tracks as well. The grid is also refined by evolving some existing models of Brott et al. (2011) to a more advanced nuclear burning stage[4] and by adding some intermediate data points with full information about the stellar structure. In all these cases, we used the same parameters and version of BEC as Brott et al. (2011). An extension to higher masses with similar parameters were numerically unstable with this version of BEC. Therefore, the grid is simply extrapolated to higher masses

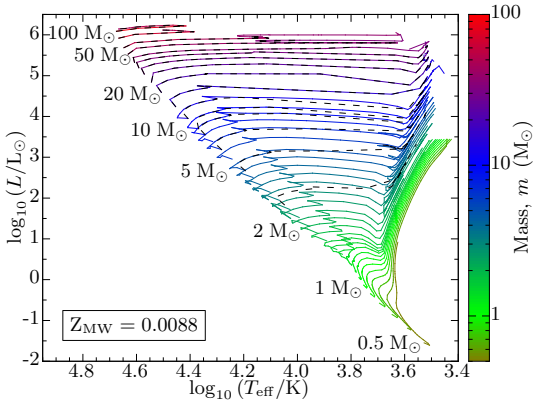

Figure 3. Hertzsprung-Russell diagram of our non-rotating stars at Milky Way metallicity, see Section 3.1.1. The mass along the tracks is colour-coded and the black dashed lines are the original models of Brott et al. (2011) which contain less full structure data. For low-metallicity tracks, see Brott et al. (2011) and Szécsi et al. (2015).

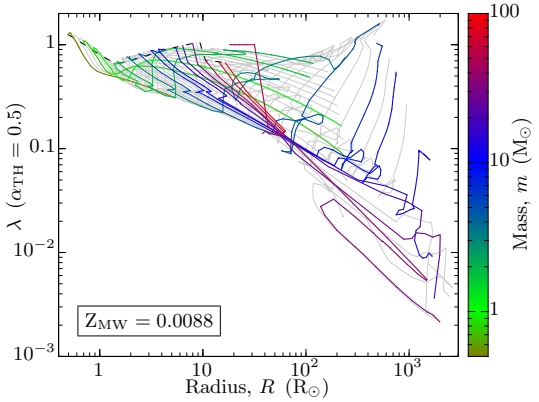

Figure 4. Dependence of the envelope binding energy parameter, λ, on stellar mass, m, and stellar radius, R. The grey models are the same as in Fig. 3. The models with an initial mass of 0.5, 0.8, 1.0, 1.5, 2.0, 3.2, 5.0, 8.0, 10.0, 15.0, 20.0, 30.0, 50.0, 80.0 and 100 $M_\odot$ are shown in colour according to their mass at a given point along the tracks. The dashed line marks the ZAMS values.

[4] The end of the calculation of the detailed stellar models is caused by numerical instabilities during carbon burning or when the density of the outermost envelope becomes too low.

if needed; see e.g. the curve beyond the last data point in the lower left panel of Fig. 2 where the wind mass loss becomes very strong.

Fig. 3 shows a Hertzsprung-Russell diagram (HRD) of the models at MW metallicity for non-rotating stars. Compared to the HRDs shown in Brott et al. (2011), Fig. 3 only contains line-connected data points where information on the full stellar structure is saved. Before using the grid data, the required quantities are extracted for ComBinE. These are the total mass, m, the time since ZAMS, t, the photospheric radius, R, the core mass, $m_{\rm core}$ – the chosen core-envelope boundary is discussed in Section 3.3 – the luminosity, L, the effective temperature, $T_{\rm eff}$ and the structure parameter of the envelope, λ (Equation (10)). Two λ-parameters are saved: one only accounting for the gravitational binding energy, and one taking the additional internal energy (including recombination energy) into account. In this way, one can choose the considered amount of internal energy when running ComBinE. To speed-up our code, with the knowledge that it uses linear interpolations, the tables of the stellar tracks are reduced to the required number of supporting points which are needed to keep a given precision[5].

Fig. 4 shows how λ depends on stellar mass and radius. This structure parameter is very crucial for the all-important CE prescription. It is clear that treating CE evolution for all stellar masses and at all evolutionary stages using a constant λ is a poor approximation given that λ varies by more than two orders of magnitude (see e.g. Dewi & Tauris 2000, 2001; Kruckow et al. 2016). In this respect, it is surprising to see the use of a constant λ-value in several recent papers on population synthesis, e.g. on DCO merger rates for LIGO, and which therefore are quite likely to lead to erroneous results.

The λ–values in Fig. 4 are calculated for $\alpha_{\rm th} = 0.5$, i.e. by taking 50 per cent of the internal energy of the envelope into account as in our default setup. The influence of the amount of internal energy included on our results is discussed in Appendix D3.

We caution against the method of applying calculated λ-values from the literature to stellar grids based on a different stellar evolution code. For example, when combining our stellar tables based on the BEC code with λ-values based on the Eggleton code (taken from Dewi & Tauris 2000, 2001), the GW merger rates change significantly compared to the self-consistent treatment applied in ComBinE. In the former case, the rates for double NS and BH-NS binaries increase by roughly 1 dex. The NS-BH systems and double BH binaries increase by roughly 2 dex. These large discrepancies demonstrate the importance of λ and stellar tracks being calculated with the same stellar evolution code.

The mass of the stellar envelope usually decreases as nuclear burning shifts material from the inner edge of the hydrogen envelope to the helium core and, at the same time, stellar wind material is lost from the outer edge of the envelope. In the most massive stars, very strong winds strip the whole envelope. The only way to increase the mass of the envelope in single star models is to mix some core material into the envelope. The radius, on the other hand, increases during the expansion phases on the giant branch(es). Usually the binding energy of the envelope, $|E_{\rm bind}|$, decreases during stellar evolution. Whether λ decreases or increases depends on the dominating term in the change of mass, radius or binding energy (e.g. Kruckow et al. 2016).

[5] All stellar quantities are restricted at all times to be precise within 2 per cent of a model based on the full available data.

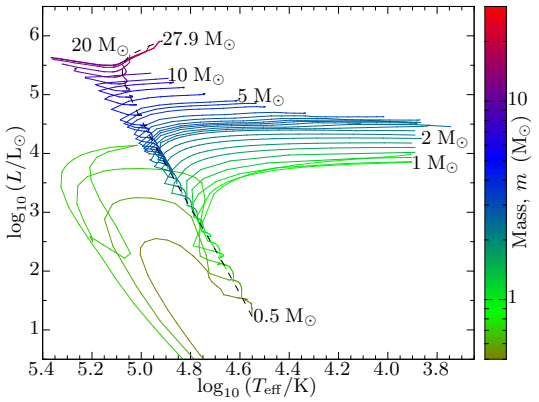

Figure 5. HRD of non-rotating naked helium stars at MW-like metallicity, see Section 3.2. The mass along the tracks is colour-coded. The black dashed line marks the He-ZAMS.

Besides our default, non-rotating simulations, a data set for rapidly rotating stars at MW-like metallicity from Brott et al. (2011) is also available in ComBinE. In this case, however, the mass range is limited to $3\ {\rm M}_\odot \leq m_{\rm ZAMS} \leq 100\ {\rm M}_\odot$. Rotating stars are not included in the study presented here.

3.1.2 Lower metallicities

In the present investigation of GW merger sources, it is important also to consider binaries in low-metallicity environments. We thus include stellar tracks for metallicities equal to those of the Large Magellanic Cloud (LMC, $Z = {\rm Z_{LMC}} \equiv 0.0047$) and the Small Magellanic Cloud (SMC, $Z = {\rm Z_{SMC}} \equiv 0.0021$), which are taken form Brott et al. (2011). Our lowest metallicity included is at a similar level as that of the dwarf galaxy IZwicky18 (IZw18, $Z = {\rm Z_{IZw18}} \equiv 0.0002 \simeq 0.02\ {\rm Z_\odot}$) and these stellar tracks are adopted from Szécsi et al. (2015) which cover a mass range from 4 $\rm M_\odot$ to 294 $\rm M_\odot$. Note, the metal distribution among the chemical elements is slightly different between the different metallicity tracks mentioned above.

3.2 Helium stars

ComBinE assumes that the mass-transfer stage peels off the whole hydrogen-rich envelope and leaves a naked helium-rich core as remnant. Fig. 5 shows the tracks of naked helium stars evolved with BEC. The plotted region with an overdensity of tracks contains the isolated helium star models of Tauris et al. (2015). We calculated additional models following the same recipe. Here again, we only plot the data points with full stellar structure data. The helium stars with the lowest masses do not evolve into a giant stage and evolve

directly onto the WD cooling track during the helium shell burning. The 0.7 $M_\odot$ model shown in Fig. 5 evolves through a helium shell flash and a thermal pulse. This phenomenon is similar to the thermal-pulse driven hydrogen shell flashes (e.g. Gautschy 2013; Istrate et al. 2016).

For the most massive of the helium stars in Fig. 5, the ZAMS turns to lower effective temperatures. At the same time they develop large inflated envelopes (Petrovic et al. 2006; Grassitelli et al. 2016). Such an inflated envelope is efficiently ejected by the winds of these stars. Therefore, their photospheric radius decreases during the first part of their evolution (evolving to higher effective temperature in Fig. 5). When a star with such an inflated envelope overfills its Roche lobe, the mass loss is not significantly increased compared to the wind mass loss (Kruckow et al. 2016). Therefore, mass-transfer algorithms like those described in Sections 2.2.3 and 2.2.4 should only be applied when the non-inflated part of the star fills its Roche lobe. To determine the boundary between the inflated and non-inflated part we follow Sanyal et al. (2015).

For helium stars with ZAMS masses up to 3.5 $M_\odot$ and evolving to the stage of Case BB RLO with a compact object accretor (i.e. post-HMXB/CE evolution), ComBinE uses the recent results of (Tauris et al. 2015) to determine their evolution.

We use the same helium star tracks for all the different metallicities. However, to account for the major effects of metallicity, we rescale the wind mass-loss rates according to Hainich et al. (2015).

3.3 Core-envelope boundary

During a mass-transfer phase (RLO or CE), it is always assumed that the whole envelope is lost and only the core remains. Therefore, a robust definition of the boundary which separates the core from the envelope is needed. Many different criteria exist to define this boundary and they often yield different results (Tauris & Dewi 2001).

On the one hand, the boundary should be located outside the hydrogen-depleted core. On the other hand, there should only be a small amount of hydrogen left within the core otherwise the exposed core would expand further and continue the mass transfer. In ComBinE, we apply the simple criterion that the hydrogen abundance in mass is $X = 0.1$ at the bifurcation point (e.g. Dewi & Tauris 2000). For further discussions on this topic we refer to Tauris & Dewi (2001); Ivanova (2011); Kruckow et al. (2016).

4 RESULTS

In this section, we present the outcomes of population synthesis runs with ComBinE. The parameters used in our default simulation are summarised in Table 2. Our choices of parameters resemble those of many other population synthesis investigations discussed in Section 5.2.2, with the exception of the accretion efficiency during RLO. We adopt highly inefficient mass transfer with an accretion efficiency of only $\epsilon \leq 0.05 = 1 - \alpha_{\rm RLO} - \beta_{\rm min}$. This choice leads to DCO results which best represent the observational data, especially the double NS systems, see below in Section 4.2.3 and Fig. 8. Furthermore, evidence to support highly non-conservative mass transfer during Case A and Case B RLO in massive binaries was investigated by Petrovic et al. (2005), and more recently presented by Shao & Li (2016) who found $\epsilon < 0.20$ to reproduce the observed Galactic population of WR/O-star binaries.

The synthesized data presented here is obtained by simulating $N = 10^9$ binary systems. In general, we find that our DCO merger rates converge for $N \geq 3 \times 10^8$ – except for the double BH systems where a statistical noise remains at the 2 per cent level. In a MW-like galaxy, we assume a constant star formation rate of one binary per year with a primary star mass > 0.8 $M_\odot$ (Hurley et al. 2002). This rate is rescaled according to the adopted primary mass range and the IMF. It is also applied at other metallicities to mimic the properties of both a young MW-like galaxy and a present-day observable MW.

As a comparison to our simulations with a MW-like metallicity, throughout this section we also present the results based on a low-metallicity case. There, the metallicity is set to $Z = Z_{\rm IZw18} = 0.0002$ although the initial mass ranges are slightly changed to $[5 : 150]\ M_\odot$ for both the primary and the secondary mass to allow more massive stars at lower metallicity (Klessen et al. 2012). In Section 5.2, we also present properties of DCO mergers based on LMC and SMC metallicities, thus simulating a total of four different metallicities for the GW sources.

4.1 Progenitor zero-age main-sequence masses

The progenitor masses of the stellar components of the binaries which form a bound system of two compact objects are shown in Fig. 6. In each pixel, the colour is a mixture reflecting the relative formation frequency of the different binary types. White regions indicate where no final DCO binary is formed.

The double NS systems (yellow) originate from binaries where both components are initially less massive than 33 $M_\odot$ (bottom left). The paucity of these systems produced from secondary stars with masses above 20 $M_\odot$ is explained by the vast majority of double NS progenitor systems evolving through a CE phase. It is difficult for an in-spiralling NS to successfully eject the envelope of a donor star with $m^{\rm s}_{\rm ZAMS} \gtrsim 20\ M_\odot$ at MW metallicity (Kruckow et al. 2016).

The more massive the primary star is, the more likely it produces a BH, eventually leading to a BH-NS binary (bottom right, red region). A slight overlap is seen, but less pronounced in the low-metallicity case. In such overlapping areas where the red region becomes yellowish or blueish, the binaries originate from a primary or secondary star too massive to produce a NS in single star evolution. However, as a result of mass transfer and mass loss these systems end up producing NSs anyway. The BH-NS binaries at the very bottom of the population with secondary ZAMS masses less than 10 $M_\odot$, especially at low metallicty, are mainly wider systems where the NS forms with small kicks, often by EC SNe.

Few NS-BH systems (green) form in our default simulations. Since mass accretion is needed for the secondary star to produce a BH in cases where the primary star produces a NS, the choice of a small accretion efficiency ϵ (Section 4) hinders the formation of NS-BH systems. Those few NS-BH binaries that do form have an initial mass ratio close to one.

Table 2. Initial values and default settings of key input physics parameters.

name	value	note
number of simulated binaries, N	10^9	our results converge for $N \geq 3 \times 10^8$
primary mass, $m^{\rm p}_{\rm ZAMS}$	$\in [4:100]$ M$_\odot$	Salpeter IMF, see Section 2.1.1
secondary mass, $m^{\rm s}_{\rm ZAMS}$	$\in [1:100]$ M$_\odot$	from mass ratio, see Equation (2) and Section 2.1.1
semi-major axis, a	$\in [2:10000]$ R$_\odot$	flat in log(P), see Section 2.1.2
eccentricity, e	0	initially circular orbit, see Section 2.1.2
metallicity, Z	$Z_{\rm MW}$	Milky Way-like, see Section 2.1.3
rotation, $v_{\rm rot}$	0 km s^{-1}	non-rotating stars, see Section 2.1.3
wind mass loss, $\alpha_{\rm RLO}$	0.20	during RLO (Soberman et al. 1997), see Section 2.2.3
minimum mass ejection by accretor, $\beta_{\rm min}$	0.75	during RLO (Soberman et al. 1997), see Section 2.2.3
circumbinary torus mass transfer, $\delta_{\rm RLO}$	0	during RLO (Soberman et al. 1997), see Section 2.2.3
circumbinary torus size, γ	2	during RLO (Soberman et al. 1997), see Section 2.2.3
CE efficiency parameter, $\alpha_{\rm CE}$	0.50	during CE, see Section 2.2.4
fraction of internal energy, $\alpha_{\rm th}$	0.50	during CE, see Section 2.2.4
mass ratio limit, $q_{\rm limit}$	2.5	criterion for stable / unstable mass transfer, see Section 2.2.3
kick velocity, w	> 0 km s^{-1}	from the distribution of SN kicks, see Table 1 in Section 2.2.6

In most cases mass transfer slows down the evolution of the primary to the extent that the secondary forms the BH first before the initial primary becomes a NS. Further discussions on the formation of NS-BH binaries are given in Section 5.3.

The largest region in Fig. 6 is blue indicating the formation of double BH binaries. Note, double BH systems occupy the largest area in the phase space of ZAMS masses but are not the most common DCO systems formed at MW-like metallicity (see Table 3 in Section 4.2 and Fig. 14 in Section 4.4). The diagonal border separating the dense and the sparse populated regions of both the double BH and the BH-NS binaries is caused by the adopted mass-ratio limit, $q_{\rm limit}$, to differentiate between stable and unstable mass transfer.

In the low-metallicity case, the formation of double BHs dominates for two reasons: i) the stellar winds are less strong and therefore create more massive BH progenitors, resulting in more massive BHs. Massive BHs can more easily eject the CE during in-spiral and thus eventually produce a BH-BH binary. The weaker stellar winds also result in more massive companion stars such that these binaries survive SN kicks more easily. ii) a low-metallicity environment allows for more massive ZAMS stars to form (Klessen et al. 2012) and, assuming the star-formation rate and the IMF slope remain constant, this leads to the formation of more BHs (Table D1).

Finally, no BHs are formed from single stars with an initial mass above 140 M$_\odot$ in our low-metallicity simulations (empty region in the lower panel of Fig. 6) because such massive stars end their life in a PISN with no compact-object remnant (Heger & Woosley 2002). In our binary systems, however, PISNe are assumed to occur at other ranges in initial mass. In ComBinE, stripped stars with initial masses exceeding 106 M$_\odot$ produce helium stars with masses above 64 M$_\odot$ which are expected to obtain lower central densities at high temperatures and result in a PISN (Heger & Woosley 2002). This explains the vertical border at 106 M$_\odot$ separating the dense and the sparse region of BH-BH systems in the lower panel of Fig. 6. Pulsational PISNe (Woosley 2017) are thought to remove a substantial amount of mass from stars shortly before their final core collapse and therefore lead to a similar effect of further reducing the upper mass limit of the BHs formed below the ordinary pair instability regime.

In Appendix C we list in detail the various formation channels leading to the different DCO binaries.

4.2 Compact object masses

Fig. 7 shows the plane of the compact object masses ($m_{\rm cobj}$) for NSs and BHs produced by our simulations. There are four distinct regions labelled in the upper panel. Those are the double NS systems in the lower left corner, the mixed BH-NS and NS-BH systems populating the regions above the x-axis at higher masses and the small population close to the y-axis around 7 M$_\odot$, and finally the double BH systems occupying the top right part of the plot ($m_{\rm cobj} > 6$ M$_\odot$). The double BH systems show two separated populations at high metallicity (upper panel). The vast majority of the systems have BH masses $m_{\rm cobj} < 13$ M$_\odot$ and the more massive of the two BHs is the remnant of the primary star. In addition, a few double BH binaries form with secondary BH masses $m^{\rm s}_{\rm cobj} > 13$ M$_\odot$. These systems have a less massive primary BH. For a more efficient mass accretion process this sub-population would be more populated (Appendix B2).

At high metallicity, the masses of the BHs are moderate because of relatively strong wind mass loss during the stellar evolution. Given that the resulting masses of BHs and NSs in our models mostly increase monotonically[6] with the mass of the progenitor stars for isolated evolution, at least all systems above the black dashed line in Fig. 7 had some binary interaction during their evolution.

At low metallicity (Fig. 7, lower panel) the DCO systems are dominated by systems containing BHs. These BHs can reach significantly higher masses because the progenitors have weaker winds and lose less mass. This also results in a higher survival rate of CE evolution where such massive BHs more easily strip-off the envelope of their donor star companion by spiral-in (Kruckow et al. 2016). The lower panel of Fig. 7 thus covers a much larger BH mass range compared to the upper panel at high metallicity.

The minimum BH mass originating from a non-stripped

[6] We are aware that many detailed studies of SN explosions and their progenitors find evidence for a rather non-monotonic mapping of (ZAMS) progenitor star mass and final compact object mass (Ugliano et al. 2012; Pejcha & Thompson 2015).

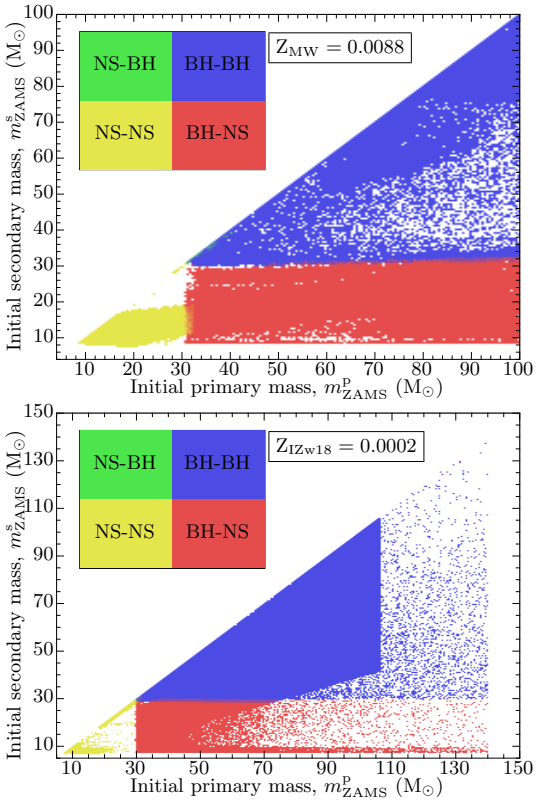

Figure 6. Progenitors of the systems forming a DCO binary. The upper panel is for a MW-like metallicity ($Z = Z_{MW} = 0.0088$) and the lower panel shows systems at low metallicity ($Z = Z_{IZw18} = 0.0002$). Their final compact object masses are shown in Fig. 7. Colour-coded is the type of the two compact objects formed from the initial primary and secondary star, respectively. This type is not necessarily the formation order. In some cases the secondary star forms a compact object first. The barely visible NS-BH systems originate from ZAMS binaries with a mass ratio close to one and $30\,M_\odot \lesssim m^p_{ZAMS} \lesssim 40\,M_\odot$ (Section 4.1).

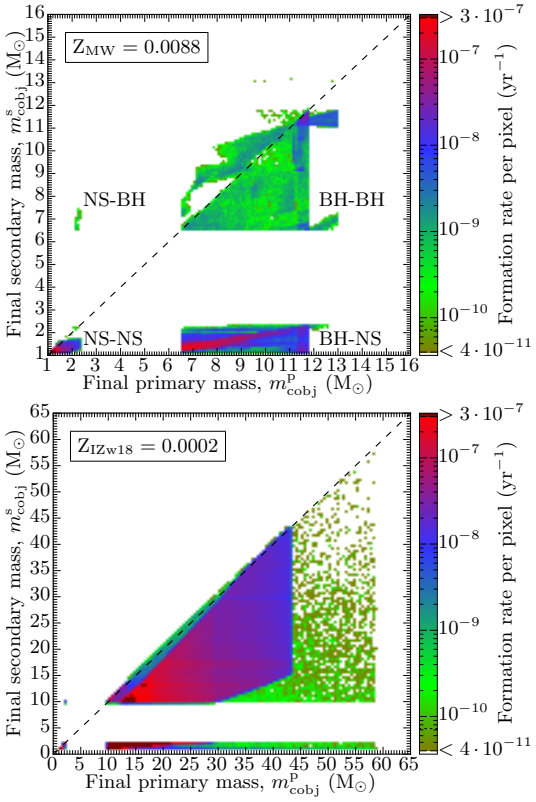

Figure 7. Masses of NSs and BHs in DCO binaries at high metallicity ($Z = Z_{MW} = 0.0088$, upper panel) and low metallicity ($Z = Z_{IZw18} = 0.0002$, lower panel). The initially more massive star produces the primary compact object with the mass, m^p_{cobj} while the secondary star produces a compact object with a mass m^s_{cobj}. The formation rate per grid cell of such systems in a MW-like galaxy is colour-coded. The minor tics show the pixel size. The black dashed line indicates equally massive compact objects. For more details see Section 4.2. A more efficient mass transfer would change this picture, cf. Fig. B2.

Table 3. Formation rates of DCO binaries in a MW-like galaxy at two different metallicities with our default setting. The binary types quote the first and second formed compact object.

Formation rates	$Z_{MW} = 0.0088$	$Z_{IZw18} = 0.0002$
NS-NS	6.81×10^{-6} yr^{-1}	1.53×10^{-5} yr^{-1}
NS-BH	5.49×10^{-9} yr^{-1}	1.65×10^{-8} yr^{-1}
BH-NS	1.49×10^{-5} yr^{-1}	4.27×10^{-5} yr^{-1}
BH-BH	2.27×10^{-6} yr^{-1}	9.65×10^{-5} yr^{-1}

star is larger the lower the metallicity, as there is more mass left in the envelope which can contribute to the BH. Table 3 shows the total formation rates of DCO binaries at two different metallicities of galaxies otherwise similar to the MW, while Fig. 7 and succeeding figures differentiate into the grid cells of different mass ranges.

In the following subsections we discuss the different binary types formed at high metallicity, as shown in the upper panel of Fig. 7.

4.2.1 Double black hole binaries

First, we look at the remnant masses in the double BH population evolved at a MW-like metallicity as shown in the upper panel of Fig. 7. The largest visible sub-population creates a triangular shape like the progenitors shown in Fig. 6. All binaries without interactions, or only minor interactions, fall into this region. The binaries where either the secondary star becomes the more massive BH or the primary BH obtains a mass above $11.8\,M_\odot$ originate from progenitor binaries which experienced intensive interactions. To obtain a secondary BH more massive than the primary BH, at an

early stage in the primary's evolution it has to lose or transfer some material to its companion star. In our simulations, mainly Case A mass transfer is responsible for a final mass ratio reversal. Furthermore, the initial mass ratio should be close to one.

At high metallicity, because of strong winds, the remnant core masses of our very massive single star models ($m^{\rm p}_{\rm ZAMS} > 80\,{\rm M}_\odot$) can become less massive than those which are left in stars which have their envelope removed by mass transfer while still on the main sequence. Therefore, our most massive Case A RLO primaries of MW metallicity can form slightly more massive BHs than compared to single stars.

4.2.2 Mixed binaries

Mixed binaries (BH-NS or NS-BH) are the most frequent DCO systems resulting from our default simulations, see Table 3. The labels in Fig. 7 refer to the compact objects resulting from the primary and secondary stars, respectively. In most cases this is also the formation order of the two remnants. However, in some rare cases the secondary star (after accretion) evolves faster than the primary star and thereby the formation order reverses. In all the cases where the primary star produces a NS while the secondary star produces a BH, the primary star has to lose or transfer mass to the secondary star. Furthermore, because of our assumption of inefficient accretion, both stars must have ZAMS masses close to the border between forming a NS or a BH.

In the vast majority (99.96 per cent) of mixed systems the primary star produces a BH and the secondary star produces a NS, cf. upper panel of Fig. 7. In those binaries the parameter range of initial configurations is much larger compared to the NS-BH systems. Here again, the most massive of the primary BHs are produced by Case A RLO from the primary progenitor star ($m^{\rm p}_{\rm ZAMS} > 80\,{\rm M}_\odot$). This is seen as an upper right extension of the red diagonal in the BH-NS binaries on the upper panel of Fig. 7. Whenever there is a limiting or preferred initial mass ratio, a diagonal structure from the lower left to the upper right is created, as more massive progenitors usually produce more massive NSs or BHs.

Additionally, there is a small over-density of systems produced at the more massive end of the BH-NS population, as one sees in double BH binaries. This feature is caused by the simple fact that a progenitor binary with more massive stars more easily remains bound following a SN explosion.

4.2.3 Double neutron star binaries

Fig. 8 shows a zoom-in on the double NS systems plotted in the upper panel of Figs 7 and B2, respectively. The black data points are measured NS masses and where we have assumed that the observed recycled pulsars originate from the primary stars. The measurement error bars are much smaller than the symbol sizes.

The observed data matches the distribution of our theoretical simulations using a highly inefficient mass-transfer process much better than in the case of efficient mass-transfer, cf. upper and lower panel, respectively. This is the main reason for the choice of $\beta_{\rm min} = 0.75$ as our default. As

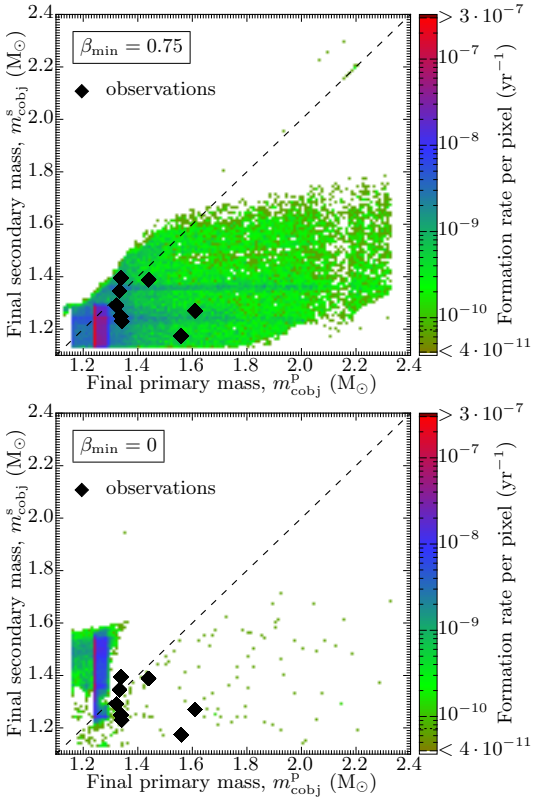

Figure 8. The upper panel shows a zoom-in on the double NS systems plotted in the upper panel of Fig. 7. Because the resolution is increased, the formation rate per grid cell is smaller. In the lower panel, more efficient mass transfer $\beta_{\rm min} = 0$ is used. For more details see Section 4.2.3. The observational data is taken from Tauris et al. (2017, and references therein), Cameron et al. (2017) and Ferdman (2017).

seen in the lower panel, efficient mass transfer strongly suppresses the formation of primary (recycled) NSs with masses $\gtrsim 1.35\,{\rm M}_\odot$. The reason for this is that the first mass-transfer phase from the primary to the secondary star becomes unstable when the mass-transfer rate exceeds the Eddington limit of the secondary star.

More than 98 per cent of the double NS binaries experience mass transfer from the primary star to its companion prior to the first SN. The majority of these systems undergo Case B RLO. Interestingly, the systems undergoing Case A RLO from the primary star only produce massive double NS binaries with $1.97\,{\rm M}_\odot < m^{\rm p}_{\rm cobj} < 2.15\,{\rm M}_\odot$. Finally, mass transfer (Case B/C RLO) onto an already evolved secondary star is responsible for the outliers from the overall shape at low primary or high secondary NS masses.

Our results in Fig. 8 show a clear over-density of primary NS masses around $1.25\,{\rm M}_\odot$. These NSs are created by an EC SN instead of an FeCC SN (e.g. Schwab et al. 2010). This NS formation channel is clearly favoured in our default

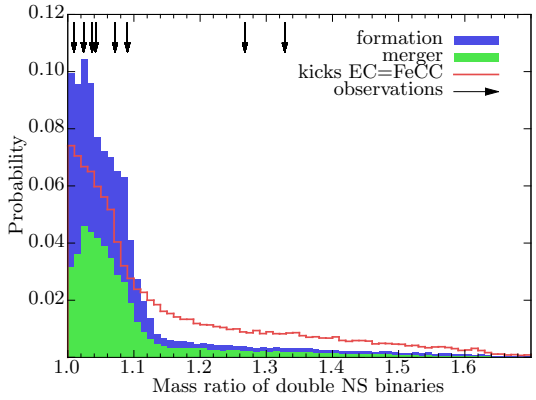

Figure 9. Histogram of the mass ratios of our simulated double NS binaries. In blue colour is shown the probability distribution for all formed a double NS systems, whereas the green colour applies to those which will merge within a Hubble time. The red line shows the mass ratio distribution of double NS systems formed when the kicks applied to EC and FeCC SNe are similar, see discussion in Section 5.1.2. The observational data of eight mass ratios from binary radio pulsars (Tauris et al. 2017; Cameron et al. 2017; Ferdman 2017) are indicated by arrows. The largest mass ratio of roughly 1.33 is that of PSR J0453+1559 (Martinez et al. 2015). GW170817 (not shown) had a mass ratio somewhere between $1.0 < q < 1.4$ (Abbott et al. 2017c).

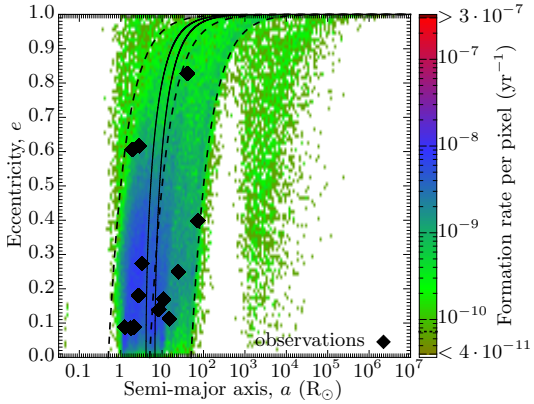

Figure 10. Eccentricity versus semi-major axis of double NS systems after the birth of the second-formed NS. Colour coded is the formation rate per grid cell of such systems in a MW-like galaxy. The minor tick marks show the grid cell size. The dashed black lines show a constant periastron separation of 0.5 $R_\odot$, 5 $R_\odot$ and 50 $R_\odot$. The solid lines are for t_{merge} equal to a Hubble time (the left one is for the minimum and the right one for the maximum NS mass configuration). The black diamonds are measurements taken from Tauris et al. (2017, and references therein), Cameron et al. (2017) and Martinez et al. (2018).

simulations. EC SNe are assumed to produce much smaller NS kicks which makes it easier for the post-SN binary to remain bound and yet often tight enough to initiate a subsequent CE phase. As the binary separation shrinks significantly during a CE and spiral-in phase, the kick of the second formed NS can be much larger without disrupting the binary (e.g. Tauris et al. 2017). Nevertheless, a clear discrepancy between our simulated primary NS masses, with a strong over-density of EC SNe, and observational data is seen and potential explanations are discussed in Section 5.1.2.

Fig. 9 shows a histogram of the mass ratios, q, of the simulated double NS systems plotted in the upper panel of Fig. 8. The agreement with observed systems looks fine, given the small number statistics. According to our simulations, a very few systems are even produced with a mass ratio > 1.7.

4.3 Orbital parameters

After the second compact object is formed in an isolated binary no further wind mass loss or mass transfer occurs until the system eventually merges. The orbital parameters will consequently only change slowly because of GW radiation.

4.3.1 Double neutron star binaries

Fig. 10 shows the orbital eccentricity and semi-major axis of the double NS binaries plotted in the upper panel of Fig. 8. Here again, the colour coding represents the formation rate per grid cell of such systems in a MW-like galaxy. The three thick dashed lines in Fig. 10 show systems with a constant periastron separation of 0.5 $R_\odot$, 5 $R_\odot$ and 50 $R_\odot$, respectively. The two solid lines indicate the boundaries to the left of which systems will merge within a Hubble time by pure GW radiation, using the least and the most massive NS combination from our simulations: $(m^{p}_{cobj}, m^{s}_{cobj}) = (1.161\ M_\odot, 1.137\ M_\odot)$ and $(2.158\ M_\odot, 2.299\ M_\odot)$, respectively.

Two main sub-populations are visible for eccentricities, $e < 0.9$ in Fig. 10. The most dominant one is the subpopulation with orbital separations of $1\ R_\odot \lesssim a \lesssim 100\ R_\odot$. All systems in this region survived one CE phase in their evolution. The widest of these systems usually had a large separation at the onset of the CE phase and a relatively massive in-spiralling NS. Both of these conditions help to unbind the CE and thus result in a wide orbit after its ejection.

The observed double NS systems coincide nicely with the peak population of our simulated systems in Fig. 10. In the bluish/purple region, all values of our simulated NS masses (≈ 1.14 to $2.30\ M_\odot$) are present. One should keep in mind that the observed systems did not necessarily evolve from progenitor binaries with the same metallicity or mass-transfer efficiency (cf. Fig. B5 first panel).

Fig. 11 shows a version of Fig. 10 in which all the systems are further evolved for 10 Gyr after the last SN. For each further 0.1 Gyr in time, the binaries contribute to this plot if they did not merge in the meantime. With the assumption that the formation rate was constant over time, this plot represents more correctly the observable systems present in our Galaxy today. The match between simulations and observations of double NS binaries looks even better here than in Fig. 10. We caution that a given observed system could, in principle, have been formed in a dense cluster and ejected afterwards, and therefore in that case it need

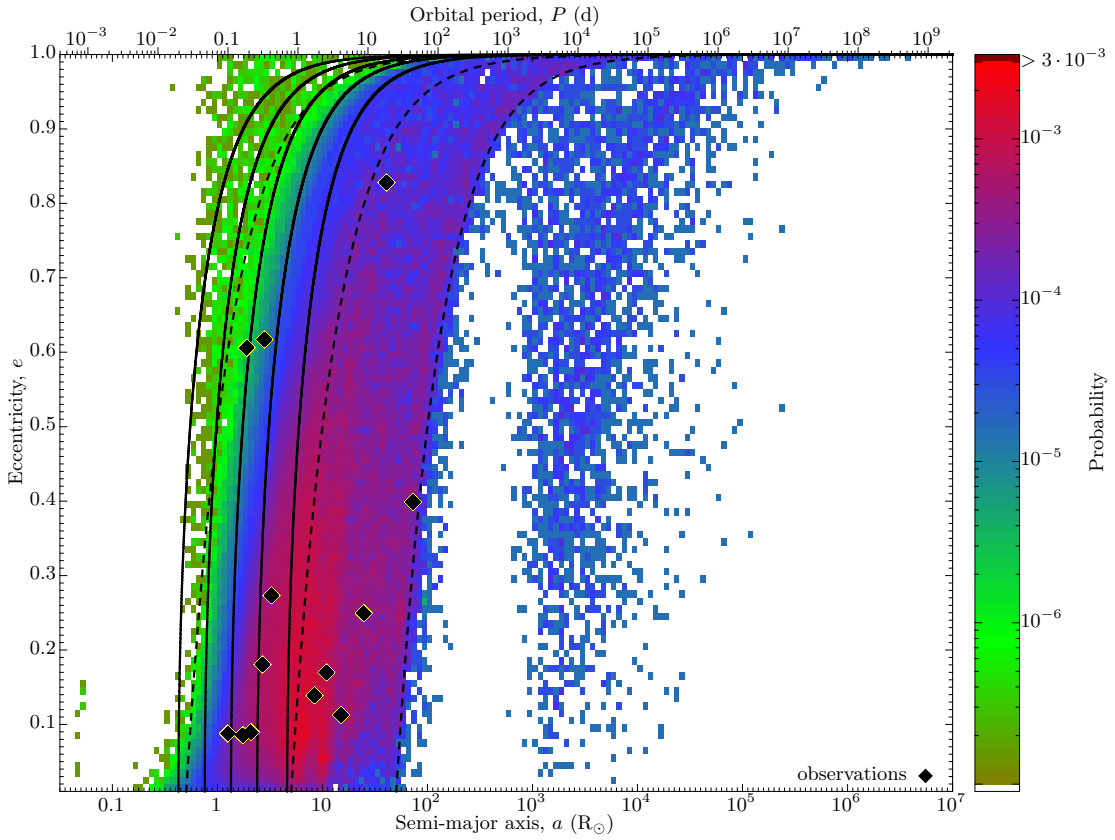

Figure 11. Eccentricity versus semi-major axis of the simulated double NS binaries where GW evolution over a timespan of 10 Gyr is included to change the observable parameters compared to their values at formation displayed in Fig. 10. The solid black lines show values of constant $t_{\rm merge} \in \{1\,\text{Myr}, 10\,\text{Myr}, 100\,\text{Myr}, 1\,\text{Gyr}, t_{\rm hubble}\}$ from left to right. The lines of constant $t_{\rm merge}$ and the orbital period scale on top assumes a mass of 1.35 $M_\odot$ for both NSs. The colour code shows the probability of each grid cell. The black diamonds are measurements taken from Tauris et al. (2017, and references therein), Cameron et al. (2017) and Martinez et al. (2018).

not be represented by our simulations of isolated binaries. However, from the shown data there are no indications that this is the case. All the observed double NS binaries are located somewhat close to the Galactic disk. The two known double NS binaries found in globular clusters have already been removed from the plotted data.

The wide binaries in Fig. 10 with $a \gtrsim 1000\,R_\odot$ are those which, after the first NS formed, avoided an unstable mass-transfer leading to a CE and spiral-in phase. The remaining bound systems which survived the second SN, and which are plotted here, experienced small kicks and are therefore likely to be dominated by NSs which underwent EC SNe. In Fig. 11, this sub-population becomes relatively more dominant as their orbital separations only decay by a marginal amount by GW damping. Therefore, they remain stationary in this plot, independent of when they were formed. A radio pulsar discovered in a double NS binary with an orbital period of the order 10 yr would thus be a good candidate to originate from an EC SN. In such wide binaries, both NSs remain non-recycled (Tauris et al. 2017), except for some negligible amount of wind accretion from its distant companion progenitor. Their lifetimes as active radio pulsars are expected to be similar to those of normal non-recycled radio pulsars (10 – 50 Myr, Lorimer & Kramer 2004; Johnston & Karastergiou 2017).

Finally, among our simulated systems there is a very minor, and probably never observed, sub-population of systems formed in very tight orbits with an orbital period of less than 2 min. These extreme systems are descendants of binaries which underwent two CE phases after the first NS formed. As the progenitor of the second NS becomes ultra-stripped the expected kick is low, leading to only small eccentricities of $e < 0.2$. GW radiation will merge these systems within 1000 yr after their formation.

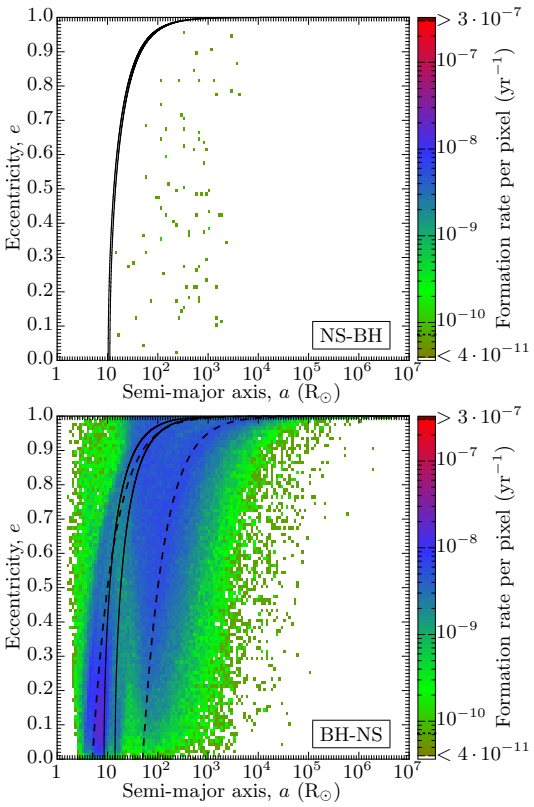

Figure 12. As Fig. 10 for the mixed systems consisting of one NS and one BH. In the upper panel the NS formed first, and in the lower panel the BH formed first. The dashed lines are constant periastron separations of 5 $R_\odot$ and 50 $R_\odot$.

4.3.2 Mixed binaries

The orbital parameters of the mixed binaries consisting of a BH and a NS are shown in Fig. 12. Compared to the double NS binaries all the different sub-populations overlap into one population.

The upper panel of Fig. 12 shows the few NS-BH systems in which the NS forms first. In all cases, there is no mass transfer after the formation of the NS. Therefore, based on our default simulations, we do not produce any recycled radio pulsars orbiting a BH (however, see the discussion in Section 5.3 on the formation of such systems). Because the NSs remain non-recycled in our default NS-BH binaries, it is impossible to differentiate them observationally from BH-NS binaries in which the NS forms second.

Among the BH-NS binaries (Fig. 12, lower panel) the widest systems are again the ones which evolved without any mass transfer after the first SN. Avoiding mass transfer from the NS progenitor to the BH means that the orbit is so wide prior to the second SN that this translates into a semi-major axis after the second SN of $a > 800\ R_\odot$.

The majority of the mixed systems belong to the thick blue band with $a \gtrsim 15\ R_\odot$. Prior to the second SN, these systems had orbital separations of $a \gtrsim 25\ R_\odot$. All these binaries only experienced stable mass transfer and no CE phase.

Only systems which had unstable mass transfer from the NS progenitor onto the BH create tighter binaries, and these contribute to observable GW events of mixed systems resulting from our default simulation. These systems, which evolved through a CE phase, follow mainly the narrow blue band with a minimum periastron separation of 2.5 to 5 $R_\odot$. The systems which become ultra-stripped may produce the binaries shown in Fig. 12 with large eccentricities and small semi-major axes, depending on the applied NS kick, see Section 2.2.6. To shrink to such a post-SN semi-major axis those kicks have to be directed close to opposite to the orbital velocity of the exploding star.

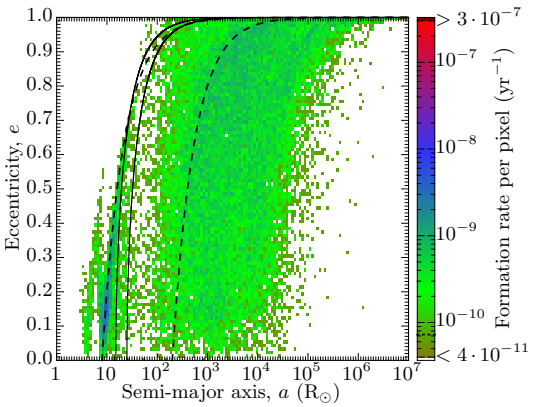

Figure 13. As Fig. 10 for the double BH systems. The dashed lines show constant periastron separations of 8 $R_\odot$ and 200 $R_\odot$, respectively.

4.3.3 Double black hole binaries

Our simulated double BH binaries also split into several sub-populations, as shown in Fig. 13. The widest systems are those without binary interactions. The systems at intermediate orbits have a stable mass transfer before the second BH forms. The tightest double BH binaries went through a CE phase.

The majority (88 per cent) of the double BH binaries in our simulations are too wide to merge within a Hubble time. Only the tightest or most eccentric double BH binaries produced will merge via GW radiation. Therefore, most of the BH-BH GW detections from a high-metallicity environment are dominated by systems which evolved through a CE phase – unless they are formed by a completely different formation channel not investigated here (Section 5.4).

4.4 Gravitational wave-driven merger rates

The orbit of a DCO binary shrinks over time because of GW radiation. Following Peters (1964), the merger time, $t_{\rm merge}$, of such a system is calculated following Equation (14). In Fig. 14, histograms of $t_{\rm merge}$ are shown for our simulated

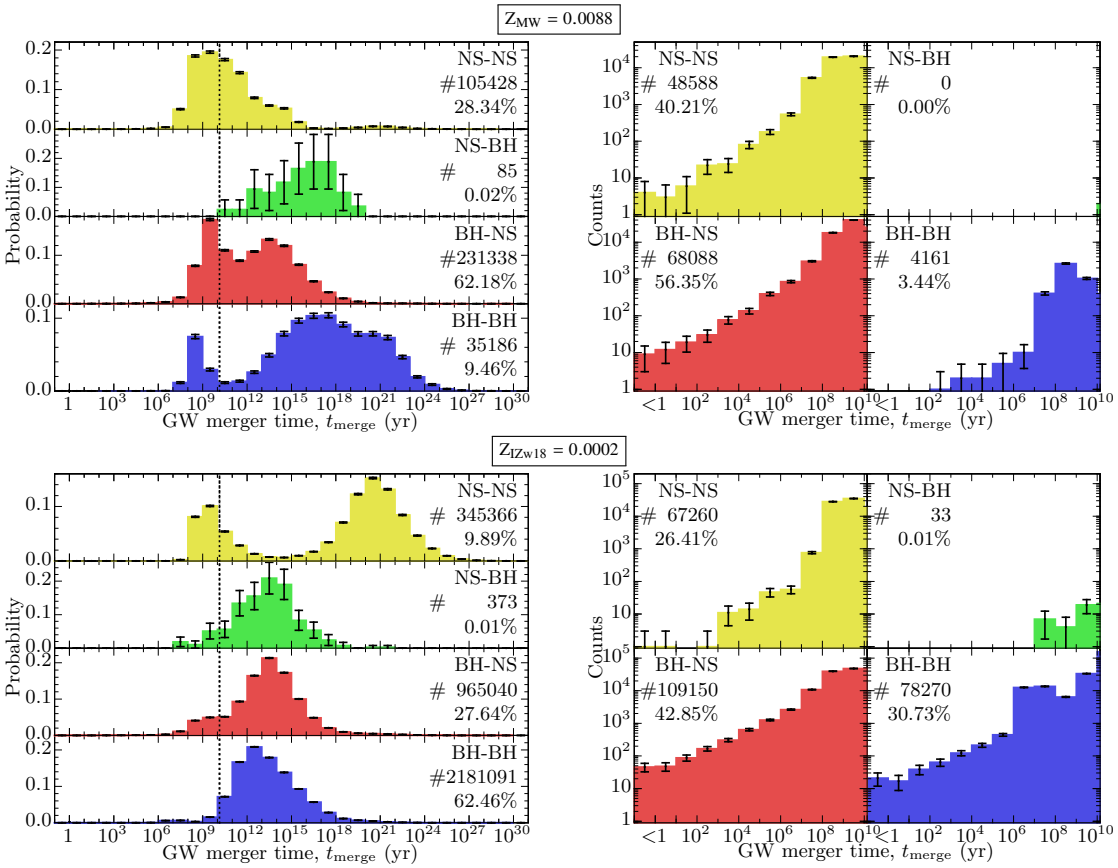

Figure 14. Left column: individually normalized probability distribution of the merger time, $t_{\rm merge}$ of our default simulation of DCO binaries. The black dotted line marks the Hubble time. Right column: Count of mergers with a given value of $t_{\rm merge}$ smaller than the Hubble time, for the same simulations shown in the left column. The order of the compact object formation is stated in the name of the binary type. Quoted in the legends are also the total and the relative number of systems shown in the sub-figures. The upper and lower rows are for different metallicities of $Z_{\rm MW} = 0.0088$ and $Z_{\rm IZw18} = 0.0002$, respectively. The error bars show the pure statistical 95 per cent confidence level.

Table 4. GW merger rates in a MW-like galaxy. The values are based on systems merging within 10^{10} yr. The upper and lower bounds are for systems merging within (10 ± 3.81) Gyr. The binary types indicate the order of the first and second-formed compact objects.

GW merger rates	$Z_{\rm MW} = 0.0088$	$Z_{\rm IZw18} = 0.0002$
NS-NS	$2.98^{+0.15}_{-0.24}\times10^{-6}$ yr^{-1}	$2.82^{+0.16}_{-0.27}\times10^{-6}$ yr^{-1}
NS-BH	$0.00^{+0.00}_{-0.00}\times10^{0}$ yr^{-1}	$1.33^{+0.13}_{-0.22}\times10^{-9}$ yr^{-1}
BH-NS	$4.05^{+0.35}_{-0.59}\times10^{-6}$ yr^{-1}	$4.57^{+0.26}_{-0.37}\times10^{-6}$ yr^{-1}
BH-BH	$2.64^{+0.05}_{-0.07}\times10^{-7}$ yr^{-1}	$2.96^{+0.50}_{-0.55}\times10^{-6}$ yr^{-1}

DCO binaries. It is clearly visible that each type of system has a main peak for $t_{\rm merge}$. Multiple peaks reflect different sub-populations of a given binary type. The most important factors affecting $t_{\rm merge}$ are the semi-major axis and the eccentricity. Given that $t_{\rm merge} \propto a^4$, a factor of 10 in semi-major axis in Figs 10–13 translates into a factor of 10^4 in $t_{\rm merge}$ in Fig. 14. The different masses of the DCO systems do not affect this behaviour by much.

The resulting merger rates of our simulated DCO binaries are shown in Table 4. At high metallicity ($Z = Z_{\rm MW} = 0.0088$, Fig. 14 upper panel) the systems which merge within a Hubble time are dominated by double NS and BH-NS binaries. The majority of double BH systems are produced with wide orbits because at high metallicity potential progenitors of tight BH-BH binaries often coalesce during the CE phase. The small peak in the double BH distribution with a merger time < 1 Gyr is caused by binaries where a massive primary BH survives the CE phase.

The lower panels of Fig. 14 show the merger time of DCO merger events in a low-metallicity environment. Although there are far more double BH and mixed binaries in this case, they do not clearly dominate the total rate of systems which merge within a Hubble time (Table 4). However, the chance of observing a merger also depends on the strain

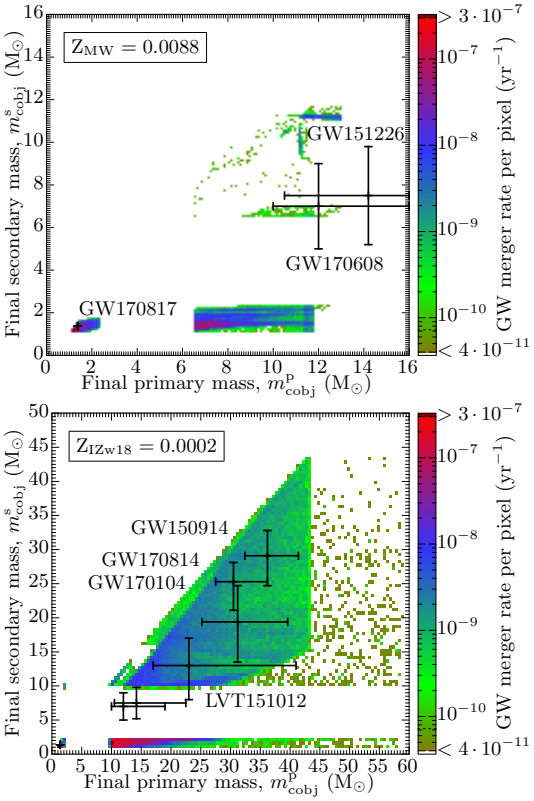

Figure 15. Distribution of simulated DCO binaries in the mass–mass plane for $Z_{MW} = 0.0088$ and $Z_{IZw18} = 0.0002$ (upper and lower panel, respectively). Colour coded are their merger rates per pixel, and for comparison, here assuming that the star formation rate is the same at both metallicities. The black data points are taken from the LIGO-Virgo events reported in Abbott et al. (2016a, 2017a,b,c); The LIGO Scientific Collaboration et al. (2017).

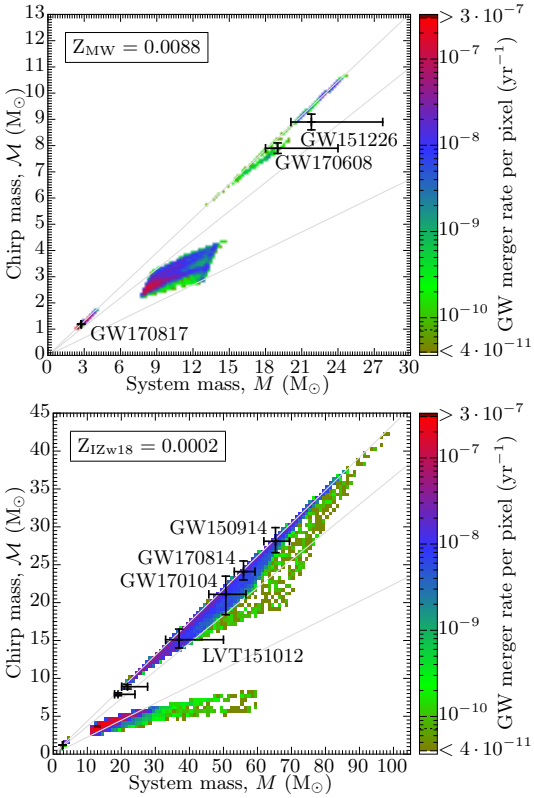

Figure 16. Distribution of simulated DCO binaries in the total mass–chirp mass plane for $Z_{MW} = 0.0088$ and $Z_{IZw18} = 0.0002$ (upper and lower panel, respectively). The three solid grey lines indicate a constant mass ratio of 1, 3 and 10 (from top to bottom). See Fig. 15 for further information.

of the GW signal, making double BH observations the most likely to be observed by far because of their larger masses, cf. Table 8.

Fig. 15 shows DCO masses and merger rates per pixel of our simulated systems in the mass–mass plane of the two compact objects. There are, as usual, four different types of binaries located at different areas in the plot: double BHs, double NSs and the two types of mixed binaries. The six announced LIGO detections of BH-BH GWs are included in the plots. Only the events GW151226 and GW170608 could have formed in a high-metallicity environment (see upper panel). The other four LIGO events need low metallicities (see lower panel) to obtain their larger BH masses, as also concluded by many other studies (e.g. Belczynski et al. 2016; Eldridge & Stanway 2016; Rodriguez et al. 2016b; Stevenson et al. 2017a). As all detected LIGO events are at distances $z = 0.1$ to 0.2, they are indeed likely to originate from a slightly lower metallicity environment than the MW (e.g. Pilyugin et al. 2013).

From GW merger observations one obtains the chirp mass and the total system mass. Fig. 16 shows this plane for high- and low-metallicity environments (upper and lower panels, respectively). Three different areas are seen corresponding to the double NS systems, the mixed systems (NS/BH) and the double BH systems. The double NS binaries have the lowest total masses and chirp masses. The mixed systems are located in the middle with large mass ratios, while the double BH binaries occupy the upper right part of the diagram at high values.

The extended parameter space of BH masses of our simulated systems at low metallicity covers all the reported GW merger events. Again, we conclude that only the events GW151226 and GW170608 could have formed in a metallicity environment like that of the Milky Way (and for GW170608 we find no solutions in a low-metallicity environment, see also Fig. 23). For more discussions about the LIGO events we refer to Section 5.2.4.

5 DISCUSSION

In the following section, we first discuss the influence of several of the input parameters applied in our simulations. We then compare our results to other population synthesis studies before we focus on the formation of the first seven events detected by LIGO-Virgo and give a general discussion on the inferred merger-rate densities. We also present a short discussion on the formation of recycled pulsars orbiting BHs and, finally, we briefly discuss alternative formation channels of DCO binaries.

5.1 Parameter studies

Most of our applied input parameters take values which are not known a priori and they are therefore uncertain to some degree. Table 5 shows how the DCO formation and merger rates are influenced by changing the different input parameters individually, compared to applying our default values given in Table 2. In the following subsections, the most important input parameters are discussed in more detail.

5.1.1 Supernova kicks

In Section 2.2.6, we outlined which kicks we apply depending on the evolutionary state of the exploding star, the type of SN and whether the compact object formed is a NS or a BH. There is some evidence to constrain these kick magnitudes, especially for double NS systems (Tauris et al. 2017), however the overall kick distribution for the various SNe remains a major uncertain aspect of modelling DCO binaries.

To test the effects of kick magnitudes, we performed a simulation in which all kick magnitudes (all types and all remnants) were reduced by a factor of 2. The third column of Table 6 shows how, as expected, smaller kicks lead to larger merger rates compared to those simulations with standard kicks. In double NS binaries, there is even an increase in the merger rate by a factor of 3. In double BH binaries, the effect of changing the kick magnitudes is relatively small because these systems have more mass to absorb the added kick momentum.

5.1.2 Electron capture vs. iron-core collapse supernovae

Specific to the NS-NS population, and to some extent the BH-NS and NS-BH populations, the ratio of EC SNe to FeCC SNe is significant in terms of the distribution of resulting NS masses. Although we can reproduce the observed distribution of NS-NS orbital separations and eccentricities (Fig. 11), our distribution of NS masses, in particular the masses of the first-formed NSs, strongly peaks at $\sim 1.25\,\mathrm{M}_\odot$, caused by NSs formed via EC SNe (Fig. 8). Using our default model, we find that for the first SNe the ratio of EC to FeCC SNe is about 1.8 in all the NS-NS systems formed and 1.1 in those which merge within a Hubble time. For the second (and in close orbits ultra-stripped) SNe, we find ratios of 0.2 and 0.07, respectively. However, in the observed distribution of NS masses in NS-NS systems, there is no evidence for such an EC SN peak.

With the empirical sample of NS-NS systems in the Galactic disk with precisely measured NS masses limited to only eight systems, it is difficult to argue that *any* of the first-formed NSs were produced via an EC SN. Depending on the NS equation-of-state, the gravitational mass of such a NS is expected to be about $1.37\,\mathrm{M}_\odot - E_\mathrm{bind}\,c^{-2}$, where the gravitational binding energy is of the order 0.10 to $0.14\,\mathrm{M}_\odot\,c^2$ (Lattimer & Yahil 1989). Thus EC SNe are expected to produce NSs with a particular gravitational mass somewhere in the interval 1.23 to $1.27\,\mathrm{M}_\odot$. However, none of the known NS-NS systems have a first-formed NS with such a small mass. It is remarkable, on the other hand, that 5 out of 9 systems have a first-formed NS within a narrow mass range of $1.32\,\mathrm{M}_\odot \lesssim m^\mathrm{p}_\mathrm{NS} \lesssim 1.34\,\mathrm{M}_\odot$. This implies that these NSs only originate from EC SNe if such SNe result in more massive NSs than assumed above and/or if these NSs have accreted of the order $0.08 \pm 0.01\,\mathrm{M}_\odot$ during the recycling phase. However, Tauris et al. (2017) recently argued that recycled NSs in double NS systems have accreted at most $\sim 0.02\,\mathrm{M}_\odot$, thus requiring EC SNe to produce NSs with birth masses of about 1.30 to $1.32\,\mathrm{M}_\odot$ to reconcile our simulations with observations.

To lower the ratio of NSs produced by EC to FeCC SNe, we made two simulations: i) applying similarly large kicks to NSs produced by EC SNe as those produced by FeCC SNe ($w_\mathrm{ECSN} = w_\mathrm{FeCCSN}$, see Table 1); and ii) decreasing the window in CO core masses producing EC SNe from $1.37\,\mathrm{M}_\odot \leq m^\mathrm{ECSN}_\mathrm{CO-core} < 1.435\,\mathrm{M}_\odot$ to $1.37\,\mathrm{M}_\odot \leq m^\mathrm{ECSN}_\mathrm{CO-core} < 1.38\,\mathrm{M}_\odot$. We now discuss the outcome of these two experiments.

Applying similar kicks to NSs produced in EC SNe as those produced in FeCC SNe (see Table 6) has a severe effect on the surviving population of NS-NS systems such that the ratio of EC to FeCC SNe in the first explosion is reduced by a factor of about 20 (e.g. the ratio for all NS-NS systems formed decreases from 1.8 to 0.08). The resulting simulated distribution of mass ratios in NS-NS systems is shown as a red line histogram in Fig. 9. Although such a small fraction of EC SNe of about 8 per cent is perhaps better in accordance with observations (also in terms of the resulting mass ratio distribution), this ratio is possibly too small, indicating that EC SNe might produce only slightly larger kicks than our default assumption of a flat probability distribution between $0 - 50\,\mathrm{km\,s^{-1}}$. More measured NS masses are needed to answer this question. The reason why larger kicks lead to such a severe reduction in the ratio of EC vs. FeCC SNe for the first-formed NSs in surviving NS-NS systems is that many of these systems will either disrupt as a consequence of the SN explosion or widen to the extent that the secondary star does not fill its Roche lobe at any time. This is a requirement for enabling CE and spiral-in evolution producing tight binaries which also survive the second SN explosion and produce NS-NS systems. In the second-formed NSs, applying larger kicks in the simulations only reduces the ratio of EC vs. FeCC SNe by a factor of 3.

Another way we can simulate a population of fewer NS-NS systems produced via EC SNe is simply by reducing the window in core masses assumed to produce an EC SN from $1.37\,\mathrm{M}_\odot \leq m^\mathrm{ECSN}_\mathrm{CO-core} < 1.435\,\mathrm{M}_\odot$ to $1.37\,\mathrm{M}_\odot \leq m^\mathrm{ECSN}_\mathrm{CO-core} < 1.38\,\mathrm{M}_\odot$, see Table 6. However, for NS-NS systems this only has the effect of decreasing the ratio of EC to FeCC SNe by a factor of ~ 2 and ~ 4 for the first and the second SN explosion, respectively. Further-

Table 5. Variations in DCO formation and merger rates for a MW-like galaxy caused by changing the values of selected key input parameters (columns 3 to 9). The default input parameters are listed in Table 2 and the resulting rates are shown in the second column. The binary types refer to the first and second compact objects formed. The pure uncertainties of Poissonian statistics are between 10^{-11} yr^{-1} and 10^{-8} yr^{-1}.

		$\alpha_{\rm CE}$	$\beta_{\rm min}$	$\alpha_{\rm RLO}$	$\alpha_{\rm th}$	$q_{\rm limit}$	$\alpha_{\rm IMF}$	$m^{\rm p}_{\rm max} = m^{\rm s}_{\rm max}$
	upper:	0.80	0.79	0.24	0.70	4.0	3	150 M$_\odot$
	lower:	0.20	0.50	0.15	0.30	1.5	2	80 M$_\odot$
Formation rates	default	$\alpha_{\rm CE}$	$\beta_{\rm min}$	$\alpha_{\rm RLO}$	$\alpha_{\rm th}$	$q_{\rm limit}$	$\alpha_{\rm IMF}$	$m^{\rm p}_{\rm max} = m^{\rm s}_{\rm max}$
NS-NS (yr^{-1})	6.81×10^{-6}	$^{+2.37}_{-1.72}\times10^{-6}$	$^{-0.63}_{+3.02}\times10^{-6}$	$^{-0.69}_{+1.06}\times10^{-6}$	$^{+0.35}_{-1.32}\times10^{-7}$	$^{+3.17}_{-1.01}\times10^{-6}$	$^{-0.33}_{+2.08}\times10^{-5}$	$^{-1.91}_{+1.05}\times10^{-8}$
NS-BH (yr^{-1})	5.49×10^{-9}	$^{+2.01}_{-0.04}\times10^{-8}$	$^{+1.20}_{-0.36}\times10^{-8}$	$^{+1.14}_{-0.50}\times10^{-8}$	$^{-0.77}_{-1.23}\times10^{-9}$	$^{+1.11}_{-0.05}\times10^{-7}$	$^{-0.35}_{+3.79}\times10^{-8}$	$^{-1.15}_{-1.69}\times10^{-9}$
BH-NS (yr^{-1})	1.49×10^{-5}	$^{+1.96}_{-3.26}\times10^{-6}$	$^{+0.17}_{-1.23}\times10^{-5}$	$^{+1.28}_{-2.73}\times10^{-6}$	$^{+1.05}_{-0.70}\times10^{-6}$	$^{+4.55}_{-1.28}\times10^{-5}$	$^{-0.10}_{+1.38}\times10^{-4}$	$^{+9.37}_{-9.15}\times10^{-7}$
BH-BH (yr^{-1})	2.27×10^{-6}	$^{+2.35}_{-0.30}\times10^{-6}$	$^{+1.06}_{-0.19}\times10^{-6}$	$^{+1.08}_{-0.28}\times10^{-6}$	$^{+2.88}_{-1.80}\times10^{-7}$	$^{+3.87}_{-0.02}\times10^{-5}$	$^{-0.16}_{+2.99}\times10^{-5}$	$^{+4.37}_{-1.11}\times10^{-6}$
GW merger rates	default	$\alpha_{\rm CE}$	$\beta_{\rm min}$	$\alpha_{\rm RLO}$	$\alpha_{\rm th}$	$q_{\rm limit}$	$\alpha_{\rm IMF}$	$m^{\rm p}_{\rm max} = m^{\rm s}_{\rm max}$
NS-NS (yr^{-1})	2.98×10^{-6}	$^{+7.75}_{-0.64}\times10^{-7}$	$^{-0.51}_{+2.71}\times10^{-6}$	$^{-5.67}_{+8.64}\times10^{-7}$	$^{-2.60}_{+1.47}\times10^{-7}$	$^{+0.85}_{-4.66}\times10^{-7}$	$^{-1.46}_{+9.68}\times10^{-6}$	$^{-3.11}_{-0.67}\times10^{-8}$
NS-BH (yr^{-1})	0.00×10^{0}	$^{+1.20}_{+0.01}\times10^{-8}$	$^{+2.58}_{+0.00}\times10^{-10}$	$^{+3.87}_{+0.00}\times10^{-10}$	$^{+1.94}_{+0.00}\times10^{-10}$	$^{+1.94}_{+0.00}\times10^{-9}$	$^{+0.00}_{+1.34}\times10^{-9}$	$^{+0.65}_{+1.93}\times10^{-10}$
BH-NS (yr^{-1})	4.05×10^{-6}	$^{+0.81}_{-2.09}\times10^{-6}$	$^{+0.25}_{-3.56}\times10^{-6}$	$^{+2.94}_{-7.65}\times10^{-7}$	$^{+4.25}_{-2.49}\times10^{-7}$	$^{+2.88}_{-2.73}\times10^{-6}$	$^{-0.26}_{+3.56}\times10^{-5}$	$^{+1.32}_{-1.61}\times10^{-7}$
BH-BH (yr^{-1})	2.64×10^{-7}	$^{+2.19}_{-0.25}\times10^{-6}$	$^{+0.01}_{+1.91}\times10^{-7}$	$^{+0.17}_{+4.45}\times10^{-8}$	$^{+3.11}_{-1.41}\times10^{-7}$	$^{+1.15}_{+0.10}\times10^{-6}$	$^{-0.19}_{+3.84}\times10^{-6}$	$^{+3.86}_{-1.96}\times10^{-7}$

Table 6. GW merger rates of a MW-like galaxy and their dependence on applied kicks and assumptions on EC SNe. The binary types refer to the first and second compact objects formed.

GW merger rates	default	small kicks*	large EC SN kicks**	small EC SN mass window***
			$w_{\rm ECSN} = w_{\rm FeCCSN}$	1.37 M$_\odot$ $\leq m^{\rm ECSN}_{\rm CO-core} <$ 1.38 M$_\odot$
NS-NS (yr^{-1})	2.98×10^{-6}	9.34×10^{-6}	1.54×10^{-6}	2.30×10^{-6}
NS-BH (yr^{-1})	0.00×10^{0}	1.94×10^{-10}	6.46×10^{-11}	1.29×10^{-10}
BH-NS (yr^{-1})	4.05×10^{-6}	7.59×10^{-6}	4.04×10^{-6}	4.04×10^{-6}
BH-BH (yr^{-1})	2.64×10^{-7}	3.05×10^{-7}	2.65×10^{-7}	2.66×10^{-7}

* half of all default kick magnitudes. ** similar to FeCC SNe, see Table 1. *** the default is 1.37 M$_\odot$ $\leq m^{\rm ECSN}_{\rm CO-core} <$ 1.435 M$_\odot$.

more, Poelarends et al. (2017) have even argued for a wider range of progenitor star masses producing EC SNe which would exacerbate the discrepancy between our theoretical simulations and observations.

To summarize our finding on EC vs. FeCC SNe, we find that our default simulations produce a majority of EC SNe for the first-formed NSs, in apparent contrast with current observations. Although the ratio of simulated EC to FeCC SNe is strongly dependent on the kicks applied in these two types of explosions, and also on the mass window for producing EC SNe, we still consider this an important and puzzling issue. Perhaps the answer is simply that EC SNe produce slightly more massive NSs than usually thought. It is anticipated that the Square-Kilometre Array (SKA) will eventually increase the number of known radio pulsars by a factor of 5 to 10 (Keane et al. 2015), thus resulting in a total of more than 100 known NS-NS systems. A large number of these systems will have their NS masses measured accurately and it will be interesting to see if an EC SN peak will be present in the NS mass distribution at that time.

For the second-born NSs in DNS systems, however, a couple of the observed masses are in agreement with a potential EC SN origin according to current expectations, e.g. PSRs J0737−3039B, J1756−2251, and J1913+1102. Our simulations (Fig. 8) show a much smaller contribution of EC SNe to the second-born NSs as most of the systems are tightened by a CE prior to the second SN, which therefore allows for larger kick magnitudes to remain bound. An additional minor factor that increases the fraction of FeCC SNe in the second SN is that their kick magnitudes are, in general, smaller than in the first SN, see Table 1.

5.1.3 *Common-envelope efficiency, $\alpha_{\rm CE}$*

Fig. 17 shows the influence of the efficiency of converting released orbital energy into kinetic energy of the CE on the early binary merger fraction. Here, early binary merger refers to systems which coalesce before a DCO binary is formed. The main reasons are CE in-spiral (i.e. failed CE ejection) or direct collision of stellar components as a result of a SN changing the orbital dynamics. A very small fraction of systems undergoing RLO will also merge. The more efficient the CE energy conversion is the more CEs are successfully ejected, and therefore the number of early mergers will decrease as most of them happen during a CE phase. However, for the entire DCO population as such, this effect is only modest. The early merger fraction decreases from 0.66 to 0.54 when $\alpha_{\rm CE}$ is increased from 0 to 1. These fractions are with respect to all binaries evolved with ComBinE, and thus we conclude that more than half of all massive binaries will suffer from an early merger during a CE event, cf. Izzard et al. (2017) for less massive stars. For a comparison, the fraction of early mergers caused by direct SN kicks in a fine-tuned direction is only about 0.0005.

In terms of DCO merger rates, Table 5 shows that changing $\alpha_{\rm CE}$ from 0.5 to 0.8 (0.2) will increase (decrease) the merger rates, as expected. For double NS systems, the changes are moderate (+26 and −2 per cent, respectively) as they almost always undergo a subsequent Case BB mass-

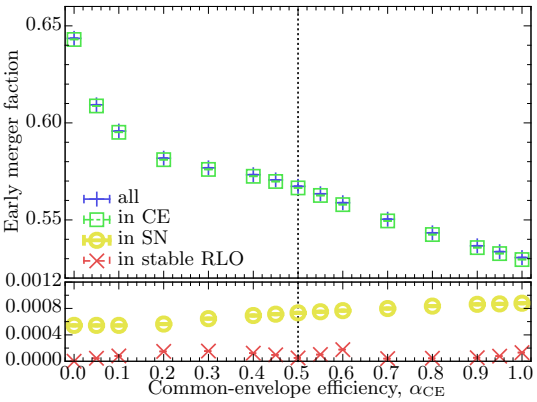

Figure 17. The fraction (number of events divided by number of systems evolved) of early coalescing systems modelled with ComBinE from binaries with $m^{p}_{ZAMS} \geq 4\,M_\odot$ and $m^{s}_{ZAMS} \geq 1\,M_\odot$, and for a MW-like metallicity ($Z_{MW} = 0.0088$), as a function of the efficiency of converting orbital energy into kinetic energy during CE evolution, α_{CE}. Also shown at the bottom is the fraction of early mergers caused by direct SN kicks and stable RLO. The vertical dotted line marks our default value of $\alpha_{CE} = 0.5$.

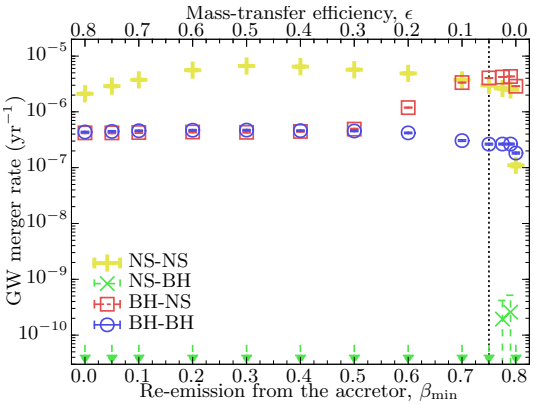

Figure 18. The GW merger rate in a MW-like galaxy as a function of the minimum mass ejection fraction in the vicinity of the accretor during RLO. The dotted line marks our default value of $\beta_{min} = 0.75$. The green arrows mark upper limits for simulated NS-BH systems.

transfer phase. However, the rate of double BH mergers is very sensitive to α_{CE} and increases by a factor 8 (decreases by a factor 19) when changing α_{CE} from 0.5 to 0.8 (0.2), respectively.

5.1.4 *Mass-transfer efficiency*

Among the chosen default values for the input parameters of our population synthesis simulations (Table 2), the minimum mass ejection fraction of the accretor during RLO is set to $\beta_{min} = 0.75$. This means that 75 per cent of the material transferred from the donor star towards the accreting star is assumed to be re-emitted with the specific orbital angular momentum of the accretor and an even higher fraction is ejected when the mass-transfer rate is super-Eddington. The reason we chose this low efficiency for accretion via RLO as our default value is the need to match our simulated population of double NS systems with observations – their orbital parameters and especially their masses, cf. Fig. 8. We now discuss the mass-transfer efficiency, ϵ, in light of the two input variables: β_{min} and α_{RLO}.

i) Re-emission from the accretor, β_{min}

The more mass a star accretes, the more massive a compact object it can produce compared to evolution in isolation as a single star. Furthermore, a more massive companion helps the binary to survive a large kick during a SN. So, naively, one would expect to produce more DCO binaries for more efficient accretion. But this is only true in wide systems. The close binaries usually evolve through a CE phase after the first compact object is formed. In this case, a more massive companion possesses a more massive envelope which is harder to eject. Consequently, tight systems more often result in an early merger via spiral in. This effect explains why the merger rate of our simulated BH-NS systems (Fig. 18) is smaller by about an order of magnitude for efficient accretion ($\beta_{min} = 0.0$, and $\alpha_{RLO} = 0.2$ corresponding to $\epsilon = 0.8$) compared to inefficient accretion ($\beta_{min} = 0.75$).

In the most common binaries producing double NS or double BH systems, however, a lower β_{min} value, i.e. more effective accretion, does not produce significantly more or fewer GW mergers – although the merger rate for double NS systems peaks near $\beta_{min} = 0.50$.

The difference in our simulated results between using our default $\beta_{min} = 0.75$ and $\beta_{min} = 0.0$ is shown in Fig. 8 for the final NS masses. For further comparison, all results using a high mass-transfer efficiency ($\beta_{min} = 0.0$) are summarised in Appendix B.

ii) Direct wind mass loss, α_{RLO}

For a given β_{min}, the fraction of material lost directly from the donor star in the form of an assumed fast wind, α_{RLO}, is constrained by conservation of mass. Given that $\epsilon \geq 0$ we have $\alpha_{RLO} \leq 1 - \beta_{min} - \delta$ (Section 2.2.3). Hence, for $\beta_{min} = 0.75$ we have $\alpha_{RLO} \in [0.0 : 0.25]$.

The dependency of the formation rate of DCO binaries on α_{RLO} has no clear trend (lower panel of Fig. D3). Nevertheless, two main effects are at work when we increase α_{RLO}. First, stronger wind mass loss widens the orbit. Secondly, the accretor gains less mass. As a consequence, the resulting wider and lighter binary is more easily disrupted in a subsequent SN. However, if a CE follows after a SN which fails to disrupt the binary then the chance of surviving the CE phase increases.

Formation rates calculated with $\alpha_{RLO} = 0.25$ are exceptional. At this value, given that $\beta_{min} = 0.75$ and thus $\epsilon = 0.0$, no mass is accreted by the accretor and thus the initially more massive star always evolves first. This suppresses in particular the formation of NS-BH systems.

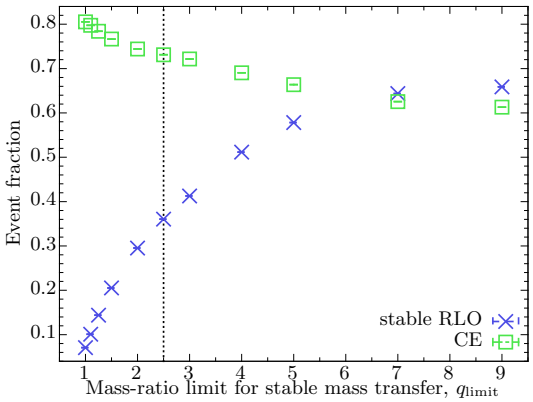

Figure 19. The mean count of stable RLO (blue) and CE (green) events per binary system evolved in a MW-like galaxy depending on the critical mass-ratio limit, $q_{\rm limit}$. The Case A or early Case B RLO events with $q < q_{\rm limit}$ are stable whereas a CE is assumed to develop for $q \geq q_{\rm limit}$. The dotted line marks our default $q_{\rm limit} = 2.5$.

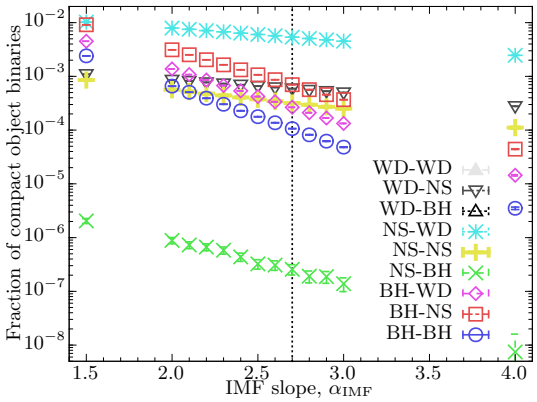

Figure 20. The relative fraction of DCO systems (here including WDs) formed in a MW-like galaxy depending on the slope of the IMF, $\alpha_{\rm IMF}$. There are no WD-BH binaries formed. The double WD systems are by far the main population with a relative formation fraction close to 1.0. The dotted line marks our default IMF (a Salpeter-IMF, $\alpha_{\rm IMF} = 2.7$).

5.1.5 Mass-ratio limit for stable mass transfer, $q_{\rm limit}$

One of our stability criteria of mass transfer is related to the mass ratio between the two stars at the onset of RLO. In Fig. 19, we show the number of stable RLO and CE events (unstable RLO) as a function of the chosen critical mass-ratio limit, $q_{\rm limit}$, for which $q < q_{\rm limit}$ will lead to a stable RLO. The general trend of having more stable RLO events with increasing $q_{\rm limit}$ is clearly visible. Note, the added number of RLO/CE events per binary system evolved can exceed 1.0 since there are sometimes multiple stages of mass transfer between the two stars (cf. Fig. 1). The total number of events (adding RLO and CE) increases when there are fewer episodes of unstable mass transfer. As discussed in Section 5.1.3, early coalescence happens mainly during a CE which suppresses the possibility of subsequent mass transfer in a given system. Therefore, also the formation rates and the GW merger rates increase clearly with larger values of $q_{\rm limit}$, cf. Table 5.

5.1.6 Initial mass function

Changing the slope of the applied IMF, and therefore the relative abundance of massive stars, makes a large difference on the formation rates of DCO binaries. Fig. 20 (here including WDs) shows the relative fractions of the different DCO binaries formed as a function of the slope of the IMF, $1.5 \leq \alpha_{\rm IMF} \leq 4.0$. These fractions change by an order of magnitude, or even more, when going from a steep to a more flat IMF. Independent of all the binary interactions, the change of the IMF slope has a simple monotonic effect on the formation fraction of the different types of DCO binaries: the steeper the IMF, the less binaries form with NSs or BHs.

Recently, Schneider et al. (2018) studied massive stars (15 to 200 $M_\odot$) in the young cluster 30 Doradus and found evidence for $\alpha_{\rm IMF} = 1.90^{+0.37}_{-0.26}$. If such an IMF is representative for the star-formation history within the observable LIGO-Virgo volume of the local Universe, then the detection rates of DCO mergers will be larger than our default results (Fig. 20).

Double WD systems are by far the most common DCOs (out of the scale shown in Fig. 20) even though our simulations do not account for the very low-mass stars below our applied mass range (Table 2). Including all low-mass stars down to e.g. 0.8 $M_\odot$ would increase the number of double WD binaries even more, but the relative ratios of DCOs without WDs would remain unaffected. The number of BH systems, however, increases by changing the upper mass limit, see Section 5.1.7. Systems in which a WD forms before a BH are not expected to be produced in nature from isolated binaries because of the excessive mass reversal required.

5.1.7 Range of the initial primary and secondary masses

For the calculation of the formation and GW merger rates of DCO binaries with NSs and BHs, there are no effects when the lower ZAMS mass boundaries of the primary and the secondary stars are changed, only the number of WD progenitors changes. However, at the high-mass end of the scale, changing the maximum mass boundary influences on the rate of BH binary formation significantly more than that of NS binaries, cf. the last column of Table 5.

5.1.8 Range of the initial semi-major axis

The initial semi-major axis is the key parameter determining whether a system will experience binary interactions or not. Fig. 21 shows how the semi-major-axis changes from the ZAMS to the time when both compact objects are formed. Because only systems which survive the binary evolution are plotted, a lack of systems in the initial separation does not mean that those systems are not simulated. For example,

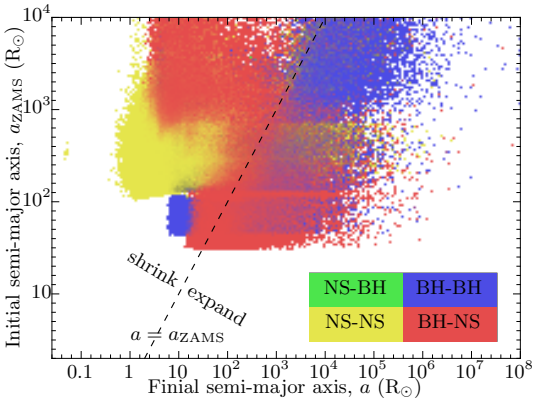

Figure 21. The initial ($a_{\rm ZAMS}$) and the final semi-major axis (a) of our simulated DCO binaries in a MW-like galaxy. Each pixel's colour shows the type of the two compact objects formed from the initial primary and secondary stars, respectively. This type is not necessarily reflecting the formation order although it is in most cases. The black dashed line indicates the binaries ending their evolution with the same semi-major axis as they started. This does not mean that they have the same orbital separation during the whole binary evolution.

there are no double NS binaries from initial ZAMS separations below 100 $R_\odot$. However, BH-NS binaries can originate from binaries with an initial orbital separation down to 30 $R_\odot$. Most of the double NS binaries shrink their orbit during their progenitor evolution. These systems are located above the dashed line.

Binaries have a Roche-lobe filling star at birth if the initial orbital separation is too small. Thus, the minimum orbital separation needed to avoid one star filling its Roche lobe on the ZAMS is $\sim 10\,R_\odot$ and $\sim 20\,R_\odot$ for double NS and double BH progenitor binaries, respectively. Changing the maximum semi-major axis at ZAMS adds or removes systems at the top of Fig. 21. Adding systems simultaneously means removing some realisations from the existing distribution. Because the survival rate is lower at longer initial separations, the total formation rate of all systems decreases for a larger upper boundary of the initial orbital separation.

Our GW merger rates are dominated by systems which have a short final separation. Therefore, the merger rate does not change in the same way as the formation rate, cf. Table D1.

5.2 Comparison to other studies and observations

We now compare our results to those of other recently published population synthesis studies on DCO binaries and to the first seven LIGO-Virgo detection events of merging double BHs and double NSs. In addition, we compare our simulated Galactic double NS merger rate with estimated constraints on CC SNe, short γ-ray bursts (sGRBs) and production of heavy r-process element events.

Table 7. Number of DCO systems present in the Milky Way as a function of the parameter $\beta_{\rm min}$, where the maximum RLO mass-transfer efficiency is given by $\epsilon_{\rm max} = 1 - \alpha_{\rm RLO} - \beta_{\rm min}$. The numbers are given for stellar evolution lasting (10 ± 3.81) Gyr. The binary types indicate the order of the first and second-formed compact objects.

Systems in MW	$\beta_{\rm min} = 0.75$	$\beta_{\rm min} = 0.5$	$\beta_{\rm min} = 0$
NS-NS	38246^{+12445}_{-13100}	41340^{+12624}_{-13405}	1616^{+499}_{-505}
NS-BH	55^{+21}_{-21}	19^{+7}_{-7}	25^{+9}_{-10}
BH-NS	108845^{+36702}_{-37811}	21303^{+7504}_{-7687}	13603^{+4532}_{-4798}
BH-BH	20073^{+7585}_{-7602}	16237^{+5934}_{-6006}	21988^{+8247}_{-8267}

5.2.1 *Number of double compact object binaries present in the Milky Way*

We predict a total Galactic population (Table 7) of the order 40 000 NS-NS binaries, 100 000 BH-NS binaries and 20 000 BH-BH binaries. Whereas the latter number is stable, the number of BH-NS and, in particular, the number of NS-NS systems present in the MW is strongly dependent on $\beta_{\rm min}$. The reason is that efficient accretion ($\beta_{\rm min} = 0$) produces relatively tighter binaries. The majority of double NS binaries formed will merge due to GWs within a Hubble time (thus removing them from the observable sample), while in the case of inefficient accretion ($\beta_{\rm min} = 0.75$) more than half of the double NS binaries are formed in wider systems which do not merge. Assuming an active radio lifetime of 100 Myr as a lower limit (i.e. slightly more than $10 - 50$ Myr typically expected for non-recycled radio pulsars Lorimer & Kramer 2004; Johnston & Karastergiou 2017), means that we expect at least of the order 400 active radio pulsars in NS-NS systems in the MW. Depending on beaming effects, probably 100 to 150 of these DNS systems will be observable from Earth.

5.2.2 *Galactic merger rates of double compact object binaries*

We first compare our new simulations to the results obtained from the old code used in Voss & Tauris (2003). The largest difference is related to systems evolved at our high metallicity case. In our new study, we find that the Galactic DCO merger rate is dominated by BH-NS and double NS systems, and not by double BH binaries (Table 5). Our predicted rate of Galactic double NS mergers is about 3.0 $\rm Myr^{-1}$, using our default values for the input physics parameters, and thus within a factor of two of Voss & Tauris (2003). Our predicted Galactic merger rate of double BHs is only 0.3 $\rm Myr^{-1}$, which is much less than the rate of 10 $\rm Myr^{-1}$ found in Voss & Tauris (2003). The reason for this is a combination of our CEs being more tightly bound, thus producing fewer DCO binaries in general, and a systematic shift in our applied threshold core mass for producing BHs.

Given that our simulated NS-NS merger rate for a MW-like galaxy is about 3.0 $\rm Myr^{-1}$, our results are among those that predict the lowest rates compared to other binary population synthesis studies (Abadie et al. 2010). There are many reasons for this, but one particular important issue is that many other codes model the CE phase with constant envelope structure parameter, λ, although it has been demonstrated that this is a poor approximation (Dewi & Tauris

2000, 2001; Podsiadlowski et al. 2003) – see also Fig. 4 and Section 3.1.1. As an example, it was shown by Voss & Tauris (2003) that using a constant value of $\lambda = 0.5$, instead of using realistic calculated values which depend on the evolutionary status of the star, increases the predicted merger rate by more than an order of magnitude. We confirm this by test simulations using ComBinE and also obtain similar discrepancies by combing our stellar tracks with λ-tables of a different source.

There are several binary population synthesis studies performed with the codes *StarTrack* (Belczynski et al. 2008; Dominik et al. 2013, 2015; Chruslinska et al. 2017), *binary_c* (Izzard et al. 2004, 2006, 2009, 2017), *BPASS* (Eldridge & Stanway 2016; Eldridge et al. 2017), *COMPAS* (Stevenson et al. 2017a; Barrett et al. 2017b), *MOBSE* (Mapelli et al. 2017; Giacobbo et al. 2017) and many more. The main differences are: the stellar evolution (i.e. applied stellar model grids and their resolution), the treatment of CE evolution, and the applied SN-kick distributions. While ComBinE interpolates large stellar evolution grids (Section 3) most other codes use fitting functions for the individual stars and their evolution. Such fitting functions (e.g. Hurley et al. 2000, 2002) do not recover some parameters well compared to more detailed stellar models. One example is the stellar structure parameter, λ. However, during a CE evolution such knowledge is important to determine if the system merges or survives the unstable mass transfer (see e.g. Kruckow et al. 2016, for discussions). Furthermore, as discussed previously, the distribution of kicks received by the NSs must depend on their formation history, i.e. the remaining envelope and the core mass of the exploding star. Some observed high-velocity pulsars need large kicks while some tight and nearby circular pulsar binaries must have experienced small kicks. We account for this in our new code in a systematic way by using different kick distributions depending on the evolutionary history of the exploding star, i.e. by considering how much of the envelope is stripped prior to the SN explosion (Section 2.2.6).

Finally, we note that our implementation of the more advanced numerical Case BB RLO modelling of Tauris et al. (2015) increases the double NS merger rate by an order of magnitude compared to our simulations based on the results of Dewi & Pols (2003) which often lead to unstable RLO.

5.2.3 *Merger-rate densities*

In Fig. 22, we plot our estimated merger-rate densities at two different metallicities. These plots are calculated from a method similar to that of figures 3 and 4 of Dominik et al. (2013) and, for a better comparison, we applied the same star-formation rate function (Strolger et al. 2004) and cosmological parameters as in Dominik et al. (2013). Furthermore, a binary fraction of 100 per cent is assumed. The two panels displayed are for a constant metallicity, showing the high- and low-metallicity cases ($Z_{MW} = 0.0088$ and $Z_{IZw18} = 0.0002$) used in our work. At high metallicity, our simulations yield merger-rate densities at redshift zero of at least 10 yr^{-1} Gpc^{-3} and 0.6 yr^{-1} Gpc^{-3}, for double NS and double BH mergers respectively, depending on the applied galaxy-density scaling. See Table 8 for detailed numbers.

When considering mergers in low-metallicity environments and at low redshift ($z < 1$), we find that

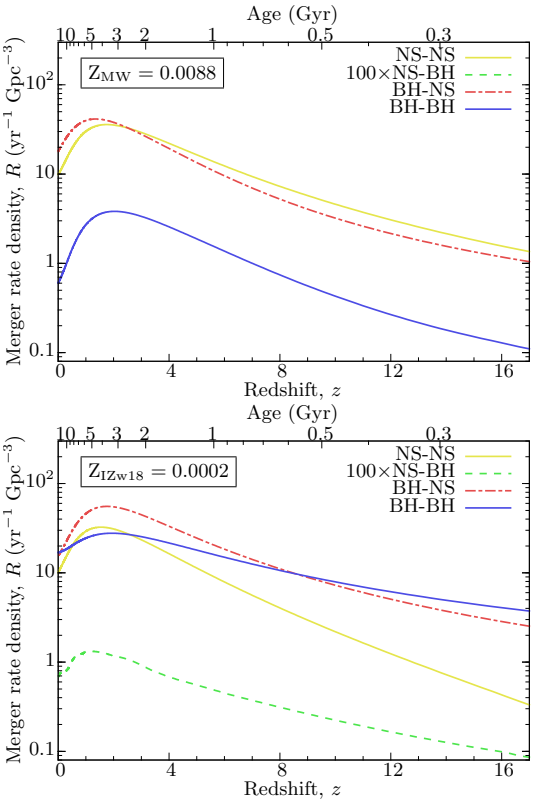

Figure 22. Merger-rate densities of the DCO binaries at MW-like (upper panel) and IZw18-like (lower panel) metallicity as a function of cosmological redshift and age of the Universe – see Table 8 for numbers. Colour-coded is the type of the two compact objects in their formation order. The values of the NS-BH binaries are multiplied with a factor of 100 to be visible in the lower plot, while they remain absent in the upper one.

the three dominant binary types (BH-BH, BH-NS and NS-NS) are more or less equally frequent (i.e. $\mathcal{R}_{z=0} \simeq 10 - 17$ yr^{-1} Gpc^{-3}). However, for NS-BH binaries we obtain $\mathcal{R}_{z=0} < 0.01$ yr^{-1} Gpc^{-3} (see Section 5.3 for a discussion on these systems). Applying efficient RLO makes the NS binaries less dominant, see Appendix B5. As our applied inefficiency of RLO is motivated by measurements of NS masses in double NS binaries in the Milky Way (Section 4.2.3), it can not be excluded that the mass-transfer efficiency is larger at lower metallicities.

In terms of anticipated LIGO-Virgo detection rates, it is evident from Table 8 that LIGO-Virgo should mainly detect GW mergers of binary BHs originating from low-metallicity environments. At a much smaller rate, LIGO-Virgo will detect mixed NS/BH and double NS mergers originating from both high- and low-metallicity environments. It should be noted that we do not expect the GW merger data analysis to be able to distinguish between NS-BH and BH-NS systems. It will not be possible to determine the formation order

Table 8. Our simulated merger-rate densities $\mathcal{R}$ at redshift zero following the two different star-formation history and galaxy-density scaling methods outlined in Dominik et al. (2013) and Abadie et al. (2010), yielding $\mathcal{R}_{z=0}$ and $\mathcal{R}_{\rm cSFR}$, respectively. Using the unweighted average $\langle\mathcal{M}^{2.5}\rangle$, some geometrical factors and assuming a signal-to-noise threshold, $\rho \geq 8$, we calculate the expected LIGO-Virgo detection rates $\mathcal{R}_{\rm D}$ and $\mathcal{R}_{\rm D,cSFR}$ (following equation (3) of Dominik et al. 2015, cf. their table 1). The merger-rate densities and detection rates are calculated for two different metallicity environments ($Z_{\rm MW} = 0.0088$ and $Z_{\rm IZw18} = 0.0002$, top and central panel, respectively) applying our default input parameter settings (Table 2). The bottom panel shows our rates calculated under an "optimistic" setting at MW metallicity to boost the NS-NS merger rate (i.e. applying $\alpha_{\rm IMF} = 2.3$, $\alpha_{\rm RLO} = 0.15$, $\beta_{\rm min} = 0.5$, $\alpha_{\rm CE} = 0.8$ and $\alpha_{\rm TH} = 0.3$). See Section 5.2.4 for a discussion.

$Z_{\rm MW}$	$\langle\mathcal{M}^{2.5}\rangle$	$\mathcal{R}_{z=0}$	$\mathcal{R}_{\rm D}$	$\mathcal{R}_{\rm cSFR}$	$\mathcal{R}_{\rm D,cSFR}$
NS-NS	1.36 $M_\odot^{2.5}$	9.85×10^{0} yr^{-1} Gpc^{-3}	0.28 yr^{-1}	3.47×10^{1} yr^{-1} Gpc^{-3}	0.98 yr^{-1}
NS-BH	20.0 $M_\odot^{2.5}$	0.00×10^{0} yr^{-1} Gpc^{-3}	0.00 yr^{-1}	0.00×10^{0} yr^{-1} Gpc^{-3}	0.00 yr^{-1}
BH-NS	15.7 $M_\odot^{2.5}$	1.80×10^{1} yr^{-1} Gpc^{-3}	5.88 yr^{-1}	4.72×10^{1} yr^{-1} Gpc^{-3}	15.43 yr^{-1}
BH-BH	233 $M_\odot^{2.5}$	6.01×10^{-1} yr^{-1} Gpc^{-3}	2.92 yr^{-1}	3.08×10^{0} yr^{-1} Gpc^{-3}	14.95 yr^{-1}
$Z_{\rm IZw18}$	$\langle\mathcal{M}^{2.5}\rangle$	$\mathcal{R}_{z=0}$	$\mathcal{R}_{\rm D}$	$\mathcal{R}_{\rm cSFR}$	$\mathcal{R}_{\rm D,cSFR}$
NS-NS	1.27 $M_\odot^{2.5}$	1.00×10^{1} yr^{-1} Gpc^{-3}	0.27 yr^{-1}	3.28×10^{1} yr^{-1} Gpc^{-3}	0.87 yr^{-1}
NS-BH	32.3 $M_\odot^{2.5}$	6.61×10^{-3} yr^{-1} Gpc^{-3}	0.00 yr^{-1}	1.55×10^{-2} yr^{-1} Gpc^{-3}	0.01 yr^{-1}
BH-NS	35.5 $M_\odot^{2.5}$	1.54×10^{1} yr^{-1} Gpc^{-3}	11.40 yr^{-1}	5.32×10^{1} yr^{-1} Gpc^{-3}	39.34 yr^{-1}
BH-BH	1720 $M_\odot^{2.5}$	1.68×10^{1} yr^{-1} Gpc^{-3}	603.02 yr^{-1}	3.45×10^{1} yr^{-1} Gpc^{-3}	1235.27 yr^{-1}
optimistic	$\langle\mathcal{M}^{2.5}\rangle$	$\mathcal{R}_{z=0}$	$\mathcal{R}_{\rm D}$	$\mathcal{R}_{\rm cSFR}$	$\mathcal{R}_{\rm D,cSFR}$
NS-NS	1.31 $M_\odot^{2.5}$	7.09×10^{1} yr^{-1} Gpc^{-3}	1.94 yr^{-1}	1.59×10^{2} yr^{-1} Gpc^{-3}	4.37 yr^{-1}
NS-BH	19.4 $M_\odot^{2.5}$	0.00×10^{0} yr^{-1} Gpc^{-3}	0.00 yr^{-1}	0.00×10^{0} yr^{-1} Gpc^{-3}	0.00 yr^{-1}
BH-NS	21.9 $M_\odot^{2.5}$	1.34×10^{1} yr^{-1} Gpc^{-3}	6.11 yr^{-1}	2.44×10^{1} yr^{-1} Gpc^{-3}	11.17 yr^{-1}
BH-BH	275 $M_\odot^{2.5}$	4.34×10^{1} yr^{-1} Gpc^{-3}	248.34 yr^{-1}	1.09×10^{2} yr^{-1} Gpc^{-3}	623.03 yr^{-1}

of the compact objects, despite potential differences in the NS spin rates depending on whether the NSs are (mildly) recycled. While the merger-rate densities of the BH-NS and double BH binaries are similar at lower metallicity, their detection rate is different by more than an order of magnitude. This difference originates from their different chirp masses which are typically $\mathcal{M}_{\rm BH/NS} \approx 4\,M_\odot$ and $\mathcal{M}_{\rm BH-BH} \approx 20\,M_\odot$, respectively (Fig. 16, lower panel). That of the double NS systems is only about $1.1\,M_\odot$.

5.2.4 *Comparison to reported LIGO-Virgo detections*

In Fig. 23, we plot the properties of the progenitor binaries of the first seven LIGO-Virgo events according to our simulations. Shown here are the distributions of the ZAMS masses and of the semi-major axis, as well as that of the final BH masses and ages of the systems at the time of the merger events. The systems selected, plotted in seven different colours, are those which will merge within a Hubble time and match the observations in both chirp mass and system mass within the uncertainties given in Abbott et al. (2016a, 2017a,b,c). At low metallicity, possible progenitors are found in our simulations for six of the reported LIGO-Virgo events – the exception is GW170608. The more massive the merging BHs are, the more likely the event happened in a low-metallicity environment. Although GW151226 could have formed at all metallicities we investigated, it is more likely that it originates from LMC-like or higher metallicity, as it is the case for GW170608. The double NS merger GW170817 could also have formed at all the metallicities we investigated.

Stevenson et al. (2017a) investigated the progenitors of the first three LIGO detections, and the second and third columns in Fig. 23 are similar to their figure 1. The results of our work and that of Stevenson et al. (2017a) are similar. However, our lowest metallicity case ($Z_{\rm IZw18} = 0.0002$) is lower than theirs at $Z = 0.001$. Our SMC metallicity simulation is similar to their $Z = 0.002$ model. The first column of Fig. 23 shows the initial semi-major axis and the age of the binaries when they merge via GW radiation. At low metallicity, there is a much larger spread in initial separations and ages of the potential progenitor systems compared to high metallicity.

The empirical merger-rate density of BH-BH systems as determined by LIGO-Virgo detections is currently reported to be $\mathcal{R} \simeq 12 - 213$ yr^{-1} Gpc^{-3} (Abbott et al. 2017a). This empirical range is consistent with our default simulations at low-metallicity environments ($Z_{\rm IZw18} = 0.0002$) where we obtain $\mathcal{R}_{z=0} = 16.8$ yr^{-1} Gpc^{-3}, but higher than our simulations of high-metallicity environment ($Z_{\rm MW} = 0.0088$) where we only obtain $\mathcal{R}_{z=0} = 0.6$ yr^{-1} Gpc^{-3}. However, as discussed in Section 5.1, variations in the assumed values of key input physics parameters can increase or decrease the merger rate significantly. As an example, the sole effect of increasing the CE ejection efficiency parameter from $\alpha_{\rm CE} = 0.5$ (our default value) to $\alpha_{\rm CE} = 0.8$ is to increase our estimated BH-BH merger rate by an order of magnitude (Table 5). Our simulated merger-rate density also increases by a factor of typically 2 to 4 when considering redshifts near $z \simeq 2$ in comparison to $z \simeq 0$ (Fig. 22).

An astonishing empirical NS-NS merger-rate density of $\mathcal{R} = 1540^{+3200}_{-1220}$ yr^{-1} Gpc^{-3} was recently reported based on the first GW detection of such a system (GW170817, Abbott et al. 2017c). This NS-NS merger event, the loudest GW signal ever recorded with a S/N ratio of 32.4, was also detected as a sGRB (Fermi-LAT Collaboration 2017; Abbott et al. 2017e) and a multiwavelength kilonova (e.g. Soares-Santos et al. 2017; Coulter et al. 2017;

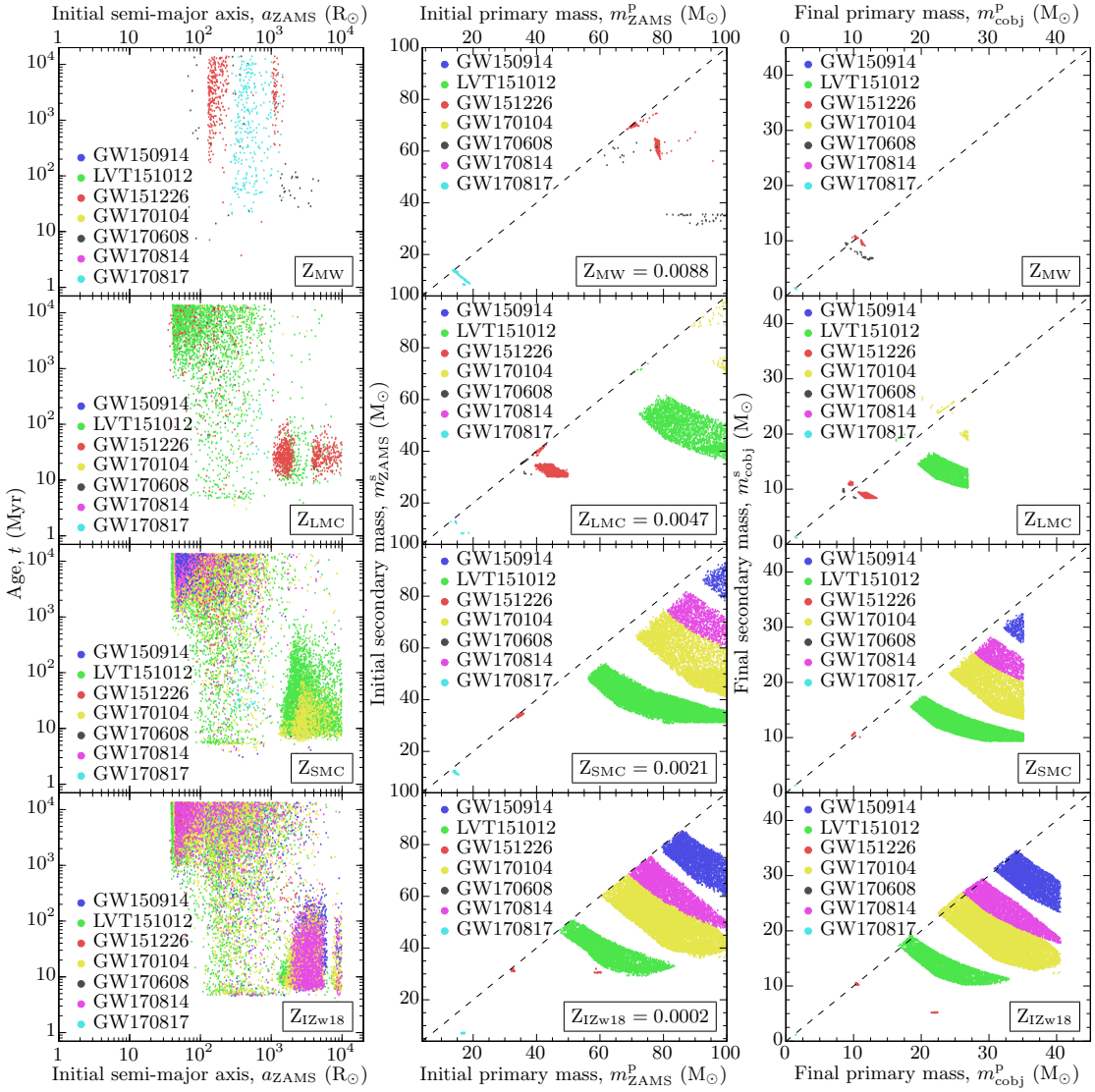

Figure 23. Simulated binary progenitor properties of the first seven LIGO-Virgo detections (GW150914 blue, LVT151012 green, GW151226 red, GW170104 yellow, GW170608 grey, GW170814 purple and GW170817 teal, Abbott et al. 2016a, 2017a,b,c). The four rows (top to bottom) correspond to metallicities of the Milky Way, the LMC, the SMC and IZw18, respectively. The dashed diagonal lines indicate similar masses.

Abbott et al. 2017d; Smartt et al. 2017; Drout et al. 2017). The combined signal seen in all three LIGO-Virgo detectors enabled an electromagnetic follow-up campaign which identified a counterpart near the galaxy NGC 4993, consistent with the localization and distance (~ 40 Mpc) inferred from GWs.

From our default simulations, we find a Galactic NS-NS merger rate of about 3.0 Myr^{-1}, translating into a merger-rate density of $R_{z=0} \simeq 10\ \mathrm{yr}^{-1}\ \mathrm{Gpc}^{-3}$, or a LIGO-Virgo detection rate of only $R_{\rm D} \simeq 0.3\ \mathrm{yr}^{-1}$ at full design sensitivity. Hence, to better match our simulated rates with that inferred from observations, we calculate an "optimistic" simulation. This optimizes our rates by changing the values of selected input physics parameters to increase our predicted NS-NS merger rate (bottom part of Table 8). To further increase the merger-rate density, we apply a local galaxy-density scaling of 0.01 MW-equivalent galaxies per Mpc^3 (Abadie et al. 2010, and references therein). Thus we are

able to obtain an "optimistic" merger-rate density of about $\mathcal{R}_{\rm cSFR} \simeq 159\ {\rm yr}^{-1}\ {\rm Gpc}^{-3}$, corresponding to a LIGO-Virgo detection rate of double NS systems of about $4\ {\rm yr}^{-1}$ at design sensitivity. By applying smaller kicks (Table 6), we increase our predicted merger-rate density of NS-NS binaries, and thus their detection rates, by an additional factor of a few. We confirmed this by additional simulations combining the "optimistic" setting with applying small kicks.

To conclude, we find that only under rather optimistic circumstances are we able to produce NS-NS merger-rate densities of up to $\mathcal{R}_{\rm max} \simeq 400\ {\rm yr}^{-1}\ {\rm Gpc}^{-3}$ in the local Universe. Although this value is within the error bar of the rate reported by Abbott et al. (2017c), we emphasize that the empirical rate of such double NS mergers is so far only based on one GW detection. From our simulations we predict that near-future GW detections or non-detections of double NS mergers from LIGO-Virgo runs O3 and O4 will decrease the empirical merger-rate density of double NSs to $\mathcal{R} \simeq 10 - 400\ {\rm yr}^{-1}\ {\rm Gpc}^{-3}$.

It is also evident from Table 8 that assuming $\beta_{\rm min} = 0.75$ we expect significantly more detections of BH-NS systems compared to double NS systems, which again illustrates GW170817 as being somewhat unexpected. The detection ratio between these two populations of DCO mergers depends on $\beta_{\rm min}$ (Fig. 18) and thus statistics from future LIGO-Virgo detections can help to constrain $\beta_{\rm min}$.

We note that also other recent population synthesis studies (Chruslinska et al. 2017; Belczynski et al. 2017) predict NS-NS merger rate densities much smaller than the empirical rate of $\mathcal{R} = 1540^{+3200}_{-1220}\ {\rm yr}^{-1}\ {\rm Gpc}^{-3}$ based on GW170817. However, we stress again that modelling the merger-rate density alone is far from the only success criterion of population synthesis. It is particularly important to be able to reproduce the characteristics of the Galactic population of double NS system (cf. Section 4.3 and Fig. 11).

For double BH and BH-NS systems, we note that under the optimistic settings discussed above, we obtain local merger-rate densities of $\mathcal{R}_{\rm max} \simeq 109\ {\rm yr}^{-1}\ {\rm Gpc}^{-3}$ and $\mathcal{R}_{\rm max} \simeq 24\ {\rm yr}^{-1}\ {\rm Gpc}^{-3}$, respectively. These theoretical values can only be increased by a factor of 2 by applying small kicks (Table 6). Our optimistic merger-rate density for double BH binaries is therefore in good agreement with the current empirical upper limit of $\mathcal{R} \simeq 213\ {\rm yr}^{-1}\ {\rm Gpc}^{-3}$ reported in (Abbott et al. 2017a). This upper limit might still be biased somewhat by GW150914 and may decrease in LIGO-Virgo observation runs O3 and O4.

5.2.5 *The progenitor system of GW170817*

The relatively massive S0 galaxy NGC 4993 is identified as the host galaxy of GW170817 (e.g. Soares-Santos et al. 2017; Coulter et al. 2017). It is located about 40 Mpc away and has a metallicity between 0.2 and $1.0\ {\rm Z}_\odot$, i.e. similar to that of the MW (e.g. Im et al. 2017). NGC 4993 is slightly less massive ($M \approx 10^{10.5}\ {\rm M}_\odot$) than the MW and shows negligible recent star formation (e.g. Pan et al. 2017). Therefore, GW170817 is expected to have an old progenitor system and a delay time of at least a few Gyr.

In Fig. 24, we show our simulations of double NS mergers in an environment with a MW metallicity of $Z = 0.0088$, similar to that of NGC 4993, and which have NS masses identical to those inferred for GW170817. We conclude that

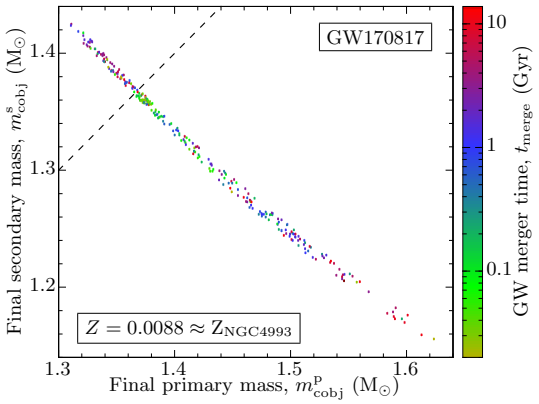

Figure 24. NS masses of simulated binary progenitors of GW170817 (Abbott et al. 2017c). The merger time (delay time) of the binary mergers is colour coded. The dashed diagonal line indicates equal masses.

we can easily reproduce the progenitor system of GW170817 which had a chirp mass of $1.188^{+0.004}_{-0.002}\ {\rm M}_\odot$ and a total mass of $2.74^{+0.04}_{-0.01}\ {\rm M}_\odot$ (Abbott et al. 2017c). We find solutions to the double NS progenitor of GW170817 which have ages from less than 100 Myr to more than 10 Gyr.

The sGRB associated with GW170817 is located within the effective radius of its host galaxy (e.g. Blanchard et al. 2017). This is not surprising given that in a massive galaxy like the MW or NGC 4993 the systemic velocities of double NS systems (resulting from NS kicks at SN birth) mainly spread out their distribution and are generally not able to eject the DCO binaries from the galactic potential. For NGC 4393, the escape velocity at the location of GW170817 is $\sim 350\ {\rm km\ s}^{-1}$ (Pan et al. 2017).

5.2.6 *Comparison to the rates of core-collapse supernovae, short γ–ray bursts and r-process element events*

In the following, we compare our simulated Galactic double NS merger rates with estimated constraints on CC SNe, sGRBs and heavy *r*-process element events.

Our default and "optimistic" estimates of a double NS merger rate of $3.0\ {\rm Myr}^{-1}$ and $14\ {\rm Myr}^{-1}$ for a MW-like galaxy translate into relative merger rates of about 3.0×10^{-4} and 1.4×10^{-3} per CC SN, assuming a Galactic CC SN rate of about $0.01\ {\rm yr}^{-1}$. These rates can be compared to that of 5.0×10^{-4} to 2.0×10^{-3}, obtained by Beniamini et al. (2016) based on an analysis of production of heavy *r*-process elements. Hence, we conclude that our simulated double NS merger rates agree with the results of Beniamini et al. (2016) based on a completely different method.

The local sGRB rate density is estimated to be $4.1^{+2.3}_{-1.9}\ f_{\rm b}^{-1}\ {\rm yr}^{-1}\ {\rm Gpc}^{-3}$ (Wanderman & Piran 2015), where $f_{\rm b}^{-1}$ is a beaming factor in the range $1 < f_{\rm b}^{-1} < 100$. Besides double NS mergers, it is expected that also mixed NS/BH mergers produce sGRBs. Adding our simulated mixed NS/BH merger-rate densities to our double NS merger-rate density, we estimate a total of $\mathcal{R}_{\rm sGRB} \simeq 25 - 28\ {\rm yr}^{-1}\ {\rm Gpc}^{-3}$ (at

$z \simeq 0$), based on our default values and almost independent on metallicity. This number agrees with that of Wanderman & Piran (2015) for any beaming factor close to $f_b^{-1} \simeq 5 - 10$ (Metzger & Berger 2012; Fong et al. 2015).

5.3 Recycled pulsars orbiting black holes

The detection of a recycled radio pulsar orbiting a BH would be of great interest, for example, to test theories of gravity (Wex & Kopeikin 1999; Liu et al. 2014; Shao et al. 2015; Yagi & Stein 2016). Unfortunately, the rarest DCO systems produced in our simulations are exactly those mixed binaries where the NS forms before the BH companion. As shown in Table 5, however, changing some of the input parameters can boost the number of these rare systems. The parameters related to the onset and outcome of CE evolution have the biggest influence on the formation rate of such NS-BH systems. The $q_{\rm limit}$ differentiates between stable and unstable mass transfer. The larger this limit, the more progenitor systems transfer mass in a stable manner. This also includes an increase in stable RLO from a naked He-star to its companion. As a result, the number of NS-BH binaries increases by avoiding a second CE phase after Case BB RLO which often leads to an early coalescence prior to the formation of a DCO binary. Similarly, an increase of the CE efficiency, $\alpha_{\rm CE}$, and/or the internal energy contribution, $\alpha_{\rm th}$, also helps NSs to successfully eject the envelope of the BH progenitor, thus producing more NS-BH systems.

Reducing the mass-transfer accretion efficiency creates more NS-BH binaries as well. Because the progenitor of the BH, the initially less massive of the two ZAMS stars, accretes under such inefficient conditions, it can only be slightly less massive than the progenitor of the NS. The reason is that it must accumulate sufficient material to pass the mass threshold for producing a BH. At the same time, the NS is probably relative massive because its progenitor star is also close to, but below, the BH formation threshold. Both of these mass conditions help the binary survive and eject its CE (Kruckow et al. 2016). When using a larger mass-transfer accretion efficiency, the number of NS-BH systems reaches a minimum before increasing again. In the most efficient case, more NS-BH systems are formed which would otherwise have become double NS systems, given the enhanced amount of material accreted by the secondary star.

Smaller SN kicks reduce the number of disrupted binaries and thus increase the formation rate of DCO binaries in general, including NS-BH binaries. Finally, a flatter, or top heavy, IMF increases the number of binaries produced which contain BHs and therefore also the number NS-BH binaries.

Combining our input physics parameters to optimize the formation of NS-BH binaries, we find that the relative number of tight NS-BH binaries (with a mildly recycled pulsar) can reach ~ 0.01 times the number of tight double NS systems. Given that the total radio pulsar population of known Galactic double NS systems is anticipated to reach about 100 with the completion of (the full) SKA (Keane et al. 2015), we therefore only expect detection of about one such NS-BH system.

In the above discussion, care must be taken to distinguish between NS-BH systems depending on whether or not the NS is recycled after its formation. Recycling requires accretion and thus only changes in input parameters which promote the survival of the CE evolution, leading to tight binaries and subsequent Case BB RLO, boost the population of recycled pulsars with BH companions. However, most of the above-mentioned modifications only increase the total number of NS-BH binaries and often only add wide-orbit systems to the sample which will end up containing a non-recycled pulsar anyway (cf. first panels of Figs 12 and B5).

Another issue to be investigated further is that NS-BH progenitor binaries often avoid Case BB RLO from the massive helium star progenitor of the BH (Tauris et al. 2015). Thus the NS only accretes inefficiently from wind accretion during the previous HMXB stage and thus the pulsar will hardly be recycled at all. This should be kept in mind when looking at the number of NS-BH binaries (and double NS systems) expected from our simulations compared to the observed populations, i.e. many of the NS-BH and double NS systems may either be in very wide-orbit systems which never merge in a Hubble time and/or only contain non-recycled radio pulsars. Such non-recycled pulsars are short-lived and their radio emission fades away after typically $10 - 50$ Myr (Lorimer & Kramer 2004; Johnston & Karastergiou 2017), which limits the chances of discovering such a system as a radio pulsar binary.

5.4 Alternative formation channels

The first LIGO event GW150914 has been suggested to form following the standard formation scenario by CE evolution (Belczynski et al. 2016). However, for massive stellar-mass BHs there are other formations channels in which a progenitor binary may evolve to become a tight pair of BHs. The three main formation channels to produce such a BH-BH pair are:

i) the CE formation channel (i.e. standard channel)
ii) the chemically homogeneous evolution (CHE) channel with or without a massive overcontact binary (MOB)
iii) the dynamical channel in dense stellar environments

In the following we discuss alternative formation channels not included in this work.

The dynamical formation channel (e.g. Portegies Zwart & McMillan 2000; Banerjee et al. 2010; Rodriguez et al. 2016a; Chatterjee et al. 2017; Banerjee 2017) produces DCO mergers via three-body and binary-binary encounter interactions in dense stellar clusters and thereby circumvents the need for mass transfer and CE evolution. In analogy to the other production channels mentioned above, the rate of DCO mergers from the dynamical formation channel is also difficult to constrain. Some recent studies predict that this channel might account for the order of only a few percent, possibly less, of all DCO mergers (e.g. Bae et al. 2014; Rodriguez et al. 2016a).

It has been suggested (e.g. Farr et al. 2017; Stevenson et al. 2017b) that the small effective inspiral spin parameters, $\chi_{\rm eff}$, inferred for the first four LIGO events (Abbott et al. 2017a) could be evidence for isotropic misalignment angles and thus a dynamical formation origin. This reasoning is based on the hypothesis that the standard formation channel, due to mass transfer, leads to aligned spins of the BHs and the orbital angular momentum vector. However, as argued by Tauris et al. (2017), it cannot be ruled out that

the spin axis of the exploding star is tossed in a new, possibly random, direction as a result of the SN similar to what has been suggested for NSs (Spruit & Phinney 1998; Farr et al. 2011). If this is the case, then all past memory from mass transfer is lost. For NSs, there is evidence for such spin axis tossing in both of the two known young pulsars found in double NS systems: PSR J0737−3039 (Breton et al. 2008) and J1906+0746 (Desvignes et al. 2017, in prep.).

An alternative and novel formation channel of relative massive BH-BH binaries, which avoids the CE phase altogether, is the the CHE channel (e.g. de Mink et al. 2009; Marchant et al. 2016; Mandel & de Mink 2016). In this scenario, the stars avoid the usual strong post-main sequence expansion as a result of effective mixing enforced through the rapidly rotating stars via tidal interactions. Therefore, the CHE scenario works only for massive stars at low metallicity in which strong angular-momentum loss due to stellar winds can be avoided. Marchant et al. (2016) presented the first detailed CHE models leading to the formation of BH-BH systems and demonstrated that massive-overcontact binaries are particularly suited for this channel. Very massive stellar-mass BH-BH mergers can form, in agreement with the detections of GW150914, GW170104 and GW170814. Double NS mergers (GW170817) and lower-mass BH-BH mergers like GW151226 ($14 + 8\ \mathrm{M}_\odot$) and GW170608 ($12 + 7\ \mathrm{M}_\odot$), however, cannot form in this scenario because the chemical mixing is insufficient in less massive progenitor stars.

Finally, it should be mentioned that in addition a "double core scenario" (Brown 1995; Belczyński & Kalogera 2001; Dewi et al. 2006) has been proposed in which CE evolution with a NS is also avoided. In this scenario, two stars with an initial mass ratio close to unity evolve in parallel and reach the giant stage roughly at the same time. Therefore, when the CE forms it will embed both stars in their giant stages, or as a giant star and a helium core, thereby avoiding the formation of a CE with a NS. The double core scenario was originally proposed (Chevalier 1993) at a time when it was thought that a NS in a CE might suffer from hypercritical accretion leading to its collapse into a BH. Thus to explain the observed double NS systems, this alternative scenario without CE evolution was invented. This formation channel, however, only works for the evolution of two stars with a mass ratio close to 1 and is thus not suited to explain the observations of tight binaries with, for example, a NS orbited by a WD companion (Tauris et al. 2012).

6 SUMMARY AND CONCLUSIONS

We have developed a new grid-based binary stellar populations synthesis code, ComBinE. The main motivation is to better understand the formation process of binaries with compact stars and the empirical merger rates reported by LIGO-Virgo based on recent GW detections of colliding double BH and double NS systems. Because the dynamical formation channel is anticipated to produce a minority of the detected DCO mergers and the CHE channel cannot produce double NSs nor low-mass double BH systems like GW151226 and GW170608, in this work we have investigated the standard (or CE) formation channel (Fig. 1) for all DCO binaries and succeeded in reproducing all GW merger events detected so far.

Our code is based on the earlier work by Voss & Tauris (2003) and simulates the evolution of typically one billion binary stars from the ZAMS until two compact objects form. In each system, the two stars are carefully followed in terms of their stellar evolution and mutual interactions via the so-called standard scenario. These interactions include stellar wind mass loss, RLO mass transfer and accretion, CEs and SNe. We apply self-consistent analyses of the binding energies of CEs and implement the results of recent numerical modelling of the subsequent Case BB RLO with a compact object accretor. In addition, we scale SN kicks according to the stripping of the exploding stars and we show that the simulated merger rates are particularly dependent on the treatment of these three interaction phases.

We demonstrate that all currently detected double BH mergers, GW150914, LVT151012, GW151226, GW170104, GW170608 and GW170814, as well as the recently reported double NS merger GW170817, can be accounted for in our models, depending on the metallicity of the progenitor stars (Figs 16 and 23). For MW-equivalent galaxies ($Z_{\mathrm{MW}} = 0.0088$), and applying default values of our input physics parameters (Table 5), we find a double NS merger rate of about $3.0\ \mathrm{Myr}^{-1}$. A similar merger rate is found for mixed BH/NS binaries, among which we predict very few, systems with a recycled pulsar orbiting a BH. The relative merger rate of double BH systems is lower by an order of magnitude at high metallicity. At low metallicity ($Z_{\mathrm{IZw18}} = 0.0002$), however, we predict the formation of double BH systems with total masses up to $\sim 100\ \mathrm{M}_\odot$ and their merger rate is similar to the merger rates of double NSs and mixed BH/NS systems (the latter two of which remain close to the values obtained for a MW-like metallicity).

The corresponding merger-rate densities in the local Universe ($z = 0$) for all types of systems combined is about $\mathcal{R} \simeq 30 - 120\ \mathrm{yr}^{-1}\ \mathrm{Gpc}^{-3}$, depending on the galaxy-density scaling (Table 8 and Fig. 22). We caution that all above-quoted rates are easily changed by more than an order of magnitude when adopting other values for some of the input physics parameters. More specifically, we find an "optimistic" merger-rate density for double NS systems of up to $\mathcal{R}_{\mathrm{max}} \simeq 400\ \mathrm{yr}^{-1}\ \mathrm{Gpc}^{-3}$ when optimizing our input physics parameters within reasonable limits, including the use of relatively small kicks. Our upper limit is still on the lower side compared to the recent empirical double NS merger-rate density of $\mathcal{R} = 1540^{+3200}_{-1220}\ \mathrm{yr}^{-1}\ \mathrm{Gpc}^{-3}$ which was recently reported based on the first GW detection of such a system (GW170817, Abbott et al. 2017c). Based on our simulations we predict that near-future GW detections (or non-detections) of double NS mergers from LIGO-Virgo runs O3 and O4 will decrease the derived empirical merger-rate density of double NSs to a level of the order $\mathcal{R} \simeq 10 - 400\ \mathrm{yr}^{-1}\ \mathrm{Gpc}^{-3}$. Such a range also seems in good agreement with comparison to the rates estimated from CC SNe, sGRBs and the production of heavy *r*-process elements (Section 5.2). We predict a NS-NS detection rate of at most 1 to 4 events per year at LIGO-Virgo design sensitivity (Table 8).

Our double BH merger simulations yield local ($z = 0$) merger-rate densities spanning the entire interval of $\mathcal{R} \simeq 0.6 - 109\ \mathrm{yr}^{-1}\ \mathrm{Gpc}^{-3}$, depending on the input physics parameters, the metallicity distribution among the sources and the applied galaxy-density scaling (Tables 5, 6 and 8). This

range is in agreement with the current empirical LIGO-Virgo rate of $\mathcal{R} = 12 - 213\ \mathrm{yr}^{-1}\ \mathrm{Gpc}^{-3}$ (Abbott et al. 2017a). Finally, for mixed BH/NS binaries we predict a local ($z = 0$) merger-rate density $\mathcal{R} \simeq 13 - 53\ \mathrm{yr}^{-1}\ \mathrm{Gpc}^{-3}$. We cannot lower the large uncertainty intervals in our predicted values due to uncertain input physics. Once the future LIGO-Virgo empirical merger rates converge, we can use these to constrain and gain new insight to the physics of binary evolution (e.g. Dvorkin et al. 2017; Barrett et al. 2017a). In addition, the possibility to measure NS spins from the GW signals of double NS mergers (Zhu et al. 2017) will enable us to compare with current models for NS spin and B-field evolution.

Our binary interaction parameters are calibrated to match the observed properties of Galactic double NS systems. Any binary population synthesis on DCO binaries must be able to reproduce the masses and orbital characteristics of binary pulsars (Fig. 8 top panel and Fig. 10). To match observational data with our simulations, we generally must invoke a low accretion efficiency during RLO. Only with this assumption are we able to match the distribution of NS masses and orbital parameters simultaneously.

Finally, we find a discrepancy between our simulated distribution of NS masses and those inferred from observations of binary radio pulsars in double NS systems, unless the formation channel of EC SNe is somehow significantly suppressed compared to that of low-mass FeCC SNe or EC SNe produce more massive NSs (about 1.30 to 1.32 $\mathrm{M}_\odot$) than usually thought (Section 5.1.2).

We conclude that the ComBinE binary population synthesis code is working well based on its initial application to GW sources and binary pulsars. The grid interpolation allows a fast and consistent replacement of up-to-date stellar evolution. Other applications with this code are currently in progress, e.g. on the formation of WD-NS binaries in which the WD forms first (Ng et al. 2018).

ACKNOWLEDGEMENTS

We thank Philipp Podsiadlowski, Pablo Marchant, Ilya Mandel, Norbert Wex, Chris Belczynski and Sambaran Bannerjee for discussions. MUK acknowledges financial support by the DFG Grant: TA 964/1-1 awarded to TMT. MK acknowledges financial support by the European Research Council for the ERC Synergy Grant BlackHoleCam under contract no. 610058. RGI thanks the STFC for funding his Rutherford fellowship under grant ST/L003910/1.

REFERENCES

Abadie J., et al., 2010, Classical and Quantum Gravity, 27, 173001
Abbott B. P., et al., 2016a, Physical Review X, 6, 041015
Abbott B. P., et al., 2016b, Physical Review Letters, 116, 061102
Abbott B. P., et al., 2016c, Physical Review Letters, 116, 241103
Abbott B. P., et al., 2017a, Physical Review Letters, 118, 221101
Abbott B. P., et al., 2017b, Physical Review Letters, 119, 141101
Abbott B. P., et al., 2017c, Physical Review Letters, 119, 161101
Abbott B. P., et al., 2017d, ApJ, 848, L12
Abbott B. P., et al., 2017e, ApJ, 848, L13
Abt H. A., 1983, ARA&A, 21, 343
Allen C., Santillan A., 1991, Rev. Mex. Astron. Astrofis., 22, 255
Antoniadis J., Freire P. C. C., Wex N., Tauris T. M., Lynch R. S., van Kerkwijk M. H., Kramer M., et al. 2013, Science, 340, 448
Bae Y.-B., Kim C., Lee H. M., 2014, MNRAS, 440, 2714
Banerjee S., 2017, MNRAS, 467, 524
Banerjee S., Baumgardt H., Kroupa P., 2010, MNRAS, 402, 371
Barrett J. W., Gaebel S. M., Neijssel C. J., Vigna-Gómez A., Stevenson S., Berry C. P. L., Farr W. M., Mandel I., 2017a, preprint (arXiv:1711.06287)
Barrett J. W., Mandel I., Neijssel C. J., Stevenson S., Vigna-Gómez A., 2017b, in IAU Symposium. pp 46–50 (arXiv:1704.03781), doi:10.1017/S1743921317000059
Belczyński K., Kalogera V., 2001, ApJ, 550, L183
Belczynski K., Kalogera V., Bulik T., 2002, ApJ, 572, 407
Belczynski K., Kalogera V., Rasio F. A., Taam R. E., Zezas A., Bulik T., Maccarone T. J., Ivanova N., 2008, ApJS, 174, 223
Belczynski K., Holz D. E., Bulik T., O'Shaughnessy R., 2016, Nature, 534, 512
Belczynski K., et al., 2017, preprint (arXiv:1712.00632)
Beniamini P., Hotokezaka K., Piran T., 2016, ApJ, 832, 149
Berger E., 2014, ARA&A, 52, 43
Bhattacharya D., van den Heuvel E. P. J., 1991, Phys. Rep., 203, 1
Bisnovatyi-Kogan G. S., Komberg B. V., 1974, Azh, 51, 373
Blanchard P. K., et al., 2017, ApJ, 848, L22
Bloom J. S., Sigurdsson S., Pols O. R., 1999, MNRAS, 305, 763
Breton R. P., et al., 2008, Science, 321, 104
Brott I., et al., 2011, A&A, 530, A115
Brown G. E., 1995, ApJ, 440, 270
Cameron A. D., et al., 2017, preprint (arXiv:1711.07697)
Chatterjee S., Rodriguez C. L., Kalogera V., Rasio F. A., 2017, ApJ, 836, L26
Chevalier R. A., 1993, ApJ, 411, L33
Chruslinska M., Belczynski K., Klencki J., Benacquista M., 2017, preprint (arXiv:1708.07885)
Clark J. P. A., van den Heuvel E. P. J., Sutantyo W., 1979, A&A, 72, 120
Coulter D. A., et al., 2017, preprint (arXiv:1710.05452)
Crowther P. A., 2007, ARA&A, 45, 177
Damour T., Taylor J. H., 1992, Phys. Rev. D, 45, 1840
De Marco O., Izzard R. G., 2017, Publ. Astron. Soc. Australia, 34, e001
Dessart L., Burrows A., Ott C. D., Livne E., Yoon S.-C., Langer N., 2006, ApJ, 644, 1063
Desvignes et al. 2017, in preparation
Dewi J. D. M., Pols O. R., 2003, MNRAS, 344, 629
Dewi J. D. M., Tauris T. M., 2000, A&A, 360, 1043
Dewi J. D. M., Tauris T. M., 2001, in Podsiadlowski P., Rappaport S., King A. R., D'Antona F., Burderi L., eds, Astronomical Society of the Pacific Conference Series Vol. 229, Evolution of Binary and Multiple Star Systems. p. 255
Dewi J. D. M., Podsiadlowski P., Pols O. R., 2005, MNRAS, 363, L71
Dewi J. D. M., Podsiadlowski P., Sena A., 2006, MNRAS, 368, 1742
Dominik M., Belczynski K., Fryer C., Holz D. E., Berti E., Bulik T., Mandel I., O'Shaughnessy R., 2012, ApJ, 759, 52
Dominik M., Belczynski K., Fryer C., Holz D. E., Berti E., Bulik T., Mandel I., O'Shaughnessy R., 2013, ApJ, 779, 72
Dominik M., et al., 2015, ApJ, 806, 263
Drout M. R., Piro A. L., Shappee B. J., et al. 2017, preprint (arXiv:1710.05443)
Dvorkin I., Uzan J.-P., Vangioni E., Silk J., 2017, preprint (arXiv:1709.09197)
Eggleton P. P., 1983, ApJ, 268, 368
Eichler D., Livio M., Piran T., Schramm D. N., 1989, Nature, 340, 126
Eldridge J. J., Stanway E. R., 2016, MNRAS, 462, 3302
Eldridge J. J., et al., 2017, preprint (arXiv:1710.02154)

Falcke H., Rezzolla L., 2014, A&A, 562, A137
Farr W. M., Kremer K., Lyutikov M., Kalogera V., 2011, ApJ, 742, 81
Farr W. M., Stevenson S., Miller M. C., Mandel I., Farr B., Vecchio A., 2017, preprint (arXiv:1706.01385)
Ferdman R. D., 2017, in talk presented at IAU Symposium 337 ed., to appear in "Pulsar Astrophysics - The Next 50 Years". Cambridge University Press
Fermi-LAT Collaboration 2017, preprint (arXiv:1710.05450)
Flannery B. P., van den Heuvel E. P. J., 1975, A&A, 39, 61
Fong W., Berger E., Margutti R., Zauderer B. A., 2015, ApJ, 815, 102
Fryer C. L., 2006, New Astron. Rev., 50, 492
Fryer C. L., Woosley S. E., Hartmann D. H., 1999, ApJ, 526, 152
Gautschy A., 2013, preprint (arXiv:1303.6652)
Giacobbo N., Mapelli M., Spera M., 2017, preprint (arXiv:1711.03556)
Glebbeek E., Gaburov E., Portegies Zwart S., Pols O. R., 2013, MNRAS, 434, 3497
Grassitelli L., Fossati L., Langer N., Simón-Díaz S., Castro N., Sanyal D., 2016, A&A, 593, A14
Habets G. M. H. J., 1986, A&A, 165, 95
Hainich R., Pasemann D., Todt H., Shenar T., Sander A., Hamann W.-R., 2015, A&A, 581, A21
Han Z., Podsiadlowski P., Eggleton P. P., 1995, MNRAS, 272, 800
Heger A., Woosley S. E., 2002, ApJ, 567, 532
Heggie D. C., 1975, MNRAS, 173, 729
Hills J. G., 1983, ApJ, 267, 322
Hjellming M. S., Webbink R. F., 1987, ApJ, 318, 794
Hobbs G., Lorimer D. R., Lyne A. G., Kramer M., 2005, MNRAS, 360, 974
Hüdepohl L., Müller B., Janka H.-T., Marek A., Raffelt G. G., 2010, Physical Review Letters, 104, 251101
Hurley J. R., Pols O. R., Tout C. A., 2000, MNRAS, 315, 543
Hurley J. R., Tout C. A., Pols O. R., 2002, MNRAS, 329, 897
Im M., et al., 2017, preprint (arXiv:1710.05861)
Istrate A. G., Marchant P., Tauris T. M., Langer N., Stancliffe R. J., Grassitelli L., 2016, A&A, 595, A35
Ivanova N., 2011, ApJ, 730, 76
Ivanova N., Belczynski K., Kalogera V., Rasio F. A., Taam R. E., 2003, ApJ, 592, 475
Ivanova N., et al., 2013, A&ARv, 21, 59
Izzard R. G., Tout C. A., Karakas A. I., Pols O. R., 2004, MNRAS, 350, 407
Izzard R. G., Dray L. M., Karakas A. I., Lugaro M., Tout C. A., 2006, A&A, 460, 565
Izzard R. G., Glebbeek E., Stancliffe R. J., Pols O. R., 2009, A&A, 508, 1359
Izzard R. G., Preece H., Jofre P., Halabi G. M., Masseron T., Tout C. A., 2017, preprint (arXiv:1709.05237)
Janka H.-T., 2012, Annual Review of Nuclear and Particle Science, 62, 407
Janka H.-T., 2013, MNRAS, 434, 1355
Janka H.-T., 2017, ApJ, 837, 84
Johnston S., Karastergiou A., 2017, MNRAS, 467, 3493
Johnston S., Manchester R. N., Lyne A. G., Bailes M., Kaspi V. M., Qiao G., D'Amico N., 1992, ApJ, 387, L37
Jones S., et al., 2013, ApJ, 772, 150
Just O., Bauswein A., Pulpillo R. A., Goriely S., Janka H.-T., 2015, MNRAS, 448, 541
Kalogera V., 1998, ApJ, 493, 368
Kaspi V. M., Johnston S., Bell J. F., Manchester R. N., Bailes M., Bessell M., Lyne A. G., D'Amico N., 1994, ApJ, 423, L43
Keane E., et al., 2015, Advancing Astrophysics with the Square Kilometre Array (AASKA14), p. 40
Kitaura F. S., Janka H.-T., Hillebrandt W., 2006, A&A, 450, 345
Klessen R. S., Glover S. C. O., Clark P. C., 2012, MNRAS, 421, 3217
Kramer M., et al., 2006, Science, 314, 97
Kroupa P., 2008, in Aarseth S. J., Tout C. A., Mardling R. A., eds, Lecture Notes in Physics, Berlin Springer Verlag Vol. 760, The Cambridge N-Body Lectures. p. 181 (arXiv:0803.1833), doi:10.1007/978-1-4020-8431-7_8
Kruckow M. U., Tauris T. M., Langer N., Szécsi D., Marchant P., Podsiadlowski P., 2016, A&A, 596, A58
Kuiper G. P., 1935, PASP, 47, 15
Langer N., 2012, ARA&A, 50, 107
Lattimer J. M., Schramm D. N., 1974, ApJ, 192, L145
Lattimer J. M., Yahil A., 1989, ApJ, 340, 426
Lewin W. H. G., van der Klis M., 2006, Compact stellar X-ray sources. Cambridge University Press
Liu K., Eatough R. P., Wex N., Kramer M., 2014, MNRAS, 445, 3115
Lorimer D. R., Kramer M., 2004, Handbook of Pulsar Astronomy. Cambridge University Press
Mandel I., 2016, MNRAS, 456, 578
Mandel I., de Mink S. E., 2016, MNRAS, 458, 2634
Mapelli M., Giacobbo N., Ripamonti E., Spera M., 2017, preprint (arXiv:1708.05722)
Marchant P., Langer N., Podsiadlowski P., Tauris T. M., Moriya T. J., 2016, A&A, 588, A50
Martinez J. G., et al., 2015, ApJ, 812, 143
Martinez J. G., et al., 2018, ApJL, accepted
Mennekens N., Vanbeveren D., 2014, A&A, 564, A134
Metzger B. D., Berger E., 2012, ApJ, 746, 48
Moe M., Di Stefano R., 2017, ApJS, 230, 15
Moriya T. J., et al., 2017, MNRAS, 466, 2085
Nandez J. L. A., Ivanova N., Lombardi Jr. J. C., 2014, ApJ, 786, 39
Nelemans G., Tauris T. M., van den Heuvel E. P. J., 1999, A&A, 352, L87
Nelson C. A., Eggleton P. P., 2001, ApJ, 552, 664
Ng C., et al., 2018, MNRAS, submitted
Nomoto K., 1987, ApJ, 322, 206
Ohlmann S. T., Röpke F. K., Pakmor R., Springel V., 2016, ApJ, 816, L9
Özel F., Freire P., 2016, ARA&A, 54, 401
Paczynski B., 1976, in Eggleton P., Mitton S., Whelan J., eds, IAU Symposium Vol. 73, Structure and Evolution of Close Binary Systems. p. 75
Pan Y.-C., et al., 2017, ApJ, 848, L30
Park D., Kim C., Lee H. M., Bae Y.-B., Belczynski K., 2017, MNRAS, 469, 4665
Passy J.-C., et al., 2012, ApJ, 744, 52
Pavlovskii K., Ivanova N., Belczynski K., Van K. X., 2017, MNRAS, 465, 2092
Pejcha O., Thompson T. A., 2015, ApJ, 801, 90
Peters P. C., 1964, Physical Review, 136, 1224
Petrovic J., Langer N., van der Hucht K. A., 2005, A&A, 435, 1013
Petrovic J., Pols O., Langer N., 2006, A&A, 450, 219
Pilyugin L. S., Lara-López M. A., Grebel E. K., Kehrig C., Zinchenko I. A., López-Sánchez Á. R., Vílchez J. M., Mattsson L., 2013, MNRAS, 432, 1217
Podsiadlowski P., 2001, in Podsiadlowski P., Rappaport S., King A. R., D'Antona F., Burderi L., eds, Astronomical Society of the Pacific Conference Series Vol. 229, Evolution of Binary and Multiple Star Systems. p. 239
Podsiadlowski P., Joss P. C., Hsu J. J. L., 1992, ApJ, 391, 246
Podsiadlowski P., Rappaport S., Pfahl E. D., 2002, ApJ, 565, 1107
Podsiadlowski P., Rappaport S., Han Z., 2003, MNRAS, 341, 385
Podsiadlowski P., Langer N., Poelarends A. J. T., Rappaport S., Heger A., Pfahl E., 2004, ApJ, 612, 1044
Poelarends A. J. T., Wurtz S., Tarka J., Adams C., Hills S. T., 2017, preprint (arXiv:1710.11143)
Portegies Zwart S. F., McMillan S. L. W., 2000, ApJ, 528, L17

Repetto S., Nelemans G., 2015, MNRAS, 453, 3341
Ricker P. M., Taam R. E., 2012, ApJ, 746, 74
Rodriguez C. L., Chatterjee S., Rasio F. A., 2016a, Phys. Rev. D, 93, 084029
Rodriguez C. L., Haster C.-J., Chatterjee S., Kalogera V., Rasio F. A., 2016b, ApJ, 824, L8
Rosswog S., 2015, International Journal of Modern Physics D, 24, 30012
Salpeter E. E., 1955, ApJ, 121, 161
Sana H., et al., 2012, Science, 337, 444
Sanyal D., Grassitelli L., Langer N., Bestenlehner J. M., 2015, A&A, 580, A20
Savonije G. J., 1978, A&A, 62, 317
Scalo J. M., 1986, Fundamentals Cosmic Phys., 11, 1
Schneider F. R. N., Sana H., Evans C. J., et al. 2018, Science, in press
Schwab J., Podsiadlowski P., Rappaport S., 2010, ApJ, 719, 722
Shao Y., Li X.-D., 2016, ApJ, 833, 108
Shao L., et al., 2015, Advancing Astrophysics with the Square Kilometre Array (AASKA14), p. 42
Smartt S. J., Chen T.-W., Jerkstrand A., et al. 2017, preprint (arXiv:1710.05841)
Soares-Santos M., Holz D. E., Annis J., et al. 2017, preprint (arXiv:1710.05459)
Soberman G. E., Phinney E. S., van den Heuvel E. P. J., 1997, A&A, 327, 620
Spruit H., Phinney E. S., 1998, Nature, 393, 139
Srinivasan G., van den Heuvel E. P. J., 1982, A&A, 108, 143
Stevenson S., Vigna-Gómez A., Mandel I., Barrett J. W., Neijssel C. J., Perkins D., de Mink S. E., 2017a, Nature Communications, 8, 14906
Stevenson S., Berry C. P. L., Mandel I., 2017b, MNRAS, 471, 2801
Strolger L.-G., et al., 2004, ApJ, 613, 200
Sutantyo W., 1974, A&A, 35, 251
Suwa Y., Yoshida T., Shibata M., Umeda H., Takahashi K., 2015, MNRAS, 454, 3073
Szécsi D., Langer N., Yoon S.-C., Sanyal D., de Mink S., Evans C. J., Dermine T., 2015, A&A, 581, A15
Taam R. E., Sandquist E. L., 2000, ARA&A, 38, 113
Tauris T. M., Bailes M., 1996, A&A, 315, 432
Tauris T. M., Dewi J. D. M., 2001, A&A, 369, 170
Tauris T. M., Savonije G. J., 1999, A&A, 350, 928
Tauris T. M., Sennels T., 2000, A&A, 355, 236
Tauris T. M., Takens R. J., 1998, A&A, 330, 1047
Tauris T. M., van den Heuvel E. P. J., 2006, in Lewin W. H. G., van der Klis M., eds, , Compact stellar X-ray sources. Cambridge University Press, Chapt. 16, pp 623–665
Tauris T. M., Fender R. P., van den Heuvel E. P. J., Johnston H. M., Wu K., 1999, MNRAS, 310, 1165
Tauris T. M., van den Heuvel E. P. J., Savonije G. J., 2000, ApJ, 530, L93
Tauris T. M., Langer N., Kramer M., 2012, MNRAS, 425, 1601
Tauris T. M., Langer N., Moriya T. J., Podsiadlowski P., Yoon S.-C., Blinnikov S. I., 2013, ApJ, 778, L23
Tauris T. M., Langer N., Podsiadlowski P., 2015, MNRAS, 451, 2123
Tauris T. M., et al., 2017, ApJ, 846, 170
The LIGO Scientific Collaboration et al., 2017, preprint (arXiv:1711.05578)
Timmes F. X., Woosley S. E., Weaver T. A., 1996, ApJ, 457, 834
Ugliano M., Janka H.-T., Marek A., Arcones A., 2012, ApJ, 757, 69
Vietri M., Stella L., 1998, ApJ, 507, L45
Voss R., Tauris T. M., 2003, MNRAS, 342, 1169
Wanderman D., Piran T., 2015, MNRAS, 448, 3026
Webbink R. F., 1984, ApJ, 277, 355
Wellstein S., Langer N., 1999, A&A, 350, 148
Wex N., 2014, preprint (arXiv:1402.5594)
Wex N., Kopeikin S. M., 1999, ApJ, 514, 388
Wheeler J. C., McKee C. F., Lecar M., 1974, ApJ, 192, L71
Woosley S. E., 2017, ApJ, 836, 244
Woosley S. E., Heger A., 2015, ApJ, 810, 34
Yagi K., Stein L. C., 2016, Classical and Quantum Gravity, 33, 054001
Yoon S., Woosley S. E., Langer N., 2010, ApJ, 725, 940
Zahn J.-P., 1977, A&A, 57, 383
Zapartas E., et al., 2017, A&A, 601, A29
Zhu X.-J., Thrane E., Osłowski S., Levin Y., Lasky P. D., 2017, preprint (arXiv:1711.09226)
de Kool M., 1990, ApJ, 358, 189
de Mink S. E., Belczynski K., 2015, ApJ, 814, 58
de Mink S. E., Cottaar M., Pols O. R., 2008, in O'Shea B. W., Heger A., eds, American Institute of Physics Conference Series Vol. 990, First Stars III. pp 217–219 (arXiv:0710.2193), doi:10.1063/1.2905545
de Mink S. E., Cantiello M., Langer N., Pols O. R., Brott I., Yoon S.-C., 2009, A&A, 497, 243
van den Heuvel E. P. J., 1994, in Shore S. N., Livio M., van den Heuvel E. P. J., Nussbaumer H., Orr A., eds, Saas-Fee Advanced Course 22: Interacting Binaries. pp 263–474
van den Heuvel E. P. J., 2004, in Schoenfelder V., Lichti G., Winkler C., eds, ESA Special Publication Vol. 552, 5th INTEGRAL Workshop on the INTEGRAL Universe. p. 185 (arXiv:astro-ph/0407451)

Table A1. Short notations in Equations (A3) to (A16).

index	i	j
11	$i_{\rm up}$	$j_{\rm up}-1$
12	$i_{\rm up}$	$j_{\rm up}$
21	$i_{\rm low}$	$j_{\rm low}-1$
22	$i_{\rm low}$	$j_{\rm low}$
up,max	$i_{\rm up}$	$j_{\rm max}(i_{\rm up})$
low,max	$i_{\rm low}$	$j_{\rm max}(i_{\rm low})$

APPENDIX A: INTERPOLATION OF STELLAR GRIDS

The stellar grids are described in Section 3. They are based on evolutionary tracks of stars with a given initial mass and describe their full stellar evolution. Each of these tracks have a number of supporting points (grid points). So the two dimensions of each grid are the initial mass and the age of the star evolved.

A1 Grid structure and interpolation

The grid points are two-dimensional matrices in each stellar variable, age $t_{i,j}$, mass $m_{i,j}$, core mass $c_{i,j}$, radius $R_{i,j}$, luminosity $L_{i,j}$, effective temperature $T_{{\rm eff},i,j}$ and the structure parameter of the envelope $\lambda_{i,j}$. The index i indicates the initial (ZAMS) mass and the index j expresses the relative time evolved. ComBinE allows for individual sets in $j \in \{0, 1, ..., j_{\rm max}(i)\}$ at a given i. Therefore, any track at a given i is scaled by the fraction of total time of the track to interpolate between two neighbouring tracks indicated by $i_{\rm up}$ and $i_{\rm low} = i_{\rm up} - 1$. For a given initial mass, $m_{\rm ini}$, there is an upper track and a lower track such that $m_{{\rm up},0} \geq m_{\rm ini} \geq m_{{\rm low},0}$[7]. In this way, the neighbouring mass indices $i_{\rm up}$ and $i_{\rm low}$ are determined for a given $m_{\rm ini}$. To interpolate on the grid, a ratio in mass is defined by,

$$r_{\rm m} = \frac{m_{{\rm up},0} - m_{\rm ini}}{m_{{\rm up},0} - m_{{\rm low},0}}, \tag{A1}$$

such that $0 \leq r_{\rm m} \leq 1$. As an example, the mass[8] at a given time is found by,

$$m = m_{\rm up} - r_{\rm m}\,\left(m_{\rm up} - m_{\rm low}\right), \tag{A2}$$

where $m_{\rm up}$ and $m_{\rm low}$ are the masses at the same relative time at the upper and lower track, respectively. The definition of the short notations in the following equations are found in Table A1. The current masses on the neighbouring tracks are interpolated as,

$$m_{\rm up} = m_{12} - r_{\rm up}\,(m_{12} - m_{11}), \tag{A3}$$

and

$$m_{\rm low} = m_{22} - r_{\rm low}\,(m_{22} - m_{21}), \tag{A4}$$

[7] Any variable $x_{i,j}$ at $i = i_{\rm up}$ or $i = i_{\rm low}$ is shortened to $x_{{\rm up},j}$ or $x_{{\rm low},j}$, respectively.

[8] In the same way, the other variables (age: t; radius: R; core mass, c; luminosity, L; effective temperature, $T_{\rm eff}$; and the structure parameter of the envelope, λ) are interpolated using the same ratios $r_{\rm m}$, $r_{\rm up}$ and $r_{\rm low}$.

with

$$r_{\rm up} = \frac{t_{12} - t_{\rm up}}{t_{12} - t_{11}} \quad \text{and} \quad r_{\rm low} = \frac{t_{22} - t_{\rm low}}{t_{22} - t_{21}}, \tag{A5}$$

where $t_{12} \geq t_{\rm up} \geq t_{11}$ and $t_{22} \geq t_{\rm low} \geq t_{21}$ holds and determines $j_{\rm up}$ and $j_{\rm low}$. Effectively there is only one time ratio because $r_{\rm up}$ and $r_{\rm low}$ depend on each other via:

$$t_{\rm rel} = \frac{t_{\rm up}}{t_{\rm up,max}} = \frac{t_{\rm low}}{t_{\rm low,max}} = \frac{t}{t_{\rm max}}. \tag{A6}$$

$t_{\rm max}$ is the lifetime of the star (from the ZAMS until a compact object is formed) and $t_{\rm rel}$ is the relative age. The two variables $m_{\rm ini}$ and $t_{\rm rel}$ determine a position in the grid and the current values of this position can be calculated with Equation (A2) and using Equations (A1) to (A6).

A2 Placing a star on the stellar grid

In principle, one can replace the two determining dimensions $m_{\rm ini}$ and $t_{\rm rel}$ by other quantities. For example, after mass transfer the two stars evolve differently compared to the evolutionary tracks they followed before the interaction. Therefore, one needs two independent quantities to place them on the new tracks interpolated from the stellar grids after the interaction. ComBinE uses the current stellar mass and the current core mass (Section 3.3) of the star as these two quantities. The combination of the two masses gives the amount of already burned material in the core and available fuel for future burning in the envelope. Furthermore, the stellar mass determines how massive a single star progenitor with such a core mass would have been on the ZAMS.

To get the new track interpolated from the stellar grids and the current position in it, a mapping from the current stellar mass, m, and the core mass, c, to the initial mass, $m_{\rm ini}(m, c)$ and the evolved time, $t_{\rm rel}(m, c)$, is needed. This mapping is not necessarily unique. Therefore, the mapping implemented in ComBinE uses the solution with the shortest age of the star as the accretor is usually a less evolved star. The two dimensions are fixed when $i_{\rm up}$, $j_{\rm up}$, $j_{\rm low}$, $r_{\rm m}$, $r_{\rm up}$ and $r_{\rm low}$ are known. The interpolated ratios $r_{\rm m}$, $r_{\rm up}$ and $r_{\rm low}$ are limited to be within $[0:1]$ and this determines the indices $i_{\rm up}$, $j_{\rm up}$ and $j_{\rm low}$.

Computationally, the indices $i_{\rm up}$, $j_{\rm up}$ and $j_{\rm low}$ are fixed first. Solutions are only possible if $\max\{m_{11}, m_{12}, m_{21}, m_{22}\} \geq m \geq \min\{m_{11}, m_{12}, m_{21}, m_{22}\}$ and $\max\{c_{11}, c_{12}, c_{21}, c_{22}\} \geq c \geq \min\{c_{11}, c_{12}, c_{21}, c_{22}\}$ are simultaneously fulfilled. The definition of the short notation is given in Table A1. Then one can solve Equations (A1) to (A6) for the stellar mass, m, and core mass, c, to get the ratios $r_{\rm m}$, $r_{\rm up}$ and $r_{\rm low}$. The two solutions are,

$$r_{\rm m}^{\pm} = \frac{-0.5\,(C - B - A) \pm \sqrt{0.25\,(C - B - A)^2 - B\,A}}{A}, \tag{A7}$$

where,

$$\begin{aligned} A = {} & (l_{22} - l_{21})\,(c_{11}\,m_{12} - c_{12}\,m_{11}) \\ & + (l_{12} - l_{22})\,(c_{11}\,m_{21} - c_{21}\,m_{11}) \\ & + (l_{22} - l_{11})\,(c_{12}\,m_{21} - c_{21}\,m_{12}) \\ & + (l_{12} - l_{21})\,(c_{22}\,m_{11} - c_{11}\,m_{22}) \\ & + (l_{21} - l_{11})\,(c_{22}\,m_{12} - c_{12}\,m_{22}) \\ & + (l_{12} - l_{11})\,(c_{21}\,m_{22} - c_{22}\,m_{21}), \end{aligned} \tag{A8}$$

$$B = (l_{22} - l_{21})\,[c\,(m_{11} - m_{12}) + c_{11}\,(m_{12} - m) + c_{12}\,(m - m_{11})], \tag{A9}$$

and

$$C = (l_{12} - l_{11})\,[c\,(m_{21} - m_{22}) + c_{21}\,(m_{22} - m) + c_{22}\,(m - m_{21})] \tag{A10}$$

with

$$l_{i,j} \equiv \frac{t_{i,j}}{t_{i,\max}}. \tag{A11}$$

For any ratio in mass, r, one then finds the ratios in time,

$$r_{\rm up} = \frac{D}{F} \tag{A12}$$

and

$$r_{\rm low} = \frac{E}{F}, \tag{A13}$$

where,

$$D = [m - m_{11}\,(1 - r)]\,(l_{22} - l_{21}) + r\,[m_{22}\,(l_{21} - l_{11}) - m_{21}\,(l_{22} - l_{11})], \tag{A14}$$

$$E = (m - m_{21}\,r)\,(l_{12} - l_{11}) + (1 - r)\,[m_{12}\,(l_{11} - l_{21}) - m_{11}\,(l_{12} - l_{21})] \tag{A15}$$

and

$$F = (m_{22} - m_{21})\,r\,(l_{12} - l_{11}) + (m_{12} - m_{11})\,(1 - r)\,(l_{22} - l_{21}). \tag{A16}$$

The solutions for $r_{\rm m}$, $r_{\rm up}$ and $r_{\rm low}$ are accepted if all values are in their domain $[0:1]$. Otherwise the next possible group of $i_{\rm up}$, $j_{\rm up}$, $j_{\rm low}$ is checked.

APPENDIX B: EFFICIENT MASS TRANSFER

This section gives additional details of our simulations using efficient mass transfer (i.e. little re-emission of transferred material reaching the accretor, $\beta_{\rm min} = 0$, and thus a high accretion efficiency, $\epsilon = 0.8$). All the other input parameters have the same values as in Table 2 in Section 4.

B1 Progenitor zero-age main-sequence masses

Fig. B1 shows the initial (ZAMS) progenitor star masses of the different types of binaries formed in our simulation with efficient mass transfer ($\beta_{\rm min} = 0$). The plot looks similar to our simulations with low mass-transfer efficiency although double NS systems are more suppressed at both metallicities, cf. Fig. 6. Furthermore, a triangular region of double BH systems appears to penetrate into the BH-NS binaries. This region is shifted in secondary mass compared to Fig. 6.

B2 Compact object masses

From Fig. B2 we see that compared to our standard case (Section 4.2), several things change in the distribution of final compact object masses when applying efficient mass transfer. Mainly the formation rates are smaller (compare Table B1 with Table 3).

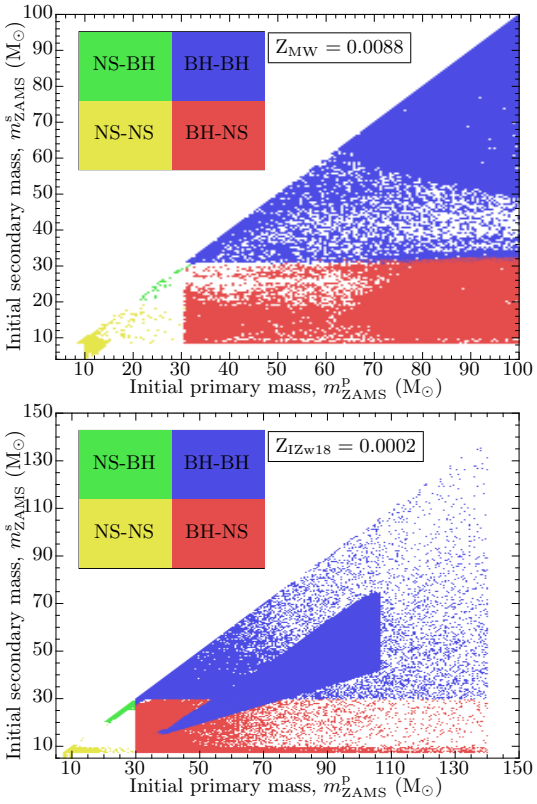

Figure B1. The upper and lower panel are our high- and the low-metallicity cases, as in Fig. 6, but with efficient mass transfer ($\beta_{\rm min} = 0$).

Table B1. Formation rates of DCO binaries in a MW-like galaxy with efficient mass transfer ($\beta_{\rm min} = 0$), cf. Table 3. The binary types refer to the first and second formed compact object.

Formation rates	$Z_{\rm MW} = 0.0088$	$Z_{\rm IZw18} = 0.0002$
NS-NS	2.27×10^{-6} yr^{-1}	7.64×10^{-6} yr^{-1}
NS-BH	2.45×10^{-9} yr^{-1}	2.58×10^{-8} yr^{-1}
BH-NS	1.78×10^{-6} yr^{-1}	2.51×10^{-6} yr^{-1}
BH-BH	2.64×10^{-6} yr^{-1}	3.93×10^{-5} yr^{-1}

In the following, we first consider the results of our MW metallicity study. Here, the population of double BH systems with large secondary BH masses is frequent and it is further extended in mass. Therefore, fewer double BH binaries are produced with inverted masses and a mass ratio close to 1. The region with most massive primary BHs and the least massive secondary BHs disappears. While the NS-BH binaries look similar, the dominant diagonal region of BH-NS systems disappears. The double NS binaries have less massive primary NSs, as shown in Fig. 8. This results in a distribution of mass ratios of double NS binaries which disagrees with observations, see Fig. B3.

We now consider our low-metallicity simulations. Sec-

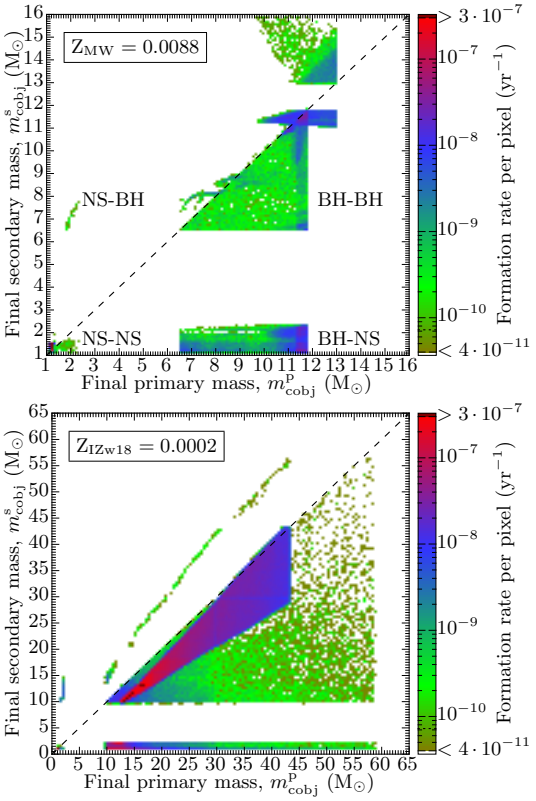

Figure B2. The upper and lower panel are our high- and the low-metallicity cases, as in Fig. 7, but with efficient mass transfer ($\beta_{\rm min} = 0$).

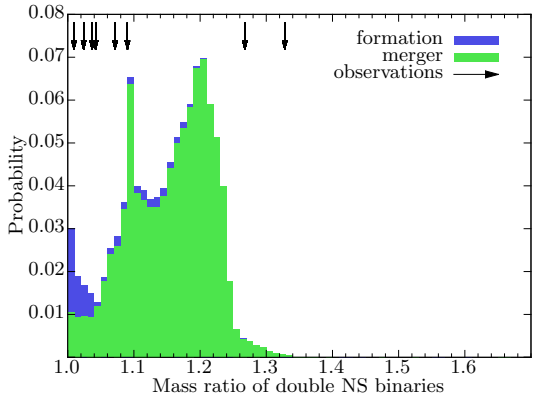

Figure B3. As Fig. 9 but with efficient mass transfer ($\beta_{\rm min} = 0$).

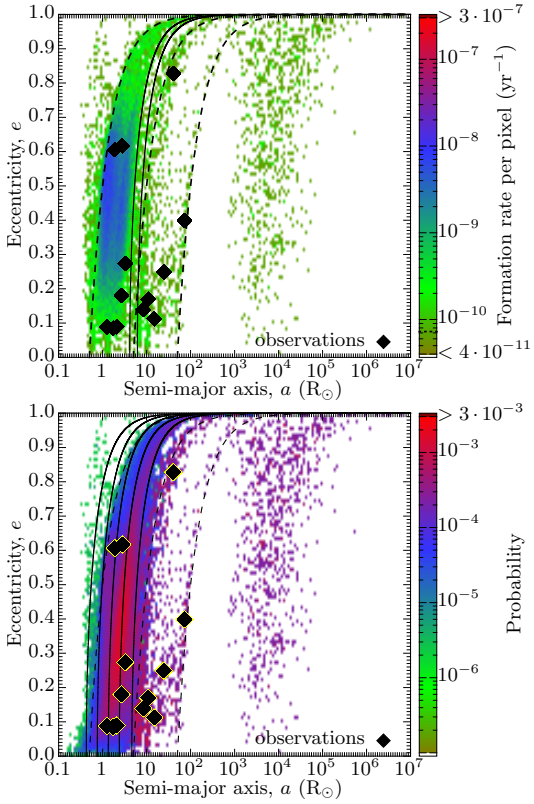

Figure B4. The upper panel shows, like Fig. 10, our double NS binaries at birth with efficient mass transfer ($\beta_{\rm min} = 0$). In the lower panel, GW evolution is considered, which changes the observable parameters compared to their values at formation, cf. Fig. 11.

ondary BHs become more massive when their progenitors accrete more mass, cf. Fig. 7. Therefore, a new line of double BH binaries appears where the secondary is more massive than the primary. The DCO systems in which the secondary becomes a NS are less common compared to our default simulation.

B3 Orbital parameters

Simulating the formation of double NS systems at MW metallicity assuming efficient mass transfer (Fig. B4 – instead of an ineffective mass transfer as in Figs 10 and 11) leads to a discrepancy compared to observations. Furthermore, in this case fewer double NS systems are produced. By assuming efficient RLO, all systems are a bit wider on average. This makes it more likely to disrupt a given binary by a SN kick. The orbital parameters of the mixed binary types (BH-NS and NS-BH in Fig. B5) look very similar to the standard case with less efficient RLO. However, because the double BH binaries (Fig. B5) become more massive in

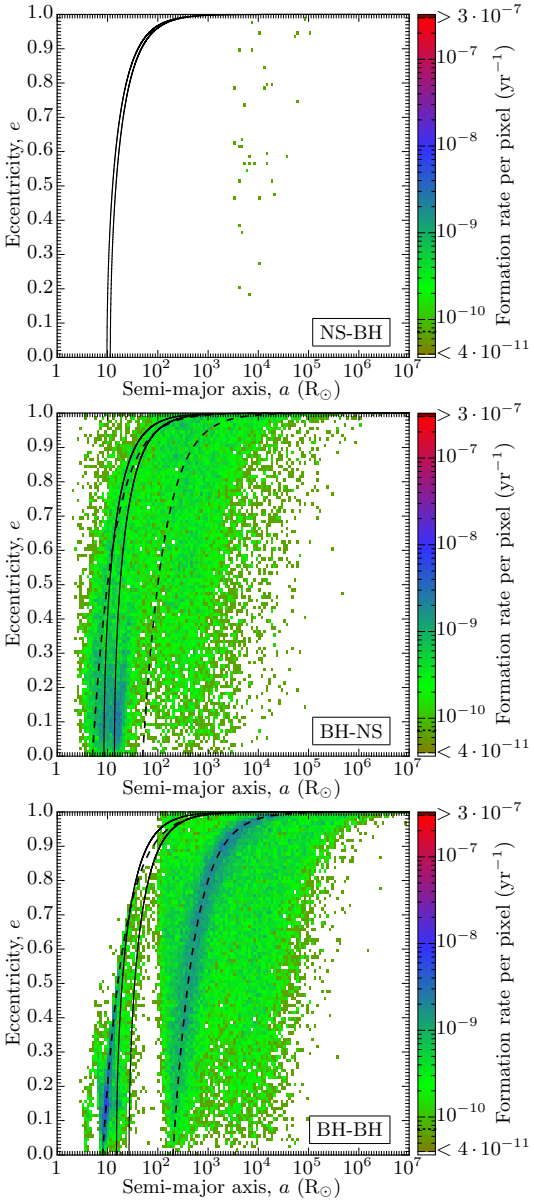

Figure B5. As the upper panel of Fig. 12 (NS-BH) and the lower panels of Fig. 12 (BH-NS) and Fig. 13 (BH-BH), with efficient mass transfer ($\beta_{\rm min} = 0$).

Table B2. GW merger rates of a MW-like galaxy with efficient mass transfer ($\beta_{\rm min} = 0$), cf. Table 4. The binary types refer to the first and second formed compact object.

GW-merger rates	$Z_{\rm MW} = 0.0088$	$Z_{\rm IZw18} = 0.0002$
NS-NS	$2.11^{+0.01}_{-0.02}\times10^{-6}$ yr^{-1}	$7.37^{+0.44}_{-0.74}\times10^{-7}$ yr^{-1}
NS-BH	$0.00^{+0.00}_{-0.00}\times10^{0}$ yr^{-1}	$4.42^{+0.00}_{-0.00}\times10^{-11}$ yr^{-1}
BH-NS	$4.21^{+0.47}_{-0.62}\times10^{-7}$ yr^{-1}	$7.84^{+0.29}_{-0.58}\times10^{-7}$ yr^{-1}
BH-BH	$4.36^{+0.09}_{-0.18}\times10^{-7}$ yr^{-1}	$3.12^{+1.14}_{-1.27}\times10^{-6}$ yr^{-1}

B4 Gravitational wave-driven merger rates

Because binaries containing at least one NS are partly suppressed when mass transfer is more efficient, double BH binaries are more frequent in the overall DCO population (Fig. B6). While double NS binaries still dominate the merger rate in the high-metallicity regime, double BH systems dominate systems which merge within a Hubble time at low metallicity, cf. Table B2.

The component masses, total masses and chirp masses of DCO binaries simulated with efficient mass transfer are shown in Figs B7 and B8. The distributions look similar to our default case with inefficient mass transfer as discussed in Section 4.4.

B5 Merger rate density

The merger-rate density changes clearly when using a more efficient mass transfer. Systems containing NSs are less common while double BH binaries are more frequent. Fig. B9 shows that the influence at low metallicity is even stronger than at MW metallicity. Therefore, further observations of GW mergers in low-metallicity environments could constrain the mass-transfer efficiency there.

average for efficient RLO, more such systems stay bound after a SN.

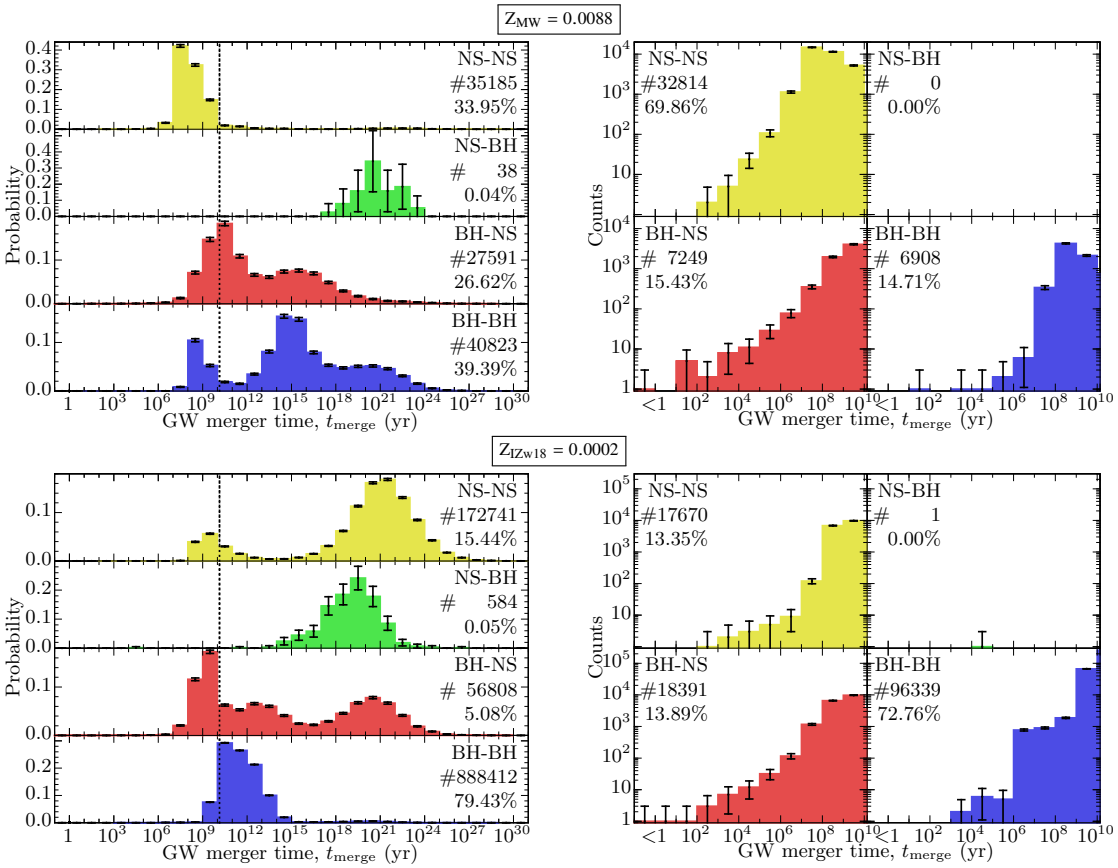

Figure B6. As Fig. 14 with efficient mass transfer ($\beta_{\rm min} = 0$).

Table B3. Merger-rate densities and detection rates, as in Table 8, with efficient mass transfer ($\beta_{\rm min} = 0$).

$Z_{\rm MW}$	$\langle \mathcal{M}^{2.5} \rangle$	$\mathcal{R}_{z=0}$	$\mathcal{R}_{\rm D}$	$\mathcal{R}_{\rm cSFR}$	$\mathcal{R}_{\rm D,cSFR}$
NS-NS	1.47 $M_\odot^{2.5}$	4.03×10^{0} yr^{-1} Gpc^{-3}	0.12 yr^{-1}	2.46×10^{1} yr^{-1} Gpc^{-3}	0.75 yr^{-1}
NS-BH	17.9 $M_\odot^{2.5}$	0.00×10^{0} yr^{-1} Gpc^{-3}	0.00 yr^{-1}	0.00×10^{0} yr^{-1} Gpc^{-3}	0.00 yr^{-1}
BH-NS	21.3 $M_\odot^{2.5}$	2.01×10^{0} yr^{-1} Gpc^{-3}	0.89 yr^{-1}	4.90×10^{0} yr^{-1} Gpc^{-3}	2.18 yr^{-1}
BH-BH	295 $M_\odot^{2.5}$	1.10×10^{0} yr^{-1} Gpc^{-3}	6.77 yr^{-1}	5.08×10^{0} yr^{-1} Gpc^{-3}	31.31 yr^{-1}
$Z_{\rm IZw18}$	$\langle \mathcal{M}^{2.5} \rangle$	$\mathcal{R}_{z=0}$	$\mathcal{R}_{\rm D}$	$\mathcal{R}_{\rm cSFR}$	$\mathcal{R}_{\rm D,cSFR}$
NS-NS	1.23 $M_\odot^{2.5}$	2.73×10^{0} yr^{-1} Gpc^{-3}	0.07 yr^{-1}	8.59×10^{0} yr^{-1} Gpc^{-3}	0.22 yr^{-1}
NS-BH	34.8 $M_\odot^{2.5}$	7.42×10^{-5} yr^{-1} Gpc^{-3}	0.00 yr^{-1}	5.15×10^{-4} yr^{-1} Gpc^{-3}	0.00 yr^{-1}
BH-NS	29.8 $M_\odot^{2.5}$	2.45×10^{0} yr^{-1} Gpc^{-3}	1.52 yr^{-1}	9.13×10^{0} yr^{-1} Gpc^{-3}	5.67 yr^{-1}
BH-BH	2370 $M_\odot^{2.5}$	3.19×10^{1} yr^{-1} Gpc^{-3}	1577.37 yr^{-1}	3.63×10^{1} yr^{-1} Gpc^{-3}	1796.42 yr^{-1}

APPENDIX C: FORMATION CHANNELS

All types of DCO binaries follow different formation channels. The most common ones which produce NSs or BHs at MW metallicity are listed in Table C1.

Table C1. Formation channels of DCO binaries (NSs or BHs) in our high-metallicity case ($Z_{MW} = 0.0088$). The first formed compact object is quoted first, even if its progenitor was the secondary star on the ZAMS. For each kind of binary the relative channel fraction is given and its main channel is marked.

relative frequency	GW merger rates (Myr^{-1})	channel index: formation channel	channel fraction of BH-BH	BH-NS	NS-BH	NS-NS
36.35%	0.422	A: RLO from primary to secondary, primary SN, RLO from secondary to primary, secondary SN	0.53%	99.47% main ch.		
36.24%	4.918	B: RLO from primary to secondary, primary SN, CE from secondary, He-RLO from secondary, ultra-stripped secondary SN		30.27%		69.73% main ch.
9.56%	1.273	C: RLO from primary to secondary, primary SN, CE from secondary, secondary SN	7.27%	86.44%		6.29%
3.98%	0.002	D: primary SN, secondary SN	89.37% main ch.	5.27%		5.35%
2.50%	0.013	E: primary SN, RLO from secondary to primary, secondary SN	8.70%	91.30%		
2.49%	0.327	F: primary SN, CE from secondary, secondary SN	7.99%	91.88%		0.13%
2.37%	0.002	G: RLO from primary to secondary, primary SN, secondary SN	70.77%	0.35%		28.88%
2.14%	0.146	H: primary SN, CE from secondary, He-RLO from secondary, ultra-stripped secondary SN		90.26%		9.74%
1.58%	0.003	I: RLO from primary to secondary, RLO from secondary back to primary, primary SN, secondary SN	98.52%		1.43% main ch.	0.05%
1.23%	0.143	J: RLO from primary to secondary, He-RLO from primary, ultra-stripped primary SN, CE from secondary, He-RLO from secondary, ultra-stripped secondary SN				100.00%
0.49%	< 0.001	K: RLO from secondary to primary, RLO from primary back to secondary, secondary SN, primary SN	99.95%		0.05%	
0.41%	0.001	L: RLO from secondary to primary, primary SN, secondary SN	100.00%			
0.23%	< 0.001	M: RLO from primary to secondary, secondary SN, primary SN	99.65%	0.35%		
0.18%	0.032	N: RLO from secondary to primary, CE from primary, secondary SN, primary SN	100.00%			
0.10%	0.004	O: RLO from primary to secondary, CE from secondary, He-RLO from primary, ultra-stripped primary SN, He-RLO from secondary, ultra-stripped secondary SN				100.00%
0.08%	0.000	P: primary SN, RLO from secondary to primary, He-RLO from secondary, ultra-stripped secondary SN		100.00%		
0.05%	0.006	Q: RLO from primary to secondary, CE from secondary, primary SN, secondary SN	94.41%			5.59%
0.02%	< 0.001	R: RLO from primary to secondary, CE from secondary, He-RLO from primary, ultra-stripped primary SN, secondary SN				100.00%
< 0.019%	0.001	S: 6 other channels	> 0%	> 0%		> 0%

- RLO from secondary to primary, secondary SN, primary SN
- RLO from secondary to primary, CE from primary, primary SN, secondary SN
- RLO from primary to secondary, primary SN, RLO from secondary to primary, He-RLO from secondary, ultra-stripped secondary SN
- RLO from primary to secondary, He-RLO from primary, primary SN, secondary SN
- RLO from primary to secondary, primary SN, CE from secondary, He-CE from secondary, ultra-stripped secondary SN
- RLO from secondary to primary, secondary SN, CE from primary, primary SN

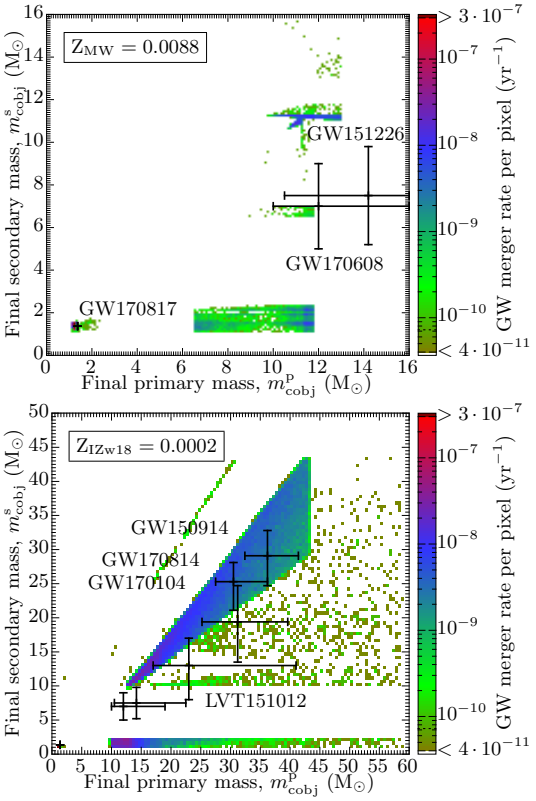

Figure B7. The upper and lower panel are our high- and the low-metallicity cases, as in Fig. 15, but with efficient mass transfer ($\beta_{min} = 0$).

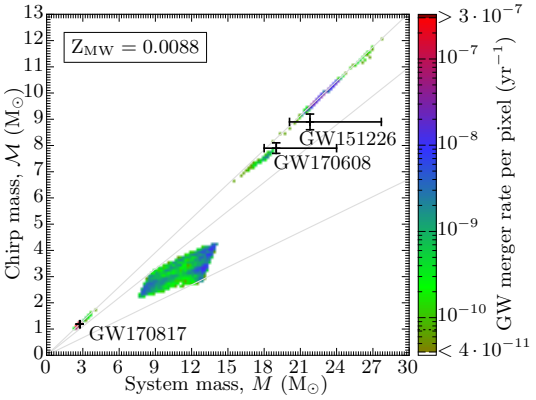

Figure B8. Our high-metallicity case as in Fig. 16 but with efficient mass transfer ($\beta_{min} = 0$).

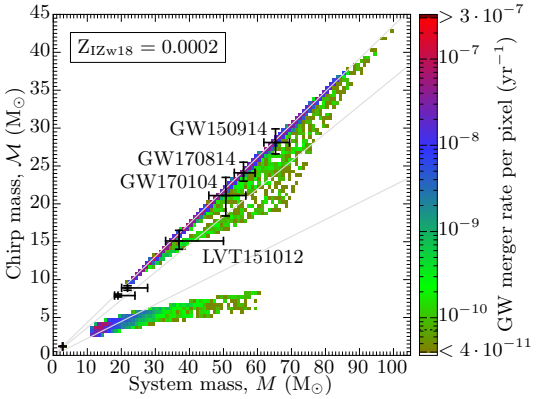

Figure B8 – *continued* . Our low-metallicity case as in Fig. 16 but with efficient mass transfer ($\beta_{min} = 0$).

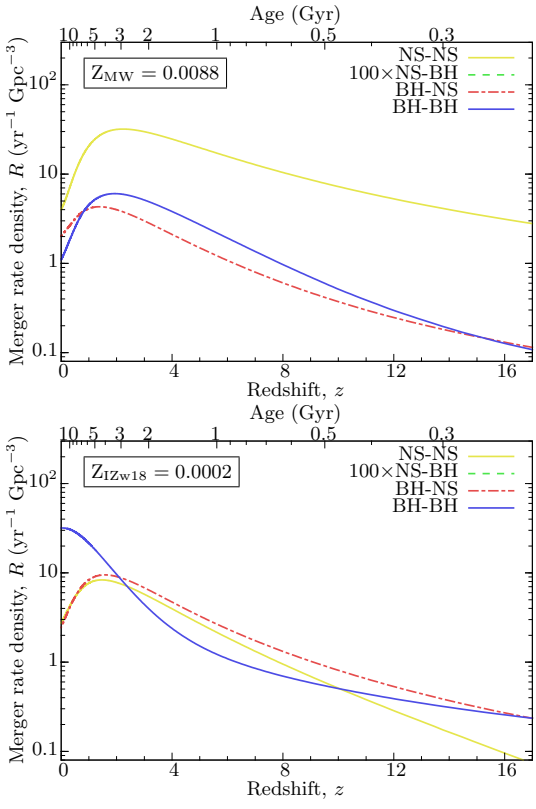

Figure B9. The upper and lower panel are our high- and the low-metallicity case, as in Fig. 22, but with efficient mass transfer ($\beta_{min} = 0$).

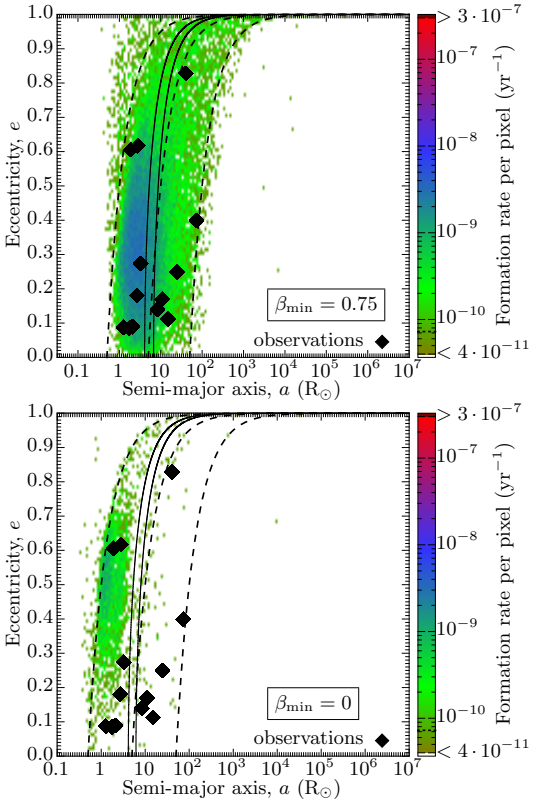

Figure D1. Our simulated orbital parameters when both NSs form by FeCC SNe. The upper and lower plots show inefficient and efficient mass transfer, respectively (cf. Fig. 10 and the upper panel of Fig. B4).

APPENDIX D: FURTHER PARAMETER VARIATIONS

Table D1 shows the changes in formation and merger rates when varying the ranges of the initial stellar masses and the semi-major axis.

D1 Iron-core collapse supernovae

There is no evidence that any observed double NS binaries contain NSs which are produced by EC SNe. Fig. D1 shows our simulated orbital parameters of systems in which both stars undergo FeCC SN. It is even clear that it is necessary to assume inefficient mass transfer to explain the observational data.

D2 Mass-transfer efficiency

The influences on the GW merger rate of the parameters β_{min} and α_{RLO} are similar (cf. Figs D2 and 18). The same holds true when comparing the formation rates in the two panels of Fig. D3. Both parameters change the mass-transfer

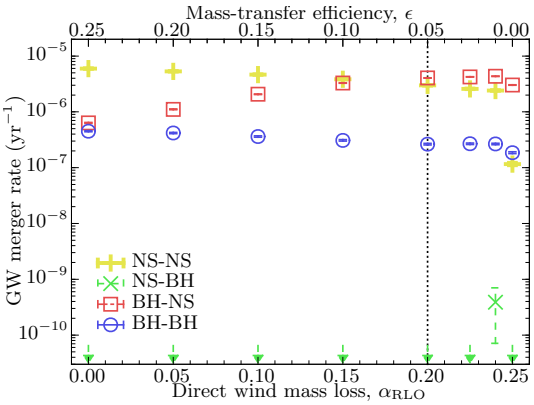

Figure D2. As Fig. 18 showing the dependence on the direct wind mass loss parameter during RLO instead.

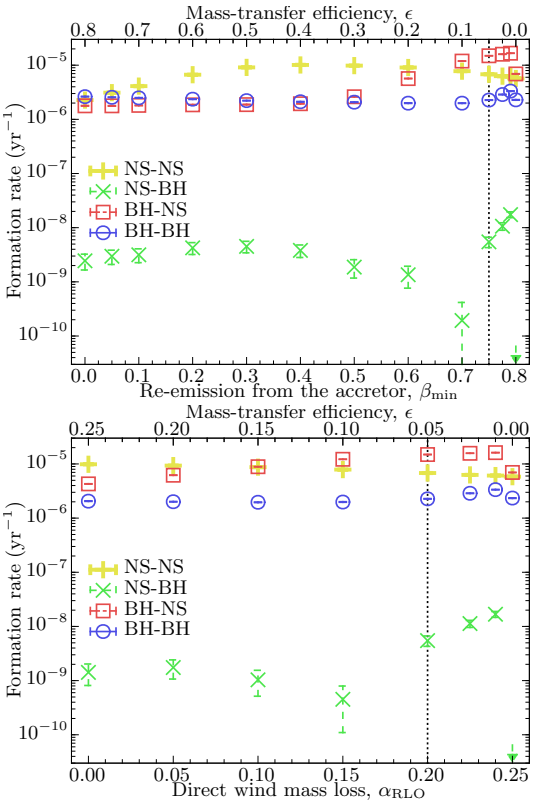

Figure D3. The formation rate of DCO binaries in a MW-like galaxy as a function of the re-emission in the vicinity of the accretor, β_{min}, (upper panel) and the direct wind mass loss parameter, α_{RLO}, (lower panel) during RLO. The dotted lines mark our default values of β_{min} and α_{RLO}, respectively.

Table D1. Formation and merger rates of DCO binaries and the effect of changing the initial ranges of stellar mass or semi-major axis, see also Table 5.

		m^{p}_{min}	m^{p}_{max}	m^{s}_{min}	m^{s}_{max}	a_{min}	a_{max}
	upper:	10 $M_\odot$	150 $M_\odot$	4.0 $M_\odot$	150 $M_\odot$	20.0 $R_\odot$	10^5 $R_\odot$
	lower:	1 $M_\odot$	80 $M_\odot$	0.5 $M_\odot$	80 $M_\odot$	0.2 $R_\odot$	10^3 $R_\odot$
Formation rates	default	m^{p}_{min}	m^{p}_{max}	m^{s}_{min}	m^{s}_{max}	a_{min}	a_{max}
NS-NS (yr^{-1})	6.81×10^{-6}	$^{+4.42}_{-9.01}\times10^{-8}$	$^{+1.05}_{+0.06}\times10^{-8}$	$^{-0.55}_{+4.90}\times10^{-6}$	$^{-1.71}_{-1.91}\times10^{-8}$	$^{+0.00}_{+5.00}\times10^{-7}$	$^{+2.89}_{-1.72}\times10^{-6}$
NS-BH (yr^{-1})	5.49×10^{-9}	$^{+6.69}_{-2.82}\times10^{-10}$	$^{-1.69}_{+0.21}\times10^{-9}$	$^{-5.16}_{+8.39}\times10^{-10}$	$^{-0.45}_{-1.15}\times10^{-9}$	$^{+0.00}_{-1.36}\times10^{-9}$	$^{+4.00}_{-1.81}\times10^{-9}$
BH-NS (yr^{-1})	1.49×10^{-5}	$^{-1.02}_{-0.08}\times10^{-7}$	$^{-0.91}_{+1.07}\times10^{-6}$	$^{-0.36}_{+2.06}\times10^{-6}$	$^{+0.30}_{+9.37}\times10^{-7}$	$^{+0.00}_{-4.62}\times10^{-8}$	$^{+1.76}_{-3.98}\times10^{-6}$
BH-BH (yr^{-1})	2.27×10^{-6}	$^{-8.86}_{-1.02}\times10^{-8}$	$^{-1.11}_{+3.75}\times10^{-6}$	$^{-0.40}_{+1.90}\times10^{-7}$	$^{-0.40}_{+4.37}\times10^{-6}$	$^{+0.00}_{-1.47}\times10^{-8}$	$^{+1.61}_{-5.03}\times10^{-7}$
GW-merger rates	default	m^{p}_{min}	m^{p}_{max}	m^{s}_{min}	m^{s}_{max}	a_{min}	a_{max}
NS-NS (yr^{-1})	2.98×10^{-6}	$^{+5.28}_{-6.50}\times10^{-9}$	$^{-0.67}_{+1.70}\times10^{-8}$	$^{-0.24}_{+1.96}\times10^{-6}$	$^{-2.08}_{-3.11}\times10^{-8}$	$^{+0.00}_{+1.91}\times10^{-7}$	$^{+1.28}_{-0.76}\times10^{-6}$
NS-BH (yr^{-1})	0.00×10^{0}	$^{+0.00}_{+9.37}\times10^{-11}$	$^{+1.93}_{+0.00}\times10^{-10}$	$^{+1.29}_{+1.29}\times10^{-10}$	$^{+1.29}_{+0.65}\times10^{-10}$	$^{+0.00}_{+6.46}\times10^{-11}$	$^{+1.94}_{+0.65}\times10^{-10}$
BH-NS (yr^{-1})	4.05×10^{-6}	$^{-6.13}_{+0.52}\times10^{-8}$	$^{-1.61}_{+1.36}\times10^{-7}$	$^{-0.94}_{+5.85}\times10^{-7}$	$^{+0.01}_{+1.32}\times10^{-7}$	$^{+0.00}_{-1.78}\times10^{-8}$	$^{-1.79}_{-1.05}\times10^{-6}$
BH-BH (yr^{-1})	2.64×10^{-7}	$^{+3.37}_{+1.56}\times10^{-9}$	$^{-1.96}_{+3.93}\times10^{-7}$	$^{-0.16}_{+2.25}\times10^{-8}$	$^{+0.12}_{+3.86}\times10^{-7}$	$^{+0.00}_{-1.29}\times10^{-9}$	$^{+1.52}_{-0.77}\times10^{-7}$

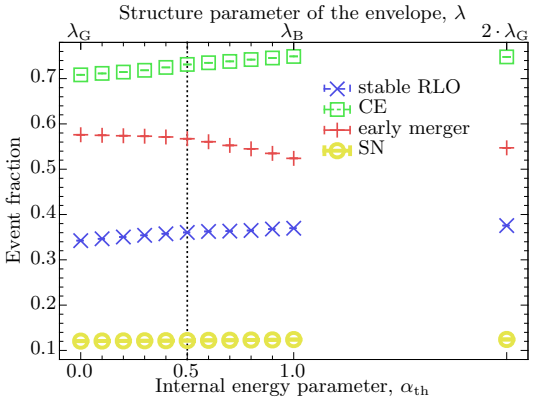

Figure D4. Mean counts of evolutionary events from relatively massive binaries modelled with ComBinE at MW metallicity as a function of the fraction of the internal envelope energy, α_{th}, included in the total binding energy of the envelope. The vertical dotted line marks our default value. The symbols to the very right ($\lambda = 2\,\lambda_G$) are from a simulation in which it is assumed that the stellar envelopes are in virial equilibrium.

efficiency, ϵ, by ejecting more or less material during stable RLO. The only difference is the specific angular momentum which is carried away by the ejecta.

D3 Internal energy parameter, α_{th}

When more internal energy is included in determining the total binding energy of the envelope (i.e. larger value of α_{th}, cf. Equation (11)) more systems survive the CE phase. This naturally increases the number of subsequent evolutionary phases (Fig. D4). Assuming the envelope is in virial equilibrium, i.e. the total binding energy is half the gravitational binding energy ($\lambda = 2\,\lambda_G$), we find similar results as with α_{th} between 0.7 and 0.8.

3.13 Supplementary material

This section provides more information about the stellar models which are interpolated in ComBinE. It is also shown how the binary evolution differs from single star evolution. Finally, further data is provided how the different parameters in ComBinE influence the binary evolution.

3.13.1 Stellar models

The stellar models are calculated with BEC. Most models are previously calculated and reported in Brott et al. (2011) and Szécsi et al. (2015). To make use of these models, also stars with lower masses are needed. Furthermore, some of the stellar models were not calculated as far as possible in their evolution, so they are recalculated and extended to a later phase of the single star evolution.

3.13.1.1 Overshooting calibration

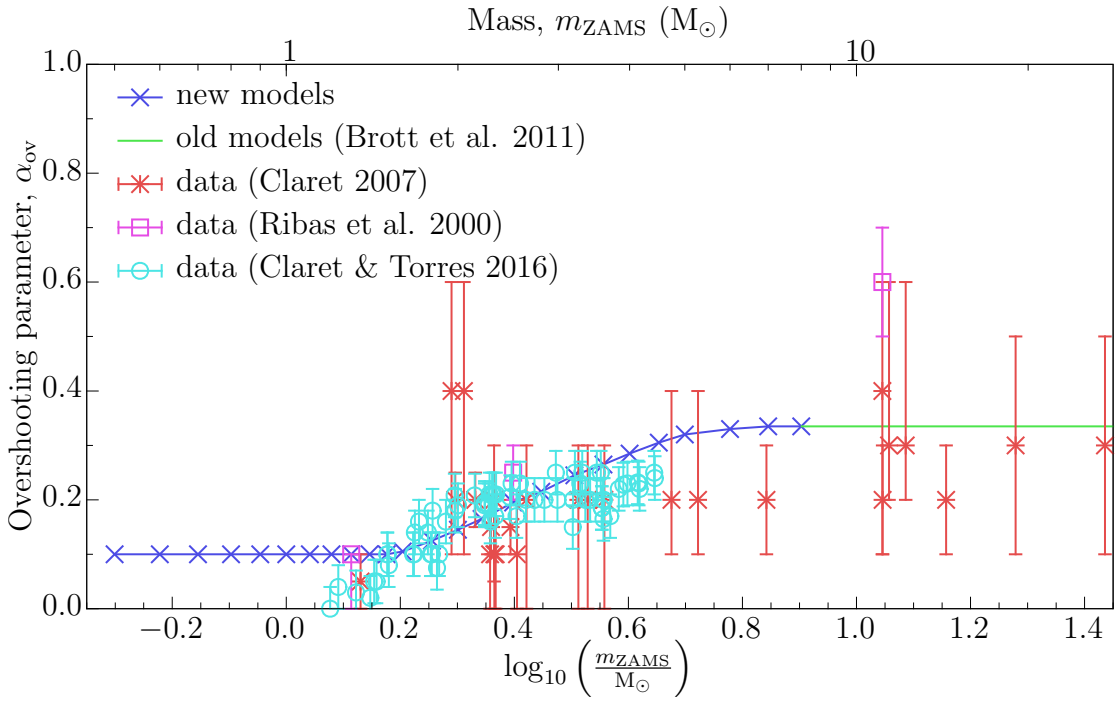

Figure 3.38: The overshooting parameter, α_{ov}, depending the on the ZAMS mass at MW-like metallicity.

For a MW like metallicity stellar models with masses below 10 $\mathrm{M}_\odot$ are added to the original models. The calibration of the overshooting parameter in Brott et al. (2011) is aimed to get the high mass models right. Therefore a mass dependent overshooting parameter for the new low-mass models is needed. The relation in comparison to observations is shown in Fig. 3.38. The calibration was done with the first two data sets. Nevertheless, the later published data of Claret & Torres (2016) seems to coincide with the calibration.

3.13.1.2 Extrapolation

The ability to calculate the models to arbitrary late stages of evolution and any initial mass is set by BEC. This makes it necessary to extrapolate some models with very low and very high masses. Five extrapolations are included in the table set used in ComBinE of stars at MW-like metallicity with initial masses of 10^{-10} $M_\odot$[1], 125 $M_\odot$, 150 $M_\odot$, 175 $M_\odot$ and 200 $M_\odot$. The extrapolation to higher masses needs to be investigated in more detail. Those models are potentially used for stars which accrete mass from its companion.

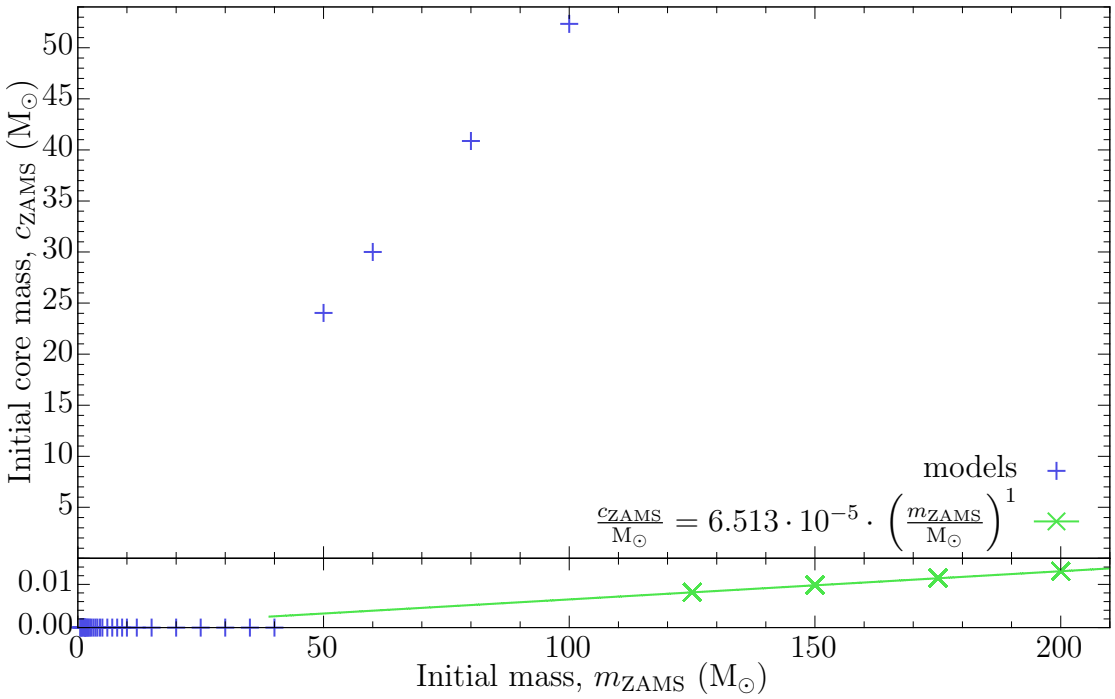

Figure 3.39: ZAMS extrapolation of the core mass, $c_{\rm ZAMS}$, to larger ZAMS masses (The extrapolations are only valid in the plotted range of the green line.).

All the stellar variables, age t, mass m, core mass $c_{\rm He}$, radius R, luminosity L, effective temperature $T_{\rm eff}$ and the structure parameter of the envelope with and without the internal binding energy $\lambda_{\rm G}$ and $\lambda_{\rm B}$ are extrapolated. Each extrapolated track contains the most important stages of the evolution: at ZAMS (Figs 3.39 to 3.44), at maximum radius (Figs B.1 to B.8), at maximum core mass (Figs B.9 to B.16), at the moment when the whole envelope is lost, at the end of the stellar calculation (Figs B.17 to B.24) and prior to collapse to the final remnant.

at ZAMS (Figs 3.39 to 3.44)

Here the mass, $m_{\rm ZAMS}$, is equal to the given initial mass. The age is set to zero, $t_{\rm ZAMS} = 0$ yr, meaning all given ages are the time since the ZAMS

[1]Only used for a smooth behaviour in ComBinE as stars below 0.5 $M_\odot$ spend more than the Hubble time on their MS.

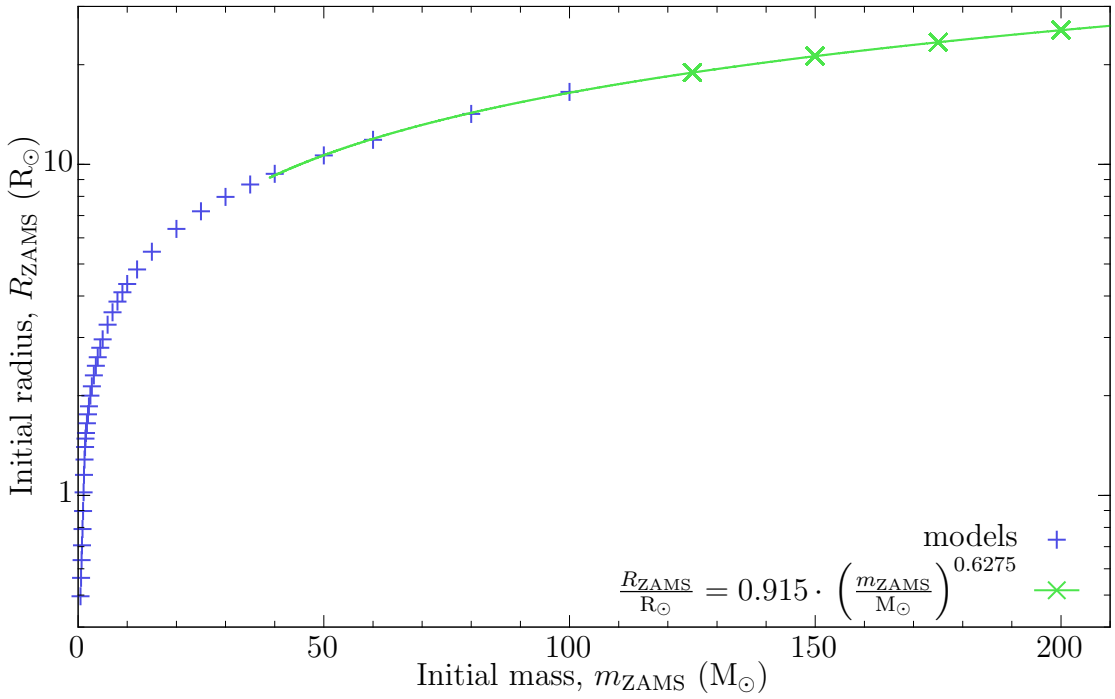

Figure 3.40: ZAMS extrapolation of the radius, R_{ZAMS}, to larger ZAMS masses.

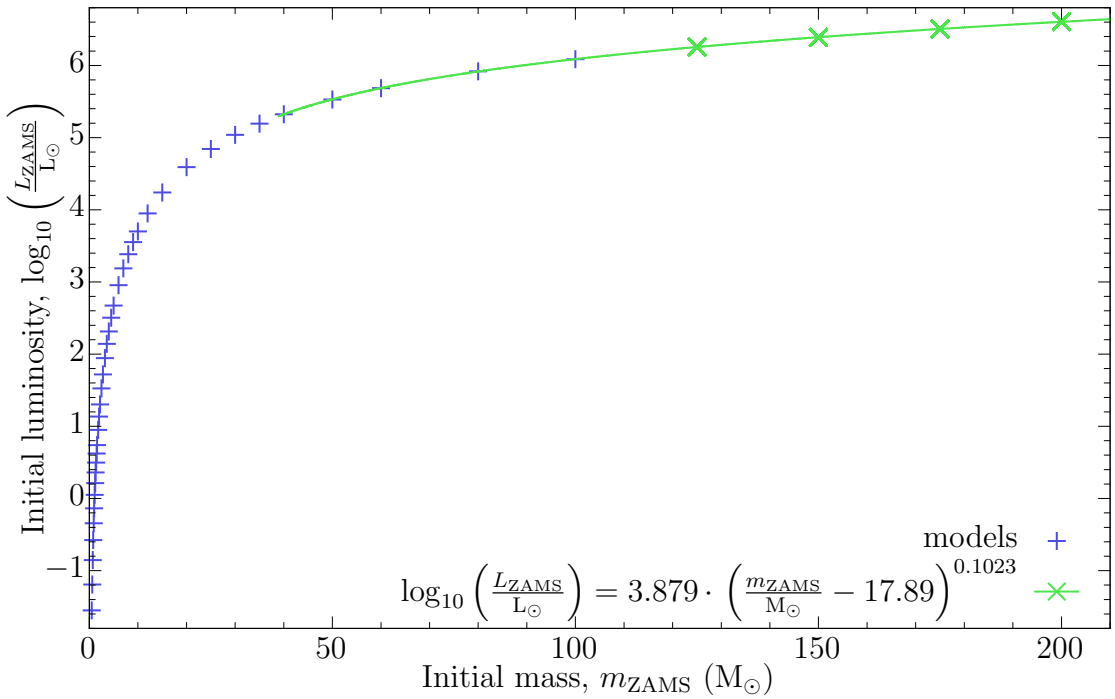

Figure 3.41: ZAMS extrapolation of the luminosity, L_{ZAMS}, to larger ZAMS masses.

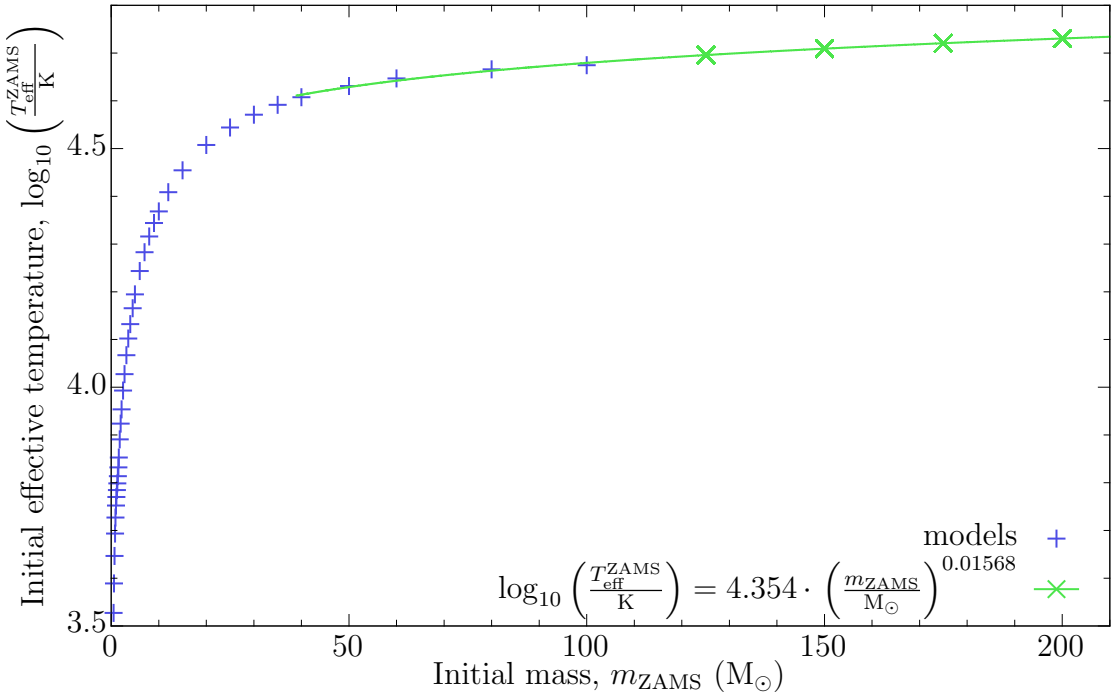

Figure 3.42: ZAMS extrapolation of the effective temperature, $T_{\rm eff}^{\rm ZAMS}$, to larger ZAMS masses.

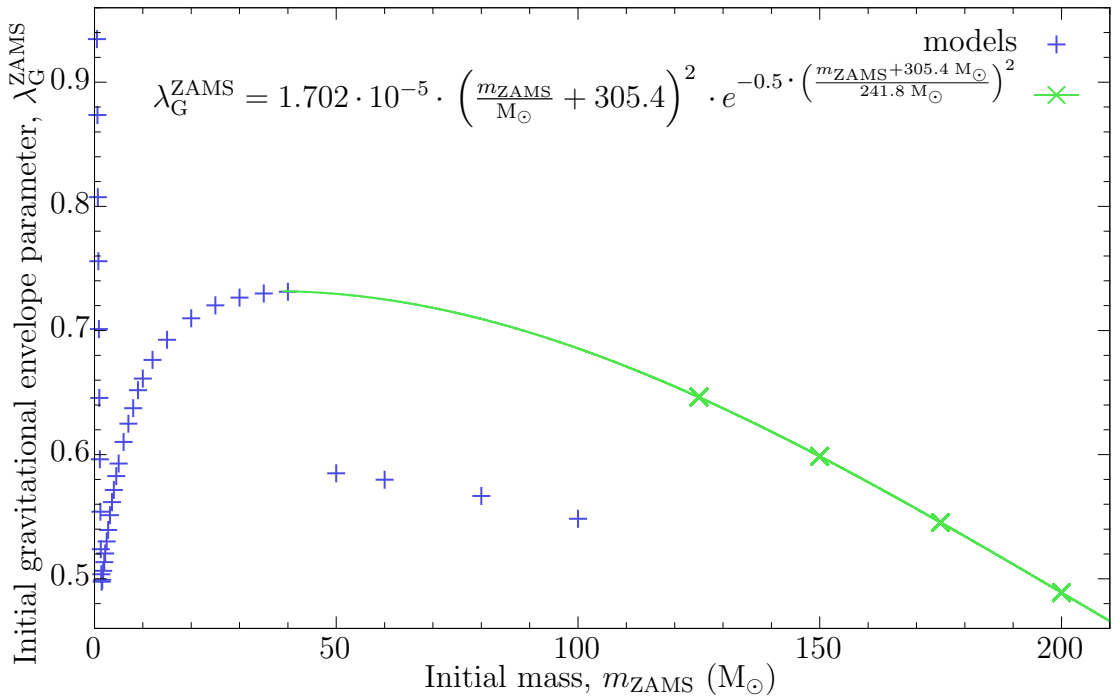

Figure 3.43: ZAMS extrapolation of the gravitational envelope binding parameter, $\lambda_{\rm G}^{\rm ZAMS}$, to larger ZAMS masses.

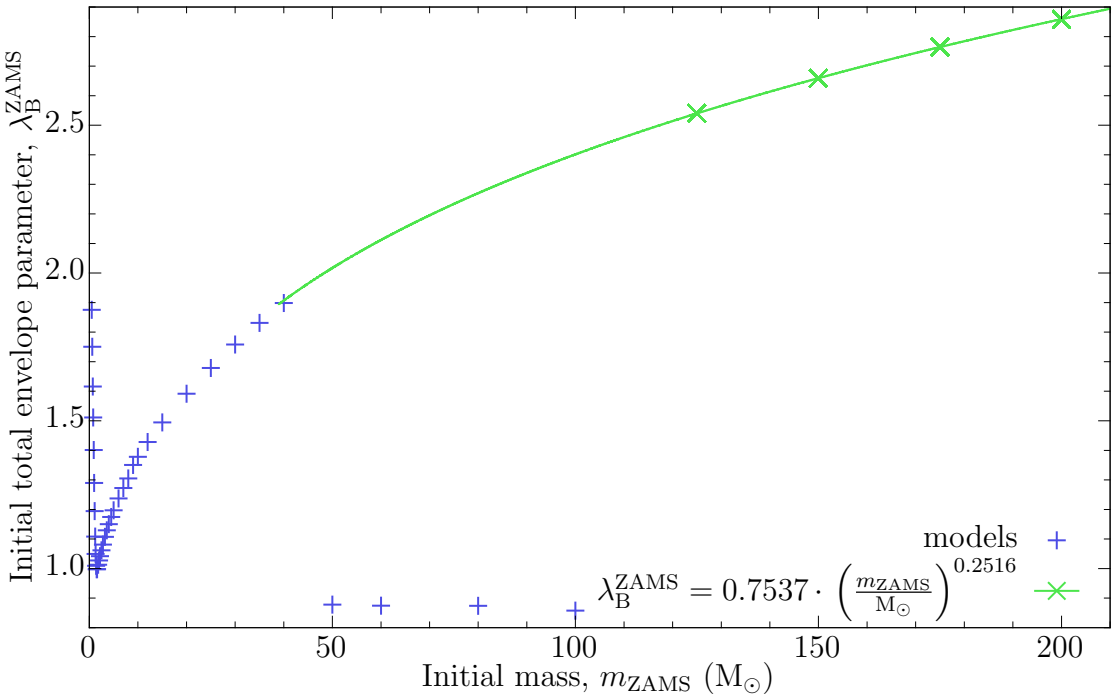

Figure 3.44: ZAMS extrapolation of the envelope binding parameter including internal binding energy, λ_B^{ZAMS}, to larger ZAMS masses.

of a star. As H burning begins at the ZAMS the He core is not existing yet. To avoid numerical instabilities, its core mass is set to a very small non-zero value. After the calculation of the extrapolated tables the effective core during core H was switched to the convective core. For this reason, the values of the massive stars in Fig. 3.39 differ much from the extrapolation line at the bottom. As the structure parameters of the envelope depend on the core boundary they are effected as well.

at maximum radius (Figs B.1 to B.8)

As some models were calculated further after the extrapolation was done a few of them evolve to larger radii and therefore differ from the extrapolation function[2]. Again the usage of the convective core as core boundary to define the core mass leads to deviations in core mass and the structure parameters of the envelope in the extrapolation.

at maximum core mass (Figs B.9 to B.16)

This point of evolution is often close to the one of maximum radius. Here, the core defined by convection and purely by abundance (Section 3.3.3) coincide so the deviations caused by this different approach in the previous points disappear.

at the moment when the whole envelope is lost

[2]This mainly holds for the models with initial masses of 50 $M_\odot$ and 60 $M_\odot$.

This data point is interpolated between the values at maximum core mass and the end of the stellar calculation. Therefore, the fitted functions of mass and core mass are used to determine the point when the core mass would become larger than the total stellar mass, which is unphysical. As there is no envelope any more, the structure parameters of the envelope do not have any physical meaning at this point and are therefore set to a fixed value[3]. This fixed values is chosen to be 1 as it is clear larger as the value previously in the simulation and close enough to minimize numerical artefacts of the discontinuity.

at the end of the stellar calculation (Figs B.17 to B.24)
As the whole envelope is already lost, the core mass is limited by the total mass (Fig. B.19). As the envelope is absent the structure parameters of the envelope are again set to 1.

prior to collapse to the final remnant
This data point is inferred from the end of the stellar calculation. This point is similar to the previous one, only the age is increased by 10%, which is on the high side, to account for later burning processes mainly completing He burning. For numerical issues the other stellar values mass, radius, core mass, luminosity and effective temperature are lowered by one part in 10^{10}.

Similarly, a number of extra He-star models are calculated by extrapolation. Their initial He masses are 10^{-10} $M_\odot$, 35 $M_\odot$, 50 $M_\odot$, 70 $M_\odot$, 100 $M_\odot$ and 150 $M_\odot$. In this case only the data points at the He-ZAMS (Figs B.25 to B.30) and at the end of the stellar calculation (Figs B.31 to B.38) are extrapolated. The most massive He stars seem to not expand during their evolution (Fig. 3.5) and therefore they are not expected to initiate any binary interaction like mass transfer caused by an expansion episode. Hence, the large uncertainties in the final structure parameters of their envelopes are unimportant as these values are practically never used.

3.13.2 How binaries evolve in ComBinE

Caused by mass transfer, the mapping from the ZAMS mass of a star to the mass of its compact remnant is not unique as it is expected for an isolated, single star. Fig. 3.45 shows the deviation between single and binary star evolution for each of the two components of the binary. A large mass loss usually results in a less massive remnant compared to single star evolution. Hence, most of the data is below the compact remnant masses of isolated stars. This holds for the primary stars, but the initially less massive (secondary) stars have a higher chance to even gain mass from binary interactions. The primary stars which become a more massive remnant compared to single star evolution with initial masses above $\gtrsim 80$ $M_\odot$ are the ones discussed at the end of Section 3.4.2.1.

The different formations channels listed in Table 3.13 cover different ranges of masses and semi-major axes on the ZAMS and also cover a wide range when

[3]This is also done in the calculated stellar models where the whole envelope is lost.

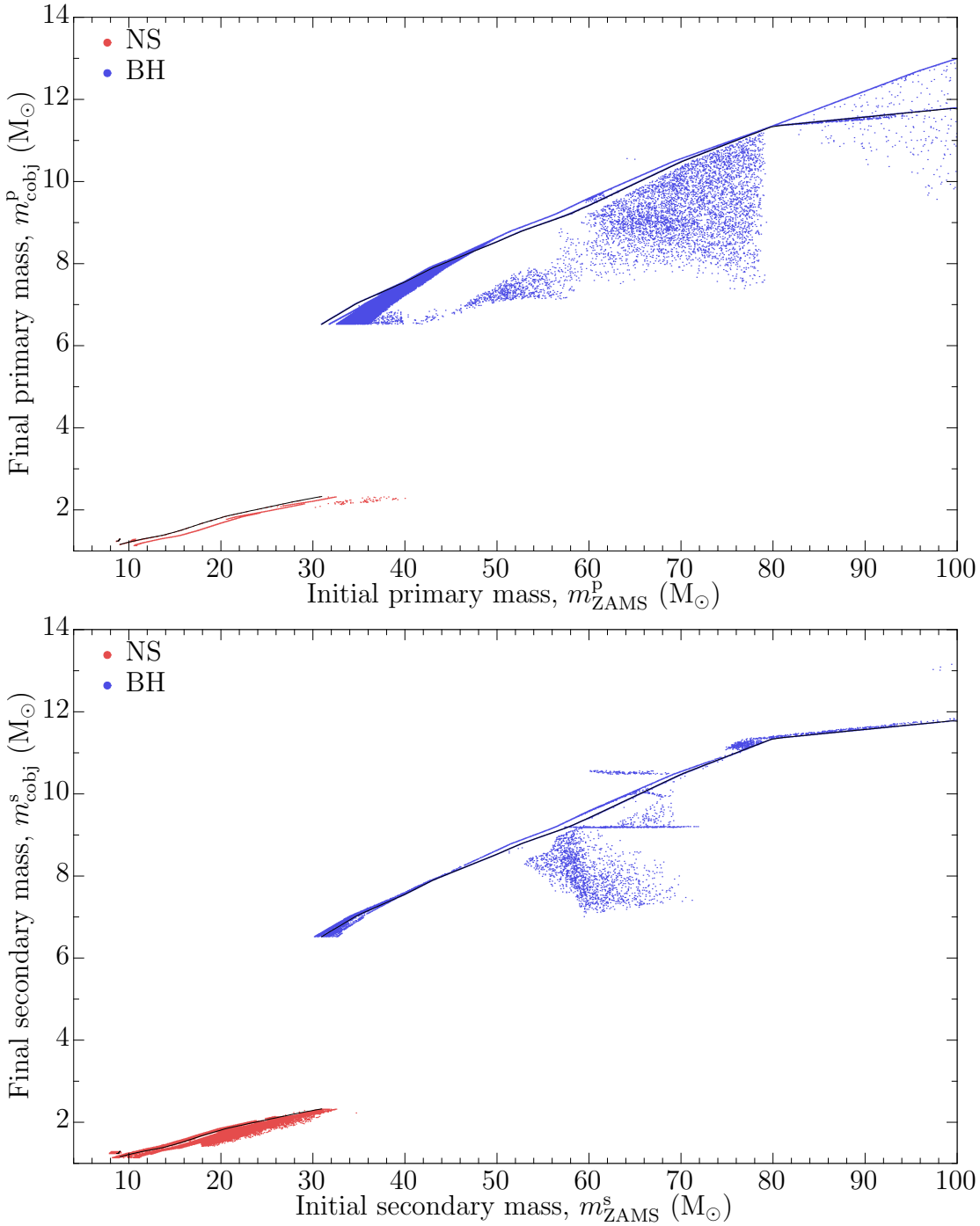

Figure 3.45: ZAMS and compact object masses of the primary (top pannel) and the secondary star (bottom pannel) at MW-like metallicity. The black lines indicate the mapping for isolated stars according to the applied stellar models and assumptions of remnant formation, see Fig. 3.2.

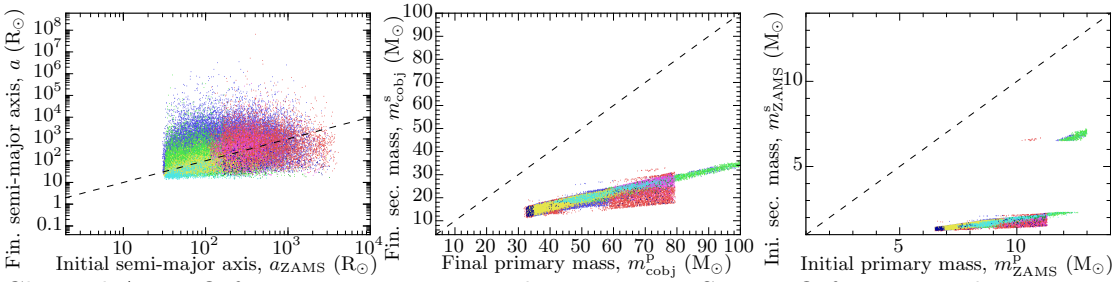

Channel A: RLO from primary to secondary, primary SN, RLO from secondary to primary, secondary SN.

Colours – merge within 10 Gyr: yellow, teal, dark blue, dark green; do not merge: blue, green, red, purple – first RLO being Case A: blue, green, yellow, teal; first RLO being Case B/C: red, purple, dark blue, dark green – early second RLO: green, purple, teal, dark green; late second RLO: blue, red, yellow, dark blue

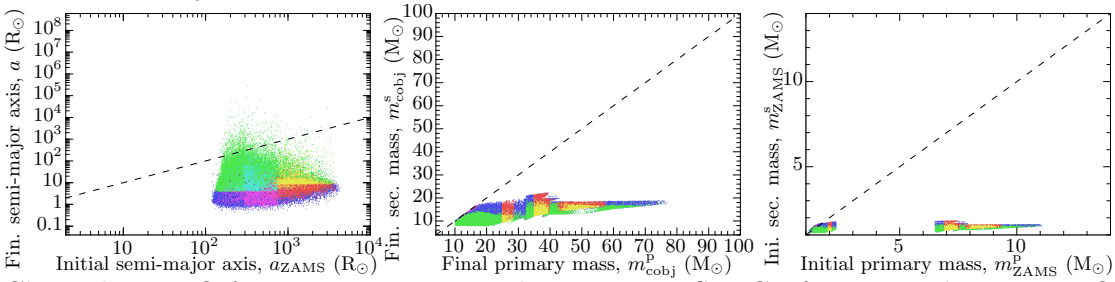

Channel B: RLO from primary to secondary, primary SN, CE from secondary, He-RLO from secondary, ultra-stripped secondary SN.

Colours – merge within 10 Gyr: blue, red, purple, dark blue, dark green; do not merge: green, yellow, teal, dark red – first RLO being Case A: red, yellow; first RLO being Case B/C onto MS star: blue, green, purple, teal, dark blue, dark red; first RLO being Case B/C onto post MS star: dark green – first SN with MS companion: blue, green, red, yellow, dark blue, dark red; first SN with post MS companion: purple, teal, dark green

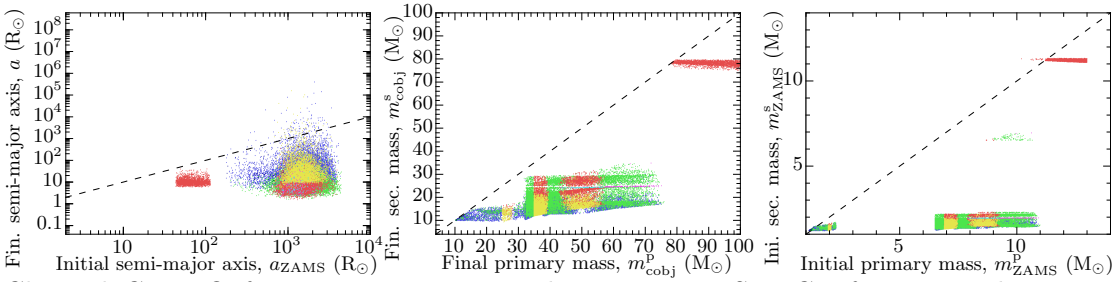

Channel C: RLO from primary to secondary, primary SN, CE from secondary, secondary SN.

Colours – merge within 10 Gyr: green, red, purple, teal, dark green; do not merge: blue, yellow, dark blue, dark red – first RLO being Case A: red, yellow, teal, dark red; first RLO being Case B/C: blue, green, purple, dark blue, dark green – first SN with MS companion: blue, green, red, yellow, purple, teal, dark red; first SN with post MS companion: dark blue, dark green – early CE: purple, teal, dark red; late CE: blue, green, red, yellow, dark blue, dark green

Figure 3.46: Primary mass, secondary mass and semi-major axis at ZAMS and directly after the formation of the second compact object of channels A to C. The colours represent the most frequent to least frequent evolution with a given channel, where the order is always: blue, green, red, yellow, purple, teal, dark blue, dark green, dark red, dark yellow, dark purple, dark teal.

both stars end their lives and become remnants. Fig. 3.46 shows the quantities for binaries evolving through the Channels A to C, at the beginning and the end of their stellar evolution. The initial separation mainly sets whether the mass transfer is Case A, B or C, shown by different colors and given in the individual legends of the channels. After the first star end its life the mass is important to differentiate between stable of unstable mass transfer (cf. Channel A and Channel B or C). As all of the parameters are important for the outcome of a potential CE the Channels B and C look very different. Even the difference of having a He-RLOF before the secondary ends its evolutions or not mainly depends only on the separation after the CE is ejected. The other channels are shown in Figs B.39–B.45 in Appendix B.2.

3.13.3 Physical parameter variations

Fig. 3.47 shows the influence of the CE efficiency in converting orbital into kinetic energy, $\alpha_{\rm CE}$, on the evolution of the binaries. The largest changes are only for very low values of $\alpha_{\rm CE}$ besides the GW merger rates of double BH binaries. This parameter influences directly the success rate of CE ejection and therefore affects the most common early mergers. As a consequence of more or fewer early mergers, fewer or more mass transfer episodes can happen. Similarly fewer or more systems survive and become a DCO.

The most important other parameters are shown in Figs B.46 to B.49. These include the mass-accretion efficiency during stable RLO, ϵ (depending on the direct wind mass loss, $\alpha_{\rm RLO}$, and the minimum re-emission from the accretor, $\beta_{\rm min}$), the mass-ratio limit to differentiate between stable and unstable mass transfer, $q_{\rm limit}$, and the internal energy parameter, $\alpha_{\rm th}$. The mass-accretion efficiency mainly influences the final mixed systems because it affects how much material can be accreted and later contribute to the compact remnant formation of the accretor. The position of the boundary between stable and unstable mass transfer has a huge impact on any subsequent evolution as the orbital separation changes easily by orders of magnitude. As tight systems with two stellar components becoming too close to one another undergo an early merger, the formation rates of all kinds of DCOs are sensitive to this bifurcation in binary evolution. The fraction of internal energy, $\alpha_{\rm th}$, available to unbind a CE has a similar effect as the CE efficiency in converting orbital into kinetic energy, but has also a dependence on the mass of the donor star.

Furthermore, the influence on the initial distributions by changing the IMF slope, $\alpha_{\rm IMF}$ (Fig. B.50), and using different initial distributions (Fig. B.51) on the mass-ratio, the semi-major axis (or period) and the eccentricity are considered. In most situations, the initial distributions have only a minor impact on the evolution of the binary. The exceptions are if the slope of the IMF is changed, affecting the frequency of massive stars in a galaxy, or if the orbital period distribution of Sana et al. (2012) is applied. This period distribution largely changes the outcome of CE evolution of low-mass stars for which it is not appropriate.

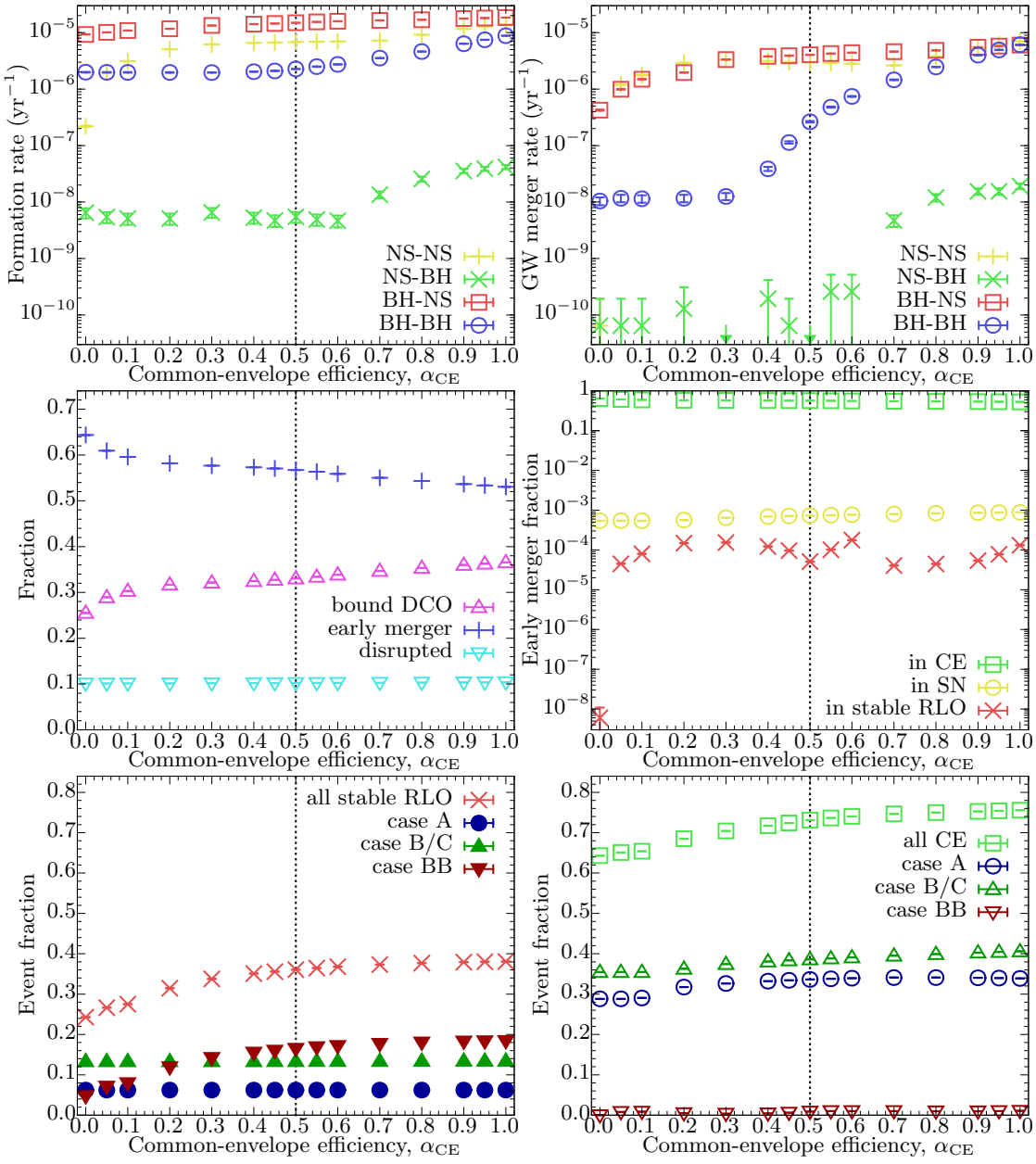

Figure 3.47: Variation of the CE efficiency, $\alpha_{\rm CE}$. The dotted line marks the default value. The rates are for a MW-like galaxy; the arrows in the top-right panel mark upper limits.

3.13.4 Intermediate efficient mass transfer

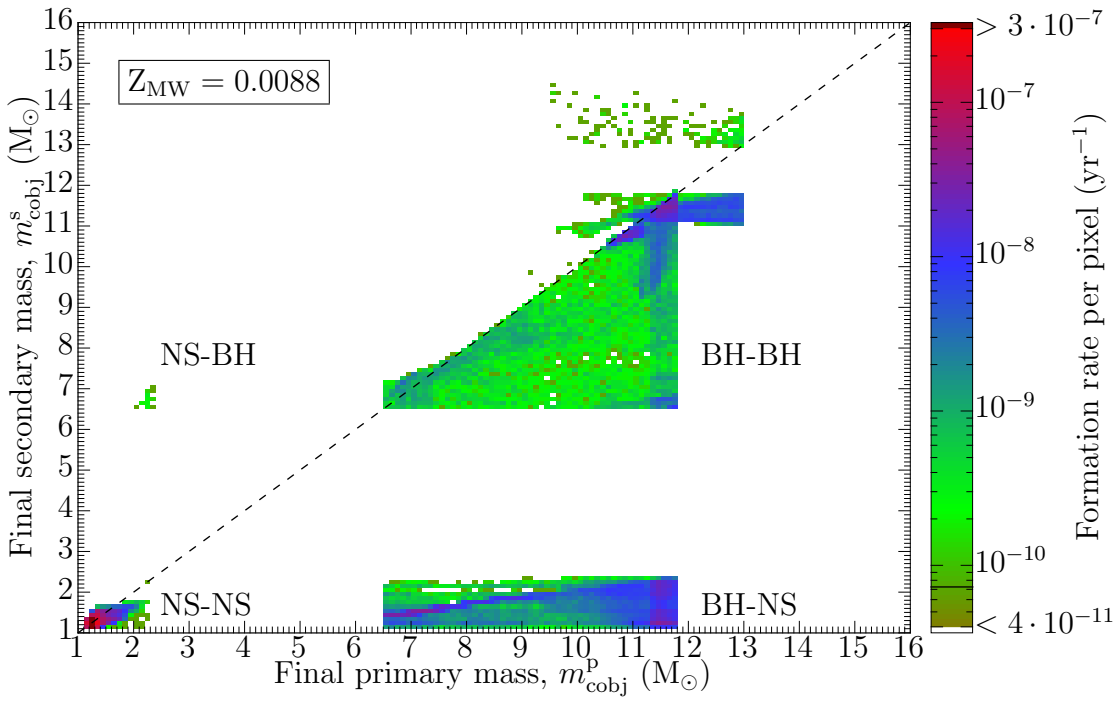

Figure 3.48: As the top panel of Fig. 3.7, but with intermediate efficient mass transfer ($\beta_{\rm min} = 0.5$).

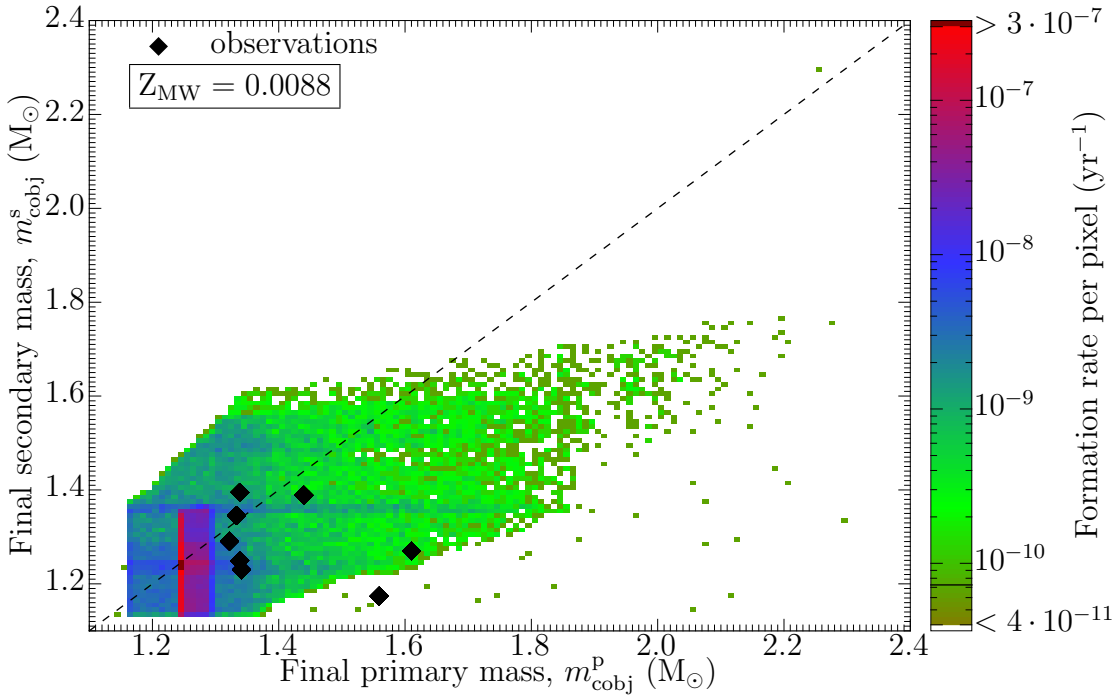

Figure 3.49: As Fig. 3.8, but with intermediate efficient mass transfer ($\beta_{\rm min} = 0.5$).

This section shows distributions of DCO binaries with intermediate efficient mass transfer ($\beta_{\rm min} = 0.5$) at MW-like metallicity. The mass distribution of the formed DCO binaries is a mixture of the two more extreme cases, cf. Fig. 3.48 to Figs 3.7 and 3.26. The BH-NS binaries are less common and the BH-BH systems with secondary BH masses above 13 $M_\odot$ appear like for efficient mass transfer ($\beta_{\rm min} = 0$). But the DNS population is similar to that of the inefficient mass-transfer case ($\beta_{\rm min} = 0.75$) and only has difficulties to explain one of the DNS binaries, cf. Fig. 3.49 to Fig. 3.8. This also holds for the mass-ratio distribution of the DNS systems (Fig. B.52).

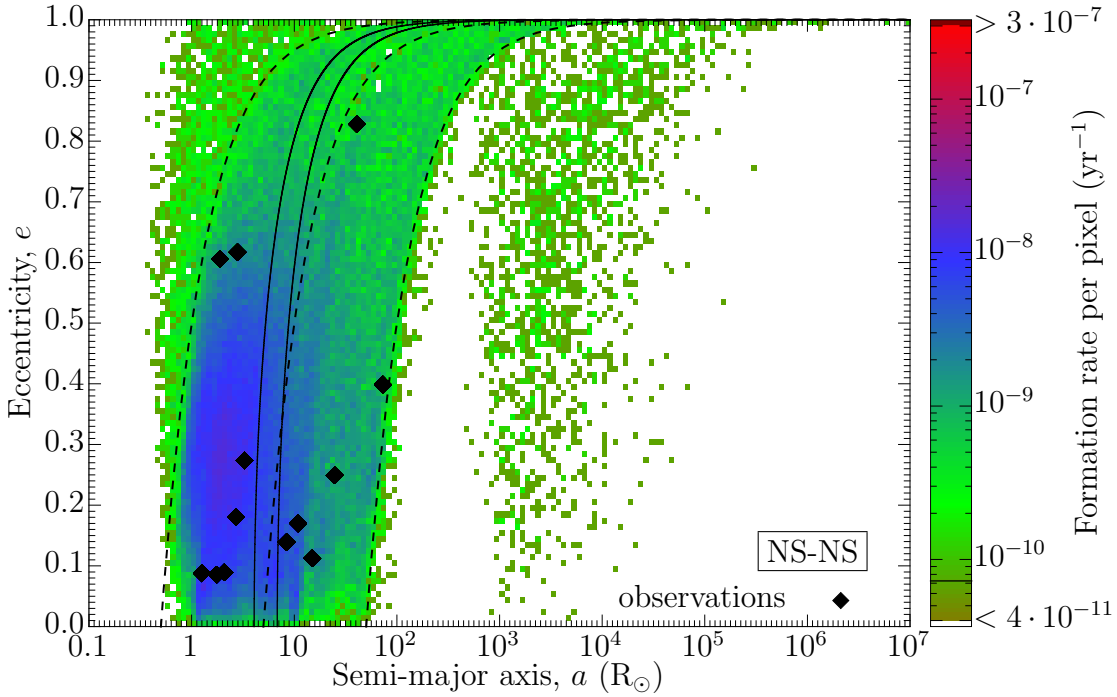

Figure 3.50: As Fig. 3.10, but with intermediate efficient mass transfer ($\beta_{\rm min} = 0.5$).

The orbital parameters shown in Figs 3.50, B.53 and B.54 are also comparable to the inefficient case presented in Section 3.4. Therefore, the statements and conclusions made there still hold for intermediate efficient mass transfer besides the BH-NS binaries being less frequent. The small deviations in the orbital separations compared to the default simulation are accordingly visible in the GW merger time (Figs B.55 and B.56). Here, the double BH binaries shift to shorter GW merger times while the mixed binaries become less frequent and tend to have larger orbital separations and therefore longer merger times.

Nevertheless, the observed GW merger events (Figs B.57 and B.58) at lower masses are similarly reproduced as in the default simulation. Hence, all the discussions (Section 3.5) about variations from the default simulation, including different kicks for newborn NSs or a shifted range for EC SNe, are expected to hold for intermediate efficient mass transfer. As the formation and merger rates of BH-NS binaries decrease when making the mass transfer a bit more efficient, this may

explain the so far non-detection of such a merging event.

Chapter 4

PSR J1755−2550: A young radio pulsar with a massive, compact companion

In this chapter, ComBinE is used to make predictions and put constraints on the unseen companion of PSR J1755−2550 (accepted for publication in MNRAS, arXiv: 1802.08248; Ng, Kruckow et al. 2018).

MNRAS **000**, 1–13 (2018) Preprint 26 February 2018 Compiled using MNRAS LATEX style file v3.0

PSR J1755−2550: A young radio pulsar with a massive, compact companion

C. Ng[1,2,3⋆], M. U. Kruckow[4], T. M. Tauris[3,4], A. G. Lyne[5], P. C. C. Freire[3], A. Ridolfi[3], I. Caiazzo[1], J. Heyl[1], M. Kramer[3,5], A. D. Cameron[3], D. J. Champion[3], B. Stappers[5]

[1] *Dunlap Institute, University of Toronto, 50 St. George St., Toronto, ON M5S 3H4, Canada*
[2] *Department of Physics and Astronomy, The University of British Columbia, Vancouver, BC V6T-1Z1, Canada*
[3] *Max-Planck-Institut für Radioastronomie, Auf dem Hügel 69, D-53121 Bonn, Germany*
[4] *Argelander-Institut für Astronomie, Universität Bonn, Auf dem Hügel 71, D-53121 Bonn, Germany*
[5] *Jodrell Bank Centre for Astrophysics, School of Physics and Astronomy, The University of Manchester, Manchester M13 9PL, UK*

Accepted XXX. Received YYY; in original form ZZZ

ABSTRACT

Radio pulsars found in binary systems with short orbital periods are usually fast spinning as a consequence of recycling via mass transfer from their companion stars; this process is also thought to decrease the magnetic field of the neutron star being recycled. Here, we report on timing observations of the recently discovered binary PSR J1755−2550 and find that this pulsar is an exception: with a characteristic age of 2.1 Myr, it is relatively young; furthermore, with a spin period of 315 ms and a surface magnetic field strength at its poles of 0.88×10^{12} G the pulsar shows no sign of having been recycled. Based on its timing and orbital characteristics, the pulsar either has a massive white dwarf (WD) or a neutron star (NS) companion. To distinguish between these two cases, we searched radio observations for a potential recycled pulsar companion and analysed archival optical data for a potential WD companion. Neither work returned conclusive detections. We apply population synthesis modelling and find that both solutions are roughly equally probable. Our population synthesis also predicts a minimum mass of $0.90\,M_\odot$ for the companion star to PSR J1755−2550 and we simulate the systemic runaway velocities for the resulting WDNS systems which may merge and possibly produce Ca-rich supernovae. Whether PSR J1755−2550 hosts a WD or a NS companion star, it is certainly a member of a rare subpopulation of binary radio pulsars.

Key words: stars: neutron — white dwarfs — pulsars: general — pulsars: individual: PSR J1755−2550

1 INTRODUCTION

The All-Sky High Time Resolution Universe (HTRU) Pulsar survey (Keith et al. 2010) conducted with the 64-m Parkes radio telescope between 2010 and 2015 has greatly increased the number of known pulsars in binary systems. Among these new discoveries is PSR J1755−2550 (Ng et al. 2015). At the time of the publication of the discovery paper, only a preliminary timing solution was available for this pulsar: it was known to have a relatively long spin period (P = 315 ms), an orbital period of 9.7 d and an orbital eccentricity of about 0.09. Further timing campaigns at the Lovell and the Effelsberg telescopes spanning 2.6 yr have significantly improved the positional uncertainty and broken its degeneracy with the spin-down rate. We find in this work that the pulsar has a large spin-down rate ($\dot{P} = 2.4 \times 10^{-15}$). These values place PSR J1755−2550 in a region of the $P - \dot{P}$ diagram that, although densely populated by normal, non-recycled, isolated pulsars, is very sparsely populated by binaries (see Fig. 1).

The only way for the binary pulsar PSR J1755−2550 to avoid having been recycled is if either it has a main-sequence (MS) star companion or it is the second-formed compact object in the system. As we shall argue later (see Section 3.3), we find that the scenario with a MS companion is the least likely. Therefore, in this paper, we focus our investigation on whether PSR J1755−2550 could be the second-formed compact object in a binary. Such a binary is very unusual; in fact there are only four known cases, which are anno-

⋆ E-mail: cherry.ng@dunlap.utoronto.ca

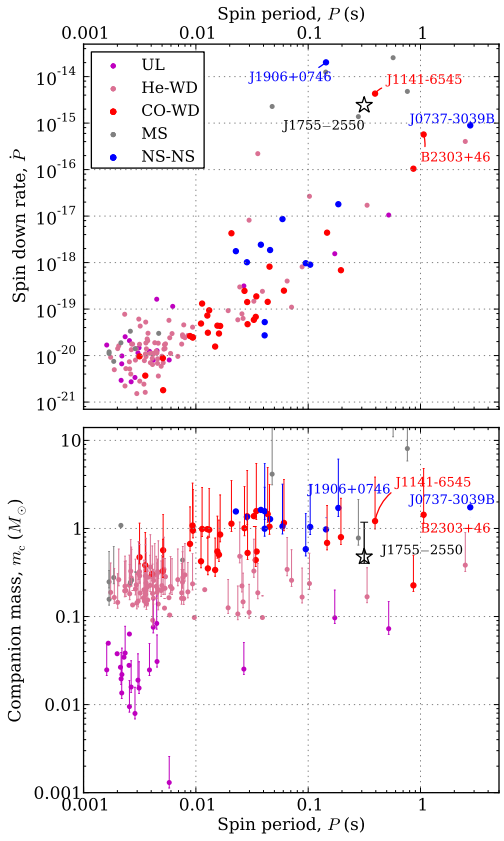

Figure 1. Top panel: The classical $P - \dot{P}$ diagram of all binary radio pulsars. Plotted here are the observed $\dot{P}$ values without any correction for the kinematic Shklovskii effect (Shklovskii 1970). Bottom panel: Companion mass versus spin period of all binary pulsars. For systems with unknown orbital inclination we plot the median companion mass instead, corresponding to $i = 60°$. The error bars indicate the range of minimum to maximum companion mass corresponding to $i = 90°$ and $i = 26°$, respectively. In both panels, the data points are colour-coded according to their binary companion type. Ultra-light (UL) companions are represented by black, helium (He) WDs by pink, carbon-oxygen (CO) WDs by red, main-sequence stars by gray and DNS (NS-NS) systems by blue. The subject of this paper, PSR J1755−2550, is shown as a star symbol. The four binary systems where the observed pulsar is the second-formed compact object are also annotated.

tated in Fig. 1 for comparison. PSRs B2303+46 (Thorsett & Chakrabarty 1999) and J1141−6545 (Manchester et al. 2000) are the only two binaries where a young neutron star (NS) is orbiting an old, massive white dwarf (WD) companion, confirmed by their optical identifications (van Kerkwijk & Kulkarni 1999; Antoniadis et al. 2011). This requires a fine-tuned formation scenario with an initial binary of two stars with typical masses in the range $6 - 10\,M_\odot$, which undergo mass reversal during the mass-transfer phase (Tauris & Sennels 2000; Davies et al. 2002). Another possible member of this population is PSR J1906+0746 (Lorimer et al. 2006b; van Leeuwen et al. 2015), however, the nature of its companion has not yet been confirmed, but given its mass ($1.322 \pm 0.011\,M_\odot$) it is likely to be a NS. That would imply PSR J1906+0746 is the second-formed NS in a double neutron star system (DNS), with the first-formed likely to be a (still undetected) recycled pulsar. Such a case is again a statistically rare find, because in a DNS the second-formed (non-recycled) NS has a much shorter radio lifetime compared to the recycled, first-formed NS. Indeed, out of all the known DNS systems, it is almost always the first-formed NS that is observed as a radio pulsar. The only confirmed case where we see the second formed pulsar is PSR J0737−3039B, but in this system we also see the first-formed pulsar, PSR J0737−3039A: this is the well-known "double pulsar" system (Burgay et al. 2003; Lyne et al. 2004).

In either case, PSR J1755−2550 has an unusual formation history and is thus an object of interest for binary stellar evolution. In Section 2 of this paper, we describe the radio observations taken and present an update of the timing solution. In Section 3 we discuss various possible formation scenarios of PSR J1755−2550, and in Section 4 we present a population synthesis investigation for WDNS binaries. Further potentially observable clues are discussed in Section 5, and we conclude our findings in Section 6.

2 RADIO TIMING OBSERVATIONS

2.1 Observational set-up

The majority of the timing observations of PSR J1755−2550 have been taken at the Jodrell Bank Observatory with the Lovell 76-m telescope, using a Digital Filterbank system (DFB) backend. The DFB is based on the implementation of a polyphase filter in FPGA processors with incoherent dedispersion. The Jodrell DFB has a bandwidth of 384 MHz with a central frequency at 1532 MHz. These observations have roughly weekly cadence and each integration is of the order of half an hour. A handful of DFB observations were also recorded at Parkes, with a bandwidth of 256 MHz and a central frequency of 1369 MHz.

A dedicated timing campaign was conducted at the Effelsberg 100-m radio telescope, with the main goal of obtaining high-quality multi-frequency polarimetry data and to perform a deep search for a potential neutron star companion of PSR J1755−2550. All Effelsberg observations were made using the PSRIX backend (Lazarus et al. 2016a) in baseband mode with a nominal bandwidth of 200 MHz. About 5 hr were spent all together observing at a central frequency of 4.8 GHz (C-band). No detection is made above a signal-to-noise ratio of 5.

2.2 Derivation of times-of-arrival and the timing solution

Our analysis of the radio timing data made use of the PSRCHIVE data analysis package (Hotan et al. 2004). Each observation is first corrected for dispersion and folded at the predicted topocentric pulse period. A high signal-to-noise template is created by co-adding all available observations. This template is then convolved with each individual profile to produce a time-of-arrival (TOA) (Taylor 1992). We

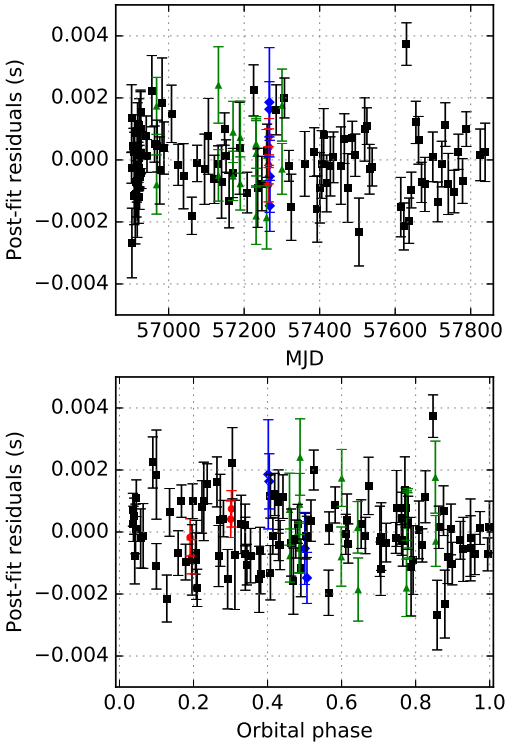

Figure 2. Post-fit timing residuals of PSR J1755−2550 with the parameters listed in Table. 1 taken into account. We use different colours to represent different data sets, with black squares being Jodrell 1.3 GHz TOAs, green triangles being Parkes 1.3 GHz TOAs, red circles being Effelsberg 1.3 GHz and blue diamonds being Effelsberg 2.6 GHz TOAs. The top panel shows residuals as a function of MJD, whereas the bottom panel plots residuals as a function of orbital phase.

generate one TOA per observation by scrunching in time and frequency to maximize the signal-to-noise ratio of each TOA. The spin and orbital periods of PSR J1755−2550 are relatively long and the high DM of 751 cm^{-3} pc means little scintillation. Hence no timing parameter should vary significantly over the course of each of the half hour integration. The DE421 Solar System ephemeris of the Jet Propulsion Laboratory (Folkner et al. 2009) is used to transform the TOAs to the Solar System barycentre.

Finally, the TEMPO2 software package (Hobbs et al. 2006) is used to fit a timing model to all TOAs, taking into account the astrometry, spin, and orbital motion of the pulsar. To describe the orbit of PSR J1755−2550 we have used the Damour-Deruelle (DD) timing model (Damour & Deruelle 1986) in TEMPO2; this is a theory-independent description of eccentric binary orbits. Since almost all of our timing data were taken at 1.3 GHz with a narrow bandwidth, we do not have a good handle on the precision of the DM and hence have fixed the DM at the nominal value of 751 cm^{-3} pc. The time span of our data set is still too short to constrain any proper motion and parallax. Given the limited timing precision typically associated with a slow pulsar, it might be years before we can reliably measure proper motion and parallax. We have held these parameters fixed at zero. As a last step, we compensate for any remaining systematic effects (e.g. instrumental or minor radio frequency interference) by calculating dataset-specific calibration coefficients (also known as 'EFAC'). These coefficients are applied to scale the TOA uncertainties such that each final respective reduced χ^2 is unity, in order to produce reliable uncertainty in the fitted parameters. See Fig. 2 for the post-fit timing residuals. If we assume a pulsar mass of 1.3 $M_\odot$, using Equation (2) of Weisberg & Taylor (1981) we obtain a predicted precession of periastron ($\dot{\omega}$) in general relativity of $0\overset{\circ}{.}0069\,\mathrm{yr}^{-1}$. Given our current precision in the measurement of ω ($0\overset{\circ}{.}015$, see

Table 1. Best-fit parameters for PSR J1755−2550. Values in parentheses are the nominal 1-σ uncertainties in the last digits.

Spin and astrometric parameters	
Right ascension, α (J2000)	17:55:38.400(4)
Declination, δ (J2000)	−25:50:22.0(18)
Spin period, P (ms)	315.1960620987(16)
Period derivative, $\dot{P}$	$2.4337(14)\times10^{-15}$
Dispersion measure, DM (cm^{-3} pc)	750.9(4)
Binary parameters	
Orbital period, P_{orb} (days)	9.6963342(6)
Projected semi-major axis, x (lt-s)	12.28441(14)
Epoch of periastron, T_0 (MJD)	56904.1265(4)
Eccentricity, e	0.08935(2)
Longitude of periastron, ω (°)	129.680(15)
Timing model	
Timing epoch (MJD)	57329
First TOA (MJD)	56901.8
Last TOA (MJD)	57848.3
Weighted RMS residuals (ms)	0.99
Reduced χ^2 ‡	1.9
Solar System ephemeris	DE421
Binary model	DD
Derived parameters	
DM-derived distance (kpc)	4.91−10.29†
Mean flux density at 1.3 GHz, $S_{1.3\,\mathrm{GHz}}$ (mJy)	0.20
Mean flux density at 2.6 GHz, $S_{2.6\,\mathrm{GHz}}$ (mJy)	0.04
Characteristic age, τ (Myr)	2.1
Characteristic dipole surface magnetic field strength at equator, B_{eq} (10^{12} G)	0.88
Mass function ($M_\odot$)	0.0211707(16)
Minimum companion mass*, $m_{\mathrm{c,min}}$ ($M_\odot$)	0.39
Median companion mass**, $m_{\mathrm{c,med}}$ ($M_\odot$)	0.47

‡ The reduced χ^2 stated here represents the value before the application of EFAC. Note that the rest of the timing solutions have EFACs incorporated, bringing the reduced χ^2 to unity.
† Using the electron density model from Yao et al. (2017) we obtain a smaller derived distance of 4.9 kpc while the Cordes & Lazio (2002) model predicts a further distance of 10.3 kpc.
* $m_{\mathrm{c,min}}$ is calculated for an orbital inclination of $i = 90°$ and an assumed pulsar mass of 1.3 $M_\odot$.
** $m_{\mathrm{c,med}}$ is calculated for an orbital inclination of $i = 60°$ and an assumed pulsar mass of 1.3 $M_\odot$.

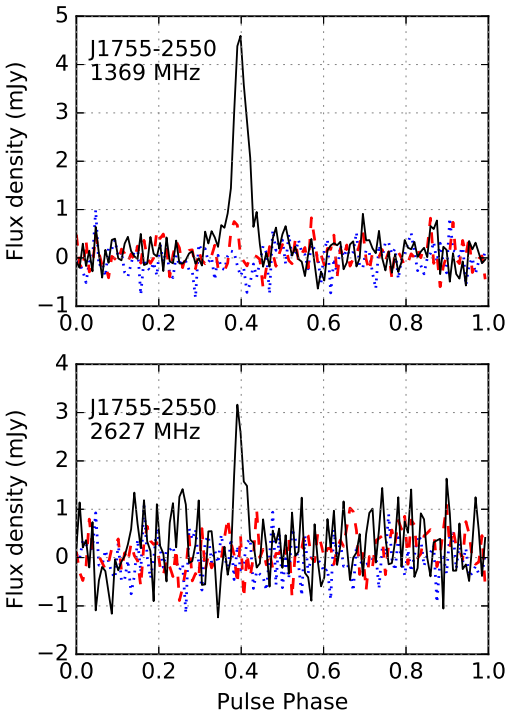

Figure 3. Pulse profiles observed at Parkes at 1.3 GHz (top panel) and at Effelsberg at 2.6 GHz (bottom panel). The integrated profiles shown here have 128 phase bins. The total intensity is represented by the black solid line, linear polarization by the red dashed line and circular polarization by the blue dotted line.

Table 1), we do not expect to be able to detect $\dot{\omega}$ in the short term.

2.3 Pulse profile and polarization study

The Parkes and Effelsberg observations record four Stokes parameters in each frequency channel and thus can be used to study the polarization profile. A calibration scan was taken before or after each of the targeted pulsar observations. This calibration scan triggers a square-wave signal of the noise diode coupled to the receptors in the feeds, which can be used to polarization calibrate for the differential gain and phase between the feeds, in turn enabling the retrieval of the true Stokes parameters.

Fig. 3 show the integrated polarization profiles of PSR J1755−2550 in total intensity, linear and circular polarization, observed at 1.3 and 2.6 GHz respectively. No significant position angle (PA) has been measured. PSR J1755−2550 has a simple profile comprising only one component and does not appear to be polarized linearly nor circularly. We also do not obtain any constraining rotation measure. It has been proposed in the literature that young, energetic pulsars with $\dot{E} > 10^{35}$ erg s^{-1} tend to have significant linear polarization (see, for example, Fig. 8 in Weltevrede & Johnston 2008). PSR J1755−2550 has a relatively high $\dot{E}$ of the order of 10^{33} erg s^{-1}. The lack of linear polarization in this case is note-worthy but not inconsistent with literature. We convolve the profile at 2.6 GHz with a scattering tail, and measured a characteristic scattering timescale of ~13.5(14) ms at 1 GHz. This small hint of scattering could also have decreased the amount of polarization.

3 FORMATION SCENARIO

3.1 Formation of binary pulsars

The standard formation scenario of a pulsar in a binary system is reasonably well established in the literature (see e.g. Bhattacharya & van den Heuvel 1991). It all begins with two main-sequence stars, where the initially more massive star evolves first, expands and transfers mass to its companion star, before it undergoes a supernova (SN) explosion to produce a NS. The newborn NS gradually spins down afterwards, as it radiates its rotational energy similar to the case of a normal radio pulsar (Lorimer & Kramer 2004). At a later stage the secondary star expands after depletion of hydrogen core burning and initiates mass transfer to the NS. In this process, known as "pulsar recycling", the NS becomes rejuvenated as it gains mass and angular momentum (e.g. Alpar et al. 1982; Tauris & van den Heuvel 2006). At the same time, the strength of its surface magnetic field is reduced (e.g. Bhattacharya 2002). Hence, the outcome of the recycling process is an old NS with rapid spin (small value of P), which enables the radio emission mechanism to reactivate, and a small $\dot{P}$ as a result of the reduced B-field.

From the $P-\dot{P}$ diagram in the top panel of Fig. 1, it can be seen that most of the binary pulsars cluster around short spin periods of millisecond duration (i.e. MSPs) and small spin-down rates of the order of 10^{-21} to 10^{-19}. The longer the duration of this recycling phase, during which the source is visible as an X-ray binary, the faster the final spin period of the pulsar and the smaller the period derivative. An important factor determining the degree of recycling is therefore the initial mass of the secondary star (see e.g. Tauris 2011, for a review). The more massive the secondary star is, the less efficient is the recycling process.

If the secondary star is sufficiently massive, it will undergo a SN explosion itself to form a younger, second NS. There are about a dozen or so of these DNS binaries known to-date (e.g. Martinez et al. 2015; Lazarus et al. 2016b). As can be seen in Fig. 1, the first-formed NSs in DNS systems tend to have relatively long spin periods and large period derivatives compared to MSPs. These NSs are therefore observed as mildly recycled pulsars and their properties are brought about by the so-called Case BB Roche-lobe overflow (Tauris et al. 2015), following the high-mass X-ray binary and common-envelope phase (Tauris & van den Heuvel 2006).

Finally, if the secondary star is not massive enough to undergo core collapse, the mass-transfer phase can last much longer (up to several Gyr, Tauris & Savonije 1999), before the companion star eventually sheds its outer layer and results in a white dwarf (WD). This often leads to very efficient recycling. As apparent from Fig. 1 (see also Fig. 9 in Tauris

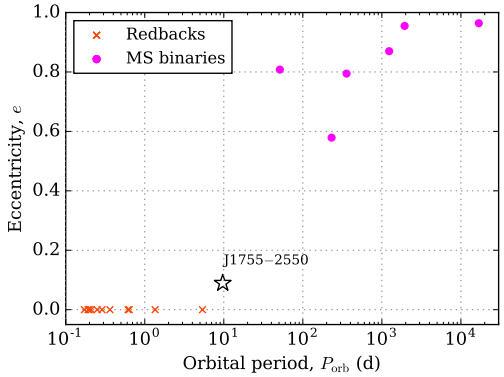

Figure 4. Eccentricity as a function of orbital period for binary radio pulsars with hydrogen-rich companions in the Galactic disk. These systems can host either so-called redbacks (stripped MS stars) or regular MS stars. PSR J1755−2550 is plotted for comparison and does not fit in either of these two populations, see Section 3.3. The error bars on all data points are much smaller than the size of the plotted dots.

et al. 2012), the most recycled systems are indeed those with ultra-light (UL) and helium WD (He WD) companions, followed by those with heavier masses, namely carbon-oxygen (CO WD) or oxygen-neon-magnesium (ONeMg WD) WDs (Lazarus et al. 2014). The NSs displaying the least amount of recycling are those found in DNS systems.

3.2 PSR J1755−2550 – the case of a young pulsar

The combination of a large $\dot{P}$ value (2.4×10^{-15}) and a relatively slow spin period (P = 315 ms) identifies PSR J1755−2550 as being a non-recycled radio pulsar (i.e. there are no signs of accretion onto the NS after its formation). The pulsar is thus relatively young and a member of a binary system with a companion star in the mass range $m_{\rm c}$ = 0.4 – 2.0 $M_{\odot}$ at the 95% C.L. (based on its measured mass function, see Section 3.4). The possibilities of the nature of the companion star, seem therefore to be restricted to the following three possibilities: a MS star, a WD or a NS. We now investigate each of these cases in more detail.

3.3 A MS star companion?

In Fig. 4, we have plotted the eccentricities as a function of orbital period for all Galactic disk binary radio pulsars with hydrogen-rich companion stars. These companions can be either so-called redbacks (stripped MS stars) or regular MS stars. The redback systems (Roberts 2011; Chen et al. 2013) are all fast-spinning MSPs with low B-fields in circular orbits. Hence, we can rule out the latter possibility for PSR J1755−2550.

We note that PSR J1755−2550 has a much smaller eccentricity ($e \simeq 0.09$) than all the known young radio pulsars with MS-star companions which have $e \gtrsim 0.60$ (see Fig. 4). Furthermore, of the six known radio pulsars with a MS-star companion only one system has a MS star with a mass which is potentially less than 3 $M_{\odot}$ (PSR B1820−11, Clifton & Lyne 1986; Lyne & McKenna 1989) and that system has an orbital period of 358 days (i.e. much larger than that of PSR J1755−2550). It has even been suggested (Portegies Zwart & Yungelson 1999) that this companion star might be a WD. Taken together, all these strongly suggests that the companion of PSR J1755−2550 is not a regular MS star, although this possibility cannot be ruled out completely (see also Section 4.3 for further discussions based on population synthesis).

However, as we will see in Section 5, there is no clear evidence for any MS star associated with PSR J1755−2550 in optical observations. Furthermore, there is no evidence for orbital variability (see bottom panel of Fig. 2) normally associated with tidal and rotational effects caused by an extended object, as observed for the pulsars with optically identified MS companions. We do not measure any variations in the orbital period ($\dot{P}_{\rm orb}$), with a statistically insignificant best-fit value of $-2(5)\times10^{-9}$. Nor do we see any evidence for any eclipses that might have been caused by outgassing of such a companion, which are also common observations in systems with identified MS companions.

In the rest of this paper, we therefore investigate the more likely case of PSR J1755−2550 being the last-formed member of a double degenerate system. The interesting question now is whether it has a WD or a NS companion star (i.e. whether it is a WDNS system, where the NS formed *after* the WD, or a DNS system). In the following, we discuss the two different possibilities based on the mass function, its orbital parameters, and the outcome of a population synthesis simulation.

3.4 Mass function of PSR J1755−2550

In Fig. 5, we have plotted the companion star mass as a function of the unknown orbital inclination angle. At first sight, the somewhat small mass function of PSR J1755−2550 (f = 0.0212 $M_{\odot}$) strongly favors a WDNS system compared to a DNS system. Based on this function alone, and assuming a pulsar mass of 1.30 $M_{\odot}$ (a typical NS mass of a young, binary, non-recycled pulsar, e.g. Tauris et al. 2017), there is only about a 5–6% chance that PSR J1755−2550 has a NS companion, requiring an almost face-on orbit with an orbital inclination angle between 26° – 17° for an assumed first-born NS mass between 1.15 – 2.1 $M_{\odot}$.

However, our population synthesis (see Section 4.1) predicts a minimum WD mass of 0.90 $M_{\odot}$ (Fig. 6) for any WD member of a WDNS system. This is not surprising since to produce such a system a mass reversal between the two stars is needed, such that the WD forms first (from the originally most massive star, i.e. the primary star) and the NS forms afterwards from the secondary star which accretes enough mass from the (giant) primary star that it undergoes core collapse to produce a NS (e.g. Tauris & Sennels 2000). Hence, a WDNS system can form from an initial zero-age main sequence (ZAMS) binary with two relatively massive stars near the threshold limit for producing a NS. As an illustrative example, consider a ZAMS binary with 9 $M_{\odot}$ and 8 $M_{\odot}$ stars. The 9 $M_{\odot}$ primary star is slightly too light to undergo core collapse, thus it necessarily forms a massive (> 0.90 $M_{\odot}$) WD. However, the 8 $M_{\odot}$ secondary star accretes enough material to go over

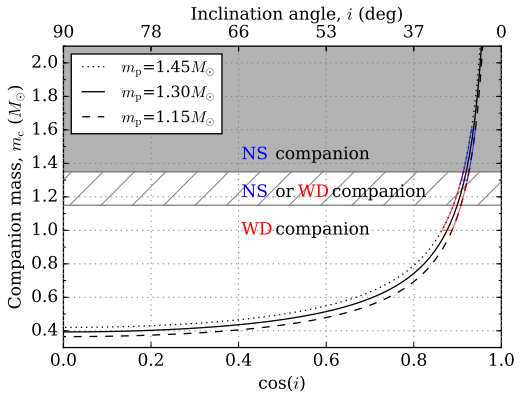

Figure 5. Companion mass (m_c) as a function of cos(i). Here i the orbital inclination angle and cos(i) is a quantity with uniform distribution for randomly oriented orbits of the PSR J1755−2550 system. The different curves correspond to the unknown mass of PSR J1755−2550 and represent typical masses of the second-formed NS in DNS systems. The grey-shaded area represents roughly the region where PSR J1755−2550 has a NS companion. The semi-shaded area marks the region where PSR J1755−2550 could have either a NS or a WD companion. The most likely companion mass ranges for NS (blue) and WD (red) are indicated in accordance with the discussion in Section 3.4. An orbital inclination of ≤ 26° is required for a DNS system.

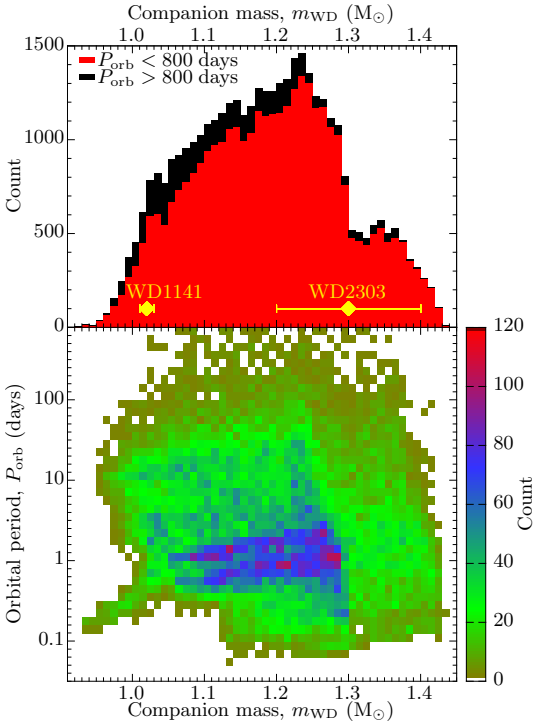

Figure 6. *Bottom plot*: Heatmap showing WD mass and orbital period for a population of WDNS binaries with an orbital period of less than 800 days obtained from our population synthesis simulations. The shown orbital period is the initial value right after the young NS has formed. The colour coding reflects the number of counts in each pixel. *Top plot*: A corresponding histogram of the WD mass distributions with orbital periods below (red) and above (black) 800 days.

the threshold (~ 10 − 11 $M_\odot$) to produce a NS. When it goes SN it produces a young pulsar, which never gets recycled.

Given that WDNS systems only form with a massive WD (> 0.90 $M_\odot$), and that NSs also have a mass above this limit, means that the first-formed compact object (i.e. the current companion star to the observed radio pulsar) must have a mass of at least 0.90 $M_\odot$. This fact, in combination with the measured mass function, means that the relative statistical probability for PSR J1755−2550 being a DNS system is much greater than the aforementioned 5-6 %.

As a first naïve guess, one could assume a first-born NS with a mass between 1.15 – 2.1 $M_\odot$. In this case, we find that the probability for PSR J1755−2550 being a DNS system is about 46%. This is estimated assuming an *a priori* randomly oriented orbit of PSR J1755−2550 with respect to Earth, and where a WD companion would have a mass between 0.9 – 1.35 $M_\odot$. However, the masses of the first-born NSs in DNS systems that have been measured thus far fall between 1.30 – 1.60 $M_\odot$ (Özel & Freire 2016). Hence, assuming this would also apply to the potential NS companion of PSR J1755−2550, we obtain an estimate for the probability of this system being a DNS system to be about 24%. Assuming a most likely WD mass in the interval 1.0 − 1.35 $M_\odot$ (see Section 4.1 and Fig. 6) the probability of PSR J1755−2550 being a DNS system converges to a final value of about ~32%. This value changes by less than 0.5% when considering a pulsar mass between 1.15 – 1.45 $M_\odot$.

This is a remarkable increase in probability (compared to that from the mass function alone) and suddenly makes a DNS system a much more likely scenario. Moreover, there are further constraints from the orbital parameters which we now discuss.

4 POPULATION SYNTHESIS

To distinguish further between a WDNS and a DNS nature of the PSR J1755−2550 system, we have taken advantage of population synthesis and simulated a large number of WDNS and DNS systems. We use ComBinE (Kruckow et al. 2018), an updated version of the population synthesis code which was previously applied to WDNS systems by Tauris & Sennels (2000) and DNS systems by Voss & Tauris (2003). At Milky Way metallicity, ComBinE interpolates the stellar models of Brott et al. (2011) and includes new calculations of their extension to lower masses. In the applied mass range, a simple power-law of −2.7 is assumed for the initial mass function. The initial binary separations are limited between 10 and 10^4 $R_\odot$ and follow a flat distribution of the logarithmic orbital period. As most interacting binaries circularise before and during mass transfer, we apply initial circular orbits.

To produce WDNS and DNS systems from progenitor stars at Milky Way metallicity, we find that the ZAMS mass range of primary and secondary stars is between 5 and 35 $M_\odot$. The binaries which evolve to a system like PSR J1755−2550 are well within this range. As the mass range is restricted and the initial mass function favours low-mass stars, we simulated 50 million systems to produce Figs. 6 and 7. All other parameters are like those in the default parameter set of Kruckow et al. (2018). This especially includes the assumption of rather inefficient mass transfer, a common envelope treatment with envelope structure information obtained from the detailed stellar models, and a SN kick distribution depending on the amount of mass stripping of the progenitor star via binary interactions prior to its explosion. In the analysis, we focus on the main population with orbital periods less than 800 days at the formation of the young NS, since wider systems would likely have avoided any binary interactions.

4.1 Orbital period and eccentricity

Fig. 6 shows the distribution of our simulated WDNS systems in the WD mass–orbital period plane and a histogram of the WD masses in these simulated WDNS systems. We note that indeed the majority (> 95%) of the simulated WDs have masses between 1.0 − 1.35 $M_\odot$. For comparison, we have plotted the WD masses of the only two known WDNS systems, PSRs J1141−6545 and B2303+46.

Fig. 7 shows the orbital period and eccentricity distribution for all simulated WDNS and DNS systems. This plot shows the orbital parameters at the birth of the double degenerate systems. However, the binaries which are born in relatively close orbits ($P_{\rm orb} \lesssim 1$ day, and especially those which are eccentric) will experience gravitational damping and evolve to shorter periods and more circular configurations. For example, the tight binary PSR J1141−6545 has a measured orbital period decay of $\dot{P}_{\rm orb} = -4.0 \times 10^{-13}$ (Bhat et al. 2008).

A zoom-in in the region near the orbital parameters of PSR J1755−2550 is shown in the bottom panel of Fig. 7. We notice that we can reproduce the location of PSR J1755−2550, and its relatively large value of $P_{\rm orb} \simeq 9.7$ d and small value of $e = 0.09$, for both WDNS and DNS systems. Based on our population synthesis modelling, we therefore conclude that from this information alone, we cannot distinguish between the two different possibilities (WDNS vs DNS) for the nature of PSR J1755−2550.

The eccentricity of PSR J1755−2550 is quite small (especially given its relatively large orbital period), compared to our simulated systems in general. This could be an indication of a small kick imparted on the NS in the SN explosion, or simply a kick direction which favors small post-SN eccentricities. For comparison, the eccentricities of PSRs J1141−6545 and B2303+46 (the two systems where we know the companions are WDs) are $e = 0.17$ and $e = 0.66$, respectively. Interestingly, the orbital eccentricities at birth for the other two young pulsars (PSR J1906+0746, which could be in a DNS, and PSR J0737−3039B, which certainly is in a DNS) are 0.085 and 0.11 respectively (Lorimer et al. 2006a). These are quite similar to the orbital eccentricity of PSR J1755−2550.

If PSR J1755−2550 is a DNS system, recent simulations

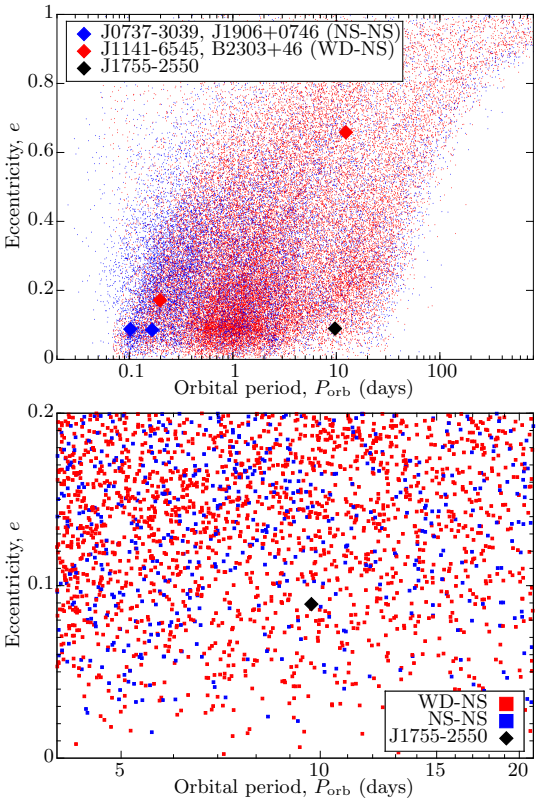

Figure 7. *Top plot*: Orbital eccentricity (e) versus orbital period ($P_{\rm orb}$) of the simulated WDNS systems (red squares) and DNS systems (blue squares) obtained from our population synthesis. The location of PSR J1755−2550 is marked with a black diamond. The colored diamonds are the other four known young pulsars in binary systems: PSRs J0737−3039B (Kramer et al. 2006), J1906+0746 (Lorimer et al. 2006b), J1141−6545 (Bhat et al. 2008) and B2303+46 (Stokes et al. 1985). *Bottom plot*: A zoom-in of the top plot. Both simulated WDNS and DNS systems are seen to populate the area close to PSR J1755−2550.

of the kinematic effects of the second SN explosion in this system (Tauris et al. 2017) indicate that the kick velocity was most likely less than 100 km s^{-1} (although a small tail of larger kick solutions exists). This is similar to their findings for PSR J0737−3039A/B and PSR J1906+0746 (which nonetheless has a much larger high-velocity tail as it is not as well constrained). The former system is strongly constrained to kicks smaller than 70 km s^{-1} if its very small proper motion is taken into account.

4.2 Relative formation rate of WDNS versus DNS systems

From our simulations, we find that the relative formation rate of WDNS and DNS systems are quite similar: 70% and 30%, respectively. A thorough investigation of this ratio, and

how it depends on initial parameters and various physical assumptions, is beyond the scope of this paper. However, we do notice that a roughly equal formation rate of these two subpopulations of binary pulsars systems does not seem unreasonable, given that (besides PSR J1755−2550) two systems of each kind have been discovered so far.

4.3 On the possibility of a MS companion star

Using the population synthesis code ComBinE (Kruckow et al. 2018), we also simulated a large population of NS–MS systems based on 50 million initial ZAMS binaries. Here, we considered MS companion stars within the mass interval of 0.4 to 1.0 $M_\odot$, given the constraint from pulsar timing on the minimum mass of the companion star (Table 1) and the lack of an optical counterpart (Section 5.1). Of these systems, only less than 2 per cent have eccentricities below 0.10 (and < 4 per cent have $e < 0.15$) right after the SN explosion. Subsequent long-term tidal interactions could in principle help to circularise more high-eccentricity systems. However, the circularisation timescale, $\tau_{\rm circ}$ (e.g. Claret & Cunha 1997, and references therein) scales with orbital period and stellar radius to large powers (up to $\tau_{\rm circ} \propto P_{\rm orb}^{7} R^{-9}$ in the case of stars with convective cores and radiative envelopes) and thus these systems with relatively wide orbits will only start to circularise efficiently once the companion star becomes a red giant star. Therefore, they will not produce NS-MS binaries with $e \sim 0.1$.

Although population synthesis always comes with uncertainties based on the applied input physics (e.g. the common-envelope phase prior to the SN creating the NS Tauris & van den Heuvel 2006), we find it reasonable to state that only relatively few NS-MS systems end up in orbits with small eccentricities and orbital periods somewhat resembling that of PSR J1755−2550. We do find many NS-MS systems with orbital periods of less than about 5 days (the progenitors of many low-mass X-ray binaries and short-orbital period binary MSPs). A thorough analysis of NS-MS systems, however, is beyond the scope of this paper.

In contrast, the NS in systems with a compact object companion (i.e. WDNS or DNS systems) and an eccentricity and period like PSR J1755−2550 (shown in Fig. 7) are more common by more than an order of magnitude (compared to NS-MS binaries) according to our population synthesis simulations. Thus based on our binary modelling alone, although we cannot exclude a MS companion star to PSR J1755−2550, we find it most likely that the companion star is a compact object.

4.4 Merging WDNS systems and Ca-rich SNe

It has been suggested that the merger event of a massive WD and a NS might produce a Ca-rich SN (Metzger 2012). These observed dim SNe (or transients) are often found at large offset distances from their associated host galaxies (Kasliwal et al. 2012; Foley 2015). For example, it was shown by Lyman et al. (2016) that about 1/3 of these Ca-rich SNe have offsets > 20 kpc. Hence, to explain this extreme offset distribution many scenarios have been proposed, including unusual formation sites such as globular clusters or dwarf satellite galaxies, which are difficult to detect. Moriya et al. (2017) argued that some of the Ca-rich gap transients might be related to explosions of ultra-stripped stars.

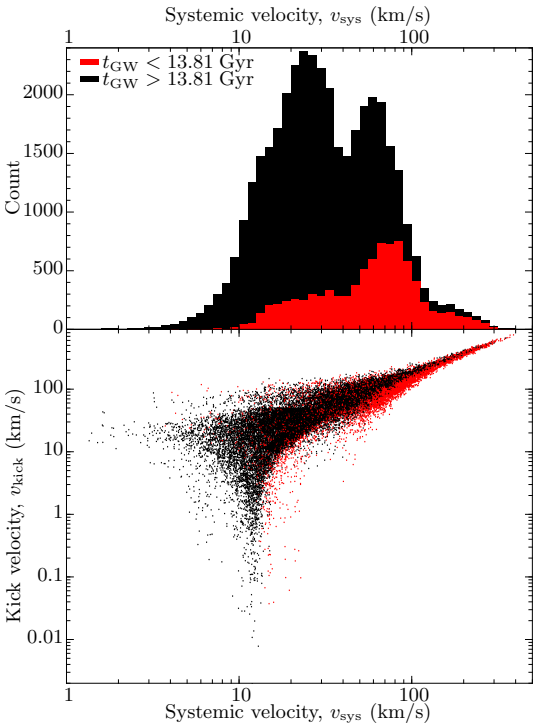

Figure 8. *Lower panel*: The relation between applied NS kick velocities and resulting 3D systemic velocities of all simulated WDNS binaries. *Upper panel*: A histogram of 3D systemic velocities from our simulated population of WDNS systems. The red and black distributions are for WDNS systems which merge via gravitational wave (GW) radiation before and after a Hubble time, respectively.

To probe whether such offset Ca-rich SNe could originate from our simulated WDNS systems escaping their birth sites, we plot in Fig. 8 the resulting 3D systemic velocities of our simulated population of WDNS binaries. It is seen that those WDNS systems which merge within a Hubble time typically have velocities of less than 100 $\rm km\,s^{-1}$, although a small high-velocity tail extends up to 350 $\rm km\,s^{-1}$.

These resulting systemic velocities depend, of course, on the applied NS kick distribution. Here, the applied NS kick distribution is taken from Kruckow et al. (2018), which reflects that many ultra-stripped SNe result in newborn NSs with small kicks (Tauris et al. 2015, 2017). In the lower panel of Fig. 8, we show the correlation between the applied NS kick velocities and the resulting systemic velocities of our simulated WDNS systems.

We conclude that our simulated WDNS systems are not able to escape the gravitational potential of somewhat massive host galaxies (like our Milky Way) if they originate from a disk population. Mergers of NSs and massive WDs, however, can also be produced from NSWD systems such as

PSR J1952+2630 (Lazarus et al. 2014), i.e. binaries with a recycled pulsar and thus where the NS forms before the WD. A kinematic investigation of those systems is beyond the scope of this paper. Finally, we note that the similar peak luminosity of Ca-rich SNe to those of SNe Ib has led to the suggestion that Ca-rich SNe may also arise from the core collapse of massive stars (e.g. Gvaramadze et al. 2017). How to account for the often observed large offsets of Ca-rich SNe with respect to their host galaxies remains to be explained in this formation model — unless multiple formation paths for Ca-rich SNe are possible.

Regardless of PSR J1755−2550 being a WDNS or a DNS system, its orbital period is much too large to produce a Galactic merger event. However, the kinematics of both populations is dominated by the SN explosion producing the last-formed compact object, and thus we predict a proper motion of PSR J1755−2550 consistent with a 3D systemic velocity of less than 100 km s^{-1}.

5 OBSERVABLE CLUES

5.1 Optical search of a first-formed WD

Any optical detection of the companion would provide definitive evidence for the WD argument in the case of PSR J1755−2550. The deepest archival data we found covering the vicinity of PSR J1755−2550 is from the pan-STARRS survey (Chambers 2006; Kaiser et al. 2010). There are five available bands (g, r, i, z, y) in total. We performed point spread function (PSF) photometry of each filter using DAOPHOT. Magnier et al. (2016) find that the mean astrometric deviation relative to the GAIA catalogue is about 5 milliarcseconds in this region of the sky, and furthermore the astrometry precision of the translation between the pulsar timing frame of reference and the GAIA frame of reference is likely to be even smaller (Wang et al. 2017), so the dominant positional uncertainties are those from the timing measurements themselves (Tab. 1) and are about two arcseconds. Since PSR J1755−2550 has a very low Galactic latitude, absorption is likely significant along the line-of-sight. We thus focus our analysis on the y−band (around 1 micrometer) data where the amount of absorption is the least among the pan-STARRS filters (Fig. 9). We find no object at the position of PSR J1755−2550 down to a detection limit of $z = 22.3$ and $y = 21.3$ from the stacked image (Fig. 10).

Using the measured DM of 751 cm^{-3}pc and the Cordes & Lazio (2002) model (hereafter NE2001) of free electron distribution in the Milky Way, we obtain a DM-derived distance of 10.3 kpc. However, a recent electron density model (Yao et al. 2017, hereafter YMW16) puts the DM-derived distance of PSR J1755−2550 much closer, at 4.9 kpc.

In Fig. 11 we plot theoretical cooling curves for WD masses ranging from 0.53 to 1.17 M$_\odot$ calculated with MESA (Paxton et al. 2013) and the DA stellar atmospheres of Holberg & Bergeron (2006), Kowalski & Saumon (2006) and Tremblay et al. (2011)[1]. The top panel shows the absolute magnitude in the pan-STARRS y-band. The uncertainty in the distance of PSR J1755−2550 makes it hard to quantify a theoretical apparent magnitude. Assuming a minimum distance of 4.9 kpc and no extinction, we have to add 13.46 magnitudes (the distance modulus corresponding to 4.9 kpc) to the values on the y-axis. As mentioned, PSR J1755−2550 is located very close to the Galactic plane and even in the y-band we have a minimum extinction of ∼5 magnitudes

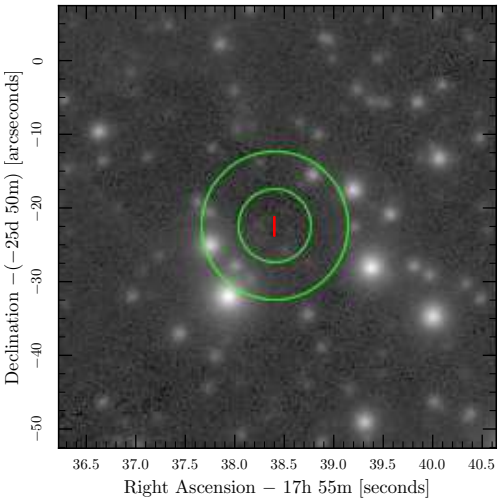

Figure 9. The stacked Pan-STARRS data in y−band. The circles indicate 5 and 10 arcsec radius around the position of PSR J1755−2550 from radio timing. The red rectangle shows the uncertainty of position from radio timing.

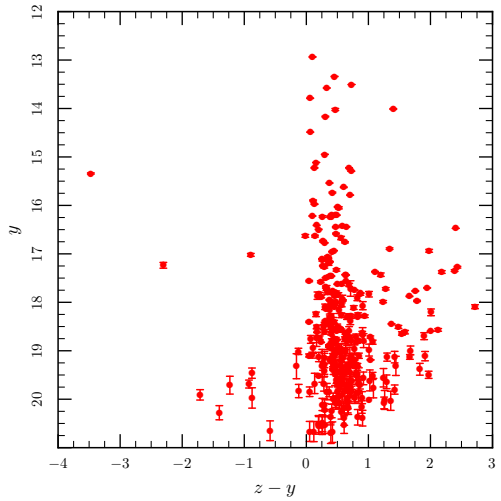

Figure 10. Colour-Magnitude Diagram of objects in the Pan-STARRS catalogue (Chambers et al. 2016) within one arcminute of the position of PSR J1755−2550 from radio timing. The 5-σ detection limit is $z = 22.3$ and $y = 21.3$.

[1] http://www.astro.umontreal.ca/~bergeron/CoolingModels

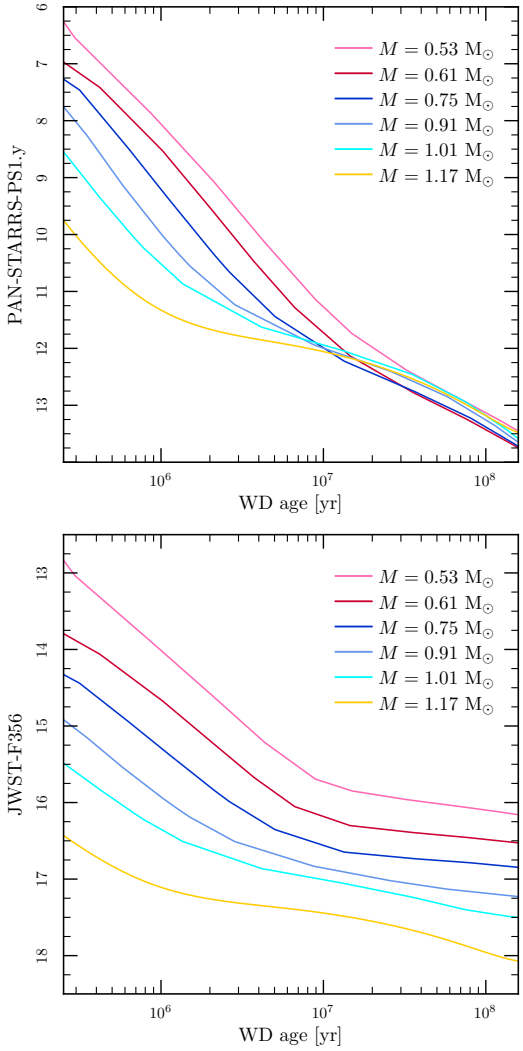

Figure 11. White dwarf cooling models for 6 different WD masses. *Top plot*: Absolute magnitude vs WD age in the pan-STARRS y–band. *Bottom plot*: Absolute magnitude vs WD age in JWST F356W filter.

(Schlegel et al. 1998; Schlafly & Finkbeiner 2011)[2]. These sum to an apparent magnitude of 25-30 for a 1 Myr-old WD (roughly the spin-down age of the pulsar) depending on its mass, which is well beyond the limit of the sensitivity of the archival pan-STARRS data, and thus our non-detection is not conclusive. In the lower panel of Fig. 11, we show the same cooling models if we were to observe with the F356W filter of the James Webb Space Telescope (JWST). WDs are fainter in this redder filter. However, the absorption in this band is much lower, less than a magnitude at a distance of ~5 kpc. A constraining optical detection with the JWST could be possible although still challenging.

In Sections 3.3 and 4.3, we discussed the scenario of the companion being a MS star. In particular eclipses and changes in the orbital period are often seen in pulsars with MS companions. Furthermore, population synthesis indicates that it is difficult to form a binary with eccentricity as low as the PSR J1755−2550 system. The pan-STARRS data can provide some additional clues. Although a low-mass MS star would have been too dim to be detected, a MS star with a mass of $\sim 0.9\,M_\odot$ would have an absolute magnitude of about 3 in the pan-STARRS y–band. Therefore, if PSR J1755−2550 was at the minimum distance of ~5 kpc, then a MS star more massive than $0.9\,M_\odot$ would have an apparent magnitude brighter than 21, and would have been detected in the pan-STARRS data studied here. This means that if we knew for certain that PSR J1755−2550 was at ~5 kpc, we could exclude a MS companion more massive than $0.9\,M_\odot$. However, at a distance of ten or more kpc, extinction would make it impossible to detect even a much higher mass MS star. A post-MS star would be even brighter. Again, the uncertainty on the distance makes it difficult to draw conclusions. There is no evidence of an MS or post-MS companion more massive than $0.9\,M_\odot$, but its presence cannot be excluded by the optical data unless the PSR J1755−2550 is about five or fewer kiloparsecs away.

5.2 Search for radio pulsation from the potential first-formed NS

If PSR J1755−2550 is indeed a DNS system, we know from observations of the first-formed (recycled) NSs in other DNS systems, that there is roughly a one-in-three chance that it would be beaming in our direction (Kramer et al. 1998), yielding an estimated 10% probability of detecting radio pulsations from the companion star of PSR J1755−2550 (given our estimation of a ~32% chance of PSR J1755−2550 being a DNS system, cf. Section 3.4). If detected, it would make PSR J1755−2550 the only other observed double pulsar system apart from PSR J0737−3039 (Burgay et al. 2003; Lyne et al. 2004).

To look for radio pulsations from the potential first-formed NS companion, we searched the seven observations available to us (Table 2). These consist of one Parkes scan in filterbank-mode taken in 2013 and six baseband observations from the Effelsberg radio telescope in 2015, covering multiple frequency bands (1.3, 2.6, and 4.8 GHz). Three observations, however, were severely affected by RFI, which made the data unusable for search purposes. We were thus left with two 1.3-GHz and two 4.8-GHz observations, each of which was processed as follows.

The `PRESTO`[3] routine `rfifind` was used to identify RFI in the time and frequency domain and the resultant mask was employed in subsequent processing. The observing band was then de-dispersed using the `prepsubband` routine. In the case of the two 4.8-GHz observations, de-dispersion was done only once, at the nominal measured DM of the pulsar (751 ± 3 cm^{-3} pc). Indeed, at such a high observing fre-

[2] http://irsa.ipac.caltech.edu/applications/DUST/

[3] http://www.cv.nrao.edu/~sransom/presto

Table 2. Search-mode observations used to search for radio pulsations from the companion of PSR J1755−2550.

Telescope	Date	Central Freq. (MHz)	Bandwidth (MHz)	Gain (K Jy^{-1})	System Temp. (K)	Sampling Time (μs)	Length (s)	Notes	$S_{\rm limit}$ (mJy)	$L_{\rm limit}$ (mJy kpc^2)
Parkes	04/04/2013	1352	340	0.74	30.6	64.00	4300		0.07	1.7–7.4
Effelsberg	30/08/2015	1347	200	1.37	22	61.44	7150		0.02	0.5–2.1
Effelsberg	31/08/2015	1347	200			248.32	3590	Severe RFI	–	
Effelsberg	01/09/2015	2627	200	1.50	17	248.32	6580	Severe RFI	–	
Effelsberg	02/09/2015	2627	200			248.32	9930	Severe RFI	–	
Effelsberg	04/09/2015	4837	200	1.55	27	61.44	8460		0.02	0.5–2.1
Effelsberg	05/09/2015	4800	125			245.76	8310		0.02	0.5–2.1

quency, the possible pulse drift across the observing band due to an incorrect DM is, within the uncertainty, negligible ($\ll$ 1 ms). On the contrary, at 1.3 GHz, an error of $\sim$ 0.75 cm^{-3} pc is sufficient to cause a pulse drift of 1 ms across an observing band of 400 MHz. This would result in a significant smearing of the signal in the case of an MSP. For this reason, the Parkes and Effelsberg 1.3-GHz observations were de-dispersed at multiple DM values, covering the 2-σ uncertainty range (745–757 cm^{-3} pc), with steps of 0.25 and 0.50 cm^{-3} pc, respectively. This guaranteed a maximum pulse drift of a fraction of a ms across the band, for the best DM trial, in both observations. After de-dispersing and taking the previously-made mask into account, the `prepsubband` routine also summed the frequency channels and referred each time sample to the Solar System barycentre (SSB), thus producing RFI-free, barycentered, de-dispersed time series.

To maximize our search sensitivity, we completely removed the effect of the orbital motion, in order to make the putative companion pulsar appear as if it were isolated. This was achieved utilizing a code that has been developed and previously used for the search of the possible pulsar companion of PSR J0453+1559 (Martinez et al. 2015). The code recalculates the time stamp of each sample of the time series by subtracting the Rømer delay due to the companion orbital motion. The time series is then made uniformly-sampled again through a linear interpolation.

The Rømer delay associated with the companion depends on the characteristics of the companion orbit. The latter are all known with the exception of the projected semi-major axis, $x_{\rm c}$. This, however, is directly related to the projected semi-major axis of the pulsar orbit, through the equation $x_{\rm c} = q\, x_{\rm p}$, where $q = m_{\rm p}/m_{\rm c}$ is the ratio between the mass of the pulsar ($m_{\rm p}$) and that of the companion ($m_{\rm c}$).

Because q is currently unknown, the parameter was searched in the range 0.32 – 3.125. Such an interval more than covers all the plausible values for the possible mass range of NSs. Indeed, assuming a minimum companion mass of 0.8 M$_\odot$ (an even more conservative value than the 0.9 M$_\odot$ derived from our population synthesis) $q \leq 3.125$ for $m_{\rm p} \leq 2.5\,{\rm M}_\odot$; on the other hand, by exchanging the roles, (thus assuming $m_{\rm p} \geq 0.8\,{\rm M}_\odot$ and $m_{\rm c} \leq 2.5\,{\rm M}_\odot$) we have $q \geq 0.32$. The choice of the step size, Δq, was also crucial to minimize the total computational time and to avoid the production of an unnecessarily large number of candidates, without degrading our sensitivity. The criterion used was the following: for each observation, we chose Δq such that, in the case of the best trial value, the residual orbital modulation would cause a maximum pulse drift, seen within the observation length, of less than 0.25 ms (i.e. less than a quarter of spin period of the fastest possible recycled MSPs allowed by theoretical models). This depends on the particular orbital phase range spanned by the companion in the considered observation, which can be easily computed through the pulsar ephemeris. The de-modulated time series was then searched with the `accelsearch` routine, summing up to 8 harmonics and with no acceleration.

The search, done for each q and DM trial, produced several hundred thousands of candidates, which were successively greatly reduced in number by sifting algorithms. The final few thousands of candidates were folded using the corresponding de-dispersed time series and the resulting plots were inspected visually. For the 79 most convincing candidates we also folded the corresponding original filterbank file, to examine the signal in the frequency domain. The vast majority of the signals turned out to be very narrow-band RFI that were not detected during the masking procedure. None of the remaining candidate signals could be clearly ascribed to a pulsar. We conclude that no signal coming from the companion was detected.

One effect that could lead to the non-detection is the degradation in detectability due to scattering broadening. The Cordes & Lazio (2002) electronic density model predicts a scattering timescale of ~66 ms along the line-of-sight of PSR J1755−2550 at an observing frequency of 1 GHz. As mentioned in Section 2.3, we measure a much smaller characteristic scattering timescale of ~13.5(14) ms at 1 GHz. Indeed, the profile of PSR J1755−2550 (see Fig. 3) does not visually appear very scattered. Nonetheless, this amount of scattering will surely prevent any MSP companion from being detected at 1.3 GHz. The scattering broadening should be less severe at 2.6 GHz, but at the same time, the pulsar flux density is also likely to get smaller.

Notwithstanding, our non-detections can be used to estimate limits on the flux density, at the different frequencies, by applying the radiometer equation and assuming a pulse duty cycle of 5 %. In turn, we can infer a luminosity limit of the putative companion. We caution that any derived luminosities are dependent on our knowledge of the pulsar distances, which is not well determined in the case of PSR J1755−2550. In Table 2, we quote the luminosity limit using both the NE2001 and YMW16 electron density model. The NE2001 model gives a higher DM distance compared to the YMW16 model which is responsible for the more conservative (higher) luminosity limit. In either case, our luminosity limit is comparable to the lower bound of the known pulsar population (see, for example, Fig. 11 in Ng et al.

2015). The existence of a weak radio pulsar companion thus cannot be entirely ruled out from our radio search.

6 CONCLUSION

We have observed the recently discovered radio pulsar PSR J1755−2550 (Ng et al. 2015) over a timespan of 2.6 yr using the Lovell Radio Telescope, the Parkes Radio Telescope and the Effelsberg Radio Telescope. We find that this pulsar has a large spin-period derivative of 2.4×10^{-15}. The combination of this value with a slow spin period ($P = 315$ ms) and a non-circular orbit ($e = 0.089$), identifies PSR J1755−2550 as being a non-recycled radio pulsar. From its mass function, we have deduced that PSR J1755−2550 is a member of a binary system with a companion star in the mass range of $0.4 - 2.0\ M_\odot$ at the 95% C.L. The nature of the companion star is most likely restricted to the following three possibilities: a MS star, a WD or a NS. From a comparison to other radio pulsars with hydrogen-rich companions, we find it unlikely that this system has a MS star companion. We thus propose that PSR J1755−2550 is the second-formed object in a double compact object binary.

Applying population synthesis modelling, we find that the chances of PSR J1755−2550 being a WDNS system or a DNS system are roughly equal. Our population synthesis also predicts a minimum companion mass of $0.90\,M_\odot$ and typically a systemic velocity of less than $100\ \mathrm{km\,s^{-1}}$. We conclude that PSR J1755−2550 could very well be a DNS system and we estimate in total a $\sim 10\,\%$ chance of detecting its companion star as a recycled radio pulsar (taking into account both the uncertainty of the nature of the companion star and the beaming fraction in case it is a DNS system). Our effort of searching for the plausible radio pulsar companion returns no detection and our luminosity limit is comparable to the lower bound of the known pulsar population. We also attempted to look for signs of a WD companion in archival Pan-STARRS data, but find no object at the position of PSR J1755−2550 down to a detection limit of $z = 22.3$ and $y = 21.3$.

Whether PSR J1755−2550 hosts a WD or a NS companion star, it will only be the third ever known WDNS, or the third ever known DNS system where we observe the second-formed NS, and thus it represents a rare subpopulation of binary pulsars in either case.

7 ACKNOWLEDGEMENTS

The Parkes Observatory is part of the Australia Telescope National Facility, which is funded by the Commonwealth of Australia for operation as a National Facility managed by CSIRO. A part of this work is based on observations with the 100-m telescope of the MPIfR (Max-Planck-Institut für Radioastronomie) at Effelsberg. Pulsar research at JBCA and access to the Lovell Telescope is supported by a Consolidated Grant from the UK Science and Technology Facilities Council (STFC). CN is supported by an NSERC Discovery Grant and Discovery Accelerator Supplement and by the Canadian Institute for Advanced Research. MUK acknowledges financial support by the DFG Grant: TA 964/1-1 awarded to TMT. AR and PCCF gratefully acknowledge financial support by the European Research Council for the ERC Starting grant BEACON under contract no. 279702, and continuing support from the Max Planck Society. AR is member of the International Max Planck research school for Astronomy and Astrophysics at the Universities of Bonn and Cologne and acknowledges partial support through the Bonn-Cologne Graduate School of Physics and Astronomy. IC and JH are supported by an NSERC Discovery Grant. The Pan-STARRS1 Surveys (PS1) and the PS1 public science archive have been made possible through contributions by the Institute for Astronomy, the University of Hawaii, the Pan-STARRS Project Office, the Max-Planck Society and its participating institutes, the Max Planck Institute for Astronomy, Heidelberg and the Max Planck Institute for Extraterrestrial Physics, Garching, The Johns Hopkins University, Durham University, the University of Edinburgh, the Queen's University Belfast, the Harvard-Smithsonian Center for Astrophysics, the Las Cumbres Observatory Global Telescope Network Incorporated, the National Central University of Taiwan, the Space Telescope Science Institute, the National Aeronautics and Space Administration under Grant No. NNX08AR22G issued through the Planetary Science Division of the NASA Science Mission Directorate, the National Science Foundation Grant No. AST-1238877, the University of Maryland, Eotvos Lorand University (ELTE), the Los Alamos National Laboratory, and the Gordon and Betty Moore Foundation. This research has made use of the NASA/IPAC Infrared Science Archive, which is operated by the Jet Propulsion Laboratory, California Institute of Technology, under contract with the National Aeronautics and Space Administration. The Dunlap Institute is funded by an endowment established by the David Dunlap family and the University of Toronto. We thank Ross Church, and other participants at the NORDITA workshop on *The Physics of Extreme-Gravity Stars*, for discussions on Ca-rich SNe.

REFERENCES

Alpar M. A., Cheng A. F., Ruderman M. A., Shaham J., 1982, Nature, 300, 728
Antoniadis J., Bassa C. G., Wex N., Kramer M., Napiwotzki R., 2011, MNRAS, 412, 580
Bhat N. D. R., Bailes M., Verbiest J. P. W., 2008, Phys. Rev. D, 77, 124017
Bhattacharya D., 2002, Journal of Astrophysics and Astronomy, 23, 67
Bhattacharya D., van den Heuvel E. P. J., 1991, Physics Reports, 203, 1
Brott I., et al., 2011, A&A, 530, A115
Burgay M., et al., 2003, Nature, 426, 531
Chambers K., 2006, in The Advanced Maui Optical and Space Surveillance Technologies Conference. p. E39
Chambers K. C., et al., 2016, preprint, (arXiv:1612.05560)
Chen H.-L., Chen X., Tauris T. M., Han Z., 2013, ApJ, 775, 27
Claret A., Cunha N. C. S., 1997, A&A, 318, 187
Clifton T. R., Lyne A. G., 1986, Nature, 320, 43
Cordes J. M., Lazio T. J. W., 2002, ArXiv: astro-ph/0207156,
Damour T., Deruelle N., 1986, Ann. Inst. Henri Poincaré Phys. Théor., Vol. 44, No. 3, p. 263 - 292, 44, 263
Davies M. B., Ritter H., King A., 2002, MNRAS, 335, 369
Foley R. J., 2015, MNRAS, 452, 2463
Folkner W. M., Williams J. G., Boggs D. H., 2009, Interplanetary Network Progress Report, 178, 1

Gvaramadze V. V., et al., 2017, Nature Astronomy, 1, 0116
Hobbs G. B., Edwards R. T., Manchester R. N., 2006, MNRAS, 369, 655
Holberg J. B., Bergeron P., 2006, AJ, 132, 1221
Hotan A. W., van Straten W., Manchester R. N., 2004, Publ. Astron. Soc. Australia, 21, 302
Kaiser N., et al., 2010, in Ground-based and Airborne Telescopes III. p. 77330E, doi:10.1117/12.859188
Kasliwal M. M., et al., 2012, ApJ, 755, 161
Keith M. J., et al., 2010, MNRAS, 409, 619
Kowalski P. M., Saumon D., 2006, ApJ, 651, L137
Kramer M., Xilouris K. M., Lorimer D. R., Doroshenko O., Jessner A., Wielebinski R., Wolszczan A., Camilo F., 1998, ApJ, 501, 270
Kramer M., et al., 2006, Science, 314, 97
Kruckow M. U., Tauris T. M., Langer N., Kramer M., Izzard R. G., 2018, MNRAS, submitted (arXiv:1801.05433),
Lazarus P., et al., 2014, MNRAS, 437, 1485
Lazarus P., Karuppusamy R., Graikou E., Caballero R. N., Champion D. J., Lee K. J., Verbiest J. P. W., Kramer M., 2016a, MNRAS, 458, 868
Lazarus P., et al., 2016b, ApJ, 831, 150
Lorimer D. R., Kramer M., 2004, Handbook of Pulsar Astronomy, Cambridge University Press
Lorimer D. R., et al., 2006a, MNRAS, 372, 777
Lorimer D. R., Stairs I. H., Freire P. C., et al. 2006b, ApJ, 640, 428
Lyman J. D., Levan A. J., James P. A., Angus C. R., Church R. P., Davies M. B., Tanvir N. R., 2016, MNRAS, 458, 1768
Lyne A. G., McKenna J., 1989, Nature, 340, 367
Lyne A. G., et al., 2004, Science, 303, 1153
Magnier E. A., et al., 2016, preprint, (arXiv:1612.05242)
Manchester R. N., et al., 2000, in Kramer M., Wex N., Wielebinski R., eds, Astronomical Society of the Pacific Conference Series Vol. 202, IAU Colloq. 177: Pulsar Astronomy - 2000 and Beyond. p. 49 (arXiv:astro-ph/9911319)
Martinez J. G., et al., 2015, ApJ, 812, 143
Metzger B. D., 2012, MNRAS, 419, 827
Moriya T. J., et al., 2017, MNRAS, 466, 2085
Ng C., et al., 2015, MNRAS, 450, 2922
Özel F., Freire P., 2016, ARA&A, 54, 401
Paxton B., et al., 2013, preprint, (arXiv:1301.0319)
Portegies Zwart S. F., Yungelson L. R., 1999, MNRAS, 309, 26
Roberts M. S. E., 2011, in Burgay M., D'Amico N., Esposito P., Pellizzoni A., Possenti A., eds, American Institute of Physics Conference Series Vol. 1357, American Institute of Physics Conference Series. pp 127–130 (arXiv:1103.0819), doi:10.1063/1.3615095
Schlafly E. F., Finkbeiner D. P., 2011, ApJ, 737, 103
Schlegel D. J., Finkbeiner D. P., Davis M., 1998, ApJ, 500, 525
Shklovskii I. S., 1970, Soviet Ast., 13, 562
Stokes G. H., Taylor J. H., Dewey R. J., 1985, ApJ, 294, L21
Tauris T. M., 2011, in Schmidtobreick L., Schreiber M. R., Tappert C., eds, Astronomical Society of the Pacific Conference Series Vol. 447, Evolution of Compact Binaries. p. 285 (arXiv:1106.0897)
Tauris T. M., Savonije G. J., 1999, A&A, 350, 928
Tauris T. M., Sennels T., 2000, A&A, 355, 236
Tauris T. M., van den Heuvel E. P. J., 2006, Formation and evolution of compact stellar X-ray sources. Cambridge University Press, pp 623–665
Tauris T. M., Langer N., Kramer M., 2012, MNRAS, 425, 1601
Tauris T. M., Langer N., Podsiadlowski P., 2015, MNRAS, 451, 2123
Tauris T. M., et al., 2017, ApJ, 846, 170
Taylor J. H., 1992, Royal Society of London Philosophical Transactions Series A, 341, 117
Thorsett S. E., Chakrabarty D., 1999, ApJ, 512, 288
Tremblay P.-E., Bergeron P., Gianninas A., 2011, ApJ, 730, 128
Voss R., Tauris T. M., 2003, MNRAS, 342, 1169
Wang J. B., et al., 2017, MNRAS, 469, 425
Weisberg J. M., Taylor J. H., 1981, General Relativity and Gravitation, 13, 1
Weltevrede P., Johnston S., 2008, Monthly Notices of the Royal Astronomical Society, 391, 1210
Yao J. M., Manchester R. N., Wang N., 2017, ApJ, 835, 29
van Kerkwijk M. H., Kulkarni S. R., 1999, ApJ, 516, L25
van Leeuwen J., et al., 2015, ApJ, 798, 118

This paper has been typeset from a TEX/LATEX file prepared by the author.

4.9 Supplementary material

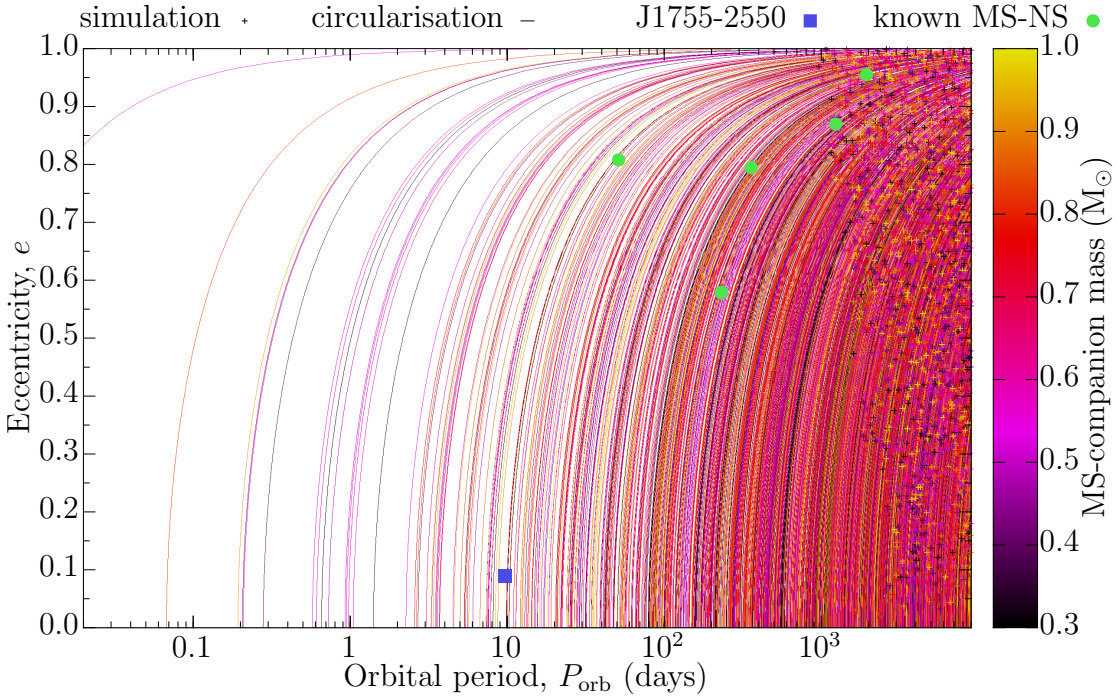

Figure 4.12: Orbital eccentricity versus orbital period of MS-NS binaries, including circularisation effects, for $\alpha_{\rm CE} = 0.5$ and $\alpha_{\rm th} = 0.5$. Furthermore, PSR J1755−2550 and known MS-NS binaries with a young pulsar (Manchester et al., 2005) are shown. The binaries in long orbits would have a circularisation timescale larger than the Hubble time.

To check the possibility of a MS companion to PSR J1755−2550, simulations show that it is very difficult to create a MS-NS binary with low eccentricity and an orbital period around 10 days (Figs 4.12 and 4.13). Even for very efficient CE ejection there are no such systems directly formed after the NS formation when limiting the companion mass to be below 1 $M_\odot$[1]. The only way is to produce them via circularisation after the NS formed. With the long orbital periods, however, an extended companion (already evolved beyond its MS) would be required to obtain an efficient circularisation via tides. Possibly some surrounding left material from the CE or the SN ejection may help to circularise faster. If the circularisation effect is enhanced for whatever reason systems like PSR J1755−2550 ($e = 0.08935$) will form this way, but the enhanced circularisation effect will quickly push the eccentricity very close to zero. This results from the strong period dependence of the circularisation timescale (Section 1.3.1.2) and makes it unlikely to observe such a short lasting phase.

When comparing Fig. 4.12 to Fig. 4.4 the Redbacks are not well represented with the default assumptions of CE ejection efficiency. Meanwhile Fig. 4.13 shows that a more efficient CE ejection would solve the problem with the Redbacks

[1]Most of the MS-NS binaries with a young pulsar shown in Figs 4.12 and 4.13 have a minimum companion mass above 3 $M_\odot$, allowing for wider systems after a CE.

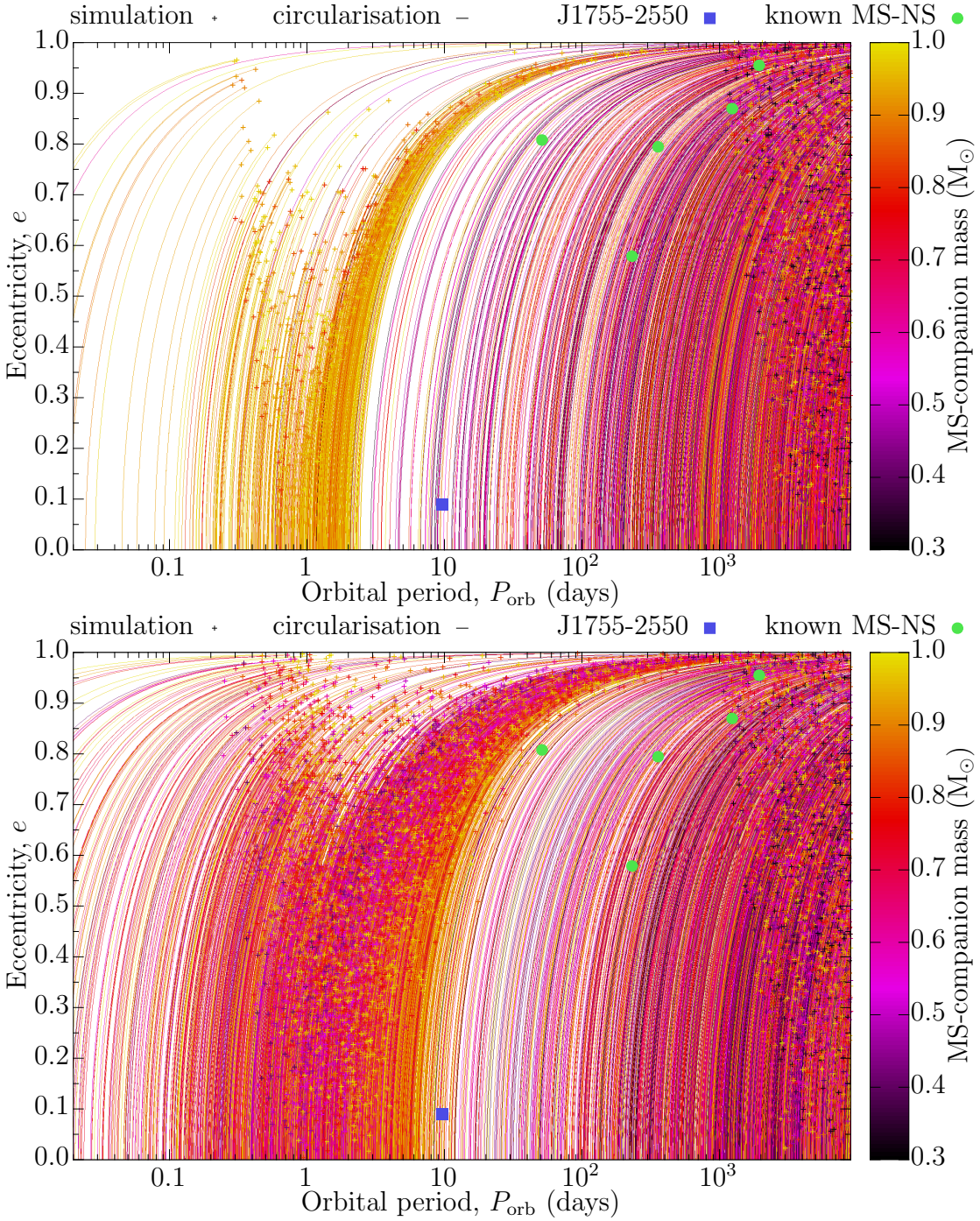

Figure 4.13: As Fig. 4.12 with more efficient CE ejection, $\alpha_{\rm CE} = 0.7$ and $\alpha_{\rm th} = 0.7$ (top panel), and $\alpha_{\rm CE} = 1.0$ and $\alpha_{\rm th} = 1.0$ (bottom panel).

appearing also in the correct period range. This leads to the conclusion that the CE ejection is either more efficient only for low-mass stars or in general. The second possibility would mainly change the high-mass end while the intermediate-mass range would be less effected by increasing the CE ejection efficiency, cf. Figs 3.47 and B.49.

Chapter 5

Conclusions and outlook

The most uncertain phase in binary evolution is the CE phase. Such a phase is short lasting and the internal processes are hidden for observations from the outside. Thus, theoretical investigation of this phase is essential. Only with the observable outcome of such a phase, the most important physical processes during a CE can be understood. The most crucial unknown is the bifurcation point which separates the ejected material from the remaining core. Which has strong implications for the energy required for the ejection of the envelope. As it is believed that the dominant energy source for the ejection is the energy released by the orbital decay during this phase, the final separation is poorly constrained. However, the resulting separation of the binary is an important factor for determining the its subsequent evolution. Various other aspects of CE evolution are also investigated here, but these are expected to have a smaller influence on the outcome. Nevertheless, additional energy sources, e.g. recombination energy or energy released by accretion onto the in-spiralling object, and losses by radiation have to be taken into account when having a better control on the bifurcation point. Finally, it is shown that double WD binaries, DNSs and double BH binaries should all be able to form via a CE phase, which is in agreement with observations. Particularly in binaries with a massive donor star of the CE, it is expected that the massive donor star collapses into a BH before GWR can lead to an early merger event. Thus, it is demonstrated that the standard formation scenario of BH-BH binaries via a CE evolution can explain the origin of the recent LIGO detections. This, in particular, includes the most massive BH-BH merger known to date, GW150914.

Binary evolution including a CE phase is believed to be the main source of close DCO binaries. These are well observed when the binary contains a NS being active as a PSR in the radio regime or when the compact object produces X-rays through accretion. Most accreting compact objects have still the progenitor of the second compact object as companion. The detection of GW signals provides a new window to observe merging DCO binaries. The distributions of observed DNS and merging binaries are investigated statistically using simulations. Therefore, the new grid-based[1] binary stellar population synthesis code ComBinE is developed

[1]The interpolation of a grid of stellar models allows for fast and consistent update of stellar evolution.

to study the standard formation channel including a CE phase. The most crucial phases of binary evolution are mass-transfer phases, CE phases and SN explosions. In the thesis, the latest results of Case BB RLO are included in the mass-transfer treatment. The implemented CE treatment makes use of self-consistent binding energies. Finally, an advanced recipe of the SNe kicks, which depend on the amount of envelope stripping during the evolution of their progenitors, is applied. Hence, the results obtained with ComBinE are based on the most recent understanding of overall binary evolution which is applicable to population synthesis methods. Population synthesis methods are used to calculate large ensembles of binaries all the way through their evolution to a possible final merger of two compact objects. Only after the formation of a DCO binary the signal of a merger event is detectable with current ground bases GW observatories at large distances. The population synthesis simulations presented here are able to reproduce all the known DNS and the reported GW merger events at the same time. The calibration with the DNS binaries, known from PSR observations, already puts some constraints on important physics during the binary evolution. The calibration mainly requires a low accretion efficiency. Remaining quantitative discrepancies in the frequency of the DNS mass distribution are deemed to be related to the EC SNe. In order to solve this deviation, the EC SNe would need to be suppressed or produce more massive NSs (about 1.30 to 1.32 $M_\odot$) than predicted by theory. Further constraints can be made by future observations of GW merger events and pulsars in binaries in combination with the presented dependence of observables on the input physics. All mergers of double BH binaries and the DNS system detected so far are represented in the models depending on metallicity. The resulting merger-rate densities of the simulations with ComBinE are in agreement with estimated rates from CC SN, short GRBs and the production of heavy r-process elements. However, for DNS mergers the merger rates are on the low side of the empirically determined rates by LIGO collaboration and the Virgo collaboration (Abbott et al., 2017a,c). Therefore, only a moderate increase in the detection rate is predicted when the observatories reach design sensitivity in the upcoming runs. Also the investigation of mixed NS/BH binaries where the NS becomes a recycled PSR yields low changes to observe such a system.

ComBinE is also applied to a different kind of problem, namely constraining the unseen companion of the young pulsar PSR J1755−2550. While an argument based on the pure assumption of a random inclination angle of the orbit with respect to the line-of-sight indicates a low-mass star or WD companion the statistical analysis with ComBinE favours a NS or massive WD as companion for the observed orbital parameters. This allows a prediction of the inclination angle of PSR J1755−2550 and give a hint for the search for the companion as the search in archival data did not facilitate identification of the companion star. If PSR J1755−2550 is a WD-NS binary, it is expected that the systemic velocity is probably below 100 km s^{-1}. Tight versions of these mixed WD/NS systems may be progenitors of calcium-rich SNe which usually show a large distance to their host galaxy. The relatively low systemic velocities expected for NS progenitors which get (ultra) stripped by a WD companion would result in a population which stays

close to its birth place in a large galaxy like the MW. On the other hand, if the NS forms first the systemic velocities are probably larger than in the case the WD forms first. As the NS-WD binaries are additionally one order of magnitude more common than the WD-NS systems, according to the simulations, calcium-rich SNe would originate from a WD/NS binary where the NS forms first.

With a population synthesis code like ComBinE more aspects of binary evolution can be studied. Those include the evolution leading to the various types of SNe, accreting binaries seen as LMXBs or HMXBs, cluster populations at different ages, runaway stars and many more topics related to astrophysical sources with an origin in a binary system. The new field of GW observation will provide unique information which cannot be inferred from observations in the usual electromagnetic spectrum. The continued development of ground based GW observatories will give more insight into merger events of compact objects in binaries. New spaceborn GW observatories will access larger parts of the GW spectrum in order to observe other sources, e.g. super massive BHs. The comparison to additional observations of different stages of binary evolution will allow further constraints on the physical processes being at work. Meanwhile, further predictions by theoretical modelling will help to refine future observations.

Appendix A

ComBinE Manual

ComBinE - Manual

Binary population synthesis code

Matthias U. Kruckow

February 2, 2018

1 Introduction

This code, ComBinE, is based on Starburst developed by Tauris & Voss in 2001, see Voss and Tauris (2003). The new version has the main goal to produce reliable event rates of mergers of stellar mass compact objects for gravitational wave detectors like LIGO. This new code is developed by Matthias Kruckow as part of a DFG-PhD project (Grant: TA 964/1-1) under supervision of Thomas Tauris.

2 Run the code

If the code is not compiled jet, you should use the makefile with the command `make ComBinE` in the `ComBinE` directory.

The easiest way to run the program is by simply typing `./ComBinE` in the main directory of ComBinE[1]. This will use some standard parameters for the run.

To run the code in a different directory you have to place a file called `tablelocation.txt` in the directory where you run the code. In this file the place of the tables[2] should be specified, the default place is `./tables/`. If you use a common directory to store the tables you should make sure that you have write access to this directory. If some integration tables, see section 3.7.1, are missing or not up to date they will be created by the code.

Note that the code will write some files in the current directory. They will be named always in the same way. So you should not run more than one simulation with ComBinE in one directory. Otherwise the output files will be overwritten, see section 2.5.

2.1 Set parameters

To change the parameters there are three ways possible. They will be described in the following sections.

2.1.1 Parameter-file: `data.in`

You can use a parameter-file called `data.in`. This has to be in the directory were you run the code. To read it in just run the command `./ComBinE -2`. An example `data.in` file looks like:

```
1 NUMBER OF PROCESSORS TO USE (<=0 AUTOMATIC): 1
2 SEED: 908070605040302010
3 NUMBER: 1000000
4 MAXIMUM PRIMARY MASS (MSUN): 100.0
5 MINIMUM PRIMARY MASS (MSUN): 4.0
6 MAXIMUM SECONDARY MASS (MSUN): 100.0
7 MINIMUM SECONDARY MASS (MSUN): 1.0
```

[1] All following commands and file references will assume the current directory to be the main directory of ComBinE.

[2] Including the stellar and integration tables, see sections 2.6 and 3.7.1.

```
 8 MAXIMUM SEMI-MAJOR AXIS (RSUN): 10000.0
 9 MINIMUM SEMI-MAJOR AXIS (RSUN): 2.0
10 WIND MASS LOSS DURING RLO (%): 20.0
11 RLO MASS EJECTION PARAMETER (%): 75.0
12 RLO RADIUS PARAMETER OF CIRCUMBINARY TORUS: 2.0
13 RLO MASS-FRACTION TO CIRCUMBINARY TORUS (%): 0.0
14 CE EFFICIENCY PARAMETER (%): 50.0
15 LAMBDA: 1.0
16 QLIMIT: 2.5
17 MHECE: -3.3
18 KICK VELOCITY (KM/S; <0 TAKE RANDOM VALUE): -1.0
19 LAMBDA INTERPOLATION FACTOR (0.0-1.0 INTERPOLATE; <0.0 OLD
       TABLES; >1.0 CONSTANT FAKTOR OF LAMBDA_G[=2.0 VIRIAL
       EQULIBRIUM]): 0.5
20 MOTION INTEGRATOR (=0 NO GALACTIC MOTION; =1 RUNGEKUTTA4): 1
21 GALACTIC POTENTIAL (=0 NO GALACTIC MOTION; =1 MW-POTENTIAL BY
       ALLEN&SANTILLAN 1991): 0
22 OUTPUT FORMAT (=M MASSIVE OUTPUT; =T TINY OUTPUT): M
23 INITIAL MASS FUNCTION (=1 SALPETER 1955; =2 KROUPA 2008): 1
24 INITIAL MASS-RATIO DISTRIBUTION (=1 KUIPER 1935; =2 FLAT; =3
       SANA+ 2012): 1
25 INITIAL SEMI-MAJOR AXIS DISTRIBUTION (=1 ABT 1983; =2 PERIOD-
       DISTRIBUTION KROUPA 2008; =3 SANA+ 2012): 1
26 INITIAL ECCENTRICITY DISTRIBUTION (=0 CIRCULAR; =1 THERMAL(
       HEGGIE 1975); =2 FLAT; =3 FLAT IN ANGULAR MOMENTUM): 0
27 INITIAL AGE DISTRIBUTION (=0 ALL AT ZAMS): 0
28 INITIAL METALLICITY DISTRIBUTION (=0 MW-METALLICITY; =-1 LMC-
       METALLICITY; =-2 SMC-METALLICITY; =-3 IZw18-METALLICITY): 0
29 INITIAL ROTATION DISTRIBUTION (=-1 SYNCHRONISED; =0 NON-
       ROTATING): 0
30 INITIAL POSITION IN THE GALAXY (=-1 SUN; =0 AT GALACTIC CENTER)
       : 0
31 INITIAL VELOCITY IN THE GALAXY (=-1 SUN; =0 AT REST): 0
32 INITIAL STELLAR DENSITY (=0 FIELD STAR): 0
```

For more information about the individual parameters see section 2.2. You should make sure, that your `data.in` file only uses ":" right before the value to read in and the order of the parameters stays the same. You can check that all parameters are read in correctly in the `data.out` file, see section 2.5.1.

2.1.2 Command line arguments

You can run the program with command line arguments. Every command line argument should be separated with a space. The first Argument specifies what kind of run is done.

`-1` Run a single model with default parameters, where
a second argument sets the primary mass ($M_\odot$),
a third argument sets the secondary mass ($M_\odot$),
a fourth argument sets the semi-major axis ($R_\odot$)
and a fifth argument sets the random seed.
Example: `./ComBinE -1 50.0 40.0 300.0 -21` this calculates one system with a primary mass of 50 $M_\odot$, a secondary mass of 40 $M_\odot$ and a semi-major axis of 300 $R_\odot$, which corresponds to an orbital period of ≈ 63.6 d as initial values. If you specify less than five arguments the not specified ones are taken from the default values or specified in the user interface.

`-2` Run with the parameters from `data.in` file, see section 2.1.1.

`-3` Run a grid between minimum and maximum values of the primary mass, secondary mass and semi-major axis in log-scale. Those values can be changed in the user interface.

`-4` Run a single model like in the old code StarBurst (Voss and Tauris, 2003), you can specify parameters like for the option `-1`.

`-11` Run a single model in debug mode, you can specify parameters like for the option `-1`.

> 0 Run with default values, see section 2.2, and this and only first argument as random seed.

When ever no random seed is specified it is generated from the current time.

2.1.3 Change the parameters in the code

The last and least way is to change the default parameters in the code, recompile it and run it. This you should only do if you want to change the default values permanently. To do it a bit more suitable, you can modify the values in the desired functions within the user interface, see section 3.9.

2.2 Input parameter description

In this section all important parameters of the program will be described. The parameters are categorised if they belong to numerics, output specifications or to the physics. Within each section the parameters are in the same order as defined in the code. The bullets are the names of the variables in the code.

2.2.1 Numerics

`parallel` The number of parallel processes which will be used by the code. Its default value is 1. It can be specified in the `data.in` file in line 1. You should make sure that the value is smaller or equal to the number of available processors.

To create one process for each processor use a value smaller or equal to 0 and then the program will determine the number of processors. The speed gain with multiple processors is not linear. To create grids of input parameters you should use one processor per ComBinE run and start several threads of ComBinE in different directories yourself.

`seed` The random seed. If it is set to its default value 0 a random seed is generated from the system time. You can also specify the seed in line 2 in the `data.in` file. In this way you can rerun a simulation with the same order of random numbers which might be useful to recreate a single model out of a population synthesis run.

`number` The number of systems which will be calculated. It can be specified in the `data.in` file in line 3 and should be larger than 0 otherwise the code does nothing. Its maximum value is 9 223 372 036 854 775 807 which is the upper boundary of the `long` integer type. The time the program runs scales for large `number` values linearly where 1 000 000 000 corresponds to about 1 d of run time.

`accuracy` The relative accuracy to which the code will check the calculations to be unaffected by numerical uncertainties. Its default value is 10^{-10}. Be aware that lowering this values to close to the precision of `double` type may cause some numerical instabilities.

`galintegrator` The integrator routine to use for the motion in the galactic potential. It can be set in line 20 in the `data.in` file. The possible values are:

- `0` no motion in the galaxy
- `1` standard Runge-Kutta 4 integrator — default value

2.2.2 Output

`screen` It enables and disables the output of the evolution information of every calculated system. As default it is `true` for the first ten calculated systems which holds for single and population synthesis runs. If it is true at the end of the calculation of a system its evolution information is printed to the screen, but the intermediate outputs only start when it is `true`.

`output` It specifies the amount of the screen-output. The possible values are `M` for massive output and `T` for tiny output. It can be set in the `data.in` file in line 22. The massive output will give you all information about the evolution of the binary system at any phase, including variable names and units. The tiny output contains only the most important values in a compressed format.

`debug` This is only for debugging and will run the program in debug mode. There it will give a lot of information during the calculation and the full tracks of the stars used for the calculation at the end. The default value is `false`.

2.2.3 Physics

Initial Parameters

Mp, Mp_max,Mp_min, IMF

The primary star is the initially more massive star. Its mass in $M_\odot$ will be taken from the given range between `Mp_max` and `Mp_min`. Their default values of 100 and 4 can be changed in lines 4 and 5 of the `data.in` file, respectively. `Mp` is the initial mass for a single system. Its default in a single run is `Mp_max` if not specified otherwise. In a population synthesis run the initial primary mass is taken randomly from a distribution function. This function is controlled by the variable `IMF`.
Possible `IMF`-values are (line 23 of the `data.in` file):

≤`-10`	user defined, see section 3.9	
`1`	Salpeter IMF (Salpeter, 1955; Scalo, 1986)	default value
`2`	canonical IMF (Kroupa, 2008)	

Ms, Ms_max,Ms_min, q,qdist

The mass of the secondary star is determined by the primary mass and the mass ratio q. Nevertheless, in the `data.in` file you specify a range for the secondary mass in lines 6 and 7, respectively. Otherwise the default range is between 1 and Mp_max. This will be converted into a range for the mass ratio depending on the primary mass, such that $q \leq 1$ holds. `qdist` tells the program from which distribution the mass ratio should be taken.
Possible `qdist`-values are (line 24 of the `data.in` file):

≤`-10`	user defined, see section 3.9	
`1`	$f(q) = \frac{2}{(1+q)^2}$, see equation (4) in Kuiper (1935)	default value
`2`	flat: $f(q) = 1$	
`3`	$f(q) \propto q^{-0.1}$ (Sana et al., 2012)	

a, a_max,a_min, adist

The semi-major axis range in $R_\odot$ is between 2 and 10000 as default or specified in lines 8 and 9 of the `data.in` file. The initial separation has a lower limit depending on the masses of the stars to create no contact systems initially.
Possible `adist`-values to determine the underlying initial orbital period distribution are (line 25 of the `data.in` file):

≤`-10`	user defined, see section 3.9	
`1`	flat in $\log(P)$, where P is the orbital period (Abt, 1983)	default value
`2`	period distribution from Kroupa (2008)	
`3`	$f(P) \propto P^{-0.55}$ (Sana et al., 2012)	

e, edist

The eccentricity `e` is determined by `edist` with possible values (line 26 of the `data.in` file):

≤`-10`	user defined, see section 3.9	

0	$e = 0$, all initially circularised	default value
1	$f(e) = 2 \cdot e$, thermal (Heggie, 1975)	
2	flat: $f(e) = 1$	
3	flat in orbital angular momentum L and constant orbital binding energy, so $e \propto \sqrt{1 - L^2}$	

t, tdist The initial age is at ZAMS for all stars as default.
The possible distribution values are (line 27 of the `data.in` file):

≤-10	user defined, see section 3.9	
0	start at ZAMS	default value

metall, Zdist The metallicity is given by `Zdist` which depend on the available stellar tables (section 2.6) and can be (line 28 of the `data.in` file):

≤-10	user defined, see section 3.9	
0	Milky Way metallicity ($Z = 0.0088$)	default value
-1	LMC metallicity ($Z = 0.0047$)	
-2	SMC metallicity ($Z = 0.0021$)	
-3	IZw18 metallicity ($Z = 0.0002$)	

omegap,omegas, rotdist The spin of the stars ω is determined by the value of `rotdist` and depend on the available stellar tables (section 2.6).
Its possible values are (line 29 of the `data.in` file):

≤-10	user defined, see section 3.9	
-1	synchronised (no effect as long as there are no rotating stellar tables provided)	
0	non-rotating	default value

x,y,z, Rdist The galactic position in Cartesian coordinates depends on `Rdist`.
Possible `Rdist`-values are (line 30 of the `data.in` file):

≤-10	user defined, see section 3.9	
-1	solar position in the Milky Way $\vec{R}^{\mathrm{T}}_{\mathrm{sun}} = (-8.5, 0.0, 0.0)$ kpc	
0	at galactic center	default value
1	random in the disk potential of Allen and Santillan (1991)	

vx,vy,vz, Vdist The three dimensional velocity of the binary system in the galaxy is determined by `Vdist` as (line 31 of the `data.in` file):

≤-10	user defined, see section 3.9	
-1	solar velocity in the Milky Way $\vec{V}^{\mathrm{T}}_{\mathrm{sun}} = (10.0, 235.0, 7.0)$ km/s	
0	at rest	default value

`1` perpendicular to the acceleration in the galactic potential to be balanced by the centrifugal force

`rhostar`, `rhodist` To estimate the encounter rate with other stars the number density of stars around a system is used. Its unit is pc^{-3}. Stellar encounters are not yet implemented.
The implemented distributions are (line 32 of the `data.in` file):

$\leq$`-10` user defined, see section 3.9

`0` field star, no encounters — default value

Evolution Parameters

`alphaRLO` The fraction[3] of material during Roche-lobe overflow which is directly lost from the system as an isotropic wind from the donor star. Its default value is 20% and it can be specified in line 10 of the `data.in` file.

`beta`, `beta_const` The fraction[3] of material which cannot be accreted by the companion during Roche-lobe overflow. This material will be isotropically re-emitted from the accretor with its specific orbital momentum. You can specify a minimum constant fraction in `beta_const` in line 11 of the `data.in` file. Its default is 75%. The final value of `beta` is at least `beta_const` but will increase if the Eddington accretion limit is reached.

`Gamma` The square root of the ratio of the radius of a circumbinary torus and the semi-major axis of the binary, see Soberman et al. (1997). The default value is 2.0 and it can be changed in line 12 of the `data.in` file.

`delta` This parameter contains the fraction[3] of the material which goes into a circumbinary torus. You can change the default value of 0% in line 13 of the `data.in` file.

`qlimit` When a normal star is filling its Roche lobe a limit in the mass ratio determines whether the outcome is a stable Roche-lobe overflow or a common envelope. The default of this limit is 2.5 and it can be specified otherwise in line 16 of the `data.in` file.

`Mhece` For a naked helium star orbiting a non-degenerate star (e.g. a main sequence star) the transition between Roche-lobe overflow and common envelope is given by the mass of the naked helium star. In line 17 in the `data.in` file you can change the default value of $-3.3\,M_\odot$. If you put a negative mass limit there it is ignored and the `qlimit` is applied for mass transfer from a naked helium star onto a non-degenerate star instead.

[3]The sum of `alphaRLO`, `beta_const` and `delta` should be between 0 and 1.

`alphaCE` The efficiency of converting the orbital energy into kinetic energy of the common envelope, to unbind it, is as default 50%. In line 14 of the `data.in` file the value can be changed.

`lambda`, `lambda_const` The λ-value represents the structure of the stellar envelope. It gives information on how easily the common envelope can be ejected. `lambda_const=1.0` is a default if no other values are available and it can be set in line 15 of the `data.in` file. The λ values are normally taken from calculated tables.

`alphaTH` This is used to interpolate between a pure gravitational λ_G and λ_B taking pressure and radiation into account, too. A value like the default of 0.5, which is between 0.0 and 1.0, interpolates the values in the stellar tables, see section 2.6. A value smaller than 0.0 uses the old tables from Dewi and Tauris (2000). A value larger than 1.0 multiplies the value with the pure gravitational λ_G so that a value of 2.0 corresponds to virial equilibrium.
The value in line 19 of the `data.in` file can be changed to:

- < 0 use the old λ tables from Dewi and Tauris (2000)
- $\in [0, 1]$ interpolate between λ_G and λ_B where the value gives the fraction of the pressure and radiation taken into account 0.5 is the default value
- > 1 use as a constant factor of λ_G

`kickv` This parameter specifies the kick velocity in km/s which a new-formed neutron star or black hole gets. A value of 0.0 corresponds to no kick and a negative value like the default -1.0 uses different distribution functions, see section 3.6.4. You can change this value at line 18 in the `data.in` file to:

- ≥ 0 fixed value in km/s for all kicks
- < 0 get kick from distributions, see section 3.6.4 default value is -1.0

`galpotential` This flag indicates which galactic potential should be used for the motion in the galaxy. Possible values are (line 21 of the `data.in` file):

- `0` no galactic potential default value
- `1` Milky Way potential by Allen and Santillan (1991)

2.3 Single run

To evolve a single system, I recommend to use the command line arguments, see section 2.1.2. With them you can specify the primary and secondary mass, the semi-major axis and a random seed for the kick generator. You can although use a `data.in` file and specify the number of systems to 1.

2.4 Population synthesis

In general, the code is designed to do population synthesis of a large number of binary systems. To check if every thing is running the first 10 calculated systems are displayed

like in the single run. With the `output` option `M`, a speed estimate is written to `stderr`. This output is written every $\frac{\texttt{number}}{100}$ systems or every 10^6 systems.

A lot of information about the run can be written to output files which will be described in the section 2.5.

2.5 Output files

ComBinE will create some files with data in the current directory. If such files are already existing they will be overwritten. Therefore you should not run ComBinE in the same directory two times if you do not want to delete the results of the first run.

The following subsections will give you an overview of which files are created and which data will be stored in them.

2.5.1 `data.out`

This file contains the main output of a population synthesis run. The input parameters are written at the top, followed by multiple counters with their descriptions and values. Here is an example file:

```
1  #parallel        seed      number   (Mp_max,Mp_min) (Ms_max,Ms_min)
       (a_max,a_min)    alphaRLO          beta_const        Gamma
       delta    alphaCE lambda_const     qlimit   Mhece    kickv
       alphaTH galintegrator    galpotential     output   IMF
       qdist    adist    edist    tdist    Zdist    rotdist  Rdist
       Vdist    rhodist
2  1        908070605040302010       1000000000       (100,4) (100,1)
       (10000,2)        0.2      0.75     2        0        0.5      1
              2.5      -3.3     -1       0.5      1        0        M
              1        1        1        0        0        0        0
              0        0        0
3  #counts RLO: total       case A  case B/C         case BB
4  360440141        62140512        133943972        164355657
5  #counts CE: total        case A  case B/C         case BB
6  731225685        336322797       386068608        8834280
7  #counts merger: total    in RLO  in CE    in SN
8  567278533        50847   566493576        734110
9  #counts SN/PN: SN        NS      BH       PN       WD
10 121905253        107597339       14307914         754149927
             754149927
11 #number of systems       survive(SS)      destroyed(DS)
12 1000000000       330457988       669542012
13 #number of SS    WD-WD   WD-NS   WD-BH   NS-WD   NS-NS   NS-BH
         BH-WD   BH-NS   BH-BH   unknown
14 330457988        328024869       195818   0       1777434  105428
        85       87830    231338   35186    0
```

```
15 #SS t_gw<1e+10yr          WD-WD   WD-NS   WD-BH   NS-WD   NS-NS
       NS-BH   BH-WD   BH-NS   BH-BH   unknown
16 20589707          20400867          39953   0       34020   46198
       0       1827    62751   4091    0
17 #number of DS     merged sys.       disrupted sys.  unknown
18 669542012         567278533         102263479       0
```

In lines 1 and 2, you find the header and the values of the input parameters, see sections 2.1.1 and 2.2. The next four pairs of lines, 3-4, 5-6, 7-8 and 9-10, contain the header and the values for the counts of events, like Roche-lobe overflow(RLO), common envelope(CE), merger and white dwarf (WD), neutron star (NS) or black hole (BH) formation, respectively.

Then follows the number of systems which survive as a binary of two compact objects or are destroyed, in lines 11 and 12. The details of survived systems are in the lines 13 to 16. The header in line 13 shows that the survived systems are grouped depending on which compact objects they host. The order of the compact objects is their formation order. The values are in line 14. The last column called `unknown` should be always 0 otherwise there are systems formed in an unconsidered way. The lines 15 and 16 represent a sub-sample of the previous two lines with the additional condition that the time to merge by gravitational wave radiation $t_{\rm gw} \leq 10^{10}$ yr. The line 18 gives more details how the systems are destroyed, while line 17 contains its header.

This output can be switched off by setting `data` to `false`.

2.5.2 `hist` files

The code provides some routines to create histograms, see section 3.8. These histograms can be written to files and will get the extension `.hist`. The first line contains some dimensional data about the histogram. The second line is the header of the following data: The first data-column contains the binned value. The second one is filled either by the histogram counts or by the normalised counts to the bin width, see section 3.8. All other columns contain the data of the sub-samples if specified.

2.5.3 `dist` files

The code can also print out tables with various specific data, e.g. all values of semi-major axis at the end of the evolution of a system. To enable writing the `.dist` files you have to set `dist=true` in the code. But be aware that this kind of output will store a lot of data when you run a large number of systems. All files with the ending `.dist` contain a header line which tells you about the content in the different columns. Each row will represent one calculated system.

As default an additional table called `distribution.csv` is created. It contains information about a specific kind of systems which appear during a population synthesis run. The systems written their as default are all surviving binaries containing only neutron stars or black holes.

2.6 Stellar tables

The code interpolates tables of stellar evolution. These tables have to be provided for ComBinE from the user. As default the tables are from Brott et al. (2011); Szécsi et al. (2015) and an extension of this grid, calculated by Matthias Kruckow (Kruckow et al., 2018). They should contain the following columns:

1. total mass m in $M_\odot$, where the first row is taken as initial mass
2. age t in yr, where 0.0 indicates the ZAMS
3. radius r in $R_\odot$
4. core mass cm in $M_\odot$
5. luminosity L as $\log_{10}\left(\frac{L}{L_\odot}\right)$
6. effective temperature $T_{\rm eff}$ as $\log_{10}\left(\frac{T_{\rm eff}}{K}\right)$
7. $\lambda = \frac{G \cdot m \cdot (m-cm)}{r \cdot E_{\rm bind}}$ using only the gravitational binding energy
8. λ using the gravitational binding and the thermodynamic energy

The code normally differentiates between main sequence and post-main sequence stars. Therefore the last line of the evolutionary tables contains the negative index of the TAMS.

The code uses tables for normal stars and helium stars. These tables have to be placed in the directories `./tables/*stars/` and `./tables/*hestars/` respectively. Here `*` indicated the grid being `MW`, `LMC`, `SMC` or `IZw18`. If you want to place the directory `tables` with its subdirectories elsewhere than in the current directory, have a look at the beginning of section 2 how to provide the location to the code.

3 Code structure

The code is split into several sub-files. The sub-files are in the directory `ComBinElib`. There is a header for all the files in this directory called `ComBinElib.h`. The main directory contains a make-file to compile the code. To make changes, or getting some other output, you can use the user interface, see section 3.9. In the following sections it will be described how the code works.

3.1 Main structure

The following flowchart in Figure 1 shows what the code is doing.

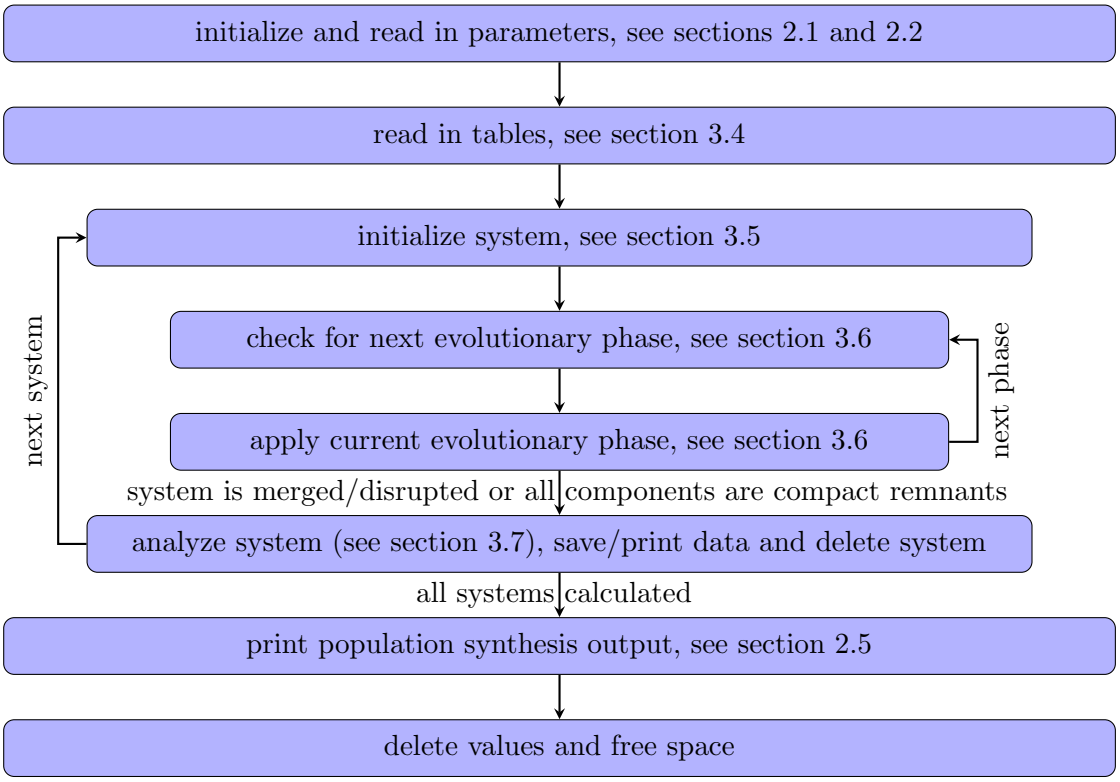

Figure 1: Flowchart of the main routine.

3.2 Constants

In the code are several constants defined which are either physical constants or conversion factors between different units, see table 1. All constants are from type `double`. The standard units in the code are $M_\odot$, $R_\odot$ and yr.

Table 1: Defined constants in the code.

name	description
`Msun`	the mass of the sun: $1\,M_\odot = 1.9885 \cdot 10^{30}$ kg (Olive and Particle Data Group, 2014)
`Rsun`	the radius of the sun: $1\,R_\odot = 6.9551 \cdot 10^{8}$ m (Olive and Particle Data Group, 2014)
`yr`	sidereal year: 1 yr = 31558149.8 s (Olive and Particle Data Group, 2014)
`Lsun`	the luminosity of the sun: $1\,L_\odot = 3.828 \cdot 10^{26}\,\mathrm{kg\,m^2\,s^{-3}}$ (Olive and Particle Data Group, 2014), in the code this value is converted to $\approx 12.5076\,M_\odot\,R_\odot^2\,\mathrm{yr}^{-3}$
`G`	the gravitational constant: $G_N = 6.67384 \cdot 10^{-11}\,\mathrm{m^3\,kg^{-1}\,s^{-2}}$ (Olive and Particle Data Group, 2014), in the code it is $\approx 3.92839 \cdot 10^{8}\,R_\odot^3\,M_\odot^{-1}\,\mathrm{yr}^{-2}$

Table 1 continued.

name	description
`c`	the speed of light: $c = 299792458\ \mathrm{m\,s^{-1}}$ (Olive and Particle Data Group, 2014), which is converted to $\approx 1.36028 \cdot 10^7\ \mathrm{R_\odot\,yr^{-1}}$ within the code
`MH`	the proton mass/mass of ionized hydrogen: $m_p = 1.672621777 \cdot 10^{-27}$ kg (Olive and Particle Data Group, 2014), the code uses the value of $\approx 8.41147 \cdot 10^{-58}\ \mathrm{M_\odot}$
`sigmaT`	the Thomson cross section of eletrons: $\sigma_T = 0.6652458734 \cdot 10^{-28}\ \mathrm{m^2}$ (Olive and Particle Data Group, 2014), while the code uses $\approx 1.37523 \cdot 10^{-46}\ \mathrm{R_\odot^2}$
`cgsEnergy`	energy conversion factor to cgs units 1 erg $\approx 1.03536 \cdot 10^{-40}\ \mathrm{M_\odot\,R_\odot^2\,yr^{-2}}$
`kms`	velocity conversion factor $1\ \mathrm{km\,s^{-1}} \approx 45.3741\ \mathrm{R_\odot\,yr^{-1}}$
`day`	sidereal day: $23^\mathrm{h}56^\mathrm{m}4.09053^\mathrm{s} \approx 2.73033 \cdot 10^{-3}$ yr (Olive and Particle Data Group, 2014)
`au`	astronomical unit: $1.495978707 \cdot 10^{11}$ m $\approx 215.091\ \mathrm{R_\odot}$ (Olive and Particle Data Group, 2014)
`pc`	parsec: $3.08567758149 \cdot 10^{16}$ m $\approx 4.43657 \cdot 10^7\ \mathrm{R_\odot}$ (Olive and Particle Data Group, 2014)

3.3 Structure definitions

In the code new structure types are defined for the physical objects. Those are `t_system` and `t_star` and will be described in the sections 3.3.1 and 3.3.2, respectively. The structure `t_SN` contains more data about the SN phase, see section 3.3.3. Additionally there is a structure `t_HRD`, see section 3.3.4, which contains all the phase space information about a star. It is also used to store the stellar gird data, see section 3.4.

3.3.1 `t_system`

This structure represents the total system. Its components are:

Table 2: Components of `t_system`.

type	name	description
`int`	`n`	number of entries in the arrays of `t_system` and its components of type `t_star`
`t_star`	`prim`	primary star, see section 3.3.2
`t_star`	`sec`	secondary star, see section 3.3.2
`double*`	`M`	array of total system mass in $\mathrm{M_\odot}$
`double*`	`qp`	array of mass ratio = mass of primary/mass of secondary
`double*`	`qs`	array of mass ratio = mass of secondary/mass of primary
`double*`	`a`	array of semi-major axis in $\mathrm{R_\odot}$
`double*`	`P`	array of orbital period in yr
`double*`	`rp`	array of Roche-lobe radius of primary in $\mathrm{R_\odot}$

Table 2 continued.

type	name	description
double*	rs	array of Roche-lobe radius of secondary in $R_\odot$
double*	e	array of eccentricity
double*	peri	array of peri-astron separation in $R_\odot$
double*	x	array of galactic x-position in pc
double*	y	array of galactic y-position in pc
double*	z	array of galactic z-position in pc
double*	vx	array of galactic x-velocity in km/s
double*	vy	array of galactic y-velocity in km/s
double*	vz	array of galactic z-velocity in km/s
double*	rhostar	array of density of surrounding stars in pc^{-3}
int*	phase	array of phases of the system, see table 8
int	stagechange	indicates if the stage of one component has changed
int	formation	indicates which formation channel is used
double	tgw	time to merge by gravitational wave emission

3.3.2 t_star

This structure is a single star. Its components are:

Table 3: Components of t_star.

type	name	description
double*	m	array of mass in $M_\odot$
double*	t	array of time in yr
double*	r	array of radius in $R_\odot$
double*	cm	array of core mass in $M_\odot$
double*	llum	array of luminosity in $\log_{10}\left(\frac{L}{L_\odot}\right)$
double*	lteff	array of effective temperature in $\log_{10}\left(\frac{T_{\text{eff}}}{K}\right)$
double*	lambda	array of λ
double*	omega	array of angular velocity
int*	stage	array of evolutionary stage, see table 4
t_HRD	track	track of this star, see section 3.3.4
int	rmax	track index where the radius is maximal
int	last	track index where the last time in track is
double	inimass	initial mass of the track
double	metal	metallicity
t_SN	SN	supernova data, see section 3.3.3

Stages

The possible stages are:

Table 4: Evolutionary stages of stars.

value	description
0	hydrogen burning
1	helium burning
2	naked helium burning
3	white dwarf (WD)
4	neutron star (NS)
5	black hole (BH)
-2	star losing its envelope and become 2
-3	star forming a PN or explode in a SN and become 3, 4 or 5, respectively

3.3.3 `t_SN`

This structure stores more data about the supernova (SN) phase. Its components are:

Table 5: Components of `t_SN`.

type	name	description
`double`	`inimass`	initial mass of the star/he-star
`double`	`Hecoremass`	pre-SN He-core mass
`double`	`COcoremass`	pre-SN CO-core mass
`double`	`remnantmass`	post-SN remnant mass
`double`	`w`	kick velocity in km/s
`double`	`theta`	kick angle θ in degree
`double`	`phi`	kick angle ϕ in degree
`double`	`vsys`	systemic velocity change by the kick in km/s
`int`	`startype`	stellar stage prior to the SN, see table 4
`int`	`type`	type of supernova: 0 no supernova 1 planetary nebula instead of SN 2 electron capture supernova 3 iron core collapse supernova 4 collapse to blackhole

3.3.4 `t_HRD`

This structure is a track of a star. Its components are:

Table 6: Components of `t_HRD`.

type	name	description
`int`	`n`	number of entries in the arrays
`int`	`TAMS`	array index of the TAMS
`double*`	`m`	array of mass in $M_\odot$
`double*`	`t`	array of time in yr

Table 6 continued.

type	name	description
`double*`	`r`	array of radius in $R_\odot$
`double*`	`cm`	array of core mass in $M_\odot$
`double*`	`llum`	array of luminosity in $\log_{10}\left(\frac{L}{L_\odot}\right)$
`double*`	`lteff`	array of effective temperature in $\log_{10}\left(\frac{T_{\text{eff}}}{K}\right)$
`double*`	`lambda`	array of λ
`double`	`inimass`	initial mass of the track

3.3.5 `t_hist`

This structure represents a histogram. It contains:

Table 7: Components of `t_hist`.

type	name	description
`int`	`n`	number of bins in the arrays
`int`	`subs`	number of subdivisions in the arrays
`long`	`ctot`	total number of counts
`long*`	`c`	array of counts
`long**`	`subc`	two dimensional array of sub counts
`double*`	`x`	array of x values of bin borders
`double`	`min`	minimum value
`double`	`max`	maximum value
`bool`	`logscale`	linear or logscale

3.4 Read stellar tables

As already described in section 2.6, the code interpolates tables for the stellar evolution of each star. To load all available tables, the code searches for them and creates `Find` files in the directory where the code runs. These files are named `Find*.*` where the type of searched tables or their location is specified.

When the tables are read in, the λ parameter is only stored as one variable depending on `alphaTH`, see section 2.2.3. Additionally the core masses of convective cores are adapted. Then the data is stored in a structure of type `t_HRD`, see section 3.3.4. Furthermore a smoothing is applied to the tables which replaces totally flat parts by very weekly changing parts, depending on the behaviour of the neighbouring data points to avoid numerical instabilities.

3.5 Initial conditions

The initial conditions of a system are either fixed values or randomly created from generating functions depending on the input parameters, see section 2.2.3. The code

can set a fixed value, choose a random value or create a grid of stars, see section 2.1.2.

The generation order of the parameters is the same as in sections 2.2.3 and 3.9. The first determined value is the primary mass, the mass of the initially more massive star. The next one is the mass ratio and accordingly the secondary mass. Then follows the semi-major axis or the period of the system. The last of the basic parameters to be determined is the eccentricity. If specified, a number of additional parameters are chosen: the initial age, the metallicity, the stellar spins, the position and velocity in a galaxy and the stellar density around the system.

3.6 Evolutionary phases

In the code all binary events are related to a phase. These considered evolutionary phases are:

Table 8: Phases for the systems.

value	description
0	wind mass loss for both stars according to the stellar evolution
12	RLO from primary to secondary
21	RLO from secondary to primary
13	CE where the primary fills its Roche-lobe
23	CE where the secondary fills its Roche-lobe
4	early merge
15	SN of primary
25	SN of secondary
16	PN of primary
26	PN of secondary
-1	destroyed, because of a disruptive kick during a SN or after an early merger
94	gravitational merger within 10^{10} yr/both stars are compact remnants
99	end stage/both stars are compact remnants

When the initial conditions, see section 3.5, are fixed the system starts always with a phase of wind mass loss for both stars.

3.6.1 Wind mass loss

During this phase both stars follow their tracks from the evolutionary tables, see section 2.6. The separation of the system changes according to Soberman et al. (1997).

This phase normally ends when either one star is filling its Roche lobe, see section 3.6.2 or the end of the stellar track is reached, see section 3.6.4. It will be followed by another wind mass loss phase when one of the stars finishes its main sequence.

3.6.2 Roche-lobe overflow

Before one star fills its Roche lobe, its is assumed that the tides in such a close orbit will circularise the system before a stable mass transfer starts. When a star is filling its Roche lobe it is checked whether the mass transfer is expected to be a stable Roche-lobe overflow (RLO) or if it will be unstable and lead to a common envelope (CE), see section 3.6.3. Depending on the evolutionary stage of the donor star, a limit on mass ratio or donor mass is used to differentiate between the two cases of mass transfer. For a normal star the two cases are distinguished by the mass-ratio limit `qlimit`, see section 2.2.3. Furthermore the fraction to maximal extend is checked to consider that convective envelopes lead to unstable mass transfer. If the star is a helium star transferring mass onto a non-degenerate star, its mass is compared to `Mhece`, see section 2.2.3. If `Mhece` is negative the `qlimit` is used for the helium stars as well. The mass transfer from a helium star to a compact object is treated as always stable if the orbital period is larger than 0.07 d (Tauris et al., 2015).

As a typical timescale of the RLO, the thermal timescale of the donor is used and is enlarged by a factor of three for a normal star. It is assumed that the donor loses its whole envelope in a RLO. The three parameters `alphaRLO`, `beta` and `delta` specify which part of the lost material leaves the system: directly from the donor, is re-emitted from the accretor, and is transferred to a circumbinary torus, respectively. While `alphaRLO` and `delta` are fixed parameters, which are given by the user, `beta` is determined dynamically. Its lowest value is `beta_const` but it could increase if the companion is not able to accrete all the material. The accretion rate is limited by the Eddington accretion rate.

The orbital parameters change according to Soberman et al. (1997). If the donor was a normal star it becomes a naked helium star after the RLO with a total mass equal to its previous core mass. If it was already a helium star it will go off in a SN or from a WD depending on its mass, see section 3.6.4. If the star does not detach after the mass transfer, the two stars will merge. The accretor will get a new stellar track according to its total and core mass after the mass transfer.

3.6.3 Common envelope

If a mass transfer is unstable the donor will expand rapidly and create a common envelope. During the CE the material of the donors envelope is ejected from the system on a typical timescale of < 1000 yr. The λ formalism is applied and the parameters `alphaCE` and `lambda_const` are fixed by the user. Depending on `alphaTH` the final λ representing the stellar structure is determined, see section 2.2.3. If the companion is a compact object, some of the envelope material will be accreted onto it which releases some energy helping to unbind the rest of the envelope. For the donor the resulting stages of the CE are the same as the ones of a stable RLO, see section 3.6.2.

3.6.4 Supernova/planetary nebula

Depending on the mass of a star it will end its life as a WD, NS or BH. A WD may form a planetary nebula (PN) around it, while a NS or a BH will be the compact remnant of

a supernova. The formation of a BH may produce a dark SN which mainly consists of neutrinos. While a system with a PN will remain bound, a SN may disrupt the binary.

Kicks

For newborn NSs and BHs kicks are expected. The code distinguishes between different kinds of SNe if `kickv` < 0. Associated with them are different kick distributions. For an electron capture SN, the kick is taken from a flat distribution up to 50 km/s, while an iron core-collapse SN uses a Maxwell-Boltzmann distribution. Depending on the mass loss during the evolution of the star the root-mean-square velocity is adjusted (Kruckow et al., 2018). All BHs get kicks from a flat distribution up to 200 km/s.

Shell Impact

A shell impact on the companion of a SN is applied following Tauris and Takens (1998). The code uses a generalisation of the formalism where the circularised semi-major axis is replaced by the separation at the moment of the explosion. After the impact the companion gets a new stellar track depending on its total and core mass. At the end it is checked whether the system remains bound or if it is disrupted or if the orbit gets so small that the system will merge.

3.7 Analysing the binary

When the system reaches its final phase the system is analysed to extract the data of interest. If the `output` option is set to the massive output, the evolution of the system is printed to the screen after the analysis.

3.7.1 Integration tables

To speed up the code, some integrations like the orbital shrinking by gravitational waves is tabulated. These tables will be created when the program runs the first time, or whenever those are missing, which requires write access to the directory with the tables, see subsection 2.

3.7.2 Galactic motion

If it is of interest, the code will follow the motion of a system in a galaxy. Therefore the flags `galintegrator` and `galpotential` have to be set, see section 2.2.

The analysed data should then be printed to the screen, written to a file or stored in a histogram, see section 3.8. The data of a system will be deleted before the next one is calculated.

3.8 Histograms

In the statistic part of the code are some general functions to create histograms during the run time. For the histograms a special type is defined. It is called `t_hist`, see

section 3.3.5.

The histogram functions are:

`void inithist(t_hist& hist, int nbin, double min, double max, bool logscale, int subs)`
This function initializes a new histogram. It will have `nbin` bins which cover a total range between `min` and `max`. If you set `logscale=true` then the bins will be of equal size on a logarithmic scale, otherwise on a linear scale. If you want to divide the counts of a bin into subbins use `subs>1`. You should use this function only in the function `PreMainLoop`, see section 3.9.

`void addtohist(t_hist& hist, double value, int sub)`
This function you should use to add data to the histogram. `value` is the new data. If you specify `sub` $\in [0, \texttt{subs-1}]$ the data will likewise add to the sub histogram with the index `sub`. Adding data to the histogram should be done in the function `AfterEvolution`, see section 3.9.

`void histout(t_hist& hist, bool perbinsize, char* name)`
This function writes the histogram data to a file. With the flag `perbinsize` you can specify whether you want only the counts printed or if you want to get the counts normalized to its bin size. The `name` is the name of the created file in the current directory. It gets an automatic extension `.hist`. For the structure of the `hist` files have a look in section 2.5.2. You should use this function only in the function `AfterMainLoop`, see section 3.9.

`void freehist(t_hist& hist)`
This routine deletes the histogram data. All data in the histogram will no longer be available and the memory of the arrays will be freed. You should use this function only when you do not need the data in the histogram any longer. The desired place of use is in the function `AfterMainLoop`, see section 3.9.

3.9 User interface

The file `ComBinElib/user.cpp` is a user interface to the code. There are several functions provided. They are called by the code and allow the user to make changes during the runtime without changing the main routines of the code. The following list describes the provided functions ordered by the usual call time.

Table 9: User functions.

function(parameter)	description
`void First()`	This function is called directly after the variable declaration in the main function.

Table 9 continued.

function(parameter)	description
`void AfterReadParameters(double& Mp_max, double& Mp_min, double& Ms_max, double& Ms_min, double& a_max, double& a_min, double& Mp, double& Ms, double& a, double& e, double& metall, double& vp, double& vs, double& x, double& y, double& z, double& vx, double& vy, double& vz, double& rhostar, int& parallel, int& galintegrator, int& galpotential)`	This function is called after the parameters are read in from the command line or `data.in` , see sections 2.1.2 and 2.1.1 respectively. All parameters are described in section 2.2. You can use this function to change the variables during the run time to rescale units if you prefer different input units.
`void PreReadTables()`	This function is called directly before the tables are read in.
`void AfterReadTables()`	This function is called after the tables are read in. You can use this function to check the tables.
`void SetSeed(long& seed, long* discard, int n)`	This function is called directly before the random seeds are set. `n` is the number of entries in `discard`. You can manipulate `seed` and `discard` to reproduce a specific system which occurred in a population synthesis run.
`void PreMainLoop()`	This function is called directly before the main loop of calculating all the systems. You can use it to set up new histograms, see section 3.8.
`double UserInitial_Mp(double Mp_max, double Mp_min)`	In this function you can define your own initial primary mass function. The return value is the primary mass in $M_\odot$.
`double UserInitial_q(double Ms_max, double Ms_min, double Mp)`	In this function you can define your own initial mass ratio function. The return value is the secondary mass in units of the primary mass or simply the mass ratio.
`double UserInitial_a(double a_max, double a_min, double Mp, double Ms)`	In this function you can define your own initial semi-major axis function. The return value is the semi-major axis in $R_\odot$.
`double UserInitial_e(double e_max, double Mp, double Ms, double a)`	In this function you can define your own initial eccentricity. The return value is the initial eccentricity the system should have.
`double UserInitial_t(double Mp, double Ms, double a, double e)`	In this function you can define your own initial age. The return value is this age in yr. (currently no effect)

Table 9 continued.

function(parameter)	description
`double UserInitial_Z(double Mp, double Ms, double a, double e, double t)`	In this function you can define your own initial metallicity. The return value is the metallicity of the system. (only metallicities corresponding to the stellar tables are considered)
`void UserInitial_omega(double& omegap, double& omegas, double Mp, double Ms, double a, double e, double t, double metall)`	In this function you can define your own initial angular spin. The values of the spin has to be stored in `omegap` and `omegas` for the primary and the secondary, respectively. Their unit is yr^{-1}. (currently no effect)
`void UserInitial_R(double& x, double& y, double& z, double Mp, double Ms, double a, double e, double t, double metall, double omegap, double omegas)`	In this function you can define your own initial position in a galactic potential. The position vector components are `x`, `y` and `z` as Cartesian coordinates of the galactic rest frame in pc.
`void UserInitial_V(double& vx, double& vy, double& vz, double Mp, double Ms, double a, double e, double t, double metall, double omegap, double omegas, double x, double y, double z)`	In this function you can define your own initial velocity in a galactic potential. The Cartesian velocity components of the galactic rest frame in km/s should be stored in `vx`, `vy` and `vz`.
`double UserInitial_rho(double Mp, double Ms, double a, double e, double t, double metall, double omegap, double omegas, double x, double y, double z, double vx, double vy, double vz)`	In this function you can define your own initial stellar density. The value of the stellar density is to be returned in pc^{-3}. (currently no effect)
`void AfterEvolution(t_system& system)`	This function is called after the system is evolved. `system` contains all the evolution information of the system, see section 3.3.1 for the structure information of the type `t_system`. Here the data should be written out or stored in the histograms.
`long ToDebug(long i)`	This function defines which system is printed with debug output, `i` is the number of the current system. Any value ≤ 0 will give non debug output.
`void AfterMainLoop()`	This function is called directly after the main loop of calculating all the systems. You can use it to write out and delete your own defined histograms, see section 3.8.

4 Warnings and errors

All warning or error messages created by the code start with `#Warning` and `#Error` respectively, see sections 4.1 and 4.2. They are written to `stderr`. Additionally there are some outputs starting with `#` to `stderr` which will be printed if some values are non-physical. All important values are checked if they are sensible in a physical context. If one of these checks fails, you will get one of the outputs summarised in table 10.

Table 10: Description of check of physical parameters.

output (* denotes some value)	description
`#prim.m=*Msun`	the primary's mass has a non-physical value
`#prim.t=*yr`	the primary's age has a non-physical value
`#prim.r=*Rsun`	the primary's radius has a non-physical value
`#prim.cm=*Msun`	the primary's core mass has a non-physical value
`#prim.llum=*`	the primary's logarithmic luminosity has a non-physical value
`#prim.lteff=*`	the primary's logarithmic effective temperature has a non-physical value
`#prim.lambda=*`	the primary's λ has a non-physical value
`#prim.omega=*/yr`	the primary's spin has a non-physical value
`#prim.stage=*`	the primary's stage has no value
`#sec.m=*Msun`	the secondary's mass has a non-physical value
`#sec.t=*yr`	the secondary's age has a non-physical value
`#sec.r=*Rsun`	the secondary's radius has a non-physical value
`#sec.cm=*Msun`	the secondary's core mass has a non-physical value
`#sec.llum=*`	the secondary's logarithmic luminosity has a non-physical value
`#sec.lteff=*`	the secondary's logarithmic effective temperature has a non-physical value
`#sec.lambda=*`	the secondary's λ has a non-physical value
`#sec.omega=*/yr`	the secondary's spin has a non-physical value
`#sec.stage=*`	the secondary's stage has no value
`#sys.M=*Msun`	the total mass of the system has a non-physical value
`#sys.qp=*`	the primary mass in units of the secondary mass has a non-physical value
`#sys.qs=*`	the secondary mass in units of the primary mass has a non-physical value
`#sys.a=*Rsun`	the semi-major axis has a non-physical value
`#sys.P=*yr`	the period has a non-physical value
`#sys.rp=*Rsun`	the Roche-lobe radius of the primary has a non-physical value
`#sys.rs=*Rsun`	the Roche-lobe radius of the secondary has a non-physical value

Table 10 continued.

output (* denotes some value)	description
`#sys.e=*`	the eccentricity has a non-physical value
`#sys.x=*pc`	the x coordinate of the system has a non-physical value
`#sys.y=*pc`	the y coordinate of the system has a non-physical value
`#sys.z=*pc`	the z coordinate of the system has a non-physical value
`#sys.vx=*km/s`	the velocity in x direction of the system has a non-physical value
`#sys.vy=*km/s`	the velocity in y direction of the system has a non-physical value
`#sys.vz=*km/s`	the velocity in z direction of the system has a non-physical value
`#sys.rhostar=*/pc^3`	the stellar density around the system has a non-physical value
`#sys.phase=*`	the phase of the system has no value
`#system.prim.lambda[n]=* ...`	the λ of the primary has a non-physical value
`#system.sec.lambda[n]=* ...`	the λ of the secondary has a non-physical value

4.1 Warning messages

Warnings should awake the curiosity of the user. Some of them only show up if the screen output is enabled, see section 2.2.2. The following list gives you an alphabetically ordered overview of possible warning messages.

Table 11: Warning messages.

warning message (* denotes some value)	description
`#Warning: accuracy not reached in RLFT2: rs=*Rsun roche=*Rsun diff=*Rsun 1.0-roche/rs=*=*`	the solution when a star fills its Roche lobe has not the required accuracy, see section 2.2.1, only displayed if `screen=true`
`#Warning: companion[0].t[*]=*yr set to *yr`	the accretor of the CE would exceed its lifetime during the CE, therefore the time of the CE phase is reduced
`#Warning: end track time newtrack.t[0]=*yr=*yr reached: newtrack.t[*]=*yr newtrack.t[0]-newtrack.t[*]=*yr Warning: newtrack.t[*]=*yr=*`	the ages in the new track exceed the determined maximum, the new track is truncated

Table 11 continued.

warning message (* denotes some value)	description
`#Warning: generate new seed(i):*`	the given random seed curses a problem during initialising of the random number generator, so a new seed is generated
`#Warning: Invalid integrator spezified: use RungeKutta 4 integrator`	the flag of the galactic integrator has an undefined value and is set to the default value, see section 2.2.1
`#Warning: Invalid potential spezified: use no potential`	the flag of the galactic potential has an undefined value and is set to the default value, see section 2.2.3
`#Warning: No initial age distribution spezified: use tdist=0`	the value of the `tdist` flag is invalid, see section 2.2.3
`#Warning: No initial eccentricity distribution spezified: use edist=0`	the value of the `edist` flag is invalid, see section 2.2.3
`#Warning: No initial mass function spezified: use IMF=1`	the value of the `IMF` flag is invalid, see section 2.2.3
`#Warning: No initial mass ratio distribution spezified: use qdist=1`	the value of the `qdist` flag is invalid, see section 2.2.3
`#Warning: No initial metallicity distribution spezified: use Zdist=0`	the value of the `Zdist` flag is invalid, see section 2.2.3
`#Warning: No initial semi-major axis distribution spezified: use adist=1`	the value of the `adist` flag is invalid, see section 2.2.3
`#Warning: No initial space distribution in a galaxy spezified: use Rdist=0`	the value of the `Rdist` flag is invalid, see section 2.2.3
`#Warning: No initial stellar density distribution in a galaxy spezified: use rhodist=0`	the value of the `rhodist` flag is invalid, see section 2.2.3
`#Warning: No initial stellar spin distribution spezified: use rotdist=0`	the value of the `rotdist` flag is invalid, see section 2.2.3
`#Warning: No initial velocity distribution in a galaxy spezified: use Vdist=0`	the value of the `Vdist` flag is invalid, see section 2.2.3
`#Warning: no solution in RLFT2`	there is no solution found when a star fills its Roche lobe, while it was expected, only displayed if `screen=true`
`#Warning: no track update, because star out of grid: star.m[*]=*Msun and star.cm[*]=*Msun`	the conditions of the star are outside of the stellar gird, therefore the mass change remains unconsidered, only displayed if `screen=true`
`#Warning: prim.t[*]=*yr prim.track.t[*]=*yr sec.t[*]=*yr sec.track.t[*]=*yr`	one of the stars got older than its age defined by its stellar evolution track

Table 11 continued.

warning message (* denotes some value)	description
`#Warning: reduce core mass from star.cm[*]=*Msun to *Msun`	the star got a too large core mass and is placed at the end of the stellar grid
`#Warning: reduce mass from star.m[*]=*Msun to *Msun`	the star got a too large mass and is placed at the end of the stellar grid
`#Warning: replace negative lambda with 1.0e+10: *`	a negative λ would mean that the envelope is unbound, instead it is replace by a very loosely bound value
`#Warning: Roche-lobe-overflow setup: prim.r[0]=*Rsun rp[0]=*Rsun sec.r[0]=*Rsun rs[0]=*Rsun`	one of the stars fills its Roche lobe form the initial conditions
`#Warning: star[0].t[*]=*yr set to *yr`	the donor of the CE would exceed its lifetime during the CE, therefore the time of the CE phase is reduced
`#Warning: The user defined eccentricity is out of range: e=* e_min=0.0 e_max=*`	The eccentricity returned by `UserInitial_e` is smaller than `e_min` or larger than `e_max`
`#Warning: The user defined semi-major axis is out of range: a=*Rsun a_min=*Rsun a_max=*Rsun`	The semi-major axis returned by `UserInitial_a` is smaller than `a_min` or larger than `a_max`
`#Warning: t=*yr star.t[*]=*yr star.track.t[j]=*yr star.track.t[j-1]=*yr j=* last=* star.rmax=* star.track.n-1=* r_ratio=* roche=*Rsun star.track.r[j]=*Rsun star.track.r[j-1]=*Rsun cloop=* cjump=*`	the time when a star filled its Roche lobe is in the past, only displayed if `screen=true`
`#Warning: wrong formation value`	the system has an unconsidered formation channel, this warning enables the screen output for this system
`#Warning: *track(s) not updated, because star out of grid`	tells you that the stellar grid is too small, for some stars the mass change is not fully considered, they are placed at the end of the stellar grid

4.2 Error messages

If an error occurs in a run you should not trust the output of the simulation. As a normal user you should never see one of the error messages. The following list gives you an alphabetically ordered overview of implemented error messages.

Table 12: Error messages.

error message (* denotes some value)	description
`#Error: can't find *-tables in *, code: *`	some tables cannot be found in the given subdirectory of `tables`, see section 2.6
`#Error: can't open data.in`	you specified with `-2` to read the `data.in` file, but there is no such file in the current directory or you have no read access to it
`#Error: can't write to text, code: *`	creating the filename for the integration table fails
`#Error: cm=*Msun t_ratio=* j=* star.track.cm[j]=*Msun star.track.cm[j-1]=*Msun`	the core mass of the star would be negative
`#Error: common envelope: system.rp[*]=*Rsun system.prim.r[*]=*Rsun system.rs[*]=*Rsun system.sec.r[*]=*Rsun`	no star is selected as donor for the common envelope
`#Error: companion[0].r[*]=*Rsun companion[0].track.r[*]=*Rsun companion[0].track.r[*]=*Rsun t_ratio=*`	the accretor gets a negative radius after common envelope
`#Error: end track time: jlow=* nlow=* jup=* nup=*`	the determined end time of the track is reached, normally it should only happen for `jlow=nlow` and `jup=nup`
`#Error: e0=* eccarray.ecc[*]=* eccarray.ecc[*]=* eratio=*`	the eccentricity cannot be interpolated from the integration table for merger time due to gravitational wave radiation, see section 3.7.1
`#Error: He-star mass of *Msun not in table`	the given initial mass of the naked He-star is outside the He-star grid
`#Error: integer overflow n=*`	the galactic integration needs more steps than `INT_MAX`
`#Error: i=*>star.rmax=*`	no zero before maximum radius found, previous checks have failed
`#Error: jlow=*<>jup=* nlow=* nup=*`	the reduction of a track by one data point failed
`#Error: j=*>jmax=*`	no zero before the companion finishes its life time found, previous checks have failed
`#Error: mass increase of the system: dm=*Msun`	the system gains mass in a non-physical way

Table 12 continued.

error message (* denotes some value)	description
`#Error: memory allocation failed: *`	the memory allocation for a variable is not possible, please check if there is enough memory available
`#Error: memory reallocation failed: *`	the memory for a variable cannot be increased, please check if there is enough memory available
`#Error: Mp/Msun=* not in [*,*]`	the generation of a random primary mass from the IMF failed
`#Error: Mp=*Msun m1=*Msun value=* int1IMF=*`	the generation of a random primary mass from the canonical IMF failed
`#Error: mratio out of range: mratio=* star.m[*]=*Msun stararray0[*].m[*]=*Msun stararray0[*].m[*]=*Msun`	the mass of the star which will get a new track cannot be found in the prior determined mass range in the stellar grid
`#Error: mratio=* not in [*,*] star.cm[*]=*Msun star.m[*]=*Msun newtrack.m[*]=*Msun newtrack.m[*]=*Msun`	the mass is outside the considered accuracy region
`#Error: mratio-cmratio=*>* mratio=*=*/*=(*-*)/(*-*) cmratio=*=*/*=(*-*)/(*-*)`	the position defined by the mass and the core mass should be the same unless the numerical errors are too large
`#Error: m=*Msun t_ratio=* j=* star.track.m[j]=*Msun star.track.m[j-1]=*Msun`	the mass of the star would be negative
`#Error: negative core mass: inimass=*Msun cm[*]=*Msun jump=*`	during the correction for convective cores a core mass gets negative, see section 3.4
`#Error: negative psi=*`	the ψ for the kick/shell impact is negative, see section 3.6.4
`#Error: newtrack of m_ini=*Msun t_max=*yr: j=* jlow=* jup=* m=*Msun t=*yr r=*Rsun core mass(cm)=*Msun`	the mass or the age of a new track gets negative
`#Error: new companion mass=*Msun companion.m[*]=*Msun companion.track.m[j]=*Msun companion.track.m[j-1]=*Msun j=* last=* companion.track.n-1=* t_ratio=* t=*yr companion.track.t[j]=*yr companion.track.t[j-1]=*yr`	the companion mass would be too small for a star or negative

Table 12 continued.

error message (* denotes some value)	description
`#Error: new star mass=*Msun star.m[*]=*Msun star.track.m[j]=*Msun star.track.m[j-1]=*Msun j=* last=* star.rmax=* star.track.n-1=* r_ratio=* roche=*Rsun star.track.r[j]=*Rsun star.track.r[j-1]=*Rsun`	the star mass would be too small for a star or negative
`#Error: not all new track points copied: j=* newtrack.n=*`	the new track consists of less track points than previously determined
`#Error: no corresponding trk1 found`	if the tables are split into `trk1` and `trk2` files the code tries to match which belong together and the matching failed
`#Error: No initial age distribution spezified! t set to 0.0`	the `tdist` flag is invalid and was not automatically changed, see section 4.1
`#Error: No initial eccentricity distribution spezified! e set to 0.0`	the `edist` flag is invalid and was not automatically changed, see section 4.1
`#Error: No initial mass function spezified! Mp set to Mp_max=*`	the `IMF` flag is invalid and was not automatically changed, see section 4.1
`#Error: No initial mass ratio distribution spezified! q set to q_max=*`	the `qdist` flag is invalid and was not automatically changed, see section 4.1
`#Error: No initial metallicity distribution spezified! metallicity set to 0.02`	the `Zdist` flag is invalid and was not automatically changed, see section 4.1
`#Error: No initial semi-major axis distribution spezified! a set to a_max=*`	the `adist` flag is invalid and was not automatically changed, see section 4.1
`#Error: No initial space distribution in a galaxy spezified! position set to center`	the `Rdist` flag is invalid and was not automatically changed, see section 4.1
`#Error: No initial stellar density distribution in a galaxy spezified! star is set in the field`	the `rhodist` flag is invalid and was not automatically changed, see section 4.1
`#Error: No initial stellar spin distribution spezified! omegap and omegas set to 0.0`	the `rotdist` flag is invalid and was not automatically changed, see section 4.1
`#Error: No initial velocity distribution in a galaxy spezified! v set to 0.0`	the `Vdist` flag is invalid and was not automatically changed, see section 4.1
`#Error: no mergertime.int`	the integration table for the merger time cannot be read

Table 12 continued.

error message (* denotes some value)	description
`#Error: no random number generator selected to get random value`	the index of the used random number generator is invalid while trying to get a random value
`#Error: no random number generator selected(i=*) to set new seed`	the index of the used random number generator is invalid while setting a new seed
`#Error: no star for supernova/planetary nebula selected: system.prim.stage[*]=* system.sec.stage[*]=*`	no star is selected to explode in a supernova or to form a planetary nebula around it
`#Error: no TAMS expected, negative mass? value=*`	a negative mass is detected in a stellar track where no TAMS value is expected, see section 2.6
`#Error: no track update: star.stage[n]=*`	the star has a stage where no track update routine is defined
`#Error: overflow: system.phase[*]=*`	no star is selected as donor for the Roche-lobe overflow
`#Error: radius out of track: r=*Rsun system.prim.track.r[*]=*Rsun system.prim.track.r[*]=*Rsun diff=*Rsun system.prim.track.n-1=* ratio_p=* system.prim.last=*`	the determined radius when the primary fills its Roche lobe cannot be found in the evolutionary track of the primary
`#Error: radius out of track: r=*Rsun system.sec.track.r[*]=*Rsun system.sec.track.r[*]=*Rsun diff=*Rsun system.sec.track.n-1=* ratio_s=* system.sec.last=*`	the determined radius when the secondary fills its Roche lobe cannot be found in the evolutionary track of the secondary
`#Error: red=*`	undefined value of `red`, possible values are only 1 and -1
`#Error: RL-radii=(*, *)Rsun stellar radii=(*, *)Rsun ratiop=* ratios=* system.prim.track.t[*]=*yr t=*yr system.prim.track.t[*]=*yr system.sec.track.t[*]=*yr t=*yr system.sec.track.t[*]=*yr system.prim.m[*]=*Msun system.sec.m[*]=*Msun`	the star which is expected to fill its Roche lobe is not doing so
`#Error: Roche lobe=*Rsun na=*Rsun new star mass=*Msun new companion mass=*Msun nq=* r_ratio=* t_ratio=*`	the Roche lobe has no value
`#Error: roche=*Rsun star.track.r[*]=*Rsun star.track.r[*]=*Rsun`	the star cannot fill its Roche-lobe, previous checks have failed

Table 12 continued.

error message (* denotes some value)	description
`#Error: r=*Rsun t_ratio=* j=* star.track.r[j]=*Rsun star.track.r[j-1]=*Rsun`	the radius of the star would be negative
`#Error: r_ratio=* roche=*Rsun star.track.r[j]=*Rsun star.track.r[j-1]=*Rsun j=*`	r_ratio has no value
`#Error: stararray0[*].TAMS=* >stararray0[*].n=*`	the TAMS is past the stellar evolution track
`#Error: System is not synchronous`	the two stars in a binary system have different ages
`#Error: system.a[*]=*Rsun system.phase[*]=*`	the semi-major axis is negative
`#Error: system.formation=* system.prim.stage[*]=* system.sec.stage[*]=*`	something went wrong when the formation channel is determined: neither the primary nor the secondary corresponds to the last formed remnant
`#Error: system.prim.r[*]=*Rsun`	the primary has a negative radius
`#Error: system.prim.r[*]=*Rsun system.prim.track.r[*]=*Rsun system.prim.track.r[*]=*Rsun ratio_p=*`	the primary got a negative radius when one star fills its Roche-lobe
`#Error: system.sec.r[*]=*Rsun`	the secondary has a negative radius
`#Error: system.sec.r[*]=*Rsun system.sec.track.r[*]=*Rsun system.sec.track.r[*]=*Rsun ratio_s=*`	the secondary got a negative radius when one star fills its Roche-lobe
`#Error: table length: stararray0[*].n=* stararray0[*].n=* Error: j=* jlow=* nlow=* jup=* nup=*`	the positions in the two neighbouring tracks are undefined
`#Error: time out of track: companion[0].t[*]=*yr companion[0].track.t[*]=*yr companion[0].track.t[*]=*yr diff=*yr companion[0].track.n-1=* t_ratio=*`	the age after the CE cannot be found in the stellar track of the accretor
`#Error: time out of track: t=*yr system.prim.track.t[*]=*yr system.prim.track.t[*]=*yr diff=*yr system.prim.track.n-1=* ratio_p=* system.prim.last=*`	the determined age when the secondary fills its Roche-lobe cannot be found in the evolutionary track of the primary
`#Error: time out of track: t=*yr system.sec.track.t[*]=*yr system.sec.track.t[*]=*yr diff=*yr system.sec.track.n-1=* ratio_s=* system.sec.last=*`	the determined age when the primary fills its Roche-lobe cannot be found in the evolutionary track of the secondary
`#Error: too many new track points: i=* star.track.n=*`	the new track consists of more track points then previously determined

Table 12 continued.

error message (* denotes some value)	description
`#Error: too massive neutron star(*):*`	the primary/secondary is a NS with a mass above the NS mass limit
`#Error: too massive white dwarf(*):*`	the primary/secondary is a WD with a mass above the Chandrasekhar limit
`#Error: t=*yr star.track.t[*]=*yr star.track.t[*]=*yr ts=" << ts << "yr r_ratio=*`	the star cannot fill its Roche-lobe, previous checks have failed
`#Error: t_ratio=* t=*yr companion.track.t[j]=*yr companion.track.t[j-1]=*yr j=*`	t_ratio has no value
`#Error: t_roche_p=*yr tp=*yr ts=*yr`	at the time when the primary fills its Roche-lobe one of the stars exceeded its life time
`#Error: t_roche_s=*yr tp=*yr ts=*yr`	at the time when the secondary fills its Roche-lobe one of the stars exceeded its life time
`#Error: unconsidered kind: *`	the kind of specified stellar grid is not implemented
`#Error: unknown calculation of age`	the positions in the two neighbouring tracks are undefined, therefore the age cannot be calculated properly
`#Error: white dwarf mass=*Msun McoreCO=*Msun star[0].cm[n]=*Msun`	the calculated WD mass exceeds the Chandrasekhar limit
`#Error: wind mass increase of primary: dm=*Msun`	the primary gains mass in a non-physical way
`#Error: wind mass increase of secondary: dm=*Msun`	the secondary gains mass in a non-physical way
`#Error: wrong time span: star.track.t[*]=*yr time=*yr star.track.t[*]=*yr t_ratio=*`	the star never reaches its given start age for the calculation
`#Error: wrong track position: star.cm[*]=*Msun star.cm[*]=*Msun star.track.cm[*]=*Msun star.track.cm[*]=*Msun`	the current core mass is compatible with the core mass at the current track position
`#Error: wrong track position: star.m[*]=*Msun star.m[*]=*Msun star.track.m[*]=*Msun star.track.m[*]=*Msun`	the current mass is compatible with the mass at the current track position
`#Error: wrong track position: star.r[*]=*Rsun star.r[*]=*Rsun star.track.r[*]=*Rsun star.track.r[*]=*Rsun`	the current radius is compatible with the radius at the current track position

Table 12 continued.

error message (* denotes some value)	description
`#Error: wrong track position: star.t[*]=*yr star.t[*]=*yr star.track.t[*]=*yr star.track.t[*]=*yr`	the current age is compatible with the age at the current track position
`#Error: zero mass`	one of the star has no mass

References

Abt, H. A. (1983). Normal and abnormal binary frequencies. ARA&A, 21:343–372.

Allen, C. and Santillan, A. (1991). An improved model of the galactic mass distribution for orbit computations. Rev. Mexicana Astron. Astrofis., 22:255–263.

Brott, I., de Mink, S. E., Cantiello, M., Langer, N., de Koter, A., Evans, C. J., Hunter, I., Trundle, C., and Vink, J. S. (2011). Rotating massive main-sequence stars. I. Grids of evolutionary models and isochrones. A&A, 530:A115.

Dewi, J. D. M. and Tauris, T. M. (2000). On the energy equation and efficiency parameter of the common envelope evolution. A&A, 360:1043–1051.

Heggie, D. C. (1975). Binary evolution in stellar dynamics. MNRAS, 173:729–787.

Hobbs, G., Lorimer, D. R., Lyne, A. G., and Kramer, M. (2005). A statistical study of 233 pulsar proper motions. MNRAS, 360:974–992.

Kroupa, P. (2008). Initial Conditions for Star Clusters. In Aarseth, S. J., Tout, C. A., and Mardling, R. A., editors, *The Cambridge N-Body Lectures*, volume 760 of *Lecture Notes in Physics, Berlin Springer Verlag*, page 181.

Kruckow, M. U., Tauris, T. M., Langer, N., Kramer, M., and Izzard, R. G. (2018). Progenitors of gravitational wave mergers: Binary evolution with the stellar grid based code ComBinE. *ArXiv e-prints*.

Kuiper, G. P. (1935). Problems of Double-Star Astronomy. I. PASP, 47:15.

Olive, K. A. and Particle Data Group (2014). Review of Particle Physics. *Chinese Physics C*, 38(9):090001.

Salpeter, E. E. (1955). The Luminosity Function and Stellar Evolution. ApJ, 121:161.

Sana, H., de Mink, S. E., de Koter, A., Langer, N., Evans, C. J., Gieles, M., Gosset, E., Izzard, R. G., Le Bouquin, J.-B., and Schneider, F. R. N. (2012). Binary Interaction Dominates the Evolution of Massive Stars. *Science*, 337:444.

Scalo, J. M. (1986). The stellar initial mass function. Fund. Cosmic Phys., 11:1–278.

Soberman, G. E., Phinney, E. S., and van den Heuvel, E. P. J. (1997). Stability criteria for mass transfer in binary stellar evolution. A&A, 327:620–635.

Szécsi, D., Langer, N., Yoon, S.-C., Sanyal, D., de Mink, S., Evans, C. J., and Dermine, T. (2015). Low-metallicity massive single stars with rotation. Evolutionary models applicable to I Zwicky 18. A&A, 581:A15.

Tauris, T. M., Langer, N., and Podsiadlowski, P. (2015). Ultra-stripped supernovae: progenitors and fate. MNRAS, 451:2123–2144.

Tauris, T. M. and Takens, R. J. (1998). Runaway velocities of stellar components originating from disrupted binaries via asymmetric supernova explosions. A&A, 330:1047–1059.

Voss, R. and Tauris, T. M. (2003). Galactic distribution of merging neutron stars and black holes - prospects for short gamma-ray burst progenitors and LIGO/VIRGO. MNRAS, 342:1169–1184.

Appendix B

Additional figures

B.1 Figures of Section 3.13.1.2

B.1.1 At maximum radius

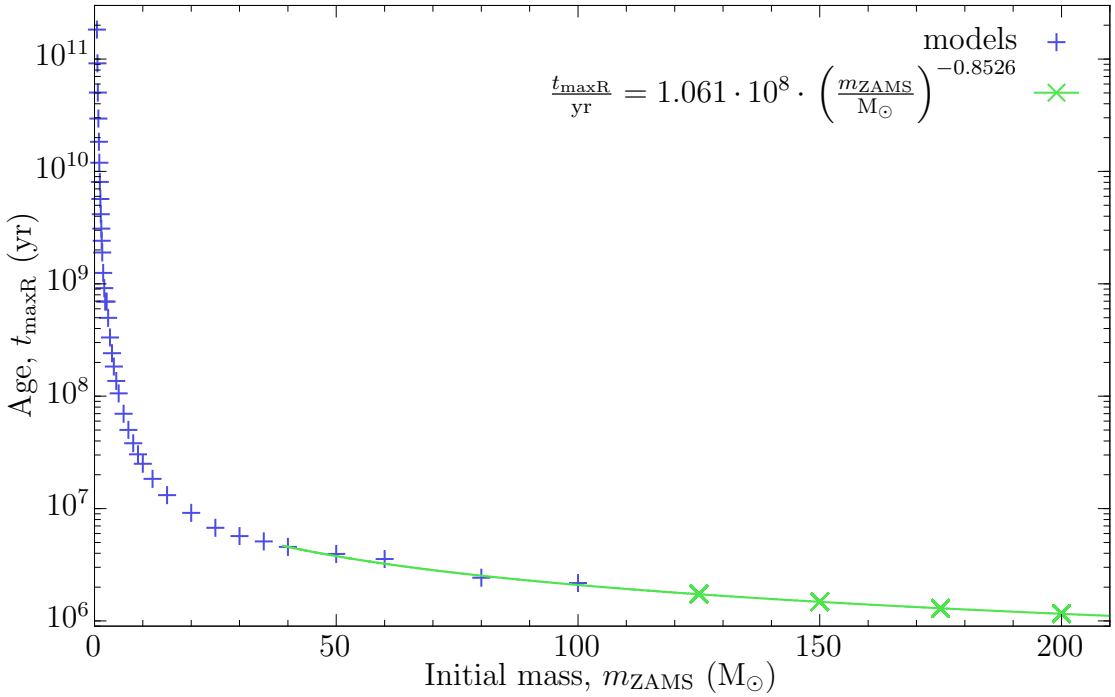

Figure B.1: Extrapolation of the age, t_{maxR}, at maximum radius to larger ZAMS masses (The extrapolations are only valid in the plotted range of the green line.).

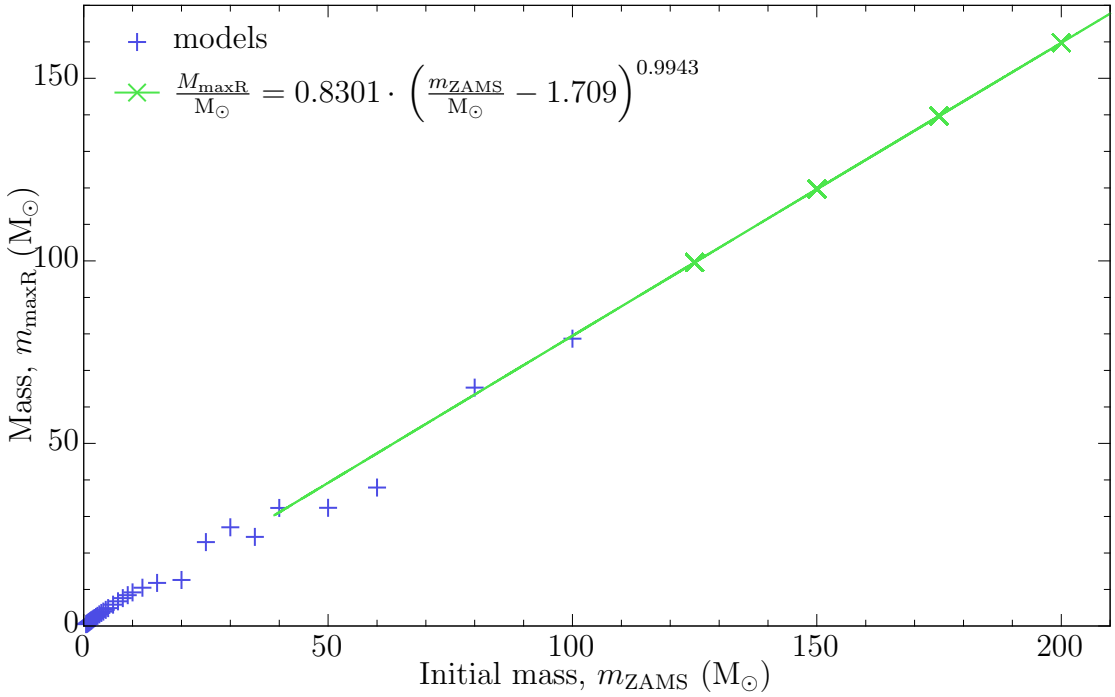

Figure B.2: Extrapolation of the mass, m_{maxR}, at maximum radius to larger ZAMS masses.

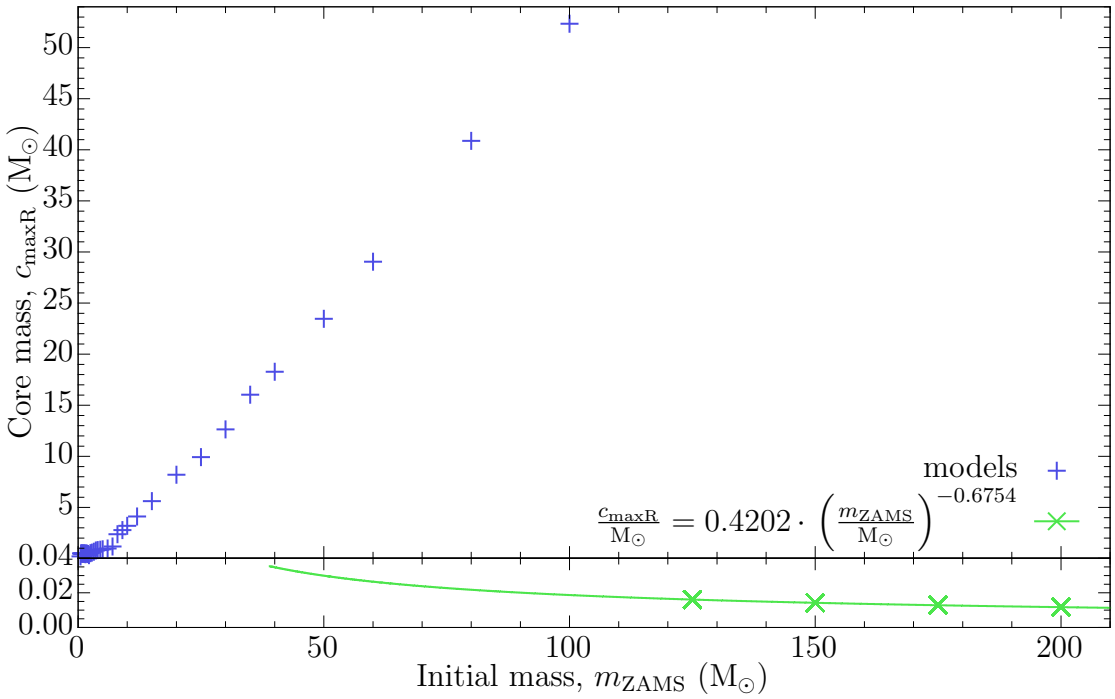

Figure B.3: Extrapolation of the core mass, c_{maxR}, at maximum radius to larger ZAMS masses.

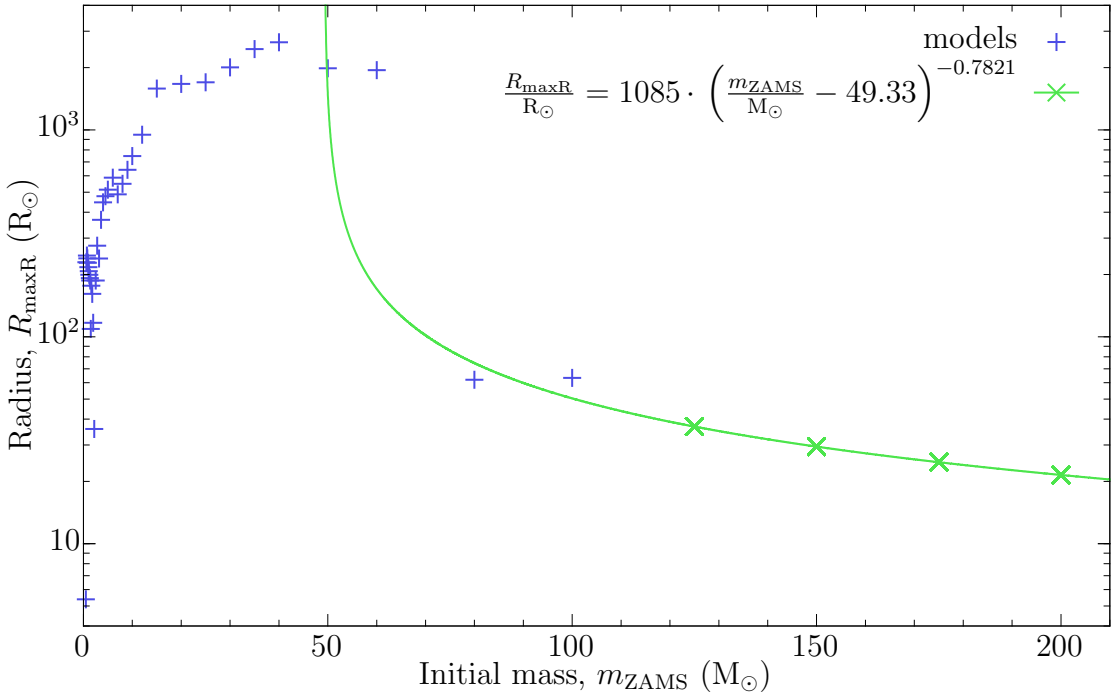

Figure B.4: Extrapolation of the radius, R_{maxR}, at maximum radius to larger ZAMS masses.

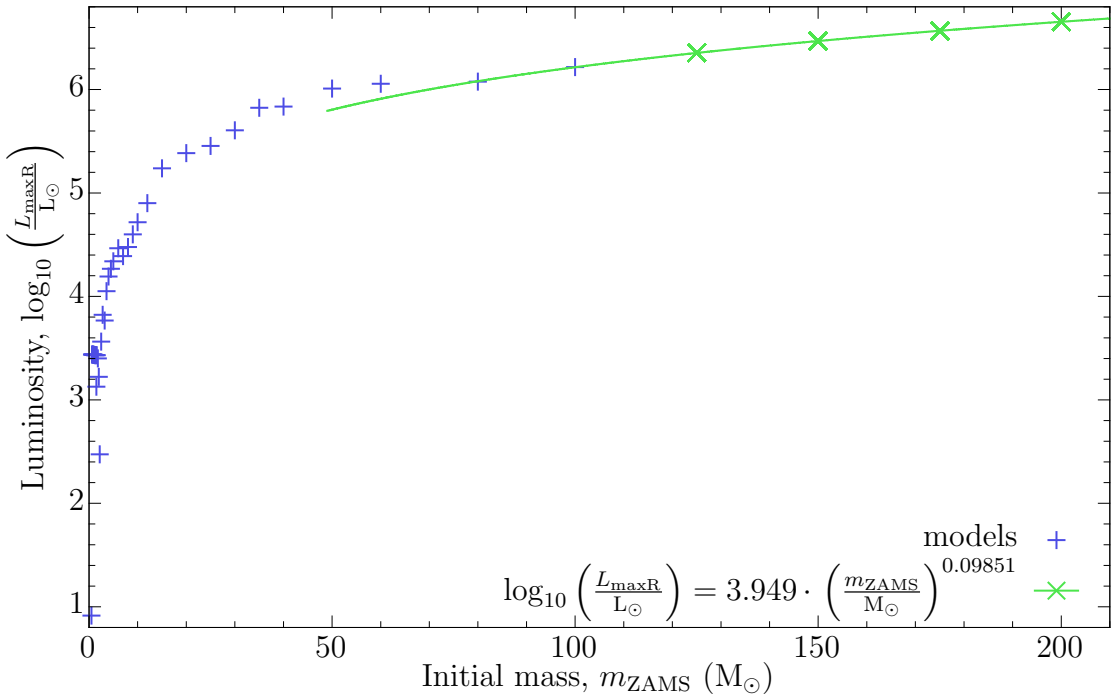

Figure B.5: Extrapolation of the luminosity, L_{maxR}, at maximum radius to larger ZAMS masses.

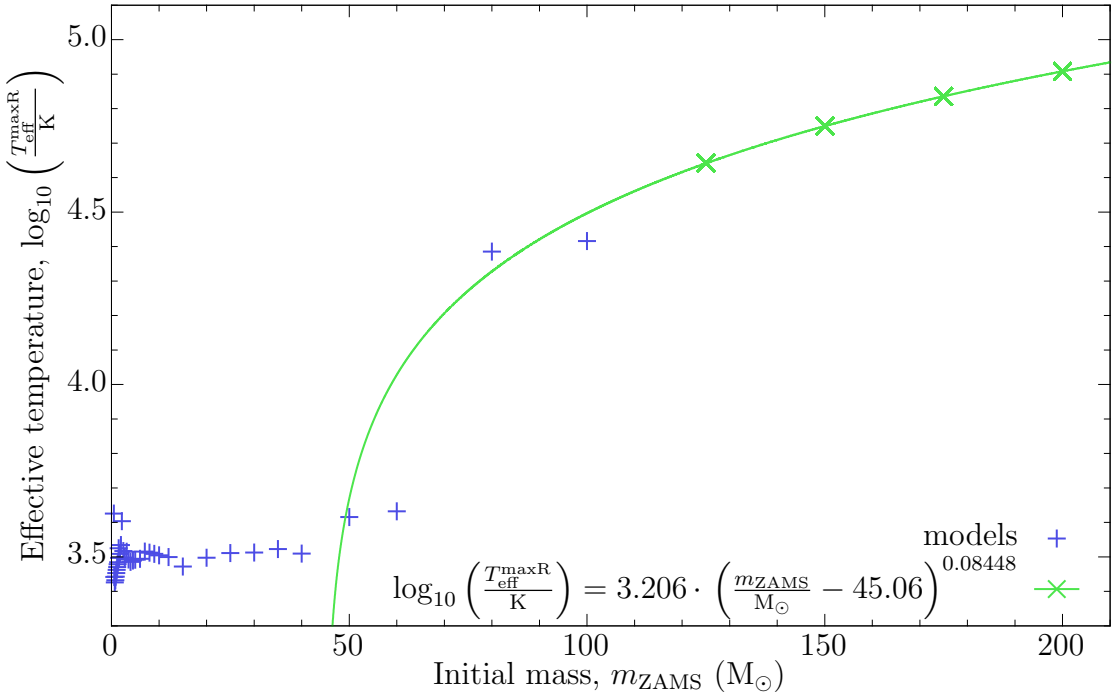

Figure B.6: Extrapolation of the effective temperature, $T_{\rm eff}^{\rm maxR}$, at maximum radius to larger ZAMS masses.

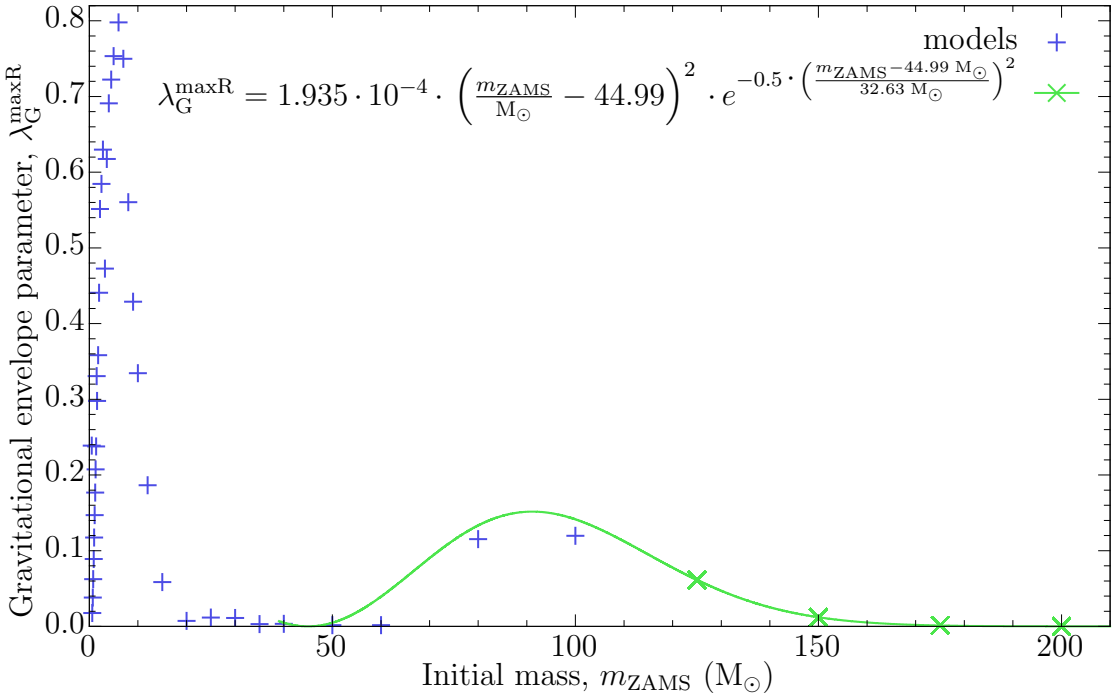

Figure B.7: Extrapolation of the gravitational envelope binding parameter, $\lambda_{\rm G}^{\rm maxR}$, at maximum radius to larger ZAMS masses.

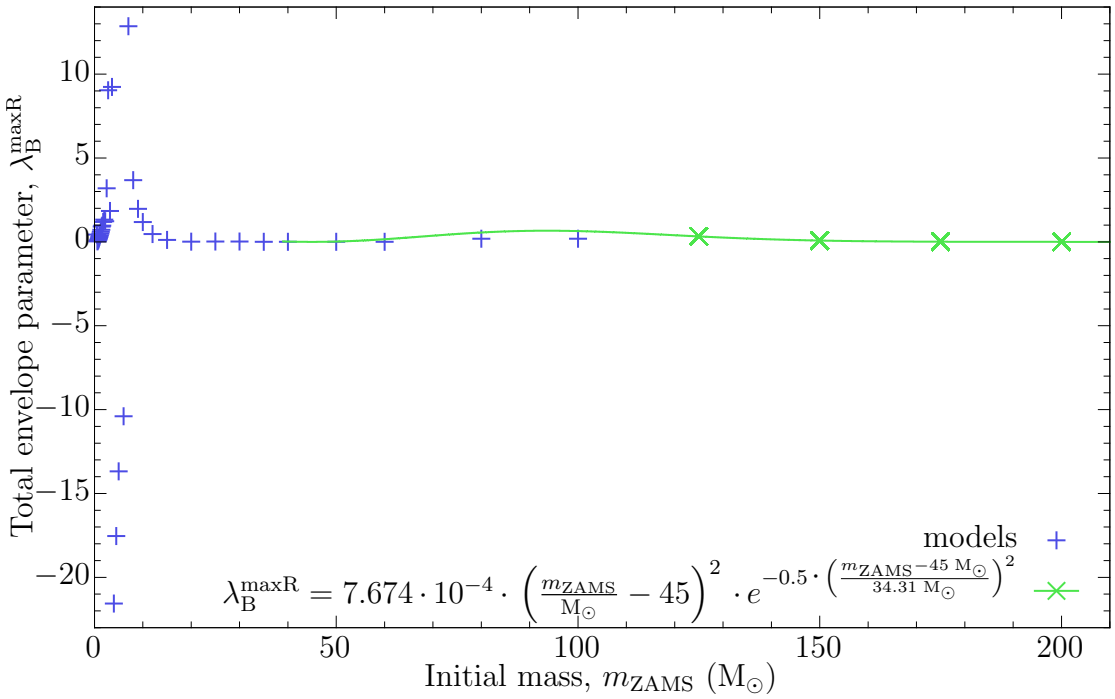

Figure B.8: Extrapolation of the envelope binding parameter including internal binding energy, λ_B^{maxR}, at maximum radius to larger ZAMS masses.

B.1.2 At maximum core mass

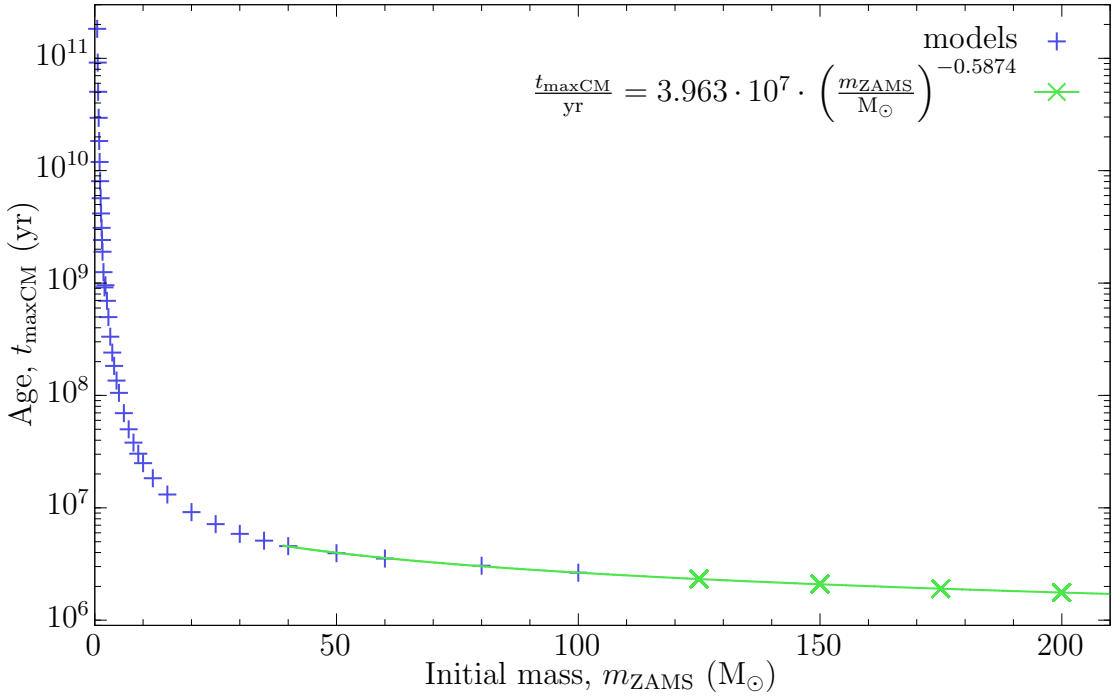

Figure B.9: Extrapolation of the age, t_{maxCM}, at maximum core mass to larger ZAMS masses (The extrapolations are only valid in the plotted range of the green line.).

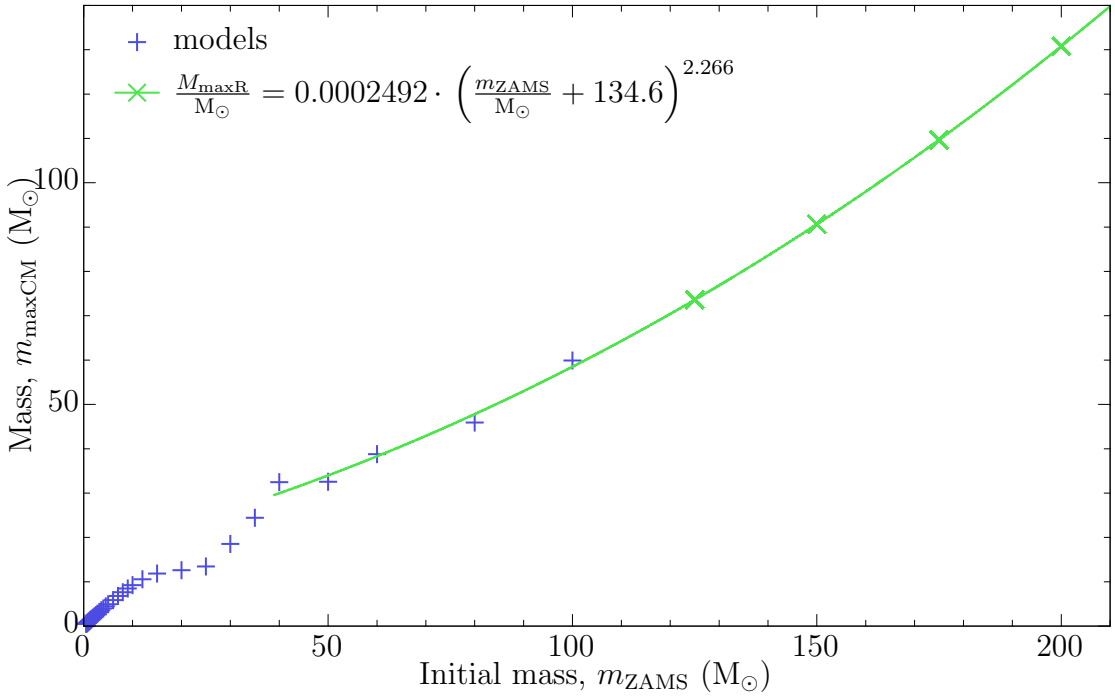

Figure B.10: Extrapolation of the mass, m_{maxCM}, at maximum core mass to larger ZAMS masses.

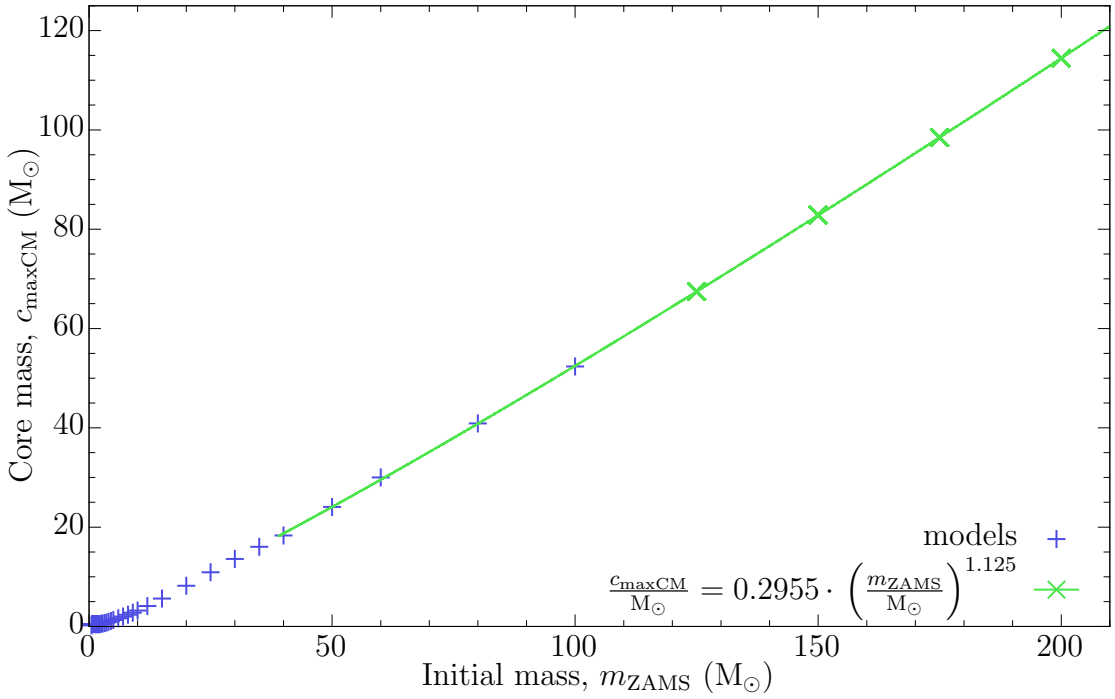

Figure B.11: Extrapolation of the core mass, c_{maxCM}, at maximum core mass to larger ZAMS masses.

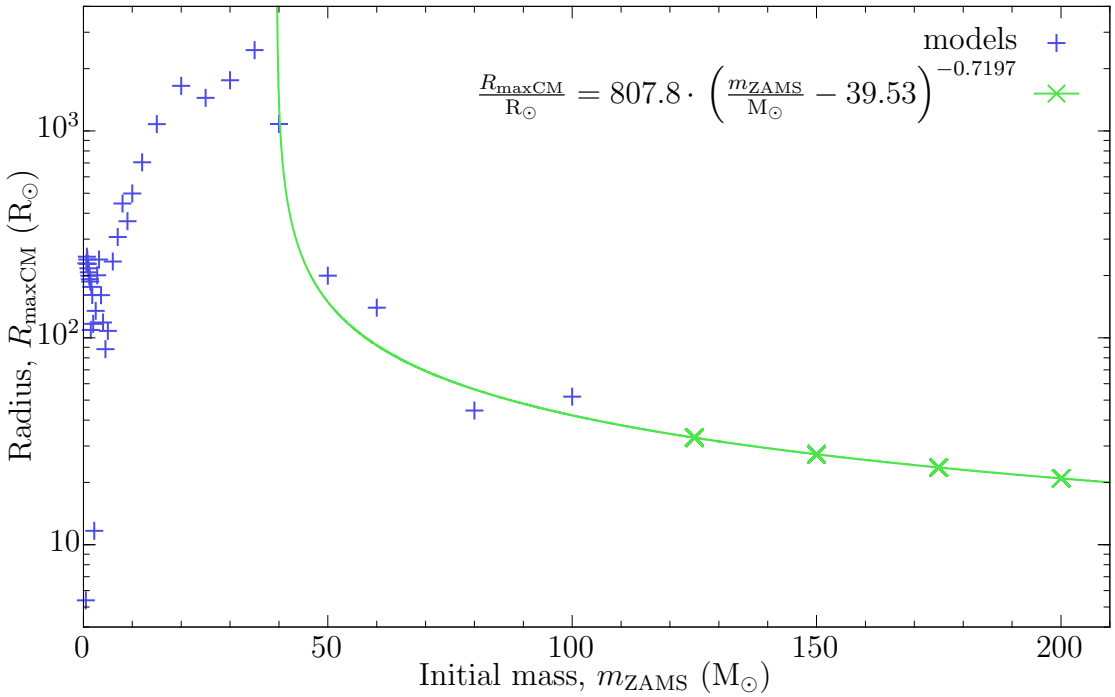

Figure B.12: Extrapolation of the radius, R_{maxCM}, at maximum core mass to larger ZAMS masses.

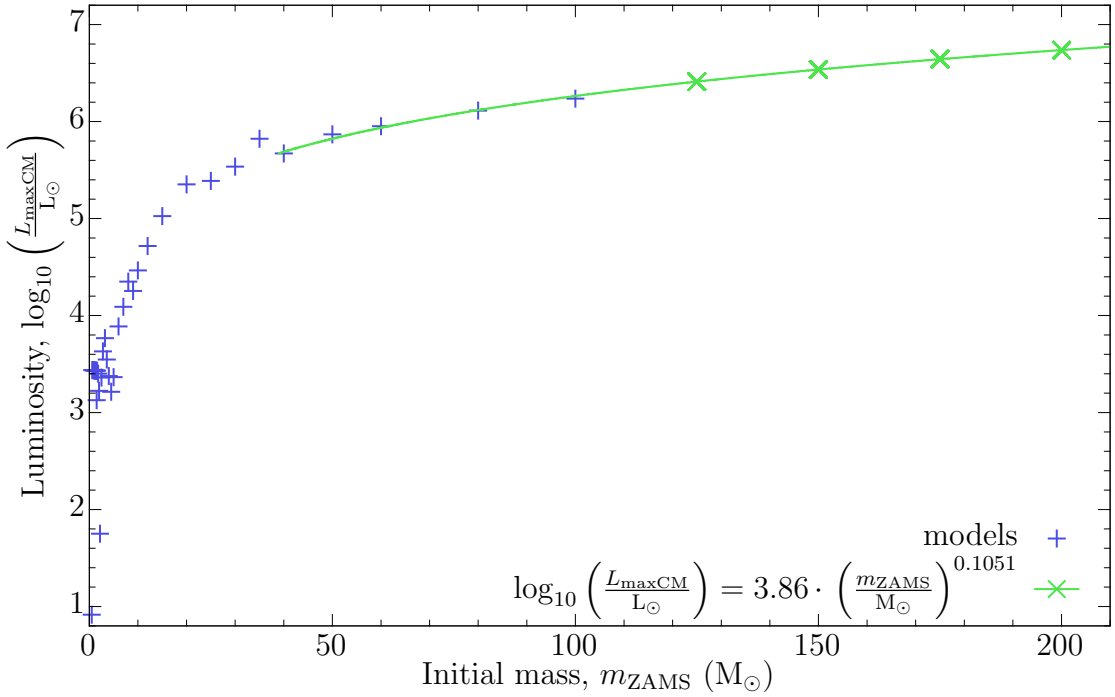

Figure B.13: Extrapolation of the luminosity, L_{maxCM}, at maximum core mass to larger ZAMS masses.

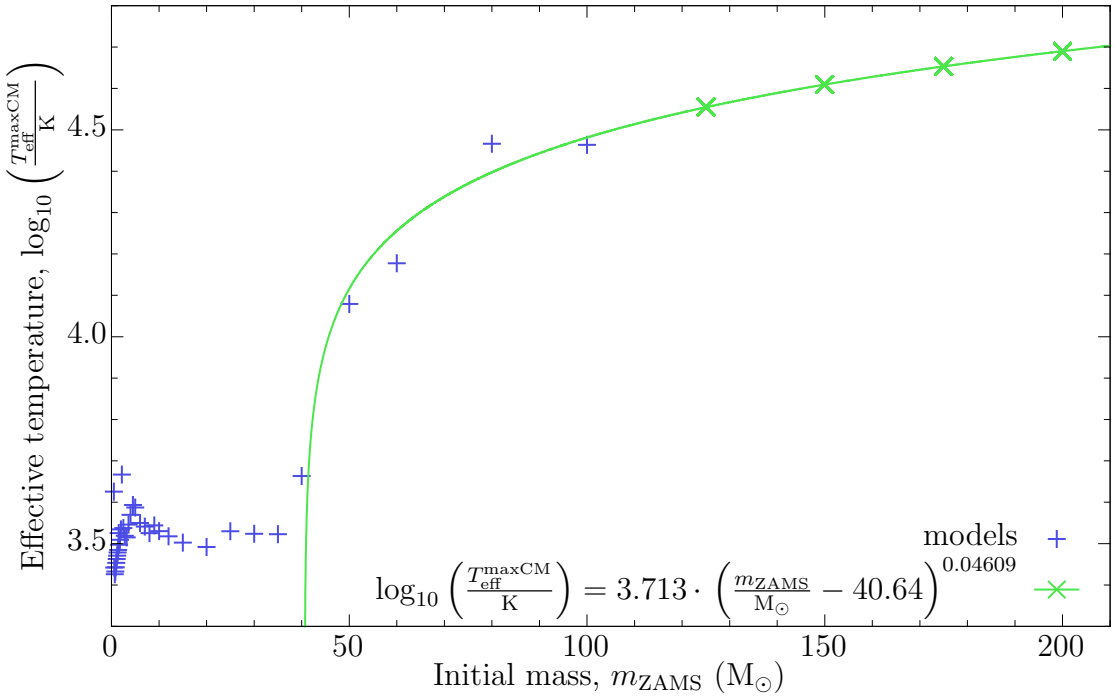

Figure B.14: Extrapolation of the effective temperature, $T_{\mathrm{eff}}^{\mathrm{maxCM}}$, at maximum core mass to larger ZAMS masses.

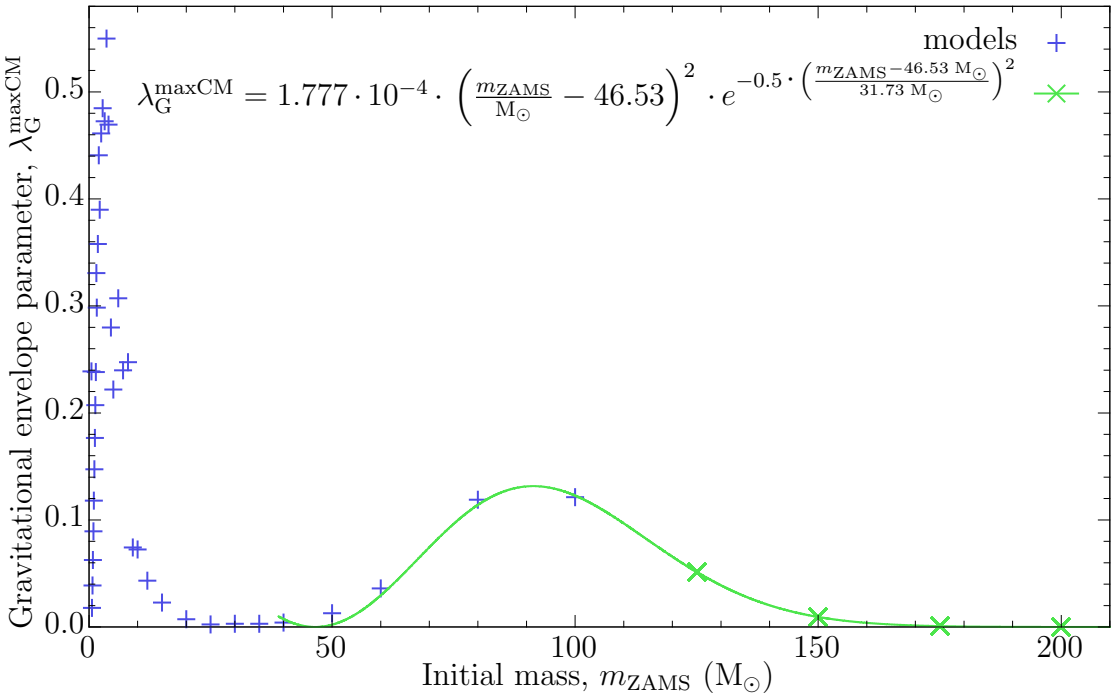

Figure B.15: Extrapolation of the gravitational envelope binding parameter, $\lambda_{\mathrm{G}}^{\mathrm{maxCM}}$, at maximum core mass to larger ZAMS masses.

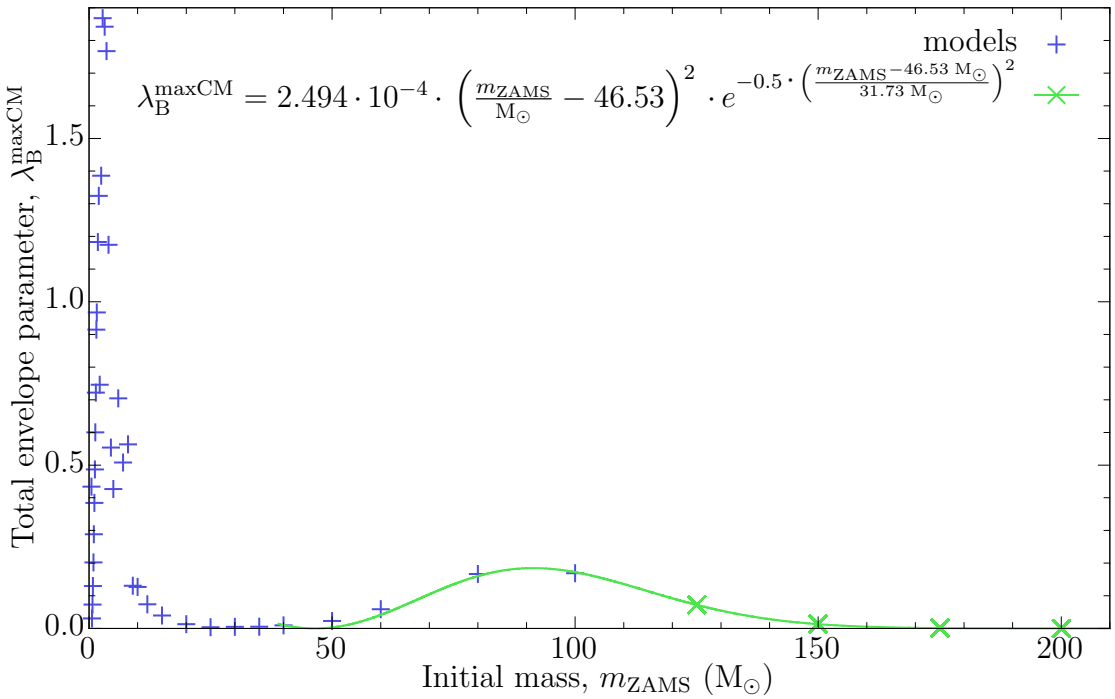

Figure B.16: Extrapolation of the envelope binding parameter including internal binding energy, $\lambda_{\mathrm{B}}^{\mathrm{maxCM}}$, at maximum core mass to larger ZAMS masses.

B.1.3 At the end of the stellar calculation

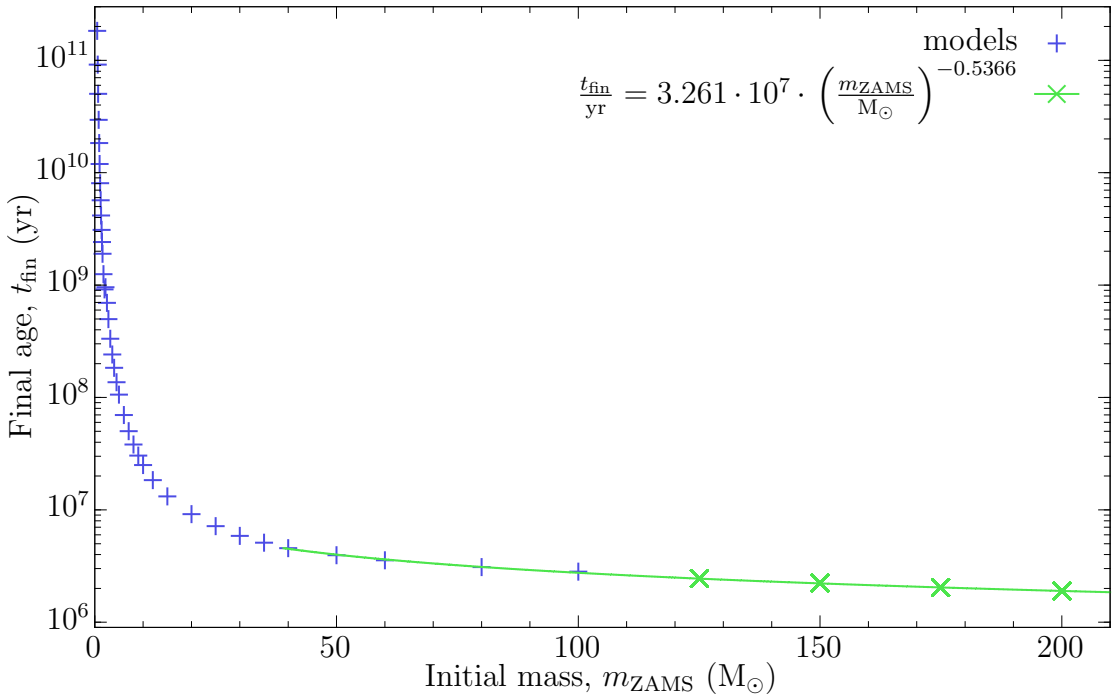

Figure B.17: Extrapolation of the age, $t_{\rm fin}$, at the end of the stellar calculation to larger ZAMS masses (The extrapolations are only valid in the plotted range of the green line.).

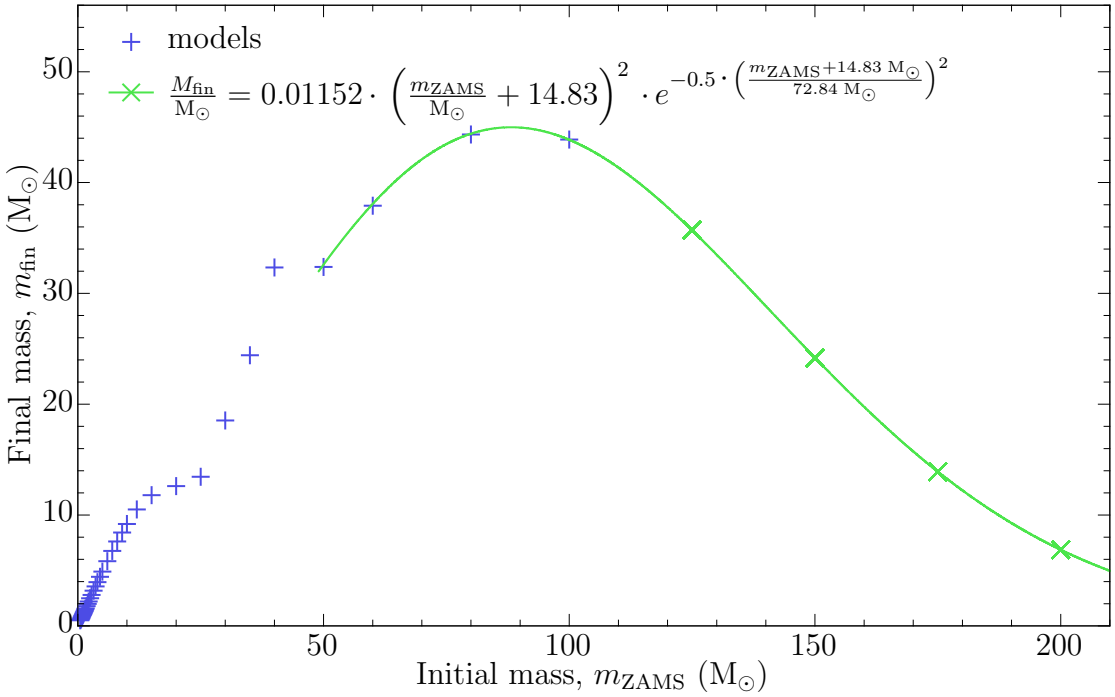

Figure B.18: Extrapolation of the mass, $m_{\rm fin}$, at the end of the stellar calculation to larger ZAMS masses.

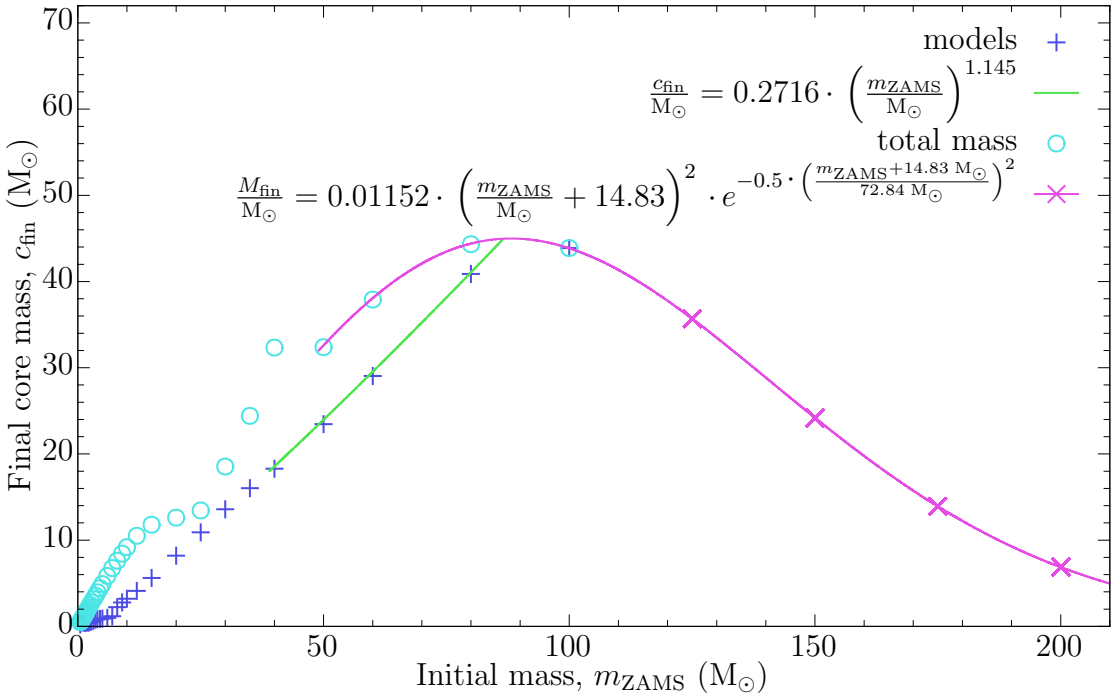

Figure B.19: Extrapolation of the core mass, $c_{\rm fin}$, at the end of the stellar calculation to larger ZAMS masses.

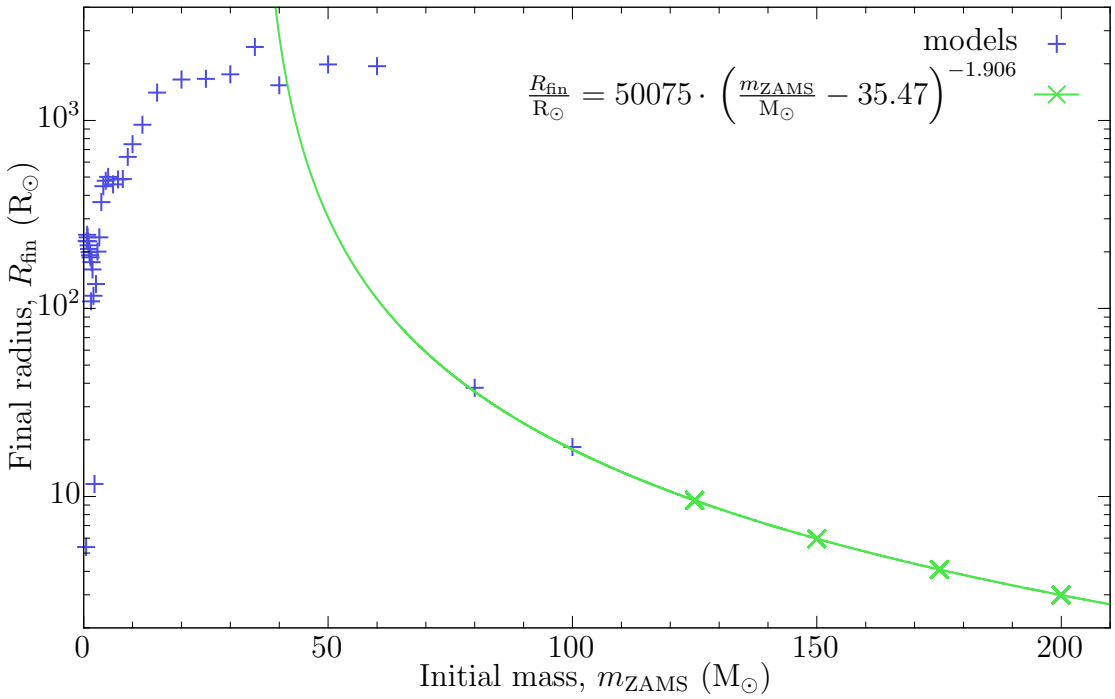

Figure B.20: Extrapolation of the radius, $R_{\rm fin}$, at the end of the stellar calculation to larger ZAMS masses.

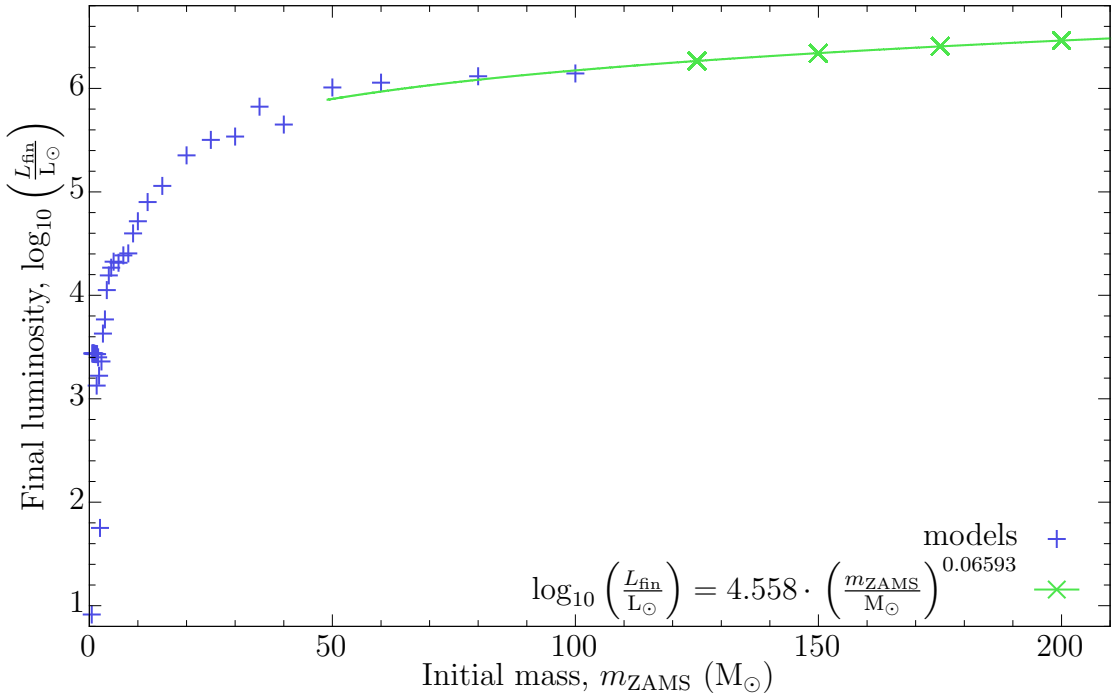

Figure B.21: Extrapolation of the luminosity, $L_{\rm fin}$, at the end of the stellar calculation to larger ZAMS masses.

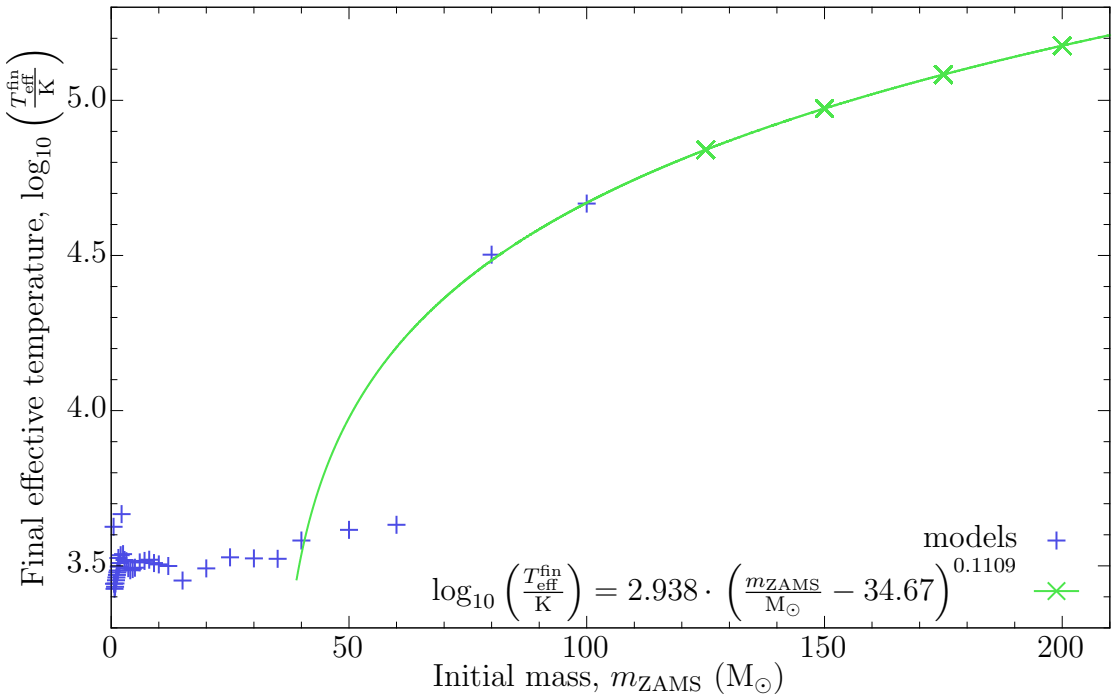

Figure B.22: Extrapolation of the effective temperature, $T_{\rm eff}^{\rm fin}$, at the end of the stellar calculation to larger ZAMS masses.

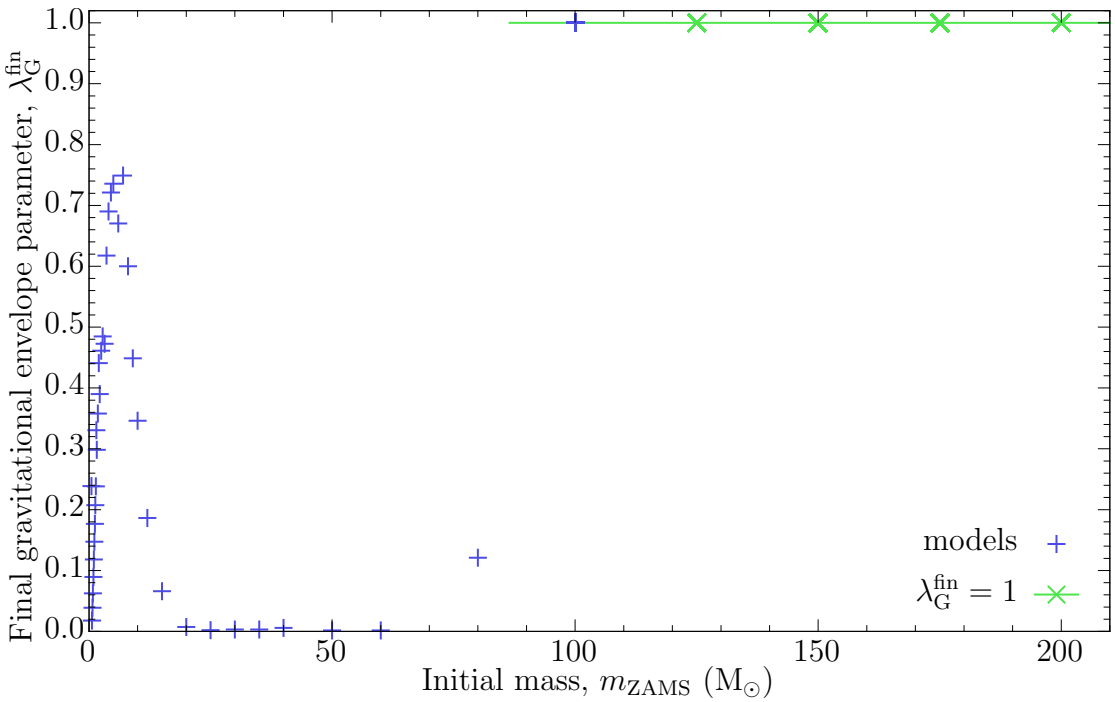

Figure B.23: Extrapolation of the gravitational envelope binding parameter, $\lambda_{\rm G}^{\rm fin}$, at the end of the stellar calculation to larger ZAMS masses.

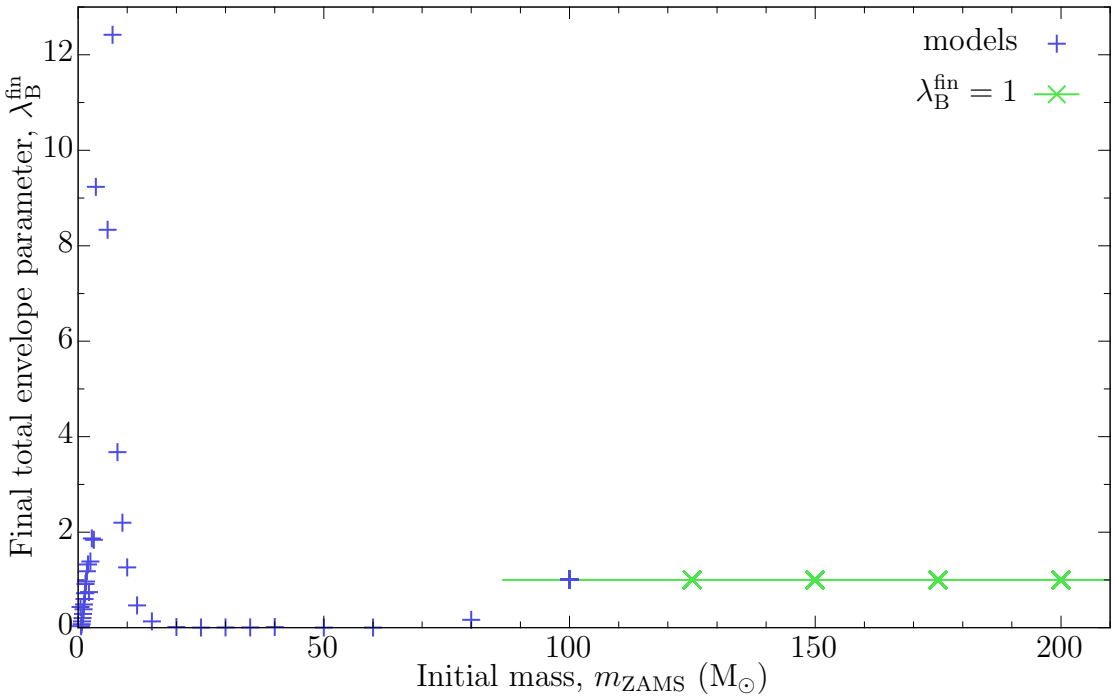

Figure B.24: Extrapolation of the envelope binding parameter including internal binding energy, λ_B^{fin}, at the end of the stellar calculation to larger ZAMS masses.

B.1.4 He-stars at He-ZAMS

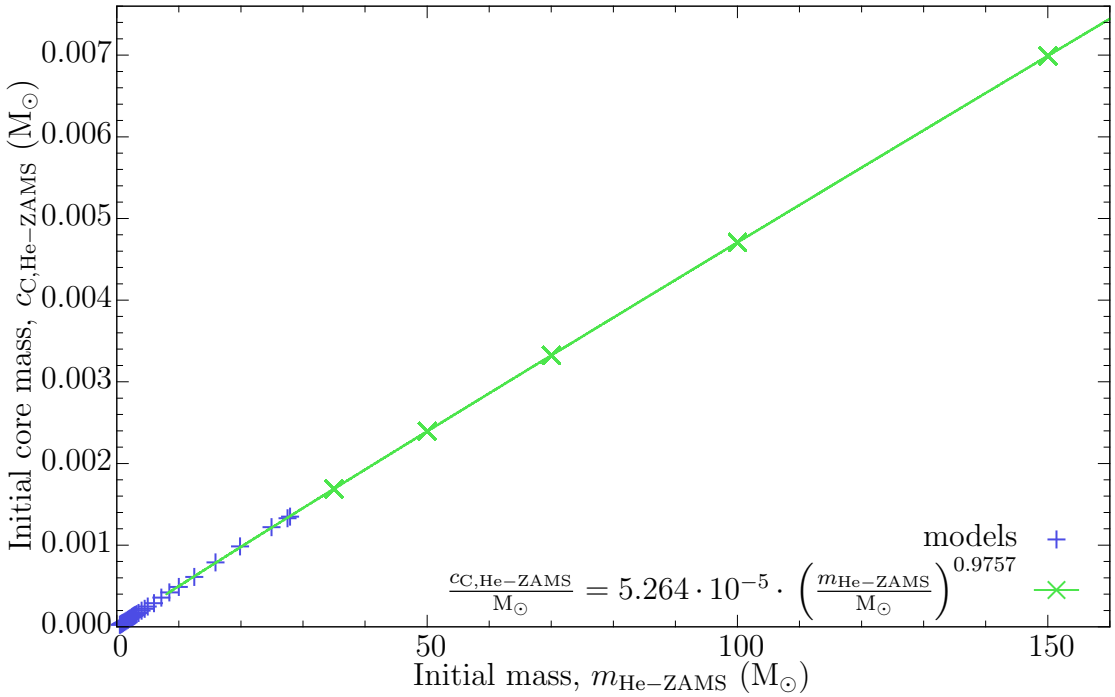

Figure B.25: Extrapolation of the He-star's carbon core mass, $c_{\mathrm{C,He-ZAMS}}$, at He-ZAMS to larger He-ZAMS masses (The extrapolations are only valid in the plotted range of the green line.).

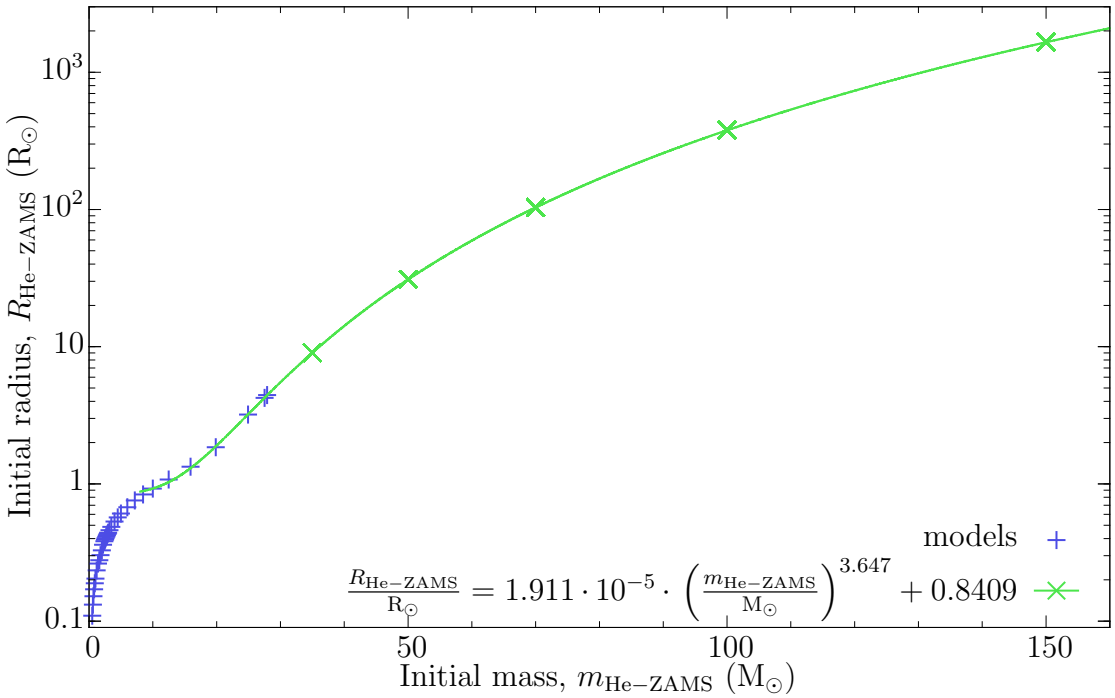

Figure B.26: Extrapolation of the He-star's radius, $R_{\mathrm{He-ZAMS}}$, at He-ZAMS to larger He-ZAMS masses.

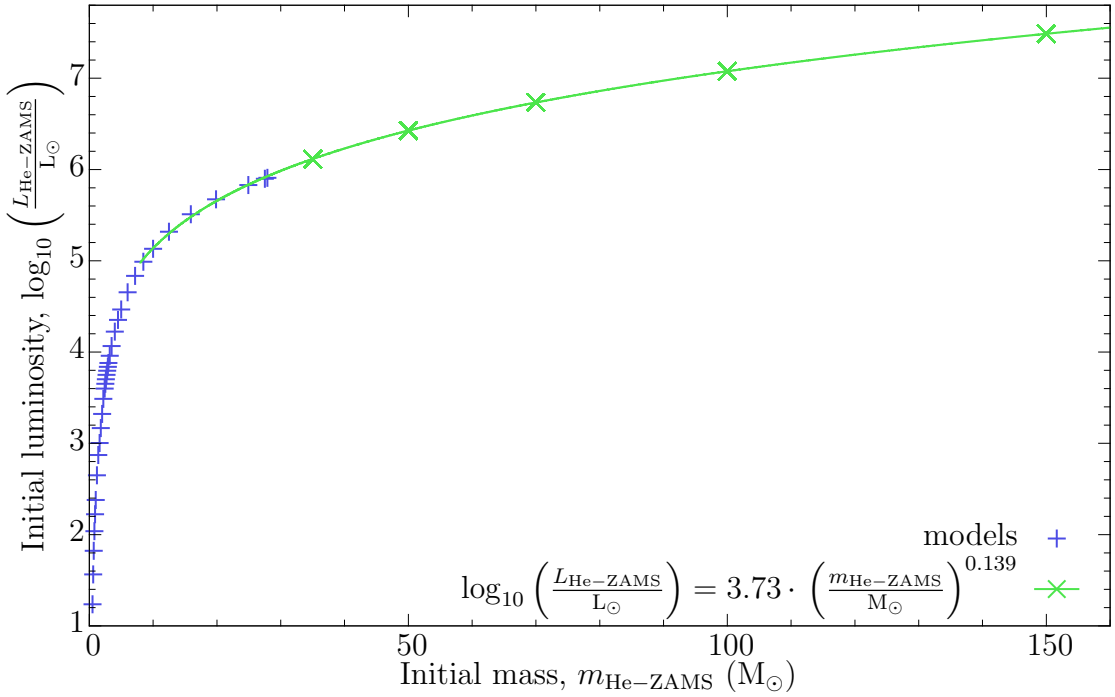

Figure B.27: Extrapolation of the He-star's luminosity, $L_{\mathrm{He-ZAMS}}$, at He-ZAMS to larger He-ZAMS masses.

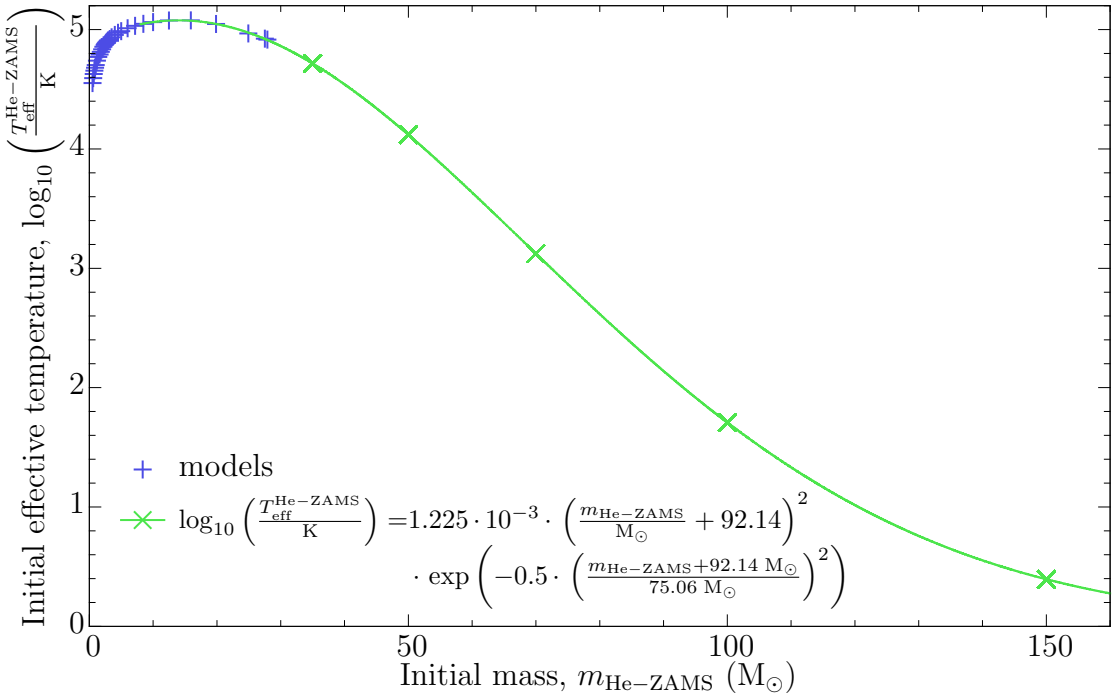

Figure B.28: Extrapolation of the He-star's effective temperature, $T_{\mathrm{eff}}^{\mathrm{He-ZAMS}}$, at He-ZAMS to larger He-ZAMS masses.

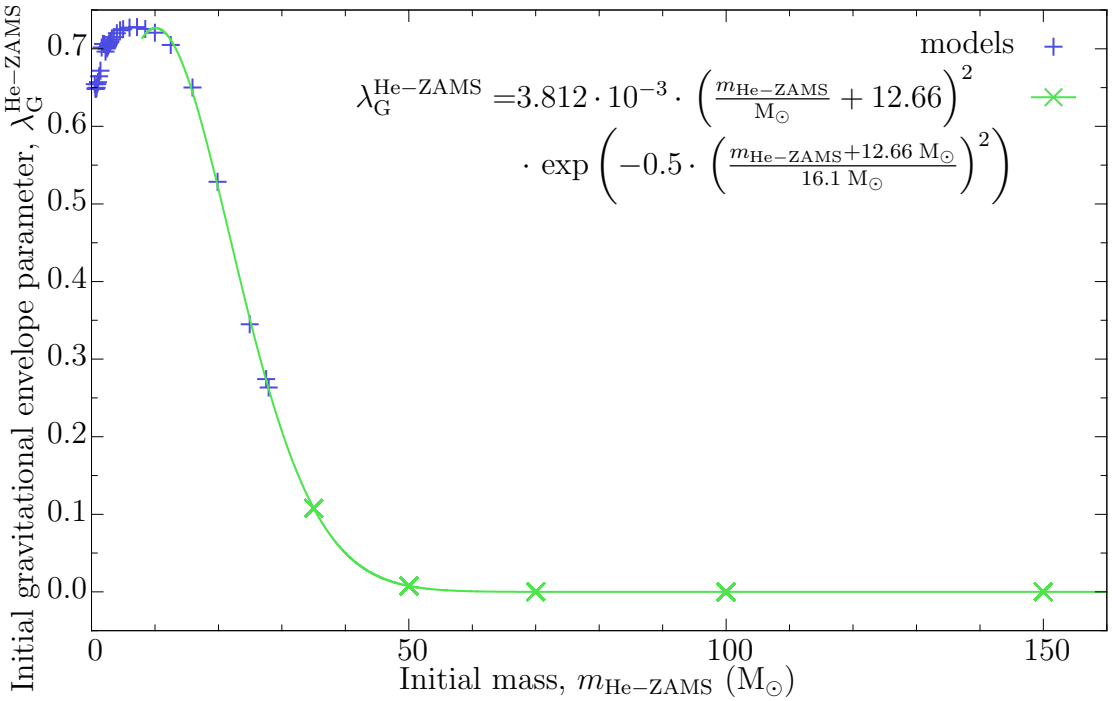

Figure B.29: Extrapolation of the He-star's gravitational envelope binding parameter, $\lambda_{\rm G}^{\rm He-ZAMS}$, at He-ZAMS to larger He-ZAMS masses.

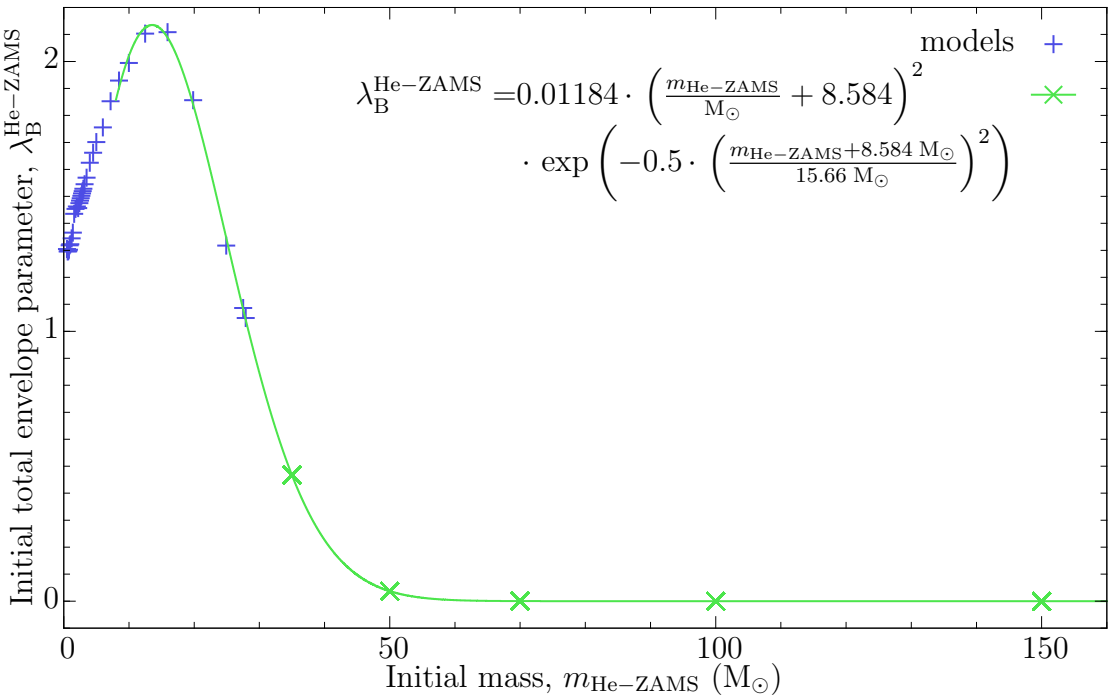

Figure B.30: Extrapolation of the He-star's envelope binding parameter including internal binding energy, $\lambda_{\rm B}^{\rm He-ZAMS}$, at He-ZAMS to larger He-ZAMS masses.

B.1.5 He-stars at their end of the stellar calculation

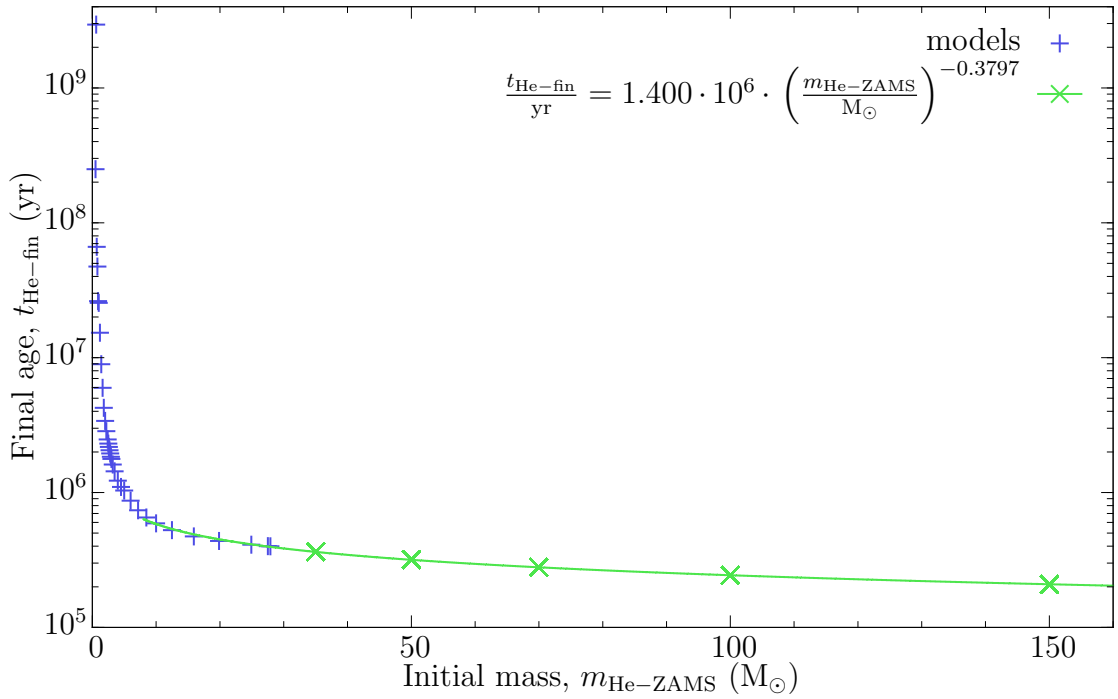

Figure B.31: Extrapolation of the He-star's age, $t_{\mathrm{He-fin}}$, at the end of the stellar calculation to larger He-ZAMS masses (The extrapolations are only valid in the plotted range of the green line.).

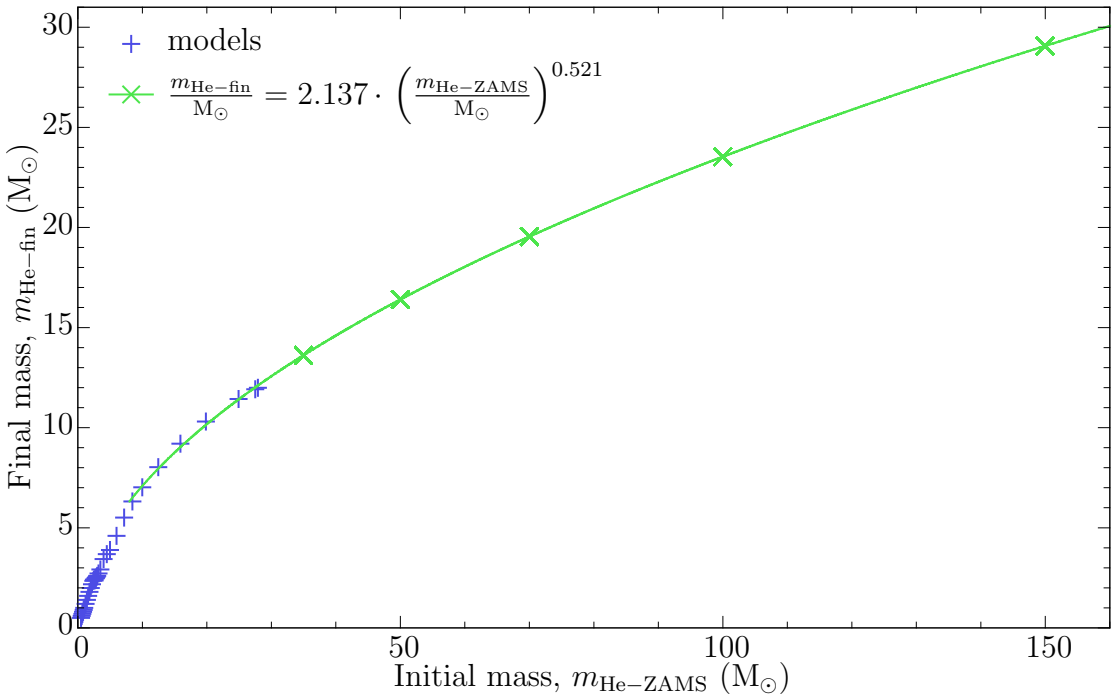

Figure B.32: Extrapolation of the He-star's mass, $m_{\mathrm{He-fin}}$, at the end of the stellar calculation to larger He-ZAMS masses.

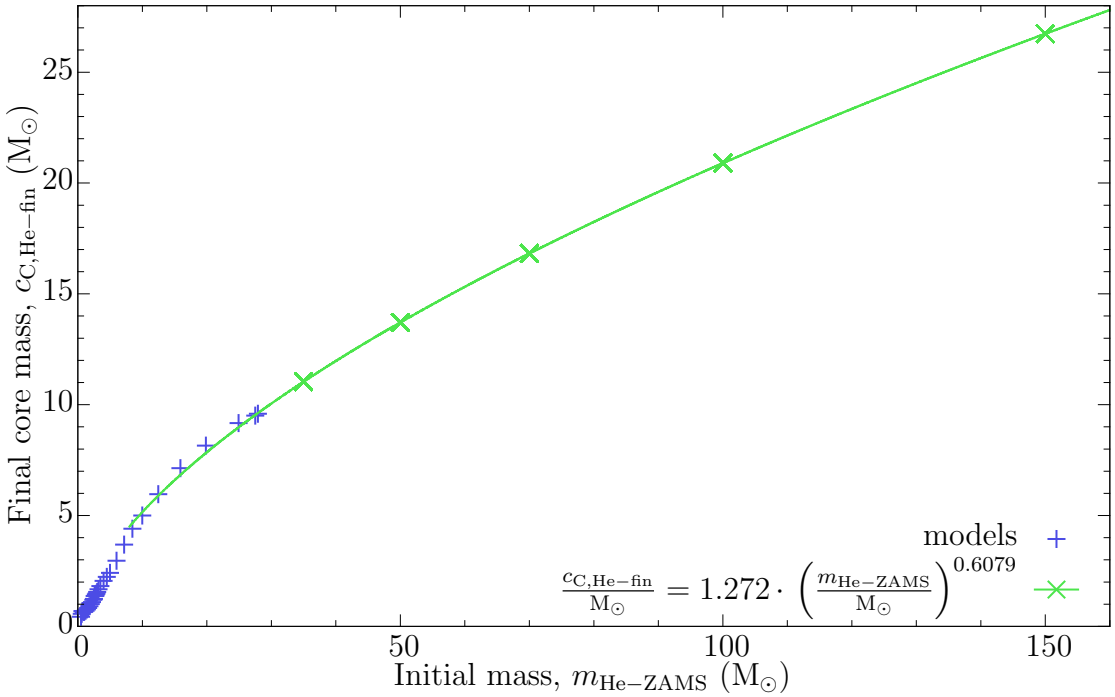

Figure B.33: Extrapolation of the He-star's carbon core mass, $c_{\mathrm{C,He-fin}}$, at the end of the stellar calculation to larger He-ZAMS masses.

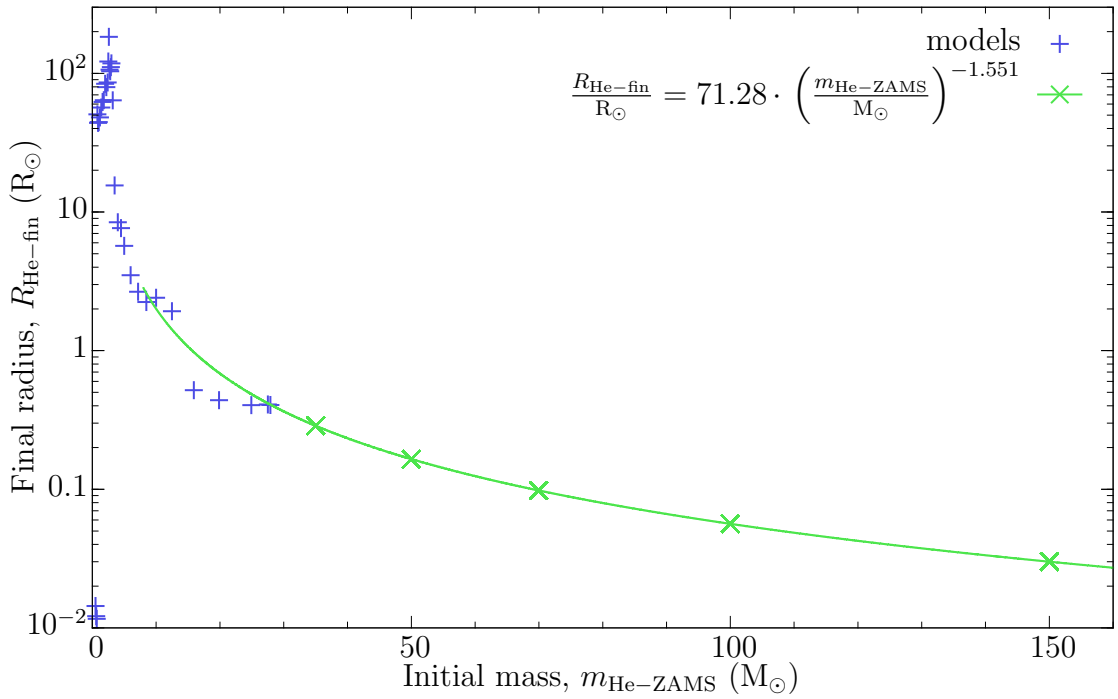

Figure B.34: Extrapolation of the He-star's radius, $R_{\mathrm{He-fin}}$, at the end of the stellar calculation to larger He-ZAMS masses.

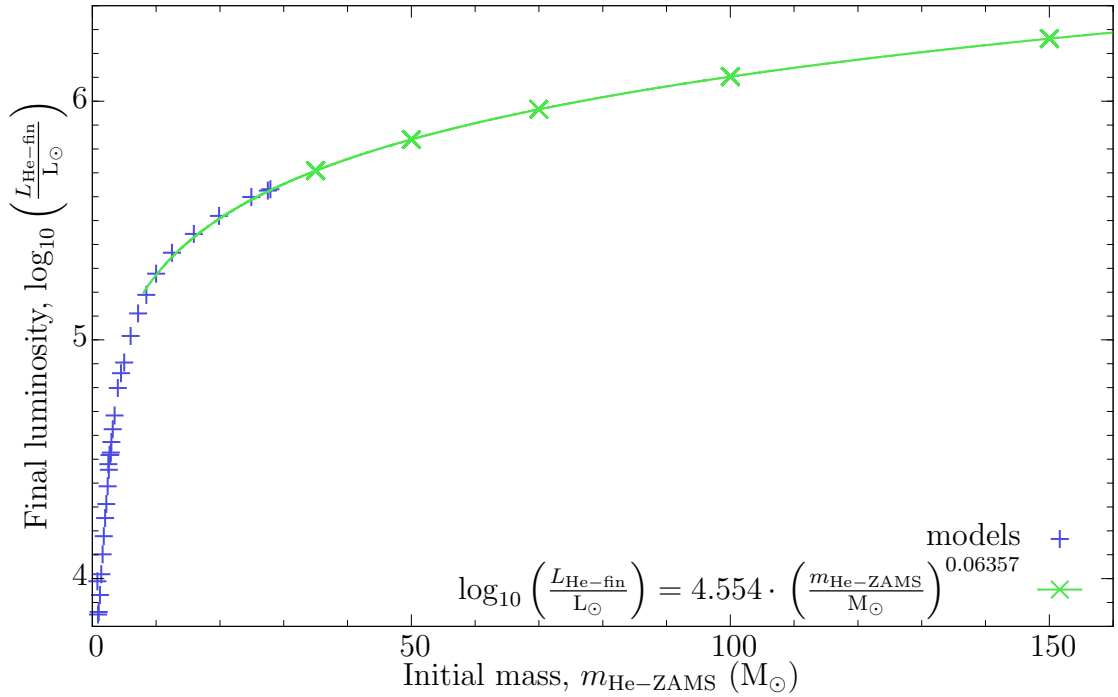

Figure B.35: Extrapolation of the He-star's luminosity, $L_{\mathrm{He-fin}}$, at the end of the stellar calculation to larger He-ZAMS masses.

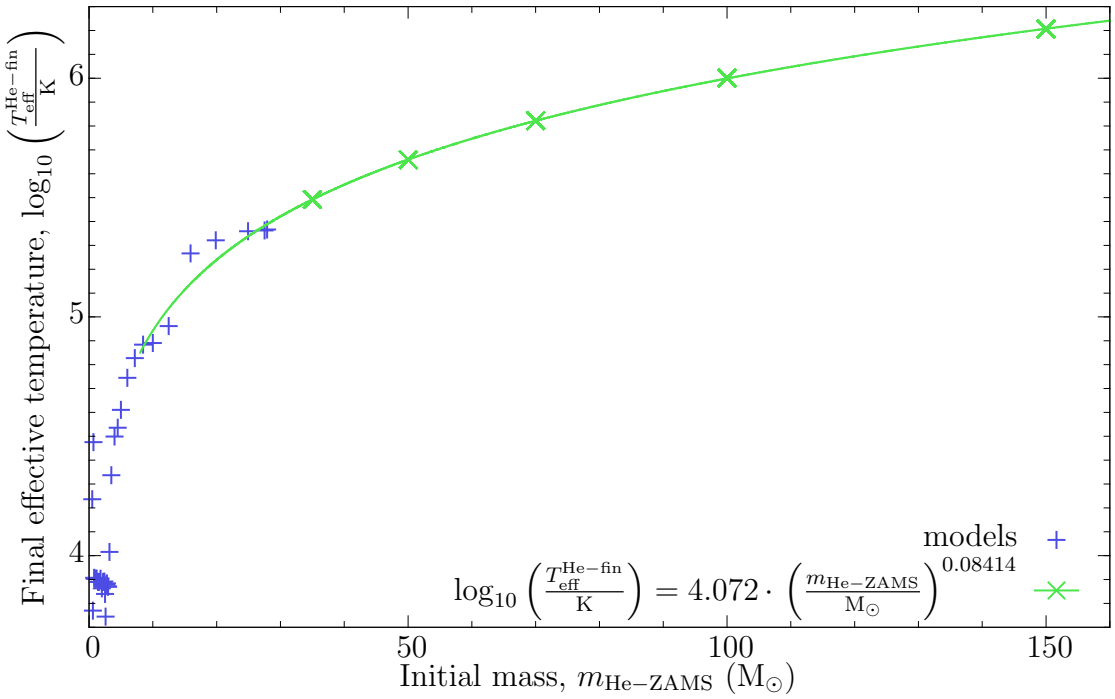

Figure B.36: Extrapolation of the He-star's effective temperature, $T_{\rm eff}^{\rm He-fin}$, at the end of the stellar calculation to larger He-ZAMS masses.

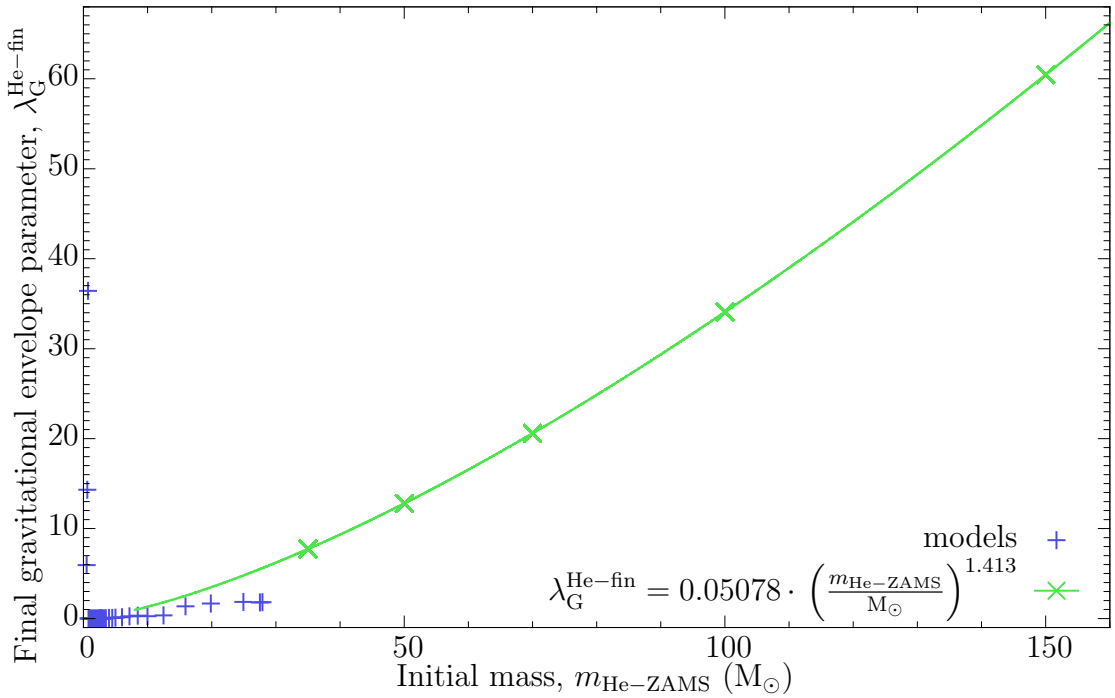

Figure B.37: Extrapolation of the He-star's gravitational envelope binding parameter, $\lambda_{\rm G}^{\rm He-fin}$, at the end of the stellar calculation to larger He-ZAMS masses.

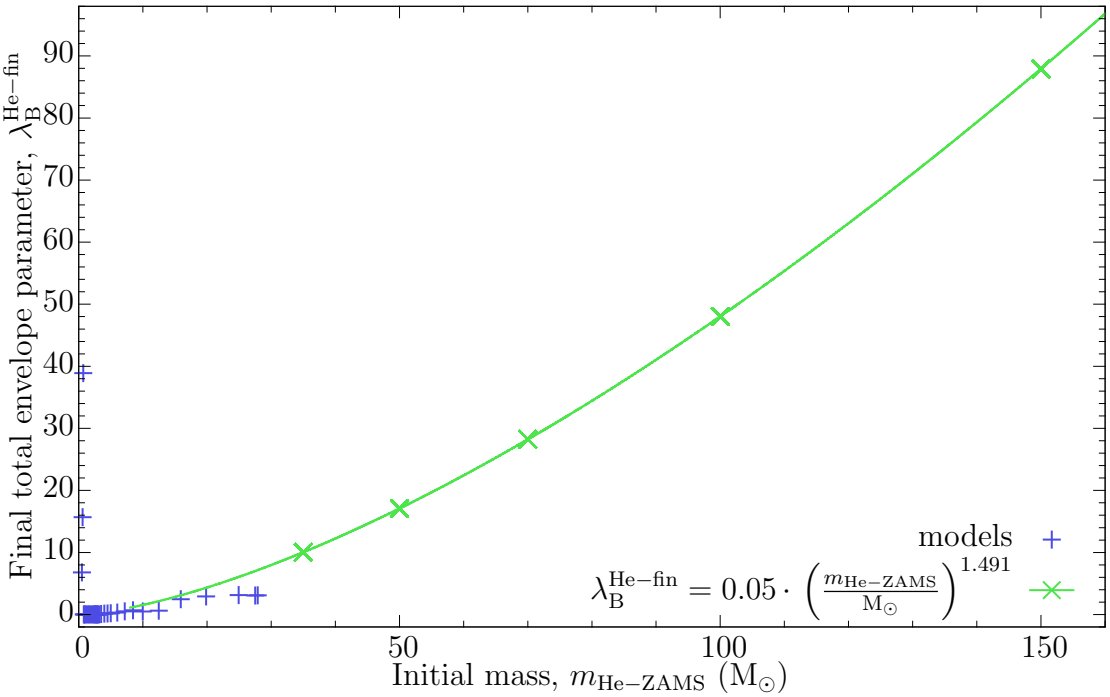

Figure B.38: Extrapolation of the He-star's envelope binding parameter including internal binding energy, λ_B^{He-fin}, at the end of the stellar calculation to larger He-ZAMS masses.

B.2 Figures of Section 3.13.2

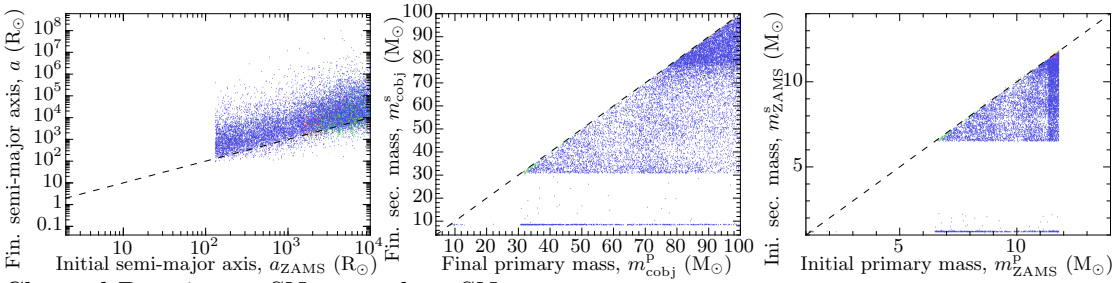

Channel D: primary SN, secondary SN.

Colours – merge within 10 Gyr: purple; do not merge: blue, green, red, yellow, teal – first SN with MS companion: blue, yellow, purple, teal; first SN with post MS companion: green, red – companion after SN is core hydrogen burning: blue, purple; companion after SN is core helium burning: green, teal; companion after SN is core carbon burning: red, yellow

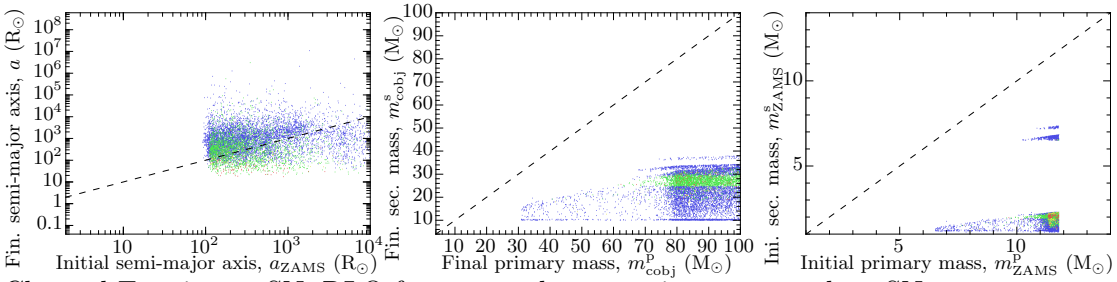

Channel E: primary SN, RLO from secondary to primary, secondary SN.

Colours – merge within 10 Gyr: red, yellow; do not merge: blue, green – early RLO: green, red; late RLO: blue, yellow

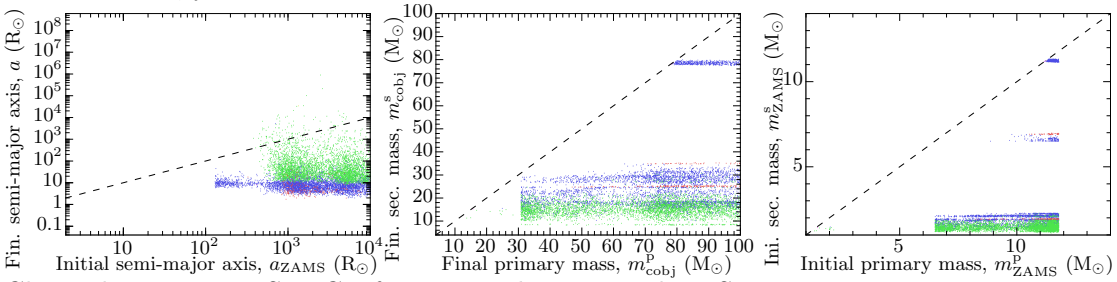

Channel F: primary SN, CE from secondary, secondary SN.

Colours – merge within 10 Gyr: blue, red, purple; do not merge: green, yellow – first SN with MS companion: blue, green, red, yellow; first SN with post MS companion: purple – early CE: red, yellow; late CE: blue, green, purple

Figure B.39: Primary mass, secondary mass and semi-major axis at ZAMS and directly after the formation of the second compact object of channels D to F. The colours represent the most frequent to least frequent evolution with a given channel, where the order is always: blue, green, red, yellow, purple, teal, dark blue, dark green, dark red, dark yellow, dark purple, dark teal.

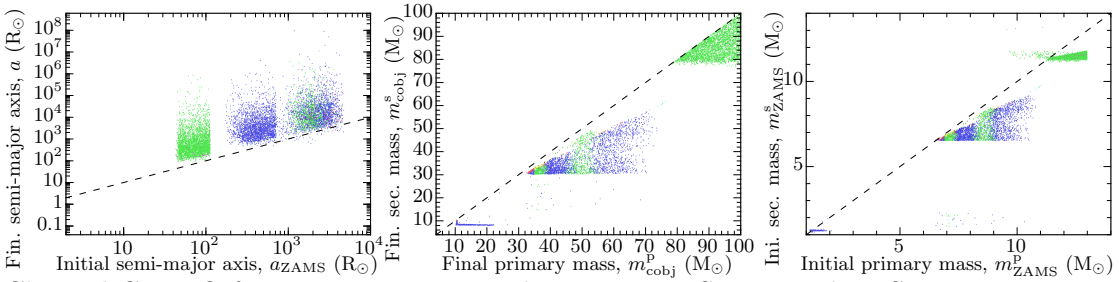

Channel G: RLO from primary to secondary, primary SN, secondary SN.

Colours – merge within 10 Gyr: purple, dark yellow; do not merge: blue, green, red, yellow, teal, dark blue, dark green, dark red – first RLO being Case A: green, yellow, purple, dark green, dark red; first RLO being Case B/C: blue, red, teal, dark blue, dark yellow – first SN with MS companion: blue, green, purple, dark blue, dark red, dark yellow; first SN with post MS companion: red, yellow, teal, dark green – companion after SN is core hydrogen burning: blue, green, purple, dark yellow; companion after SN is core helium burning: red, yellow, dark blue, dark red; companion after SN is core carbon burning: teal, dark green

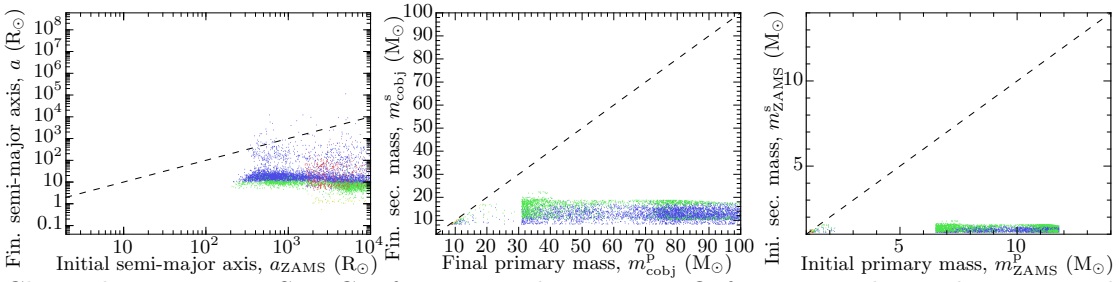

Channel H: primary SN, CE from secondary, He-RLO from secondary, ultra-stripped secondary SN.

Colours – merge within 10 Gyr: green, yellow; do not merge: blue, red – first SN with MS companion: blue, green; first SN with post MS companion: red, yellow

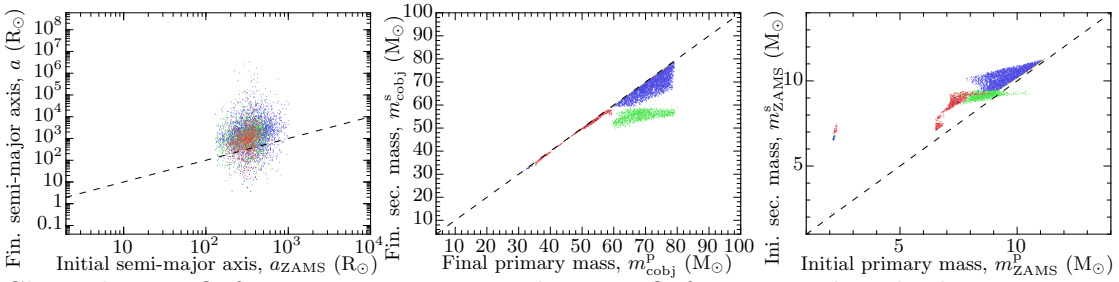

Channel I: RLO from primary to secondary, RLO from secondary back to primary, primary SN, secondary SN.

Colours – merge within 10 Gyr: purple, teal, dark blue, dark red; do not merge: blue, green, red, yellow, dark green – first RLO being Case A: red, dark blue, dark green; first RLO being Case B/C onto MS star: blue, green, purple, teal; first RLO being Case B/C onto post MS star: yellow, dark red – early second RLO: green, red, teal, dark blue; late second RLO: blue, yellow, purple, dark green, dark red

Figure B.40: Primary mass, secondary mass and semi-major axis at ZAMS and directly after the formation of the second compact object of channels G to I. The colours represent the most frequent to least frequent evolution with a given channel, where the order is always: blue, green, red, yellow, purple, teal, dark blue, dark green, dark red, dark yellow, dark purple, dark teal.

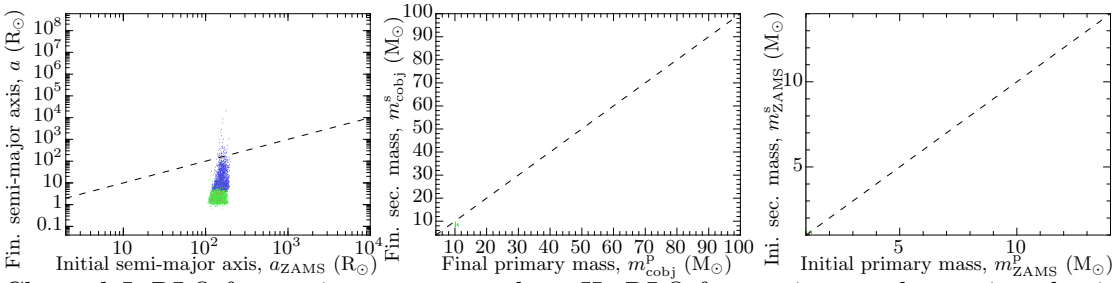

Channel J: RLO from primary to secondary, He-RLO from primary, ultra-stripped primary SN, CE from secondary, He-RLO from secondary, ultra-stripped secondary SN.
Colours – merge within 10 Gyr: green, red; do not merge: blue, yellow – first RLO being Case B/C: all – second RLO onto MS star: blue, green; second RLO onto post MS star: red, yellow

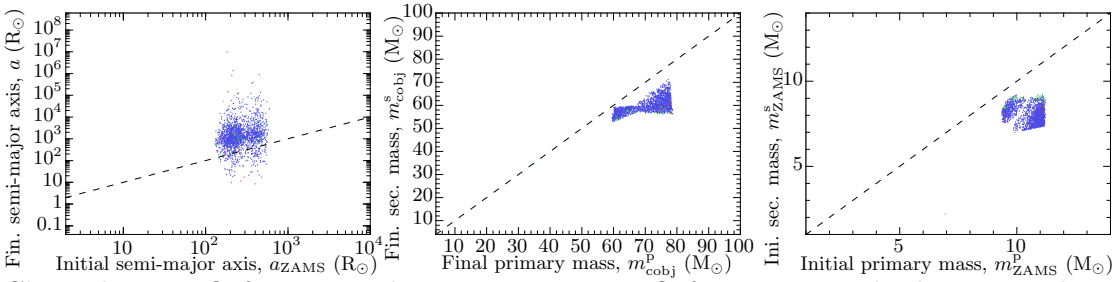

Channel K: RLO from secondary to primary, RLO from primary back to secondary, secondary SN, primary SN.
Colours – merge within 10 Gyr: red; do not merge: blue, green – first RLO being Case A: blue, red; first RLO being Case B/C: green

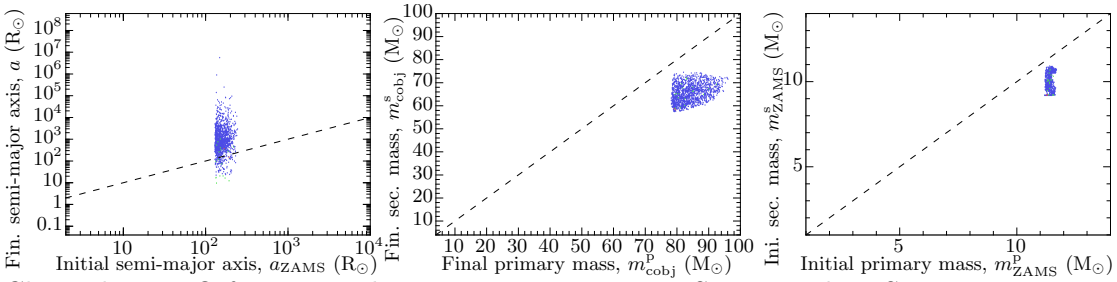

Channel L: RLO from secondary to primary, primary SN, secondary SN.
Colours – merge within 10 Gyr: green; do not merge: blue, red – first RLO being Case A: blue, green; first RLO being Case B/C: red

Figure B.41: Primary mass, secondary mass and semi-major axis at ZAMS and directly after the formation of the second compact object of channels J to L. The colours represent the most frequent to least frequent evolution with a given channel, where the order is always: blue, green, red, yellow, purple, teal, dark blue, dark green, dark red, dark yellow, dark purple, dark teal.

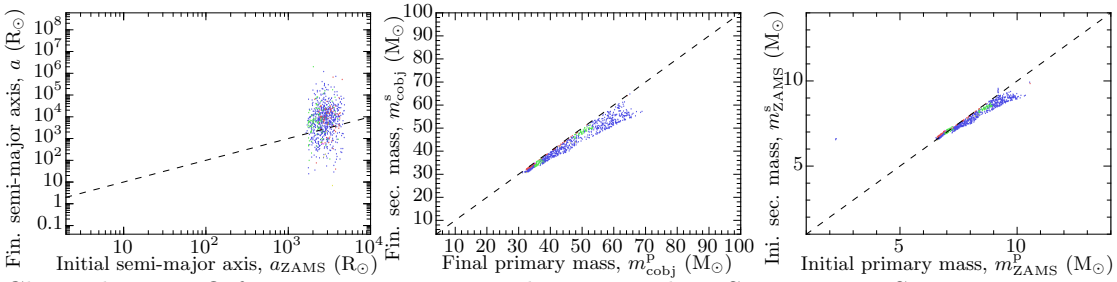

Channel M: RLO from primary to secondary, secondary SN, primary SN.

Colours – merge within 10 Gyr: yellow; do not merge: blue, green, red, purple – first RLO being Case A: green; first RLO being Case B/C onto MS star: blue, yellow, purple; first RLO being Case B/C onto post MS star: red – companion after RLO is core hydrogen burning: blue, green, yellow; companion after RLO is core helium burning: red, purple

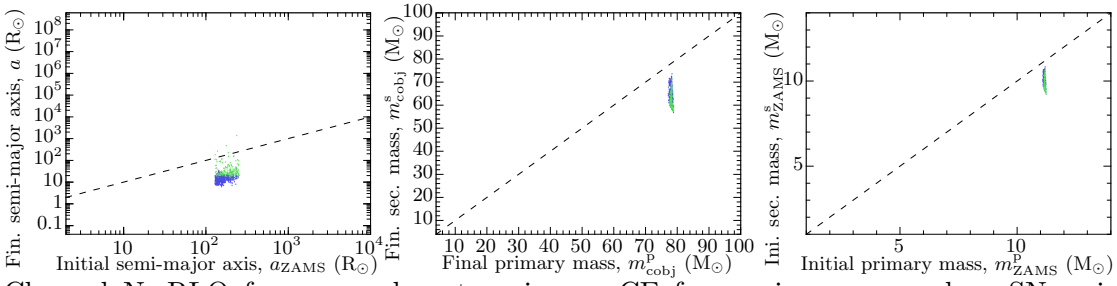

Channel N: RLO from secondary to primary, CE from primary, secondary SN, primary SN.

Colours – merge within 10 Gyr: blue; do not merge: green – first RLO being Case A: all

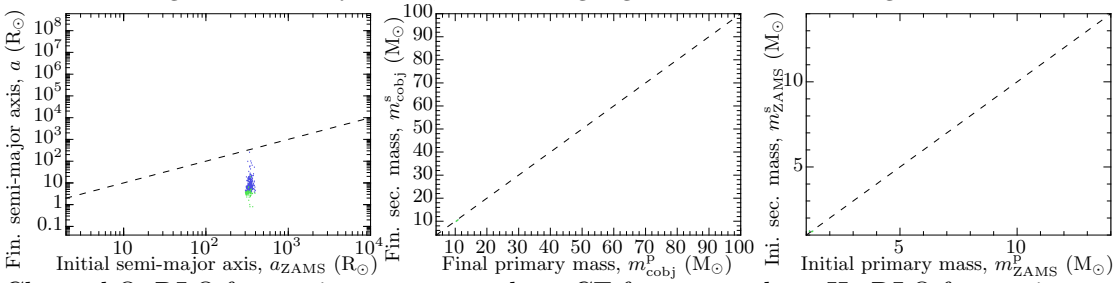

Channel O: RLO from primary to secondary, CE from secondary, He-RLO from primary, ultra-stripped primary SN, He-RLO from secondary, ultra-stripped secondary SN.

Colours – merge within 10 Gyr: green; do not merge: blue – first RLO being Case B/C onto post MS star: all

Figure B.42: Primary mass, secondary mass and semi-major axis at ZAMS and directly after the formation of the second compact object of channels M to O. The colours represent the most frequent to least frequent evolution with a given channel, where the order is always: blue, green, red, yellow, purple, teal, dark blue, dark green, dark red, dark yellow, dark purple, dark teal.

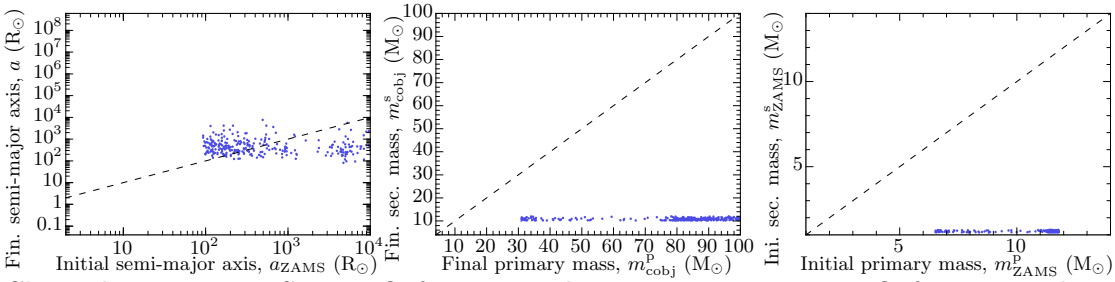

Channel P: primary SN, RLO from secondary to primary, He-RLO from secondary, ultra-stripped secondary SN.

do not merge within 10 Gyr – RLO being Case B/C

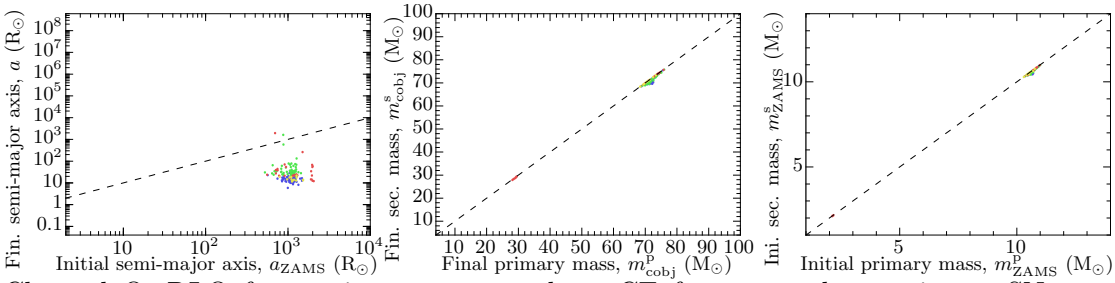

Channel Q: RLO from primary to secondary, CE from secondary, primary SN, secondary SN.

Colours – merge within 10 Gyr: blue, yellow; do not merge: green, red – first RLO being Case B/C onto MS star: blue, green; first RLO being Case B/C onto post MS star: red, yellow

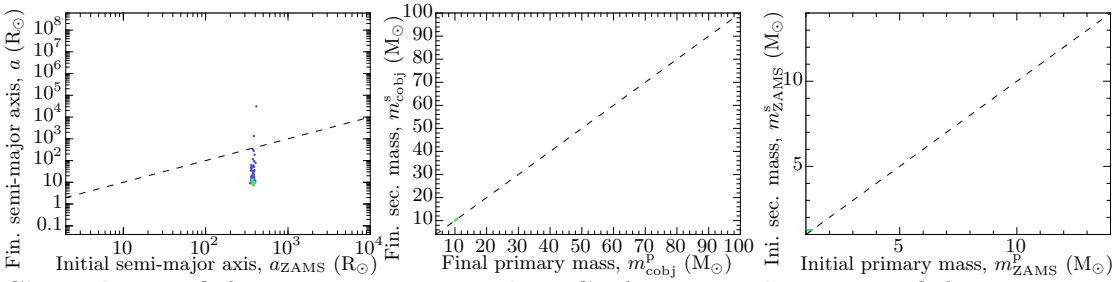

Channel R: RLO from primary to secondary, CE from secondary, He-RLO from primary, ultra-stripped primary SN, secondary SN.

Colours – merge within 10 Gyr: green; do not merge: blue – first RLO being Case B/C onto post MS star: all

Figure B.43: Primary mass, secondary mass and semi-major axis at ZAMS and directly after the formation of the second compact object of channels P to R. The colours represent the most frequent to least frequent evolution with a given channel, where the order is always: blue, green, red, yellow, purple, teal, dark blue, dark green, dark red, dark yellow, dark purple, dark teal.

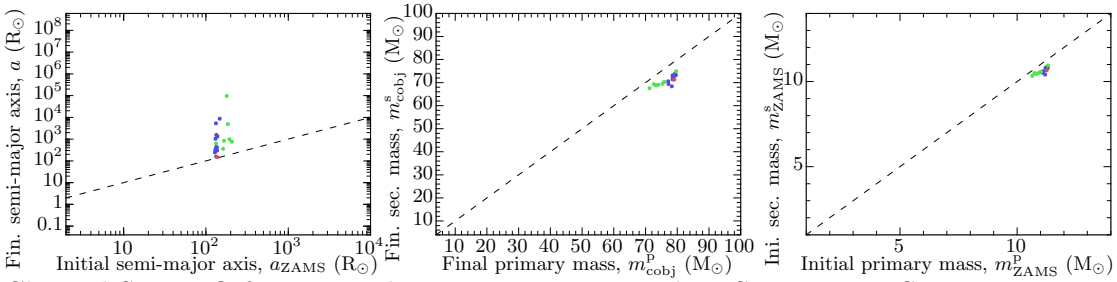

Channel S1: RLO from secondary to primary, secondary SN, primary SN.

Colours – do not merge within 10 Gyr: all – first SN with MS companion: blue; first SN with post MS companion: green, red – companion after SN is core hydrogen burning: blue; companion after SN is core helium burning: red; companion after SN is core carbon burning: green

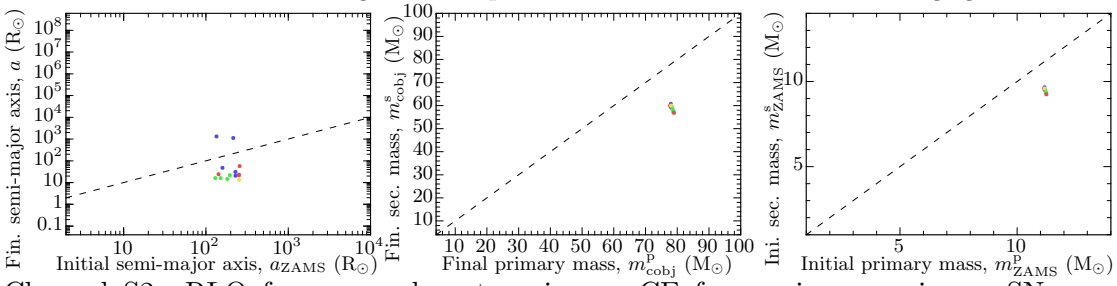

Channel S2: RLO from secondary to primary, CE from primary, primary SN, secondary SN.

Colours – merge within 10 Gyr: green, yellow; do not merge: blue, red – first RLO being Case A: blue, green; first RLO being Case B/C: red, yellow

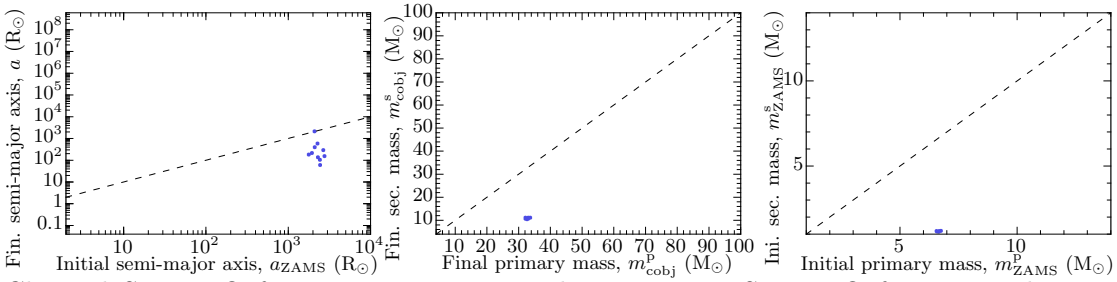

Channel S3: RLO from primary to secondary, primary SN, RLO from secondary to primary, He-RLO from secondary, ultra-stripped secondary SN.

do not merge within 10 Gyr – first RLO being Case B/C

Figure B.44: Primary mass, secondary mass and semi-major axis at ZAMS and directly after the formation of the second compact object of channels S1 to S3. The colours represent the most frequent to least frequent evolution with a given channel, where the order is always: blue, green, red, yellow, purple, teal, dark blue, dark green, dark red, dark yellow, dark purple, dark teal.

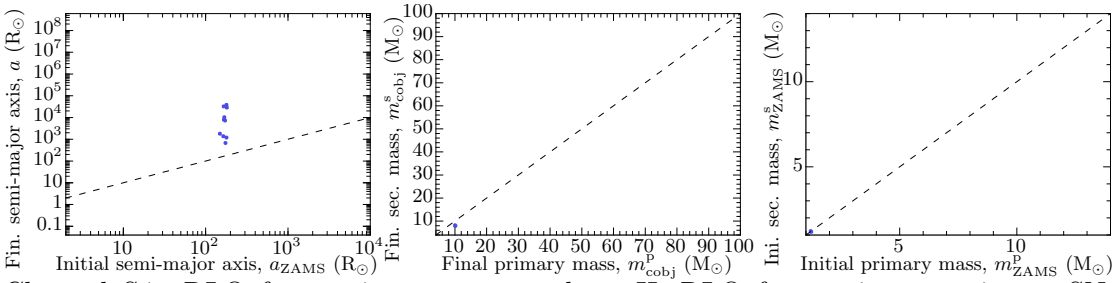

Channel S4: RLO from primary to secondary, He-RLO from primary, primary SN, secondary SN.

do not merge within 10 Gyr – first RLO being Case B/C

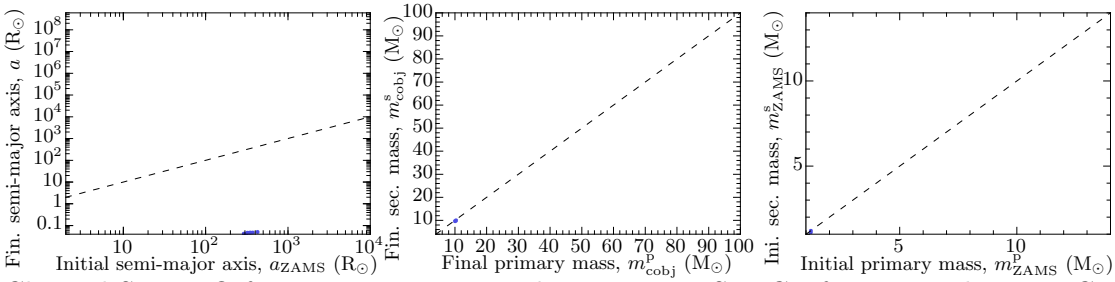

Channel S5: RLO from primary to secondary, primary SN, CE from secondary, He-CE from secondary, ultra-stripped secondary SN.

merge within 10 Gyr – first RLO being Case B/C

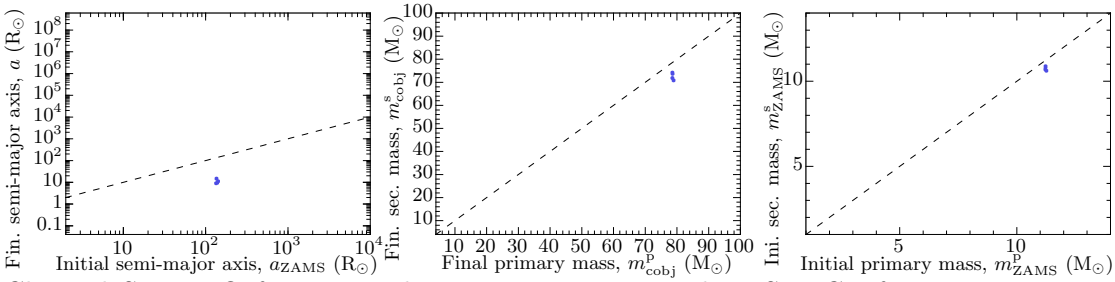

Channel S6: RLO from secondary to primary, secondary SN, CE from primary, primary SN.

merge within 10 Gyr – first RLO being Case A

Figure B.45: Primary mass, secondary mass and semi-major axis at ZAMS and directly after the formation of the second compact object of channels S4 to S6. The colours represent the most frequent to least frequent evolution with a given channel, where the order is always: blue, green, red, yellow, purple, teal, dark blue, dark green, dark red, dark yellow, dark purple, dark teal.

B.3 Figures of Section 3.13.3

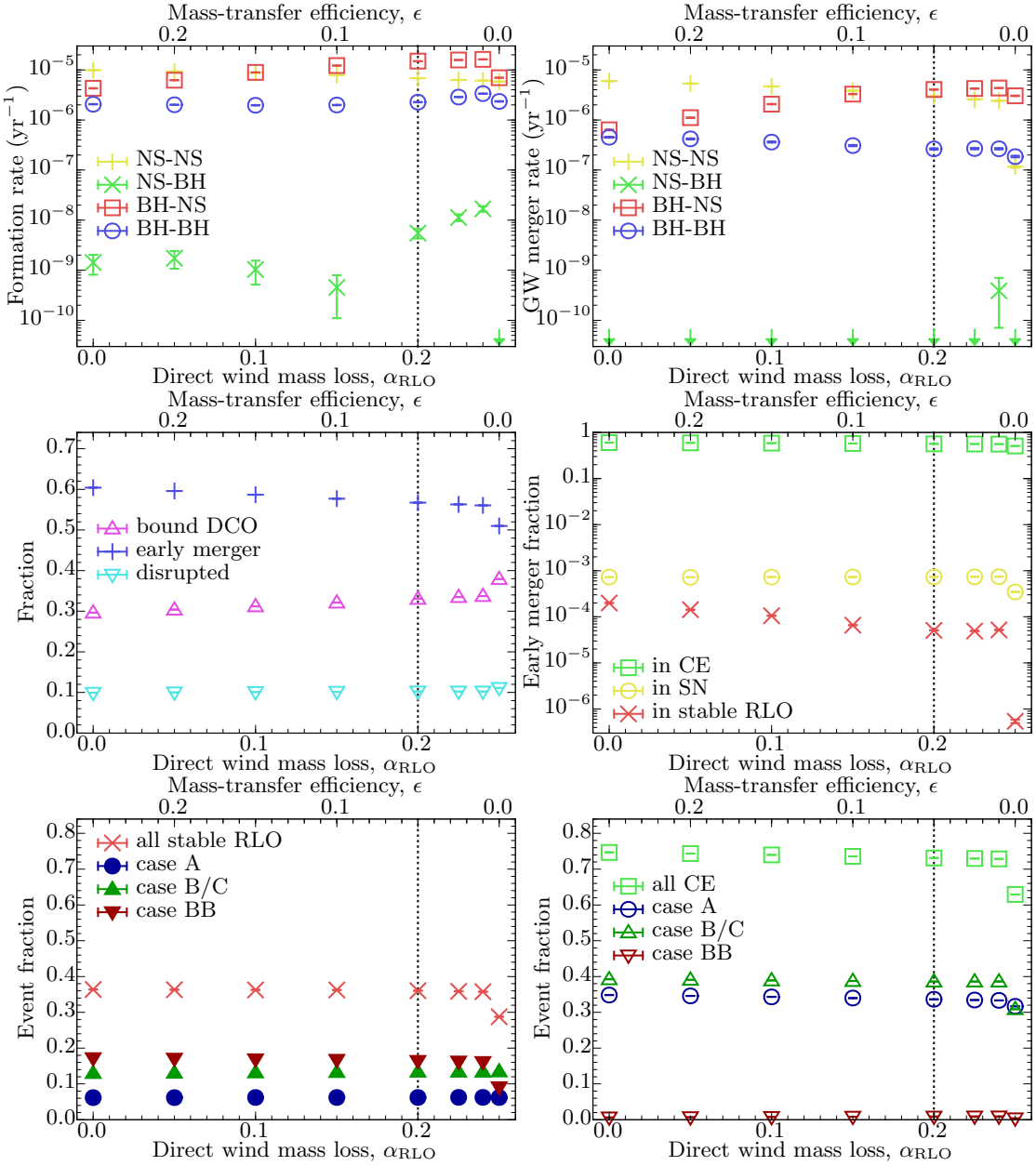

Figure B.46: Variation of the direct wind mass loss during stable RLO, $\alpha_{\rm RLO}$, and the resulting mass-transfer efficiency, ϵ. The dotted line marks the default value. The rates are for a MW-like galaxy; the arrows in the top panels mark upper limits.

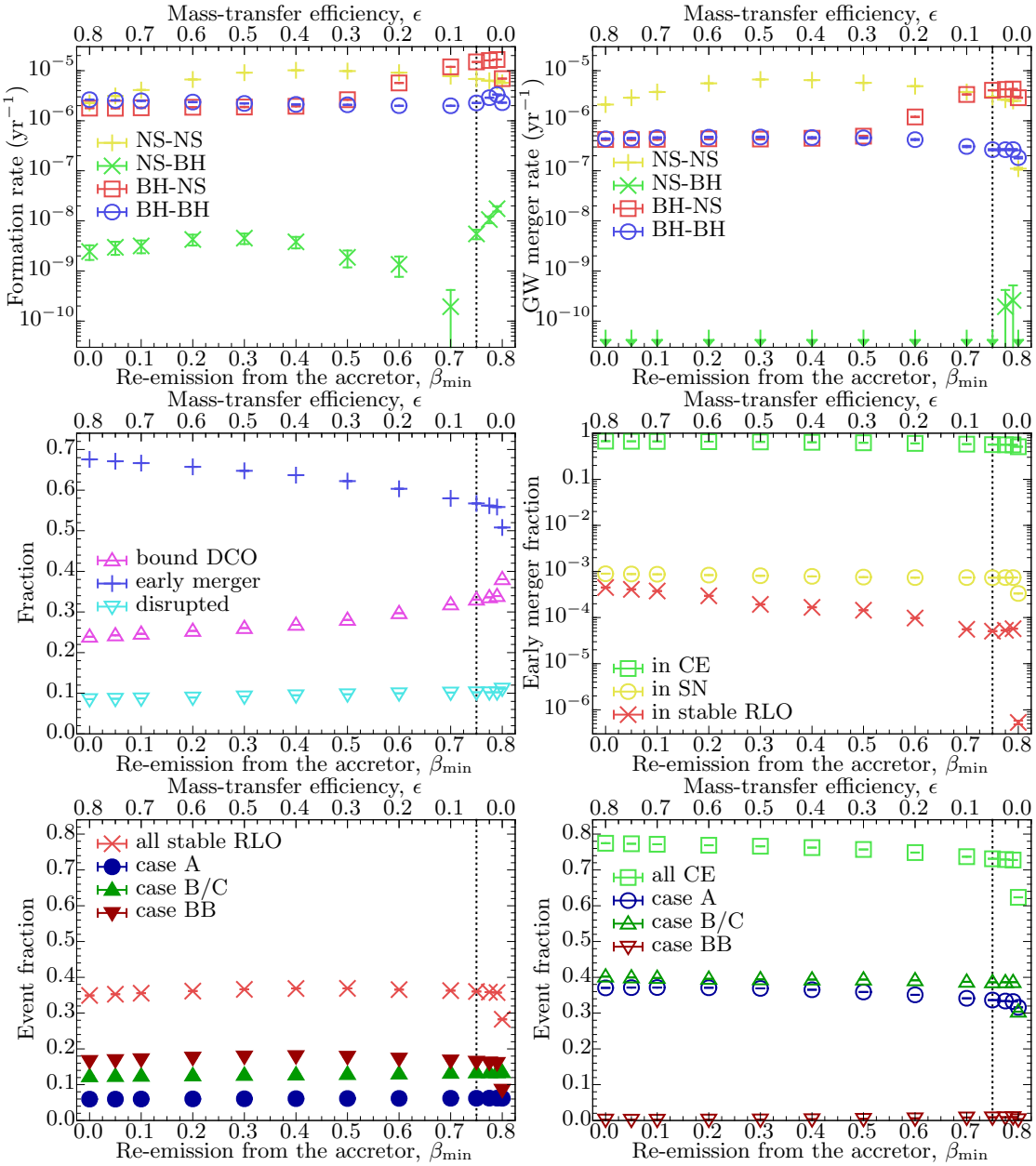

Figure B.47: Variation of the minimum re-emission from the accretor during stable RLO, $\beta_{\rm min}$, and the resulting mass-transfer efficiency, ϵ. The dotted line marks the default value. The rates are for a MW-like galaxy; the arrows in the top-right panel mark upper limits.

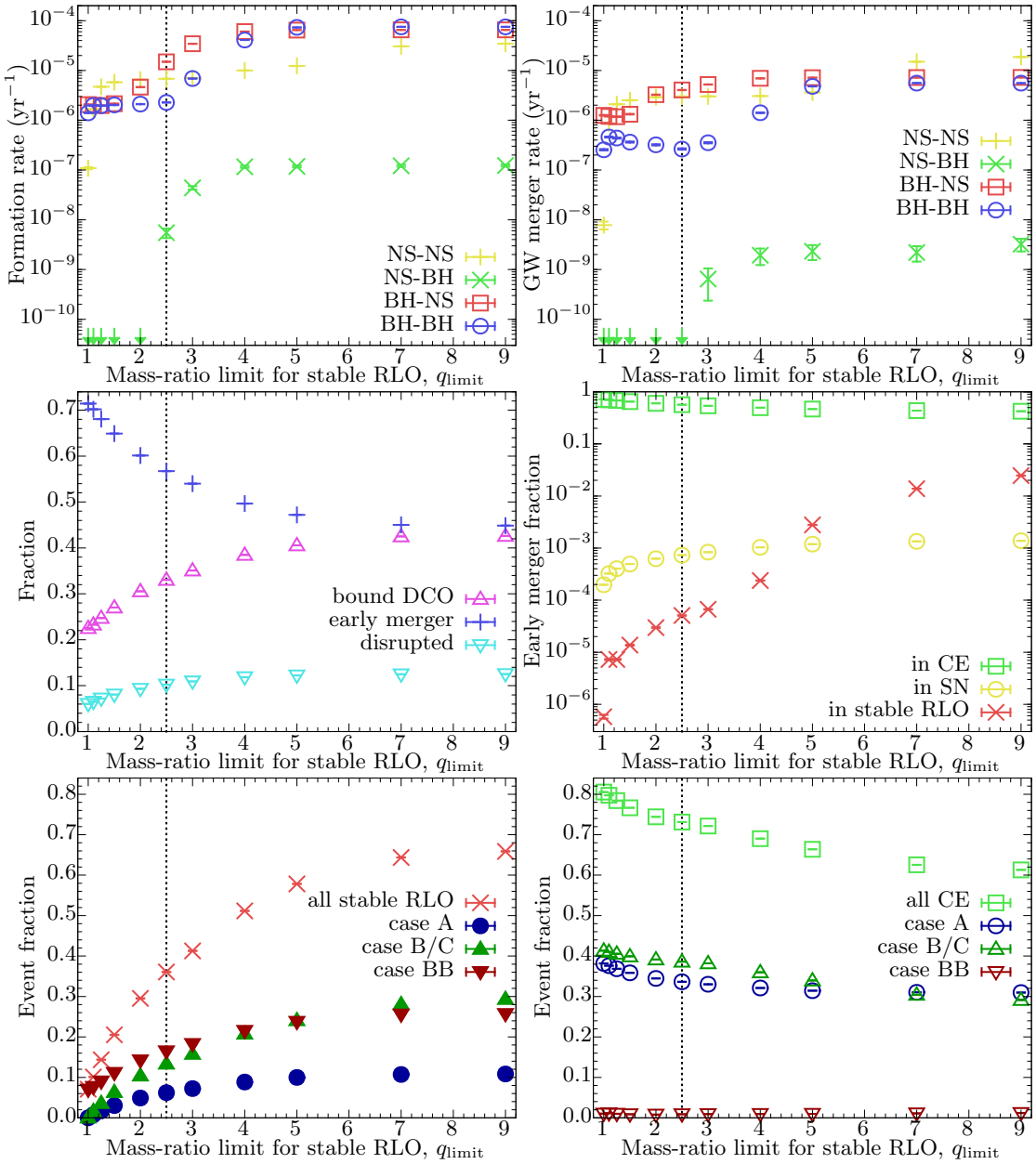

Figure B.48: Variation of the mass-ratio limit for stable mass transfer, $q_{\rm limit}$. The dotted line marks the default value. The rates are for a MW-like galaxy; the arrows in the top panels mark upper limits.

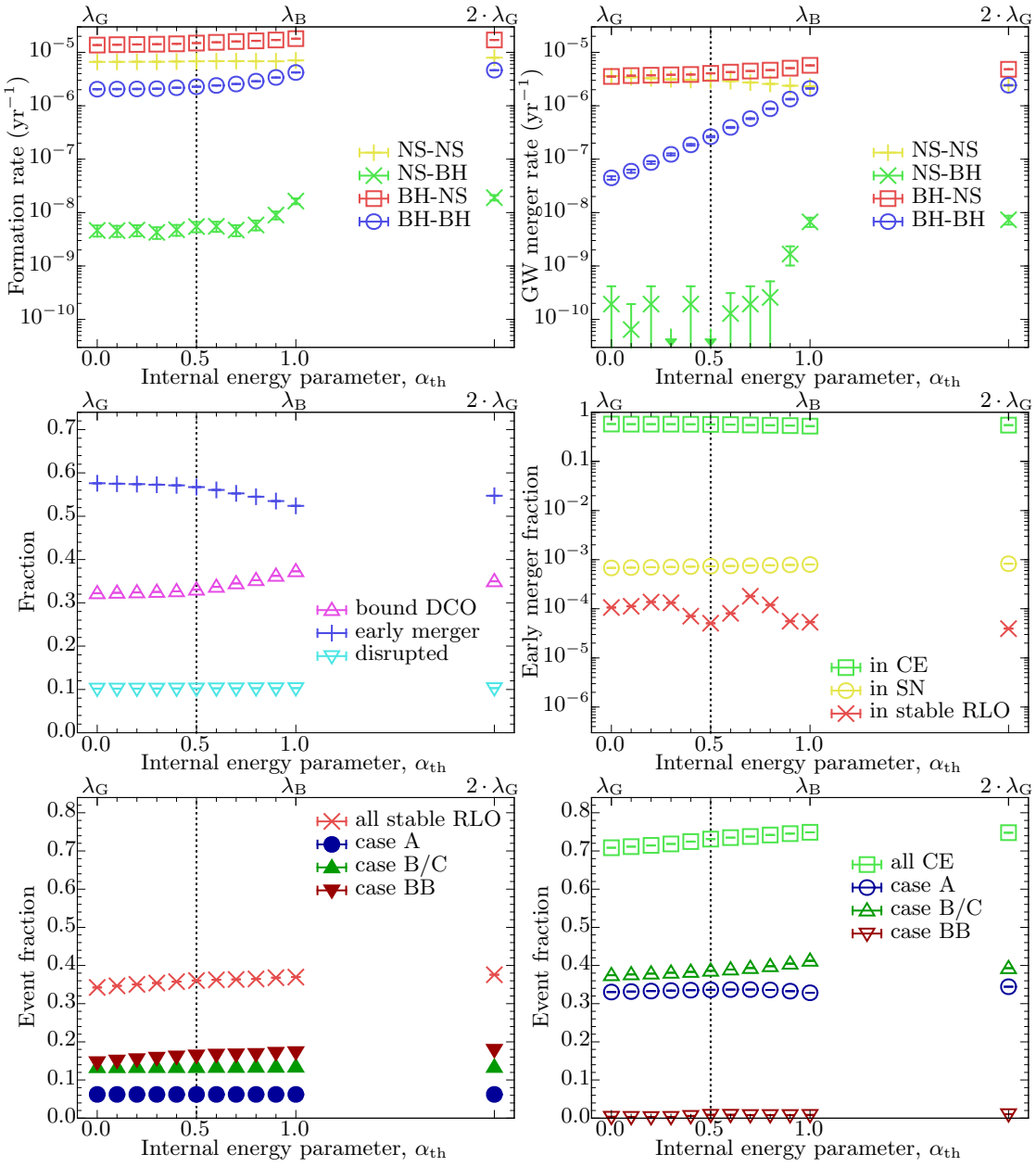

Figure B.49: Variation of the internal energy parameter, α_{th}. The dotted line marks the default value. The rates are for a MW-like galaxy; the arrows in the top-right panel mark upper limits.

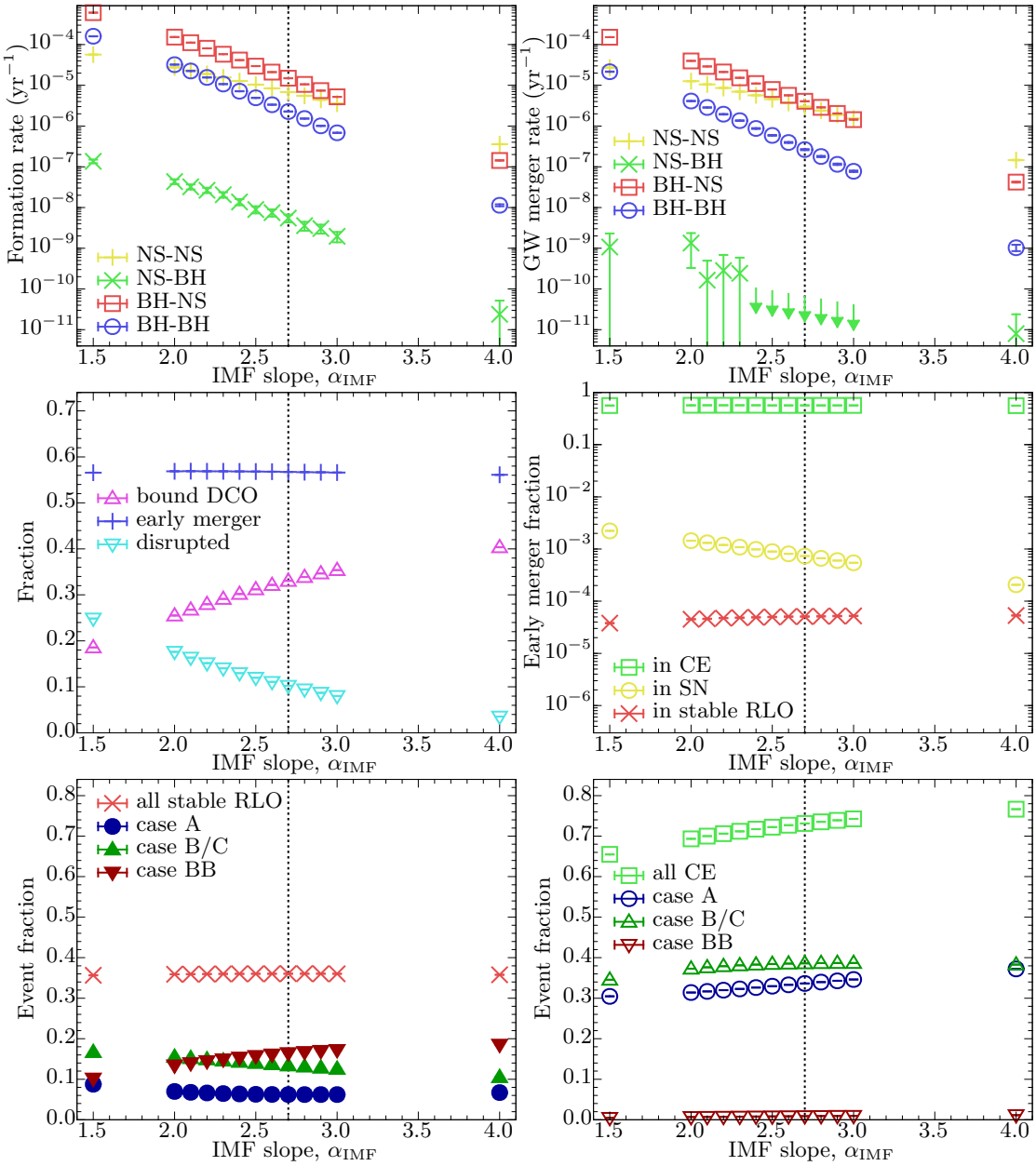

Figure B.50: Variation of the IMF slope, $\alpha_{\rm IMF}$. The dotted line marks the default value. The rates are for a MW-like galaxy; the arrows in the top-right panel mark upper limits.

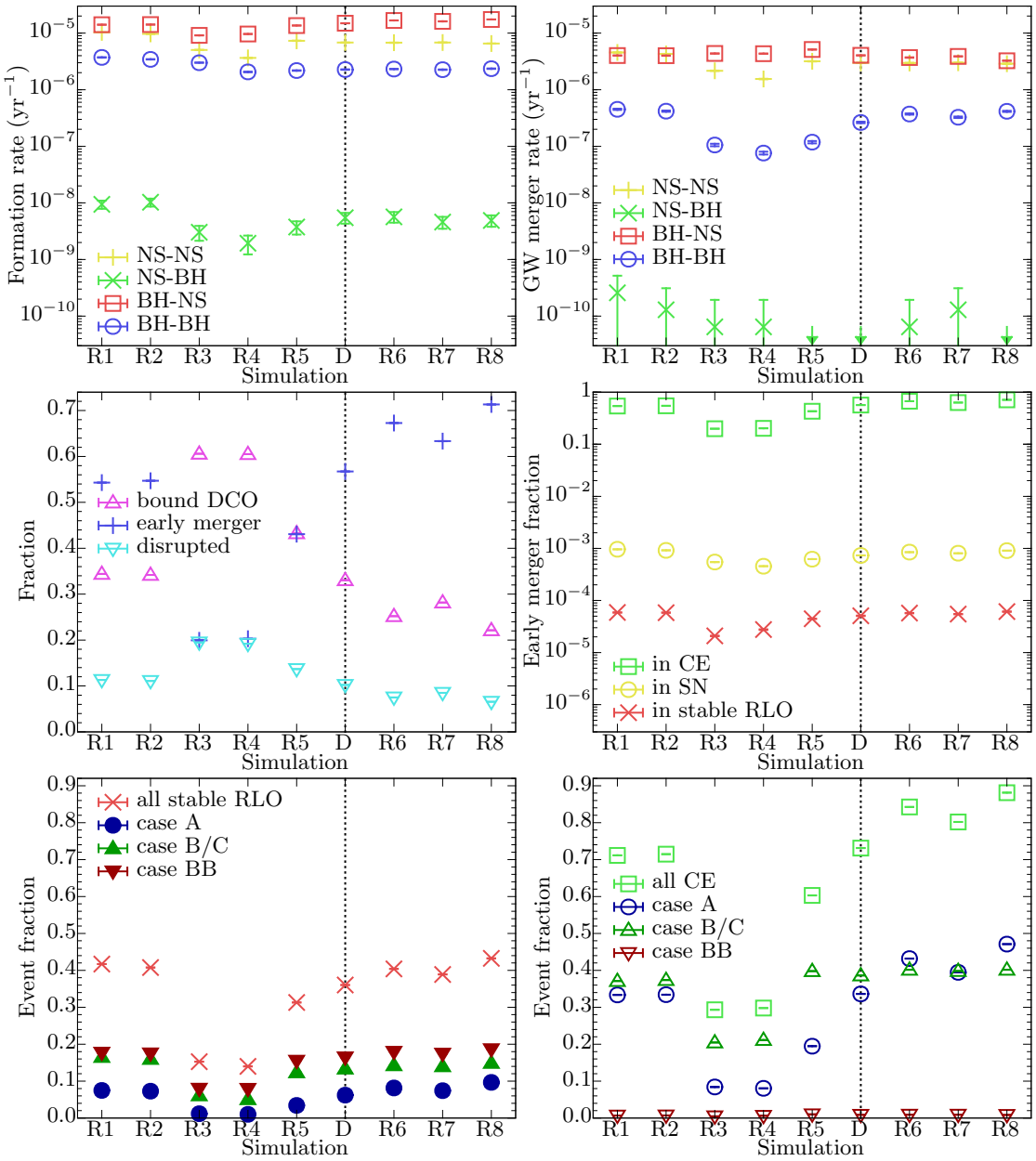

Figure B.51: Variation of initial distributions. The different runs are R1: q-flat; R2: q-Sana; R3: q-Sana and a (P-Sana); R4: a (P-Sana); R5: a (P-Kroupa); D : default (dotted line); R6: e-thermal; R7: e-flat; R8: e (flat in angular momentum). The rates are for a MW-like galaxy; the arrows in the top-right panel mark upper limits.

B.4 Figures of Section 3.13.4

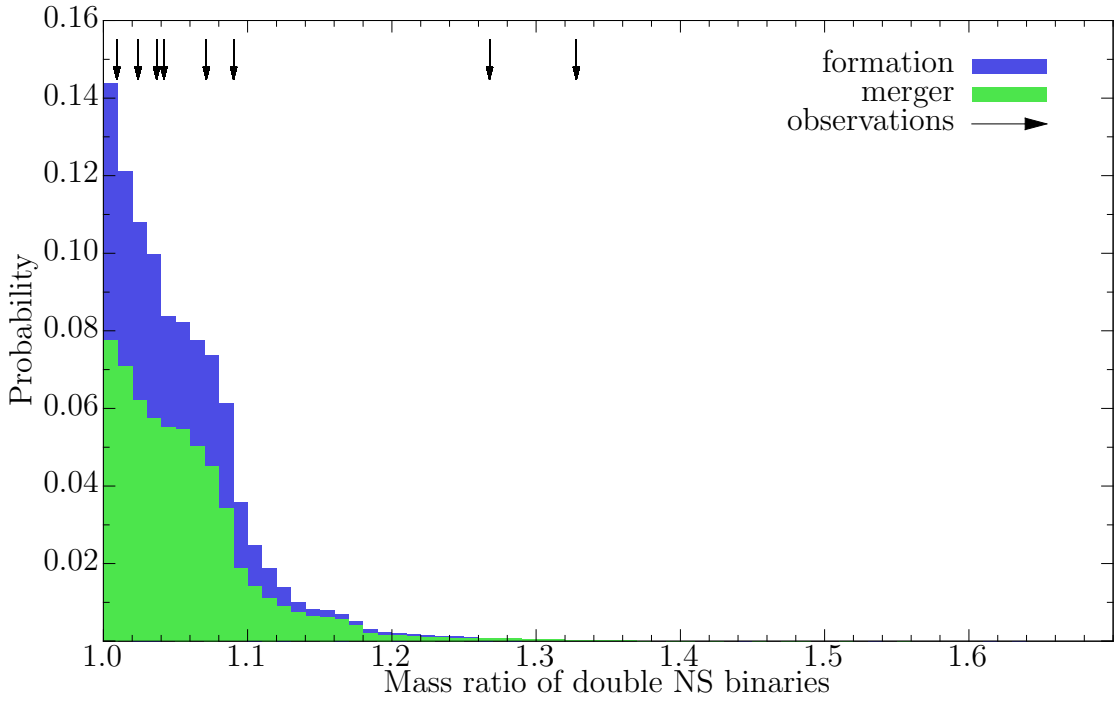

Figure B.52: As Fig. 3.9, but with intermediate efficient mass transfer ($\beta_{\min} = 0.5$).

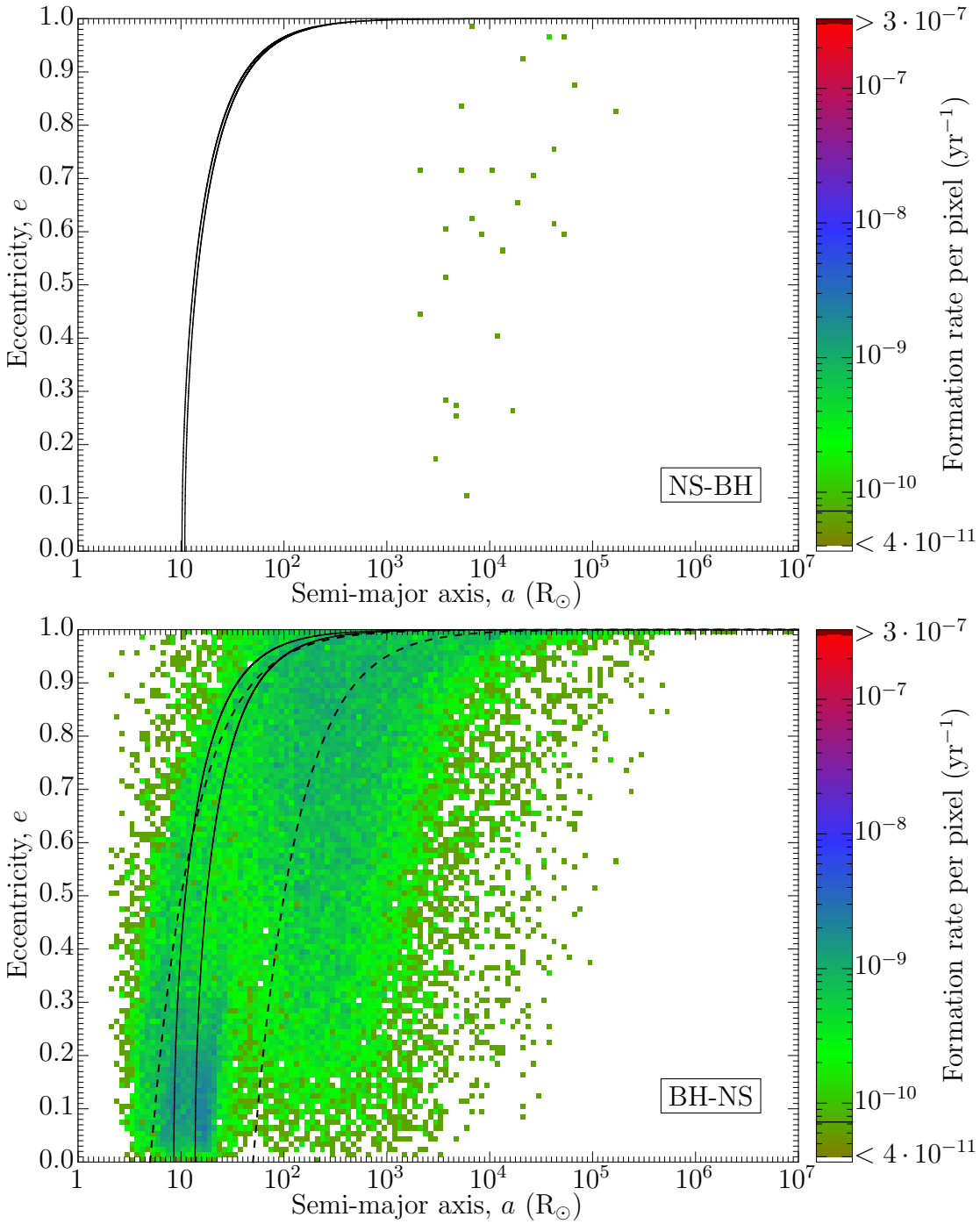

Figure B.53: As Fig. 3.12, but with intermediate efficient mass transfer ($\beta_{\min} = 0.5$).

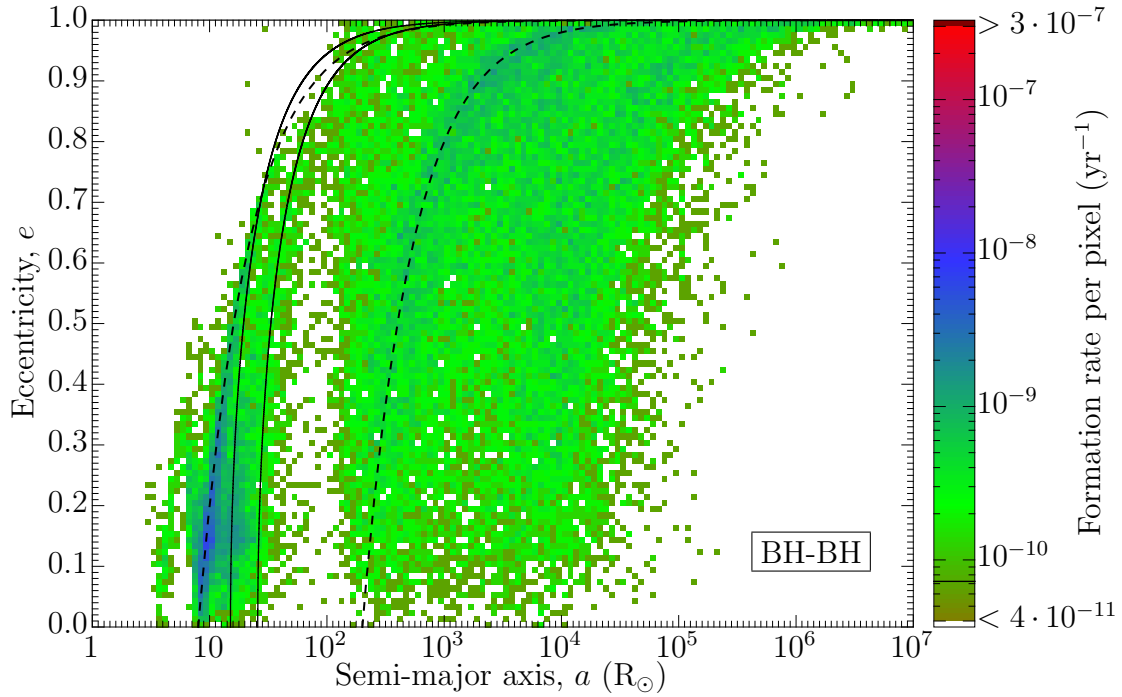

Figure B.54: As Fig. 3.13, but with intermediate efficient mass transfer ($\beta_{\min} = 0.5$).

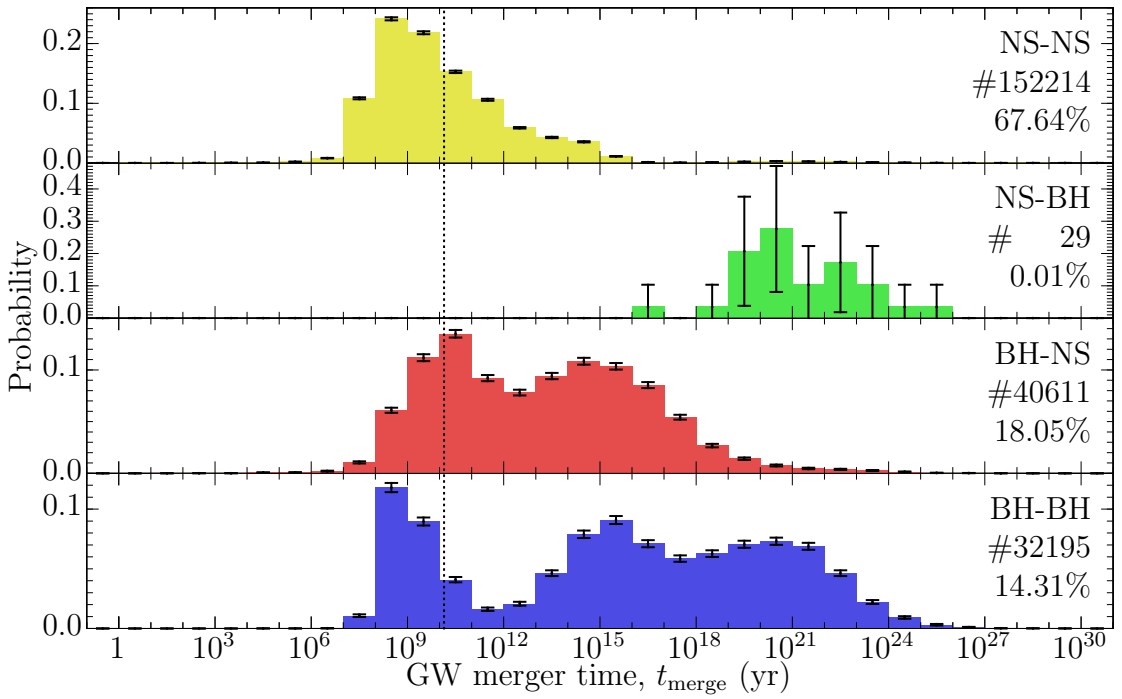

Figure B.55: As the top-left panel of Fig. 3.14, but with intermediate efficient mass transfer ($\beta_{\min} = 0.5$).

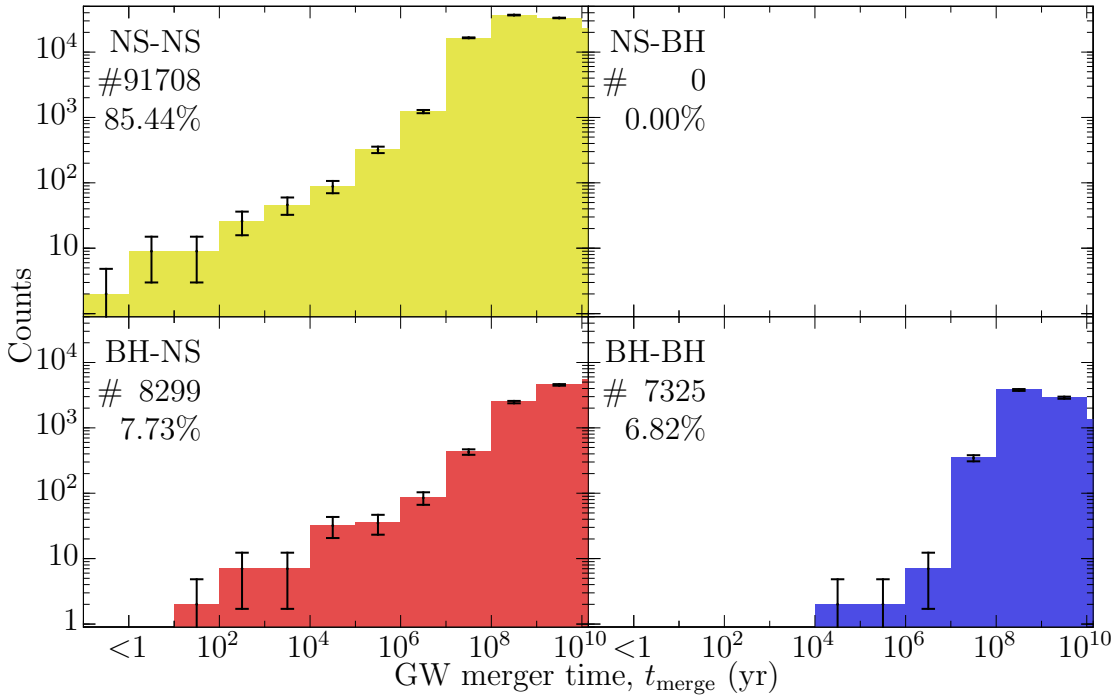

Figure B.56: As the top-right panel of Fig. 3.14, but with intermediate efficient mass transfer ($\beta_{\rm min} = 0.5$).

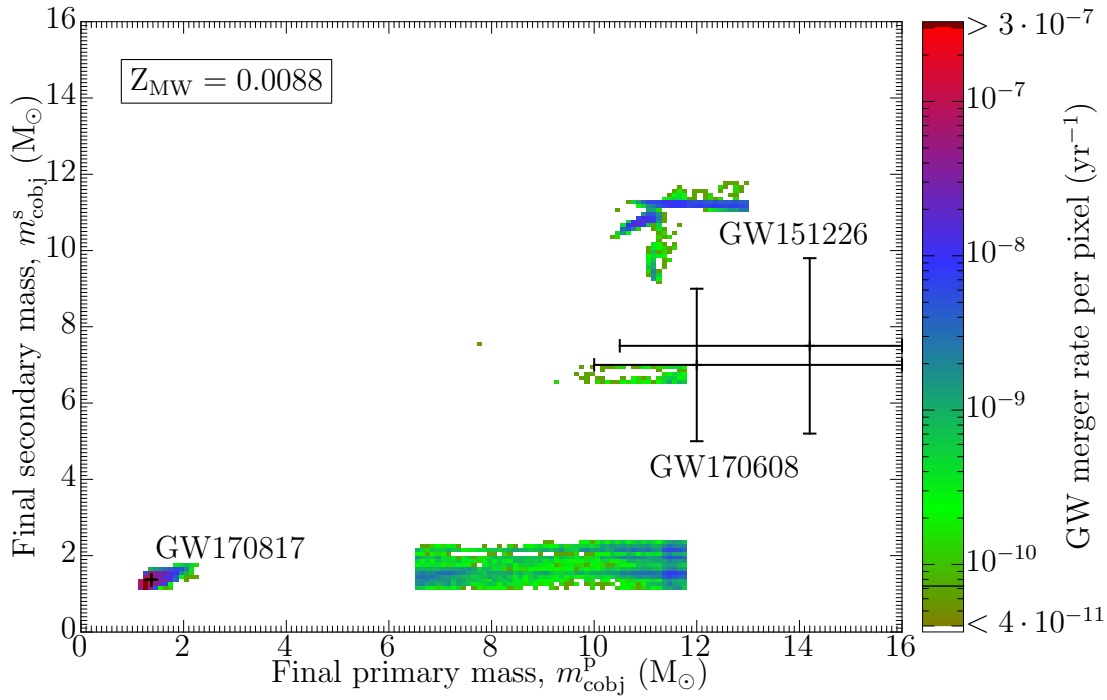

Figure B.57: As the top panel of Fig. 3.15, but with intermediate efficient mass transfer ($\beta_{\rm min} = 0.5$).

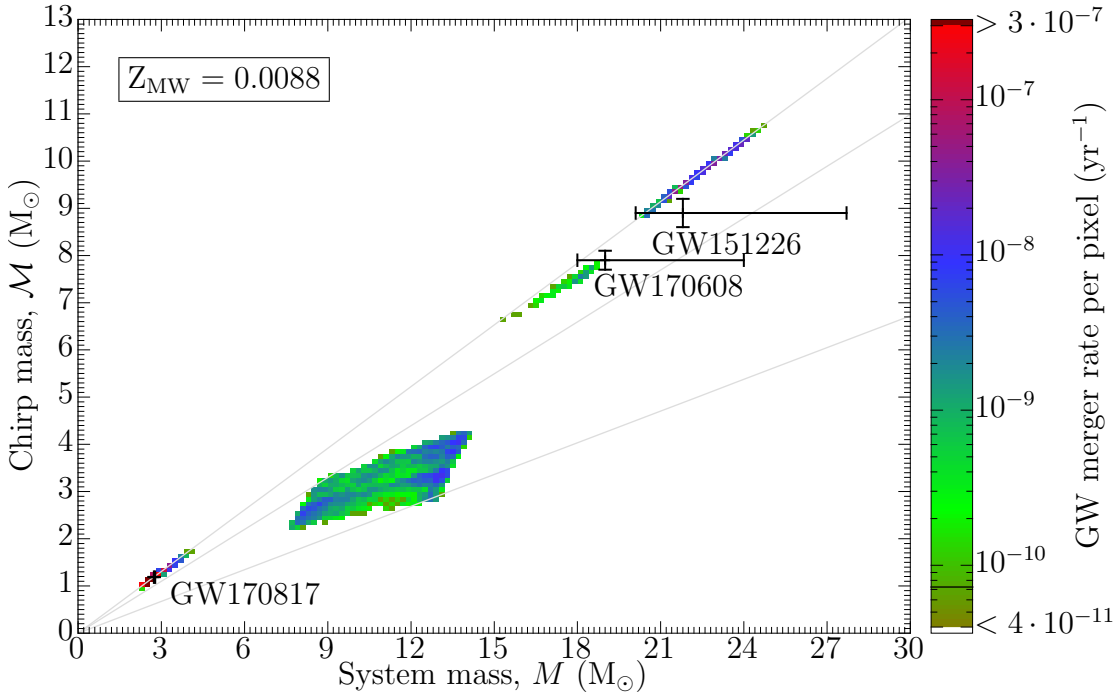

Figure B.58: As the top panel of Fig. 3.16, but with intermediate efficient mass transfer ($\beta_{\rm min} = 0.5$).

Acknowledgements

It was an inspiring and challenging time to work on this thesis. To complete such a thesis one needs to work hard, to excel oneself and to get support.

First, I would like to thank my supervisors Thomas and Norbert. Whenever there was a need for discussion, they always take the time to help with their experience. For me it was a great pleasure to have these two as my supervisors.

During the different projects of this thesis I worked with several people to realize these projects. Therefore, I would like to thank all my co-authors of the articles for their contribution. Dori's models of low metallicity stars and her BEC interface were very helpful to analyse the structure of these stars. The comparison to detailed models of binary evolution provided by Pablo Marchant closed the bridge between the single stars and the population synthesis. My thanks also belongs to Phillip Podsiadlowski, who shared his experience of CE evolution. Insights to fast binary star evolution were irreplaceable for what Rob Izzard deserves my gratitude. The pulsar people, including Michael Kramer, Cherry Ng and many more, gratefully contribute with precise measurements of NSs to compare the models to observations.

The atmosphere of the daily work environment is set by nice office mates. In my case, I like to thank Patrick, Abel and David for long working hours having always a bit of humour around. I would not like to miss the administrative help of Elisabeth Kramer. Also all the other members of the stellar group were a friendly and beneficial enrichment to my work.

I acknowledge financial support by the Deutsche Forschungsgemeinschaft Grant: TA 964/1-1 awarded to Thomas Tauris. I would also like to thank the Argelander-Institut für Astronomie and the Bonner Graduiertenzentrum of the university Bonn to gave me the possibility of part time jobs to finish this thesis.

Last but not least, I like to thank my friends and family. Here, I would like to point out Patrick times two. Particularly, I thank my parents and grandparents for their sympathy and their absolute assistance.

List of figures

1.1 Theoretical Hertzsprung-Russell diagram 2
1.2 Illustration of postburning stellar composition 12
1.3 Illustration of an orbit 16
1.4 Illustration of mass transfer 19

2.1 Envelope binding energy/parameter depending on stellar radius . . 28
2.2 Minimum mass of the in-spiralling object depending on ZAMS mass of the donor star 29
2.3 Energy budget depending on mass coordinate 31
2.4 Energy budget depending on radius coordinate 31
2.5 Recombination energy importance depending on ZAMS mass 33
2.6 Pre-CE to post-CE orbital separations 35
2.7 Merger time due to GW radiation depending on post-CE orbital separation 35
2.8 Convective envelopes depending on ZAMS mass 39

3.1 Illustration of the formation of a BH-NS system 43
3.2 Mapping ZAMS masses to compact object masses 48
3.3 HRD at MW metallicity 50
3.4 Dependence of the envelope binding energy parameter on stellar radius and stellar mass 50
3.5 HRD of naked helium stars 51
3.6 Progenitors of the systems forming a DCO binary 54
3.7 Masses of formed NSs and BHs in DCO binaries 54
3.8 Masses of double NS binaries 55
3.9 Histogram of the mass ratios of double NS binaries 56
3.10 Eccentricity versus semi-major axis of double NS systems 56
3.11 Eccentricity versus semi-major axis of evolving double NS binaries . 57
3.12 Eccentricity versus semi-major axis of mixed NS/BH systems 58
3.13 Eccentricity versus semi-major axis of double BH systems 58
3.14 Histograms of GW merger time 59
3.15 Masses of merging NSs and BHs in DCO binaries 60
3.16 Chirp und total masses of merging DCO binaries 60
3.17 Early coalescing systems as a function of the CE efficiency 63
3.18 The GW merger rate as a function of the mass-transfer efficiency . 63
3.19 Stability of mass transfer as a function of the mass-ratio limit . . . 64

3.20 Fraction of DCO systems as a function of the IMF slope 64
3.21 The initial and the final semi-major axis of DCO systems 65
3.22 Merger-rate densities of the DCO binaries 66
3.23 Progenitor properties of the first seven LIGO-Virgo detections . . . 68
3.24 NS masses of progenitors of GW170817 69
3.25 Progenitors of the systems forming a DCO binary (efficient mass transfer) 76
3.26 Masses of formed NSs and BHs in DCO binaries (efficient mass transfer) 77
3.27 Histogram of the mass ratios of double NS binaries (efficient mass transfer) 77
3.28 Eccentricity versus semi-major axis of (evolving) double NS systems (efficient mass transfer) 77
3.29 Eccentricity versus semi-major axis of mixed NS/BH and double BH systems (efficient mass transfer) 78
3.30 Histograms of GW merger time (efficient mass transfer) 79
3.31 Masses of merging NSs and BHs in DCO binaries (efficient mass transfer) 81
3.32 Chirp und total masses of merging DCO binaries (efficient mass transfer) 81
3.33 Merger-rate densities of the DCO binaries 81
3.34 Eccentricity versus semi-major axis of double NS systems only formed via FeCC SN 82
3.35 The GW merger rate as a function of the mass-transfer efficiency 2 82
3.36 The formation rate as a function of the mass-transfer efficiency . . . 82
3.37 Mean counts of evolutionary events as a function of internal envelope energy used during CE 83
3.38 Calibration of the overshooting parameter 84
3.39 ZAMS extrapolation of the core mass 85
3.40 ZAMS extrapolation of the radius 86
3.41 ZAMS extrapolation of the luminosity 86
3.42 ZAMS extrapolation of the effective temperature 87
3.43 ZAMS extrapolation of the gravitational envelope binding parameter 87
3.44 ZAMS extrapolation of the total envelope binding parameter 88
3.45 ZAMS and compact object masses 90
3.46 Masses and semi-major axis of formation channels A-C 91
3.47 Variation of the common-envelope efficiency 93
3.48 Masses of formed NSs and BHs in DCO binaries (intermediate efficient mass transfer) 94
3.49 Masses of formed NSs binaries (intermediate efficient mass transfer) 94
3.50 Eccentricity versus semi-major axis of double NS systems (intermediate efficient mass transfer) 95

4.1 Spin down rate and companion mass depending on spin period . . . 99
4.2 Timing residuals 100

4.3 Pulse profiles . . . 101
4.4 Eccentricity as a function of orbital period for binary radio pulsars with hydrogen-rich companions . . . 102
4.5 Companion mass as a function of inclination . . . 103
4.6 Heatmap of WD mass and orbital period of WDNS binaries . . . 103
4.7 Orbital eccentricity versus orbital period of WDNS and NSNS binaries 104
4.8 NS kicks and resulting 3D systemic velocities of WDNS binaries . . 105
4.9 The stacked Pan-STARRS data in yband . . . 106
4.10 Colour-Magnitude Diagram of objects in the Pan-STARRS catalogue 106
4.11 White dwarf cooling models . . . 107
4.12 Orbital eccentricity versus orbital period of MS-NS binaries . . . 111
4.13 Orbital eccentricity versus orbital period of MS-NS binaries (more efficient CE) . . . 112

A.1 Flowchart . . . 129

B.1 Extrapolation of the age at maximum radius . . . 153
B.2 Extrapolation of the mass at maximum radius . . . 154
B.3 Extrapolation of the core mass at maximum radius . . . 154
B.4 Extrapolation of the radius at maximum radius . . . 155
B.5 Extrapolation of the luminosity at maximum radius . . . 155
B.6 Extrapolation of the effective temperature at maximum radius . . . 156
B.7 Extrapolation of the gravitational envelope binding parameter at maximum radius . . . 156
B.8 Extrapolation of the total envelope binding parameter at maximum radius . . . 157
B.9 Extrapolation of the age at maximum core mass . . . 158
B.10 Extrapolation of the mass at maximum core mass . . . 158
B.11 Extrapolation of the core mass at maximum core mass . . . 159
B.12 Extrapolation of the radius at maximum core mass . . . 159
B.13 Extrapolation of the luminosity at maximum core mass . . . 160
B.14 Extrapolation of the effective temperature at maximum core mass . 160
B.15 Extrapolation of the gravitational envelope binding parameter at maximum core mass . . . 161
B.16 Extrapolation of the total envelope binding parameter at maximum core mass . . . 161
B.17 Extrapolation of the age at the end of the stellar calculation . . . 162
B.18 Extrapolation of the mass at the end of the stellar calculation . . . 163
B.19 Extrapolation of the core mass at the end of the stellar calculation . 163
B.20 Extrapolation of the radius at the end of the stellar calculation . . . 164
B.21 Extrapolation of the luminosity at the end of the stellar calculation 164
B.22 Extrapolation of the effective temperature at the end of the stellar calculation . . . 165
B.23 Extrapolation of the gravitational envelope binding parameter at the end of the stellar calculation . . . 165

B.24 Extrapolation of the total envelope binding parameter at the end of the stellar calculation . . . 166
B.25 Extrapolation of the He-star's carbon core mass at He-ZAMS 167
B.26 Extrapolation of the He-star's radius at He-ZAMS 167
B.27 Extrapolation of the He-star's luminosity at He-ZAMS 168
B.28 Extrapolation of the He-star's effective temperature at He-ZAMS . 168
B.29 Extrapolation of the He-star's gravitational envelope binding parameter at He-ZAMS . . . 169
B.30 Extrapolation of the He-star's total envelope binding parameter at He-ZAMS . . . 169
B.31 Extrapolation of the He-star's age at the end of the stellar calculation 170
B.32 Extrapolation of the He-star's mass at the end of the stellar calculation 171
B.33 Extrapolation of the He-star's carbon core mass at the end of the stellar calculation . . . 171
B.34 Extrapolation of the He-star's radius at the end of the stellar calculation . . . 172
B.35 Extrapolation of the He-star's luminosity at the end of the stellar calculation . . . 172
B.36 Extrapolation of the He-star's effective temperature at the end of the stellar calculation . . . 173
B.37 Extrapolation of the He-star's gravitational envelope binding parameter at the end of the stellar calculation . . . 173
B.38 Extrapolation of the He-star's total envelope binding parameter at the end of the stellar calculation . . . 174
B.39 Masses and semi-major axis of formation channels D-F 175
B.40 Masses and semi-major axis of formation channels G-I 176
B.41 Masses and semi-major axis of formation channels J-L 177
B.42 Masses and semi-major axis of formation channels M-O 178
B.43 Masses and semi-major axis of formation channels P-R 179
B.44 Masses and semi-major axis of formation channels S1-S3 180
B.45 Masses and semi-major axis of formation channels S4-S6 181
B.46 Variation of the direct wind mass loss 182
B.47 Variation of the minimum re-emission from the accretor 183
B.48 Variation of the mass-ratio limit for stable mass transfer 184
B.49 Variation of the internal energy parameter 185
B.50 Variation of the IMF slope 186
B.51 Variation of initial distributions 187
B.52 Histogram of the mass ratios of double NS binaries (intermediate efficient mass transfer) . . . 188
B.53 Eccentricity versus semi-major axis of mixed NS/BH systems (intermediate efficient mass transfer) . . . 189
B.54 Eccentricity versus semi-major axis of double BH systems (intermediate efficient mass transfer) . . . 190
B.55 Histogram of GW merger time (intermediate efficient mass transfer) 190

B.56 Histogram of GW merger time below the Hubble time (intermediate efficient mass transfer) 191
B.57 Masses of merging NSs and BHs in DCO binaries (intermediate efficient mass transfer) 191
B.58 Chirp und total masses of merging DCO binaries (intermediate efficient mass transfer) 192

List of tables

1 Units . . . viii
2 Constants . . . viii
3 Variables . . . ix

3.1 SN kicks . . . 49
3.2 Initial values and default settings . . . 53
3.3 Formation rates of DCO binaries . . . 54
3.4 GW merger rates of DCO binaries . . . 59
3.5 Variations in DCO formation and merger rates . . . 62
3.6 GW merger rates depending on kicks and assumptions on EC SNe . 62
3.7 Number of DCO systems present in the MW . . . 65
3.8 Merger-rate densities in the local Universe and their detection rates 67
3.9 Short notations . . . 75
3.10 Formation rates of DCO binaries (efficient mass transfer) . . . 76
3.11 GW merger rates of DCO binaries (efficient mass transfer) . . . 78
3.12 Merger-rate densities in the local Universe and their detection rates (efficient mass transfer) . . . 79
3.13 Formation channels of DCO binaries . . . 80
3.14 Variations in DCO formation and merger rates 2 . . . 83

4.1 Best-fit parameters for PSR J1755−2550 . . . 100
4.2 Search-mode observations used to search for radio pulsations from the companion of PSR J1755−2550 . . . 108

A.1 Constants . . . 129
A.2 `t_system` components . . . 130
A.3 `t_star` components . . . 131
A.4 Stages . . . 132
A.5 `t_SN` components . . . 132
A.6 `t_HRD` components . . . 132
A.7 `t_hist` components . . . 133
A.8 Phases . . . 134
A.9 User functions . . . 137
A.10 Physical checks . . . 140
A.11 Warning messages . . . 141
A.12 Error messages . . . 144

Bibliography

Abadie J., et al., 2010, Classical and Quantum Gravity, 27, 173001

Abbott B. P., et al., 2016a, Physical Review X, 6, 041015

Abbott B. P., et al., 2016b, Physical Review Letters, 116, 061102

Abbott B. P., et al., 2016c, Physical Review Letters, 116, 241103

Abbott B. P., et al., 2017a, Physical Review Letters, 118, 221101

Abbott B. P., et al., 2017b, Physical Review Letters, 119, 141101

Abbott B. P., et al., 2017c, Physical Review Letters, 119, 161101

Abbott B. P., et al., 2017d, ApJ, 848, L12

Abbott B. P., et al., 2017e, ApJ, 848, L13

Abt H. A., 1983, ARA&A, 21, 343

Allen C., Santillan A., 1991, Rev. Mexicana Astron. Astrofis., 22, 255

Alpar M. A., Cheng A. F., Ruderman M. A., Shaham J., 1982, Nature, 300, 728

Antoniadis J., Bassa C. G., Wex N., Kramer M., Napiwotzki R., 2011, MNRAS, 412, 580

Antoniadis J., Freire P. C. C., Wex N., Tauris T. M., Lynch R. S., van Kerkwijk M. H., Kramer M., et al. 2013, Science, 340, 448

Bae Y.-B., Kim C., Lee H. M., 2014, MNRAS, 440, 2714

Banerjee S., 2017, MNRAS, 467, 524

Banerjee S., Baumgardt H., Kroupa P., 2010, MNRAS, 402, 371

Barrett J. W., Gaebel S. M., Neijssel C. J., Vigna-Gómez A., Stevenson S., Berry C. P. L., Farr W. M., Mandel I., 2017a, preprint (`arXiv:1711.06287`)

Barrett J. W., Mandel I., Neijssel C. J., Stevenson S., Vigna-Gómez A., 2017b, in IAU Symposium. pp 46–50 (`arXiv:1704.03781`), doi:10.1017/S1743921317000059

Belczyński K., Kalogera V., 2001, ApJ, 550, L183

Belczynski K., Kalogera V., Bulik T., 2002, ApJ, 572, 407

Belczynski K., Kalogera V., Rasio F. A., Taam R. E., Zezas A., Bulik T., Maccarone T. J., Ivanova N., 2008, ApJS, 174, 223

Belczynski K., Holz D. E., Bulik T., O'Shaughnessy R., 2016, Nature, 534, 512

Belczynski K., et al., 2017, preprint (arXiv:1712.00632)

Beniamini P., Hotokezaka K., Piran T., 2016, ApJ, 832, 149

Berger E., 2014, ARA&A, 52, 43

Bhat N. D. R., Bailes M., Verbiest J. P. W., 2008, Phys. Rev. D, 77, 124017

Bhattacharya D., 2002, Journal of Astrophysics and Astronomy, 23, 67

Bhattacharya D., van den Heuvel E. P. J., 1991, Phys. Rep., 203, 1

Binney J., Tremaine S., 1987, Galactic dynamics. Princeton University Press

Bisnovatyi-Kogan G. S., Komberg B. V., 1974, AZh, 51, 373

Blanchard P. K., et al., 2017, ApJ, 848, L22

Bloom J. S., Sigurdsson S., Pols O. R., 1999, MNRAS, 305, 763

Bours M. C. P., et al., 2014, MNRAS, 438, 3399

Breton R. P., et al., 2008, Science, 321, 104

Brott I., et al., 2011, A&A, 530, A115

Brown G. E., 1995, ApJ, 440, 270

Brown W. R., Kilic M., Hermes J. J., Allende Prieto C., Kenyon S. J., Winget D. E., 2011, ApJ, 737, L23

Burgay M., et al., 2003, Nature, 426, 531

Cameron A. D., et al., 2017, preprint (arXiv:1711.07697)

Castro N., Fossati L., Langer N., Simón-Díaz S., Schneider F. R. N., Izzard R. G., 2014, A&A, 570, L13

Chabrier G., 2003, ApJ, 586, L133

Chambers K., 2006, in The Advanced Maui Optical and Space Surveillance Technologies Conference. p. E39

Chambers K. C., et al., 2016, preprint (arXiv:1612.05560)

Chandrasekhar S., 1931, ApJ, 74, 81

Chatterjee S., Rodriguez C. L., Kalogera V., Rasio F. A., 2017, ApJ, 836, L26

Chatzopoulos E., Wheeler J. C., 2012, ApJ, 748, 42

Chen H.-L., Chen X., Tauris T. M., Han Z., 2013, ApJ, 775, 27

Chevalier R. A., 1993, ApJ, 411, L33

Chruslinska M., Belczynski K., Klencki J., Benacquista M., 2017, preprint (arXiv:1708.07885)

Claret A., 2007, A&A, 475, 1019

Claret A., Cunha N. C. S., 1997, A&A, 318, 187

Claret A., Torres G., 2016, A&A, 592, A15

Clark J. P. A., van den Heuvel E. P. J., Sutantyo W., 1979, A&A, 72, 120

Clifton T. R., Lyne A. G., 1986, Nature, 320, 43

Cordes J. M., Lazio T. J. W., 2002, ArXiv: astro-ph/0207156

Coulter D. A., et al., 2017, preprint (arXiv:1710.05452)

Crowther P. A., 2007, ARA&A, 45, 177

Damour T., Deruelle N., 1986, Ann. Inst. Henri Poincaré Phys. Théor., Vol. 44, No. 3, p. 263 - 292, 44, 263

Damour T., Taylor J. H., 1992, Phys. Rev. D, 45, 1840

Davies M. B., Ritter H., King A., 2002, MNRAS, 335, 369

Davis P. J., Kolb U., Knigge C., 2012, MNRAS, 419, 287

De Marco O., Izzard R. G., 2017, PASA, 34, e001

Deinzer W., von Sengbusch K., 1970, ApJ, 160, 671

Dessart L., Burrows A., Ott C. D., Livne E., Yoon S.-C., Langer N., 2006, ApJ, 644, 1063

Desvignes et al. 2017, in preparation

Dewi J. D. M., Pols O. R., 2003, MNRAS, 344, 629

Dewi J. D. M., Tauris T. M., 2000, A&A, 360, 1043

Dewi J. D. M., Tauris T. M., 2001, in Podsiadlowski P., Rappaport S., King A. R., D'Antona F., Burderi L., eds, Astronomical Society of the Pacific Conference Series Vol. 229, Evolution of Binary and Multiple Star Systems. p. 255

Dewi J. D. M., Pols O. R., Savonije G. J., van den Heuvel E. P. J., 2002, MNRAS, 331, 1027

Dewi J. D. M., Podsiadlowski P., Pols O. R., 2005, MNRAS, 363, L71

Dewi J. D. M., Podsiadlowski P., Sena A., 2006, MNRAS, 368, 1742

Dominik M., Belczynski K., Fryer C., Holz D. E., Berti E., Bulik T., Mandel I., O'Shaughnessy R., 2012, ApJ, 759, 52

Dominik M., Belczynski K., Fryer C., Holz D. E., Berti E., Bulik T., Mandel I., O'Shaughnessy R., 2013, ApJ, 779, 72

Dominik M., et al., 2015, ApJ, 806, 263

Drout M. R., Piro A. L., Shappee B. J., et al. 2017, preprint (arXiv:1710.05443)

Dvorkin I., Uzan J.-P., Vangioni E., Silk J., 2017, preprint (arXiv:1709.09197)

Eggleton P. P., 1983, ApJ, 268, 368

Eichler D., Livio M., Piran T., Schramm D. N., 1989, Nature, 340, 126

Einstein A., 1916, Annalen der Physik, 354, 769

Einstein A., 1918, Sitzungsberichte der Königlich Preußischen Akademie der Wissenschaften (Berlin), Seite 154-167.

Eldridge J. J., Stanway E. R., 2016, MNRAS, 462, 3302

Eldridge J. J., et al., 2017, preprint (arXiv:1710.02154)

Falcke H., Rezzolla L., 2014, A&A, 562, A137

Farr W. M., Kremer K., Lyutikov M., Kalogera V., 2011, ApJ, 742, 81

Farr W. M., Stevenson S., Miller M. C., Mandel I., Farr B., Vecchio A., 2017, preprint (arXiv:1706.01385)

Ferdman R. D., 2017, in talk presented at IAU Symposium 337 ed., to appear in "Pulsar Astrophysics - The Next 50 Years". Cambridge University Press

Fermi-LAT Collaboration 2017, preprint (arXiv:1710.05450)

Flannery B. P., van den Heuvel E. P. J., 1975, A&A, 39, 61

Foley R. J., 2015, MNRAS, 452, 2463

Folkner W. M., Williams J. G., Boggs D. H., 2009, Interplanetary Network Progress Report, 178, C1

Fong W., Berger E., Margutti R., Zauderer B. A., 2015, ApJ, 815, 102

Fryer C. L., 2006, New A Rev., 50, 492

Fryer C. L., Woosley S. E., Hartmann D. H., 1999, ApJ, 526, 152

Gautschy A., 2013, preprint (arXiv:1303.6652)

Giacobbo N., Mapelli M., Spera M., 2017, preprint (arXiv:1711.03556)

Glebbeek E., Gaburov E., Portegies Zwart S., Pols O. R., 2013, MNRAS, 434, 3497

Gräfener G., Owocki S. P., Vink J. S., 2012, A&A, 538, A40

Grassitelli L., Fossati L., Langer N., Simón-Díaz S., Castro N., Sanyal D., 2016, A&A, 593, A14

Gvaramadze V. V., et al., 2017, Nature Astronomy, 1, 0116

Habets G. M. H. J., 1986, A&A, 165, 95

Hainich R., Pasemann D., Todt H., Shenar T., Sander A., Hamann W.-R., 2015, A&A, 581, A21

Han Z., Podsiadlowski P., Eggleton P. P., 1994, MNRAS, 270, 121

Han Z., Podsiadlowski P., Eggleton P. P., 1995, MNRAS, 272, 800

Heger A., Woosley S. E., 2002, ApJ, 567, 532

Heger A., Fryer C. L., Woosley S. E., Langer N., Hartmann D. H., 2003, ApJ, 591, 288

Heggie D. C., 1975, MNRAS, 173, 729

Hills J. G., 1983, ApJ, 267, 322

Hjellming M. S., Webbink R. F., 1987, ApJ, 318, 794

Hobbs G., Lorimer D. R., Lyne A. G., Kramer M., 2005, MNRAS, 360, 974

Hobbs G. B., Edwards R. T., Manchester R. N., 2006, MNRAS, 369, 655

Hobson M. P., Efstathiou G. P., Lasenby A. N., 2006, General Relativity. Cambridge University Press, doi:10.2277/0521829518

Holberg J. B., Bergeron P., 2006, AJ, 132, 1221

Hotan A. W., van Straten W., Manchester R. N., 2004, PASA, 21, 302

Hüdepohl L., Müller B., Janka H.-T., Marek A., Raffelt G. G., 2010, Physical Review Letters, 104, 251101

Hulse R. A., Taylor J. H., 1975, ApJ, 195, L51

Humphreys R. M., Davidson K., 1994, PASP, 106, 1025

Hurley J. R., Pols O. R., Tout C. A., 2000, MNRAS, 315, 543

Hurley J. R., Tout C. A., Pols O. R., 2002, MNRAS, 329, 897

Hut P., 1981, A&A, 99, 126

Iben Jr. I., Livio M., 1993, PASP, 105, 1373

Im M., et al., 2017, preprint (arXiv:1710.05861)

Ishii M., Ueno M., Kato M., 1999, PASJ, 51, 417

Istrate A. G., Marchant P., Tauris T. M., Langer N., Stancliffe R. J., Grassitelli L., 2016, A&A, 595, A35

Ivanova N., 2011, ApJ, 730, 76

Ivanova N., Chaichenets S., 2011, ApJ, 731, L36

Ivanova N., Belczynski K., Kalogera V., Rasio F. A., Taam R. E., 2003, ApJ, 592, 475

Ivanova N., et al., 2013, A&A Rev., 21, 59

Ivanova N., Justham S., Podsiadlowski P., 2015, MNRAS, 447, 2181

Izzard R. G., Tout C. A., Karakas A. I., Pols O. R., 2004, MNRAS, 350, 407

Izzard R. G., Dray L. M., Karakas A. I., Lugaro M., Tout C. A., 2006, A&A, 460, 565

Izzard R. G., Glebbeek E., Stancliffe R. J., Pols O. R., 2009, A&A, 508, 1359

Izzard R. G., Preece H., Jofre P., Halabi G. M., Masseron T., Tout C. A., 2017, preprint (arXiv:1709.05237)

Janka H.-T., 2012, Annual Review of Nuclear and Particle Science, 62, 407

Janka H.-T., 2013, MNRAS, 434, 1355

Janka H.-T., 2017, ApJ, 837, 84

Johnston S., Karastergiou A., 2017, MNRAS, 467, 3493

Johnston S., Manchester R. N., Lyne A. G., Bailes M., Kaspi V. M., Qiao G., D'Amico N., 1992, ApJ, 387, L37

Jones S., et al., 2013, ApJ, 772, 150

Just O., Bauswein A., Pulpillo R. A., Goriely S., Janka H.-T., 2015, MNRAS, 448, 541

Kaiser N., et al., 2010, in Ground-based and Airborne Telescopes III. p. 77330E, doi:10.1117/12.859188

Kalogera V., 1998, ApJ, 493, 368

Kasliwal M. M., et al., 2012, ApJ, 755, 161

Kaspi V. M., Johnston S., Bell J. F., Manchester R. N., Bailes M., Bessell M., Lyne A. G., D'Amico N., 1994, ApJ, 423, L43

Kawabata K. S., et al., 2010, Nature, 465, 326

Keane E., et al., 2015, Advancing Astrophysics with the Square Kilometre Array (AASKA14), p. 40

Keith M. J., et al., 2010, MNRAS, 409, 619

Kippenhahn R., Weigert A., 1990, Stellar Structure and Evolution. Springer, Berlin

Kitaura F. S., Janka H.-T., Hillebrandt W., 2006, A&A, 450, 345

Klessen R. S., Glover S. C. O., Clark P. C., 2012, MNRAS, 421, 3217

Kowalski P. M., Saumon D., 2006, ApJ, 651, L137

Kramer M., Xilouris K. M., Lorimer D. R., Doroshenko O., Jessner A., Wielebinski R., Wolszczan A., Camilo F., 1998, ApJ, 501, 270

Kramer M., et al., 2006, Science, 314, 97

Kroupa P., 2001, MNRAS, 322, 231

Kroupa P., 2008, in Aarseth S. J., Tout C. A., Mardling R. A., eds, Lecture Notes in Physics, Berlin Springer Verlag Vol. 760, The Cambridge N-Body Lectures. p. 181 (arXiv:0803.1833), doi:10.1007/978-1-4020-8431-7˙8

Kruckow M. U., Tauris T. M., Langer N., Szécsi D., Marchant P., Podsiadlowski P., 2016, A&A, 596, A58

Kruckow M. U., Tauris T. M., Langer N., Kramer M., Izzard R. G., 2018, MNRAS, submitted (arXiv:1801.05433)

Kuiper G. P., 1935, PASP, 47, 15

LIGO Scientific Collaboration 2017, LIGO, https://www.ligo.org/

Langer N., 2012, ARA&A, 50, 107

Langer N., Hamann W.-R., Lennon M., Najarro F., Pauldrach A. W. A., Puls J., 1994, A&A, 290

Lattimer J. M., Schramm D. N., 1974, ApJ, 192, L145

Lattimer J. M., Yahil A., 1989, ApJ, 340, 426

Lazarus P., et al., 2014, MNRAS, 437, 1485

Lazarus P., Karuppusamy R., Graikou E., Caballero R. N., Champion D. J., Lee K. J., Verbiest J. P. W., Kramer M., 2016a, MNRAS, 458, 868

Lazarus P., et al., 2016b, ApJ, 831, 150

Lewin W. H. G., van der Klis M., 2006, Compact stellar X-ray sources. Cambridge University Press

Liu K., Eatough R. P., Wex N., Kramer M., 2014, MNRAS, 445, 3115

Livio M., Soker N., 1988, ApJ, 329, 764

Lombardi Jr. J. C., Proulx Z. F., Dooley K. L., Theriault E. M., Ivanova N., Rasio F. A., 2006, ApJ, 640, 441

Lorimer D. R., Kramer M., 2004, Handbook of Pulsar Astronomy. Cambridge University Press

Lorimer D. R., et al., 2006a, MNRAS, 372, 777

Lorimer D. R., Stairs I. H., Freire P. C., et al. 2006b, ApJ, 640, 428

Loveridge A. J., van der Sluys M. V., Kalogera V., 2011, ApJ, 743, 49

Lyman J. D., Levan A. J., James P. A., Angus C. R., Church R. P., Davies M. B., Tanvir N. R., 2016, MNRAS, 458, 1768

Lyne A. G., McKenna J., 1989, Nature, 340, 367

Lyne A. G., et al., 2004, Science, 303, 1153

MacLeod M., Ramirez-Ruiz E., 2015a, ApJ, 798, L19

MacLeod M., Ramirez-Ruiz E., 2015b, ApJ, 803, 41

Magnier E. A., et al., 2016, preprint (`arXiv:1612.05242`)

Manchester R. N., Taylor J. H., 1977, Pulsars. W. H. Freeman, San Francisco

Manchester R. N., et al., 2000, in Kramer M., Wex N., Wielebinski R., eds, Astronomical Society of the Pacific Conference Series Vol. 202, IAU Colloq. 177: Pulsar Astronomy - 2000 and Beyond. p. 49 (`arXiv:astro-ph/9911319`)

Manchester R. N., Hobbs G. B., Teoh A., Hobbs M., 2005, AJ, 129, 1993

Mandel I., 2016, MNRAS, 456, 578

Mandel I., de Mink S. E., 2016a, MNRAS, 458, 2634

Mandel I., de Mink S. E., 2016b, MNRAS, 458, 2634

Mapelli M., Giacobbo N., Ripamonti E., Spera M., 2017, preprint (arXiv:1708.05722)

Marchant P., Langer N., Podsiadlowski P., Tauris T. M., Moriya T. J., 2016, A&A, 588, A50

Martinez J. G., et al., 2015, ApJ, 812, 143

Martinez J. G., et al., 2018, ApJL, accepted

McDonald I., Zijlstra A. A., Watson R. A., 2017, MNRAS, 471, 770

Mennekens N., Vanbeveren D., 2014, A&A, 564, A134

Metzger B. D., 2012, MNRAS, 419, 827

Metzger B. D., Berger E., 2012, ApJ, 746, 48

Meynet G., Maeder A., 2005, A&A, 429, 581

Miller G. E., Scalo J. M., 1979, ApJS, 41, 513

Moe M., Di Stefano R., 2017, ApJS, 230, 15

Moriya T. J., et al., 2017, MNRAS, 466, 2085

Nandez J. L. A., Ivanova N., Lombardi Jr. J. C., 2014, ApJ, 786, 39

Nandez J. L. A., Ivanova N., Lombardi J. C., 2015, MNRAS, 450, L39

National Aeronautics and Space Administration (NASA) 2017b, Fermi, https://fermi.gsfc.nasa.gov/

National Aeronautics and Space Administration (NASA) 2017a, James Webb Space Telescope, https://jwst.nasa.gov/

Nelemans G., Tout C. A., 2004, in Tovmassian G., Sion E., eds, Revista Mexicana de Astronomia y Astrofisica Conference Series Vol. 20, Revista Mexicana de Astronomia y Astrofisica Conference Series. pp 39–40

Nelemans G., Tauris T. M., van den Heuvel E. P. J., 1999, A&A, 352, L87

Nelemans G., Verbunt F., Yungelson L. R., Portegies Zwart S. F., 2000, A&A, 360, 1011

Nelson C. A., Eggleton P. P., 2001, ApJ, 552, 664

Ng C., et al., 2015, MNRAS, 450, 2922

Ng C., et al., 2018, MNRAS,

Nomoto K., 1987, ApJ, 322, 206

Ohlmann S. T., Röpke F. K., Pakmor R., Springel V., 2016, ApJ, 816, L9

Olive K. A., Particle Data Group 2014, Chinese Physics C, 38, 090001

Özel F., Freire P., 2016, ARA&A, 54, 401

Paczynski B., 1976, in Eggleton P., Mitton S., Whelan J., eds, IAU Symposium Vol. 73, Structure and Evolution of Close Binary Systems. p. 75

Pan Y.-C., et al., 2017, ApJ, 848, L30

Park D., Kim C., Lee H. M., Bae Y.-B., Belczynski K., 2017, MNRAS, 469, 4665

Passy J.-C., et al., 2012, ApJ, 744, 52

Pavlovskii K., Ivanova N., Belczynski K., Van K. X., 2017, MNRAS, 465, 2092

Paxton B., et al., 2013, preprint (`arXiv:1301.0319`)

Pejcha O., Thompson T. A., 2015, ApJ, 801, 90

Perets H. B., et al., 2010, Nature, 465, 322

Perets H. B., Gal-yam A., Crockett R. M., Anderson J. P., James P. A., Sullivan M., Neill J. D., Leonard D. C., 2011, ApJ, 728, L36

Peters P. C., 1964, Physical Review, 136, 1224

Peters P. C., Mathews J., 1963, Physical Review, 131, 435

Petrovic J., Langer N., van der Hucht K. A., 2005, A&A, 435, 1013

Petrovic J., Pols O., Langer N., 2006, A&A, 450, 219

Pilyugin L. S., Lara-López M. A., Grebel E. K., Kehrig C., Zinchenko I. A., López-Sánchez Á. R., Vílchez J. M., Mattsson L., 2013, MNRAS, 432, 1217

Podsiadlowski P., 2001, in Podsiadlowski P., Rappaport S., King A. R., D'Antona F., Burderi L., eds, Astronomical Society of the Pacific Conference Series Vol. 229, Evolution of Binary and Multiple Star Systems. p. 239

Podsiadlowski P., Joss P. C., Hsu J. J. L., 1992, ApJ, 391, 246

Podsiadlowski P., Rappaport S., Pfahl E. D., 2002, ApJ, 565, 1107

Podsiadlowski P., Rappaport S., Han Z., 2003, MNRAS, 341, 385

Podsiadlowski P., Langer N., Poelarends A. J. T., Rappaport S., Heger A., Pfahl E., 2004, ApJ, 612, 1044

Poelarends A. J. T., Wurtz S., Tarka J., Adams C., Hills S. T., 2017, preprint (arXiv:1710.11143)

Portegies Zwart S. F., McMillan S. L. W., 2000, ApJ, 528, L17

Portegies Zwart S. F., Yungelson L. R., 1999, MNRAS, 309, 26

Repetto S., Nelemans G., 2015, MNRAS, 453, 3341

Ribas I., Jordi C., Giménez Á., 2000, MNRAS, 318, L55

Ricker P. M., Taam R. E., 2012, ApJ, 746, 74

Roberts M. S. E., 2011, in Burgay M., D'Amico N., Esposito P., Pellizzoni A., Possenti A., eds, American Institute of Physics Conference Series Vol. 1357, American Institute of Physics Conference Series. pp 127–130 (arXiv:1103.0819), doi:10.1063/1.3615095

Rodriguez C. L., Chatterjee S., Rasio F. A., 2016a, Phys. Rev. D, 93, 084029

Rodriguez C. L., Haster C.-J., Chatterjee S., Kalogera V., Rasio F. A., 2016b, ApJ, 824, L8

Rosswog S., 2015, International Journal of Modern Physics D, 24, 30012

Russell H. N., 1914, Nature, 93, 252

SKA Organisation 2017, Square Kilometre Array, https://www.skatelescope.org/

Salpeter E. E., 1955, ApJ, 121, 161

Sana H., et al., 2012, Science, 337, 444

Sanyal D., Grassitelli L., Langer N., Bestenlehner J. M., 2015, A&A, 580, A20

Savonije G. J., 1978, A&A, 62, 317

Scalo J. M., 1986, Fund. Cosmic Phys., 11, 1

Schlafly E. F., Finkbeiner D. P., 2011, ApJ, 737, 103

Schlegel D. J., Finkbeiner D. P., Davis M., 1998, ApJ, 500, 525

Schneider F. R. N., Sana H., Evans C. J., et al. 2018, Science, in press

Schwab J., Podsiadlowski P., Rappaport S., 2010, ApJ, 719, 722

Shao Y., Li X.-D., 2016, ApJ, 833, 108

Shao L., et al., 2015, Advancing Astrophysics with the Square Kilometre Array (AASKA14), p. 42

Shapiro S. L., Teukolsky S. A., 1983, Black holes, white dwarfs, and neutron stars: The physics of compact objects. Wiley-Interscience, New York

Shklovskii I. S., 1970, Soviet Ast., 13, 562

Sigurdsson S., Hernquist L., 1993, Nature, 364, 423

Smartt S. J., Chen T.-W., Jerkstrand A., et al. 2017, preprint (arXiv:1710.05841)

Smith N., Vink J. S., de Koter A., 2004, ApJ, 615, 475

Soares-Santos M., Holz D. E., Annis J., et al. 2017, preprint (arXiv:1710.05459)

Soberman G. E., Phinney E. S., van den Heuvel E. P. J., 1997, A&A, 327, 620

Soker N., 2004, New A, 9, 399

Soker N., 2015, ApJ, 800, 114

Soker N., 2016, preprint (arXiv:1605.02672)

Space Telescope Science Institute (STScI) 2017, Hubble Space Telescope, http://hubblesite.org/

Spruit H., Phinney E. S., 1998, Nature, 393, 139

Spruit H. C., Taam R. E., 2001, ApJ, 548, 900

Srinivasan G., van den Heuvel E. P. J., 1982, A&A, 108, 143

Steiner A. W., Lattimer J. M., Brown E. F., 2013, ApJ, 765, L5

Stevenson S., Vigna-Gómez A., Mandel I., Barrett J. W., Neijssel C. J., Perkins D., de Mink S. E., 2017a, Nature Communications, 8, 14906

Stevenson S., Berry C. P. L., Mandel I., 2017b, MNRAS, 471, 2801

Stokes G. H., Taylor J. H., Dewey R. J., 1985, ApJ, 294, L21

Strolger L.-G., et al., 2004, ApJ, 613, 200

Sutantyo W., 1974, A&A, 35, 251

Suwa Y., Yoshida T., Shibata M., Umeda H., Takahashi K., 2015, MNRAS, 454, 3073

Szécsi D., Langer N., Yoon S.-C., Sanyal D., de Mink S., Evans C. J., Dermine T., 2015, A&A, 581, A15

Taam R. E., Ricker P. M., 2010, New A Rev., 54, 65

Taam R. E., Sandquist E. L., 2000, ARA&A, 38, 113

Tauris T. M., 2011, in Schmidtobreick L., Schreiber M. R., Tappert C., eds, Astronomical Society of the Pacific Conference Series Vol. 447, Evolution of Compact Binaries. p. 285 (arXiv:1106.0897)

Tauris T. M., Bailes M., 1996, A&A, 315, 432

Tauris T. M., Dewi J. D. M., 2001, A&A, 369, 170

Tauris T. M., Savonije G. J., 1999, A&A, 350, 928

Tauris T. M., Sennels T., 2000, A&A, 355, 236

Tauris T. M., Takens R. J., 1998, A&A, 330, 1047

Tauris T. M., van den Heuvel E. P. J., 2006, in Lewin W. H. G., van der Klis M., eds, , Compact stellar X-ray sources. Cambridge University Press, Chapt. 16, pp 623–665

Tauris T. M., Fender R. P., van den Heuvel E. P. J., Johnston H. M., Wu K., 1999, MNRAS, 310, 1165

Tauris T. M., van den Heuvel E. P. J., Savonije G. J., 2000, ApJ, 530, L93

Tauris T. M., Langer N., Kramer M., 2012, MNRAS, 425, 1601

Tauris T. M., Langer N., Moriya T. J., Podsiadlowski P., Yoon S.-C., Blinnikov S. I., 2013, ApJ, 778, L23

Tauris T. M., Langer N., Podsiadlowski P., 2015, MNRAS, 451, 2123

Tauris T. M., et al., 2017, ApJ, 846, 170

Taylor J. H., 1992, Royal Society of London Philosophical Transactions Series A, 341, 117

The LIGO Scientific Collaboration et al., 2017, preprint (arXiv:1711.05578)

The Virgo Collaboration 2017, The Virgo experiment at the European Gravitational Observatory, http://www.virgo-gw.eu/

Thorsett S. E., Chakrabarty D., 1999, ApJ, 512, 288

Timmes F. X., Woosley S. E., Weaver T. A., 1996, ApJ, 457, 834

Tremblay P.-E., Bergeron P., Gianninas A., 2011, ApJ, 730, 128

Ugliano M., Janka H.-T., Marek A., Arcones A., 2012, ApJ, 757, 69

Ulmer A., Fitzpatrick E. L., 1998, ApJ, 504, 200

Vietri M., Stella L., 1998, ApJ, 507, L45

Vink J. S., de Koter A., Lamers H. J. G. L. M., 2001, A&A, 369, 574

Voss R., Tauris T. M., 2003, MNRAS, 342, 1169

Wanderman D., Piran T., 2015, MNRAS, 448, 3026

Wang C., Jia K., Li X.-D., 2016, ArXiv:1605.03668

Wang J. B., et al., 2017, MNRAS, 469, 425

Webbink R. F., 1984, ApJ, 277, 355

Weisberg J. M., Taylor J. H., 1981, General Relativity and Gravitation, 13, 1

Wellstein S., Langer N., 1999, A&A, 350, 148

Weltevrede P., Johnston S., 2008, MNRAS, 391, 1210

Wex N., 2014, preprint (arXiv:1402.5594)

Wex N., Kopeikin S. M., 1999, ApJ, 514, 388

Wheeler J. C., McKee C. F., Lecar M., 1974, ApJ, 192, L71

Woosley S. E., 2017, ApJ, 836, 244

Woosley S. E., Heger A., 2015, ApJ, 810, 34

Woosley S. E., Heger A., Weaver T. A., 2002, Reviews of Modern Physics, 74, 1015

Yagi K., Stein L. C., 2016, Classical and Quantum Gravity, 33, 054001

Yao J. M., Manchester R. N., Wang N., 2017, ApJ, 835, 29

Yoon S., Woosley S. E., Langer N., 2010, ApJ, 725, 940

Zahn J.-P., 1975, A&A, 41, 329

Zahn J.-P., 1977, A&A, 57, 383

Zahn J. P., 1984, in Maeder A., Renzini A., eds, IAU Symposium Vol. 105, Observational Tests of the Stellar Evolution Theory. p. 379

Zapartas E., et al., 2017, A&A, 601, A29

Zhu X.-J., Thrane E., Osłowski S., Levin Y., Lasky P. D., 2017, preprint (arXiv:1711.09226)

Zorotovic M., Schreiber M. R., Gänsicke B. T., Nebot Gómez-Morán A., 2010, A&A, 520, A86

de Kool M., 1990, ApJ, 358, 189

de Marco O., Passy J., Moe M., Herwig F., Mac Low M., Paxton B., 2011, MNRAS, p. 28

de Mink S. E., Belczynski K., 2015, ApJ, 814, 58

de Mink S. E., Mandel I., 2016, preprint (arXiv:1603.02291)

de Mink S. E., Cottaar M., Pols O. R., 2008, in O'Shea B. W., Heger A., eds, American Institute of Physics Conference Series Vol. 990, First Stars III. pp 217–219 (arXiv:0710.2193), doi:10.1063/1.2905545

de Mink S. E., Cantiello M., Langer N., Pols O. R., Brott I., Yoon S.-C., 2009, A&A, 497, 243

van Kerkwijk M. H., Kulkarni S. R., 1999, ApJ, 516, L25

van Leeuwen J., et al., 2015, ApJ, 798, 118

van den Heuvel E. P. J., 1994, in Shore S. N., Livio M., van den Heuvel E. P. J., Nussbaumer H., Orr A., eds, Saas-Fee Advanced Course 22: Interacting Binaries. pp 263–474

van den Heuvel E. P. J., 2004, in Schoenfelder V., Lichti G., Winkler C., eds, ESA Special Publication Vol. 552, 5th INTEGRAL Workshop on the INTEGRAL Universe. p. 185 (arXiv:astro-ph/0407451)

List of publications

C. Ng, **M. U. Kruckow**, T. M. Tauris, A. G. Lyne, P. C. C. Freire, A. Ridolfi, I. Caiazzo, J. Heyl, M. Kramer, A. D. Cameron, D. J. Champion, and B. Stappers. PSR J1755-2550: A young radio pulsar with a massive, compact companion. MNRAS*, submitted*, February 2018. doi: 10.1093/mnras/sty482.

M. U. Kruckow, T. M. Tauris, N. Langer, M. Kramer, and R. G. Izzard. Progenitors of gravitational wave mergers: Binary evolution with the stellar grid based code ComBinE. MNRAS*, submitted (arXiv:1801.05433)*, January 2018.

T. M. Tauris, M. Kramer, P. C. C. Freire, N. Wex, H.-T. Janka, N. Langer, P. Podsiadlowski, E. Bozzo, S. Chaty, **M. U. Kruckow**, E. P. J. van den Heuvel, J. Antoniadis, R. P. Breton, and D. J. Champion. Formation of Double Neutron Star Systems. ApJ, 846:170, September 2017. doi: 10.3847/1538-4357/aa7e89.

M. U. Kruckow, T. M. Tauris, N. Langer, D. Szécsi, P. Marchant, and P. Podsiadlowski. Common-envelope ejection in massive binary stars. Implications for the progenitors of GW150914 and GW151226. A&A, 596:A58, November 2016. doi: 10.1051/0004-6361/201629420.

H. K. Dreiner, M. Becker, M. Borzyszkowski, M. Braun, A. Faßbender, J. Hampel, M. Hansen, D. Hebecker, T. Heepenstrick, S. Heinz, K. Hortmanns, C. Jost, M. Kortmann, **M. U. Kruckow**, T. Leuteritz, C. Lütz, P. Mahlberg, J. Müllers, T. Opferkuch, E. Paul, P. Pauli, M. Rossbach, S. Schaepe, T. Schiffer, J. F. Schmidt, J. Schüller-Ruhl, C. Schürmann, L. Ubaldi, and S. Wagner-Carena. "What's (the) Matter?", A Show on Elementary Particle Physics with 28 Demonstration Experiments. *ArXiv e-prints (arXiv:1607.07478)*, July 2016.

Z.-W. Liu, T. M. Tauris, F. K. Röpke, T. J. Moriya, **M. Kruckow**, R. J. Stancliffe, and R. G. Izzard. The interaction of core-collapse supernova ejecta with a companion star. A&A, 584:A11, December 2015. doi: 10.1051/0004-6361/201526757.